TSME ICOME 2020

Challenging Trends in Mechanical Engineering

Ubon Ratchathani University

The 11th TSME International Conference on Mechanical Engineering

CONFERENCE PROCEEDINGS

1st – 4th December 2020

Sunee Grand Hotel & Convention Center

Ubon Ratchathani, Thailand

Proceedings of

The 11th TSME International Conference on Mechanical Engineering (ICoME 2020)

1st – 4th December 2020
Sunee Grand Hotel & Convention Center,
Ubon Ratchathani, Thailand

Hosted by: Department of Mechanical Engineering,
Faculty of Engineering,
Ubon Ratchathani University
Cooperated by: Thai Society of Mechanical Engineering (TSME)

Welcome Speech

The 11th TSME
International Conference on Mechanical Engineering
(TSME - ICoME 2020)

Sunee Grand Hotel & Convention Center, Ubon Ratchathani

Dear our honored guests,

First of all, please, may I warmly welcome you to the the 11th International Conference on Mechanical Engineering (ICoME 2020). It is my great pleasure to be here for the opening session. As far as I knew, this conference is one of the greatest international conference in engineering and on behalf of Ubon Ratchathani University, it is our greatest honor to be a host.

Mechanical engineering is one of the important fields necessarily to lead this world to better future. As we knew well that the world these days, especially Thailand, are facing lot of challenges such as shortage of energy and global warming, rising of aging society, shortage of human power and demanding of robot and AI technologies, safer and more efficient transportation in Covid 19 crisis ect. These challenges need knowhow, technique, technology and innovations from mechanical engineers. And I believe this conference will play a main roll to deliver solutions for those.

On behalf of UBU which our vision is to be "A Leading University in ASEAN Focusing on Transforming Life Quality and Innovations" together with our staffs in Mechanical Engineering Department, we are ready to work side by side with mechanical engineers around Thailand and around the world to accomplished our mission to lift up life quality of people.

Lastly, I wish to thank all staffs of the department of Mechanical Engineering, UBU, to host this conference. I also wish to pay my gratefulness to the Thai Society of Mechanical Engineers (TSME) for providing a chance for UBU to serve as a host. I hope all delegates will enjoy and happy while attending every session of this conference. I also hope this conference will be fruitfully perfectly and smoothly completed.

Thank you.

Assistant Professor Dr.Chutinunt Prasitpuripreecha
Rector of Ubon Ratchathani University

Welcome Speech

The 11^{th} TSME
International Conference on Mechanical Engineering
(TSME - ICoME 2020)

Sunee Grand Hotel & Convention Center, Ubon Ratchathani

International Conference on Mechanical Engineering is an annual conference which is held by the Thai Society of Mechanical Engineers (TSME). The conference is aimed bring together leading scientists, researchers and research scholars to exchange and share their experiences and research results in the field of Mechanical Engineering. The conference has been carrying out for more than 10 years continuously.

This year conference is the 11^{th} and hosted by Department of Mechanical Engineering, UBU. The theme of this year conference is “Challenging Trends in Mechanical Engineering” and is held for 4 days during 1^{st} – 4^{th} December 2020 at Sunee Grad Hotel and Convention Center, Ubon Ratchathani, Thailand. This year, there are about 132 papers submitted for presentation and there are 180 delegates from many countries join the conference including on line and in person.

On behalf of organizer of the conference we wish to thank partners who has been supporting this conference, which are the Research and Service on Energy Center (RSEC), Total Engineering (Thailand) Company Limited, Kinetics Company Limited, FT Energy Company Limited, the Japanese Society of Mechanical Engineers (JSME) and the Korean Society of Mechanical Engineers (KSME).

Assistant Professor Dr.Prachasanti Thaiyasuit
Head of Mechanical Engineering Department, Ubon Ratchathani University

Welcome Speech

The 11th TSME International Conference on Mechanical Engineering (TSME - ICoME 2020)

Sunee Grand Hotel & Convention Center, Ubon Ratchathani

Lady and Gentleman, on behalf of TSME, I would like to welcome all of you to this conference: the 11th Thai Society of Mechanical Engineers, International Conference on Mechanical Engineering, TSME-ICoME 2020 at the Sunee Grand Hotel & Convention Center Ubon Ratchathani, Thailand.

I especially want to welcome our colleagues, our honorary guests and our partners: The Japan Society of Mechanical Engineers (JSME), Korean Society of Mechanical Engineers (KSME) and all participants coming from outside Thailand.

The TSME-ICoME conference bring together people from all different geographical areas who share a common discipline or field and they are a great way to meet new people in your fields. In conclusion, the Mechanical Engineering research pays an important role to enhance the growth of country especially in the academic and industry sectors.

In this regard, I would like to express my congratulation and appreciation to the Department of Mechanical Engineering, Ubon Ratchathani University for the dedication to organize the TSME-ICoME 2020 where held at the Sunee Grand Hotel & Convention Center Ubon Ratchathani, Thailand during 1st – 4th December 2020. Thank you for your supporting team and all staff for hard working to make this conference possible. This is a very special year in which 2 options are organized, both in the on-site and online presentations.

I hope the conference will be success and belief that this collaboration will be further strengthened not only the network of mechanical engineers in Thailand but also the network of mechanical engineers in the region.

Thank you.

P. Rattanadecho

Professor Dr.Phadungsak Rattanadecho
President of Thai Society of Mechanical Engineers (TSME)

About the Conference

The 11th TSME
International Conference on Mechanical Engineering
(TSME - ICoME 2020)
Sunee Grand Hotel & Convention Center, Ubon Ratchathani

Since 1987, the Thai Society of Mechanical Engineers (TSME) has been holding national conferences in Mechanical Engineering yearly. These conferences are called Mechanical Engineering Network of Thailand (ME-NETT). The objectives of the conferences are to encourage students, researchers, and interested persons to present their works, to create researching networks, to publish the research works for industry sectors, to find the needs of public and private organizations, to fulfill these demands to enhance the growth of country, and to be a hub in the field of Mechanical Engineering for anyone with an interest. In 2010, with collaboration from the American Society of Mechanical Engineers (ASME), the Japan Society of Mechanical Engineers (JSME), and the United Kingdom's Institute of Mechanical Engineers (IMechE), TSME started to hold yearly international conferences under the name of the International Conference on Mechanical Engineering (ICoME)

It is our great pleasure to invite you to the ICoME 2020 which will be held in the nice city of Ubon Ratchathani (Thailand) from 1st - 4th December, 2020. The conference is organized by the Thai Society of Mechanical Engineers (TSME) that aims to bring together leading scientists, researchers and research scholars to exchange and share their experiences and research results in the field of Mechanical Engineering. You will walk away with new perspectives, concrete ways to shape a better future and a brand-new group of collaborators.

Members of Thai Society of Mechanical Engineering (TSME)

The 11th TSME International Conference on Mechanical Engineering (TSME - ICoME 2020)

Sunee Grand Hotel & Convention Center, Ubon Ratchathani

1. Burapha University
2. Chiang Mai University
3. Chulachomklao Royal Military Academy
4. Chulalongkorn University
5. Kasetsart University
6. Kasetsart University Sriracha Campus
7. Khon Kaen University
8. King Mongkut's Institute of Technology Ladkrabang
9. King Mongkut's University of Technology North Bangkok
10. King Mongkut's University of Technology Thonburi
11. Mahasarakham University
12. Mahidol University
13. Mahonakorn University of Technology
14. Naresuan University
15. Navaminda Kasatriyadhiraj Royal Air Force Academy
16. Pathumwan Institute of Technology
17. Phathumthani University
18. Prince of Songkla University
19. Rajamangala University of Technology Lanna
20. Rajamangala University of Technology lsan
21. Rajamangala University of Technology Ratanakosin
22. Rajamangala University of Technology Srivijaya
23. Rajamangala University of Technology Thanyaburi
24. Rangsit University
25. Royal Thai Naval Academy
26. Saint John's University
27. Siam University
28. Silpakorn University
29. Srinakharinwirot University
30. Sripatum University
31. Suranaree University of Technology
32. Thai-Nichi Institute of Technology
33. Thammasat University
34. Ubon Ratchathani University

Conference Committee

The 11th TSME
International Conference on Mechanical Engineering
(TSME - ICoME 2020)
Sunee Grand Hotel & Convention Center, Ubon Ratchathani

International Advisory Board

1.	Prof.Dr.Phadungsak Rattanadecho	President of Thai Society of Mechanical Engineers (TSME)
2.	Prof.Dr.Ashwani K. Gupta	University of Maryland, USA
3.	Prof.Dr.Ning Zhu Shizuoka	Institute of Science and Technology, JAPAN
4.	Prof.Dr.Katsunori Hanamura	Tokyo Institute of Technology, JAPAN
5.	Prof.Dr.Jens Nørkær Sørensen	Technical University of Denmark, DENMARK
6.	Prof.Dr.Ashim K. Datta	Cornell University, USA
7.	Prof.Dr.Kambiz Vafai	University of California, USA
8.	Prof.Dr.Naoki Maruyama	Mie University, JAPAN
9.	Assoc.Prof.Dr.Seokwoo Jeon	KAIST, REPUBLIC OF KOREA
10.	Prof.Dr.Elmi Abu Bakar	University Sains Malaysia, MALAYSIA
11.	Prof.Dr.Pham Tuan Anh	Ho Chi Minh City University of Technology, VIETNAM
12.	Assoc.Prof.Dr.lman K.	Reksowardojo Institute of Technology, Bandung, INDONESIA
13.	Prof.Dr.Le Anh Tuan	Hanoi University of Science and Technology, VIETNAM
14.	Prof.Dr.Ocktaeck Lim	University of Ulsan, REPUBLIC OF KOREA
15.	Prof.Dr.Huynh Thanh Cong	Ho Chi Minh City University of Technology, VIETNAM
16.	Prof.Dr.Hendri Syamsudin	Institut Teknologi Bandung, INDONESIA
17.	Prof.Dr.Pham Huu Tuyen	Hanoi University of Science and Technology, VIETNAM
18.	Prof.Dr.Hironori Saitoh	Sojo University, JAPAN
19.	Prof.Dr.Jau-Huai Lu	National Chung Hsing University, Republic of China
20.	Dr.Norazila Binti Othman	Mechanical Engineering, University Teknologi Malaysia

Local Organizing Committee

The 11th TSME
International Conference on Mechanical Engineering
(TSME - ICoME 2020)
Sunee Grand Hotel & Convention Center, Ubon Ratchathani

Ubon Ratchathani University

1.	Asst.Prof.Dr.Mongkol Pusayatanont	Conference Advisor
2.	Asst.Prof.Dr.Prachasanti Thaiyasuit	Conference Chair
3.	Assoc.Prof.Dr.Thanarath Sriveerakul	Associate Conference Chair
4.	Asst.Prof. Dr.-Ing.Nantawatana Weerayuth	Subcommittee Chair of Venue and Formalities
5.	Asst.Prof.Dr.Ratchada Sopakayang	Subcommittee Chair of Academic Affairs
6.	Asst.Prof.Dr.Wirapan Seehanam	Subcommittee Chair of Public Relations
7.	Assoc.Prof.Dr.Kulachate Pianthong	Subcommittee Chair of Funding and Special Events
8.	Assoc.Prof.Dr.Umphisak Teeboonma	Subcommittee Chair of Finance and Registration
9.	Assoc.Prof.Dr.Chawalit Thinvovgpituk	Committee
10.	Assoc.Prof.Dr.Anirut Matthujak	Committee
11.	Assoc.Prof.Dr.Lt.JG.Somya Poonaya	Committee
12.	Asst.Prof.Dr.Adun Janyalertadun	Committee
13.	Asst.Prof.Dr.Apinunt Namkhat	Committee
14.	Asst.Prof.Rattapong Patikanung	Committee
15.	Dr.Komsan Rattanakijsuntorn	Committee
16.	Dr.Patinya Samanuhut	Committee
17.	Chakrit Pongarm	Committee
18.	Songsupa Pumchumpol	Committee
19.	Bongkot Juntamas	Committee
20.	Krittaya Chaiyot	Committee
21.	Nitikorn Promduang	Committee
22.	Paryat Samanmit	Committee
23.	Pakawat Naosopa	Committee
24.	Samak Intha	Committee
25.	Suk Dampatik	Committee
26.	Watcharaporn Chantharakan	Committee
27.	Jirapreeya Ok-Oon	Committee
28.	Narongrit Majan	Committee

Local Scientific Committee

The 11th TSME
International Conference on Mechanical Engineering
(TSME -ICoME 2020)

Sunee Grand Hotel & Convention Center, Ubon Ratchathani

1. Prof.Dr.Sumrerng Jugjai	King Mongkut's University of Technology Thonburi Alternative Energy and Combustion (AEC)
2. A.M.Prof.Dr.Noppol Hanklar	Navaminda Kasatriyadhiraj, Royal Thai Air Force Academy Automotive, Aerospace and Marine Engineering (AME)
3. Assoc.Prof.Dr.Vitoon Uthaisangsuk	King Mongkut's University of Technology Thonburi Applied Mechanics, Materials and Manufacturing (AMM)
4. Assoc.Prof.Dr.Jackrit Suthakorn	Mahidol University Biomechanics and Bioengineering (BME)
5. Prof.Dr.Phadungsak Rattanadecho	Thammasat University Computation and Simulation Techniques (CST)
6. Prof.Dr.Suwat Kuntanapreeda	King Mongkut's University of Technology North Bangkok Dynamic Systems, Robotics and Controls (DRC)
7. Assoc.Prof.Dr.Ratchaphon Suntivarakorn	Khon Kaen University Engineering Education (EDU)
8. Assoc.Prof.Dr.Jaruwat Charoensuk	King Mongkut's Institute of Technology Ladkrabang Energy Technology and Management (ETM)
9. Prof.Dr.Somchai Wongwises	King Mongkut's University of Technology Thonburi Thermal System and Fluid Mechanic (TSF)

Thai Society of Mechanical Engineers (TSME)
Organizing Committee

The 11th TSME
International Conference on Mechanical Engineering
(TSME - ICoME 2020)
Sunee Grand Hotel & Convention Center, Ubon Ratchathani

1.	Assoc.Prof.Dr.Worawut Wisutmethangoon	Senior Advisor
2.	Assoc.Prof.Dr.Withaya Yongchareon	Senior Advisor
3.	Prof.Dr.Sumrerng Jugjai	Senior Advisor
4.	Asst.Prof.Dr.Chinda Charoenphonphanich	Senior Advisor
5.	Manit Koothanapath	Adviser
6.	Yuthana Charoenwong	Adviser
7.	Dr.Payung Sukdasawit	Adviser
8.	Apichit Lumlertpongpana	Adviser
9.	Assoc.Prof.Dr.Yossapong Laoonual	Adviser
10.	Assoc.Prof.Dr.Pongpan Kaewtatip	Adviser
11.	Assoc.Prof.Dr.Perapong Tekasakul	Adviser
12.	Jiraboon Vityakraisign	Adviser
13.	Maj.Gen.Chukiat Chuaypetch	Adviser
14.	Tinakon Pongluxna	Adviser
15.	Prof.Dr.Kulachate Pianthong	Vice President
16.	Assoc.Prof.Dr.Jaruwat Charoensuk	Vice President
17.	Asst.Prof.Dr.Pornthip Keangin	Secretary
18.	Asst.Prof.Dr.Warakom Nerdnoi	Treasurer
19.	Dr.Nattadon Pannucharoenwong	Receptionist
20.	Dr.Nopparat Khamporn	Registrar
21.	Dr.Montana Rungsiyopas	Public Relations
22.	A.M.Prof.Dr.Noppol Hanklar	Committee
23.	Assoc.Prof.Dr.Smith Eiamsa-ard	Committee
24.	Assoc.Prof.Dr.Preechar Karin	Committee
25.	Prof.Dr.Tanakorn Wongwuttanasatian	Committee
26.	Dr.Sopida Sungsoontorn	Committee
27.	Assoc.Prof.Dr.Kanit Wattanavichien	Committee
28.	Assoc.Prof.Dr.Amornrat Kaewpradap	Committee
29.	Assoc.Prof.Dr.Anchasa Pramuanjaroenkij	Committee
30.	Dr.Samroeng Netpu	Committee
31.	Dr.Taperit Thongshoob	Committee
32.	Asst.Prof.Dr.Wirachai Roynarin	Committee
33.	Asst.Prof.Dr.Nattawoot Depaiwa	Committee

List of Reviewers

The 11th TSME International Conference on Mechanical Engineering (TSME - ICoME 2020)

Sunee Grand Hotel & Convention Center, Ubon Ratchathani

1.	Prof.Dr.Ashwani K.Gupta	University of Maryland
2.	Prof.Dr.Sakamon Devahastin	King Mongkut's University of Technology Thonburi
3.	Prof.Dr.Somchai Hanklar	Navaminda Kasatriyadhuraj Royal Air Force Academy
4.	Prof.Dr.Sujin Bureerat	Khon Kaen University
5.	Prof.Dr.Suwat Kuntanapreeda	King Mongkut's University of Technology North Bangkok
6.	Prof.Dr.Thananchai Leephakpreeda	Thammasat University
7.	Assoc.Prof.Dr.Amornrat Kaewpradap	King Mongkut's University of Technology Thonburi
8.	Assoc.Prof.Dr.Anirut Matujak	Ubon Ratchathani University
9.	Assoc.Prof.Dr.Chakrit Suvanjumrat	Mahidol University
10.	Assoc.Prof.Dr.Chonlathis Eiamworawutthikul	Sripatum University
11.	Assoc.Prof.Dr.Ekachai Juntasaro	King Mongkut's University of Technology North Bangkok
12.	Assoc.Prof.Dr.Jarruwat Charoensuk	King Mongkut Institute of Technology Ladkrabang
13.	Assoc.Prof.Dr.Kampanart Theinnoi	King Mongkut's University of Technology North Bangkok
14.	Assoc.Prof.Dr.Kulachate Pianthong	Ubon Ratchathani University
15.	Assoc.Prof.Dr.Naoki Maruyama	Mie University
16.	Assoc.Prof.Dr.Nopdanai Ajavakom	Chulalongkorn University
17.	Assoc.Prof.Dr.Pairod Singhatanadgid	Chulalongkorn University
18.	Assoc.Prof.Dr.Petch Jearanaisilawong	King Mongkut's University of Technology North Bangkok
19.	Assoc.Prof.Dr.Prasan Sathitruangsak	Mahanakorn University of Technology
20.	Assoc.Prof.Dr.Preechar Karin	King Mongkut’s Institute of Technology Ladkrabang
21.	Assoc.Prof.Dr.Smith Eiamsa-ard	Mahanakorn University of Technology
22.	Assoc.Prof.Dr.Somchai Chanchaona	King Mongkut's University of Technology Thonburi
23.	Assoc.Prof.Dr.Somya Poonaya	Ubon Ratchathani University
24.	Assoc.Prof.Dr.Thanarath Sriveerakul	Ubon Ratchathani University
25.	Assoc.Prof.Dr.Wanchai Asvapoositkul	King Mongkut's University of Technology Thonburi

List of Reviewers

The 11th TSME International Conference on Mechanical Engineering (TSME - ICoME 2020)

Sunee Grand Hotel & Convention Center, Ubon Ratchathani

26.	Assoc.Prof.Dr.Wiroj Limtrakarn	Thammasat Univeristy
27.	Asst.Prof.Dr.Apinunt Namkhat	Ubon Ratchathani University
28.	Asst.Prof.Dr.Arrsara Chaikittiratana	King Mongkut's University of Technology North Bangkok
29.	Asst.Prof.Dr.Boonrit Prasartkaew	Rajamangaly University of Technology Thanyaburi
30.	Asst.Prof.Dr.Bundit Krittacom	Rajamangala University of Technology Isan
31.	Asst.Prof.Dr.Hataitep Wongsuwarn	Kasetsart University Kampangsean
32.	Asst.Prof.Dr.Kittisak Khuwaranyu	Silpakorn University
33.	Asst.Prof.Dr.Kunnayut Eiamsa-ard	Kasetsart University
34.	Asst.Prof.Dr.Mana Saedan	Chiangmai University
35.	Asst.Prof.Dr.-Ing.Nantawatana Weerayuth	Ubon Ratchathani University
36.	Asst.Prof.Dr.Pakpong Jantapremjit	Burapha University
37.	Asst.Prof.Dr.Panya Aroonjarattham	Mahidol University
38.	Asst.Prof.Dr.Phacharaporn Bunyawanichakul	Kasetsart University
39.	Asst.Prof.Dr.Phongsak Phakamach	The Army Research and Development Office
40.	Asst.Prof.Dr.Pornthip Keangin	Mahidol University
41.	Asst.Prof.Dr.Prachasanti Thaiyasuit	Ubon Ratchathani University
42.	Asst.Prof.Dr.Preecha Khantikomol	Rajamangala University of Technology Isan
43.	Asst.Prof.Dr.Pumyos Vallikul	King Mongkut's University of Technology North Bangkok
44.	Asst.Prof.Dr.Ratthasak Prommas	Rajamangla University of Technolygy Rattanakosin
45.	Asst.Prof.Dr.Sathaporn Chuepeng	Kasetsart University
46.	Asst.Prof.Dr.Suwimon Saneewong Na Ayuttaya	Chulachomklao Royal Military Academy
47.	Asst.Prof.Dr.Thanapat Wanichanon	Mahidol University
48.	Asst.Prof.Dr.Thibordin Sangsawang	Silpakorn University
49.	Asst.Prof.Dr.Usa Makmool	King Mongkut's University of Technology Thonburi
50.	Asst.Prof.Dr.Wirapan Seehanam	Ubon Ratchathani University

List of Reviewers

The 11th TSME International Conference on Mechanical Engineering (TSME - ICoME 2020)

Sunee Grand Hotel & Convention Center, Ubon Ratchathani

51.	Asst.Prof.Mr.Suttipong Paksuttipol	Royal Thai Naval Academy
52.	Dr.Attaporn Wisessint	Kasetsart University
53.	Dr.Chalothorn Thumthae	Suranaree University of Tachnology
54.	Dr.Denchai Woradechjumroen	Sripatum University
55.	Dr.Kitchanon Ruangjirakit	King Mongkut's University of Technology Thonburi
56.	Dr.Komsan Rattanakijsuntorn	Ubon Ratchathani University
57.	Dr.Manop Masomtob	National Metal and Materials Technology Center
58.	Dr.Mason Thammawichai	Royal Thai Air Force Academy
59.	Dr.Maturose Suchatawat	King Mongkut’s Institute of Technology Ladkrabang
60.	Dr.Nattadon Pannucharoenwong	Thammasat University
61.	Dr.Nattawut Suwannapum	Rajamangala University of Technology Rattanakosin
62.	Dr.Patinya Samanuhut	Ubon Ratchathani University
63.	Dr.Pornporm Boonporm	Suranaree University of Tachnology
64.	Dr.Prakorb Chartpuk	Rajamangala University of Technology Phra Nakhon
65.	Dr.Rattana Borrisutthekul	Suranaree University of Technology
66.	Dr.Sarawuth Srinakaew	Royal Thai Naval Academy
67.	Dr.Snunkhaem Echaroj	Thammasat University
68.	Dr.Sopida Sungsoontorn	Rajamangala University of Technology Rattanakosin
69.	Dr.Teerapot Wessapan	Rajamangala University of Technology Thanyaburi
70.	Dr.Waraporn Klinbun	PANYAPIWAT Institute of Management
71.	Mr.Aphilak Lonklang	Suranaree University of Tachnology
72.	Mr.Kajorndej Phimphilai	Chiang Mai University
73.	Mr.Krittaya Chaiyot	Ubon Ratchathani University
74.	Mr.Rittipol Chantarat	Rajamangala University of Technology Rattanakosin
75.	Ms.Prapaporn Prasertpong	Rajamangala University of Technology Thanyaburi

Keynote Speaker

The 11th TSME
International Conference on Mechanical Engineering
(TSME - ICoME 2020)
Sunee Grand Hotel & Convention Center, Ubon Ratchathani

Mr.Yukio Yoshida
Vice President of Technical External Affairs Division
Toyota Daihatsu Engineering and Manufacturing Limited company

2017 ~ Present : Vice president of Technical External Affairs Division, Toyota Daihatsu Engineering and Manufacturing Limited company

2013 ~ 2016 : Project General Manager, Powertrain Planning Department, Powertrain Unit Management Division, Toyota Motor Corporation, Japan, Strategy Making and Product Planning of Powertrain

2010 ~ 2012 : Group Manager, Strategy Management Department, Product Development Management Division, Toyota Motor Corporation, Japan, Powertrain Strategy Making

2005 ~ 2009 : Vice President Toyota Motor Asia Pacific Engineering and Manufacturing, Thailand, Powertrain Engineering Division, Technical Research Division and Vehicle Evaluation Division.

1983 ~ 2004 : Engineer, Engine Development Division, Technical Center Toyota Motor Corporation, Japan, C-Type Diesel Engine Development, L-Type & KD-Type Diesel Engine Development and Localization for Thailand Product.

Mr.Yukio Yoshida
Vice President of Technical External Affairs Division
Toyota Daihatsu Engineering and Manufacturing Limited company

Keynote Speaker

The 11th TSME International Conference on Mechanical Engineering (TSME - ICoME 2020)

Sunee Grand Hotel & Convention Center, Ubon Ratchathani

Asst.Prof.Dr.Wirachai Roynarin

Department of Mechanical Engineering, Rajamangala University of Technology Thanyaburi

Education

1995	: B. Eng. Mechanical Engineering Rajamangala University of Technology Thanyaburi, Thailand
1999	: MSc. Mechanical Engineering Northumbria University, Newcastle, England
2004	: Ph.D. Mechanical Engineering Northumbria University, Newcastle, England

Fields of Interest : Renewable Energy, Wind Water and Wave Energy

Full Biography Such as Experiences

1998 – Present	: Lecturer of Department of Mechanical Engineering, Faculty of Engineering Rajamangala University of Technology Thanyaburi (RMUTT), Ministry of Education, Thailand.
1999 – 2000	: Vice- Head of Mechanical Engineering Department, Faculty of Engineering, RMUTT
2006 – Present	: Director of Research Centre of Renewable Energy Division, RMUTT
2010 – Present	: Assistance of Dean of Engineering Faculty, RMUTT
2012- Present	: President of Thailand Renewable Energy for Community Associations (TRECA)
2016- Present	: Head of Research and Service Energy Center Faculty of Engineering, RMUTT

Asst.Prof.Dr.Wirachai Roynarin
Department of Mechanical Engineering,
Rajamangala University of Technology Thanyaburi

TSME Memory Awards

The 11th TSME International Conference on Mechanical Engineering (TSME - ICoME 2020)

Sunee Grand Hotel & Convention Center, Ubon Ratchathani

Prof.Dr.Somchai Wongwises

Institutions

Department of Mechanical Engineering, Faculty of Engineering, King Mongkut's University of Technology Thonburi

Bio

Prof.Dr.Somchai is dedicated to his teaching, service, and research work to serve the society. He is the recipient of several awards such as Outstanding researcher award from the Thailand Research Fund (TRF) (1996-1997), TRF Senior Research Scholar (2003 – 2009), Outstanding Researcher Award in Engineering and Industrial Research from the National Research Council (2004), Outstanding Scientist Award from the Foundation for the Promotion of Science and Technology under the Patronage of His Majesty the King (2006) and the Outstanding Research Professorship from TRF and OHEC (2010).

Awards

- Highly Cited Researcher in the field of Engineering - 2020
- Highly Cited Researcher in the field of Engineering - 2019
- Highly Cited Researcher in the field of Engineering - 2018
- Highly Cited Researcher in the field of Engineering - 2017

https://recognition.webofscience.com/awards/highly-cited/2020/

Prof.Dr.Somchai Wongwises
Department of Mechanical Engineering,
Faculty of Engineering, King Mongkut's
University of Technology Thonburi

Conference Venue

The 11th TSME International Conference on Mechanical Engineering (TSME - ICoME 2020)

Sunee Grand Hotel & Convention Center, Ubon Ratchathani

Welcome to Sunee Grand Hotel & Convention Center

Sunee Grand Hotel & Convention Center is a standard 5 star hotel in Ubon Ratchathani Province. There are 222 guest rooms under the concept of Business and Family Hotel which has the standard of service. And have facilities Complete comfort Travel is convenient and safe. Since the hotel is located in the heart of the city and the main road of Ubon Ratchathani You can reach the international airport within 10 minutes and you can easily travel to other destinations.

Sunee Grand Hotel can be said that it is a place that will make the user unforgettable with all the convenience in one. Due to its central location and the Sunee Tower shopping center, a complex Containing Sunee Grand Hotel The largest and most modern wedding seminar meeting room in the Isan region. With a shopping mall Large supermarket IT equipment distribution center Finance and securities companies More than 7 financial banks and a variety of interfoods Entertainment Center, modern entertainment without limits, fun movie theaters in SF and Water Wonder Park, the only water park in the heart of Ubon Ratchathani.




Conference Venue

The 11th TSME
International Conference on Mechanical Engineering
(TSME - ICoME 2020)

Sunee Grand Hotel & Convention Center, Ubon Ratchathani

Conference Venue

The 11th TSME International Conference on Mechanical Engineering (TSME - ICoME 2020)

Sunee Grand Hotel & Convention Center, Ubon Ratchathani

Private Car

Take Highway No.1 (Phahon Yothin) to Saraburi, turn onto Highway No.2 (Mittraphap), continue with Highway No.24 (Chokchai-Dejudom) to Ubon Ratchathani. Either way, take the Bangkok - Nakhon Ratchasima road and continue onto the Highway No.226 through Buriram, Surin, Sisaket and enter Ubon Ratchathani Province.

Bus

Take the bus from Morchit bus station to Ubon Ratchathani bus station. It costs around 600 baht for the bus fare. At the Ubon Ratchathani bus station, take the local taxi to the hotel. It costs around 50 baht for the taxi fare.

Train

There are express train from Bangkok to Ubon Ratchathani and regular train from Nakhon Ratchasima to Ubon Ratchathani every day.

Ubon Ratchathani airport

Sunee Grand Hotel & Convention Center is located on Chayangkul Road. Approximately **2** km from the Ubon Ratchathani airport.
The aircraft are Thai Smile, Vietjetair, AirAsia, Nok Air, Thai Lion Air.

Conference Map

The 11th TSME International Conference on Mechanical Engineering (TSME - ICoME 2020)

Sunee Grand Hotel & Convention Center, Ubon Ratchathani

Sinsap Progressive Corporation Company Limited

Sunee Tower 512/8 Chayangkun 16 Road.
Nai-muang Sub District
Mueang Ubon Ratchathani District
Ubon Ratchathani Province 34000

+668 0265 3388, +66 4535-2900

+66 4535 2999

www.suneegrandhotel.com/

https://web.facebook.com/suneegrandhotel.ubon

suneegrandhotel.sm.fo@gmaiI.com

Web Reservaton Prices

Room Type	Rate	Prices
Superior Room	~~1,800 ฿~~	1,500 ฿
Deluxe Room	~~2,000 ฿~~	1,800 ฿
Junior Suite Room	~~3,200 ฿~~	2,800 ฿
Royal Suite Room	~~3,600 ฿~~	3,200 ฿

Sunee Grand Hotel

Conference Map

The 11th TSME International Conference on Mechanical Engineering (TSME - ICoME 2020)

Sunee Grand Hotel & Convention Center, Ubon Ratchathani

Conference Program

The 11th TSME
International Conference on Mechanical Engineering
(TSME - ICoME 2020)
Sunee Grand Hotel & Convention Center, Ubon Ratchathani

1st December 2020

16.00-18.00 Register

2nd December 2020

	Time\Room	1-Patumwan	2-Patummas	3-Patumchart	4-Patumtip	5-Tabtimsiam4
Session 1	09.00-09.20	AEC0001	AME0001	AMM0001	BME0003*	CST0001
	09.20-09.40	AEC0006*	AME0004	AMM0002	BME0005	CST0002
	09.40-10.00	AEC0008*	AME0005*	AMM0003*	BME0001*	CST0003
	10.00-10.20	AEC0009*	AME0011*	AMM0018*	BME0002*	CST0004
	10.20-10.40	**Coffee Break**				
Session 2	10.40-11.00	DRC0002	ETM0003	TSF0002*	AME0006	AMM0005
	11.00-11.20	DRC0004	ETM0011*	TSF0004*	AME0008	AMM0006
	11.20-11.40	DRC0007*	ETM0012*	TSF0008*	AME0010	AMM0007
	11.40-12.00	DRC0008*	ETM0017*	TSF0013*	AME0013	AMM0008
	12.00-13.00	**Lunch (Tabtimsiam3)**				
Session 3	13.00-13.20	CST0005	ETM0004	TSF0003	AMM0010	AEC0003
	13.20-13.40	CST0015	ETM0006	TSF0006	AMM0021*	EDU0001
	13.40-14.00	CST0011*	ETM0008	TSF0007	AMM0022*	EDU0002
	14.00-14.20	CST0016*	ETM0009	TSF0009	AMM0024*	EDU0003*
	14.20-14.40	CST0018*		TSF0012	AMM0025*	
	14.40-15.00	**Coffee Break**				

15.00-15.50 ***Opening Ceremony*** (Tubtimsiam2)
15.50-16.00 ***TSME Memory Awards***
16.00-16.40 ***"Trends of Future Technology Transforming the Automotive Industry"***
By Mr. Yukio Yoshida, Vice President Technical External Affairs Division
Toyota Daihatsu Engineering & Manufacturing Co., Ltd.
16.40-17.20 ***"Innovation of Low-Speed Wind Machine for Thailand and ASEAN Wind Resource"***
By Asst. Prof. Dr.Wirachai Roynarin, Rajamangala University of Technology Thanyaburi

17.45-19.45 ***City Tour*** (Wat Phra That Nong Bua, Wat Maha Wanaram, Thoung Sri Mueang)

Remark : *online presentation

Conference Program

The 11th TSME
International Conference on Mechanical Engineering
(TSME - ICoME 2020)
Sunee Grand Hotel & Convention Center, Ubon Ratchathani

3rd December 2020

	Time\Room	1-Patumwan	2-Patummas	3-Patumchart	4-Patumtip	5-Tabtimsiam4
Session 4	09.00-09.20	AEC0004	ETM0013	CST0008	AMM0011	BME0007
	09.20-09.40	AEC0010	ETM0014	CST0009	AMM0012*	BME0008
	09.40-10.00	AEC0012	ETM0015*	CST0012	AMM0013	BME0009
	10.00-10.20	AEC0013	ETM0016	CST0014*	AMM0014	
	10.20-10.40	**Coffee Break**				
Session 5	10.40-11.00	AMM0015	DRC0009	AEC0002	AME0003	TSF0001
	11.00-11.20	AMM0019	DRC0010	AEC0007	AME0007	TSF0005
	11.20-11.40	AMM0020	DRC0011*	AEC0011	AME0009	TSF0010
	11.40-12.00	AMM0023		AEC0014*	AME0012	TSF0011
	12.00-13.00	**Lunch (Tabtimsiam3)**				
Session 6	13.00-13.20	BME0006	CST0010	DRC0001*	ETM0001	AMM0016
	13.20-13.40	BME0010	CST0013	DRC0003*	ETM0002	AMM0004*
	13.40-14.00	BME0011	CST0006*	DRC0005*	ETM0005	AMM0009*
	14.00-14.20	BME0004*	CST0007*	DRC0006*	ETM0007	AMM0017*
	14.20-14.40	**Coffee Break**				
Session 7	14.40-15.00	AME0014	CST0017*	ETM0019		
	15.00-15.20	AME0015	CST0019	ETM0018*		
	15.20-15.40	AME0016	AMM0026*	ETM0010*		
	15.40-16.00	TSF0014	AMM0027			

16.00-17.00 ***Developing the Curriculum of Mechanical Engineering Seminar*** (Tabtimsiam4)
17.00-18.00 ***TSME Committee / Head of Department Meeting*** (Tabtimsiam4)
18.00-22.00 ***Closing Ceremony and Conference Banquet*** (Tubtimsiam2)

Remark : *online presentation

4th December 2020

09.00-12.00 Cultural Tour
(Khampun Museum, Warinjamrap, Ubon Ratchathani, Thailand)

Contents

The 11th TSME International Conference on Mechanical Engineering (TSME - ICoME 2020)

Sunee Grand Hotel & Convention Center, Ubon Ratchathani

Contents

The 11th TSME International Conference on Mechanical Engineering (TSME - ICoME 2020)

Sunee Grand Hotel & Convention Center, Ubon Ratchathani

Contents

The 11th TSME
International Conference on Mechanical Engineering
(TSME - ICoME 2020)
Sunee Grand Hotel & Convention Center, Ubon Ratchathani

Contents

The 11th TSME International Conference on Mechanical Engineering (TSME - ICoME 2020)

Sunee Grand Hotel & Convention Center, Ubon Ratchathani

AEC0002

An Experimental Investigation of ABE-Diesel Blend on Performance, Combustion, and Emissions in a Compression Ignition Engine

Kan Komanee, Sathaporn Chuepeng, Ob Nilaphai*

ATAE Research Unit, Department of Mechanical Engineering,
Faculty of Engineering at Sriracha, Kasetsart University
199 Sukhumvit Road, 20230 Chonburi, Thailand

*Corresponding author, E-mail: ob@eng.src.ku.ac.th

Abstract. The intermediate product of the butanol production process, acetone-butanol-ethanol (ABE), is currently interested as an alternative fuel for vehicles as its key properties are similar to butanol. This paper aims to investigate the effect of ABE-diesel blend (20% by volume) on the single-cylinder diesel engine. The engine performance, combustion characteristics, and emissions, particularly nitric oxide and smoke, are investigated at loads 10, 20 and 30 Nm and 1,600 rpm speed. The result shows that the specific fuel consumption and combustion phenomena are slightly different from diesel. It is found that the smoke reduced by 46.67%, but the trade-off emissions between smoke and nitric oxide, especially at high load conditions exist.

1. Introduction

In the last few decades, diesel is a main fuel in the Thailand transportation sector, which yearly consumed around 50% to 60% [1]. For that, Thailand has imported crude oil more than 50 million liters per day since 2012 [2] as causes of Thai economics and energy are dependent on world oil price situation. Thai government by Ministry of Energy has focused on promoting alternative diesel fuel, biodiesel, which can be domestically produced. However, biodiesel can be slightly substituted diesel only by 6% of total amount as reported by Energy Policy and Planning Office in 2018 [1].

In order to determine the new alternative fuels for the compression ignition (CI) engines, the researchers have considered the alcohol as an alternative fuel for diesel engines i.e. ethanol and butanol [3], [4]. Butanol seems to be the best candidate for diesel engine as its properties are more suitable with diesel engines than other alcohol fuels such as higher auto-ignition ability, higher energy content, higher viscosity, higher density, lower water solubility, and no separation problem when blending with diesel [5], [6], [7]. Moreover, the use of butanol-diesel blend can be also simultaneously reduce the soot and nitrogen oxides (NO_x) emissions without affecting on engine performance [8]. Although, butanol presents the several advantages in the literature reviews, it does not success as a fuel for diesel engine due to high production cost and energy in terms of feedstock requirement and low yield productivity [6].

Bio-butanol is produced by acetone-butanol-ethanol (ABE) fermentation process, producing an ABE mixture in the intermediate production. Generally, ABE mixture contains an acetone, butanol, and ethanol with a ratio of 3:6:1, respectively [9]. To obtain the pure butanol, the mixture is distillated and dehydrated in the last process, consuming higher energy and production cost. As seen, the ABE mixture consists of hydrocarbon alcohol fuels; therefore, it can be considered as an alternative fuel for CI engines. In previous studies [10], [11], [12], they reported that the ABE-diesel blend at blending ratio 20% by volume (20% v/v), called ABE20, presenting a similar physical and chemical properties to diesel. Moreover, they also investigated the spray and combustion parameters by using the optical technique measurement in combustion chamber to simulate the realistic diesel operating conditions. They found that the spray characteristics of ABE20 also performed similar to reference fuel; a difference of liquid spray length of less than 1 mm can be observed during steady state of injection, while the difference of vapor spray penetration of less than 5% can be seen for the whole time of injection [11]. For the combustion characteristics, they found that ABE20 performed a longer ignition delay and lift-off flame position due to the lower auto-ignition ability of ABE in the mixture. Meanwhile, by using the illumination light extinction technology, Wu et al. found that the soot luminosity of ABE20, related to soot formation, was lower than diesel for all testing conditions [12].

As presented in the literature reviews, ABE20 presents high possibility to use in the diesel engines as presenting similar spray and combustion to diesel. Therefore, this work aims to study the feasibility of the use ABE20 in diesel engines in term of the engine performance, combustion, emissions and engine stability. All parameters was carried on the single-cylinder diesel engine in different engine torques (loads) 10, 20, and 30 Nm at the same engine speed 1,600 rpm. The experimental results of ABE20 are compared with the results of reference diesel fuel.

2. Methodology

2.1 Fuel preparation

This part presents the details of preparation and main properties of the test fuels. According to the general production of ABE, the ratio between acetone, butanol and ethanol of ABE mixture (A:B:E) is approx. 3:6:1 [13]. Therefore, this ratio was used in this study. The volumetric blending ratio of 20% between ABE and diesel was chosen as its spray and combustion parameters similar to diesel [10]. To avoid the effect of fuel properties variation, the purity 99.5% of acetone, 99.8% of butanol, and 99.5% of ethanol were blended to form the neat ABE. Then, the 20% v/v of ABE was blended with 80% v/v of diesel, called "ABE20".

Table 1. Physical properties of the test fuels.

Fuel properties	D100	ABE20
Density at 25 ˚C (g/cm^3)	0.83	0.82
Viscosity at 40 ˚C (mm^2/s)	3.5	2.3
Oxygen concentration (wt.%) [14]	-	4.77%
Lower heating value (MJ/kg)	45.6	41.9
Latent heat of vaporization at 298 K (kJ/kg) [11]	362	411
Cetane number (-)	58	Not provided

Table 1. shows the main fuel properties of ABE20 compared with the reference diesel fuel (D100). As seen, the densities of ABE20 and D100 are slightly different (1.2% difference), but significantly different in the viscosity, approx. 34% difference. These properties would affect to the vaporization process and spray development. Additionally, the LECO AC-350 was used to measure the lower heating value (LHV) in order to analyze impacts on fuel consumption. As seen, the ABE20 has a lower LHV than D100 by approx. 8%. One parameter that would effect on spray development and ignition process is the latent heat of vaporization (Lv) [15] in which the ABE20's Lv is higher than that of D100 by 13.5%. For the main important fuel property, cetane number is an indicator of auto-ignition ability of fuel for CI engine. Only cetane number of D100 is presented in this table and no cetane data of ABE20 in this work and literature reviews. However, it would be expected that cetane number of ABE20 should

be lower than D100, as presenting lower cetane number of alcohol fuel contained in ABE mixture, such as 25 for butanol and 8 for ethanol [10], [12].

2.2 Experimental set-up

The experiment was carried on an agricultural single-cylinder diesel engine (Kobota, Model RT100), that gives the maximum torque and power by 33.4 Nm at 1,600 rpm and 7.4 kW at 2,400 rpm, respectively [16]. The bore and stroke of this engine are 88 mm and 90 mm, respectively while the compression ratio is 18:1. To control the engine load, the engine was equipped with the engine dynamometer [16], as depicted in Figure 1.

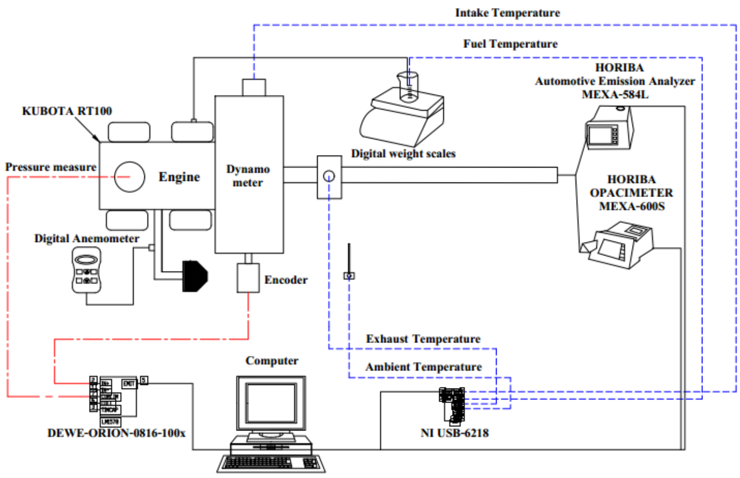

Figure 1. Diagram the experimental set-up on top view.

In this study, the all investigated parameters were measured in different engine torque loads by 10, 20 and 30 Nm measured by dynamometer at the same engine speed of 1,600 rpm. The thermal efficiency (η_{th}) is the ratio between produced work per cycle and chemical energy in the fuel [16], calculated by:

$$\eta_{th} = \frac{1}{SFC \times LHV} \tag{1}$$

where *SFC* is specific fuel consumption, and LHV is fuel lower heating value. To analyze the effect of different properties of test fuels on combustion behaviour, the heat release rate (HRR) was calculated based on the cylinder pressure and crank angle data, by:

$$HRR = \frac{\gamma}{\gamma - 1} p \frac{dV}{d\theta} + \frac{1}{\gamma - 1} V \frac{dP}{d\theta} \tag{2}$$

where γ , θ , and V are specific heat ratio, position of crank angle and cylinder volume, respectively. In this study, the working fluid (air) condition was assumed as the ideal gas and based on crank angle degree domain.

By using the HRR data, the auto-ignition ability of fuels, ignition delay (ID), was determined by the interval time between the start of injection (SOI) and the start of combustion (SOC). The SOI of this study is fixed at 20° before top dead center (bTDC). Meanwhile, the SOC is defined as the first time of HRR return to positive value [17].

In order to measure the cylinder pressure data, a pressure transducer (Kistler, Model 6052C) was installed at the crown of the combustion chamber. The pressure signal was interfaced with a charge amplifier (Dewetron, Model DEWE-30-4) to filter and amplify the signal before recorded by data acquisition system (Dewetron, Model DEWE-ORION-0816-100x). While the crank angle data can be obtained by an incremental shaft encoder (Baumer Electric, Model BDK 16.05A360-5-4) with 1-degree crank angle of resolution (360 pulses per revolution).

The fuel consumption in each test was measured by digital weight scale (CST, Model CDR-3) with the accuracy of ±0.05 g. To measure the air inlet, the flow meter (Benetech, Model GM8901) was used to measure the volume flow rate and temperature of air at the position after the engine air filter. The temperatures for all test conditions such as ambient temperature, fuel temperature, cooling temperature, intake temperature, and exhaust temperature were measured by K-type thermocouple and recorded by in-house developed LabVIEW data acquisition system (National Instruments, NI USB-6218).

The effect of the use of ABE on the exhaust gas emission was investigated by certain emission analyzers. The gaseous emission analyzer (Horiba, Model MEXA-584L) were used to measure the nitric oxide (NO), while the black smoke of exhaust gas at the tail pipe was measured by the smoke meter (Horiba, Model MEXA-130S), based on light intensity absorbed and presented in opacity percentage.

3. Result and Discussion

3.1. Engine Performance

To investigate the effect of fuels on the engine performance, the fuel consumption (FC) of ABE20 and D100 in different engine loads is illustrated in Figure 2. (a). As seen, the FC is increased by increasing engine loads because of the higher energy requirement. In the effect of fuel on this parameter, ABE20 shows the higher FC for all conditions, especially in high loads. This is due to its lower the heating value than D100 by approx. 8% (see Table 1.). This relates to the higher FC by 8.7 % and 6% for 20 and 30 Nm, respectively. For another parameter of engine performance, the thermal efficiency of ABE20 is higher that D100 at the lowest load of 10 Nm by 8.84%, as seen in Figure 2. (b). This is due to ABE20 has a higher the latent heat of vaporization (Lv) than D100, leading to higher absorbed heat around chamber in vaporization process. As a result, the air-fuel mixture can be enhanced and improved the thermal efficiency [18]. However, there is no significant difference in thermal efficiency at the high load conditions.

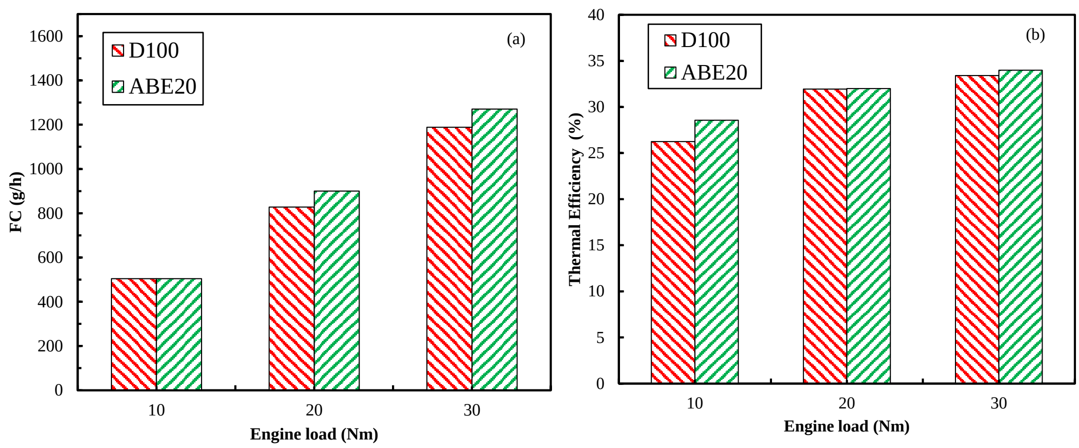

Figure 2. Comparative results of (a) fuel consumption and (b) thermal efficiency of ABE20 and D100 in different engine loads of 10, 20, and 30 Nm at 1,600 rpm.

3.2. Combustion characteristics

Figure 3. compares the experimental results of cylinder pressure (CP) and the heat release rate (HRR) between ABE20 and reference fuel in different engine loads. For clearer visibility, the CP profile is shown only at the loads of 10 and 30 Nm in Figure 3. (a). The CP increased with engine load due to more fuel amount injected in the combustion chamber. In the effect of fuel, the CP profile of ABE20 starts to rise up after D100 and performs higher peak pressure more than D100 for all condition. The

peak pressure of ABE20 is higher than D100 in the range of 0.8 bar to 5.7 bar, or 1.26% to 8.4% greater for all conditions.

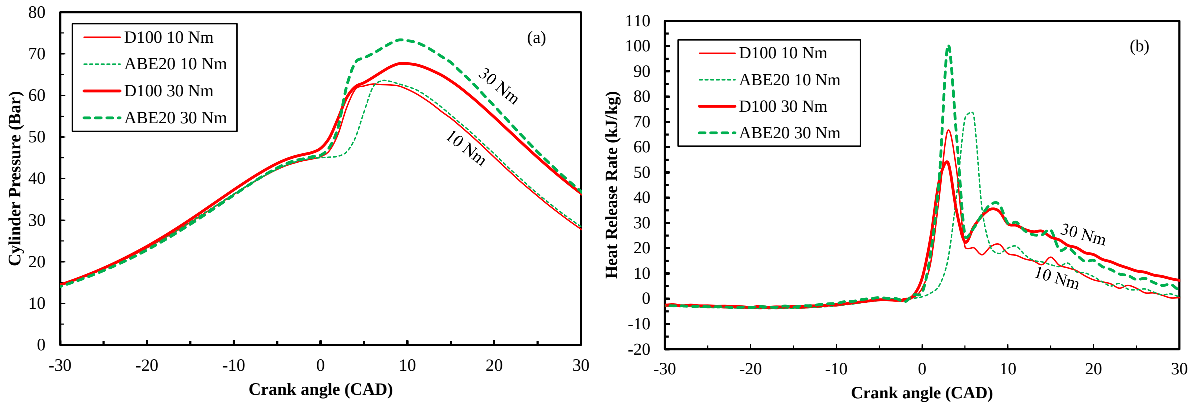

Figure 3. Combustion analysis of ABE20 and D100 in different engine loads of 10 and 30 Nm at 1600 rpm; (a) cylinder pressure and (b) heat release rate

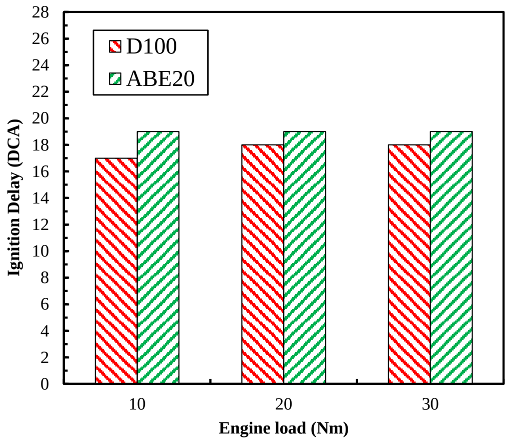

Figure 4. The ignition delay of ABE20 and D100 in different engine loads of 10, 20, and 30 Nm at 1,600 rpm.

Figure 3. (b) shows the heat release rate (HRR) profile from the combustion of the test fuels. The HRR profile of D100 starts to rise up around 3˚ bTDC, taking place early ABE20 around 1˚ to 2˚ crank angle (CAD). Generally, after fuel injection into the combustion chamber, the heat surrounding the jet entrains the fuel to vaporize, inducing the HRR in negative value in this period. Due to the higher latent heat of vaporization of ABE20 than D100 around 13.5% (see in Table 1.), the cooling effect was induced around the fuel jet in the combustion chamber [19]. As a result, ABE20 takes more time in vaporization process and accumulates more initial energy in this period, before rising up in the premixed-combustion phase [19], [20]. Therefore, the longer ID, higher peak of CP and higher HRR profile are observed from the ABE20 combustion. As seen in Figure 4. the ID of ABE20 is longer than D100 in the range of 1˚ and 2˚ for all engine loads.

4. Emissions

4.1 Smoke and Nitric Oxide

Smoke emission can be presented as the state of incomplete combustion in the combustion chamber, in the rich zone of air-fuel mixture. Figure 5. (a) shows the smoke dramatically increased by the increasing engine load for all fuels. At 30 Nm, the smoke is higher than 10 and 20 Nm by 27.6% and 8.3 %, respectively. At the same engine speed, the amount of inlet air was constant but the FC was increased by engine load; therefore, poor air-fuel mixture and increasing the rich zone of combustion chamber can be obtained, leading to higher smoke in high load. For the effect of different fuel properties, the smoke of ABE20 is lower than D100 for all testing conditions by 46.67%, 25.18% and 42.76% for torque 10, 20 and 30 Nm, respectively.

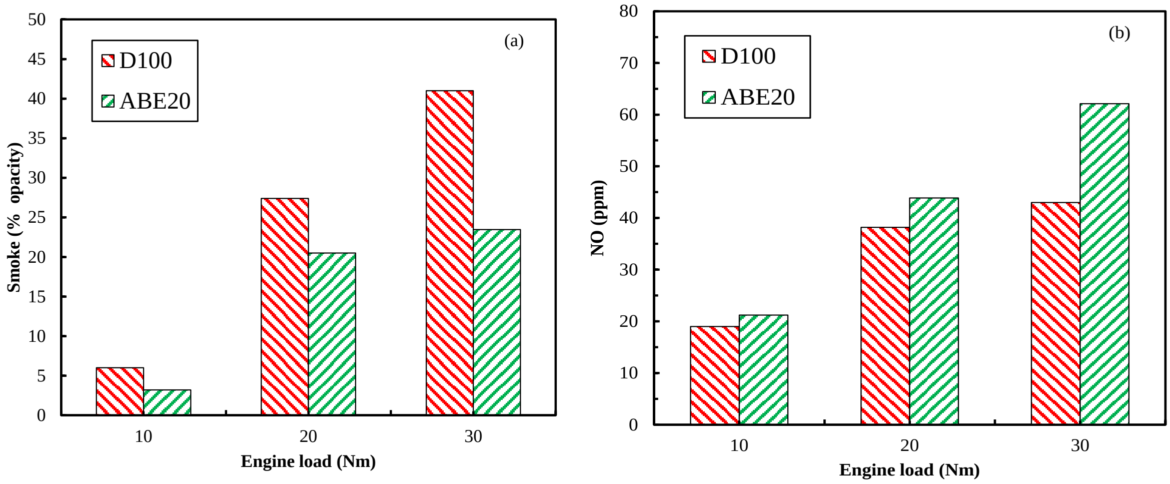

Figure 5. Exhaust gas analysis of ABE20 and D100 in different engine loads 10 and 30 Nm at 1600 rpm; (a) Smoke and (b) Nitric oxide

The oxides of nitrogen (NO_x) formation of diesel engines, mainly occupied by nitric oxide (NO), are dependent on oxygen content and combustion temperature in combustion chamber [21]. As seen in Figure 5. (b), the trend of NO is increased at high load for all fuels. NO at 30 Nm is higher than 10 and 20 Nm by 24 and 4.8 ppm for D100 and 40.91 and 18.26 ppm for ABE20. This is as the fuel at the high load was consumed in greater amount than the low load, causing a stronger combustion behaviour, as observed in the higher HRR profile in Figure 3. (b). Therefore, the higher combustion temperature and NO formation can be presented at the high load conditions [22], [23]. This result can be explained by that ABE contains higher oxygen in molecule with delaying the ignition that spikes a higher peak CP and HRR and promoting the higher combustion temperature and NO formation of ABE20 when compared with D100 [21].

5. Conclusions

This study investigates the effect of the use a new candidate of alternative diesel fuel, called ABE20, in the single cylinder-diesel engine. The results of performance, combustion and emissions are compared with reference diesel fuel (D100) in different engine loads at the same engine speed of 1,600 rpm. As observed by the most literature reviews, ABE20 performs the higher fuel consumption for high engine loads compared to D100 due to the lower heating value of alcohol fuels contained inside the ABE mixture. However, it presents the advantage of higher thermal efficiency than diesel by 8.84%. The trade-off between smoke and NO is yet observed in this work. ABE20 presents a lower smoke opacity than D100 in the range of 25% to 47%, due to the higher oxygen content and better air-fuel mixing as presenting a long ignition delay. Meanwhile, the higher combustion temperature of ABE20, expected by the peak of CP and HRR profile, generates the high NO emission, especially in high loads.

Finally, although the ABE20 performs a good attractive to be used as a fuel for diesel engines, however, the economic worthiness in practical use, stability, durability, and material compatibility would be considered and investigated in the future work.

6. Acknowledgements

The authors would like acknowledge the Kasetsart University Research and Development Institute (KURDI) for the research funding (Grant number: KURDI No. R-M 29.62), and wish to thank Thai Oil Public Company Limited for supporting the test fuel and their properties.

7. Reference

[1] Energy Policy and Planning Office, "Energy statistics of Thailand 2018," 2018.

[2] Energy Policy and Planning Office, "Import of crude oil classified by sources," 2018.

[3] Y. Li, J. Gong, Y. Deng, W. Yuan, J. Fu, and B. Zhang, "Experimental comparative study on combustion, performance and emissions characteristics of methanol, ethanol and butanol in a spark ignition engine," *Appl. Therm. Eng.*, vol. 115, pp. 53–63, 2017, doi: 10.1016/j.applthermaleng.2016.12.037.

[4] Z. Chen, L. Wang, and K. Zeng, "A comparative study on the combustion and emissions of dual-fuel engine fueled with natural gas/methanol, natural gas/ethanol, and natural gas/n-butanol," *Energy Convers. Manag.*, vol. 192, no. February, pp. 11–19, 2019, doi: 10.1016/j.enconman.2019.04.011.

[5] M. Lapuerta, O. Armas, and R. García-Contreras, "Stability of diesel-bioethanol blends for use in diesel engines," *Fuel*, vol. 86, no. 10–11, pp. 1351–1357, 2007, doi: 10.1016/j.fuel.2006.11.042.

[6] C. Jin, M. Yao, H. Liu, C. F. F. Lee, and J. Ji, "Progress in the production and application of n-butanol as a biofuel," *Renewable and Sustainable Energy Reviews*, vol. 15, no. 8. Elsevier Ltd, pp. 4080–4106, 2011, doi: 10.1016/j.rser.2011.06.001.

[7] S. Y. No, "Application of biobutanol in advanced CI engines – A review," *Fuel*, vol. 183, pp. 641–658, 2016, doi: 10.1016/j.fuel.2016.06.121.

[8] J. Kujawski, A. Rozicka, M. Bryjak, and W. Kujawski, "Pervaporative removal of acetone, butanol and ethanol from binary and multicomponent aqueous mixtures," *Sep. Purif. Technol.*, vol. 132, pp. 422–429, Aug. 2014, doi: 10.1016/j.seppur.2014.05.047.

[9] H. Wu *et al.*, "Impacts of Acetone-Butanol-Ethanol (ABE) ratio on spray and combustion characteristics of ABE-diesel blends," *Appl. Energy*, vol. 149, pp. 367–378, 2015, doi: 10.1016/j.apenergy.2014.11.053.

[10] O. Nilaphai, C. Hespel, S. Chanchaona, and C. Mounaïm-Rousselle, "Spray and combustion characterizations of ABE/Dodecane blend in comparison to alcohol/Dodecane blends at high-pressure and high-temperature conditions," *Fuel*, vol. 225, no. March, pp. 542–553, 2018, doi: 10.1016/j.fuel.2018.03.184.

[11] H. Wu, K. Nithyanandan, J. Zhang, Y. Lin, T. H. Lee, and C. F. Lee, "Impacts of Acetone –

Butanol – Ethanol (ABE) Ratio on Spray and Combustion Characteristics of ABE – Diesel Blends," *Appl. Energy*, vol. 149, pp. 367–378, 2015, doi: 10.1016/j.apenergy.2014.11.053.

[12] I. Veza, M. Farid, M. Said, and Z. A. Latiff, "Progress of acetone-butanol-ethanol (ABE) as biofuel in gasoline and diesel engine : A review," *Fuel Process. Technol.*, vol. 196, no. May, p. 106179, 2019, doi: 10.1016/j.fuproc.2019.106179.

[13] T. Lee, Y. Lin, H. Wu, L. Meng, A. Hansen, and C. F. Lee, "Characterization Spray and Combustion Processes of Acetone-Butanol-Ethanol (ABE) in a Constant Volume Chamber," *SAE Tech. Pap.*, vol. 1, pp. 1–8, 2015, doi: 10.4271/2015-01-0919.

[14] M. Karabektas and M. Hosoz, "Performance and emission characteristics of a diesel engine using isobutanol-diesel fuel blends," *Renew. Energy*, vol. 34, no. 6, pp. 1554–1559, Jun. 2009, doi: 10.1016/j.renene.2008.11.003.

[15] C. Vipavanich, S. Chuepeng, and S. Skullong, "Heat release analysis and thermal efficiency of a single cylinder diesel dual fuel engine with gasoline port injection," *Case Stud. Therm. Eng.*, vol. 12, no. January, pp. 143–148, 2018, doi: 10.1016/j.csite.2018.04.011.

[16] John B. Heywood, *Internal Combustion Engine Fundamentals*. Singapore: McGraw-Hil, 1988.

[17] K. Nithyanandan *et al.*, "Improved SI engine efficiency using Acetone-Butanol-Ethanol (ABE)," *Fuel*, vol. 174, pp. 333–343, 2016, doi: 10.1016/j.fuel.2016.01.001.

[18] A. K. Agarwal *et al.*, "Effect of fuel injection pressure and injection timing of Karanja biodiesel blends on fuel spray, engine performance, emissions and combustion characteristics," *Energy Convers. Manag.*, vol. 91, pp. 302–314, 2015, doi: 10.1016/j.enconman.2014.12.004.

[19] A. K. Agarwal, D. K. Srivastava, A. Dhar, R. K. Maurya, P. C. Shukla, and A. P. Singh, "Effect of fuel injection timing and pressure on combustion, emissions and performance characteristics of a single cylinder diesel engine," *Fuel*, vol. 111, pp. 374–383, 2013, doi: 10.1016/j.fuel.2013.03.016.

[20] Y. C. Chang, W. J. Lee, S. L. Lin, and L. C. Wang, "Green energy: Water-containing acetone-butanol-ethanol diesel blends fueled in diesel engines," *Appl. Energy*, vol. 109, pp. 182–191, 2013, doi: 10.1016/j.apenergy.2013.03.086.

[21] S. Rajendran, "Effect of antioxidant additives on oxides of nitrogen (NOx) emission reduction from Annona biodiesel operated diesel engine," *Renew. Energy*, vol. 148, no. x, pp. 1321–1326, 2020, doi: 10.1016/j.renene.2019.10.104.

[22] Y. C. Chang, W. J. Lee, T. S. Wu, C. Y. Wu, and S. J. Chen, "Use of water containing acetone-butanol-ethanol for NOx-PM (nitrogen oxide-particulate matter) trade-off in the diesel engine fueled with biodiesel," *Energy*, vol. 64, no. x, pp. 678–687, 2014, doi: 10.1016/j.energy.2013.10.077.

AEC0004

Wood Vinegar Production from Cassava Rhizome by Downdraft Gasifier

T Poowadin[1,*], M Polsongkram[1], P Khantikomol[1], A Wongniyom[1], S Bunchan[1] and W Apisitpinyo[1]

[1]Renewable Energy Technology Research Laboratory (RTER)
Department of Mechanical Engineering, Rajamangala University of Technology Isan, 744 Suranarai Rd., Muang, Nakhonratchasima, 30000, Thailand

* Corresponding Author: poowadin@gmail.com

Abstract. This research article aims to study the production of wood vinegar from cassava rhizome by downdraft gasifier. The gasifier has 30 cm diameter and 250 cm high which consists of pyrolysis chamber, cyclone and condenser. The gas produced in the system was condensed inside the condenser. Cassava rhizomes 4-6 kg was used as a biomass with the moisture content 10.23%. The air flow rate of the experimentation was set at $0.760 x 10^{-3}$, $1.013 x 10^{-3}$, $1.267 x 10^{-3}$, $1.520 x 10^{-3}$ and $1.773 x 10^{-3}$ m^3/s, respectively. The experimental results showed that the amount of wood vinegar increased according to the air flow rate increase. The optimum conditions for the production of wood vinegar from cassava rhizomes by downdraft gasifier was 4 kg of biomass with the air flow rate at $1.773 x 10^{-3}$ m^3/s, wood vinegar production efficiency was 24.50%. The specific gravity of wood vinegar was 1.0138 and the acidity-pH was 4.29. In addition, it was found that the amount of the sticky liquid obtained from the experiment decreased with the air flow rate increase. The smallest amount of the sticky liquid from this experiment obtained at 6 kg of biomass with the air flow rate at $1.773 x 10^{-3}$ m^3/s. The amount of the sticky liquid per mass equal to 1.27% by weight.

Keywords: Wood Vinegar, Cassava Rhizome, Downdraft Gasifier.

1. Introduction

When biomass is heated in a closed vessel or in an air-tight environment, it is pyrolysis process. The pyrolysis is process of gasification that convert fuel from biomass through incomplete combustion at high temperature to produce syngas. Gasification technology is environmentally friendly that is to reduce carbondioxide (CO_2) from the burning of biomass fuels. Gasifier is the reactor of gasification technology that it is used for producing syngas. There are many types of gasifiers including updraft gasifier, downdraft gasifier, crossdraft gasifier and fluidized bed gasifier. Other types of gasifiers are currently under development. This research use downdraft gasifier to produce wood vinegar because of the information from previous study about tar levels from gasifiers shows that the relative of tar production, with downdraft gasifier being the cleanest [1, 2]. In the pyrolysis process starts to destroy structure of biomass at temperature about 200-400°C. Char, water vapour, methanol, acetic acid and any gases are produced to be syngas. If this syngas is cooled, a liquid can be collected. This liquid, if left to sit about 2-3 mounts, it will be separated into three layers. An oily liquid is on the top layer while thick wood tar settles on the bottom. The middle layer is raw wood vinegar. Raw wood vinegar has more than 200 chemicals, such as acetic acid, formaldehyde, ethyl-valerate, methanol, tar, etc. [3] Wood vinegar has been used in a variety of ways, including as an ingredient in medicines, an additive to animal feeds, soil improvement, pest repellent, a deodorizer, a facilitator in the fermentation process and a raw material in various other industries. In agriculture, recently farmers in many countries use wood vinegar as alternatives to chemicals in improving crop yields, helps plants develop stronger roots and controlling pests. Wood vinegar can be collected in the carbonization process. The quantity of wood vinegar depends on the water content of the wood and on the method of collecting, normally the weight of the raw wood vinegar is about 8% that of the original wood and 5% useable wood vinegar. For example, 100kg of wood yields 25kg charcoal, about 8kg raw wood vinegar and 5 kg useable, refined vinegar. [4] The different kind of wood produce different compounds in wood vinegar. Also, different technique for collecting them produce different one. During process for collecting wood vinegar, the first stage (white smoke) and the last stage (purple smoke), should both be avoided. Because of the first stage contains too much water and the last stage contains large quantities of tar. Therefore, vinegar from both stages is unusable for agriculture. There are many attempts to develop of charcoal kiln and the way to collecting wood vinegar that expects of removing tar and making large quantities of wood vinegar. However, it is not easy to find new technique or design that can fulfill all requirements. Installing a downdraft gasifier to produce wood vinegar from cassava rhizome is the main study of this research.

2. Materials and methods

2.1 Characteristics of fuel

Cassava rhizome is biomass that can be processed into energy and it has plentiful in northeast region of Thailand. There are available in large quantity of cassava rhizome after harvesting, as shown in figure 1. Molecular formula for cassava rhizome is $CH_{1.54}O_{0.59}$ Cassava rhizome chip was used as fuel for producing wood vinegar by downdraft gasifier. The consumption of biomass was varied at 4, 5, and 6 kg with the size was 5-10 cm length and the moisture content 10.23%.

2.2 Experimental Setup and Measuring Devices Used

The downdraft gasifier for producing wood vinegar was design to small size with capacity of 0.18 m^3. The diameter of the air inlet nozzle was 2.5 cm and the air flow into the combustion chamber was set at 1.5-3.5 m/s. As shown in figure 2, several type-K thermocouples were employed to measure the temperatures at combustion, reduction, pyrolysis and drying zone. The syngas was cooled down by the condenser and wood vinegar can be collected at the bottom of condenser. Production of crude wood vinegar from cassava rhizome can be stated as follows: (a) 4-6 kg. of cassava rhizome was introduced into the downdraft gasifier at the top. (b) Primary air flow into the combustion chamber at above the oxidation zone and syngas removed from bottom of the downdraft gasifier. (c) Syngas moves into the cyclone and some sticky liquid can be collected here. (d) Then syngas moves into the condenser and condensed to be wood vinegar.

Figure 1. Cassava rhizome chip

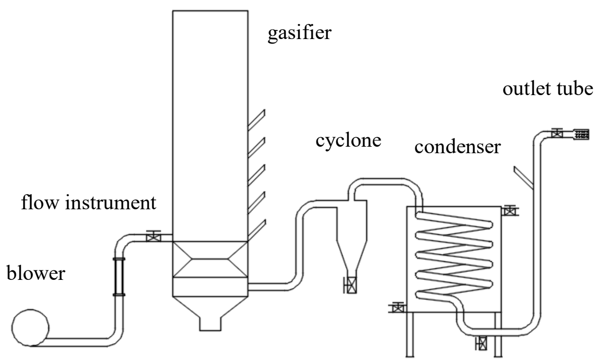

Figure 2. Schematic of downdraft gasifier

As shown in figure 3, The downdraft gasifier for producing wood vinegar was made of the steel with 250 cm high and 30 cm base diameter. The kiln was insulated by thermal insulator outside the combustion zone. An air was used to be a working fluid blew by the blower (1) through the flow meter into the combustion chamber. The air temperature in front of the gasifier was 30-32 ºC and volume flow rate (2) was 0.760x10^{-3}-1.773x10^{-3} m^3/s. Type K-thermocouples (3) were used to measure the temperatures of the downdraft gasifier. Moreover, the sticky liquid can be collected (7) at the cyclone (4) and wood vinegar can be collected (8) at the condenser (5) then syngas moves to outlet tube (6).

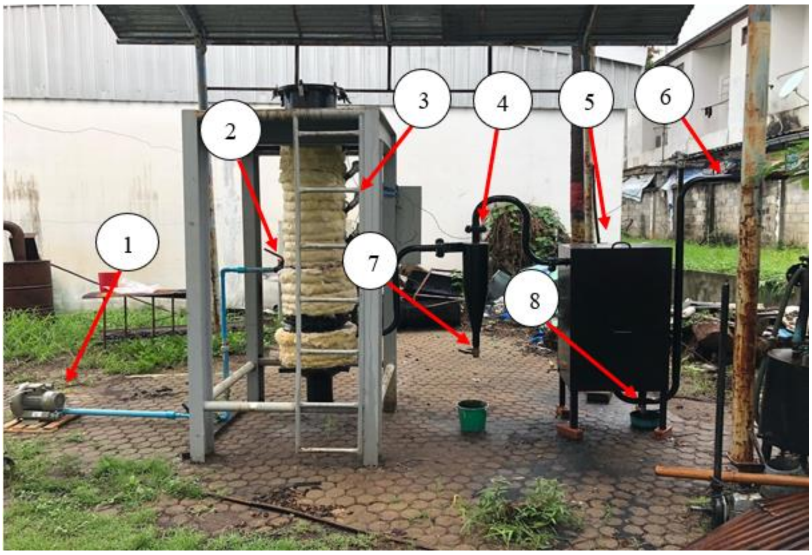

Figure 3. The downdraft gasifier for producing wood vinegar

3. Data processing

Generally, the cassava plant is composed of root (76% w/w), top/leaf (5% w/w), stem (11%w/w) and rhizome (8% w/w) [5]. In Thailand after harvest, it is estimated that about 3-4 million tons of cassava rhizome is obtainable annually. There is information from previous study explain that from its availability and characteristics, cassava rhizome has a great potential to be utilized for heat and power generation. In the present study, Cassava rhizome was used as a biomass to produced wood vinegar by the process of gasification. Cassava rhizome was chopped into pieces of 5-10 cm length with the moisture content 10.23%. Moisture content indicates the amount of water contained in the material compared to the mass of material. Moisture content can be determined by using the equation as follow:

$$M_w = \frac{w-d}{w} \times 100 \tag{1}$$

Where, M_w is the moisture content (%), w is the mass of material (kg), d is the mass of dry material (kg)

The wood vinegar production efficiency (η_v) of the downdraft gasifier can be evaluated by the ratio of mass of wood vinegar production (m_v) and the consumption of biomass (m_f) which was expressed in equation (2).

$$\eta_v = \frac{m_v}{m_f} \times 100 \tag{2}$$

Where, η_v is wood vinegar production efficiency (%), m_v is mass of wood vinegar production (kg), m_f is the consumption of biomass (kg)

4. Results and Discussion

4.1. wood vinegar production

In the present work, cassava rhizome 4, 5, and 6 kg with the moisture content 10.23% were examined. Wood vinegar production by downdraft gasifier with air flow rate 0.760×10^{-3} m^3/s was shown in figure 4. The results indicated that at a biomass of 4 and 5 kg, the production of wood vinegar was highest at time of 20 min. then wood vinegar production was collected decrease slowly. At low air flow rate effects to burn slowly, resulting wood vinegar can be collected slowly and amount of wood vinegar production is low (16.12% of the original biomass). The experimental result for high air flow rate 1.773×10^{-3} m^3/s was shown in figure 5. It was found that at high air flow rate effects to burn easily, resulting almost of wood vinegar can be collected in the first half period and amount of wood vinegar production is high (24.50% of the original biomass). The experimental results showed that more space for combustion zone (low amount of biomass) with high air flow rate affects to collected wood vinegar increasingly.

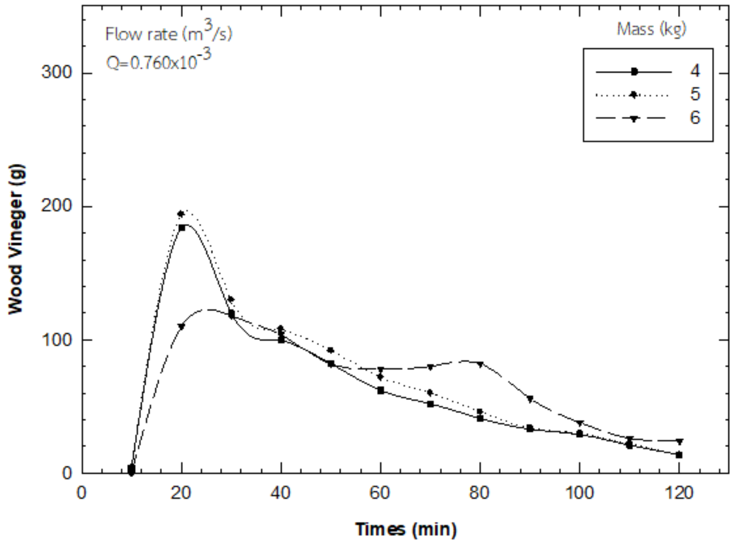

Figure 4. Wood vinegar production by downdraft gasifier with air flow rate 0.760×10^{-3} m^3/s

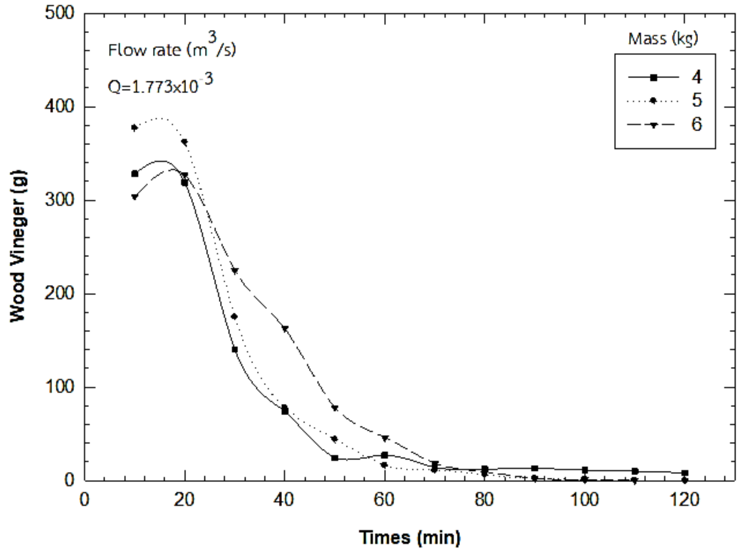

Figure 5. Wood vinegar production by downdraft gasifier with air flow rate 1.773×10^{-3} m^3/s

4.2. wood vinegar production efficiency

Wood vinegar production efficiency was calculated by the ratio of mass of wood vinegar production and the consumption of biomass. As shown in figure 6, the graph shows the effect of air flow rate and wood vinegar production efficiency. It was found that increasing of biomass consumption affect to decrease wood vinegar production efficiency. Increasing of air flow rate affect to increase wood vinegar production efficiency. However, the experimental results indicated that the optimum condition for producing wood vinegar by downdraft gasifier was 4 kg of biomass consumption with air flow rate 1.773×10^{-3} m^3/s. The highest wood vinegar production efficiency was 24.50%. And the amount of the sticky liquid per mass equal to 1.27% by weight.

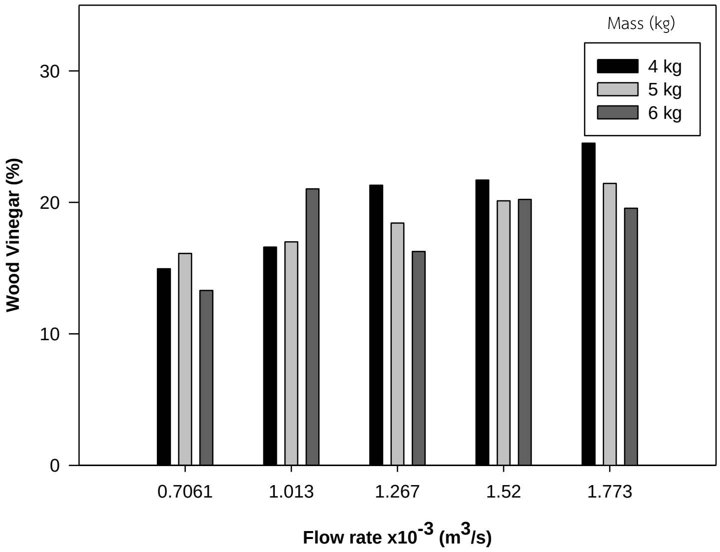

Figure 6. Wood vinegar production efficiency

Wood vinegar production efficiency and their properties was shown in table 1. The results showed that wood vinegar production efficiency by downdraft gasifier decrease with biomass consumption increase. The specific gravity of wood vinegar was 1.0138-1.0217 and the acidity-pH was 3.99-4.53. In addition, it was found that the amount of the sticky liquid (collected at the cyclone) obtained from the experiment decreased with the air flow rate increase.

Table 1. Wood vinegar production efficiency and their properties

Cassava rhizome (kg)	Flow rate $\times 10^{-3}$ (m^3/s)	Wood vinegar production efficiency (%)	Wood vinegar properties	
			pH	SG
4	0.760	14.95	4.25	1.0138
4	1.267	21.30	4.31	1.0133
4	1.773	24.50	4.29	1.0138
5	0.760	16.12	4.40	1.0217
5	1.267	18.43	4.21	1.0138
5	1.773	20.12	4.34	1.0178
6	0.760	13.30	4.38	1.0158
6	1.267	16.27	3.99	1.0103
6	1.773	19.55	4.53	1.0139

Conclusion

The present study conducted about wood vinegar production from cassava rhizome by downdraft gasifier. The downdraft gasifier was modified by installing the cyclone to collected sticky liquid from syngas before send to condenser. From the experimental results and discussion of experimental data, the issue can be summarized as follows:

1. Wood vinegar production efficiency was increase with increasing of the air flow rate. For this study the air flow rate at 1.773×10^{-3} m^3/s shows the highest value of wood vinegar production efficiency.

2. Wood vinegar production efficiency was decrease with biomass consumption increase. For this study the biomass consumption at 4 kg shows the highest value of wood vinegar production efficiency.

3. The optimal condition for producing wood vinegar by downdraft gasifier was 4 kg of biomass consumption and air flow rate at 1.773×10^{-3} m^3/s that showed the highest value of wood vinegar production efficiency equal to 24.50%

4. Wood vinegar production was collected increase fastly with increasing of the air flow rate and collected slowly with increasing of biomass consumption.

Acknowledgments

We are grateful to all staffs in Mechanical Engineering Department, Rajamangala University of Technology Isan for their active help and guidance during the construction and testing of the downdraft gasifier to produce wood vinegar from cassava rhizome.

References

]1[Milne T A, Evans R J and Abatzoglou N 1998 *Biomass Gasifier “Tars”: Their Nature, Formation, and Conversion* (Colorado: NREL/TP-570-25357)
[2] Kivisaari T, Bjornbom P and Sylwan C 2002 J. of Power Sources. **104** pp 115-124
[3] Food and Fertilizer Technology Center 2005 *Wood Vinegar*. Retrieved from http://www.agnet.org/ library/pt/2005025/pt2005025.pdf
[4] Sadakichi, Kishimoto and Hirowaka Tsuyoshi 2015 *Wood Vinegar and Biochar in Agriculture*. Retrieved from http://www.warrencc.org.au/wp-content/uploads/2015/12/CharcoalVinegar-with-pictures.pdf
[5] Nakorn T, Prasert R, Pruk A and Adisak P 2017 *Biochar Production from Cassava Rhizome in a Semi-continuous Carbonization System* Energy Procedia **141** pp 109-113
[6] Godfrey O, Sarah W, Jeffrey S, Noble B, Isa K, Ahamada Z and Nicholas K 2017 *Characterization of Slow Pyrolysis Wood Vinegar and Tar from Banana Wastes Biomass as Potential Organic Pesticides* Journal of Sustainable Development vol 10 no 3 pp 81-92
[7] Kari T, Leena F and Jasse T 2010 *History and Use of Wood Pyrolysis Liquids as Biocide and Plant Protection Product* The Open Agriculture Journal **4** pp 111-118
[8] Sungwarn B, Tinnakorn P and Kittichai T 2017 *A Study of Throat Size Effect on Downdraft Biomass Gasifier Efficiency* Energy Procedia **138** pp 745-750
[9] Adisak P, James O. T and Anthony V. B 2006 *Fast Pyrolysis of Agricultural Residues from Cassava Plantation for Bio-oil Production Proc. Int. Conf. on Sustainable Energy and Environment (SEE 2006)* p 1-5

AEC0011

Improvement of Combustion Efficiency for Synthetic Natural Gas Flame on IDF Axial Burner

T. Sudjan, K. Thaworamongkon, N. Thogsrisomboon, K. Yuenying, M. Poothornsri, J. Charoensook, J. Wongwiwat, S. Jugjai and A. Kaewpradap*

Department of Mechanical Engineering, Faculty of Engineering,
King Mongkut's University of Technology Thonburi, 126 Pracha Uthit Rd.,
Bang mod, Thungkru, Bangkok, 10140 Thailand.

* Corresponding Author: amornrat.kae@kmutt.ac.th

Abstract. This study is to improve the combustion efficiency of synthetic natural gas on IDF (Inverse Diffusion Flame) axial burner with numerical investigation. The IDF axial burner was studied with non-premixed combustion to improved safety and improved combustion efficiency. Therefore, this study focused on port recession, burner shape and nozzle exit at unity equivalence ratio (Φ=1.0) which affected to mixture flow, flame temperature (1877 °C) and heat flux (3238 kW/m^2) of synthetic natural gas flames on IDF axial burner. The enhancement of flame temperature and heat flux were resulted by the numerical model of synthetic natural gas flames on IDF axial burner with recession and dome shape of nozzle exit. This investigation concluded that the combustion efficiency could be improved by the dome shape and recession of nozzle exit for synthetic natural gas combustion on IDF axial burner due to an increase of residence time and better mixing between air and fuel.

Keywords: IDF axial burner, Non-premixed combustion, Natural gas synthetic, Numerical model, Flame temperature.

1. Introduction

Currently, the demand of energy increases while sources of energy are limited—the heat energy to be used for other forms of energy. Most of the energy is obtained from fossil fuel combustion. Simultaneously, the fuel limitation that has to use for high efficiency. Natural gas is the most widely used gas in the industry section or even used as a fuel in the transportation section [1]. Normally in Thailand have the main component of natural gas, 89% of methane, and 11% of carbon dioxide [2]. In industrial combustion, axial burners are used to burning as symmetrical burners suitable for many applications, such as gas turbine combustion. The premixed combustion was using for enhancing higher flame temperature. However, Flashback flames occur when the improper fuel-air ratios. It is extremely dangerous to burning [3]. Therefore, safety is essential to concern to active combustion; many researchers have tried to design the combustion for more safely without flashback flame. More commonly used today is a change to the type of combustion as non-premixed combustion for eliminates the problem at the root cause. Reducing the chance of spread of the mixture between air and fuel mixture when burning velocity is more significant than flow velocity. Simultaneously, the diffusion flame occurs with air, and fuel was poorly mixed [4].

Several studies have been proposed to improve the flame on a normal diffusion flame (NDF) with a fuel-air inversion with an inverse diffusion flame (IDF). The air and fuel were mixing well with air at surrounding were induce to combustion from IDF type. The premixed flame replaces to diffusion flame [5]. The flame length is shorter, and the flame stability is increased when the IDF burner was used in combination with the Swirl [6]. Other research confirms the IDF Burner's effectiveness in emission reduction and more flame stability [7]. However, the IDF burner effect to diluted flame temperature by air on the inside nozzle. The small nozzle exit size affected the flame temperature to be increased [8]. Enhancing mixing between air and fuel and the increase of the reaction zone can increase the flame temperature. The addition technique is to install a swirl at the nozzle exit to increase slight turbulence and mixing [9]. In addition, extending residence time for combustion is important to enabling the air and fuel were good mixings and into complete combustion.

Therefore, to improve the combustion efficiency of the synthetic natural gas non-premixed combustion on the IDF burner, this studied was focused on using the techniques mentioned above. To analyze the combustion characteristic such as structure of distribution temperature, flow pattern of air fuel velocity and analyze to heat flux, and thermal efficiency by uses a technique to increase fuel mixing with the nozzle exit type on the head IDF burner to achieve the highest energy efficiency

2. Numerical Model

2.1 Geometry of IDF burner

Figure 1(a) shows smooth IDF burner geometry to study the improvement of the combustion of natural gas simulated with 89% of methane (CH_4) and 11% of carbon dioxide (CO_2). The IDF burner consists of an air nozzle (inside) and a fuel nozzle (outside). The design of the nozzle of air and fuel area was 44.2 mm^2 and 42.2 mm^2, respectively, with the equivalent ratio of 1.00 or at Firing of 2.00. The air velocity at 1.59 m/s and fuel velocity at 13.4 m/s for overall of simulation. Figure 1(b)-(f) shows the shape of the head burner was designed for increasing air-fuel mixing. The details are as shown in Table 1.

2.2 Numerical method

The Numerical model was used with the ANSYS-Fluent student 2019 R3 version for simulation non-premixed combustion model. Transition SST viscous model, radiation model, and k-ε turbulent model were applied. The mesh amount of 500,000 elements are used in this IDF model. That was a maximum mesh of the Ansys program version. The mesh elements were used in the IDF model's outer region and the region around the IDF head elaborate than another region. CH_4 was mixed with CO_2 at the ration of 89:11. Inlet fuel and inlet air were set to 300 K, while the outlet was set to 1.01 bar and set up flow type to non-slip condition. The recording result was collected when the data into a steady state.

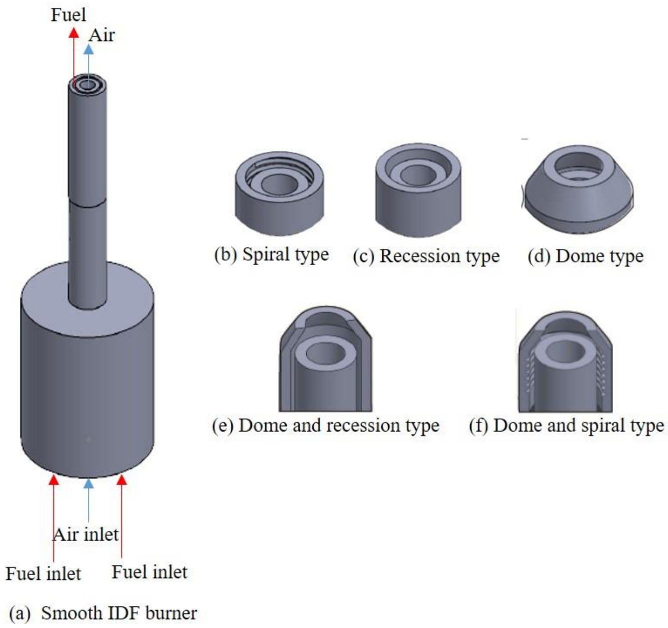

Figure **1.** Schematic of (a) Geometry of smooth IDF burner (b)**-**(f) geometry of IDF burner type**.**

Table 1. The detail of IDF burner type

Type of IDF burner	Fuel nozzle	Air nozzle
Smooth	Smooth surface	Smooth surface
Spiral	Spiral surface	Smooth surface
Recession	Smooth surface	0.25 mm of recession tube
Dome	5 mm of dome height	Smooth surface
Dome with recession	5 mm of dome height	0.25 mm of recession tube
Dome with spiral	5 mm of dome height	Spiral surface

3. Methodology

The methodology for this study consists of two-part. The first part explained the theory of air and fuel quantity calculation for combustion in the numerical model, such as combustion equation, equivalence ratio, firing rate, flow velocity, and last part, which shows the resulting calculation for analysis combustion efficiency. In this study improve combustion efficiency that can illustrated by the result of combustion characteristic, heat flux, and thermal efficiency on the IDF model implied.

3.1 Combustion equation

Combustion equation was calculated by 89**%** of methane (CH_4) and 11**%** of carbon dioxide (CO_2) as fuel with the air is an oxidizer for the analysis of a percentage by volume as show in equation (1)**.**

$$C_xH_y+zO_2 \rightarrow xCO_2+\frac{y}{2}H_2O+3.77zN_2 \quad (1)$$

3.2 Equivalence ratio

Equivalence ratio is the ratio between the actual fuel-air ratio and the theoretical fuel-air ratio that results in complete combustion are defined as shown in equation (2).

$$\Phi=\frac{(F/A)_{actual}}{(F/A)_{stoi}} \tag{2}$$

3.3 Firing rate

Firing rate is the input rate of fuel can be calculated from the mass flow rate and low heating value of the fuel as shown in equation (3).

$$F.R. = \dot{m}_{f} \times LHV \tag{3}$$

3.4 Flow velocity

The air flow velocity and fuel flow velocity for this study. The air and fuel flow velocity are the ratio between volume flow rate and nozzle area as shown in equation (4) and (5) respectively.

$$U_{a}= \frac{Q_{a}}{A_{a}} \tag{4}$$

$$U_{f}= \frac{Q_{f}}{A_{f}} \tag{5}$$

3.5 Combustion characteristic

Combustion characteristics represent the combustion temperature distribution and flow pattern of fuel and air velocity vector. The temperature distribution indicates the fuel and air combustion reaction's flame temperature, while the flow pattern indicates the flow field of fuel and air during mixing.

3.6 Heat flux

The rate of heat energy transfer can operate heat flux (W/m^2) through a given surface (W) per unit area (m^2). The multi-dimensional were using calculate for the heat flux of this model, that proportional to the parameters thermal conductivity (k) and the temperature gradient as shown in (6)

$$\vec{q} = -k\nabla T \tag{6}$$

3.7 Thermal efficiency

Thermal efficiency is calculated by the ratio of the heat output and the fuel inserted or firing rate (kW). Heat output of this model calculate by mass flow rate (kg/s) and enthalpy (kJ/kg) as show in (7).

$$\eta_{th}= \frac{Q_{out}}{F.R.} \tag{7}$$

4. Result and discussion

4.1 Combustion characteristic of Smooth IDF burner

The structure of the natural gas non-premixed combustion flame on the smooth IDF burner is shown in Figure 2(a), the photographic flame was obtained from the experiment based on stoichiometry combustion. The flame showed the premixed flame as symmetrical for both the left and right flames. Simultaneously, Figure 2(b) showed the contours of temperature distribution obtained from an Ansys Fluent model. The flame temperature structure of the IDF burner formed a premixed zone. The premixed flame temperature was higher than the outside flame temperature because of the ambient air diffuse effect. It resulted in a lower temperature around the outside of the smooth IDF flame model as temperature as the maximum temperature of 879 °C and the same condition the result of temperature on IDF burner from experiment was 658 °C it was lower than IDF model because of the experiment occurred heat loss to surrounding.

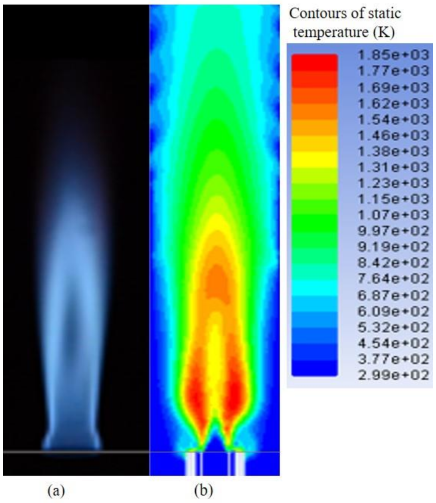

Figure 2. The flame structure of IDF burner (a) The photographic flame (b) The contours of temperature distribution by smooth IDF burner model

4.2 Combustion characteristics

Figure 3 shows the structure of the temperature distribution and the flow pattern on the side view and top view of the non-premixed combustion IDF model with the spiral, recession, and dome type on the nozzle exit as shown in Figure.1. The natural gas combustion at an equivalent ratio of 1.00 or 2.00 kW. The contour of the temperature distribution of the three types of IDF burner was similar. Clearly, at the inside zone (red contour) occur the high temperature has a wide area in the recession and spiral type of burner. In contrast, the dome type had a higher temperature than those types of IDF burners, but only a narrow area.

The flow pattern on the side and top view show the air and fuel velocity vector on the flow field were mixtures, as shown in Figure 3 The spiral type produces a high-velocity vector in the fuel flow because of slight turbulence from the spiral area and high flow velocity in that area. Simultaneously, the recession and dome types were similar velocities of flow field intensities. Still, the dome-type flow field occurs the vector of velocity plunging into the air on the centre of flame and velocity vector into mixing with the air before ejection from the burner and more residence time for mixing between air and fuel.

Figure 4 shows the structure of the temperature distribution and the flow pattern of the IDF model with a combination type of IDF burner. The dome with recession type of IDF burner and the dome with a spiral type of IDF burner. The temperature distribution shape is clearly observed in the dome with recession type and higher temperature distribution and high-temperature zone (red zone) than dome with spiral type. The intensive velocity vector occurs in the premixed zone. The air and fuel were more mixed at side view and top view on the dome with recession type due to the more temperature distribution characteristic of recession type. It can support more temperature distribution than only dome type.

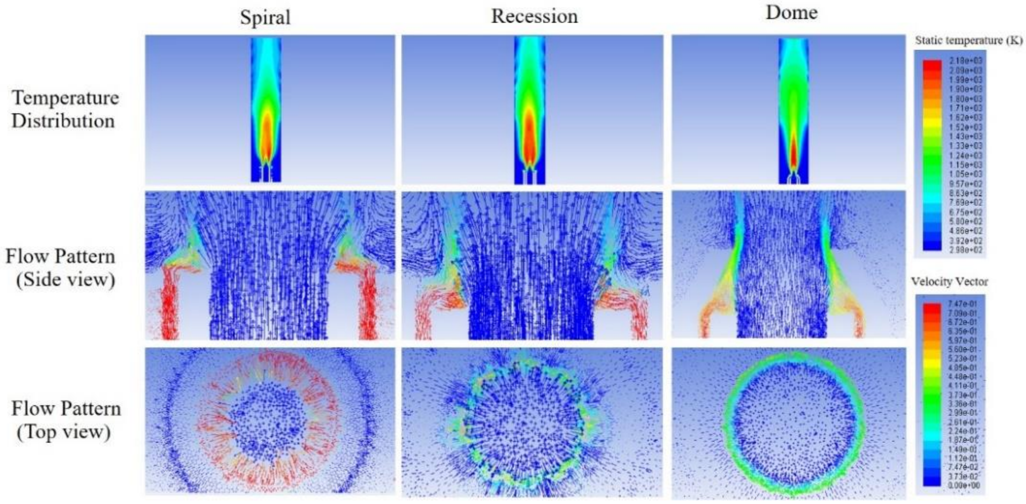

Figure 3. The structure of the distribution temperature and the flow pattern on the side view and top view of the non-premixed combustion IDF model with the spiral, recession, and dome type

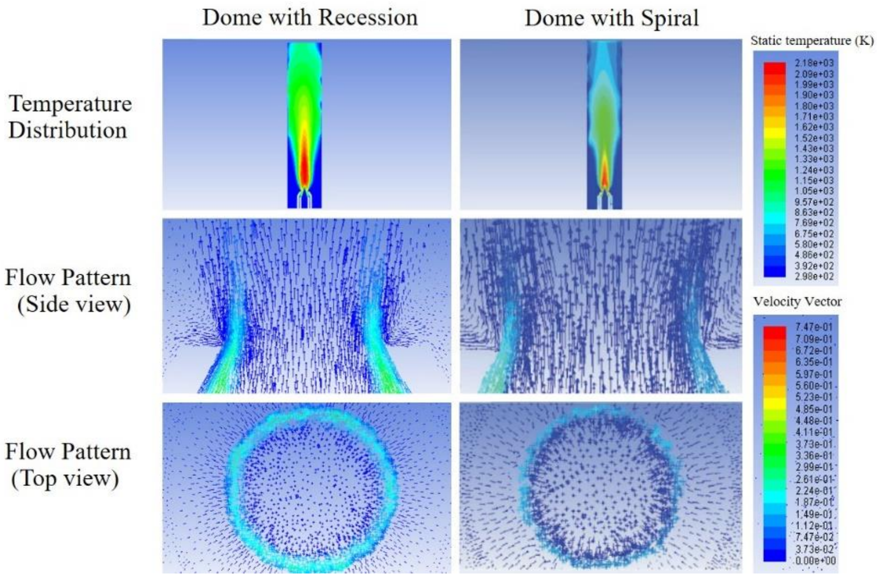

Figure 4. The structure of the temperature distribution and the flow pattern of the IDF model with a combination type of IDF burner.

4.3 Heat flux

Figure 5 shows the maximum temperature and heat flux of the IDF burner type flames. It was found that the maximum temperature of 1759°C on dome type and the flame temperature of 1342°C and 917°C, of recession and spiral type, respectively. Simultaneously, the highest heat flux distribution at 2899 kW/m^2 on the recession type was due to the increasing air-fuel mixing residence time more than those types—the influence of fuel flow on recession type similar to the partially premixed combustion. Thus, when comparing the maximum temperature and heat flux, it was found that dome type was closest to the adiabatic flame characteristics while combination type of the IDF burner. The flame temperature as 1877°C and the heat flux 3238 kW/m^2 on the dome with recession type while the temperature was 1690°C and the heat flux as 2787 kW/m^2 on the dome with spiral type.

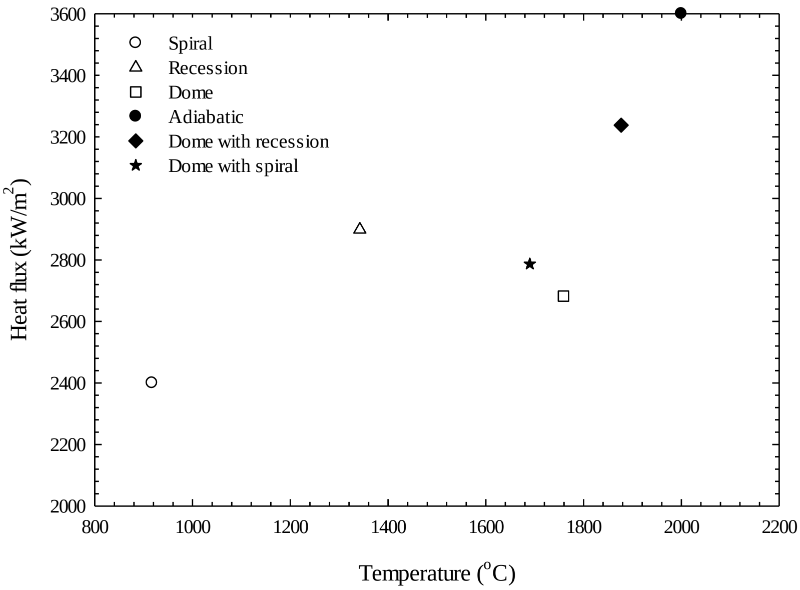

Figure 5. The maximum temperature and heat flux of the IDF burner type

4.4 Thermal efficiency

Figure 6 shows the maximum temperature and thermal efficiency of the IDF burner flame. Recession and dome type of IDF burners have a similar thermal efficiency of 58**%** and 54**%**, respectively. Both two type it can provide higher temperature heat dissipation while the spiral shape has the lowest thermal efficiency of 48**%**, indicating lower heat distribution and temperature. However, dome shape burners were found to be closest to the adiabatic of the flame characteristics. The dome with recession type increased the thermal efficiency as 65**%** with the increasing residence time on recession characteristic for mixing well between air and fuel. The results show the high temperature, heat flux, and thermal efficiency closer to adiabatic flame characteristic on a dome with recession type of IDF burner.

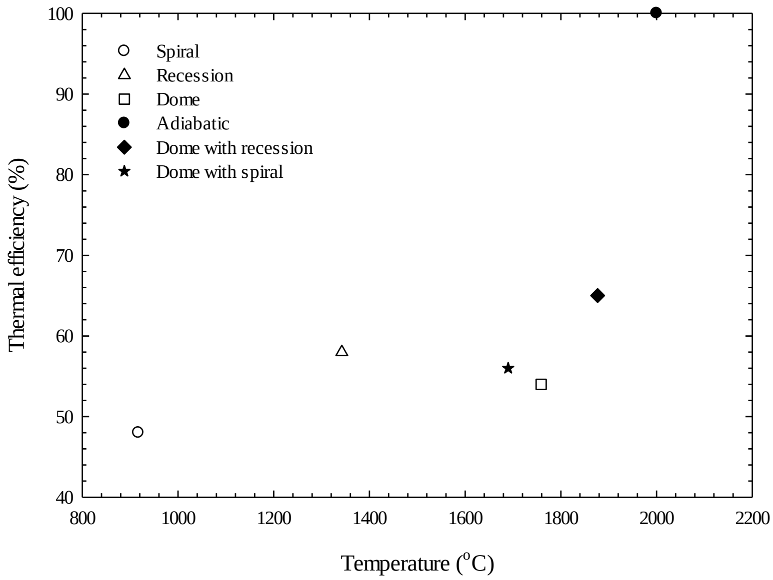

Figure 6. The maximum temperature and thermal efficiency of the IDF burner type.

5. Conclusion

In this study of non-premixed combustion on IDF burners with nozzle exit type as the spiral, recession, dome, and combination types to improve natural gas combustion at 89% of CH_4 and 11% of CO_2, the results were summarized as follows.

1. Numerical models can predict the structure of flames, similar to images of experimental flames from photographic.

2. The shape of the nozzle exit type affects the flame characteristics: dome type can provide the highest flame temperature with the characteristic of changing the direction of the fuel for mixing with air. The recession type can provide the highest heat flux with an increased residence time of combustion.

3. The combination of the dome with recession type was obtained the greatest increase of flame temperature and heat flux, and thermal efficiency and increase of 998 °C from a smooth IDF burner.

Acknowledgments

The author would like to thank for CERL lab, Department of Mechanical Engineering, Faculty of Engineering, King Mongkut's University of Technology Thonburi (KMUTT) for facility supports.

References

[1] Energy Policy and Planning Office, Ministry of Energy 2019 Energy situation
[2] PTT distribution service center PTT public company limited, Online gas quality 2019 online: https://dscng.pttplc.com/(S(ax11gt3h1rmn3lniznp1hwpe))/Home/Home.aspx.
[3] Alireza Kalantari and Vincent McDonell 2017 *Prog. Energy Combust. Sci.* 61 p 249-292
[4] M. Angsuchoti, A. Kaewpradap and S. Jugjai 2017 *The 8th TSME-ICoME* p 582–589
[5] A. Kaewpradap and S. Jugjai 2019 *Proc. Int. Conf. on Earth Environmental science* vol 265 p 012002.
[6] Vipul Patel and Rupesh Shah 2018 *Appl. Therm. Eng.*137 p 377-385
[7] J. Miao, C. W. Leung, C. S. Cheung, Z. Huang, and W. Jin 2016 *Int. J. Hydrogen Energy*. 41 p 9653–9663
[8] B. A. Rabee 2018 *Energy*. 160 p. 1201–1207
[9] A. M. Elbaz and W. L. Roberts 2016 *Fuel*. 169 p 120–134

AEC0012

Properties of Roof Tiles Produced From Agricultural Residue Materials

A Pasilo, E Boonthum, U Teeboonma, A Namkhat, and S Pumchumpol*

Department of Mechanical Engineering,
Faculty of Engineer, Ubon Ratchathani University
85 Sathonlamark Road, Warin Chamrap, Ubon Ratchathani, 34190, Thailand

* Corresponding Author: songsup.p@ubu.ac.th

Abstract. The objectives of this paper were to study on physical properties, mechanical properties and thermal properties of roof tiles produced from agricultural residue materials. Agricultural residue materials consist of kenaf fiber, corncob fiber, palm fruit bunch fiber and water hyacinth fiber. The adhesive on this research was synthetic urea-formaldehyde resins. Physical properties, mechanical properties and thermal properties were conducted according of industry standards such as JIS A 5908-2003, TIS 535-2556, ASTM D 256-2006a and ASTM C 117- 2010. Additionally, the properties of these roof tiles were compared on by commercial roof tiles. The results shown that the rupture modulus and elastic modulus were within standard. Moreover, thermal conductivity of these roof tiles was similar to that of commercial roof tiles.

1. Introduction

Energy crisis and global warming are occurring in all regions of the world, including Thailand. Reusing agricultural and industrial waste materials such as rice straw, bagasse, corncobs, wood chips, etc., is another way to reduce the impact of the emerging crisis. Since Thailand is an agricultural country, it has plenty of crop residues such as straw, corncobs, bagasse pulp fiber, water hyacinth, sisal, palm fruit bunch, oil palm fiber and water hyacinth fiber. Agricultural waste is widely available in developing countries. Agricultural waste materials have a fibrous structure, so they can be used as raw materials for the production of residential building materials [1-3]. Especially used to produce roof tiles. The advantages of using plant fibers are low cost and resistance to environmental changes [4-6]. Therefore, the development of roof tiles from crop residues becomes as an alternative to energy and environments conservation as well as economy. Many researchers [1,3,5,6] had researched to recycle these agricultural residues materials, in hoping that it will help decrease the demand of using natural resources. For example, many kinds of crop residues were recycled and reused; such as kenaf, sugar cane pulp was blended in plywood. They found that the strength and ability of moisture absorbance of these types of plywood are similar to other commercial plywood. Agricultural residues materials are suitable materials for brittle reinforcement, even though relatively poor durability performance [8]. Designing a suitable of materials ratio for the mechanical properties of fibers can develop materials with optimal properties for construction. Anyway, the aim of this research was to apply agricultural residue materials products for the highest benefits by the development of roof tiles produced from agricultural residue materials, such as kenaf fiber, corncob fiber, palm fruit bunch fiber and water hyacinth fiber. Physical properties, mechanical properties and thermal properties of roof tiles produced from agricultural residue materials which testing according to industry standards, JIS A 5908-2003, ASTM D 256-2006a and ASTM C 117- 2010. The adhesive on this research was synthetic urea-formaldehyde resins. The ratio of urea-formaldehyde resin was 12% by mass. Expecting that the roof tiles can perform as a good insulation with lightweight, durability and low cost.

2. Materials and Methods

Agricultural residue materials studied in this study were kenaf fiber, corn cob fiber, palm fruit bunch fiber and water hyacinth fiber. The synthetic urea-formaldehyde resin adhesive was selected as an adhesive. Each ingredient was grounded by a jet mill, about 1-2 mm, then sifted through a sieve to give it a similar size. Subsequently, it was, opened sun, dried until the final moisture content was about 5-6 percent of wet basis. To produce the roof tile, mold of roof tile was constructed with a size of 11x22x1.5 cm^3 as shown in Figure 1.

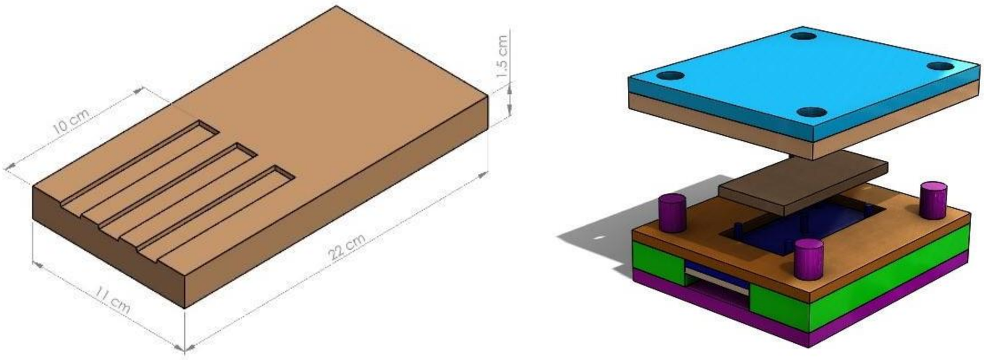

Figure 1. Mold of roof tiles.

Figure 2. The hydraulic machine for producing the roofing tiles.

Figure 2 shown the hydraulic machine used for forming the roofing tiles. To produce roof tiles, the composition was mixed with urea formaldehyde resin at the amount of 12 percent by mass because this proportion is appropriate for agricultural material. After that, the mixture was put into the mold. The specimen was formed by a 100-ton hydraulic machine under pressure of 180 kg/m^2 and temperature of mold at 150°C, for 15 minutes. The roof tile were made triplicate for repeated testing and the roof tile example produced in this work were shown in Figure 3. Physical properties testing, mechanical properties testing and thermal properties testing were tested according to industry standard as shown in table 1. Furthermore, scanning electron microscopy (SEM) technique was used for investigating microstructural characteristics of roof tiles. Finally, the thermal properties of roof tiles produced in this work were compared to commercial roof tiles.

Figure 3. The example of roof tiles.

Table 1. Standard test specification method for roof tiles.

Property	Standard test specification
Density (D)	JIS A 5908-2003
Modulus of rupture (MOR)	TIS 535-2556
Modulus of elasticity (MOE)	ASTM D 256-2006a
Thermal conductivity (K)	ASTM C 117-2010

3. Results and Discussion

3.1 Cross-sectional photos using Scanning electron microscopy (SEM) technique

Figure 4 shown fiber cross-sectional using SEM technique of roof tiles made from kenaf, corncob, palm fruit bunches and water hyacinth. The result of a cross-sectional photograph of the roof tiles produced from kenaf, corncob, palm fruit bunches and water hyacinth. It was found that there were gaps between the fibers to allow the binder to penetrate, resulting in the fibers to bond well. Especially in the case of tiles made from water hyacinth fibers, it was found that there was the greatest gap for adhesives to penetrate, resulting in high density and strength tiles. Consistent with the density and strength tests presented in Figure 5-7 for roof tiles with gaps for infiltration, the roof tiles made from palm fruit bunches, corncob and kenaf, respectively.

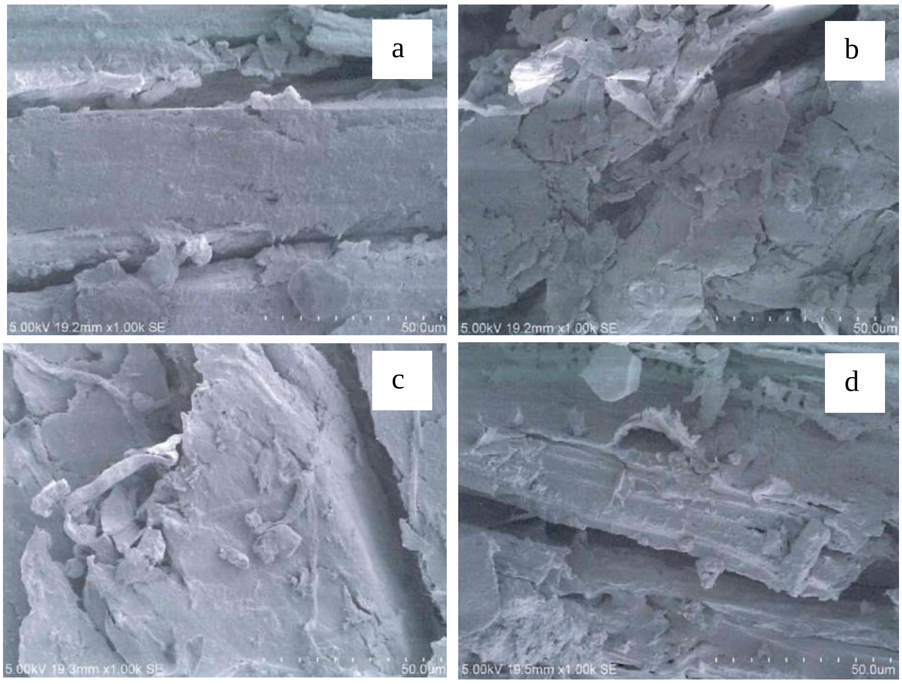

Figure 4. Microstructure of roof tiles: (a) kenaf fiber, (b) corncob fiber, (c) palm fruit fiber and (d) water hyacinth fiber.

The deformation of specimens were kenaf fiber, corncob fiber, palm fruit bunch fiber and water hyacinth fiber. Four specimens were tested for each in order to receiver more accurate results. Similar progressive pattern was also observed in other specimens. The presented laboratory results, the extrusion of roof tiles is according to the factors defined in all respects. Figure 4-8 displays the results of roof tiles product.

3.2 Physical testing

Figure 5 shown the results of the density testing for roof tiles made from kenaf, corncob, palm fruit bunch and water hyacinth, tested in accordance with JIS A 5908-2003**.** The density of roof tiles made from kenaf fibers, corncob, palm fruit bunches and water hyacinth were 343 kg.m^{-3}, 362 kg.m^{-3}, 420 kg.m^{-3} and 581 kg.m^{-3}, respectively**.**

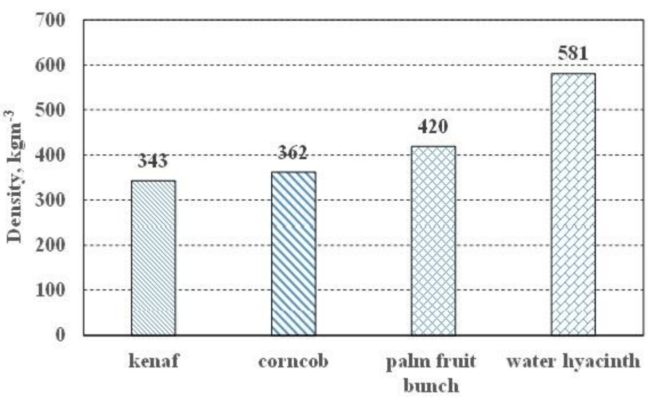

Figure 5. Density of roof tiles.

The results shown that the roof tiles made from water hyacinth fiber have the highest density. Because of the adhesive could be penetrated better between the hyacinth fibers than the palm bunch fibers. The density of the roof tiles made from water hyacinth fiber were 41%, 38% and 28% higher than those produced from corncob and palm fruit bunch, respectively.

3.3 Mechanical testing

Figures 6 and 7 shown the modulus of rupture (MOR) and modulus of elasticity (MOE) of the roof tiles produced from kenaf, corncob, palm fruit bunches and water hyacinth. The testing was done in accordance with TIS 535-2540 and ASTM D 256- 2006a. The results shown that the modulus of rapture (MOR) of roof tiles made from kenaf, corncob, palm fruit bunches and water hyacinth were 1.05 MPa, 1.83 MPa, 1.92 MPa and 1.97 MPa, respectively. Modulus of elasticity (MOE) of the roof tiles made from kenaf, corncob, palm fruit bunches and water hyacinth were 130 MPa, 182 MPa, 197 MPa and 199 MPa, respectively. The results from experimental found that the strength of the roof tiles made from water hyacinth fibers was the highest. This was because the adhesive penetrated better between the hyacinth fibers than the palm bunch fibers, corncobs and kenaf. Modulus of elasticity (MOE) of roof tiles made from water hyacinth fibers was 47%, 7% and 3% higher than kenaf, corncob, and palm fruit bunch, respectively. The values of the roof tiles made from water hyacinth fiber were 35%, 9% and 1% higher than those made from kenaf, corncob and palm fruit bunch, respectively. The mechanical properties of the roof tiles were tested in accordance with TIS 535-2540 standard.

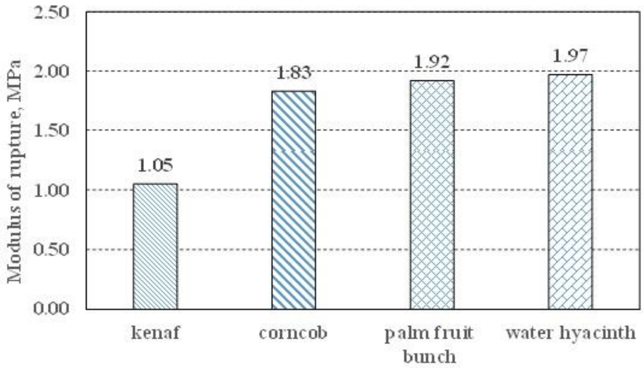

Figure 6. The modulus of rupture

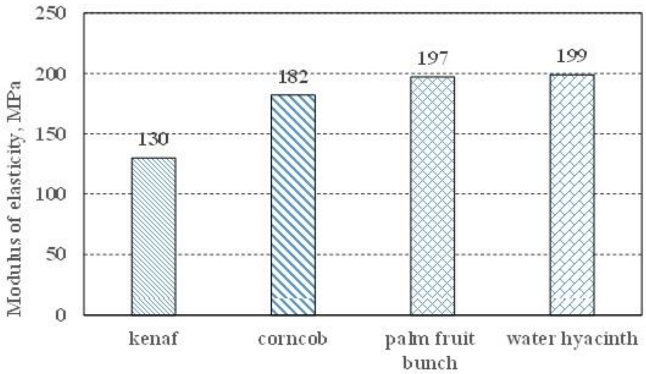

Figure 7. The modulus of elasticity.

3.4 Thermal properties testing

Figure 8 shown the test results for the thermal conductivity of roof tiles produced from kenaf, corncob, palm fruit bunch and water hyacinth. The results shown that thermal conductivity of roof tiles produced from kenaf, corncob, palm fruit brunch and water hyacinth were 0.024 W(mK)$^{-1}$, 0.030 W(mK)$^{-1}$, 0.095 W(mK)$^{-1}$ and 0.098 W(mK)$^{-1}$, respectively. The roof tiles made from water hyacinth had the highest thermal conductivity or lowest insulation. This was because the gap or porosity of the roof tiles made from water hyacinth fibers was low. This was due to adhesive penetrated well into the gaps between the water hyacinth fibers compared to others. Thermal conductivity of roof tiles made from water hyacinth fibers were 76%, 69% and 3% higher than those made from kenaf, corncob, and palm fruit bunch, respectively.

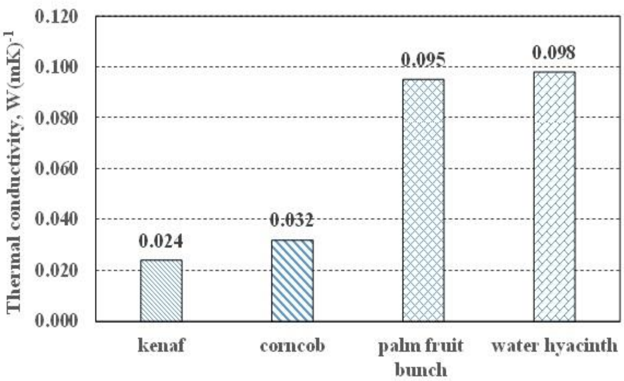

Figure 8. Thermal conductivity.

3.5 Comparison of thermal conductivity with commercially roof tiles.

Table 2 shown the results of the test for thermal conductivity of roof tiles produced from kenaf, corncob and water hyacinth and 4 types of commercially roof tiles. The results shown that thermal conductivity of roof tiles produced in this research was similar to that of commercially roof tiles, and found that the roof tiles made from kenaf had the lowest thermal conductivity. In other words, it had the best insulation compared to other types.

Table 2. The comparison between experiment and commercial roof tiles.

Type of roof tiles	Thermal conductivity, W(mK)$^{-1}$
Kenaf fiber	0.024
Corn cob fiber	0.032
Palm fruit bunch fiber	0.095
Water hyacinth fiber	0.098
Commercial Roof tiles: A	0.229
Commercial Roof tiles: B	0.030
Commercial Roof tiles: C	0.040
Commercial Roof tiles: D	0.041

4. Conclusions

From studying properties of roof tiles produced from agricultural residue materials. The results could be summarized as follows;

a) The results of the fiber cross-sectional imaging by SEM technique showed that the adhesives were able to penetrate the fiber gap well. The fibers with which the adhesives penetrate the gap the most were water hyacinth.
b) The mechanical properties of roof tiles made from kenaf, corncob, palm fruit bunch and water hyacinths were measured in density and strength.
c) Thermal conductivity of roof tiles produced from kenaf, corncob, palm fruit bunch and water hyacinth were found to have similar thermal conductivity as those in commercially roof tiles. In addition, it was found that roof tiles made from kenaf had the lowest thermal conductivity.

The results of the study and data analysis could be concluded that it was possible to use agricultural residue materials as raw materials in the production of roof tiles.

Acknowledgments

The authors would like to express their sincere thanks to Faculty of Engineering, Ubon Ratchathani University for financial support.

References

[1] Darsana, P., Abraham, R., Joseph, A., Jasheela, A., Binuraj, P.R., Sarma, J 2016 *Procedia Technology* **24** 169 – 178
[2] Pickering, K.L., Aruan M.G., Le, T.M 2016 *Applied Science and Manufacturing* **83** 98–112
[3] Sen T and Reddy H. N. J 2011 *International Journal of Innovation, Management and Technology* **2** 186-191
[4] Bentchikou, M., Guidoum, A., Scrivener, K., Silhadi, K., Hanini, S 2012 *Construction and Building Materials* **34** 451–456
[5] Humphrey D 2017 *Procedia Engineering* **200** 1–9
[6] Raut, P., Ralegaonkar, R.V., Mandavgane, S.A 2011 *Construction and Building Materials* **25** 4037–42
[7] Andrade, F., Romildo, S., Toledo, D., João, F., Melo, A., Eduardo, F., Fairbairn, R 2010 *Construction and Building Materials* **24** 777–785
[8] Danso, H., Martinson, D.B., Ali, M., Williams, J.B 2015 *Construction and Building Materials* **101** 797–809

AME0007

Characterization of metal oxide ashes in diesel particulate filter utilizing electron microscopy

Sattatad Rodvanna[1,*], Preechar Karin [1,*], Nuwong Chollacoop[2] and Katsunori Hanamura[3]

[1]Faculty of Engineering, King Mongkut's Institute of Technology Ladkrabang, Bangkok 10520, Thailand
[2]National Metal and Materials Technology Center, National Science and Technology Development Agency, Pathumthani 12120, Thailand
[3]School of Engineering, Tokyo Institute of Technology, Tokyo 152-8552, Japan

* Corresponding Author: ton230937@gmail.com

Abstract. Physicochemical characteristics of metal oxide ashes derived from the actual passenger cars' diesel particulate filter (DPF) were investigated utilizing an electron microscopy, energy dispersive spectroscopy, X-Ray Fluorescence, and X-Ray Diffractometer. A deposition of ash particles mainly took place at the end plug with various deposited length depending on channels. The majority of ash components, derived from lubricant additives, consisted of Fe, Si, Ca, Cu, S, P, Zn, Al and minor Cr, Ni, Mn. These ash components resulting in a clogging which is the main concern of a diesel vehicle equipped with DPF.

Keywords: Diesel engine; Particulate filter; Metal oxide ash; Fuel additives; Engine wear

1. Introduction

Nowadays, automotive trends are focusing to the future of the vehicles, for example, autonomous vehicle, Plug-in Hybrid Electric Vehicle (PHEV), and the most popular one Electric vehicles (EV). These future developments require a revolutionized of the infrastructure in which only a few countries are well-prepared. Therefore, internal combustion engines will continue to be used as a main power source for transportation. Among the engines, diesel engine is widely used [1] due to its highest thermal efficiency among others [2]. However, the diesel exhaust gas contains high amount of particulate matter (PM), which is harmful for our body and environment. A solid fraction of diesel PM composed of soot formed by an incomplete combustion, and ash which mainly derived from fuel or engine oil additives [3]. Diesel Particulate Filter (DPF) was introduced as the most effective way to mitigate this emission because the PM removal efficiency is more than 98% [4]. As PM continuously trapped in DPF, the filter back pressure is increased resulting in a reduction of engine efficiency. As a result, DPF need to be regenerated by oxidizing of trapped PM. Unlike to soot particles, an incombustible metal oxide ash cannot be removed from DPF by burning and will deposit in it. There are two types of ash deposition: wall ash [5] and plug ash [6]. Wall ash covers the DPF wall and performs as a membrane filter resulting in a high filtration efficiency, but too much deposition can restrict the channel diameter. On the other hand, plug ash completely fills the channel and reduces the effective length of the filter [7].

Previous research [8], suggested that the mechanism of ash distribution process depended on the DPF regenerative way. By using active regeneration ash tends to accumulate at the end of the channel as plug ash, while wall ash was formed by the passive regeneration. In addition, the ash formation can be influenced by the attractive forces between particles. Based on the previous results of in-situ optical system [9], revealed that wall ash can be removed and accumulated at the end plug as the plug ash through the process of soot oxidizing at 600°C. This process can occur even in the absence of any flow through the channel due to the presence of substantial cohesive. Although the different mechanisms of the ash distribution process were proposed, the debate about the complex ash formation, accumulation, as well as fundamental mechanisms of ash property, are still ongoing without firm evidence. Therefore, the investigations on the ash physico-chemical property and the ash formation process by using advanced analytical tools will be helpful to solve the abovementioned issues.

In this study, the actual DPF was disassembled and accumulated ashes were investigated their distribution pattern. Furthermore, morphological, nanostructures and chemical composition characteristics of ash particles were investigated utilizing electron microscopy techniques.

2. Experiments

2.1 Investigated DPF system

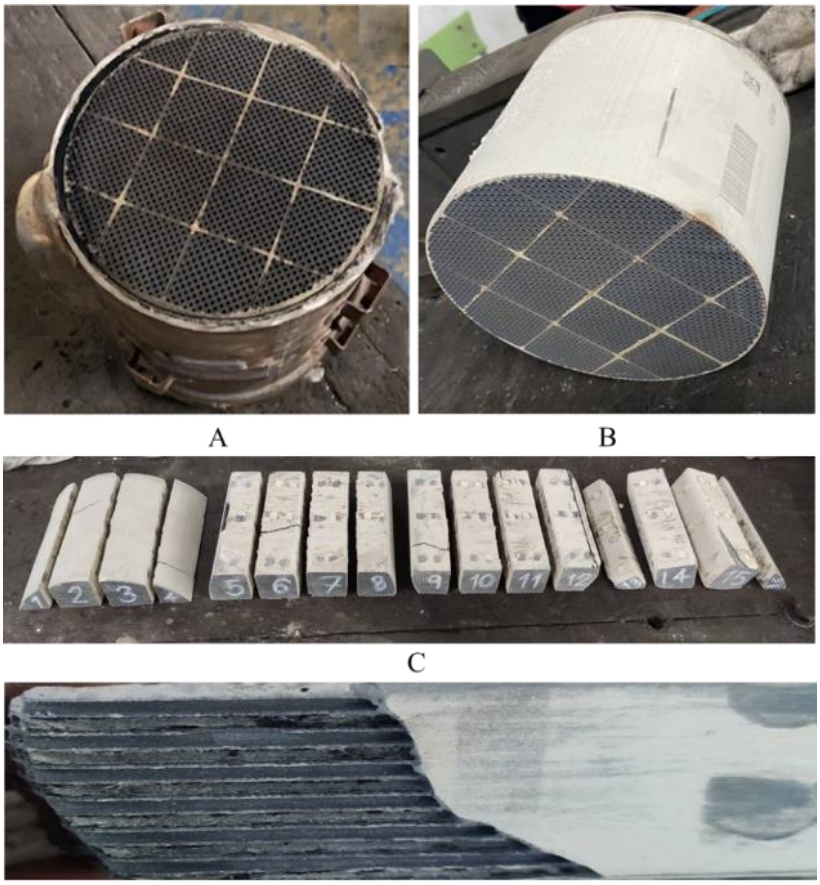

Figure 1. Passenger cars' DPF assembly (A), DPF with honey-comb structure (B), 16 segments of DPF after it was disassembled (C), a removed top wall DPF (D).

Figures 1(A) presents DPF assembly obtained from a diesel passenger car which was used in this experiment. The investigated DPF had ‘honey-comb’ structures (figure 1B) and consists of different ‘segments’, there were disassembled in their segment constituents as shown in figure 1(C). Then, the horizon top wall of each segment was removed layer by layer utilizing abrasive papers and grinding machine (figure 1D). The macroscale analysis data of ash accumulation length, as well as distribution patterns in each layer were collected, as trapped within the filter channels. In order to confirm the reproducibility of data, several DPF from the same car manufactures were investigated in this experiment.

In addition, a mechanical removal of ash from the filter also performed as the microscale analysis. Characterization and chemical components analysis of ash particles were carried out by X-Ray Fluorescence (XRF), and X-Ray Diffractometer (XRD) at NSTDA Characterization and Testing Service Center (NCTC). For the microscopic investigations, a field emission scanning electron microscope (FE-SEM), and a transmission electron microscope (TEM) analytical facility were used at the National Nanotechnology Center (NANOTEC). The FE-SEM instrument was Hitachi SU5000 combined with an energy dispersive X-Ray spectroscopy (EDX) for qualitative chemical analysis. The majority of TEM study was made by using a transmission electron microscope (JEOL model JEM 2100) also equipped with an energy dispersive X-Ray spectroscopy (EDX), this instrument was operated at 200kV acceleration voltage.

3. Results and Discussion

3.1 The macroscale analysis of plug ash in DPF

3.1.1. Ash accumulation in DPF

Figure 2 (A) presents the twelfth DPF segment in which the horizontal top wall has already removed. This segment has the total of 9 inflow channels, as indicated on the right-hand side of figure 2 (A). Ash in DPFs tends to loosely accumulate, as a brown brittle powdery, and entirely filled up at the end of inflow channels (plug ash). The asymmetrical can be observed in this sample as the plug ash lengths are varied depending on channels. Channel 1 has about 18 mm. which is a highest compare to others. The plug ash length drastically reduced to about 6.5 mm. in channel 7, however, the length gradually increased again to 7 and 7.3 mm. in channel 8 and 9, respectively. The amount of ash diminishing distinctively toward the inflow. The channels area without plug ash had a very thin ash layer (wall ash) attached on the channel wall, as well as deposited deep inside the surface pore along the filter length (figure 2 B). The mechanisms that altered ash particles from the channel walls to the end plug consists of flow-induced transport and regeneration-reduced transport [6]. Flow induced transport is a detachment and transport of ash particles by a shear force from the exhaust that can overcome the force of adhesion between the particle and filter wall (or neighboring particles).

Figures 2. Accumulation of plug ash inside the DPF.

During the regeneration process, soot cake continuously oxidized from the bottom [10]. The adhesive force between soot and ash, as well as DPF substrate are reduced. As a result, ash particles detach from DPF surface and subsequent transport to the end plug. The term “regeneration-reduced transport” can be used to describe this phenomenon.

3.1.2. Ash distribution in DPF

Figure 3 presents plug ash length distribution in 16 segments of the DPFs. The horizontal axis represents “Segments number “in which each segment consists of 6-9 channels, depending on locations. The vertical axis represents plug ash length in millimeter (mm.). From this figure, deposited ash length fluctuates between 2-21 mm. with the average of 4.7 mm. from the 125 mm. long filter channel. Ash distribution in most of segments were corresponding to the asymmetrical parabolic flow profile. At the filter center, ash length is varied between 2 to 8 mm., no significance difference of ash deposition in the same DPF segment. However, there were some significant increase of ash deposited length at the outer channel in the segments numbers 8,12 and 16 which are close to filter periphery. The maximum length is up to 21 mm. which is almost 5 times more than the average. Previous study [11] on morphology and size of ash PM from the light truck DPF, found such a contradict result that the center part contained higher amounts of ash deposited than the periphery. One Possibility is the unique design of DPF inlet pipeline which is a characteristic of each vehicle. Thus, resulting in the difference inflow pattern inside the DPF.

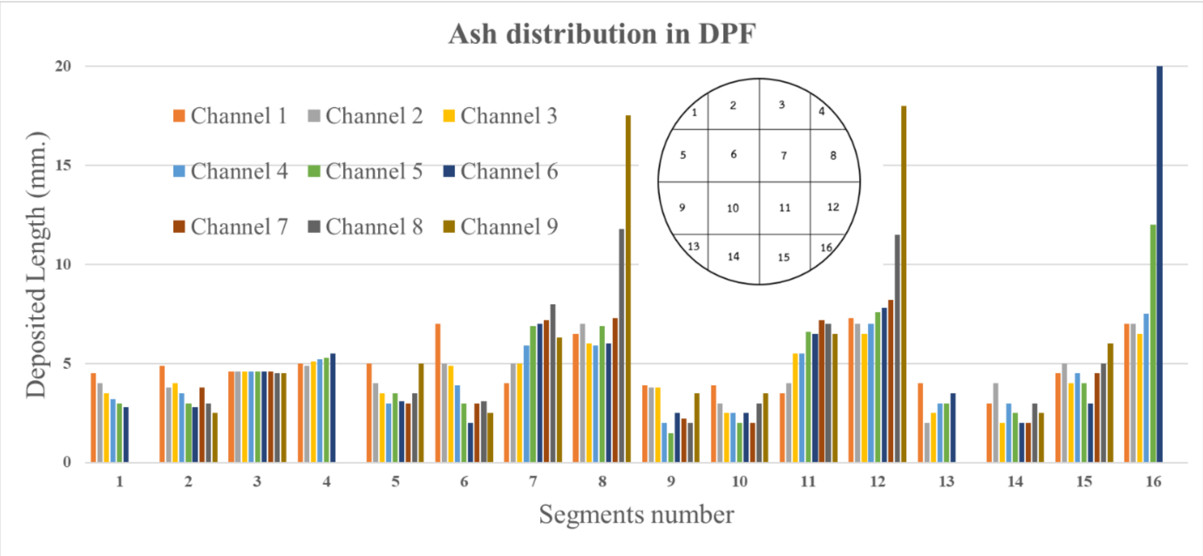

Figure 3. Ash distribution and deposited length inside the DPF.

3.2 The microscale analysis of ash powder

3.2.1 XRD analysis of DPF material

Before further investigation on ash elemental composition, the material analysis of DPF need to be conducted. Thus, a small piece of DPF was cut and made approximately 2 g. into a powder for XRD analysis. The main composition of this DPF is SiC as shown in XRD spectra figure 4. There is no signal of catalyst materials such as Pt, Pd, therefore, it can be concluded that the investigated DPF in this experiment is a non-coated type.

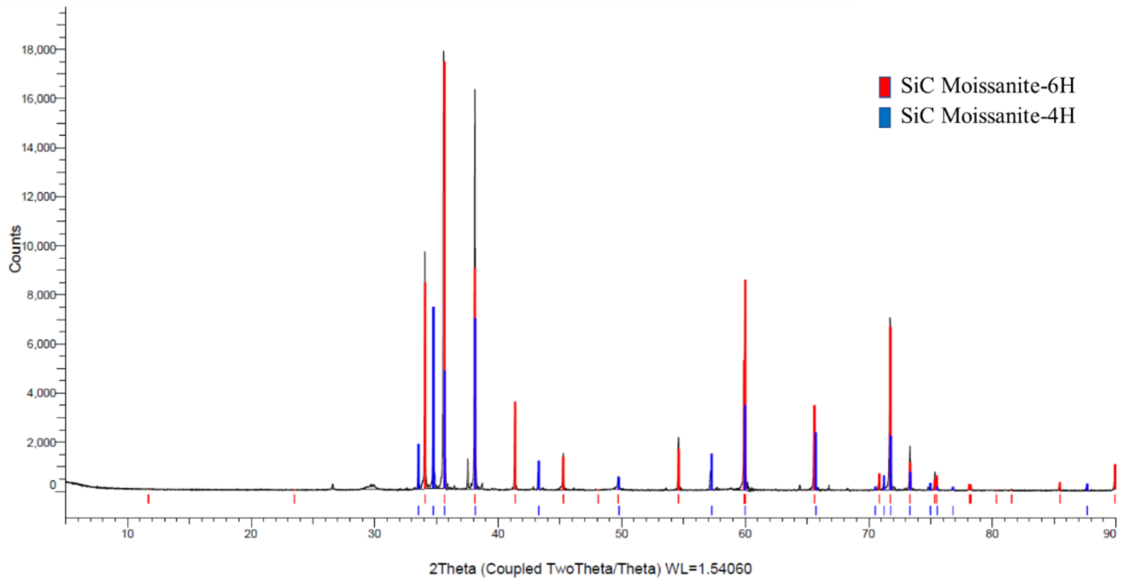

Figure 4. XRD spectra analysis of DPF material.

3.2.2 XRF and XRD analysis of ash components

Table 1 presents XRF analysis of elemental contained (wt.%) in ash sample. From the XRF result, the large proportion elements constitution of ash are Fe, Si, Ca, Cu, S, P, Zn, and Al which often presents in forms of $Cu_{0.5}Zn_{0.5}Cr_{1.1}Fe_{0.9}O_4$, $Ca(SO_4)$, Fe_2O_3 and $Ca_{19}Cu_2(PO_4)_{14}$, as shown in XRD spectra result (figure 5). It is well-known that metal oxide ashes mainly derived from metal in the diesel fuel, engine wear, and lubricating oil. Sine Fe is the main constituent of ash, it is expected that a majority of Fe might produce from the fuel-borne additive (ferrocene) which is the Fe-based catalyst used to reduce the soot ignition and burning temperature. Another possibility is that Fe with minor Ni and Cr may originate from the engine wear which blended in lubricating oil [12].

Table 1. XRF elemental analysis of ash powder.

Elements	Wt%	Elements	Wt%
Fe	30.88	Zn	7.46
Si	16.18	Al	4.78
Ca	10.88	K	1.17
Cu	9.47	Ni	0.99
S	9.16	Cr	0.71
P	7.92	Mn	0.41

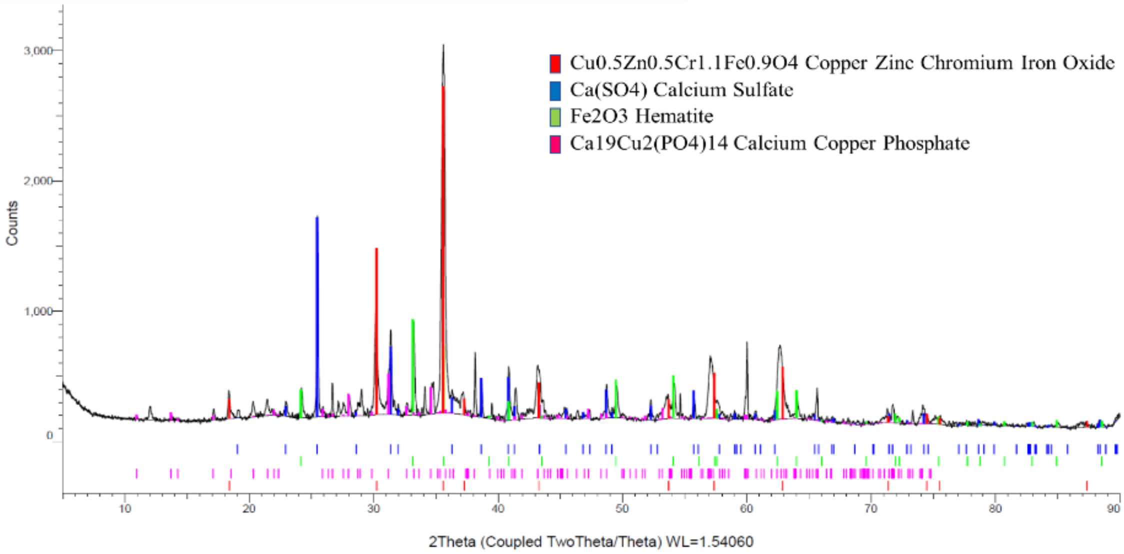

Figure 5. XRD spectra analysis of elements contained in deposited ash.

3.3.3 SEM-EDS imaging of ash particles

Figure 6 presents SEM image (A) and EDS elemental analysis (B) of Fe-oxide ash particle. This nearly spherical particle, with approximately 5 microns. in diameter, is a common type ash found in this sample. The elemental analysis revealed that Fe and O are the major elements included in this particle while Cu, Si, Zn, Al, P, Ca also found as minor components. This particle generated during the melting of iron at 1538℃ in cylinder. A surface tension draws the molten material into is spherical shape and rapidly solidified [11]. As a result, this particle has a cubic aggregation on its surface. Subsequently, transported by the exhaust gas and deposited in DPF as shown.

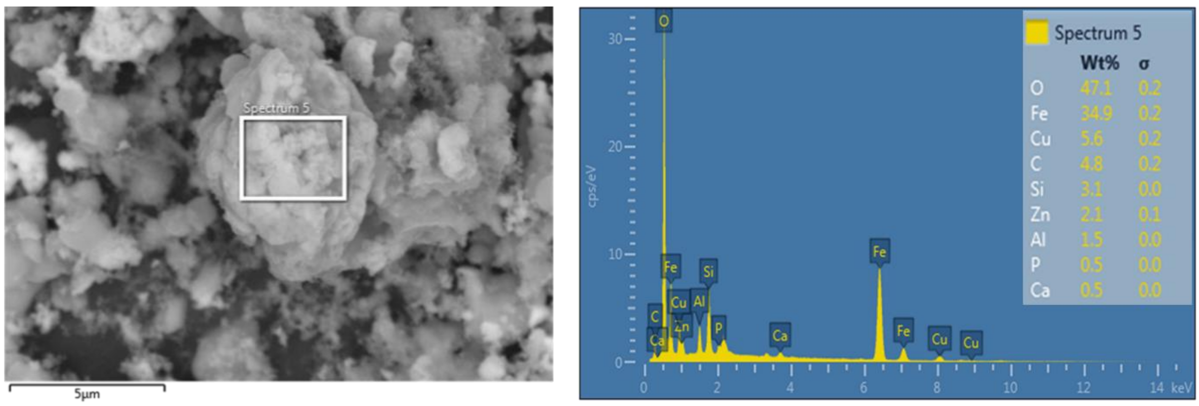

A B

Figure 6. SEM image (A) and EDS elemental analysis of ash particle (B).

3.3.4 TEM imaging

The bright field TEM image in figure 7 presents an agglomeration of ash particles with irregular round outlines shapes. Previous study suggested that this round ash particles derived from a condensation of hot combustion vapors from S which is a volatile species [13]. The right image (B) presents a higher magnification image of finer individual particle with approximately 25 nm. in diameter. A parallel straight-line hatch patterns can be clearly observed, indicated a crystalline structure which is similar to a nanostructure of metals. This particle has a strong tendency to form an aggregation, and resulting in a densification of ash particle caused by repeated regenerations.

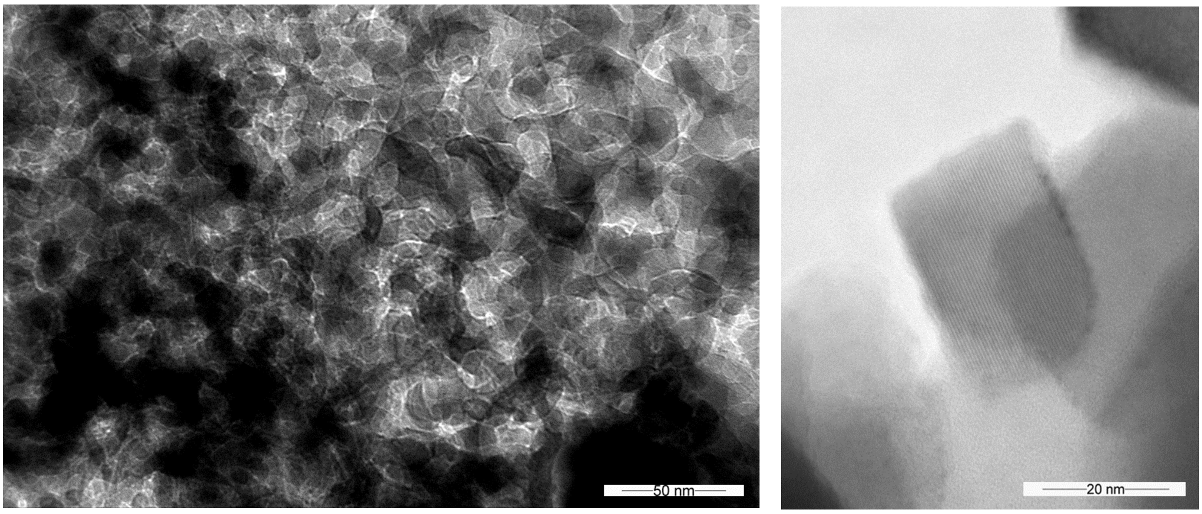

A B

Figure 7. Bright field TEM image of various agglomerated ash particles (A), and bright field TEM presents nanostructure of metal oxide ash (B).

The top left figure 8 presents bright field TEM image of ash agglomeration, the EDS elemental mappings also shown. The agglomerates usually have round outlines with irregular shape, as shown in the bright field TEM image. EDS spectra mappings show an inhomogeneous of elemental distribution. Elements of Fe, O, Zn, Al, Ni, Cr and S are found in greater amounts, while Ca and P show some local concentrated. The presence of Ca, S, P, Fe, Zn and O are usually in form of $CaSO_4$, $Zn_3(PO_4)_2$, $FePO_4$ and $Ca_3(PO_4)_2$ which are a common diesel ash [14]. The EDS spectra mappings reveal some interesting information of element distribution. P, S, Ca and O showed similar pattern, thus, formed compounds such as -O, -SO4 and -PO4 of Ca. Additionally, oxides of Fe, Al, Zn and minor Cr, Ni are considered to be the majority of ash compounds found within this sample. These compounds might be abrasion products of engine wear formed during movement of pistons. This inference is in compliance with previous XRD, XRF analysis of ash powder which also show the presence of anhydrite ($CaSO_4$), hematite (Fe_2O_3), as well as minor fragment of Ni and Cr.

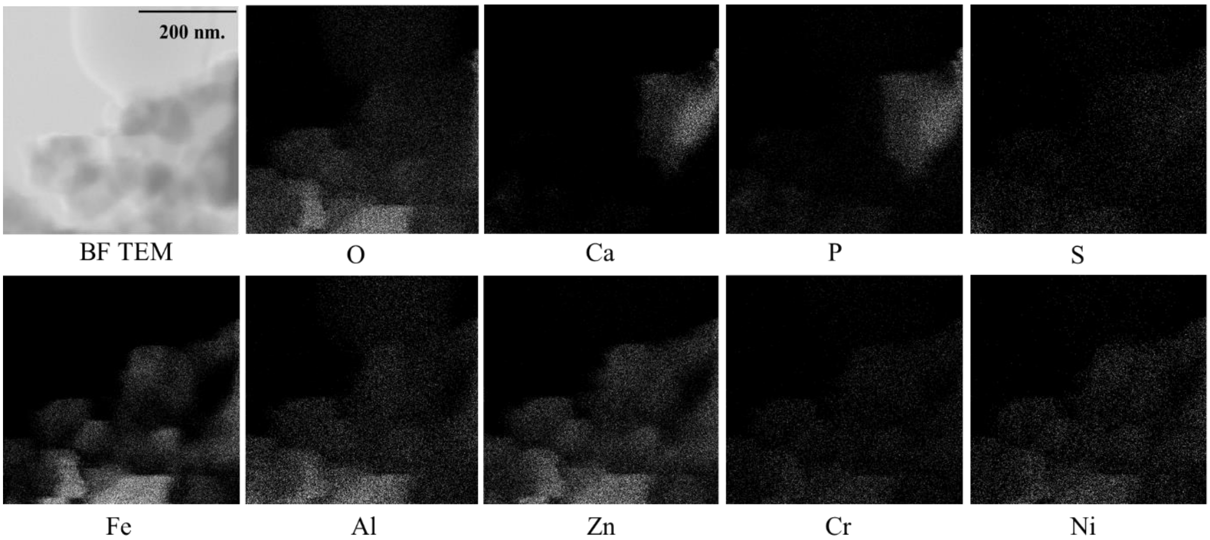

Figure 8. Bright field TEM image (Top-left) and EDS elemental distribution mappings.

4. Conclusion

The actual DPFs acquired from a diesel passenger car was disassembled for an investigation of macro/microscale analysis of metal oxide ashes. The macroscale analysis results found that ash entirely filled up the end plug of channels and distribution in most segments were corresponding to the asymmetrical parabolic flow profile. Much amounts of ash were deposited at the filter periphery with the maximum length of 21 mm. due to the unique design of DPF inlet pipeline. The XRF microscale analysis revealed that Fe is the main component of deposited ash on the SiC non-coated DPF, while XRD analysis confirmed the presence of $Cu_{0.5}Zn_{0.5}Cr_{1.1}Fe_{0.9}O_4$, $Ca(SO_4)$, Fe_2O_3 and $Ca_{19}Cu_2(PO_4)_{14}$. The TEM results confirmed that the agglomerated ashes are mostly round and consist chemically of Fe, O, Zn, Al, Ni, Cr, S and minor Ca and P in form of sulfates, phosphates and oxides. It was clarified that majority of ash components found within DPFs samples are oxides of Fe, Al, Zn and minor Cr, Ni. These components originated from engine wear metal, exhaust corrosion products, as well as fuel and lubricant additives. In the future, the further investigation on additive elements of fuel and lubricant oil will be helpful to precisely confirm sources of this deposited ash in DPF.

5. Acknowledgements

The authors would like to express their sincere appreciation for financial support from National Research Council of Thailand (Diesel Engine’s Particulate Matters Reduction using Ethanol-Biodiesel-Diesel Blends and Particulate Filter 398/2563), technical support from King Mongkut’s Institute of Technology Ladkrabang (KMITL) and National Science and Technology Development Agency.

6. References

[1] Plotkin, S. and Ribeiro, S. K. Energy Efficiency Technologies for Road Vehicles 2009; 2:125-137

[2] Heywood, J. B. Internal Combustion Engine Fundamentals. McGraw-Hill. Singapore; 1988.

[3] Bagi, S., R. Bowker, and R. Andrew. 2016. Understanding chemical composition and phase transitions of ash from field returned DPF units and their correlation with filter operating conditions. SAE International Journal of Fuels and Lubricants 9:239–59. doi:10.4271/2016-01-0898.

[4] Gao, J., C. Ma, S. Xing, L. Sun, and L. Huang. 2018. A review of fundamental factors affecting diesel pm oxidation behaviors. Science China-Technological Sciences 61:330–45. doi:10.1007/s11431-016-9117-x.

[5] Viswanathan, S., Rakovec, N., and Foster, D. ：Microscale Study of Ash Accumulation Process in DPF Walls Using the Diesel Exhaust Filtration Analysis (DEFA) System, ASME, ICEF 2012-92104, (2012)

[6] Sappok, A., Wang, Y. et al. ：Theoretical and Experimental Analysis of Ash Accumulation and Mobility in Ceramic Exhaust Particulate Filters and Potential for Improved Ash Management, SAE Technical paper, 2014-01-1517, (2014)

[7] Sappok, A. ：The Nature of Lubricant-Derived Ash-Related Emissions and Their Impact on Diesel Aftertreatment System Performance, PhD Thesis, Massachusetts Institute of Technology, 2009.

[8] Ishizawa, T., H. Yamane, H. Satoh, K. Sekiguchi, M. Arai, N. Yoshimoto, and T. Inoue. 2009. Investigation into ash loading and its relationship to DPF regeneration method. SAE International Journal of Commercial Vehicles 2:164–75. doi:10.4271/2009-01-2882.

[9] Sappok, A., I. Govani, C. Kamp, Y. Wang, and V. Wong. 2013. In-situ optical analysis of ash formation and transport in diesel particulate filters during active and passive DPF regeneration processes. SAE International Journal of Fuels and Lubricants 6:336–49. doi:10.4271/2013-01-0519.

[10] Rodvanna, S., Srilomsak, M., Mitsuhiro S., and Katsunori H.: Scanning electron microscopic time-lapse visualization of ash movement during regeneration of Diesel Particulate Filters, International Journal of Automotive Engineering, Vol. 11,No.2(2020).

[11] Liati, A., P. Dimopoulos Eggenschwiler, E. Müller Gubler, D. Schreiber, and M. Aguirre. 2012a. Investigation of diesel ash particulate matter: A scanning electron microscope and transmission electron microscope study. Atmospheric Environment 49:391–402. doi:10.1016/j.atmosenv.2011.10.035.

[12] Sappok, A., Wong, V., 2007. Detailed Chemical and Physical Characterization of Ash Species in Diesel Exhaust Entering Aftertreatment Systems SAE Technical Paper,2007-01-0318.

[13] Buhre, B.J.P., Hinkley, J.T., Gupta, R.P., Wall, T.F., Nelson, P.F., 2005. Submicron ash formation from coal combustion. Fuel 84, 1206e1214.

[14] Nemoto, S., Kishi, Y., Matsuura, K., Miura, M., Togawa, S., Ishikawa, T., Hashimoto, T., Yamazaki, T., 2004. Impact of Oil-derived Ash on Continuous Regeneration-type Diesel Particulate Filter- JCAPII Oil WG Report JCAPII Oil WG Report SAE Technical Paper 2004-01-1887.

AME0016

Study of Aerodynamic Characteristics of a Passive Morphing Airfoil

Tewa Khansiriwong[1,*] and Kitchanon Ruangjirakit[1]

Department of Mechanical Engineering, Faculty of Engineering, King Mongkut's University of Technology Thonburi, Bangkok, 10140, Thailand

* Corresponding Author: tewa.kh@mail.kmutt.ac.th

Abstract. This research aims to highlight aerodynamic characteristics of a passive morphing airfoil concept which utilizes pressure distribution acting on the upper and lower surfaces of the airfoil to change its shape. In this study, NACA 0010 airfoil is used as the base airfoil. The structure of the airfoil is hollow and leading edge and trailing edge of the airfoil are fixed. To evaluate the effects of shape change, three morphing strategies are proposed: upper surface morphing, lower surface morphing and both surfaces morphing. Lift coefficient, drag coefficient and lift-to-drag ratio are evaluated using XFoil for each morphing strategy. The results suggest that upper surface morphing provides better aerodynamic benefits than the lower surface morphing and both surfaces morphing. The upper surface morphing provides higher lift, lower drag and higher lift-to-drag ratio while the lower surface morphing provides lower lift, higher drag and lower lift-to-drag ratio. The lift and drag of both surfaces morphing are not significantly different with NACA 0010 at low angle of attack. The results from this study can be used to design suitable stiffness for upper and lower surfaces in order to achieve desired airfoil shape during operation.

1. Introduction

In recent years, morphing or adaptive airfoil concept has become an emerging technology due to its advantages in reduction of mechanical complexity and higher aerodynamic performance. The morphing airfoil can be defined as an airfoil which its shape can be seamlessly altered. There are several design approaches of the morphing airfoil depending on the requirements, design goals and applications. Flight envelope of aircrafts equipped with morphing wing technology can be extended and smooth transition during flight can be achieved and be used for multi-mission aircraft [1]. Apart from the applications in aircraft industry, morphing technology is also applicable to other applications such as small wind turbines and spoilers or aerodynamic parts of ground vehicles. The small wind turbines with morphing capability can delay stall through shape change at suitable point of operation; hence, more energy extraction is possible [2]. The car spoiler and aerodynamic parts can benefit from the morphing technology to sustain required downforce at different driving conditions [3].

The morphing concept can be divided into two main groups, which are active morphing and passive morphing. The active morphing uses actuator such as motor or force actuator to activate shape change. For the active morphing there are the several concept. The interested active morphing concept use the piezoelectric to control the flow separation around an airfoil [4]. The passive morphing utilizes aerodynamic loads to achieve desired shape through design of the internal structure [5], proper selection of skin material and design of skin stiffness [6]. The main advantage of the passive morphing concept is that complicated actuating mechanism is not required in order to enable shape change; therefore, small morphing applications that has the limitation of space for mechanism can be solved and designed by applying the surface morphing. However, the main challenge of the passive morphing airfoil is to identify suitable shape change in various operating conditions.

The aforementioned benefits of the morphing wing airfoil in various applications lead to the main concept of this paper, which aims to study passive morphing concept in details and investigate aerodynamic characteristics of a NACA0010 airfoil section with upper surface morphing, lower surface morphing and both surfaces morphing using numerical analysis through XFoil in order to obtain suitable shape change strategy at different conditions. The results from this study will highlight the extent of benefits of the morphing airfoil over a baseline NACA0010 airfoil.

2. Model Setup

In order to investigate the aerodynamic characteristics of the morphing airfoil, NACA 0010 airfoil section is used as a baseline. The upper surface and the lower surface are morphed in turn to NACA 0015 and NACA 0020, respectively. Then, both surfaces are morphed continuously in a similar manner as the single surface morphing mentioned above. The summary of all airfoil shapes as well as the designated name of each configuration are shown in Figure 1. In this study, XFoil, which was developed using panel method [7], is used as a computational tool to explore the characteristics of each 2-D airfoil configuration. The analysis is conducted in viscous mode and the airfoil is discretized into 200 panels. The lift and drag coefficients as well as the lift-to-drag ratio for each configuration are computed at angles of attack ranging from 0 to 20 degrees.

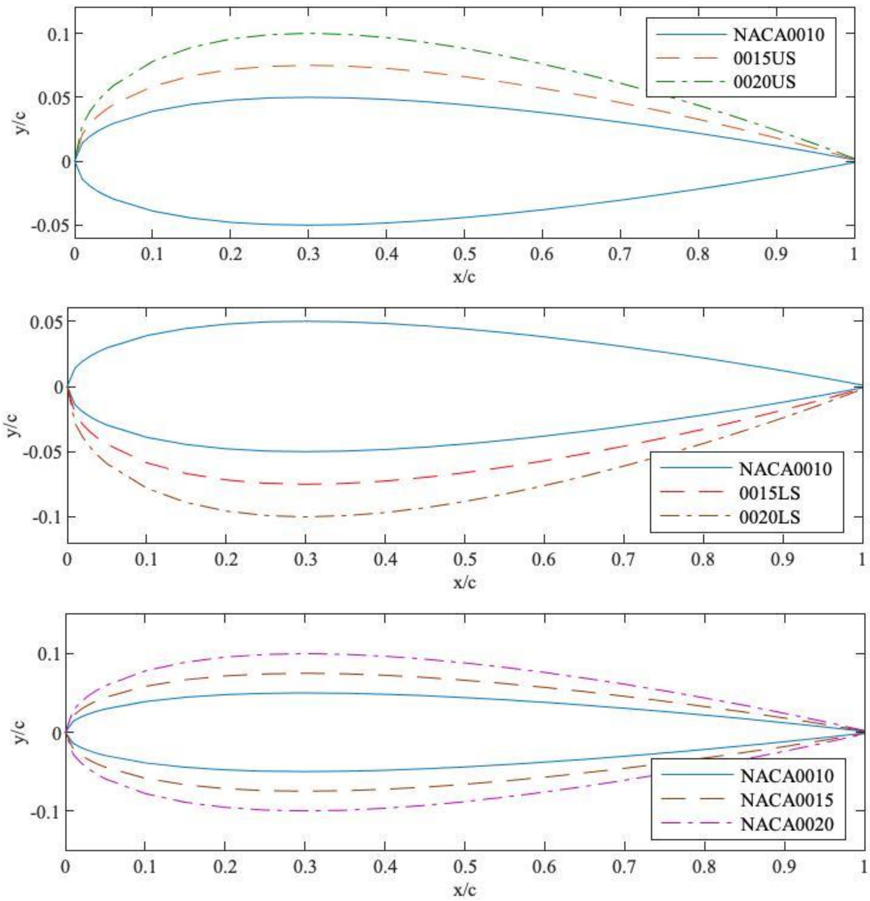

Figure 1. Shape and designated name of each morphing configuration.

3. Model Validation

In order to confidently use XFoil [7] as a tool to study the aerodynamic effects of baseline NACA 0010 airfoil under various morphing configurations in this paper, NACA 0012 airfoil is modeled and tested using XFoil at Reynold's number of 6,000,000. Nodes are 200 nodes and Ncrit is equal 9 for this simulation. Then, the lift coefficient results are compared with the experimental results by Abbot and Doenhoff [8] as shown in Figure 2. It can be clearly observed that the computational and experimental results are in good agreement, especially at low angles of attack. At higher angles of attack, the experimental results show earlier stall point than the numerical results because XFoil uses the panel method, which complex turbulence models are not included. Therefore, near wall skin friction drag cannot be correctly captured. However, for this study, the aerodynamic characteristics computed using XFoil are considered sufficient to provide useful benefits of morphing airfoil technology.

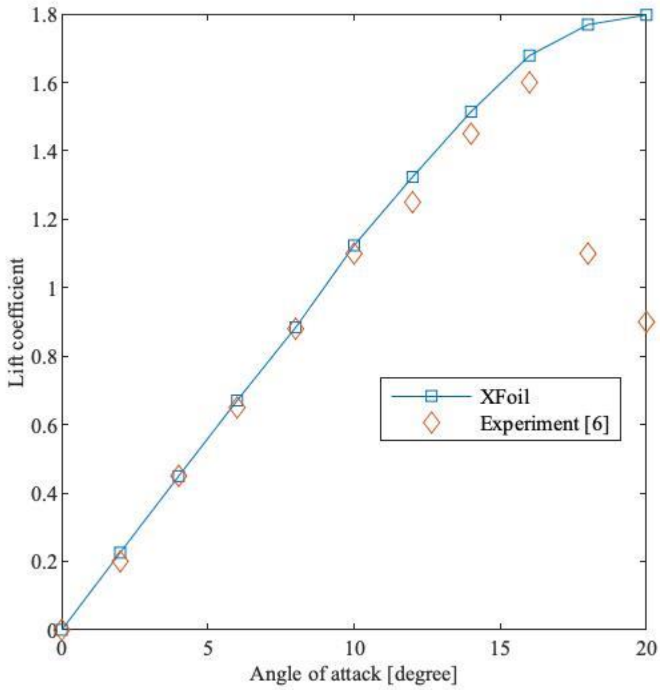

Figure 2. Comparison of lift coefficient of NACA 0012 airfoil between XFoil and experiment.

4. Result and Discussion

The results of upper surface morphing of NACA 0010 airfoil at Reynold's number of 100,000 are presented in Figure 3. All strategies of morphing use 200 nodes and Ncrit is equal 9 for simulation. It can be clearly observed that a higher lift coefficient and lower drag coefficient as well as delayed stall are achieved through deflection of upper surface. This is due to an increase in camber, which results in a change in aerodynamic characteristics of the airfoil. In terms of lift-to-drag ratio of upper surface morphing as shown in Figure 3., 0015US and 0020US gives higher lift-to-drag ratio than the NACA0010. As a result, morphing the upper surface of NACA0010 to 0015US and 0020US, respectively, provides better aerodynamics characteristics. When investigating the effects of freestream velocity, two values of Reynold's number are considered: 500,000 and 1,000,000. As the velocity of the air flow increases, the lift and drag coefficients of the unmorphed configuration becomes relatively similar to those of morphed configurations, especially at low angle of attack. However, when comparing the lift-to-drag ratio of the unmorphed and morphed configurations, it is found that the upper morphing airfoil can provide favorable aerodynamic benefits.

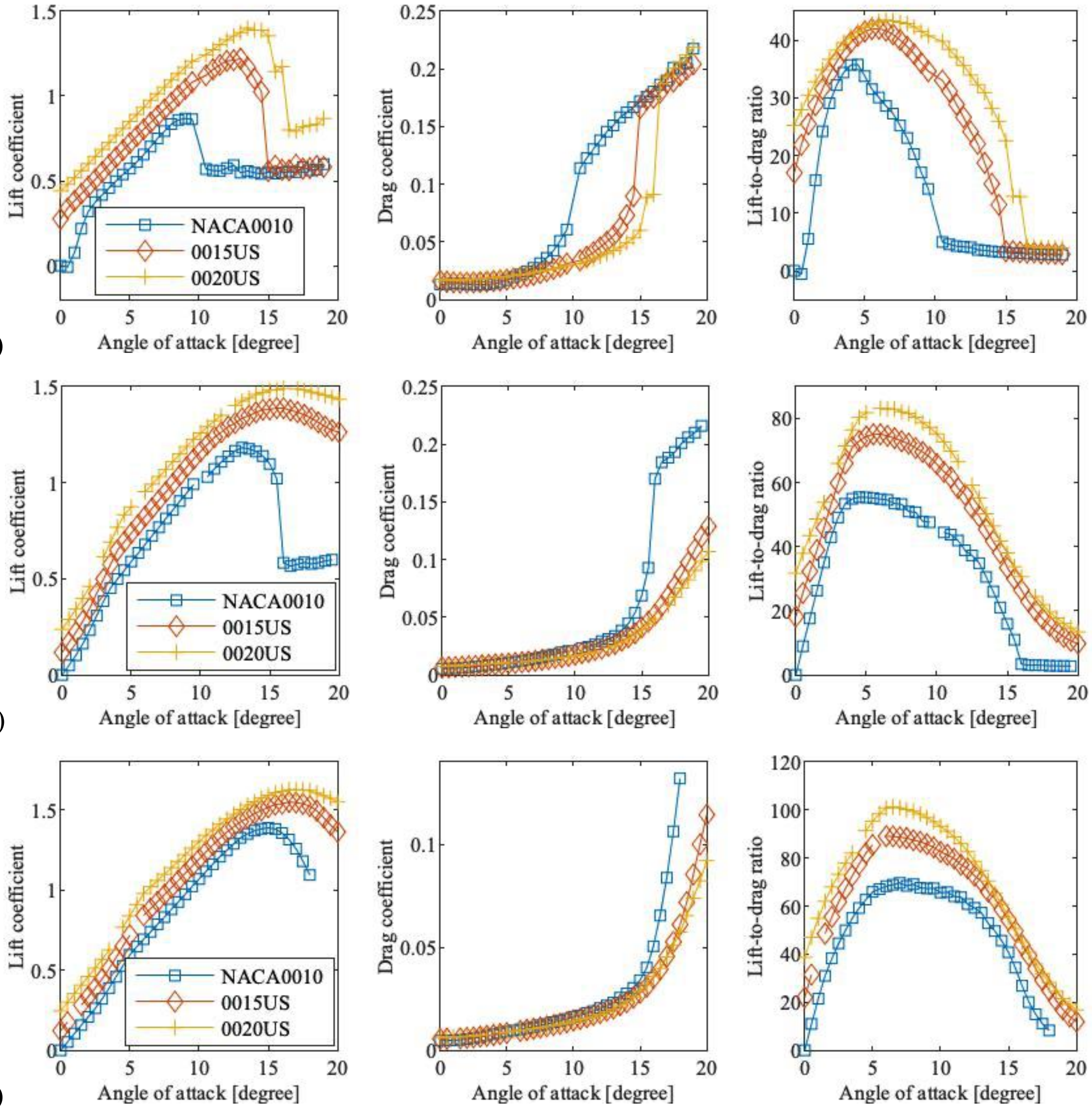

(a)

(b)

(c)

Figure 3. Aerodynamic characteristics of upper surface morphing airfoil at (a) Re = 100,000 (b) Re = 500,000 (b) and (c) Re = 1,000,000.

For the lower surface morphing, it provides opposite effects of the upper surface morphing. The lift coefficient and lift-to-drag ratio of 0015LS and 0020LS are less than 0010 at all angles of attack. Therefore, the lower surface morphing is not an attractive morphing approach.

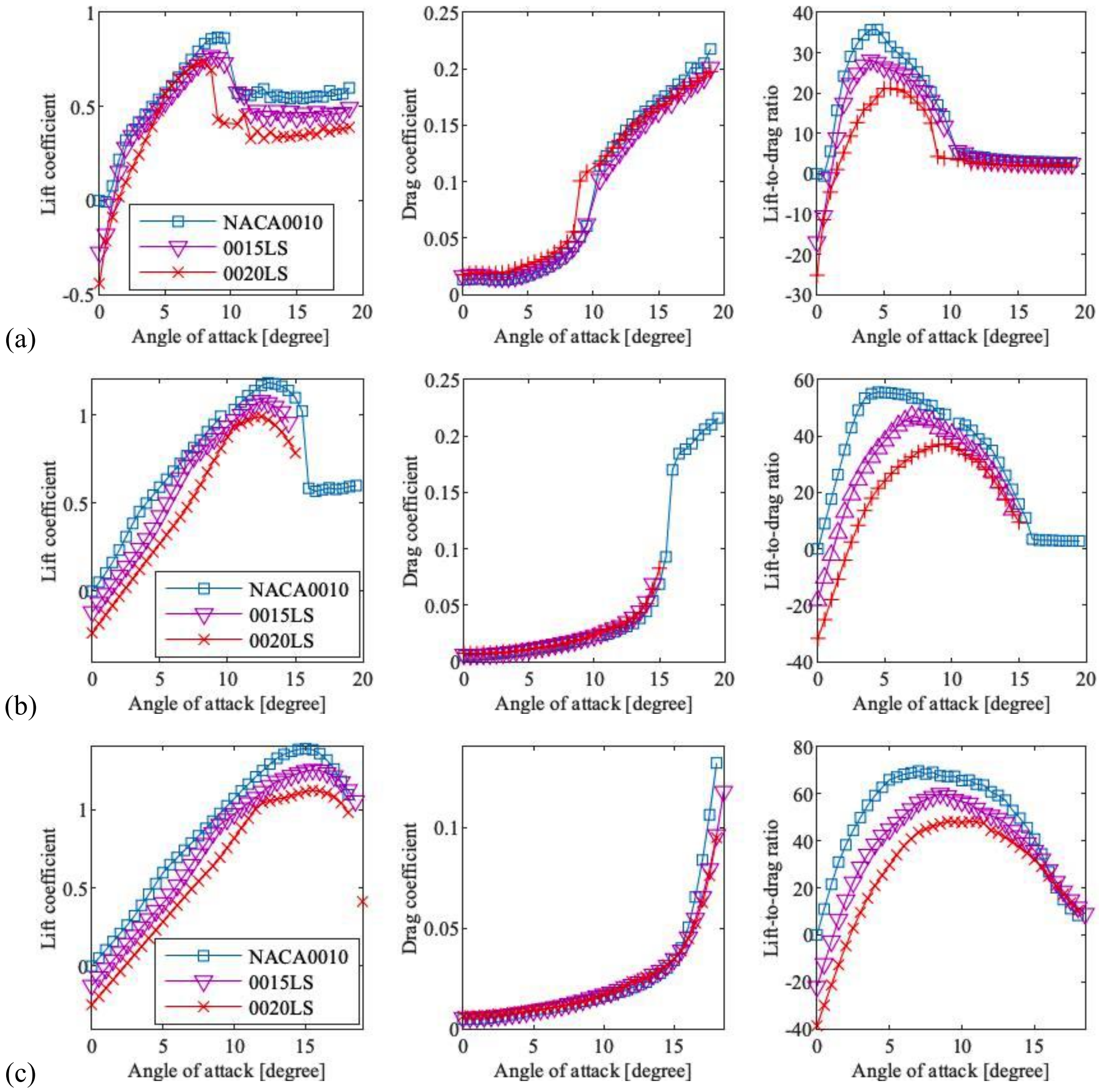

Figure 4. Aerodynamic characteristics of lower surface morphing airfoil at (a) Re = 100,000 (b) Re = 500,000 and (c) Re = 1,000,000.

For both surfaces morphing, the lift coefficient of NACA0010, NACA0015 and NACA0020 are not significantly different but NACA0015 and NACA0020 airfoils provide higher stall angle. For drag coefficient, NACA0015 and NACA0020 sections exhibit less drag than the NACA0010 airfoil at high angle of attack. In terms of the lift-to-drag ratio, NACA0010 shows the best lift-to-drag ratio at low angle of attack, while at high angle of attack, NACA0015 and NACA0020 provide better lift-to-drag ratio. Therefore, the advantages of using both surfaces morphing cannot be clearly identified.

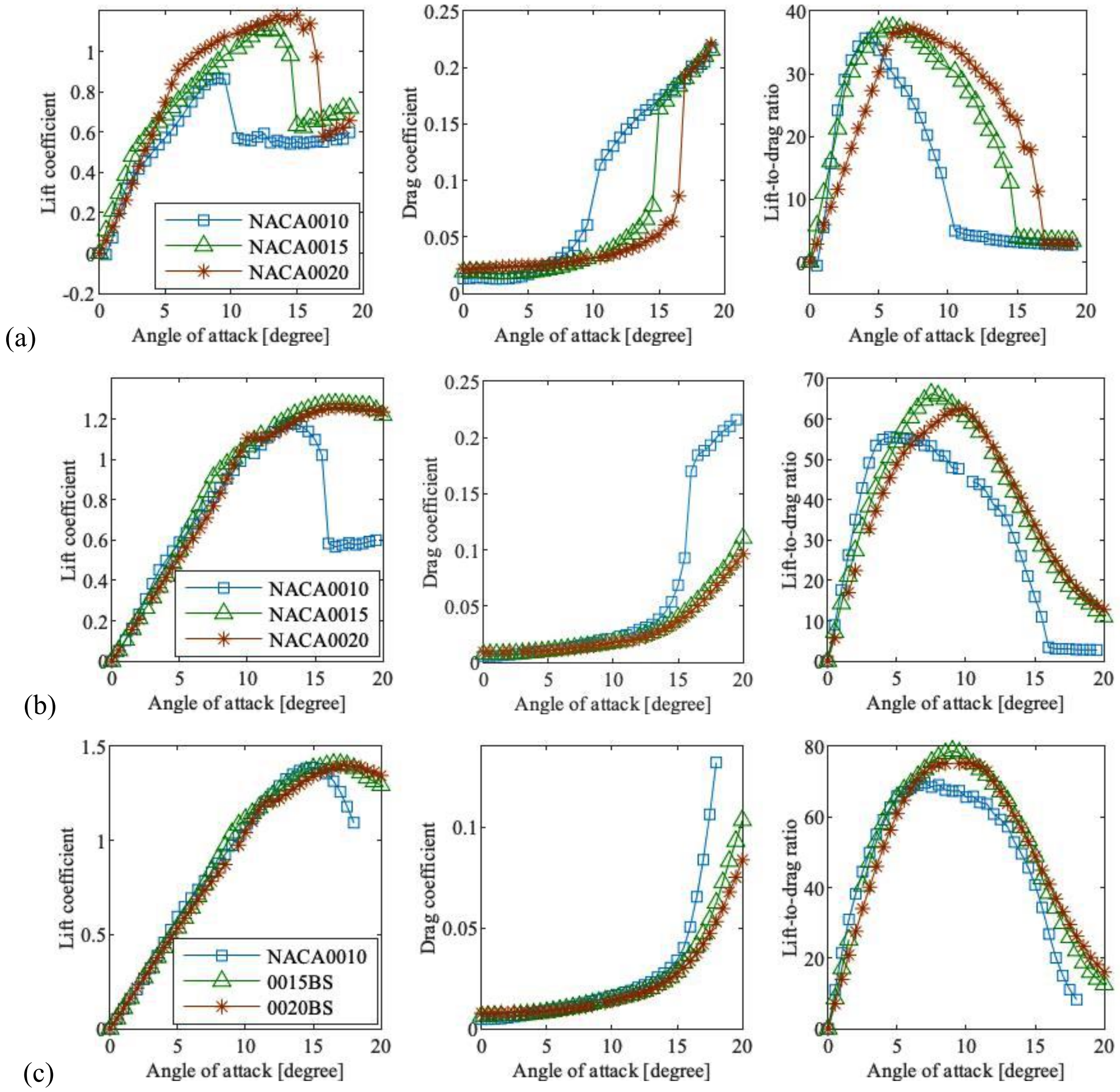

Figure 5. Aerodynamic characteristics of both surfaces morphing airfoil at (a) Re = 100,000 (b) Re = 500,000 and (c) Re = 1,000,000.

In order to clearly identify the benefits of passive morphing concept and the most suitable morphing approach, the lift and drag coefficients and the lift-to-drag ratio of each morphing method are plotted against angle of attach as shown in Fig. 6. It can be clearly seen that the upper surface (US) morphing provides the highest lift and low drag, which results in the highest lift-to-drag ratio at every angle of attack. Hence, the upper surface morphing is the most suitable approach for passive morphing. The second suitable morphing approach is the both surfaces (BS) morphing. The most unfavorable morphing strategy is the lower surface (LS) morphing.

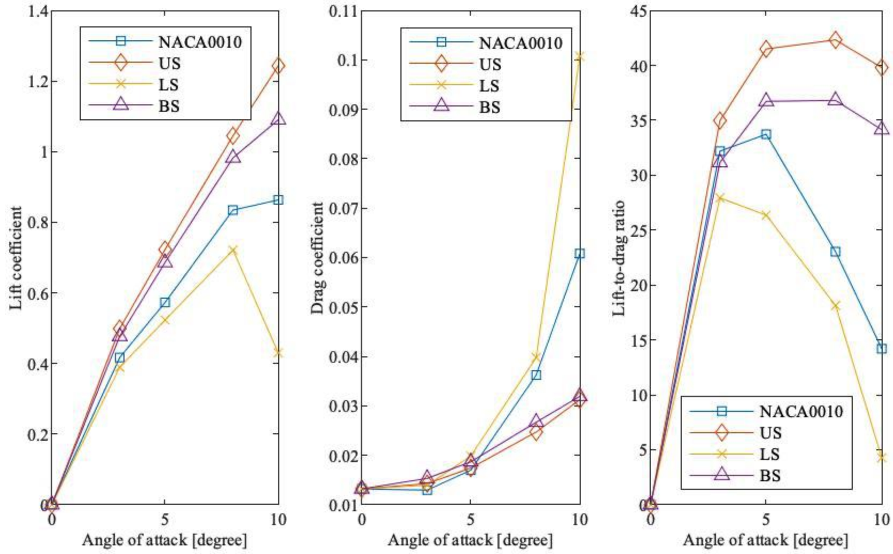

Figure 6. Comparison of different morphing approach at Re = 100,000.

5. Conclusion and Future Work

The morphing airfoil in this study is based on the concept that the airfoil can change the shape using pressure difference between the pressure inside and outside of the airfoil. The shape of the morphing airfoil can be controlled by designing proper structural properties. Three morphing strategies are investigated, which are upper surface morphing, lower surface morphing and both surfaces morphing. According to the results obtained from analysis using panel code implemented through XFoil, the upper surface morphing is the best strategy because it provides better lift coefficient, drag coefficient and lift-to-drag ratio as the angle of attack increases. The most unfavorable morphing approach is the lower surface morphing as it provides less lift and more drag than the NACA0010 airfoil used as a benchmark. The results from this study provide preliminary analysis of aerodynamic characteristics of the passive morphing airfoil concept in order to identify the best morphing approach and shape. Further steps in the designing of the passive morphing airfoil is to investigate suitable skin material and thickness to achieve desired shape change. If the suitable skin material and thickness of this passive morphing airfoil can be design, this passive morphing airfoil may be the choice for the small application that can not apply the mechanism of the morphing airfoil.

References

[1] C. Thill, J. Etches, I. Bond, K. Potter and P. Weaver, 2008, morphing skin.
[2] Xavier Lachenal, Stephen Daynes and Paul M. Weaver, 2012, Review of morphing concept and materials for wind turbine blade applications.
[3] Stephen Daynes and Paul M. Weaver, 2013, Review of shape-morphing automobile structure: concept and outlook.
[4] G. Jones, M. Santer, M. Debiasi, G. Papadakis, 2017, Control of flow separation around an airfoil at low Reynolds numbers using periodic surface morphing.
[5] Hyeonu Heo, Jaehyung Ju, 2013, Compliant cellular structure: Application to a passive morphing airfoil
[6] Diangui Huang and Guoqing Wu, 2012, preliminary study on the aerodynamic characteristics of an adaptive reconfigurable airfoil.
[7] Mark Drela, 1989, XFoil: An analysis and design system for low Reynolds number airfoils.
[8] Ira H. Abbott and Albert E. Von Doenhoff, 1959, theory of wing sections including a summary of airfoil data, General publishing company, Ltd., publish in Canada, p.462

AMM0006

Development of Cassava Pulp Belt Filter-press Squeezing Machine

B Nopphawong Na Ayutthaya[1], M Polsongkram[1], W Apisitpinyo[1], A Wongniyom[1]. and, P Khantikomol[1*]

[1] Renewable Energy Technology Research Laboratory (RTER)
Department of Mechanical Engineering, Rajamangala University of Technology Isan, 744 Suranarai Rd., Muang, Nakhonratchasima, 30000, Thailand

* Corresponding Author: preecha@rmuti.ac.th

Abstract. This article aims to propose the development of cassava pulp belt filter-press squeezing machine. The series of roller pairs were used to squeeze the cassava pulp. Five initial moisture contents were varied as 70, 75, 80, 85, and 90 (%w.b.). Five rolling belt gapes were varied as 0.50, 0.75, 1.00, 1.25, and 1.50 mm. The belt speed ware varied 5 values as 0.3, 0.4, 0.5, 0.6, and 0.7 m/s. The rollers were varied 5, 6, 7, 8, and 9 pairs. Finally, the cassava pulp feed rates were varied 5 values as 0.1, 0.2, 0.3, 0.4, and 0.5 kg/s. The experimental results indicated that the removed moisture content and the moisture removing efficiency decrease with increasing the initial moisture content, the belt speed, the rolling belt gap, and the feed rate.

Keywords: Cassava pulp, Belt filter-press, Squeezing machine, Removed water efficiency.

1. Introduction

The information from Office of Agricultural Economics [1] reported in 2019, the cassava planted over 8 million rais of land in 48 provinces with total products over 30 million tons per year. The almost 80% crop was developed to be cassava starch product [2]. From the report of Thai Tapioca Starch Association of Thailand, Nakhon Ratchasima province is highest crop area and yields of the Northeast region of Thailand. In Nakhon Ratchasima province, there are 27 starch factories for Cassava roots developed to the starch. The massive waste from manipulative process is going to water treatment for environment. For the cassava pulp, generally, the manufacturing waste is left moisture content approximately 60-80 (%w.b). The method to recovery these cassava pulps is very valuable. From Thai Agricultural Standard [3], the quality of cassava pulp is following requirements moisture content less than or equal to 14%, starch content greater than or equal to 35%, crude fiber content is less than or equal to 18% and sand / silica content less than or equal to 3%. The dewatering technique is applied to reduce liquid from cassava pulp. From literature, a study of thin layer drying model for cassava pulp [4] using model BINDER Inculcator BD 53 with initial moisture content of cassava pulp 80% was undergone at temperature 50, 60 and 70ºC and monitoring mass of cassava pulp at interval 20 minute until mass constant. Hence, the increasing drying time decreases for moisture ratio. Drying temperature decreases for drying time. Oluwole A. Odetunmibi et al [5] studies the effects of kinetics properties to drying cassava industries;

namely, the drying temperature, drying air velocity, and dewatering time. The each of property has 5 levels, and the experiment was recreated three times. for the interesting outputs, drying rate and drying time obtained, were observed. In summary, the time of drying is depended on the remaining liquid, which performed dewatering, the initial moisture content, and increasing initial moisture content as well. The air velocity increases the capability drying process. Finally, the drying kinetics influenced to these processing parameters. In mechanism topic for dewatering such as main centrifuge, extrusion and belt press filter. The belt press filter method; that is, the effective technique in removing moisture well and inexpensive. The technique uses belt-press cassava pulp squeezing machine was studied [6] by the initial moisture content was varied 85, 90 and 95 (%w.b.). Moreover, the belt speed varied 0.5, 0.6 and 0.7 m/s. The experimental results reveal that, the removed water efficiency decreases with increasing the initial moisture content and the belt speed, but low efficiency dewatering performance. In this study, the development of the belt-filtered cassava pulp squeezing machine uses compressing belt which is high flexible and absorbent water less properties; while, be feeding system for cassava pulp.

Nomenclature

M_w	Wet standard moisture content (%w.b.)
w	The mass of the material before drying (kg)
d	The mass of the material after drying (kg)

2. Theory

To develop and complete the Cassava Pulp Belt Filter-press squeezing machine, research data and equipment function have to study. This chapter is about the research results and the working principles of the devices involved in this project. The moisture determination of the cassava pulp samples referenced to ASTM D3173, which have two methods namely the dry and the wet basic. The Wet method is the ratio between the weight of water to the total weight of the sample and the Dry method is the ratio between wetted and dried mass sample. The Wet method is suitable for since wetted pulp. The method is drying by in a hot air oven at 105 °C for 24 hours (or until the mass of sample was remained constantly). The moisture quantity of cassava residue was determined by the Association of Official Agricultural Chemists (AOAC) has published standard method, at the wet standard moisture (Wet basic) method was shown in Equation (1)

$$M_w = \frac{w-d}{w} \times 100 \tag{1}$$

3. Experimental setup

In this section, the performance of the components are described the principle to fabricated the Cassava Pulp Belt Filter-press squeezing machine as shown in Figure 2.

First, wet cassava pulp was scaled for the initial moisture weight and was fed by polyester conveyor belt on through the squeezing mechanisms. For the dewatering process, the first roller pair is function to controls pressing belt which its force the wet pulp undergoes the specific gap between roller is the main driver ejects liquid out to drier pulp. The roller is distinctive with 18 mm holes mesh to contribute the liquid flow out easily and fall to the bottom tray, and accumulated liquid for the sewage system. After that, the others supporting rollers maintain to serve pressing and transporting to pulp by high tension belt conveyer. Lastly dewatering process, dried cassava sample have to scale for the ended moisture weight as the removed moisture content.

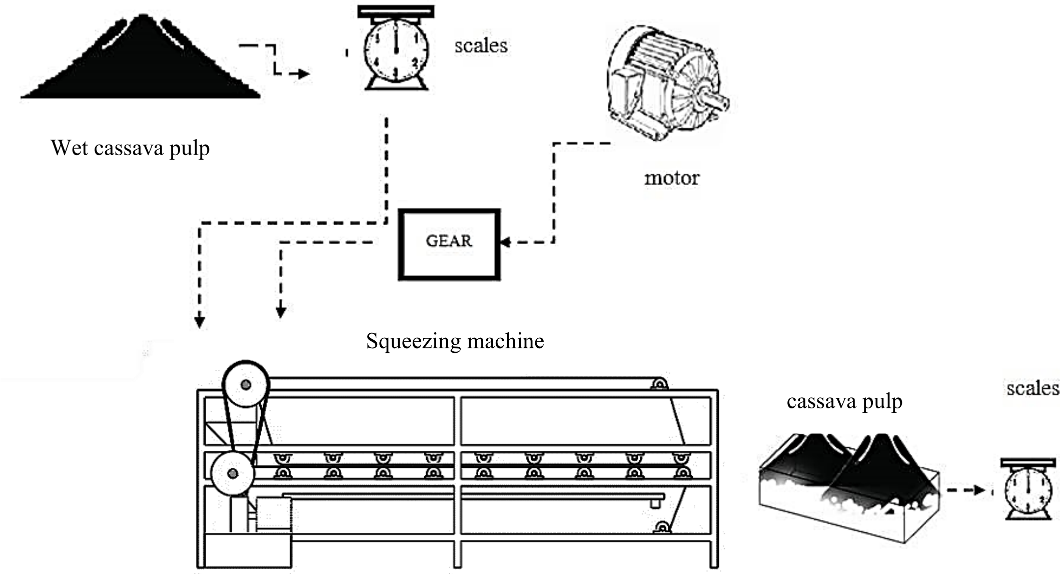

Figure 1 schematic diagram of equipment.

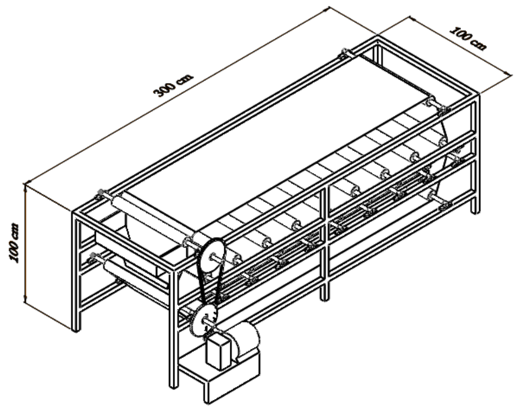

Figure 2 Cassava Pulp Belt Filter-press squeezing machine

4. Results and Discussion

This section shows the experimental results and the possibilities of the curve for each period.

4.1. Influence of Initial Moistures of Cassava Pulp

Figure 3(a) shows the curves of the removed moisture against the initial moisture content of cassava pulp. The initial moisture content, (Mi) from 70 to 90% w.b., and the rolling belt gaps are 0.25 mm step down from 1.5 to 0.5 mm. The most narrow gap engaged 70% w.b. was the maximum ability to remove liquid out of pulp, but the curve was gradually decrease, when initial moisture content was higher moisture. Similarly, the other variations, the curves of removed moisture content were gradually decrease contrast with the adding initial moisture content. That causes were the amount of liquid exceed from absorbable pulp and the without pressing from roller, due to pulp density was insufficient for pressing while.

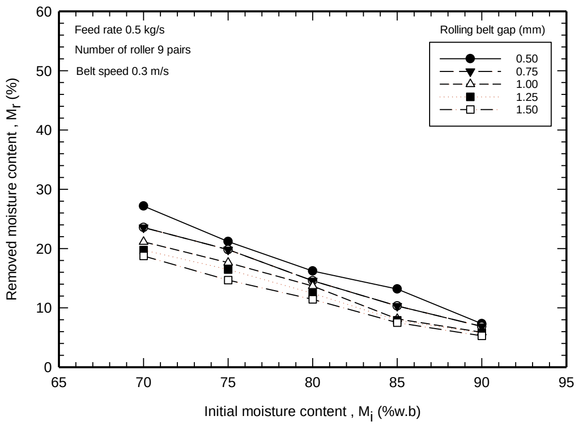

(a)

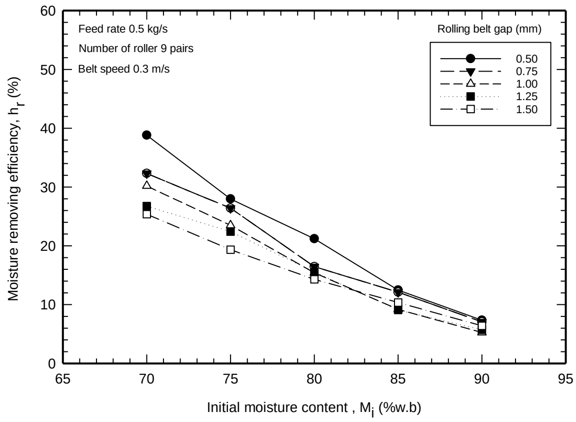

(b)

Figure 3 Influence of the initial moisture contents of cassava pulp to (a) removed moisture content and (b) moisture removing efficiency.

Figures 3(b) shows the moisture removing efficiency depend on the initial moisture content, and the rolling belt gap. The initial moisture content which was absorbed by cassava pulp, related to the ability of squeezing roller gap. 0.5mm gap and with 70% w.b. is the maximum of efficiency, because the moisture of cassava pulp can set shape, when it was pressed. After the increased more than 70 % w.b. the cassava pulp become almost wet matter which was exceed liquid from the cassava pulp absorption, and liquid spread out before pressing and may be muddy, that cause of the graph continuously down. Consequently, the initial moisture content that was amount of liquid which inside cassava pulp effects to the moisture removing efficiency.

4.2. Influence of belt speed.

The effect of the belt speed to the removed moisture content and the moisture removing efficiency, considered that the varied speed from 0.3 to 0.7 m/s., 0.5 to 1.5 mm rolling belt gap, and 70% w.b. initial moisture content are the conditions. The result reveals the percentages of the removed moisture content in each gap are only different in 1-2%, and the 0.5 mm of rolling belt gap is most effective to squeeze cassava pulp for removed liquid, show in Figure 4(a). Consequently, the effect of the belt speed is less effect to percentage of the removed moisture content changing. Similarly, the moisture removing efficiency undergoes the varied belt speeds, the narrowest gap distinguish in whole belt speed. The dewatering process ended on compression roller pair, although the speed was increased, the efficiency still gradual. Therefore, the belt-speed just transports the pulp matter out of the dewatering process. In the point of efficiency, the belt speed reduces cassava pulp moisture after left from the dewatering process, show on Figure 4(b). After ended pressing, the reconstructing pulp mechanism was reduced moisture by air around pulp surfaces. Consequently, the lower belt-speed enhances the moisture removing efficiency.

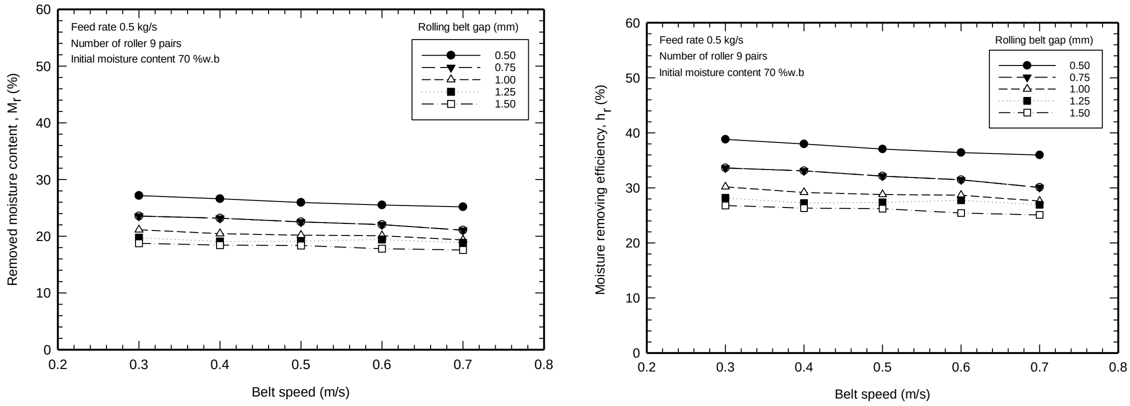

(a) (b)

Figure 4 Influence of belt speed to (a) removed moisture content and (b) moisture removing efficiency.

4.3. Influence of rolling belt gap.

The rolling belt gap is a vital parameter in dewatering process. The fit gap for pulp moves through the rolling, and ejected liquid out from the pulp, simultaneously. The gap varied from 0.5 to 1.5 mm., 0.5 kg/s feed rate, and set constantly 0.3 m/s belt-speed. The result reveals in Figure 5(a), the 0.5 mm. gap is the highest of removed moisture content for whole of initial moisture content. When the gap was increased, the removed liquid was gradually. In part of higher moisture, the graph tend was gradually, and appeared almost flat line in 90 % w.b. initial moisture content. For the highest moisture indicated that, the narrowest gap in performance inability to press muddy pulp. The tends in Figure 5(b) seem like in Figure 5(a), the moisture removing efficiency grows up, due to the rolling belt gap was reduced to contribute pressing domination.

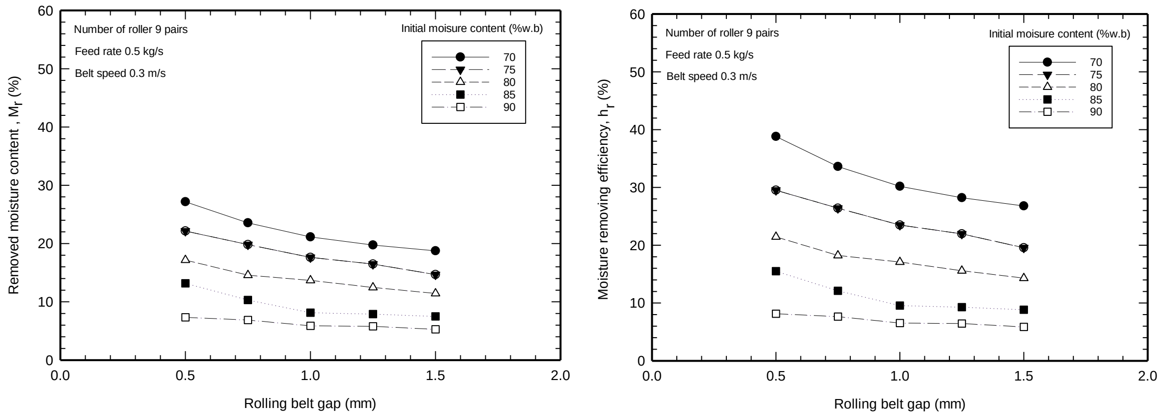

(a) (b)

Figure 5 Influence of rolling belt gap to (a) removed moisture content and (b) moisture removing efficiency.

4.4. Influence of Number of Roller pairs.

Figure 6(a) shows the influence of number of roller pairs to the removed moisture content and the removing moisture content efficiency. When the number of pairs of rollers was reduced, the moisture content was also decrease, and need to compensate time rolling operation. Obviously, the number of roller pair enhances removing moisture process.

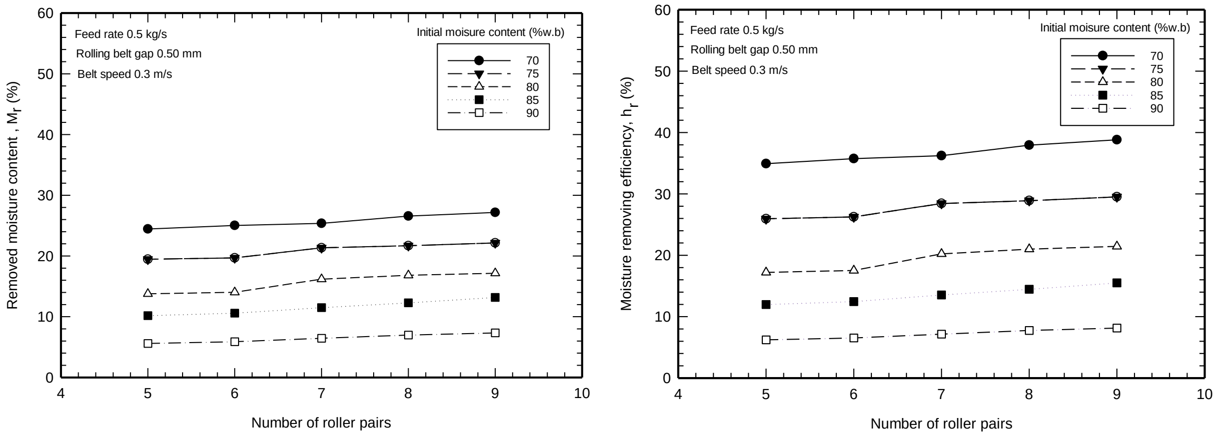

(a) (b)

Figure 6 Influence of Number of Roller pairs to (a) removed moisture content and (b) moisture removing efficiency.

Figure 6(b) explains that, the number of pairs of rollers effects to the amount of moisture removing efficiency. Accordingly, the removed moisture content and moisture removing efficiency enhancement was achieved by adding number of roller pairs.

4.5. Influence of feed rates.

The feed rate regulated the amount of cassava pulp into the dewatering process. The effect of overload not appeared through performance, since the gently pulp and the high power of the driver motor where occupies at first rolling pair. Instantly, the cassava pulp intake spread to the first rolling pair; consequently, the pulp was pressed to be flat. Therefore, the curves slightly rise and similarly tend, show on Figure 7(a).

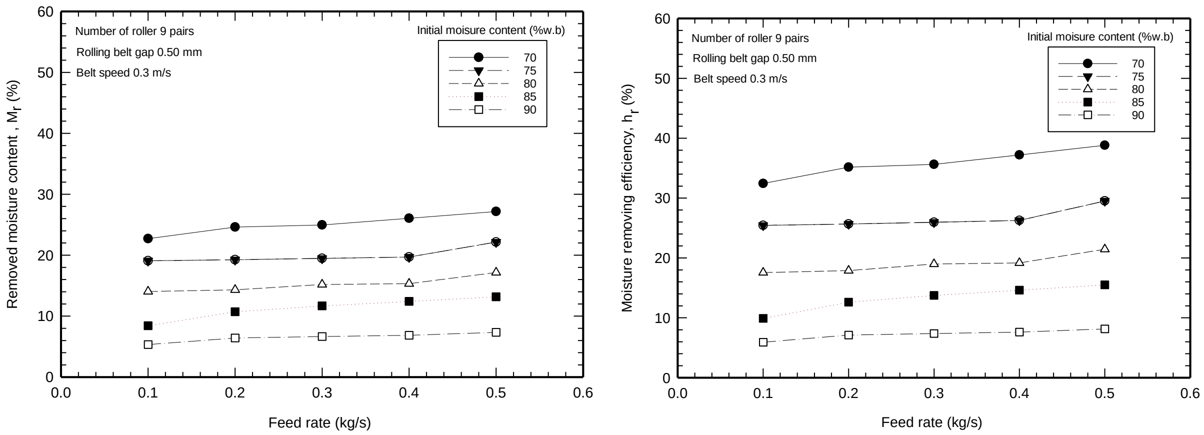

(a) (b)

Figure 7 Influence of feed rates to (a) removed moisture content and (b) moisture removing efficiency.

The removed moisture content and moisture removing efficiency curves are conformed, since the cause of feed rate is simple performed for feed matter. The feed rate contributed the efficiency and curve tend to grow up, consequently the initial moisture content is lower than 80% w.b., show no Figure 7(b), that mean, the efficiency can extend if feed rate is more developed, till to overload.

Conclusion

From a study, the development of cassava pulp belt filter-press squeezing machine and a test for the moisture removing efficiency of squeezing machine describe as follows.

The dewatering process for reduced liquid by pressing belts which are driven by rolling and motor unit consist of several parameters namely initial moisture content, rolling belt gap, belt speed, number of roller pairs, and feed rate. The vital part for generating pressing ejects liquid, drives the belt, and makes belt tension. The maximum efficiency is about 40% in all parameters. The maximum of each parameter explain as follows, 70% w.b. initial moisture content, 0.5 mm. rolling belt gap, 9 number of roller pairs, 0.5 kg/s feed rate, and belt speed is indifferent.

Acknowledgments

Thank you for the author of the article**.** Mr**.** Watthana Watchareerat**.** Mr**.** Mark Dulsanthia and Mr**.** Asadakorn Mekkhuang students in mechanical engineering Rajamangala University of Technology Isan to provided assistance in data collection trials and thank you to the Department of Mechanical Engineering Rajamangala University of Technology Isan that has provided funding and a place to study and perform this research until it has been successfully completed**.** wishing to acknowledge assistance or encouragement from colleagues, special work by technical staff or financial support from organizations should do so in an unnumbered Acknowledgments section immediately following the last numbered section of the paper.

References

[1] Office of Agricultural Economics. 2019. *Table showing details of cassava.* Retrieved Sep 10, 2020. From .www.oae.go.th/assets/portals/1/fileups/prcaidata/files/casava62.pdf

[2] Thai Tapioca Strach Association . 2020. *Tapioca Background*. Retrieved Sep 10, 2020. From. www.thaitapiocastarch.org/en/information/learning_industry/tapioca_background

[3] National Bureau of Agricultural Commodity and Food Standards. 2018. *Thai Agricultural Standard TAS 8803-2018.* Retrieved Sep 29, 2020. From http://web.acfs.go.th/standard/download/TAPIOCA-RESIDUE_TAPIOCA-BY-PRODUCT.pdf

[4] Suparerk Charmongkolpradit and Ratinun Luampon. 2017. *Study of Thin Layer Drying Model for Cassava Pulp*. *Energy Procedia*, 2017(138)**,** 354–359.

[5] Oluwole A. Odetunmibi et al. 2017. *Drying kinetic of industrial cassava flour: Experimental data in view. Data in Brief***,** 2017(15), 501-510.

[6] Benyapa Nopphawong Na Ayutthaya et al. 2020. *Study for Cassava Pulp Water Removing by Fabric Belt-press Squeezing Machine*

[7] ASTM International. (2011). ASTM D3173. *Standard Test Method for Moisture in the Analysis Sample of Coal and Coke.* West Conshohocken. PA

[8] Chainarong Simaworapongphan et al. 2018. *Study and Construct Cassava Pulp Squeezing Machine*. Thesis, Rajamangala University of Technology Isan, Nakhon Ratchasima.

AMM0007

Analysis and Optimization of Adhesive-Bonded Tubular-Coupler joint with Variable Stiffness Composite Adherend under Tension and Torsion Loadings

Marco Jongrakwattana[1,*] and Sontipee Aimmanee [1]

Advanced Materials and Structures Laboratory (AMASS), Center for Lightweight Materials Design and Manufacturing, Department of Mechanical Engineering, Faculty of Engineering, King Mongkut's University of Technology Thonburi, Bangkok, 10140, Thailand

* Corresponding Author: marco.j@mail.kmutt.ac.th

Abstract. This study aims to investigate an adhesive-bonded tubular coupler joint with a variable stiffness composite coupler. The adhesive-bonded joint is considered as an axisymmetric linearly elastic joint, which is under either uniform tension or torsion loading. The adhesive-bonded joint is composed of two cylindrical adherends, an inner isotropic adherend as well as an outer adherend made of composite material. Both adherends are bonded by a very thin adhesive layer. A mathematical model based on the three-dimensional elasticity is ulitzed for the adherends, whereas the adhesive is governed by the modified force equilibrium equations. To find the optimum variable fiber orientation in the outer adherend that minimizes adhesive stresses, the tubular coupler joint is divided into a finite number of small segments, each of which is assumed to have a uniform fiber angle. The results show that stress concentration in the adhesive bonded joint is significantly reduced for both the tension and torsion cases because nearly uniform load distributions in the adherends are achieved.

Keywords: Adhesive bonded joint, Variable-stiffness composite, Torsion, Tension, Stress concentration.

1. Introduction

Recently, adhesive and adhesion technology is an alternative solution to the conventional assembly such as fastening and welding because of light weight, low stress concentration, and high corrosion resistance. The structure assembly consists inner and outer adherends, which are joined together by an adhesive glue. There are many important literatures studying stresses in adhesive bonded tubular lap joints, which involve in the present study. For example, Lubkin and Reissner [1] studied adhesive stress distributions of tubular-lap joints under axial loading. Adhesive shear and normal stresses were predicted analytically. Pugno and Surace [2] analyzed and designed the optimum tubular bonded joint under torsion loading by modifying the joint profile. Both papers considered inner and outer adherends as isotropic materials. Regarding analysis of a fiber-reinforced composite adherend, Xu and Li [3] studied stress developed in adhesive-bonded composite joints by finite difference method without uniform stressed assumption in adhesive and adherends. Aimmanee, et. al [4] formulated a simplified mathematical model and investigated stress distribution of a tubular-lap joint under an axial loading. Aimmanee [5] also published a unified mathematical model for stress analysis in adhesive-bonded cylindrical coupler joints under three loading conditions, i.e. tension, torsion and internal or external pressure. The literature reviews show that stress distributions over adhesive bonding always accumulate and peak at either end of bondline due to load path and material discontinuities.

In order to reduce adhesive stress concentration, many studies paid attention on designing the optimum joints that modified geometry or properties of adherend for reducing adhesive stress concentration. Boss et al. [6] studied a single-lap composite joint under tension and compared the responses between modulus grading, varied fiber orientation, and geometry grading such as varied geometry thickness profile. The results show that changing fiber orientation offered an acceptable solution for reducing the adhesive stress concentration. Advanced manufacturing technology such as Automated Fiber Placement (AFP) and Continuous Tow shearing (CTS) [7] could apply for modulus graded composite adherend by varying fiber orientation. These advanced manufacturing techniques cause non-uniform elastic properties, also known as variable stiffness properties. Aimmanee and Hongpimolmas [8] proposed a theory to design a variable stiffness composite tubular coupler joint subjected to torsion by varying fiber orientation that enables the effective reduction in adhesive stress concentration. As a refined and extended work, a present study aims to develop a highly accurate mathematical model to analyze the adhesive-bonded tubular-coupler joint with variable composite adherend under either a tension or a torsion loading. The adhesive-bonded joint considered is composed of two cylindrical tubes, an inner isotropic tube and an outer tube made of composite material. Elasticity theory of a laminated cylindrical structure is utilized to capture the behaviors of relatively thick adherends. Formulation of the tubular-lap joint model, results obtained and conclusions will be discussed in the following sections.

2. Elasticity theory of a laminated cylindrical structure

An adhesive-bonded coupler joint configuration is shown in figure 1(a). The adhesive-bonded joint consists of the inner tube (adherend 1) made of an isotropic material and the outer coupler tube (adherend 2) as *N*-layer laminated composite material. The adherends are joined with very thin adhesive layer. Due to the symmetry of the coupler joint, the model can be analyzed in half around the middle as shown in figure 1(b). The elasticity theory developed in [5,9] is applied to calculate the stresses and displacements in the adherends. The coordinates (x, θ, r) is adopted as shown in figure 2. The coupler is considered as a symmetric-balanced($[\pm\theta]_s$) composite material with varying fiber orientation along the x direction. Similarly, the inner isotropic material adherend can also be calculated the same way by letting N = 1.

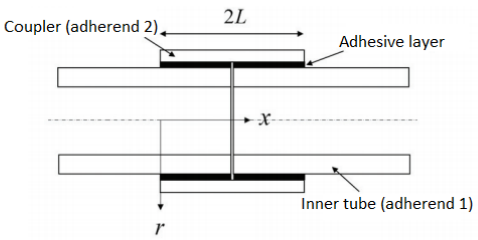

Figure 1(a). Full coupler joint model.

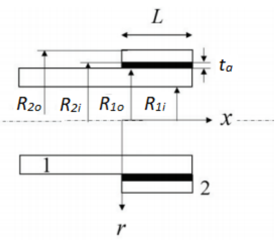

Figure 1(b). Half coupler joint model.

Three displacement directions of k^{th} layer laminated cylindrical tube are expressed in table 1 as follows: axial ($u^{(k)}$), tangential ($v^{(k)}$) and radial ($w^{(k)}$) displacement directions. Note that subscript k defines the layer number of the laminated tube. From three laminated displacements, there are *2N+2* unknowns need to be solved to obtained the adherend elastic responses, i.e. ($\varepsilon_x^0, \gamma_{x\theta}^0, A_1^{(1)}, A_2^{(1)}, \dots, A_1^{(N)}, A_2^{(N)}$). The quantities ε_x^0 and $\gamma_{x\theta}^0$ are axial strain and angle of twist per unit length, respectively, and $A_1^{(k)}, A_2^{(k)}$ are integration constants of the k^{th} layer. Therefore, all the unknowns require *2N+2* equations to satisfy. Four equations are obtained from force and torque (F and T) equilibrium equations and surface normal traction (p_i and p_o) boundary conditions. The remaining 2*N-2* equations are obtained from normal traction and displacement continuity at the interface between each layer [5,9].

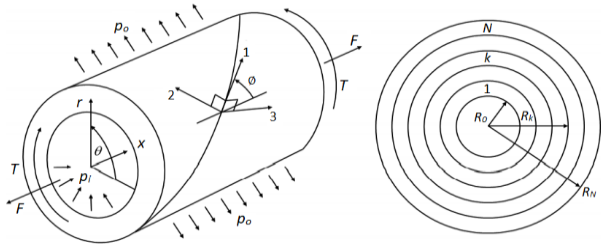

Figure 2. A laminated cylindrical tube and coordinates.

After utilizing the abovementioned boundary conditions, the equilibrium equations of the *N*-layer laminate can be written in term of global stiffness matrix as listed on the right side in table 1. k_{ij} $(i, j = 1, 2, 3, \ldots, 2N+2)$ are stiffness coefficients obtained from the 2*N*+2 satisfied equations [5]. Consequently, the 2*N*+2 unknowns can be solved and the laminated displacements can be evaluated as illustrated on the left side in table 1. These layer displacments will be applied in the adhesive governing equation presented in next section.

Table 1. Laminated displacements and Global stiffness matrix equation.

Laminated displacements		Global matrix equation
Axial direction	$u^{(k)}(x)=\varepsilon_x^0 x$	$$\begin{bmatrix} k_{11} & k_{12} & k_{13} & \cdots & k_{1,2N+2} \\ k_{21} & k_{22} & k_{23} & \cdots & k_{2,2N+2} \\ k_{31} & k_{32} & k_{33} & \cdots & k_{3,2N+2} \\ k_{41} & k_{42} & k_{43} & \cdots & k_{4,2N+2} \\ \vdots & \vdots & \vdots & \ddots & \vdots \\ k_{2N+2,1} & k_{2N+2,2} & k_{2N+2,3} & \cdots & k_{2N+2,2N+2} \end{bmatrix} \begin{Bmatrix} F \\ T \\ p_i \\ p_o \\ 0 \\ 0 \\ \vdots \\ 0 \end{Bmatrix} = \begin{Bmatrix} \varepsilon_x^0 \\ \gamma_{x\theta}^0 \\ A_1^{(1)} \\ A_2^{(2)} \\ \vdots \\ A_1^{(N)} \\ A_2^{(N)} \end{Bmatrix}$$
Tangential direction	$v^{(k)}(x,r)=\gamma_{x\theta}^0 x$	
Radial direction	$w^{(k)}(r)=A_1^{(k)}r^{\lambda(k)}+A_2^{(k)}r^{-\lambda(k)}$ $+\Gamma^{(k)}\varepsilon_x^0 r+\Omega^{(k)}\gamma_{x\theta}^0 r^2$	
where	$\lambda^{(k)^{*1}}=\sqrt{\dfrac{\bar{C}_{22}^{(k)}}{\bar{C}_{33}^{(k)}}}, \Gamma^{(k)^{*2}}=\left(\dfrac{\bar{C}_{12}^{(k)}-\bar{C}_{13}^{(k)}}{\bar{C}_{33}^{(k)}-\bar{C}_{22}^{(k)}}\right), \Omega^{(k)^{*3}}=\left(\dfrac{\bar{C}_{26}^{(k)}-2\bar{C}_{36}^{(k)}}{4\bar{C}_{33}^{(k)}-\bar{C}_{22}^{(k)}}\right)$	

*1, *2 and *3 Note that these parameters are in terms of components of the transformed stiffness matrix, $\bar{C}_{ij}^{(k)}$ [5,9].

3. Formulation of equivalent tubular-lap joint

3.1. Governing equations

The dimension of a tubular coupler lap joint is defined in figure 1(a). The adhesive thickness and the bonding length are denoted by t_a and L, repectively. Additionally, the adhesive is very thin compared to inner and outer adherends. Parameters R_{2i} and R_{2o} denote inner and outer radius of adherend 2, respectively. Similarly, paremeter R_{1i} and R_{1o} symbolize inner and outer radius of adherend 1. There are mainly two out-of-plane shear stresses that are considered in the adhesive for torsion and tension loadings: hoop shear stress ($\tau_{\theta r}^a$) for the former and longitudinal shear stress (τ_{xr}^a) for the latter. However, only tension loading needs to consider adhesive radial normal stress (σ_r^a) that is significantly coupled with tension loading [4]. The adhesive stress is considered as a uniform stress through the adhesive thickness. The present study initially uses the governing equations developed in the work of Aimmanee and coworkers [4,5,8]. As a result, the adhesive shear stresses $\tau_{\theta r}^a$ and τ_{xr}^a can be related with the internal resultant torque $T_2(x)$ and force $F_2(x)$ in adherend 2, which are listed on the left side in table 2. For torsion and tension governing equations displayed on the right side in the table, the additional adherend deformations associated with in-plane shear strain ($\gamma_{x\theta}$) and axial normal strain (ε_x) marked with **1* and **2* must be taken into account. This correction in the governing equations is done because the hoop and longitudinal shear stresses at inner and outer surfaces of both adherends presented in section 2 are orignially assumed to be zero, but the adherend-adhesive interaction causes the nonzero shear stresses. As also shown table 2, the normal traction in tension loading or the adhesive radial normal stress is considered to equal pressure distribution on the inner (p_{2i}) and outer (p_{1o}) surfaces of both adherends. Parameters E^a and G^a denotes adhesive young modulus and shear modulus, respectively.

Table 2. The governing equations for cylindrical tube.

	Adhesive stress	Governing equation
Torsion	$\frac{1}{2\pi R_{2i}^2}\frac{dT_2(x)}{dx}=\tau_{\theta r}^a=G^a\gamma_{\theta r}^a$	$\frac{d^2T_2(x)}{dx^2}=\frac{2\pi R_{2i}^2G^a}{t_a}\left[\left(\gamma_{x\theta}^{2i}+\frac{dv_{2i}}{dx}^{*1}\right)+\left(\gamma_{x\theta}^{1o}+\frac{dv_{1o}}{dx}^{*1}\right)\right]$
Tension	$\frac{1}{2\pi R_{2i}}\frac{dF_2(x)}{dx}=\tau_{xr}^a=G^a\gamma_{xr}^a$	$\frac{d^2F_2(x)}{dx^2}=\frac{2\pi R_{2i}G^a}{t_a}\left[\left(\varepsilon_x^{2i}+\frac{du_{2i}}{dx}^{*2}\right)+\left(\varepsilon_x^{1o}+\frac{du_{1o}}{dx}^{*2}\right)\right]$
Normal traction	$\sigma_r^{a*3}=E^a\varepsilon_r^a=p_{1o}=p_{2i}$	

*1 and *2 Note that these adherend deformations are caused by the influence of shear stresses in the adhesive.
*3 Note that adhesive radial normal stress is calculated from the constitutive relation in the adhesive.

3.2 Implementation of elasticity theory for adherends
The governing equations in table 2 are formulated to determine the resultant loads in adherend 2 and the adhesive shear stresses in the coupler joint. However, according to the global matrix equation in table 1, the resultant loads, T, F, p_i, p_o are coupled and must be solved altogether. To simplify this complexity, the problem is separated into two parts involving the primary and secondary effects of both loadings as conceptualized in Aimmanee and Hongpimolmas's works [4,8]. Consequently, the final form of the modified governing equations are listed in table 3. Note that the external applied torque (T) and force (F) equal $T = T_1 + T_2$ and $F = F_1 + F_2$, where subscript *1* and *2* define the resultant load in adherend 1 and adherend 2, respectively.

Table 3. Modified torque and force governing equations.

Torsion	Tension
$\frac{d^2T_2(x)}{dx^2}=K_TT_2(x)+K_C$	$\frac{d^2F_2(x)}{dx^2}=k_FF_2(x)+k_pp_{2i}(x)+k_c$
$;K_T=\frac{2\pi R_{2i}^2G^a}{t_a}\left(\gamma_{x\theta,T}^{2i\ *1}+\gamma_{x\theta,T}^{1o\ *1}+\frac{dv_{2i}}{dx}-\frac{dv_{1o}}{dx}\right)$	$;k_F=\frac{2\pi R_{2i}G^a}{t_a}\left(\varepsilon_{x,F}^{2i\ *2}+\varepsilon_{x,F}^{1o\ *2}+\frac{du_{2i}}{dx}-\frac{du_{1o}}{dx}\right)$
$;K_C=\frac{2\pi R_{2i}^2G^a}{t_a}\left(-\gamma_{x\theta,T}^{1o}T\right)$	$;k_p=\frac{2\pi R_{2i}G^a}{t_a}\left(\varepsilon_{x,p}^{2i\ *3}-\varepsilon_{x,p}^{1o\ *3}\right),k_C=\frac{2\pi R_{2i}G^a}{t_a}\left(-\varepsilon_{x,F}^{1o}F\right)$

*1, *2 and *3 Note that the terms are strains per unit torque, force and pressure, respectively.

3.3 Optimum fiber angle evaluation by finite segment method
The finite segment method [4,5,8] is a solution methodology that divides an adherend into a finite number in order to evaluate the optimum fiber orientation in each segment that as a whole equalizes adhesive shear stress into uniform fashion through overlap region instead of accumulating at the ends. This phenomenon is directly resulted from linear internal resultant load distribution. According to table 2, the adhesive stresses from torsion and tension loadings are constant if torque or force distribution in adherend 2 is linear (*Tx/L* or *Fx/L*). By implementing the finite segment method, the governing equations are modified into *n* segments as are shown in table 4. The purpose is to find the strain per unit load for minimizing adhesive shear stresses that are related to T_2 and F_2 as expressed in the general solutions in table 4. The strain per unit load is subsequently used to determine the corresponding fiber angle $\emptyset_2^{(i)}$ as delineated in [8]. Remark that fiber orientation within each segment is considered to be constant. The modified governing equations for n segment need 3n satisfied boundary and continuity conditions to

solve for 3n unknowns. All 3n boundary and continuity conditions are also shown in table 4, and subscript *i* denotes the i^{th} segment number.

Table 4. Governing equations and General solutions in finite segment form.

	Torsion	Tension
Governing equation	$\frac{d^2T_2^{(i)}(x)}{dx^2} = K_T^{(i)}T_2^{(i)}(x) + K_C^{(i)}$	$\frac{d^2F_2^{(i)}(x)}{dx^2} = k_F^{(i)}F_2^{(i)}(x) + k_p^{(i)}p_{2i}^{(i)}(x) + k_C^{(i)}$
General solution	$T_2^{(i)} = T_2^{(i)}\left(x; C_1^{(i)*a}, C_2^{(i)*a}, \gamma_{x\theta,T}^{2i(i)}(\phi_2^{(i)})^{*c}\right)$	$F_2^{(i)} = F_2^{(i)}\left(x; G_1^{(i)*b}, G_2^{(i)*b}, \varepsilon_{x,F}^{2i(i)}(\phi_2^{(i)})^{*d}\right)$
	$T_2^{(1)}(0) = 0, T_2^{(n)}(L) = T$	$F_2^{(1)}(0) = 0, F_2^{(n)}(L) = F$
	$\left.\frac{dT_2^{(i)}}{dx}\right\|_{x_i} = \left.\frac{dT_2^{(i+1)}}{dx}\right\|_{x_i} = \frac{T}{L}^{*e}, (i = 1,2,3,\ldots n-1)$	$\left.\frac{dF_2^{(i)}}{dx}\right\|_{x_i} = \left.\frac{dF_2^{(i+1)}}{dx}\right\|_{x_i} = \frac{F}{L}^{*e}, (i = 1,2,3,\ldots n-1)$
	$T_2^{(i)}(x_i) = T_2^{(i+1)}(x_i), (i = 1,2,3,\ldots n-1)$	$F_2^{(i)}(x_i) = F_2^{(i+1)}(x_i), (i = 1,2,3,\ldots n-1)$
	$\left.\frac{dT_2^{(i+1)}}{dx}\right\|_{x_n} = \frac{T}{L}^{*e}, (Boundary\ \&\ Continuity\ conditions)$	$\left.\frac{dF_2^{(i+1)}}{dx}\right\|_{x_n} = \frac{F}{L}^{*e}, (Boundary\ \&\ Continuity\ conditions)$

*a and *b Notes are integration constants in general solutions of torsion and tension loadings, respectively.
*c and *d Notes are required strain per torque and force that have relationship with fiber angle.
*e Note is the perfect condition for adhesive shear stress minimization.

4. Results and discussion

4.1 Model validation

In order to validate the developed methodology, the computational results obtained from the finite segment method for 40 segments is compared to the finite element analysis conducted in ABAQUS. The adhesive shear stresses are illustrated in figure 3 and 4 for both loadings. Adherend 2 is 4-layer symmetric balanced carbon/epoxy, adherend 1 made of steel, and epoxy used as an adhesive in the validation model.The mechanical properties and dimensional geometry of the coupler joint are described in table 5 and 6. The constant fiber angles of 45° and 0° in adherend 2 resisting the applied torque and force of 1 *N.m* and 1 *N* are considered for torsion and tension cases, respectively. The results show that the developed model gives very good agreement with the finite-element simulation along the entire bounding length except the small regions at the ends where differences are caused by the mesh sensitivity to the peak stresses in the finite-element analysis.

Table 5. Mechanic,al properties of coupler joint.

Properties	Epoxy(Adhesive)	Steel (Adherend 1)	Carbon/Epoxy (Adherend 2)
$E_1(GPa)$	1.30	200.00	128.00
$E_{2,3}(GPa)$	1.30	200.00	10.00
$G_{12,13}(GPa)$	0.46	76.90	4.49
$G_{23}(GPa)$	0.46	76.90	3.58
$\nu_{12,13}$	0.41	0.30	0.28
ν_{23}	0.41	0.30	0.47

Table 6. Dimensional geometry of coupler joint.

Geometry	Adhesive	Adherend 1	Adherend 2
Outer radius, R_{1o} (mm)	-	10	-
Bonding Length, L (mm)	40	-	-
Thickness, t (mm)	0.1	5	5

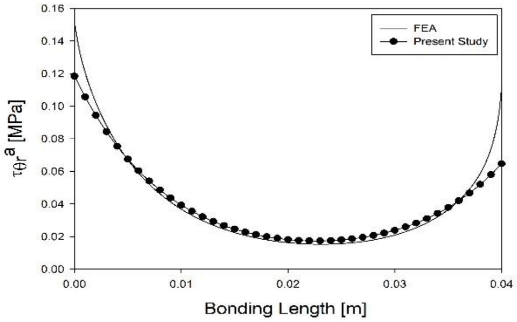

Figure3. Adhesive hoop shear stress in torsion case.

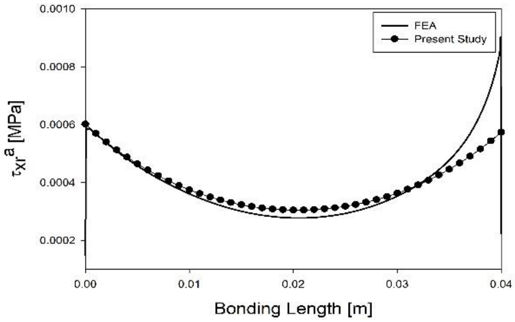

Figure 4. Adhesive longitudinal shear stress in tension case.

4.2 Adhesive shear stress minimization

From mathematical model, the optimum fiber angle for minimizing adhesive shear stress are shown in figure 5(a) and (b). It is seen that 40 segments is a sufficient number of secments for the convergent solution. The optimized fiber angle starts from 90º that yields the maximum corresponding strains for both loadings, making the left end area as the most compliant zone. Along the bonding length, the optimum fiber angle decreases (signifying increased stiffness) until to 45º and 0º that provide minimum strains for torsion and tension loadings, respectively, making the right end area as the stiffest zone. It should be noted here that the optimal fiber orientations plotted in the figure are not of the perfect coupler joints that possess the uniform adhesive shear stress in the two loading cases. The perfect joints require higher and lower strains than the unidirectional carbon/expoxy can provide in the compliant and stiff zone mentioned. Therefore, the cut-off constant fiber angles are employed near the both ends, and cause the resulting optimized joint to be different from the perfect joint. Figure 6(a) and (b) show that the distributions of the internal resultant forces obtained from the optimal variable stiffness adherends are closer to the linear load distributions than the constant fiber angle. Figures 6(c) and (d) on the other hand show the normalized adhesive shear stress as expressed in equation (1) and (2), where $\tau^a_{m,T}$ and $\tau^a_{m,F}$ denote the adhesive mean shear stress in the case of torsion and tension loadings respectively. The optimized solutions approach more closely to the uniform stress distribution occurring in the perfect joint than the constant fiber angle model. In conclusion, the adhesive shear stress minimization provides significant lower stress concentration at the left end and the slightly higher at right end of the both loadings.

$$\tau^a_{m,T} = \frac{T}{2\pi R_{2i}^2 L} \quad (1) \qquad \tau^a_{m,F} = \frac{F}{2\pi R_{2i} L} \quad (2)$$

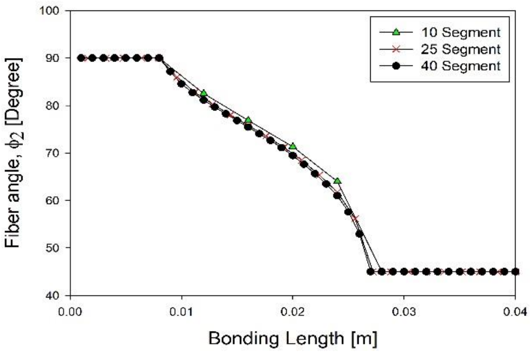

(a). Optimum fiber angle in torsion case.

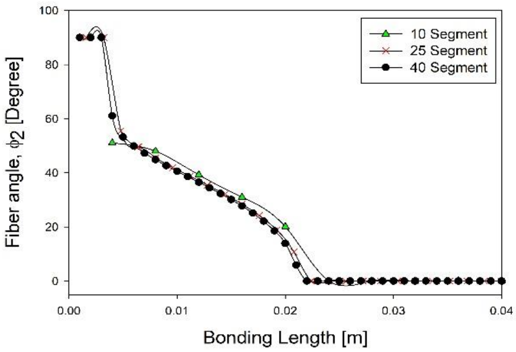

(b). Optimum fiber angle in tension case.

Figure 5. Optimum fiber angle in torsion and tension case.

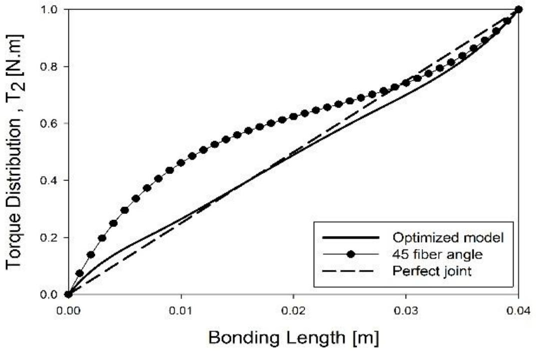

(a). Torque distribution in torsion case.

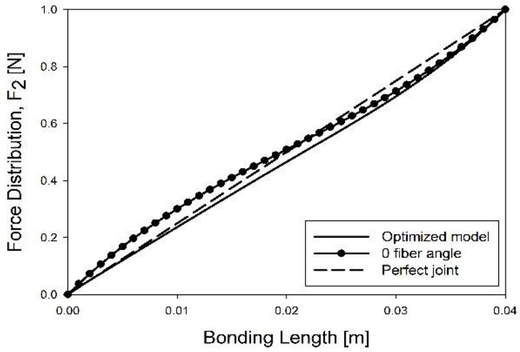

(b). Force distribution in tension case.

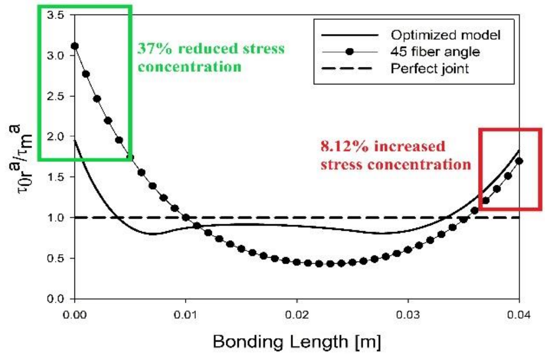

(c). Normalized adhesive hoop shear stress in torsion case.

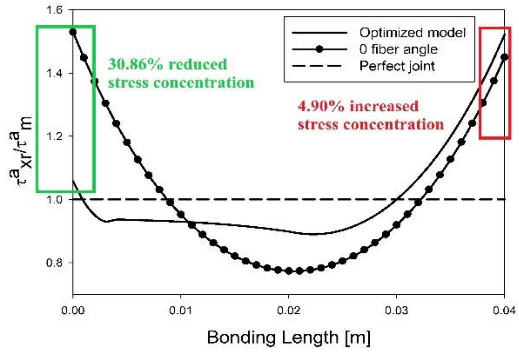

(d). Normalized adhesive longitudinal shear stress in torsion case.

Figure 6. Load distribution and normalized adhesive shear stress of adherend 2 in torsion and tension case.

5. Conclusions

The finite segment method solution is developed to evaluate the optimum fiber orientation in variable stiffness composite coupler. The purpose is to reduce the adhesive shear stress in the joint. The results show that the optimized fiber angles in overall can reduce the adhesive shear stress in both loadings considered. The stress concentration at left end is significantly decreased but the right end is slightly increased. Explicitly, the optimized joint models performs better than those composed of constant fiber orientations. However, due to the limitations of material properties the adhesive stresses cannot be minimized such that they are uniform over the entired bonding length mentioned as presented in the perfect joint conditions.

References

[1] Lubkin J.L. and Reissner E. 1956 *Transactions of the ASME* pp. 1213-1221
[2] Pugno N. and Surace G. 2001 *Journal of Strain Analysis* vol 36 No. 1 pp. 17-24
[3] Xu W. and Li G. 2010 *International Journal of Adhesion & Adhesives* vol 30 pp. 191-199
[4] Aimmanee S., Hongpimolmas P. and Ruangjirakit K. 2018 *International Journal of Adhesion and Adhesive* vol 86 pp. 59-72
[5] Aimmanee S. 2018 *Applied Adhesive Bonding in Science and Technology* chapter 2 pp. 11-31
[6] Boss J.N., Ganesh V.K. and Lim C.T 2003 *Composite Structures* vol 62 pp. 113-121
[7] Kim B.C., Potter K. and Weaver P.M. 2012 *Composites: Part A* vol 43 pp. 1347-1356
[8] Aimmanee S. and Hongpimolmas P. 2017 *Composite Structures* vol 164 pp.76-89
[9] Herakovich and Carl T. 1998 Mechanics of Fibrous Composites *USA: John Wiley& Sons, Inc* chapter 10 pp.362-380

AMM0013

An Investigation of Hybrid AL/CFRP Tubes with Fiber Orientation Angle Parallels to Its Axis

Chuangchai Chupava*, Chawalit Thinvongpituk and Komsan Rattankijsuntorn

Department of Mechanical Engineering, Faculty of Engineering, Ubon Ratchathani University, Ubonratchathani, 34190, Thailand

* Corresponding Author: pui2006me@gmail.com

Abstract. This study investigated the effects of fiber orientation on the axial impact characteristics of cylindrical aluminum tubes wrapped with carbon fiber reinforced polymers (CFRP). The tubes were made of aluminum 6063-T5 with a diameter of 44.45 mm, a thickness of 1.15 mm and a length of 100 mm. The outer surface of the aluminum tube was reinforced by wrapping epoxy carbon fiber. Effect of number of fiber/epoxy layers and fiber orientation on crush characteristic of specimens were investigated. The specimens were tested under impact loading using a drop-hammer of 30 kg at a speed of 6.9 m/s in axial direction. Progressive collapse, failure mode of specimens as well as reaction load were recorded for further investigation. The results revealed that the average and maximum loads of the hybrid tubes were higher than those of aluminum tubes without reinforcement. The stacking sequence and fiber orientation were found to have influence on failure mode and hence the crashworthiness behavior of specimens. The fibers with angle of 0 degree in outer layer of specimen provided higher value of maximum and mean loads than naked tube. However, their load value increments were not as high as those of 90 degree. The 1, 2, and 3-layer specimens with (0), (0,0), and (0,0,0) fiber/epoxy were found to resist lower impact load than those of other combinations. The average loads of hybrid tubes with (0), (0,0), and (0,0,0) fiber/epoxy were higher than those of naked aluminum tubes by 4.91%, 4.68% and 1.33% respectively. In addition, the maximum loads of those hybrid tubes were higher than aluminum tubes by 1.51%, 14.52% and 25.88% respectively.

Keyword: impact load, hybrid tube, carbon fiber, composite material, CFRP

1. Introduction

The choice of materials for a vehicle is the first and most important factor for automotive designs as it will keep passengers travelling in a car secure and even protect the important parts of vehicles during a crash. Recently, related studies focus on improving the energy absorption efficiency and reducing the vehicle weight. As a result, fiber reinforced polymers (FRP) are one of the most popular composite materials used in vehicle design as well as sports equipment and building structures due to the high strength-to-weight ratio. However, automotive design should not focus only on the weight of materials and fuel economy, but also the safety of the passengers [1].

Within the last decade, a number of studies were completed on the use of fiber reinforced polymer products for the strengthening of various metallic structures. Bambach et al. [2] conducted a set of tests on square hollow section (SHS) composite steel/CFRP tubes subjected to axial impact. Kathiresan et al. [3] examined the crushing behavior and energy absorption of glass fiber/epoxy resin composite overwrapped aluminum under low-speed collisions. Golzar and Poorzeinolabedin [4] investigated the impact resistance, strength and stiffness of composite glass fiber material used in the lateral structure of cars. Jung-Seok Kim et al. [5] studied the failure modes and energy absorption capabilities of different kinds of circular tubes made of carbon, Kevlar, and carbon–Kevlar hybrid fibers composites with epoxy resin. The test was conducted with a constant velocity of 10 mm/min with a load of 100 kN. It was found that the pipes made of carbon fibers provided the highest energy absorption, while unidirectional carbon fibers wrapped in unidirectional Kevlar fibers provided the largest material deformation. Some studies were also interested in studying the shape of composite material [6-9] and the failure mode of composite materials as well as the fiber orientation that affect the ability to absorb energy [9]. A number of researchers studied the shape of aluminum tube used to absorb energy and found that cylindrical tube has a good ability to absorb energy [9-10]. The finite element analysis and analytical results compared to the experiment were performed in order to know the effect of parameters that are used in composite material design [7-9]. The influence of fiber orientation on circular and rectangular hybrid tube was also investigated [11].

The present work aimed to investigate the influence of fiber orientation and the number of reinforced layers on the impact behavior of circular aluminum tubes reinforced with carbon fiber/epoxy under axial impact loading by a weight-drop test.

2. Research Methodology

2.1 Workpiece preparation

The specimens used in the study are composite cylindrical AL/CFRP tubes, as shown in Figure 1. They consisted of an inner layer of aluminum tubes (6063- T5) with a diameter of 44.45 mm, a thickness of 1.15 mm and a length of 100 mm. The outer surface of the aluminum tube was wrapped with unidirectional epoxy carbon fiber as a reinforced material of 300 g/m^2. For the adhesive, epoxy ER 550 was used in study. The workpieces were molded by vacuum molding. The maximum number of wrapped fibers was 3 layers which each layer has a thickness of 0.50 mm and the fiber angle was arranged differently, that are (0), (90), (0,0), (90,0), (0,90), (90,90), (0,0,0), (0,0,90), (0,90,0), (90,0), (0,90,90), (90,0,90), (90,90,0) and (90,90,90).

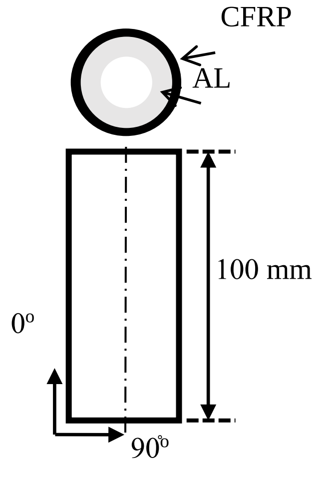

Figure 1. Schematic presentation of specimens.

2.2 Material properties

The mechanical properties of aluminum tubes are based on the tensile test using the ASTM E8M standard as shown in Table 1. The properties of carbon epoxy are in accordance to the ASTM 3039 standard as shown in Table 2.

Table 1. Mechanical properties of aluminum tube.

Property	Description	Value
ρ	Density (kg/m^3)	2,700
E	Young's modulus (GPa)	42.92
υ	Poisson's ratio	0.33

Table 2. properties of carbon epoxy laminate.

Property	Description	Value
ρ	Density (kg/m^3)	1,500
E_{11}	Young's modulus in longitudinal direction (GPa)	66.34
E_{22}	Young's modulus in transverse direction (GPa)	7.152
υ_{12}	Poisson's ratio	0.269
X_t	Longitudinal tensile strength (MPa)	1,142.14
X_c	Longitudinal compressive strength (MPa)	263.78
Y_t	Transverse tensile strength (MPa)	18.23
Y_c	Transverse compressive strength (MPa)	35.25
S_{12}	Longitudinal shear strength (MPa)	28.83
S_{23}	Transverse shear strength (MPa)	30.50

2.3 Experimental method

In this study, axial impact testing was performed using a vertical impact testing machine, as shown in Figure 2. The weight of hammer head can be adjusted from 20 kg to 60 kg. A load cell used in the test has a capacity of measuring loads up to 200 kN. It converts impact loading into electrical signals sent to the data locker that can record a maximum of 10,000 values per second. Signals recorded in the data locker were processed by the computer, and appeared as the result of the relationship between the load and time.

In this experiment, a hammer head with a weight of 30 kg was released freely from a height of 2.43 m. thus leading to an impact energy of 714.15 J. The images of specimens deforming during impact tests were recorded by a camera at a speed of 1200 images/second. Each test was repeatedly performed three times aiming to basically prove the reproducibility. The impact testing data was calculated and presented in the form of maximum and average loads on the bare aluminum tubes and the composite carbon fiber tubes with different fiber orientations.

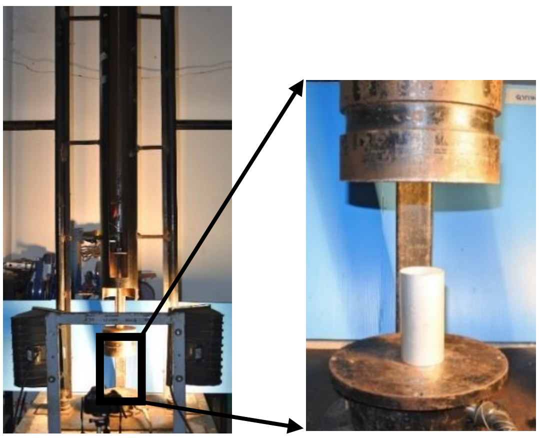

Figure 2. Vertical impact test setup.

2.4 Variables used in the study

In this study, there are two main variables indicating the impact strength of a structure, i.e. maximum load and average load, which are generally referred from the correlation graph between the force and time as shown in Figure 3.

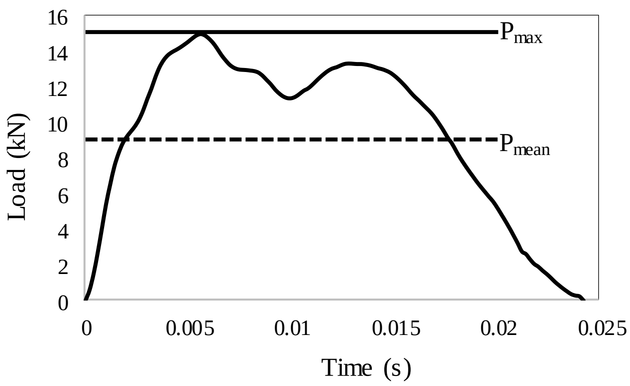

Figure 3. The correlation graph between the force and time.

1. Maximum load (P_{max})
Maximum load is the highest load that occurs throughout the period that hammer impacting on the specimen on the specimen as shown in Figure 3. The maximum load should be within the appropriate range, otherwise it can cause too high reflectance in the event of a shock occurs.
2. Mean load (P_{mean})
Mean load is the average load throughout the period that hammer impacting on the specimen on the specimen as shown in Figure 3. Generally, the average load should have a high value because it is a variable indicating the ability to withstand the force arise from shocks.

3. Results

3.1 Collapse Behavior of Specimens
The results from the impact tests cause different collapse behaviors of specimens. The details of these collapse behaviors found in the tests are discussed as followed.

3.1.1. The collapse mode of the aluminum tube without reinforced fiber laminate
The collapse mode of an aluminum tube without reinforced fiber laminate failed in the diamond mode which consisted of a number of lobes stacking on each other as shown in Figure 4. The damage caused by the impact on the bare aluminum tube in the axial direction resulted in the asymmetric folding.

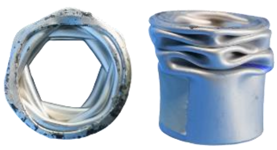

Figure 4. Collapse mode of the aluminum tube without reinforced fibers.

3.1.2. The collapse modes of the aluminum tube with a single carbon fiber/epoxy laminate
According to Figure 5, the collapse mode of the inner aluminum tubes failed in diamond mode. However, the (0) carbon fiber/epoxy laminate failed in lamina bucking mode, i.e. the outer reinforced fibers bended and broke out from the surface of the main structure as shown in Figure 5A, while the

5A (0) 5B (90)

Figure 5. The collapse modes of aluminum tubes with single layer carbon fiber/epoxy laminate; 5A with (0) carbon fiber/epoxy laminate; 5B with (90) carbon fiber/epoxy laminate.

(90) carbon fiber/epoxy laminate failed in fiber breaking mode, i.e. the fibers were broken in various directions. Some of the broken fibers penetrated in the folds of the main structure and some failed out of the main structure as shown in Figure 5B.

3.1.3. The collapse modes of the aluminum tube with 2-layer carbon fiber/epoxy laminate

The collapse behaviors of aluminum tubes with 2-layer carbon fiber/epoxy laminate oriented in (0,0), (0,90), (90,0) and (90,90) are shown in Figure 6. For the (0,0) carbon fiber/epoxy laminate, the collapse mode of the inner aluminum tubes failed in diamond mode, while both of carbon fiber/epoxy layers failed in lamina bucking as illustrated in Figure 6A.

For the (0,90) carbon fiber/epoxy laminate, the first layer with (0) carbon fiber/epoxy laminate failed in local bucking mode and sprang out of the aluminum tube, while the second layer with (90) failed in fiber breaking mode entering into the folds of the main structure as appeared in Figure 6B.

In case of the (90,0) carbon fiber/epoxy laminate, the first layer with (90) failed in fiber breaking mode penetrating into the folds of the main body, while the second layer with (0) failed in laminar bending and sprang out of the aluminum tube as shown in Figure 6C.

Finally, tubes with the (90,90) carbon fiber/epoxy laminate, the collapse behaviors of both layers appeared in fiber breaking mode piercing into the folds of the main structure as seen in Figure 6D.

6A (0,0) 6B (0,90) 6C (90,0) 6D (90,90)

Figure 6. The collapse modes of aluminum tubes with 2-layer carbon fiber/epoxy laminates 6A (0,0); 6B (0,90); 6C (90,0); 6D (90,90).

3.1.4. The collapse modes of the aluminum tubes with 3-layer carbon fiber/epoxy laminate

The collapse behaviors of aluminum tubes with 3-layer carbon fiber/epoxy laminate oriented in (0,0,0), (0,0,90), (0,90,0), (0,90,90), (90,0,0), (90,90,0) and (90,90,90) are presented in Figure 7. As evidenced by the images, the inner aluminum tubes failed in diamond mode for all setups.

For the (0,0,0) carbon fiber/epoxy laminate, the collapse behavior of each layer appeared in laminar bending mode and bended out from the aluminum tube as illustrated in Figure 7A. On the contrary, for (90,90,90) laminate, all layers failed in fiber breaking mode and penetrated into the folds of the main structure as shown in Figure 7G.

In case of the tubes having mix composite layers between (0) and (90) orientation, it was found that impact behaviors of each layer depend on the position of those layers. The interior layers with (0) alignment failed in local buckling mode and infiltrated into lobes of aluminum tubes as presented in Figure 7B, 7C and 7D. These impact behaviors are different from the case where internal layers aligned in (90) direction. For the tube with (90) as interior layers, these layers failed in fiber breaking mode piercing into the main body as appeared in Figure 7C, 7D, 7E and 7F.

7A (0,0,0) 7B (0,0,90) 7C (0,90,0) 7D (0,90,90)

7E (90,0,0) 7F (90,90,0) 7G (90,90,90)

Figure 7. The collapse modes of the aluminum tubes with 3-layer carbon fiber/epoxy laminates; 7A (0,0,0); 7B (0,0,90); 7C (0/90/0); 7D (0,90,90); 7E (90,0,0); 7F (90,90,0); 7G (90,90,90).

In the matter of exterior layers, tubes with the external (0) composite layer failed in laminar bending mode as shown in Figure 7C, 7E and 7F, whereas tubes with the external (90) layer failed in fiber breaking mode as presented in Figure 7B and 7D.

3.2 Maximum and Mean Load

The maximum load and mean load on the specimens can be obtained from the relationship between the load and time resulting from the axial impact tests, as shown in Figure 8.

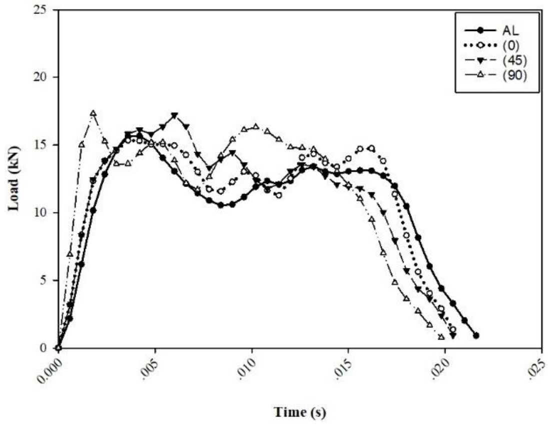

8A 1-fiber layer

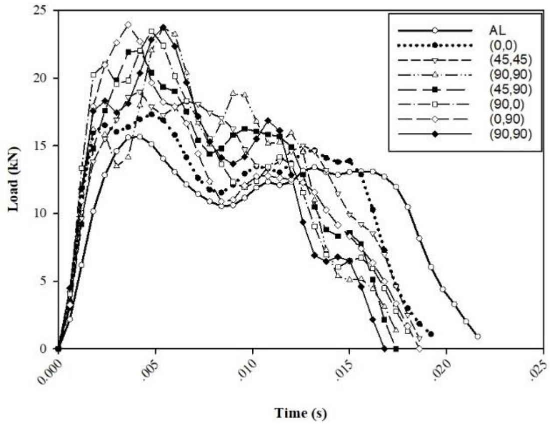

8B 2-fiber layers

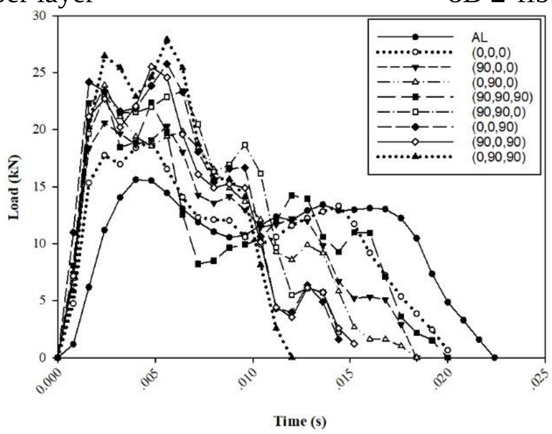

8C 3-fiber layers

Figure 8. The relationship between the load and the time of aluminum tubes with and without a single layer carbon fiber/epoxy laminate oriented in different ply angles; 8A 1-layer; 8B 2-layers; 8C 3-layers

The maximum and mean load of specimens under impact are shown in Figure 8A, 8B and 8C. From those figures, it was found that there was no immediate damage occur on the specimens in all setups. The workpiece received the load at the beginning and slowly failed down at the end of the test.

As shown in Table 3, the maximum and mean load of specimens with reinforcement are higher than those of the bare aluminum tubes. Considering the influence of number of layers, it is obviously seen that the maximum load is increasing significantly as number of layers increases. Nevertheless, the mean load doesn't increase much when number of fiber layer is increasing except for (0,0,90), (90,90,0) and (0,90,90) hybrid tube. This indicated that the increasing of fiber layers may help increasing the resistance of impact load but may be not able to significantly enhance energy absorption capacity of specimens. The orientation of fiber and its' sequence look like to have significant influence on the maximum load and mean load, especially for the tubes with 2 and 3 fiber layers. It can be seen from the amount of those loads when the sequence of fiber orientation is changed in Table 3. It can be noticed that the difference in ply angles resulted in the difference of maximum and average loads applied on the specimens. The result revealed that the hybrid tube with (0,90,90) carbon fiber/epoxy laminate offer most the maximum load and mean load by 58.56% and 84.58% respectively. Whereas, the maximum and mean load of specimens with (0), (0,0) and

(0,0,0) fiber/epoxy were found to resist lower impact load than those of other combinations. This is due to the collapse behavior of each specimens appeared in laminar bending mode and bended out from the aluminum tube.

Table 3. Maximum load and Mean load on the specimens from axial impact tests.

Specimens	P_{mean} (kN)	P_{max} (kN)
AL	10.86	15.18
(0)	11.39	15.40
(90)	11.73	17.31
(0,0)	11.37	17.38
(90,0)	12.28	19.88
(90,90)	12.29	22.52
(0,90)	12.32	23.95
(0,0,0)	11.00	19.10
(0,90,0)	11.38	21.30
(90,90,90)	11.57	24.53
(90,0,0)	12.17	20.66
(90,0,90)	13.37	25.84
(0,0,90)	14.60	25.77
(90,90,0)	15.42	26.99
(0,90,90)	17.22	28.02

4. Summary

From the experimental study on the composite aluminum tubes under the axial impact, it was found that the maximum and mean load increased as the number of CFRP layers increased, yet the position and the orientation of CFRP layers played important roles in changing the capacity as well. According to the results of this study, in case of the 3-layer carbon fiber tubes, the composite tube with (0,90,90) offer most the maximum capacity that improved the maximum load and mean load by 58.56% and 84.58% respectively. Whereas, the 1, 2, and 3-layer specimens with (0), (0,0), and (0,0,0) fiber/epoxy were found to resist lower impact load than those of other combinations. The average loads of hybrid tubes with (0), (0,0), and (0,0,0) fiber/epoxy were higher than those of naked aluminum tubes by 4.91%, 4.68% and 1.33% respectively. In addition, the maximum loads of those hybrid tubes were higher than aluminum tubes by 1.51%, 14.52% and 25.88% respectively.

References

[1] A.n. Jambor, M.t. Beyer: Materials & Design. 18 (1997) 203-209.
[2] M.R. Bambach, M.Elchakani, X.L.Zhao: Composite Structures. 87 (2009) 282-292.
[3] M. Kathiresan, K. Manisekar, V. Manikandan: Composite Structures. 94 (2012) 3510-3519.
[4] M.Golzar, M.Poorzeinolabedin: International Journal manufacturing technology. 49 (2010) 1037-1045.
[5] Jung-Seok Kim, Hyuk-Jin Yoon, Kwang-Bok Shin: International Journal of impact engineering. 38 (2011) 198–207.
[6] Nikola Schmidova, Tereza Zavrelova, Michal Vasicak, Filip Zavadil, Milan Ruzicka, Martin Rund: Materials Today. Proceedings 5 (2018) 26784 – 26791.
[7] Xuan Zhao, GuoHua Zhu, Chenyu Zhou, Qiang Yu: Composite Structures. 222 (2019) 110-120.
[8] Haiyan Yu, Huiru Shi, Siji Chen: Composite Structures. 209 (2019) 579-589.
[9] Peng Feng, Lili Hu, Peng Qian, Lieping Ye: Composite Structures. 140 (2016) 749-757.
[10] Muhammed Emin Erdin, Cengiz Baykasoglu, Merve Tunay Cetin: Procedia Engineering. 149 (2016) 559 – 565.
[11] D. Hu, C. Zhang, X. Ma and Bin Song: Composites Part A 90 (2016) 489-500.

AMM0026

Recording and analysis of exercise ergonomics in running cases using microcontroller

Sitthichai Wongnor[1], Kunchorn Sarawong [2,*], and Peter Srisoontorn-Persons

[1,2,3,]Department of Mechanical Engineering, Faculty of Engineering and Technology, North-Chiang Mai University, Chiang Mai, 50230, Thailand

* Corresponding Author: chang.sarawong @gmail.com

Abstract. Running is becoming more popular in the modern days and there has been an increase of the use of technology to increase the efficiency of each runner. By integrating technology into running ergonomics there can be many improvements made to running ergonomics. This project is created to research the efficiency of the runner with technology by using microcontrollers to control the ergonomics of the runner. By connecting gyroscopes to the runner, we can record and analyse the running ergonomics which can then be used to correct the running ergonomics of the runner. The right movement of the body is crucial to the runner. The origins of ergonomics started in the 5th century. In 1970 physicians were sure that running is the control of the oxygen only but in 1980 there was a research that stated that body ergonomics had an impact on running in both short and long distances. Running researchers began to reveal that there were other variables that contributed to running success notably running ergonomics. The correct ergonomics can help reduce osteoarthritis, muscle strain, imbalanced oxygen levels and fatigue. Research states that 50% of runners have injuries from the wrong ergonomics. Thus the integration of modern technology is crucial to running ergonomics to help reduce the strain on the body of the runner. Thus by controlling the ergonomics of the runner and analysing the ergonomics is part of the solution to the problem.

1. Introduction

Running ergonomics has become crucial in modern days for exercising, and numerous runners utilize wearable technologies in order to improve their exercise and training. This paper investigates the running ergonomics by using technology to record and analyse the efficiency of the runner by readjusting the angle in which is the correct form of running by using technology Marcus Peikriszwili Tartaruga et al. [1] studied about the relationship between running economy and the changes in physical factors in long distance runners and the results were that running ergonomics can be used to help sustain running economics and can help save energy while running Richard N. Hinrichs [2] results showed that while the body possessed varying amounts of angular momentum about all three coordinate axes, the arms made a meaningful contribution to only the vertical component. The arms were found to generate an alternating positive and negative during the running cycle. This tended to cancel out the opposite pattern of the legs. The trunk was found to be an active participant in this balance of angular momentum, the upper trunk rotating back and forth with the arms and, to a lesser extent, the lower trunk with the legs. The result was a relatively small total-body throughout the running cycle. The inverse relationship between upper- and lower-body angular momentum suggests that the arms and upper trunk provide the majority of the angular impulse about the z axis needed to put the legs through their alternating strides in running. Lawrence ,J, P. [3] running ergonomics is the study of the relationship of the human and devices to help receive data from running and using the data to help improve the running form which is an closed loop system by receiving the data and using the data to analyse and see if the running form is correct. In order for the running economy to work perfectly the system needs 2 things which are the design must work correctly and the elements must be in sync in order for any system to work to the designated target and the running form that is used to run the farthest is [4] Palladino, S. (.(2016 As figure1

Figure 1. Correct running form

[5] Wilson,D. The correct running form must be as follow. The runner must look straight, shoulders should be relaxed, upright torso, unclenched fists, arms relaxed swinging at sides, hips pointing straight ahead, legs beneath body with knees slightly bent and landing between heel and midfoot. By doing so, it can help save energy while running and make the runner run farther. [6] Spong, M. W., & Vidyasagar, M. basic dynamic theory of rigid body is the study about the movement of a coordinate system and the coordinate is the representation of the movement of a rigid body and is normally in 3 dimensions in all sides of the movement. The 2 types of movements used is translation and rotation as figure 2

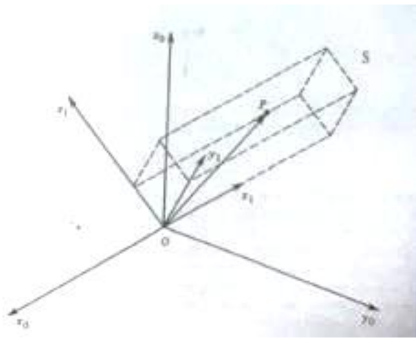

Figure 2. Coordinates in rigid bodies

With the help of modern technology, running injuries can be prevented by controlling the ergonomics of the runner using sensors to measure and analyse the correct running form of the body

2. Research Methodology

The recording of the running ergonomic the system will have many different parts which are the Microcontroller, Gyroscopes and the SD-Card Writer. The microcontroller used is the Arduino UNO R3 connected to 2 Gyroscopes and connected to an Arduino SD card shield. The type of gyroscope used is the GY-50 L3G4200D and the MPU6050 gyroscope. The Arduino UNO is connected to the 9V battery which is connected to the push start push stop button. The recording of both the values received from the gyroscope is recorded into the SD-CARD as shown in figure 3

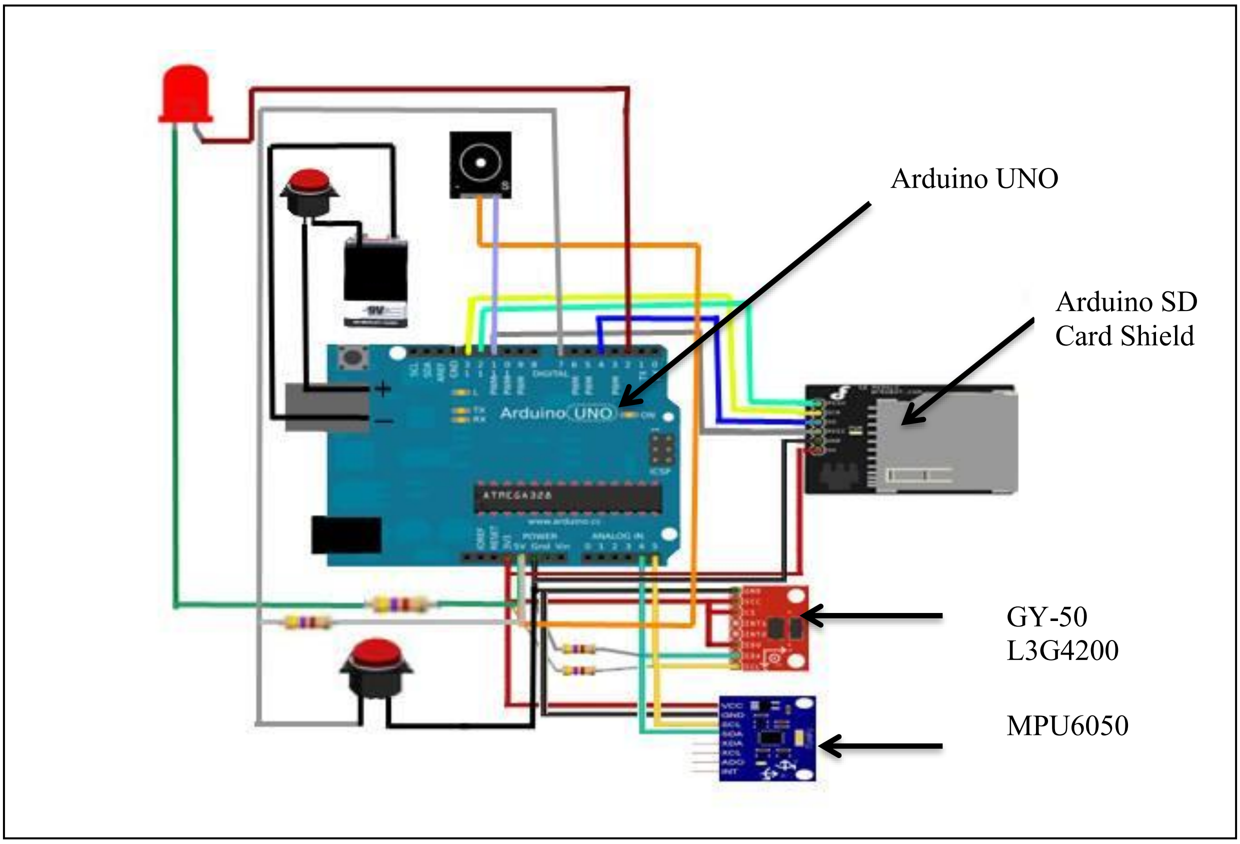

Figure 3. Parts used in the recording device

The process of the program used to record the running ergonomics will be as written in the program transferred to the microcontroller which will be as the following flowchart and the example data received from the gyroscope will be as figure 4

There will be 4 recorded data every second and the total time used will be 40 seconds which will be averaged for every second and then to total average will be averaged to calculate the average angle of the runner in total and the data will be recorded in degrees per second

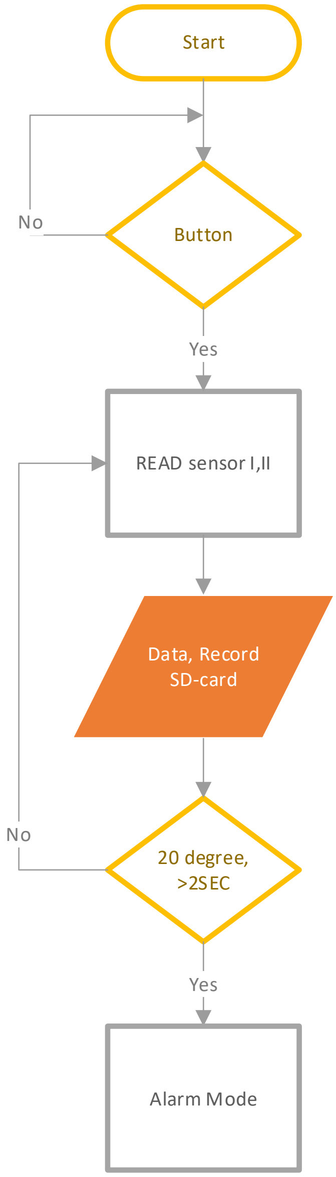

Figure 4. Work process flowchart of the device

To setup the device onto the body. The first gyroscope is suggested to be at 55% of the height of the runner from the floor. The picture setup has a shirt that has both gyroscopes installed and microcontroller on the side which will be as figure 5

Figure 5. Installation of the recording device onto the runner

Point number 1 is the first gyroscope which is at 55% of the runners' height from the floor. Point number 2 is the second gyroscope used to analyse the data which will be installed in the middle of the back between shoulder blades and number 3 is the microcontroller which is installed on the side of the body which will receive the values from the gyroscopes and record the values received into the SD-CARD. If the average running angle between each second is more than 20 degrees the buzzer which is connected to the arduino will buzz.

3. Research Results and Discussions

The results found that from the 8 participants, the participants that have an average of 20 less than 20 degrees or don't fluctuate much is 25% which is shown in figure 6 and 75% of the participants have running ergonomics that should be improved shown in figure 7

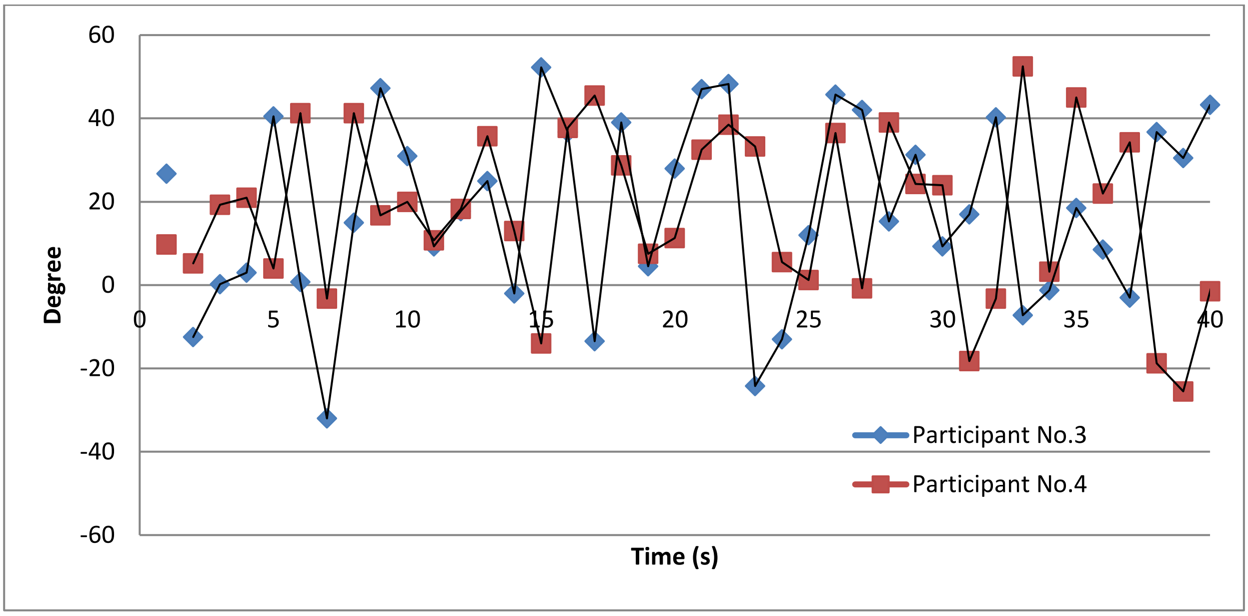

Figure 6. Participants with good running ergonomics

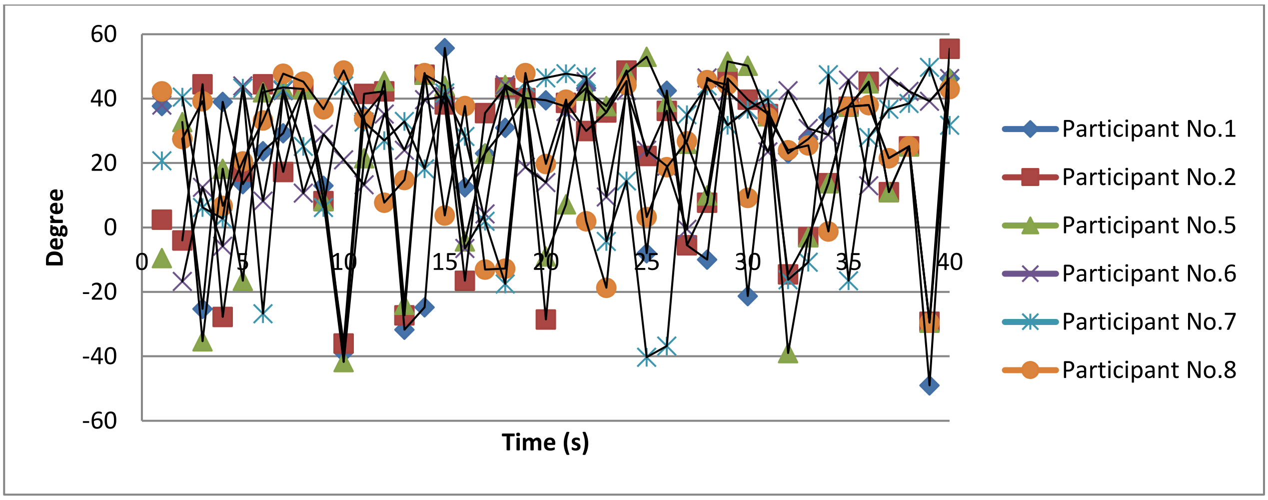

Figure 7. participants which have running ergonomics that should be improved

The runners with good running form have less fluctuation in each second and have a running angle of less than 20 degrees forward. The runners with good form have a total average running angle of 17.19 degrees per second as for the runners which have running ergonomics that should be improved have a total average angle of 22.61 degrees which is calculated from the table shown.

Table 1. Average running angle of participants

Name	Average angle (degree)
Participant No. 1	21.4
Participant No. 2	20.7
Participant No. 3	16.9
Participant No. 4	17.5
Participant No. 5	21.1
Participant No. 6	26.4
Participant No. 7	21.4
Participant No. 8	24.7

From the table participant number 3 and 4 have a running angle of less than 20 degrees which is good and the other participants have an angle of more than 20 degrees. We can conclude that 25% of the participants have good running ergonomics and 75% have running ergonomics that must be improved on which means that 75% of the participants with running ergonomics that should be improved on might be injured from running.

Conclusions

The values of the recording of the participants can be used to analyse the running form of the participants at any given point. The result of analysing the participants found that 75% of the participants have running ergonomics that must be improved on and 25% of the participants have good running ergonomics. By analysing the running ergonomics of the participants with bad running ergonomics found that in many moments in time there is a swing in the upper body which results in change in momentum and may cause the body to loose balance and lead to injuries.

Recommendations

Using the same type of gyroscope which connects using the I^2C with the same address may cause connection problems thus the usage of 2 models of gyroscopes will make the connection easier

To improve on this paper the usage of the proper program which can filter and plot the data may prove to be helpful and be clearer. The addition of other gyroscopes can help get more accurate data of the running ergonomics.

Acknowledgment

We would like to thank you North-Chiangmai University for the usage of the university campus.

References

[1] Marcus Peikriszwili Tartaruga, Jeanick Brisswalter, Leonardo Alexandre Peyre-Tartaruga, Alusio Otavio Vargas Avila, Cristine Lima Alberton, Marcelo Coertjens, Eduardo Lusa Cadore, Carlos Leandro Tiggemann, Eduardo Maeczwski Silva and Luiz Fernado Mrtins Kruel, 2012 *The Relationship Between Running Economy and Biomechanical Variables in Distance Runners* (Tatlor and Francis, Volume 83:Issue 3) p 367-375

[2] Richard N. Hinrichs, *Upper Extremity Function in Running. II: Angular Momentum Considerations* (Journal of Applied Biomechanics, Volume3:Issue 3) p 242-236

[3] Lawrence, J, P. 2012 *Effect of Adopting Proper Running Form Techniques on Hip Strength in Healthy Females* (Honors Projects) p 133.

[4] Palladino, S. 2016 *Understanding Running Effectiveness and its Uses* (WKO4) USA

[5] Wilson,D. 2014 *Correct Running Technique explained by a Physiotherapist* https://myphysiosa.com.au/physio-correct-running-technique/

[6] Spong, M. W., & Vidyasagar 2004 *Robot dynamics and control* (New York :Wiley–Interscience)

AMM0027

Development of Creep Testing Machine and Validation Cases of ASTM A36 Steel Property

Pavaret Preedawiphat[1], Numpon Mahayotsanun[1,*], Keerati Sa-Ngoen[2], Mai Noipitak[3], Pongsak Tuengsook[3], Sedthawatt Sucharitpwatskul[4], and Sasawat Mahabunphachai[4]

[1]Department of Mechanical Engineering, Faculty of Engineering, Khon Kaen University, Muang, Khon Kaen, 40002, Thailand
[2]LPN Metallurgical Research Center, Prasamutjedee, Samutprakarn, 10290, Thailand
[3]King Mongkut's University of Technology Thonburi, Thung Khru, Bangkok, 10140, Thailand
[4]National Metal and Materials Technology Center, Khlong Luang, Pathum Thani, 12120, Thailand

* Corresponding Author: numpon@kku.ac.th

Abstract. Premature failures of creep-resistant steels have been causing critical damages and high maintenance costs worldwide. As a result, it is necessary to carry out creep tests to calculate creep life to reduce creep failure during the service. In Thailand, the number of creep testing machines is limited, and some organizations need to rely on services abroad, which are costly and time-consuming. This project aimed to develop a creep testing machine that met the standards and the increased demands of the local service. The in-house creep testing machine was developed, and the finite element analysis was used to determine the creep testing machine's structural performance. The ASTM A36 steel specimen was tested under high stress and temperatures to determine the developed machine's function.

1.Introduction

Creep failures must be avoided when structural systems are exposed to high stresses and temperatures, particularly in thermal, chemical, petroleum, and nuclear power plants [1]. The strains under fixed stresses at the elevated temperature over time are commonly carried out to observe creep behaviors [2]. The creep testing results can be evaluated and analyzed to identify the service life and creep mechanisms [3]. Loads, temperatures, and time are the major factors influencing creep service life. Typically, the minimum number of nine creep tests is conducted to take into account these three factors. Recently, creep-resistant steels have developed to enhance service life under high-temperature operations [4]. As a result, the demand for creep testing commonly used in power plants and the petroleum industry has increased. Nevertheless, the number of creep testing machines in Thailand does not meet the increasing demand. Besides, carrying out creep testing by using the universal testing machine does not meet the ASTM E139 - 11 standard [5] or ISO 204:2009 standard [6], and cannot carry out many creep tests at a time. The testing facility must also be certified by ISO/IEC 17025 [7] to ensure that testing operations and reports can be internationally accepted. Relying on sending the samples to perform creep testing abroad is too costly and time-consuming. Thus, developing a certified facility in Thailand having multiple creep machines or potentially a creep machine farm (40-100 machines) would be the ideal situation. Not only does each creep machine need to be accurate and reliable, but the cost of each machine development must also be minimum. This work's objective was to develop an affordable, accurate, and reliable creep testing machine that could potentially be simply replicated to develop a creep machine farm in the future. The structural analysis using the finite element method (FEM) was used to determine the machine's stiffness and feasibility. The creep testing experiment was also carried out to determine the function of the machine.

2.Creep Machine Development

The creep machine design used in this work was adapted from Zubair Khan et al. [8]. The lever-type (lever arm indirect load) was selected because the lever arm could increase the loads up to 100 times without the need to enlarge the machine's size, as illustrated in Figure 1. The main components of the developed creep machine consist of weights, a lever, and an oven. The dead weights could be stacked up to 3000 kgf, which could provide the loads up to 1000 ton-force by way of the lever. The body frame material was JIS G3101 SS400. The electric heating furnace (oven) was designed to provide the temperature range of 200°C - 1000°C by using the nichrome heating wires. Three heating zones were arranged to ensure uniform temperature distribution throughout the tested sample. Over time, the displacement of the tested specimen was recorded by the linear variable differential transformer (LVDT) attached to the pull rod (on top of the oven). The displacement data was sent to the data logger and converted to strain data over time.

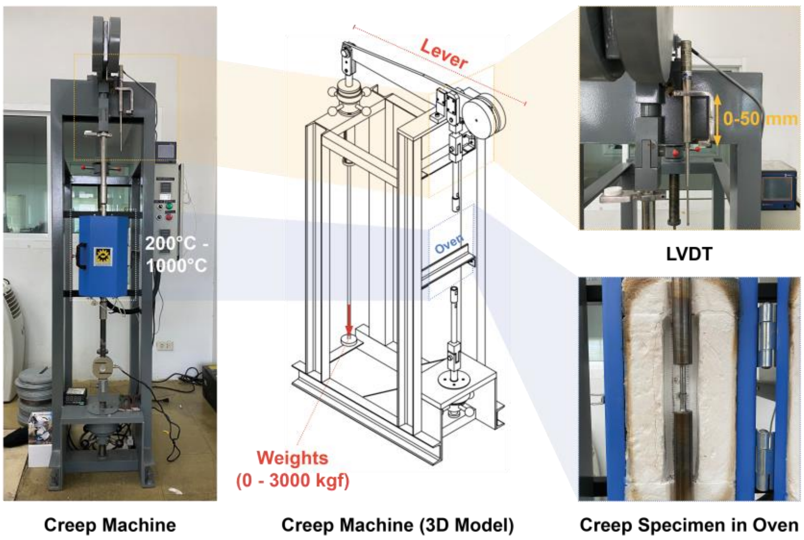

Figure 1. Developed creep machine.

Three subsystems were calibrated with the standard methods to validate the performance of the developed creep machine. The thermocouples (Type K) of the electric heating furnace were calibrated against the standard thermocouple by Miracle International Technology (MIT). The measured temperatures were within ±1 °C and certified by MIT. The displacement readings were calibrated with the digital dial gauge (Mitutoyo Absolute Digimatic Indicator), and the compared results were within ±0.01 mm. Regarding the weight calibration, the deadweight was compared with the load cell, according to ASTM E4 [9].

Typically, a creep test could be carried out up to 1,000 hours. With such high loads and long durations, the machine's overall structure was carefully designed to take into account the components under tension, compression, bending, shear stress, and creep. The static structural analysis was then performed to determine the creep machine design's feasibility, as displayed in Figure 2. ANSYS Workbench 2012R was the commercial finite element analysis (FEA) software used to carry out the stiffness analysis. The elements used were 10-node tetrahedral, having 203,146 nodes and 183,489 elements with less than 5% errors. The FEA loading condition was seen on the left of Figure 2. The deadweight of 325 kg (3188.3 N) was added. The top and bottom specimen holders were fixed. The FEA results showed that the maximum deformation was 2.0683 mm. The overall effective stresses (von Mises stress) were relatively low but having high-stress concentration up to 547.74 MPa at the pin location. As a result, the pin material was then changed to be JIS S45C steel to obtain the safety factor of 1.5 - 2.0.

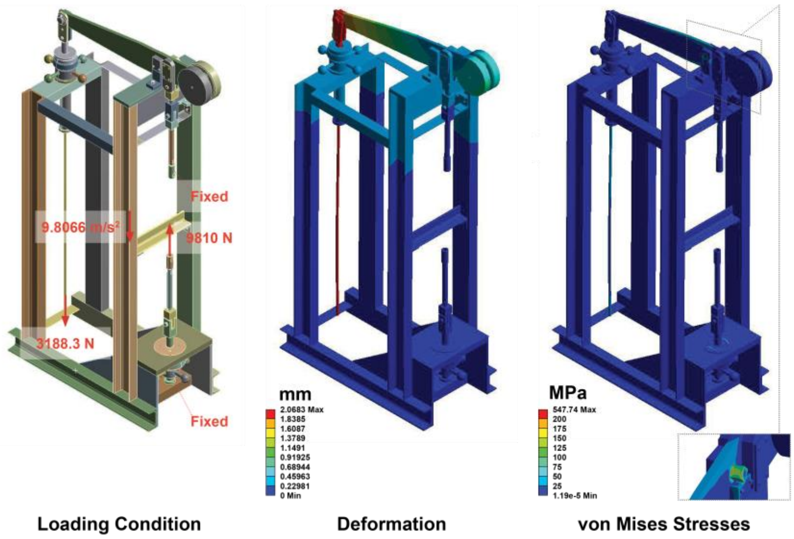

Figure 2. Structural analysis of the creep machine.

3.Creep Test

The creep test following ASTM E139 - 11 standard [5] was carried out to determine the developed machine's function. The creep specimen was prepared according to the standard, as shown in Figure 3. ASTM A36 was the commonly used material in power plants and selected here for the creep specimen. The creep specimen was then tested at 600°C and 110 MPa for 465 minutes (7.75 hours). Figure 4 presents the displacement, strain, and strain rate results obtained from the creep test. The image of the tested specimen is also displayed in the displacement vs. time graph. The obtained graphical results indicate the typical creep behaviors of ASTM A36, similar to the standard ASTM study [10]. Also, no deformation or bending of the creep machine was noticed during the entire testing period. Based on the obtained result, the performance of the developed creep testing machine met the standards. The agreed results also indicated that the machine offered accuracy and reliability. Thus, the machine's replication would be further planned and developed to develop the creep machine farm in Thailand eventually.

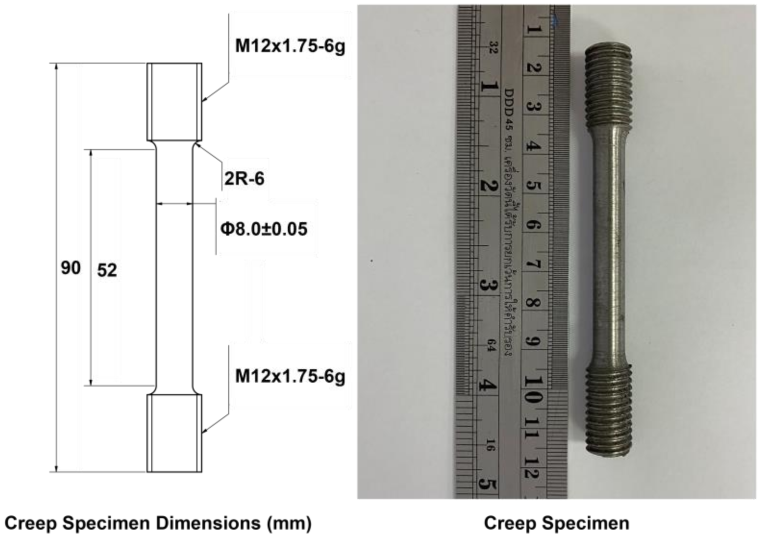

Figure 3. Creep specimen.

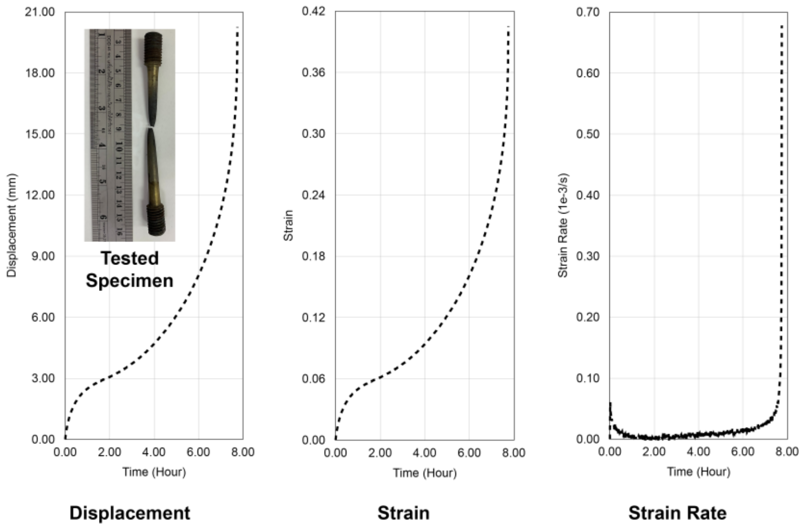

Figure 4. Creep testing results.

Conclusion

The lever-type creep testing machine was developed to provide up to 1000 ton-force, 1000°C, and 1000 hours. The machine's structural analysis was carried out by using the finite element analysis, and the pin material was changed from JIS G3101 SS400 to JIS S45C steel to obtain the safety factor of 1.5 - 2.0. With the obtained machine stiffness results, the ASTM A36 creep specimen was tested for 7.75 hours at 600°C and 110 MPa. The experimental results met with the ASTM standard and proven to be accurate and reliable.

Acknowledgments

This research was funded by the Thailand Research Fund (TRF) grant number PHD5910086, and the National Innovation Agency (NIA). The authors would like to acknowledge the supports of LPN Metallurgical Research Center; Department of Mechanical Engineering, Faculty of Engineering, Khon Kaen University; King Mongkut's University of Technology Thonburi; and National Metal and Materials Technology Center (MTEC).

References

[1] Fabricius A, Jackson PS 2016 *Eng. Fail. Anal.* **66** 398-406.
[2] Kassner ME 2015 *Fundamentals of Creep in Metals and Alloys* (Butterworth-Heinemann).
[3] Nabarro FRN, Villiers Fd 2018 *Physics Of Creep And Creep-Resistant Alloys* (CRC Press).
[4]Abe F, Kern T-U, Viswanathan R 2008 *Creep-Resistant Steels Woodhead Publishing Series in Metals and Surface Engineering* (Elsevier).
[5] ASTM E139-11(2018), Standard Test Methods for Conducting Creep, Creep-Rupture, and Stress-Rupture Tests of Metallic Materials, ASTM International, West Conshohocken, PA, 2018, www.astm.org.
[6] https://www.iso.org/standard/37601.html.
[7] https://www.iso.org/ISO-IEC-17025-testing-and-calibration-laboratories.html.

[8] Zubair Khan M, Saleem H, Mahi A, Aleemullah, Ahmed Khalid F, Asad Ali Naqvi S, Lim TH, Song RH, 2020 Am. J. Mater. Eng. Technol. **3**(3) 51-57.
[9] ASTM E4-01, Standard Practices for Force Verification of Testing Machines, ASTM International, West Conshohocken, PA, 2001, www.astm.orgASTM E4-01, Standard Practices for Force Verification of Testing Machines, ASTM International, West Conshohocken, PA, 2001, www.astm.org
[10] T. Z. Harmathy and W. W. Stanzak, "Elevated-Temperature Tensile and Creep Properties of Some Structural and Prestressing Steels," in Fire Test Performance, (West Conshohocken, PA: ASTM International, 1970), 186-208. https://doi.org/10.1520/STP44718S.

BME0001

Characteristic and geometry analysis for soft robotic fingers by fully 3D printing with commercial silicone rubber

C Musikapan[1] and R Chancharoen[1]

[1]Department of Mechanical Engineering, Faculty of Engineering, Chulalongkorn University, 254 Phayathai Road, Wang Mai, Pathum Wan, Bangkok, 10330, Thailand.

Corresponding Author: ratchatin.c@chula.ac.th and chaiyawat.cuengineer@gmail.com

Abstract. At the present, we found that many Stroke survivors, Parkinson's disease and Orthopedic patients were loss the muscle controlling and neural network damaged. They need a hand functional assistance in medical rehabilitation to support them during their normal activities of daily life (ADL). In this work, we proposed a humanoid soft robotic finger by fully 3D printing technology with a commercial silicone rubber mixture. This practice available in a short time to manufacture without the molding process. In additional, we demonstrated an inner characteristic and mechanical design by geometry analysis, and numerical method which we called a multi cavity cells (MC-Cells). Consequently, MC-Cells had optimized a curvature surface and bending motion on the top of soft actuator which its thickness wall properties had expand with high fluidic pressurization. Finally, we evaluated soft robotic flexor in the range of motion (ROM) on Distal Interphalangeal joint (DIP) in biomechanics that it active with several air pressure generating during 75 kPa to 175 kPa into the model.

Keywords: Hand functional assistance, geometry analysis, multi cavity cells, soft robotic flexor and range of motion.

1. Introduction

Recently, hand rehabilitation has been assisting patients about movement disorders significantly reduce in the case neurologically based disorders. There are various approaches to restore the functionality of the upper specifically limit disorders e.g., stroke, Parkinson, stroke with Parkinson, trigger fingers and orthoses [1][2]. For this reason, neurologically based disorders affected with finger's grasping and flexor [3]. The mainly causes of disease which it affected their muscle disorders and motor disabilities [4]. These reasons had already assisted them by repetitive activities training during primary rehabilitation and ADL [1][2][5]. The counteract these problems have been using soft robotic finger as soft actuator that it takes the finger's joints and muscle passive flexor [6]. It assists to support their movement in biomechanics by soften material. The soft actuators have already assistive with their finger joints on Metacarpophalangeal (MCP), Proximal interphalangeal (PIP) and Distal interphalangeal (DIP) in ROM [7]-[9]. In addition, soft actuators by 3D printing technique are generate forces to support bidirectional finger movements in flexion and extension [10][11].

In this paper, we present our assistive model with mathematic solving in characteristic and geometry analysis of MC-Cells.

2. Model and method

Recently, we aim to design a model of soft actuator to assist the real human finger bone flexor. Its characteristic models have design under geometry analysis. Then, its dimension are lengths 80 mm and 118 mm, both sizes have width 14 mm and height 15 mm. In addition, the models have been several block roofing with tracks on the top surface. We propose this technique with fully 3D printing that we call MC-Cells to support our soft actuator bending. Also, the soften inner structure have been design with double mainly air tapping that it connects with multi cavity as MC-Cells. So, the soft actuator driven after the pneumatic system generated a pressure into the mainly air tapping. Consequently, the MC-Cells have been active by elongation passive flexor.

In this work, we have used silicone sealants by TOA productivity which its mainly soften material are safety for human body. Its properties have possible worked to elongation more than 600 % during expansion. In addition, we used 3D Bio-plotter printer with 0.28 mm in tips glue needle type 18G during process of printing. Furthermore, time process of printing has been using for 40 minutes in model length 80 mm and an hour for model length 118 mm.

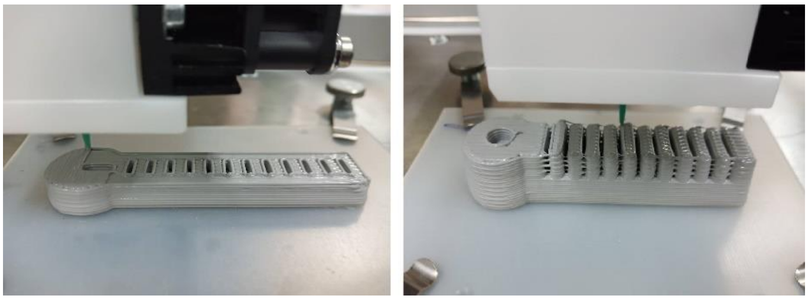

A B

Figure 1. Soft robotic fingers in fully 3D printing process by 3D Bio-plotter printer, A) Base of block roofing in printing process and B) Fully printing process of soft actuator.

3. Mathematic solving

In this paper, we propose geometry analysis in soft actuator which its flexible finger bending have summarized the elongation with linearization method like a novel work and another researches [5][6][12]. Consequently, we analyze the flexible moment in biomechanics with several pressure generated due to compare with natural finger flexor in efficiency.

3.1. Bending angle

In this work, we have been solving the surface expansion which its wall properties have elongation like an equation (1). Where λ_1 is the total area on top surface over MC-Cells and N is the number of block roofing in MC-Cells. While Q is the area on block roofing that it is include the surface over MC-Cells and mainly air tapping like equation (2). In addition, a_1 is the length of block roofing in MC-Cells. Where, a_2 is length of track between any block roofing. Furthermore, b_1 and b_2 is thickness walls of MC-Cells.

For instance, λ_1 = 37.5 mm^2 in model lengths 80 mm and 61.1 mm^2 for model length 118 mm. Q have been solving like equation (2) if a_1 = 1.3 mm, a_2 = 1.1 mm, b_1 = 3 mm, b_2 = 10.2 mm.

$$\sum \lambda_1 = N\,Q \tag{1}$$

$$Q = a_1 b_1 + 2a_1 b_2 + a_2 b_1 \tag{2}$$

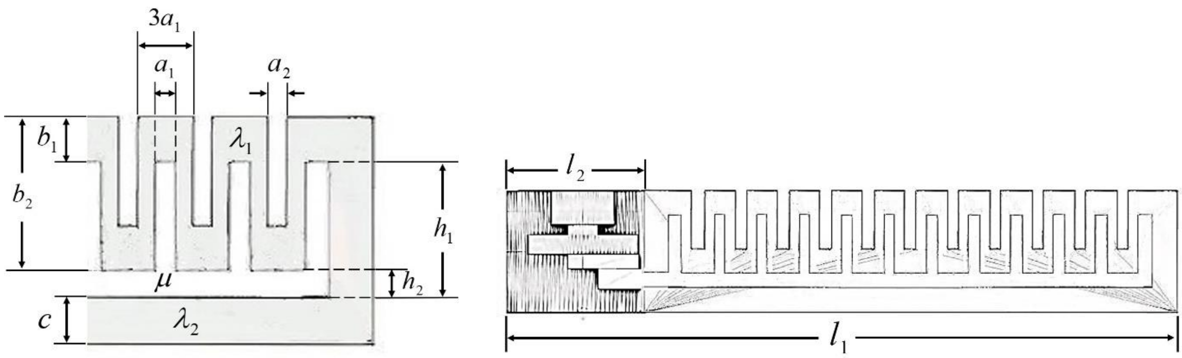

A B

Figure 2. Model diagram A) The MC-Cells segments and B) Model's diagram in side view.

Next, we defined λ_2 is the base layer which it has been solving like an equation (3). Also, L_1 is the total length of model and c is the thickness of base layer. In this work, λ_2 = 2.4 mm^2 in model length 80 mm and 3.54 mm^2 for model length 118 mm if c = 3 mm.

$$\lambda_2 = L_1 c \tag{3}$$

Assuming, μ is the inner coefficient that its active with mainly air tapping. Also, μ have been vary on the pressure generated into the model which it has been solving like an equation (4). So, A is the area of inner body that it defined as $A = N\, w_1\, a_1\, \Delta h + n\, w_2\, h_2\, \Delta l$.

$$\mu = \frac{P\,A}{\Delta l} \tag{4}$$

Additionally, P is the pressure to generate into the model. Also, l_1 is the total length of model and l_2 is the air pressure chamber distance before mainly air tapping zones. So, Δl that it defined as $\Delta l = l_1 - l_2$. In addition, Δh is an inner cavity of MC-Cells that it possible mathematic solving as 7.2 mm for both sizes. Furthermore, w_1 is the width of block roofing that it is 8 mm and the width of mainly air tapping is 1.8 mm as w_2. Then, n = 2 that it is the number of mainly air tapping.

Finally, θ_{active} is the bending angle of distal finger that we propose a simplified linearization platform to explain our flexor experiment [5][12]. We defined k is the elongation of MC-Cells area which it directly affects with λ_1. The results have been showing the elongation effects and bending angle in table 1 that it had been solving like an equation (5).

$$\theta_{active} = \sin^{-1}\left(\frac{\lambda_1\, k\, \lambda_2\, \mu}{\lambda_2^{\,2} + \lambda_1\, k\, \mu^2}\right) \tag{5}$$

3.2. Biomechanics

In biomechanics, it possible to explain and analyze the distal angle active by trigonometry analysis. From my perspective, l_{MP} is the length of finger bone between MCP and PIP joint and l_{PD} is the length from PIP to DIP joint. While, θ_1 and θ_2 are the internal components angle in MCP joint. Also, γ_{MD} is the displacement line from MCP to DIP joint. Where, $\hbar_1$ is the reference line from PIP joint which its perpendicular with γ_{MD}. So, $\hbar_1$ that it defined as $\hbar_1 = l_{MP} \sin\theta_2$. Then, φ_1 is the angle active of PIP joint by trigonometry characteristic which it defined as $\varphi_1 = 90° - \dot{\theta}_2$. Consequently, φ_2 should be solving like an equation (6).

$$\varphi_2 = \cos^{-1}\left(\frac{\hbar_1}{l_{PD}}\right) \tag{6}$$

Furthermore, γ_{MD} from MCP to DIP joint in complementary which it defined as $\gamma_{MD} = \gamma_1 + \gamma_2$. It possible to find γ_{MD} as $\gamma_{MD} = \sqrt{l_{MP}^2 - \hbar_1^2}$. In addition, φ_3 that it is enable solving like an equation (7). However, φ_3 related with angle flexor in DIP joint as follows PIP joint's flexor like α which it defined as α = 180° - ($\varphi_1 + \varphi_2$).

$$\varphi_3 = \cos^{-1}\left(\frac{\gamma_2}{l_{PD}}\right) = 90^\circ - \cos^{-1}\left(\frac{l_{MP}\sin\theta_2}{l_{PD}}\right) \tag{7}$$

Although, DIP joint flexor that it has been composed with corners φ_4 and φ_5. Also, l_{DE} is the length of finger bone from DIP joint to distal. So, γ_3 and γ_4 are displacement lines active in mathematic solving as $\gamma_{ME} = \gamma_3 + \gamma_4$. Then, γ_3 and γ_4 that it defined as $\gamma_3 = \sqrt{\gamma_{MD}^2 - \hbar_2^2}$, $\gamma_4 = \sqrt{l_{DE}^2 - \hbar_2^2}$. Consequently, φ_4 that it defined as $\varphi_4 = 180° - \dot{\theta}_3$. Therefore, $\hbar_2$ is the reference line connect with γ_{ME} which it is the displacement line from MCP joint to distal fingers. So, $\hbar_2$ that it defined as $\gamma_{MD}\sin\theta_3$. Consequently, φ_5 should be solving like an equation (8).

$$\varphi_5 = \cos^{-1}\left(\frac{\hbar_2}{l_{DE}}\right) \tag{8}$$

Hence, we have been solving to find β which it is the active angle of flexor in DIP joint like 180° - ($\varphi_3 + \varphi_4 + \varphi_5$) in an equation (9).

$$\beta = 180^\circ - \cos^{-1}\left(\frac{\gamma_2}{l_{PD}}\right) - \left(90^\circ - \dot{\theta}_3\right) - \cos^{-1}\left(\frac{\gamma_{MD}\sin\theta_3}{l_{DE}}\right) \tag{9}$$

Consequently, the percentage of biomechanics movement efficiency which it is possible to calculate in mathematic solving like an equation (10). In addition, ROM of MCP joint have been active from 0° to 90°, 0° to 110° in PIP joint and DIP joint from 0° to 80°. For instance, η is the percentage of finger active efficiency that it has been solving in flexor ability to perform the result in table 2.

$$\eta = \left(\frac{ROM - active\ angles}{ROM}\right) \times 100\% \tag{10}$$

4. Results

As a result, flexible angle of soft actuator experiment when it packs on the finger. We found that the bending angle of soft actuator related with finger bone and joints active movement. Also, the bending angle measurement shows the result like mathematic solving. Soft actuators have been bending when we are generates air pressure into our model like figure 3.

However, the bending angle of soft actuator with retaining strap which it takes lowly angle movement from inertia. So, we found the opposite result when we pack our soft actuator with pocket glove or soften fabric material like figure 3A. In addition, the bending angle of soft actuator related with finger bone and joints movement like diagram in figure 3B.

Figure 3. A) Soft actuator active on fingers B) Soft actuator packs on finger and C) Soft actuator affects the finger joints movement.

Therefore, the result of bending angle in model length 80 mm and 118 mm by measurement after we generate air pressure into our model with 75 kPa, 100 kPa, 125 kPa, 150 kPa and 175 kPa. The results have shown the elongation rate k affects to λ_1 in Table 1, and percentage in figure 4.

Table 1. Result of the bending angle experiment for soft actuator with several air pressure inputs.

Pressure	Model length 80 mm		Model length 118 mm	
(kPa)	Measurment	k	Measurment	k
75	14.5°	0.763	24.5°	1.108
100	21°	0.835	34°	1.136
125	31°	0.997	48.5°	1.260
150	37°	1.004	60°	1.278
175	49.5°	1.153	77.5°	1.284

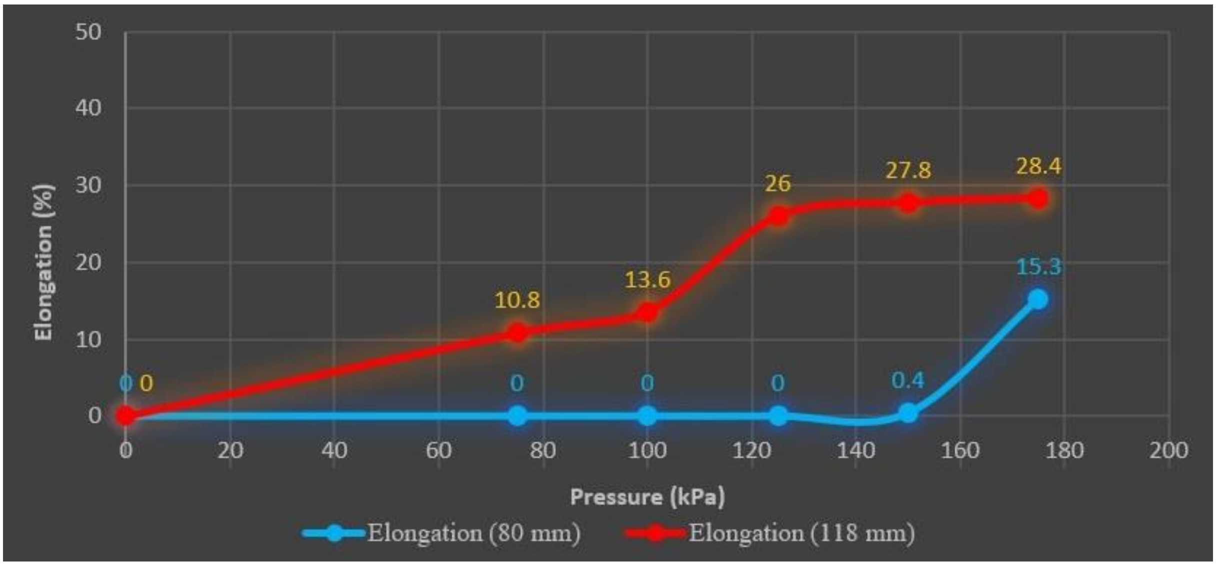

Figure 4. Result of surface elongation by MC-Cells active ($\lambda_1 k$).

Thus, soft actuator which it assists finger bone movement and joints flexor. Also, distal soft actuators have been supporting the human fingers on diagram that it has shown that as figure 5.

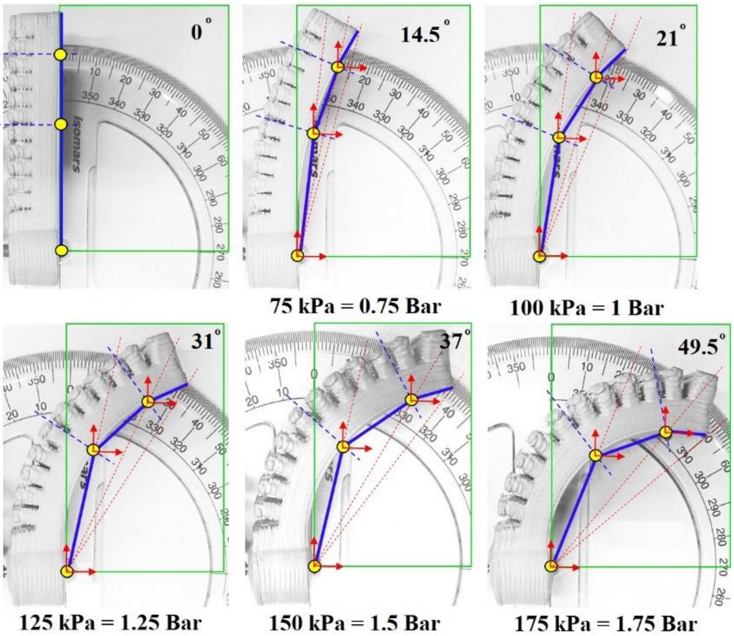

Figure 5. Bending angle of soft actuator with several air pressure generating into the model that it assists the finger bone movement (blue solid line) and finger joints flexor (yellow point).

For this reason, soft actuator affects with finger joints in biomechanics which it driven as well as the several air pressures generating. Similarly, the experimental results have showed that the percentage of biomechanics efficiency for both size models in Table 2.

Table 2. Biomechanics efficiency (in percentage) of finger joints movement ability after the soft actuator driven with several air pressure generating.

Pressure (kPa)	Model length 80 mm			Model length 118 mm		
	MCP	PIP	DIP	MCP	PIP	DIP
75	6.67%	11.82%	11.25%	12.22%	21.91%	9.38%
100	7.78%	20.45%	18.13%	17.78%	29.36%	11.63%
125	12.78%	27.27%	28.75%	27.22%	41.91%	5.75%
150	14.44%	34.54%	28.75%	31.67%	45.91%	45.13%
175	24.44%	42.73%	21.25%	46.67%	49.82%	66.75%

5. Discussion and Conclusion

This research has succeeded to study about of soft actuator characteristics which it produces by fully 3D printing with silicone rubber. So, its properties able to support the highest air pressure more than 175 kPa and assist the bending angle of finger for 77.5°. However, we found that the model less than a highest force to active because the limits of soften light weight properties to use. For this reason, it affects with the patient have strong muscle or heavy fingers.

Although, these reason as follows on above which we can select a new material in higher grade silicone rubber to driven soft actuator for grasping. Furthermore, about the force problem to assist the neurological patient in training which we can design new inner mainly air tapping which it supports flexible finger ability with higher force. Finally, 3D printing technology have very important for assisting the neurological patients in medical rehabilitation.

References

[1] Fischer H.C., Triandafilou K.M., Thielbar K.O., Ochoa J.M., Lazzaro E.D., Pacholski K.A. and Kamper D.G. 2016 Use of a portable assistive glove to facilitate rehabilitation in stroke survivors with severe hand impairment *2016 IEEE Transactions on Neural Systems and Rehabilitation Engineering* **24(3)** 344–351.

[2] Yap H.K., Yeow R.C., Lim J.H. and Nasrallah N. 2017 Design and preliminary feasibility study of a soft robotic glove for hand function assistance in stroke survivors *2017 Frontiers in Neuroscience* **11**.

[3] Polygerinos P., Galloway K.C., Savage E., Herman M., O'Donnell K. and Walsh C.J. 2015 Soft robotic glove for hand rehabilitation and task specific training *ICRA 2015* (Seattle, USA).

[4] Heung K.H., Tong R.K., Lau A.T. and Li Z. 2019 Robotic glove with soft-elastic composite actuators for assisting activities of daily living *2019 Soft Robotics* [Accessed: 2019 March] Available: https://www.researchgate.net/publication/331793050.

[5] Polygerinos P., Lyne S., Wang Z., Nicolini L.F., Mosadegh B., Whitesides G.M. and Walsh C.J. 2013 Towards a soft pneumatic glove for hand rehabilitation *2013 In Proc. IEEE/RSJ International Conference on Intelligent Robots and Systems* (Tokyo, Japan).

[6] Polygerinos P., Wang Z., Overvelde J.T., Galloway K.C., Wood R.J., Bertoldi K. and Walsh C.J. 2015 Modelling of soft fiber-reinforced bending actuators *2015 IEEE Transaction on Robotics* **31(3)**.

[7] Yap H.K., Kamaldin N., Lim J.H., Nasrallah F.A., Goh J.C. and Yeow C.H. 2017 A magnetic resonance compatible soft wearable robotic glove for hand rehabilitation and brain imaging *2017 IEEE Transactions on Neural Systems and Rehabilitation Engineering* **25(6)** 782-793.

[8] Polygerinos P., Wang Z., Galloway K.C., Wood R.J. and Walsh C.J. 2014 Soft robotic glove for combined assistance and at home rehabilitation *2014 Robotic and Autonomous System* **73** 135-143.

[9] Tarvainen T.V.J. and Yu W. 2017 Pneumatic multi-pocket elastomer actuators for metacarpophalangeal joint flexion and abduction-adduction *Journal of Actuators MDPI 2017* (Basel, Switzerland), **6(27)**.

[10] Yap H.K., Ng H.Y. and Yeow C.H. 2016 High-force soft printable pneumatics for soft robotic applications *Soft Robotics 2016* **3(3)**.

[11] Yap H.K., Liang X. and Yeow R.C. 2017 A fully fabric-based bidirectional soft robotic glove for assistance and rehabilitation of hands impaired patients *2017 IEEE Robotics and Automation Letters* **2(3)**.

[12] Feng N., Shi Q., Wang H., Gong J., Lin C. and Lu Z. 2018 A soft robotic hand: design, analysis, Semg control, and experiment *2018 International of Journal Advanced Manufacturing Technology* **97** 319-333.

BME0007

Design of Microfluidic System for Detecting Percentage Parasitemia of Malaria-Infected Red Blood Cells Using Impedance Measurement

Prapapan Sonridhi[1], Pakpum Somboon[1], Morakot Kaewthamasorn[2], Werayut Srituravanich[3], Nattapol Damrongplasit[3] and Alongkorn Pimpin[3,*]

[1] Biomedical Engineering Program, Faculty of Engineering, Chulalongkorn University, 254 Phayathai Road, Pathumwan, Bangkok 10330, Thailand
[2] Faculty of Veterinary Science, Chulalongkorn University, 254 Phayathai Road, Pathumwan, Bangkok 10330, Thailand
[3] Department of Mechanical Engineering, Faculty of Engineering, Chulalongkorn University, 254 Phayathai Road, Pathumwan, Bangkok, 10330, Thailand

* Corresponding Author: alongkorn.p@chula.ac.th

Abstract. Malaria is one of the global leading infectious diseases transmitted by the bite of *Anopheles* female mosquitos during their 'blood meat'. Parasites that cause this disease are *Plasmodium* parasites including *P. falciparum*, *P. vivax*, *P. ovale*, *P. malariae*, and *P. knowlesi*. Severe malaria when it is late for treatment occurs with enormous numbers of malaria-infected blood cells. The speed of disease examination such as the detection of percentage parasitemia plays an important role in having the chance of patient's survival. Unfortunately, the conventional microscopy technique is not a proper choice in this aspect. Therefore, this research focuses on how to develop the new way of malaria diagnosis method that is faster and yet more reliable. Three components such as microchannel, electromagnetic device and impedance measurement are combined together to achieve the goal. Microchannel helps confining the stream of blood cells, electromagnetic device creates the force to manipulate and enrich the malaria-infected blood cells containing hemozoin, and impedance measurement detects the relative amount of healthy and malaria-infected blood cells or percentage parasitemia. Unlike the microscopy technique does, an expert to run the diagnosis is not needed. In addition, less diagnostic time could assist a doctor to initiate treatment on time and save the patient's life.

1. Introduction

Malaria is a world's infectious disease caused by *Plasmodium* parasites, including *P. falciparum, P. vivax, P. ovale, P. malariae,* and *P. knowlesi,* transmitted by *Anopheles* female mosquitos. There were 228 million people who infected Malaria and approximate 405,000 deaths in 2018, mostly in sub-Saharan Africa, following World malaria report 2019 by WHO [1]. The symptoms of malaria are varied between no sign of symptoms to severe symptoms that can lead to death in later. Mostly, symptoms appear 10-15 days after the mosquito's bite. The initial symptoms are similar to a flu, such as fever with alternating chills and sweats, headache, and body aches, that are hard to diagnosis. If *P. falciparum* malaria is left untreated for 24-48 hours, it will develop the severe symptoms, such as severe anemia, respiratory distress, or cerebral malaria, because of rapid multiplication of malaria-infected cells. Generally, these severe symptoms which are together with high percentage parasitemia could refer to severe malaria that is the main cause of deaths. Thus, if we can early detect high percentage parasitemia before the symptoms occurred, it would be a great benefit for managing diseases and preventing deaths.

The gold standard of malaria diagnosis is microscopy that is widely used because of its capability to identify malaria species and percentage parasitemia to assess the treatment. Especially, finding percentage parasitemia is almost exclusively in microscopic diagnosis because it came from figuring out malaria density in thick or thin blood film under microscope [2]. However, the main disadvantages of this method are requiring an expert in order to read the results, time consuming, and not suit for field test. For using in fields, a rapid diagnostic tests (RDTs) is commonly used instead because of the speed of running a test in minutes, but this method can only identify some species of malaria that is specific in test tools. If patients are infected by the other malaria species, RDTs would not indicate that they are malaria-infected patients. Moreover, RDTs cannot tell percentage parasitemia. Thus, the information from the tests was not enough for treating diseases.

According to these difficultly of gold standard diagnosis, there is another technique so called microfluidics presented to deal with a micro scale of fluid sample. The system greatly reduces the experimental time from an hour to a few minutes as it got attention in the biomedical engineering field recently. So far, microfluidics is widely used to deal with malaria in many aspects. For example, relying on paramagnetic property of malaria-infected red blood cells (iRBCs) when malaria cells invaded into red blood cells and produced compounds containing iron, microfluidics was used for increasing density to measure as much as possible malaria infected cells by using magnetic force. For example, Sumari et al. made the cytosmears that contained most of the infected cells [3], and Bhakdi et al. optimized high gradient magnetic separation in order to isolate infected cells [4].

In addition, microfluidics was also integrated with other new techniques to detect the infected blood cells. For example, microfluidics was used for finding malaria infected cells by sensing electrical signal instead of obtaining images under microscope. Using the electrical signal is good for clarify the result of experiment since it could save time of diagnosis. Du et al. deployed electric impedance of single cell for characterizing the state of malaria, even in early stages [5]. For finding electric impedance in cell suspension, Mansor et al. carried out the experiment using microfluidic device with integrated microneedles to detect a group of *Saccharomyces cerevisiae* cells [6]. For parasitemia fast screening, Rosa and Yang used synchronous multi-tone injection of current and voltage detection of their device to figure out that the minimum parasitemia level difference was 0.0078% (390 parasites/µl) [7].

Despite of that, this is an early stage for this research field, and the improvement to find an effective method is required. In this work, we combined the advantages of microfluidics for malaria diagnosis in order to create a system that can detect malaria infection and percentage parasitemia effectively. We used cell enrichment technique to increase the density of infected cells by using electromagnetic forces and electric impedance measurement to investigate the distinguishing signal outputs for different percentage parasitemia samples. To achieve the goal, we designed a microfluidic system to manipulate the ratio between malaria-infected red blood cells (iRBCs) and healthy red blood cells (hRBCs) by using electromagnetic force to pull infected cell mostly to one outlet comparing to the other one, and measuring the impedance signals compared the magnitude and phase changes in both outlets for the possibility of detecting percentage parasitemia of malaria.

2. Principle

2.1. Electromagnetic force

When a malaria parasite invaded into red blood cells in bloodstream, it will consume hemoglobin and leave a compound of heme (a prosthetic group consisting of an iron), which developed to be hemozoin (a crystal-like form of heme) [8]. Malaria parasites keep consuming hemoglobin and increasing hemozoin that alters paramagnetic property of cell (Table 1). Using this property, external magnetic field could be used to manipulate malaria-infected red blood cells (iRBCs) and healthy red blood cells (hRBCs). Electromagnetic forces occurred on the magnetic particles when they passed through the magnetic fields. The particles will be pulled to move close to the strong magnetic field area [9].

Table 1. Relative magnetic susceptibilities of each type of RBC to water [9].

Type of RBC	Relative magnetic susceptibilities ($\Delta\chi$) 10^{-6}
hRBC	0.01
Early ring from-iRBC	0.82
Late trophozoite-iRBC	0.91
Schizont-iRBC	1.80

2.2. Cell manipulation
Microfluidics or lab-on-a-chip (LOC) is the technique that allows handling fluid in micro-and-nano scales by designing microchannel and using a proper flow rate. Because of its scale, microfluidics is using to deal with many applications in biology. In this research, we focused on how to design a microfluidics with microchannel for separating the samples to two outlets. We used T-shaped microchannel to divide fluid equally in general. To manipulate more cells to one outlet, we deployed electromagnetic force to pull malaria-infected red blood cells (iRBCs) close to fluid stream that goes to the outlet. This could make a difference in number of cells between the two outlets that we can figure out percentage parasitemia from the difference created.

2.3. Impedance measurement
Impedance measurement helps to detect specific cells from the sensing of electrical properties of samples. The dielectric properties of malaria-infected red blood cells (iRBCs) and healthy red blood cells (hRBCs) are different according to Table 2 [9].

Table 2. Dielectric properties of iRBC and hRBC (σ_m is the electrical conductivity of the suspension medium) [9].

Cell type	Position	Electrical conductivity (S/m)		Relative dielectric permittivity	
		Host	Parasite	Host	Parasite
iRBC	Membrane	$7 \pm 2 \times 10^{-5}$	$< 10^{-6}$	9.03 ± 0.82	8 ± 4
	Interior	$(0.95 \pm 0.05)\ \sigma_m$	1.0 ± 0.4	58 ± 10	70 ± 5
hRBC	Membrane	$< 10^{-6}$	-	4.44 ± 0.45	-
	Interior	0.31 ± 0.03	-	59 ± 6	-

3. Design
We designed two components, i.e. cell enrichment and impedance measurement as shown in Figure 1. For cell enrichment, an electromagnet was employed to generate electromagnetic forces at the straight channel before T-Shaped channel to pull malaria-infected red blood cells (iRBCs) to the specific outlet. After the T-junction, pairs of electrodes were employed to monitor the changes of impedance of samples in both outlets. The difference could be possibly used to tell the severity of malaria infection.

The system is consisted of three parts; PDMS microchannel, electrodes, and 3D-printed mechanical holder.

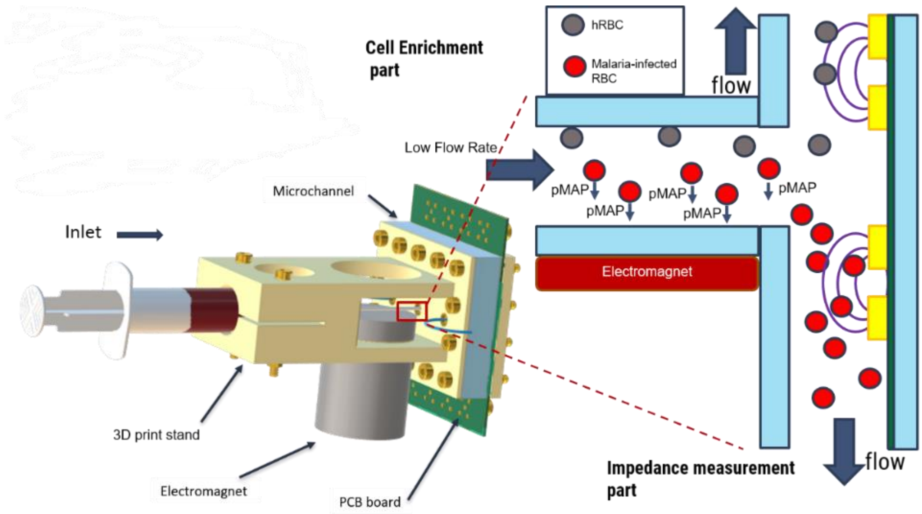

Figure 1. The schematic diagram of system.

3.1. Microchannel

The microchannel was designed to have one inlet at the middle and two outlets both to the left and right that are symmetry as shown in Figure 2a. Each side labelled as Output 1 (left side) and Output 2 (right side) has approximately 77 mm long and 40 µm height. A Polydimethylsiloxane (PDMS) microchannel was casted using the aluminium mold to create this microchannel.

3.2. Electrodes

To keep low-cost manufacturing, Printed Circuit Board (PCB) is used. The size of electrode line in PCB cannot be smaller than 2 mil (~ 50 µm). Eight pairs of electrodes were designed with two different sizes of sensing area, small (sensing area = 150 µm x 50 µm) for observing small groups of cells and large (sensing area = 150 µm x 200 µm) for observing huge groups of cells by insulating coating all PCB except the sensing area as shown in Figure 2b.

3.3. 3D-printed holder

To combine the system together, 3D-printed holder was used as illustrated in Figure 2c. Figure 3 shows the assemble of all components together.

(a)

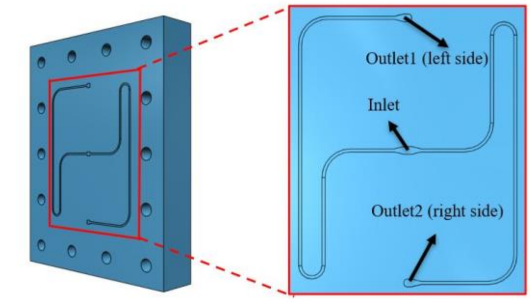

(b)

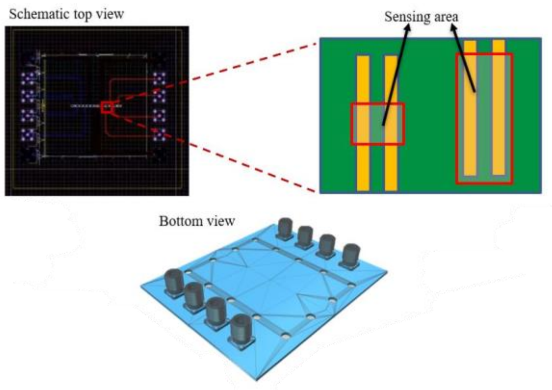

(c)

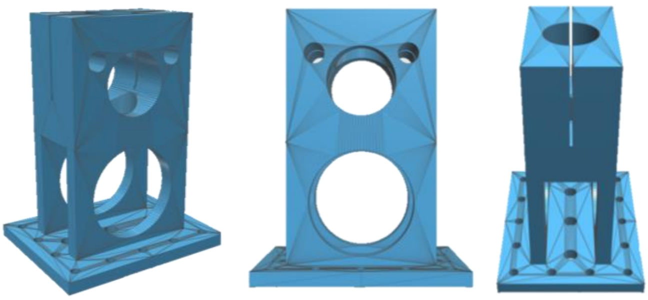

Figure 2. The design of (a) microchannel, (b) electrodes on PCB, and (C) 3D-printed holder.

(a)

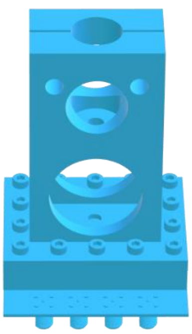

(b)

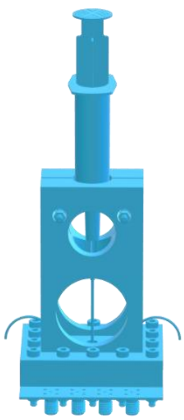

(c)

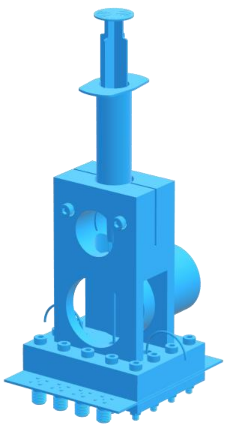

Figure 3. The assemble of all components: (a) arranging all components and fixing with screws, putting (b) syringe and outlet tubes, and (c) electromagnet generator.

4. Prototyping

All components were combined to be one assembly as shown in Figure 4. After that, electromagnet generator with DC power supply to activate electromagnetic forces was attached. Then, PCB with impedance analyser to monitor the changes of signal was connected. In experiments, proper flow rate was firstly set using a syringe pump and waiting for 30 minutes to achieve the steady state before turning on electromagnet and collecting the signal data from impedance analyser. At present, we are conducting an experiment to test the system and checking leakage of assembly and starting to test with plastic particles (diameter: 10µm) to test the effectiveness of the microchannel. The preliminary test in the buffer-volume fraction between the volume from left side and right side of microchannel and the initial volume at the inlet was comparable about 45-55%. Moreover, the percentage of the number of plastic particles from left side and right side of microchannel and the initial one at the inlet was about 20% equally, and it implied that half of particles was adhered in the microchannel.

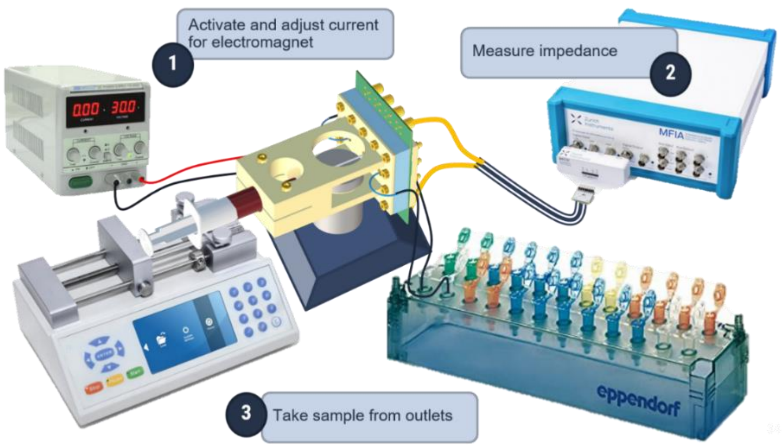

System Prototype

Figure 4. The overview of system.

5. Conclusion

New system for malaria diagnosis which could tell the patients illness and, importantly, how severity of illness they are was designed in this work. T-shaped microchannel was designed for separating the flow to be two ways symmetrically. Electromagnetic generator was deployed to manipulate the iRBCs to the specific outlet. At both outlets, pairs of electrodes were used to measure the difference of impedance, and the severity of infection could be detected. The prototype was built and the test was ongoing.

References

[1] WHO 2019 *World malaria report 2019* (Geneva: World Health Organization)
[2] Manser M, Olufsen C, Andrews N and Chiodini P L 2013 *Malar. J.* **12** 428
[3] Sumari D, Grimberg B T, Blankenship D, Mugasa J, Mugittu K, Moore L, Gwakisa P and Zborowski M 2016 *Malar. J.* **15** 113
[4] Bhakdi SC, Ottinger A, Somsri S, Sratongno P, Pannadaporn P, Chimma P, Malasit P, Pattanapanyasat K and Neumann HP 2010 *Malar. J.* **9** 38
[5] Du E, Ha S, Diez-Silva M, Dao M, Suresh S and Chandrakasan AP 2013 *Lab. Chip.* **13**(19) 3903–3909
[6] Mansor MA, Takeuchi M, Nakajima M, Hasegawa Y and Ahmad MR 2017 *Appl. Sci.* **7** 2–170
[7] Rosa BG and Yang G-Z 2020 [published online ahead of print, 2020 Apr 27] *IEEE Trans Biomed Eng.*
[8] Coronado LM, Nadovich CT and Spadafora C 2014 *Biochim. Biophys. Acta.* **1840**(6) 2032-2041
[9] Kasetsirikul S, Buranapong J, Srituravanich W, Kaewthamasorn M and Pimpin A 2016 *Malar. J.* **15**(1) 358

BME0008

Comparative Study of Kinematics and Kinetics between Normal Knee and Total Knee Arthroplasty during Squatting

Kasiwat Chaiyasit[1], Supakit Rooppakhun[2,*], and Chotchuang Phombut[2]

[1]School of Biomedical Innovation Engineering, Institute of Engineering, Suranaree University of Technology 111 University Avenue, Muang, Nakhon Ratchasima 30000, Thailand
[2]School of Mechanical Engineering, Institute of Engineering, Suranaree University of Technology 111 University Avenue, Muang, Nakhon Ratchasima 30000, Thailand

* Corresponding Author: supakit@sut.ac.th

Abstract. The objective of this study is to evaluate the kinematics and kinetics of knee joint during squatting based on the data of three-dimensional (3D) inverse dynamics analysis. A total of fifty-five subjects was collected which consisted of thirty-one normal knee and twenty-four total knee arthroplasty-TKA with the average age and body mass index (BMI) of 24.8 ± 2.2 years, 25.14 ± 6.6 kg/m^2 and 66.45 ± 6.8 years, 28.05 ± 4.2 kg/m^2, respectively. The 3D motion capture technique included the inverse dynamics analysis of the musculoskeletal (MSK) model was performed to analyze the dynamic movement of the knee joint during squatting based on computer simulation software. The contact-forces and moments of the knee joint were evaluated and then were compared between two groups using statistical mean different analysis. According to the results, there was a statistically significant difference ($p < 0.05$) of the knee joint forces and moments between the normal knee group and the TKA group during the squatting. The magnitude of maximum resultant joint force in the normal group and TKA group revealed an average of 4.35 ± 1.0, and 3.14 ± 1.3 times bodyweight, respectively. The maximum value of the axial and lateral moment of a knee joint in the normal group revealed higher than the TKA group. Also, the average maximum flexion angle in the normal knee and TKA group was 143.1 ± 12.9 degrees and 86.2 ± 20.1 degrees, respectively. There were statistical differences in squatting movement between normal and total knee replacement patients, especially in the kinematics of flexion angle. The evaluation of knee joint movement enables used for diagnosing and following the knee joint function after total knee replacement such as Oxford knee score (OKS) during daily living activities.

Keywords: Squatting, Inverse dynamics, Knee Joint, Total Knee Arthroplasty

1. Introduction

Squatting posture is a common activity that is found in Asian daily living, especially in Thailand such as resting, toileting, and meditation. The knee joint is the most vulnerable and susceptible joint, as the main lower limb motor joint during squatting activity. Normally, the squatting activity to the knee joint movement which related to the flexion angle of above 120 degrees. High-flexion or deep squatting often referred to the angle of the knee joint that over a range of 130 to 165 degrees [1, 2]. The biomechanical evaluation of the knee joint was associated with the analysis of kinematics and kinetics data. Kinematics analysis described the motion of multi-link systems as the human skeleton without the consideration of motion cause, for example, flexion angle, velocity, as well as acceleration. While, kinetics is the study of the relationship between the motion of bodies and its causes from both static and dynamic, such as the equilibrium of forces and moments.

According to squatting posture, the occurred force and moment of the knee joint which related to the ligaments and the knee joint included shank and thigh. Recent studies have shown squatting or high knee flexion for long periods which is common in Asian cultures is considered as one of the risk factors to cause a higher rate of knee osteoarthritis. The increase of knee flexion angle during squatting causes greater contact pressure in femur, tibia, and patella cartilage. Also, the large moments and forces that will result in high stress at the knee joint will reach damage to cartilage [2, 3, 4].

Nowadays, total knee arthroplasty (TKA) has become one of the most successful orthopedic procedures in providing pain relief and rehabilitation of knee function. The TKA patients were post-surgery need to return to their daily life activities that need a different range of knee flexion angles such as walking, ascending stairs, sitting, and working on the ground that needs over 60 to 130 degrees of knee flexion angle. The biomechanical study of the knee joint is even more important after arthroplasty because the knee joint forces are therefore directly implicated in joint articular wear and damage, especially to the polyethylene component. In many studies of TKA patients, the knee forces have been reported for a variety of activities, for example, the contact forces during walking increased at 2.8 times body weight. Stair descent were contact forces at 3.2 to 3.5 times bodyweight more than stair ascent at 2.9 to 3 times bodyweight, respectively. While during squatting, the knee forces were in a range of 2.8 to 3.8 times body weight at different knee flexion angles [5, 6].

In the present, 3D motion capture is the most common technique to detect the movement for the analysis of kinetics and kinematics of knee joint including forces, moments, and range of motion, that used the 3D retro-reflective tracking markers located at the anatomical joints and segments, which are obtained by the 3D infrared cameras. While, inverse dynamics technique is the most comprehensive method used to calculate the joint reaction forces and moments which require the kinematics data and the ground reaction forces acquired with force plate synchronized with the cameras based on computer simulation software [7, 8]. For example, the studies of biomechanics of knee joint during squatting, that used a musculoskeletal model by 3D marker motion capture data based on computer simulation and force plate to collect kinematic and kinetic data to examine knee forces and moments [1, 4, 9]. Furthermore, some studies of TKA patients and knee osteoarthritis were used the same technique and constructed subject-specific models to examine the knee biomechanics [3, 6].

Also, the diagnostics and rehabilitation in post-surgery follow-up of TKA patients are using Oxford knee score (OKS) and the knee movement assessment to examine the knee function, range of motion, and pain after total knee replacement (TKR) surgery which related directly to the force and moment of knee joint during daily living. The recent study to validate the Oxford knee score (OKS) in patients with knee osteoarthritis were collected by the New Zealand Joint Registry, which found the OKS are useful predictors of early rehabilitation after TKR and use for the monitoring of the outcome and potential failure in TKA patients. It can be considered a reliable and valid measurement [10].

This study was to examine significant differences in knee joint biomechanics based on inverse dynamic and 3D-motion analysis. By focusing on the study of posture in daily activities under the activity of squatting from fifty-five subjects consisting of thirty-one normal knee group and twenty-four TKA group. Kinematics and kinetics of knee joints were considered directly and then compared between groups. The information on knee joint movement can be clinically applied in diagnosing and following the knee joint function after total knee replacement such as Oxford knee score (OKS), which useful for predicting medical treatment. Finally, for implant designers to develop of high range of motion the knee replacements.

2. Biomechanics of knee joint

Knee biomechanics is simple concerning the type of motion. The knee functions that characterize the biomechanics are complex because they needed knee mobility and stability. The knee joint offers a wide range of motion with high resistance to external stress. Loads are transmitted by a combination of compressive force between the articular surfaces and tensile force in the ligaments and muscles. Ligaments are considered passive elastic structures and can only be loaded in tension. Muscle and tendons are considered active elastic structures and can only act under tension. Bones are non-elastic structures and work under compressive loads [11].

A. Kinematics of knee joint

Joint kinematics is the study of the relative motion between two consecutive segments of the human body without considering the forces that cause them to move. Squatting is one of the postures that was used for the kinematics study of the knee joint. During knee flexion, knee joint motion is a combination of sliding and rolling between the contracting tibia and femoral condyle surfaces with a range of motion about 0° to 135° of flexion. The internal and external rotation about the knee is approximately 5° to 10° in each direction [9]. In daily activities, the range of knee flexion angle extends from 10° to 160° as shown in figure 1. First, the screw-home mechanism of flexion was in a range between 5° to 20° with the rotation between the tibia and femur occurs automatically. Next, the range of motion between 20° to 120° of flexion angle was considered as the fundamental of active arc, which involves most of the daily activities. Finally, the passive arc between 120° to 160° of flexion angle, which is most commonly used in the Asian population [12].

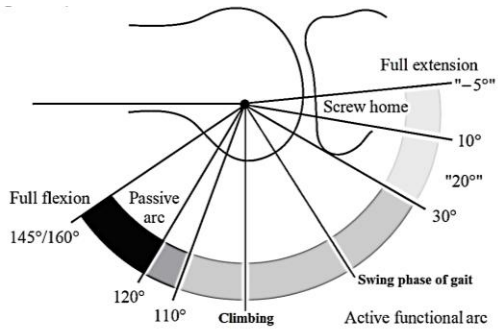

Figure 1. Range of motion during squatting of a human knee joint.

B. Inverse dynamics of knee joint

The inverse dynamics technique is the most comprehensive method used in the solution of biomechanical problems to calculate the joint reaction forces and moments that the musculoskeletal system or load-bearing on prosthetic components during human locomotion. Consideration using input data is needed to carry out this analysis, for example, body weight, body segment parameters, kinematics, and kinetics information [7, 13].

The lower limb consists of three rigid points including thighs, shank, and foot as shown in figure 2. There are connected with a single hinge joint and internal muscle forces are acting on this joint to counterbalance the moment due to external forces. The relationship of the internal forces and moments developed at the ankle, knee, and hip joint are determined in the weight, a moment of inertia, accelerations, angular velocity, and angular acceleration of the segments, and the orientation during walking and squatting. The components of forces along the positive direction of axes and clockwise moment at joints are positive values. The dynamic equations in the thigh, shank, and foot segments are written as in equation (1) to equation (9), respectively.

Component of joint forces X_H and Y_H along the plane of progression x and vertical direction y respectively. While X_K and X_{AN} along the plane of progression x and Y_K and Y_{AN} along vertical y are given by, Hip Joint Model:

$$X_H = X_K + \frac{W_T}{g}[\ddot{x}_H - \dot{\theta}_H^{\,2}(r_T cos\theta_H) - \ddot{\theta}_H(r_T sin\theta_H)] \tag{1}$$

$$Y_H = Y_K + W_T + \frac{W_T}{g}[\ddot{y}_H - \dot{\theta}_H^{\,2}(r_T sin\theta_H) + \ddot{\theta}_H(r_T cos\theta_H)] \tag{2}$$

And joint moment M_H is given by

$$\begin{aligned} M_H &= M_K - X_K(l_T sin\theta_H) + Y_K(l_T cos\theta_H) + W_T(r_T cos\theta_H) \\ &+(I_T + \frac{W_T}{g} r_T^{\,2})\ddot{\theta}_H - \frac{W_T}{g}[\ddot{x}_H(r_T sin\theta_H) - \ddot{y}_H(r_T cos\theta_H)] \end{aligned} \tag{3}$$

Knee Joint Model:

$$X_K = X_{AN} + \frac{W_S}{g}[\ddot{x}_K - \dot{\theta}_S^{\,2}(r_s cos\theta_S) - \ddot{\theta}_S(r_s sin\theta_S)] \tag{4}$$

$$Y_K = Y_{AN} + W_S + \frac{W_S}{g}[\ddot{y}_K - \dot{\theta}_S^{\,2}(r_s sin\theta_S) + \ddot{\theta}_S(r_s cos\theta_S)] \tag{5}$$

And joint moment M_K is given by

$$\begin{aligned} M_K &= M_{AN} - X_{AN}(l_S sin\theta_S) + Y_{AN}(l_S cos\theta_S) + W_S(r_s cos\theta_S) \\ &+(I_S + \frac{W_S}{g} r_s^{\,2})\ddot{\theta}_S - \frac{W_S}{g}[\ddot{x}_K(r_s sin\theta_S) - \ddot{y}_K(r_s cos\theta_S)] \end{aligned} \tag{6}$$

Ankle Joint Model:

$$X_{AN} = -X_G + \frac{W_F}{g}[\ddot{x}_{AN} - \dot{\theta}_F^{\,2}(r_F cos\theta_F) - \ddot{\theta}_F(r_F sin\theta_F)] \tag{7}$$

$$Y_K = -Y_G + W_F + \frac{W_F}{g}[\ddot{y}_{AN} - \dot{\theta}_F^{\,2}(r_F sin\theta_F) + \ddot{\theta}_F(r_F cos\theta_F)] \tag{8}$$

And joint moment M_{AN} is given by

$$\begin{aligned} M_{AN} &= -X_G Y_{AN} - Y_G(X_G - X_{AN}) + W_F(r_F cos\theta_F) \\ &+(I_F + \frac{W_F}{g} r_F^{\,2})\ddot{\theta}_F - \frac{W_F}{g}[\ddot{x}_{AN}(r_F sin\theta_F) - \ddot{y}_{AN}(r_F cos\theta_F)] \end{aligned} \tag{9}$$

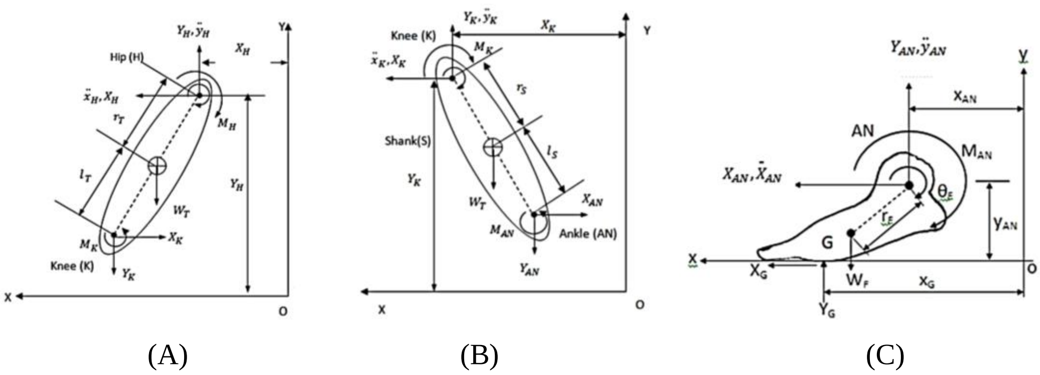

(A) (B) (C)

Figure 2. External forces acting on the segment: (A) thigh, (B) shank, and (C) foot.

Where X_G and Y_G are longitudinal and vertical components of ground reaction forces. The X_{AN} and Y_{AN} are coordinated ankle joint. X_G is the longitudinal coordinate of the ground reaction force. W_T, W_S, and W_F are the weight of the thigh, shank, and foot segments $\ddot{x}_H, \ddot{y}_H, \ddot{x}_K, \ddot{y}_K, \ddot{x}_{AN}$ and $\ddot{y}_{AN}$ are the component of translation acceleration of hip, knee, and ankle joint along axes of reference. $\theta_H, \dot{\theta}_H, \ddot{\theta}_H, \theta_S, \dot{\theta}_S, \ddot{\theta}_S, \theta_F, \dot{\theta}_F$ and $\ddot{\theta}_F$ are the angular rotation, angular velocity, and angular acceleration of axis of the thigh, shank measured clockwise from x-direction. While the axis of the foot concerning the forward direction. The l_T and l_S are the lengths of the thigh and shank. r_T, r_S and r_F are the distance of the mass center of the thigh, shank, and foot from its proximal joint. The I_T, I_S, and I_F are the mass moment of inertia of the thigh, shank, and foot about its centroidal axis. g is the acceleration due to gravity [15].

3. Materials and Methods

3.1 Data acquisition

The 3D motion data of volunteers were collected, which is human research and experimental, and preserved by the Human Research Ethics Committee (HREC), Suranaree University of Technology. The biomechanical evaluation of the knee joint in two different groups of subjects consisted of the normal knee group and the total knee arthroplasty group was considered. The thirty-one normal knee subjects which healthy and had no history of knee surgery (average body mass index-BMI of 25.14 ± 6.65 kg/m^2) were used and the average age, height, and weight of 24.8 ± 2.2 years, 1.66 ± 0.06 m., and 69.48 ± 18.77 kg, respectively. While the TKA group consisted of twenty-four subjects (average body mass index-BMI) of 28.05 ± 4.28 kg/m^2) and the average age, height, and weight of 66.45 ± 6.8 years, 1.56 ± 0.07 m., and 68.20 ± 10.78 kg. TKA group were performed by the same surgeon and were 1-year post-surgery at the time of the data collection. All subjects were installed with reflective markers on their bodies before data acquisition using a 3D tracking camera and force sensor plate during the squatting posture as shown in figure 3.

(A) (B)

Figure 3. Anatomical locations used the reflective marker placement on the body during squatting: (A) normal subject and (B) TKA subject.

3.2 The 3D motion analysis system

The inverse dynamic technique which required kinematics and kinetics of a knee joint during squatting was performed in this study. The motion data were collected and processed using musculoskeletal modeling to calculate knee joint force including moment. Each subject was tracked the 3D positions of 43 retro-reflective spherical marker points on the anatomical locations according to the Vicon's Plug-in-Gait marker placement protocol as shown in figure 3. The marker-based motion data analysis was obtained using a 6-camera (MX40) 3D motion system (Vicon). The ground reaction forces were obtained from a force sensor plate for each foot during the trial using two force plates (Kistler-type

9281B). The motion data were recorded and analyzed using the Qualisys Track Manager (QTM) software (Qualysis, Savedalen, Sweden). The kinematics input data and ground reaction force were then evaluated and used to calculate the knee joint force as well as moment. The body segments were also scaled using the measured data obtained from each subject included age, gender, body weight, and height. The kinematics, kinetics, and inverse dynamic MSK model of the subject-specific were analyzed by using the AnyBody Modeling System (AnyBody Technology) software as shown in figure 4.

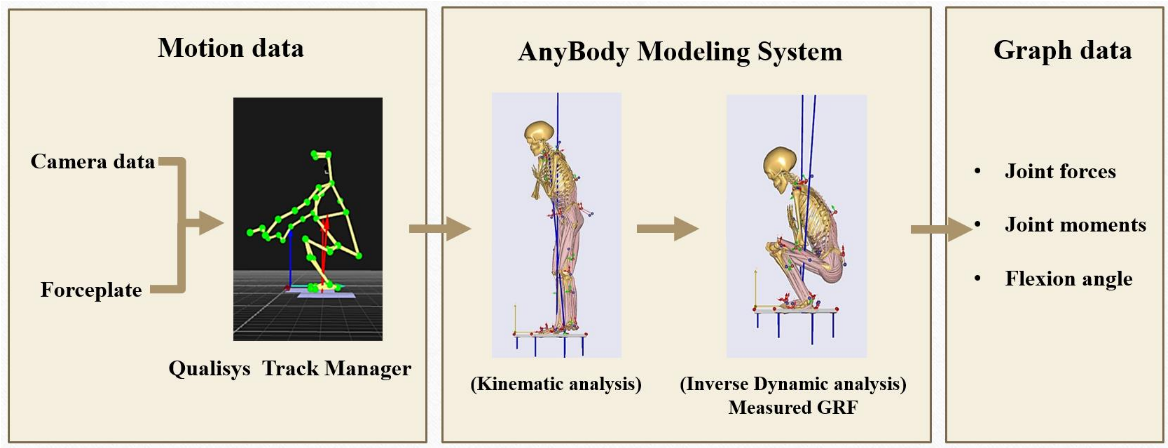

Figure 4. Three-dimensional maker-based models data flowchart.

3.3 Protocol for the squatting activity
Before the squatting, all subjects step up on the force plates and putting the feet flat to each force plate with both feet parallel to each other. To collect data, the squat position was repeated for each volunteer. During the squatting motion, the subject has to keep three conditions:

1) Stand still until recording the statics mode for five seconds,
2) Squatting with maximum knee flexion angle within tolerance and with preferred trunk flexion. Both heels flat on the force plate.
3) Each subject completed three trials of squatting activity.

3.4 Statistical analysis
The statistical analysis was considered by using statistical and data analysis software MedCalc program. The biomechanical parameter consisted of knee joint forces, moment, and flexion angles during the squatting cycle were then compared between the normal knee group and TKA group. The analyzed data including means, standard deviation (SD) was evaluated. Also, the comparison of the mean difference (t-test) at the level of significant differences of p-value < 0.05 was performed.

4. Results & Discussion
The purpose of this study was to examine knee kinematics and kinetics in the normal knee and TKA group during squatting activity based on 3D-motion techniques and inverse dynamic analysis. The parameter consisted of the knee force (anterior-posterior; -AP, medial-lateral; -ML and proximal-distal; -PD), knee moment (axial and lateral), and knee flexion angle. Table 1 showed the results of the squatting analysis included knee joint parameters and the comparison between the normal knee and TKA groups. During squatting, the average of AP-force and PD-force that occurred in the knee joint displayed a higher value than the PD-force in both groups. However, there was a statistically significant difference between the normal knee and TKA groups. The joint force in the normal knee group revealed a higher value than the TKA group. Similarly, the result of the average resultant moment included the axial and lateral moment in the normal knee group displayed significantly higher than TKA groups.

Table 1. Comparison of knee joint parameters between the normal knee and TKA group at the maximum average as mean (±SD)

Parameters	Normal (n=31)	TKA (n=24)	P value
AP force (BW)	3.56 ± 1.1	2.91 ± 1.2	0.0419
ML force (BW)	0.44 ± 0.2	0.04 ± 0.1	0.0001
PD force (BW)	3.09 ± 0.8	0.45 ± 1.2	0.0001
Resultant force (BW)	4.35 ± 1.0	3.14 ± 1.3	0.0003
Axial moment (N-m)	8.84 ± 5.1	5.68 ± 4.8	0.0233
Lateral moment (N-m)	34.57 ± 8.2	15.73 ± 16.1	0.0001
Resultant moment (N-m)	35.99 ± 8.0	20.71 ±11.3	0.0001
Maximum flexion angle (Degree)	143.1° ± 12.9°	86.2° ± 20.1°	0.0001

*Significant difference between normal and TKA ($P < 0.05$)

Figure 5 showed the results of the average resultant force and average knee force in AP, ML, and PD direction during the squatting cycle of both groups. During the squatting phase, the maximum AP- force of the normal knee group displayed 3.5 times body weight at 53% of the squatting cycle. While the TKA group exhibited 2.9 times body weight at 86% of the squatting cycle. However, the result of ML- force showed a low value and closely between the normal knee and TKA group with approximately 0.44 and 0.04 times body weight at 49% and 28% of the squat cycle, respectively. The result of PD-force revealed that there was 3 times body weight at 77% of the squat cycle in the normal knee group and 0.45 times body weight at 100% of the squat cycle for TKA. Also, the resultant force of the normal knee group and TKA group were 4.35 times bodyweight and 3.14 times bodyweight, respectively. The average maximum force of the knee joint in the normal knee group was higher than the TKA group during the squat cycle. Also, there was a statistically significant difference ($p < 0.05$) between the two groups. This result of knee forces was similar to the previous studies. For example, the average maximum forces displayed in a range of 2.8 and 3.8 times body weight at the flexion angle of 125 degrees to 139 degrees for different types of squatting in subjects without arthritis or TKA [9]. The previously also reported the maximum force of TKA subject-specific model of squatting approximating 2.2 to 2.3 and 3.25 times body weight at different maximum knee flexion angles [3, 6]. According to the studies that used the same technique also reported the maximum resultant force in a range of 1.8 to 3 times bodyweight and 3.2 times bodyweight for TKA subject [17, 18]. The maximum values of the anterior-posterior force nearly always acted in the posterior direction. The medial-lateral force was small and nearly close to zero during the squat cycle. In addition, the anterior-posterior force was generally higher than the medial-lateral force, while the proximal-distal force was the highest of those forces, respectively.

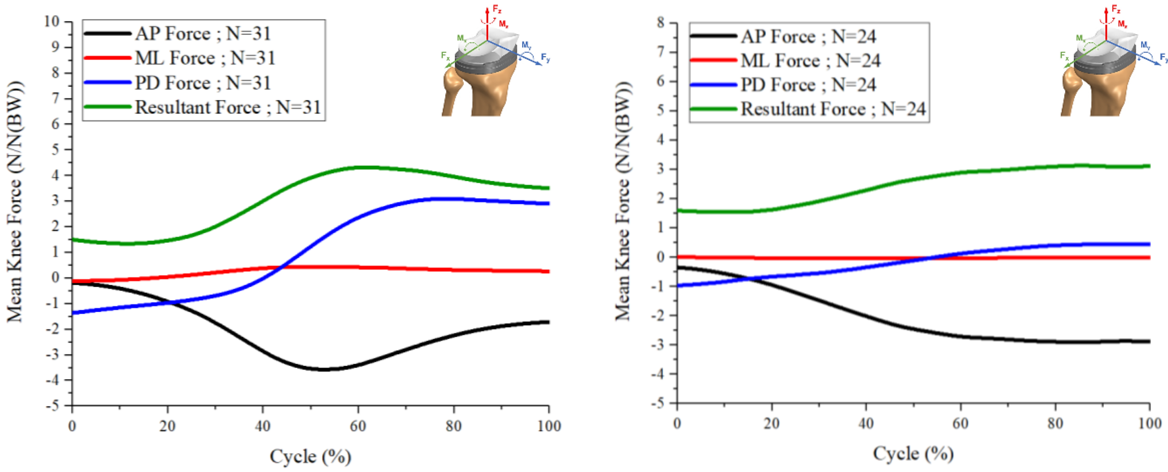

(A) (B)

Figure 5. Comparison of average knee forces measured during squatting for both groups with (A) normal knee group and (B) TKA group; the anterior-posterior force (black line); the medial-lateral force (red line); the proximal-distal force (blue line) and the resultant force (green line).

Figure 6(A) and 6(B) showed the result of the average resultant moment and average knee moment in the axial and lateral direction during the squatting cycle of both groups. In general squatting, the knee moments were increased varied the high flexion angle. Comparatively, the average maximum moments of a knee joint in the normal knee group were higher than the TKA during the squat cycle. The average axial moment in the normal knee and TKA group displayed the maximum value of 8.8 N-m and 5.7 N-m at 89% and 98% of the squat cycle, respectively. While the average lateral moment showed the maximum value of 34.6 N-m and 15.7 N-m at 88% and 98% of the squat cycle for the normal knee and TKA group, respectively. The resultant moment of the normal knee group was 35.99 N-m while the TKA group was 20.71 N-m, respectively. Also, there was a statistically significant difference ($p < 0.05$) between the knee moment of the normal knee and the TKA group. For previous studies, the variation of the axial moment value was close to zero or small negative and positive during the entire loading cycle of squatting activity. The value of lateral moment was negative or close to zero and starts increasing to positive values while during the initial phase of squatting. The axial moment was generally higher than the lateral moment [14, 17] that similar to this study, respectively. In addition, the increase of resultant force during squatting will increase the stress on the patellar tendon as well as the contact forces in the tibiofibular joint. The force and moment exerted on the knee joint varied with the knee flexion angle during squatting [15].

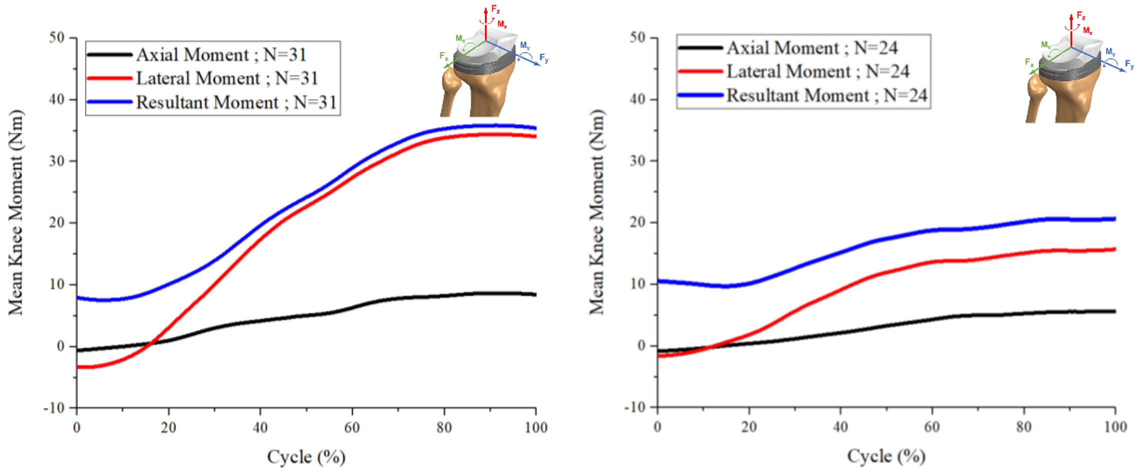

(A) (B)

Figure 6. Comparison of average knee moment measured during squatting between both groups with (A) normal knee group and (B) TKA group: the axial moment (black line); the lateral moment (red line), and the resultant moment (blue line).

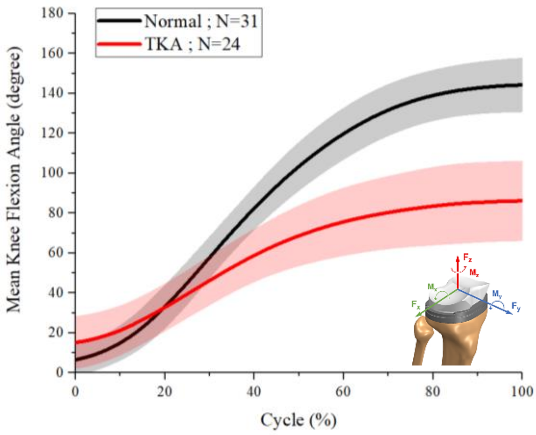

Figure 7. Comparison of average knee flexion angle during squatting between both groups with normal knee group (black line) and TKA group (red line).

Figure 7 represented the results of the flexion angle in each percentage of the squatting cycle between the normal knee group and the TKA group. The knee flexion angle started in a knee extension position of 6 degrees and 15 degrees for the normal knee and TKA group. The average maximum flexion angle in the normal knee group and TKA group were 143.1 degrees and 86 degrees, respectively. Clearly, there was a significant difference in knee flexion angle between the normal knee and TKA group. The normal knee group can be squatting with a higher value of knee flexion angle than the TKA group. According to the risk assessment studies, the factors that affected to the range of motion postoperatively for TKA patients included the preoperative range of motion, underlying disease, age, weight and height of the patients, surgical technique, implant design, and postoperative physiotherapy [16]. For the previous report, the normal knee flexion angle of Asian squatting was approximate 138 degrees, and the average flexion angle in a range of 125 degrees to 146 degrees for different types of squatting in subjects without arthritis or TKA [1, 9]. In addition, the maximum flexion angle during squatting for the TKA group was average in a range of 92 degrees to 98 degrees [6, 14]. The previous studies that used the same technique reported the flexion angle was approximately 80 degrees to 105 degrees [17, 18].

5. Conclusion

In this study, the kinematics and kinetics data of the squatting activity using inverse dynamic and 3D-motion analysis between the normal knee and TKA group were presented. During the squatting cycle, the magnitude of maximum force, moment, and flexion angle in the normal knee group were higher than the TKA group. The result of the maximum resultant force in the normal group was an average of 4.3 times body weight while the TKA group was an average of 3.1 times body weight. The average maximum flexion angle of the normal knee and TKA group was 143 degrees and 86 degrees, respectively. The result of this study may enable diagnosing or following knee joint disease, analyze the knee joint function after total knee replacement surgery during daily activities, and for the knee implant development to the high range of motion.

6. Acknowledgments

The research is partly supported and funded by the Health Systems Research Institute. The authors would like to acknowledge Assoc. Prof. Pornthep Rachnavy, School of Sports Science, Institute of Science, Suranaree University of Technology for the suggestion of AnyBody Modeling System software and 3D motion technique. Also, the authors would like to thank all subjects for their cooperation from Suranaree University of Technology Hospital.

7. Reference

[1] Dela Peña MS. The Biomechanics of the Knee during High Flexion Posture: Asian kinetically different from Caucasians. Philippine Normal University, Faculty of Science Technology and Mathematics, 2018.

[2] Fox J, editor Knee and Ankle Biomechanics during Squatting with Heels On and Off of the Ground, with and Without Weight Shifting 2016.

[3] Nagura T, Matsumoto H, Kiriyama Y, Chaudhari A, Andriacchi TP. Tibiofemoral joint contact force in deep knee flexion and its consideration in knee osteoarthritis and joint replacement. J Appl Biomech. 2006.

[4] Ashvin Thambyah. How critical are the tibiofemoral joint reaction forces during frequent squatting in Asian populations? The Knee 15 (2008) 286–294

[5] D'Lima DD, Fregly BJ, Patil S, Steklov N, Colwell CW, Jr. Knee joint forces: prediction, measurement, and significance. Proc Inst Mech Eng H. 2012.

[6] Mizu-Uchi H, Colwell CW, Jr., Flores-Hernandez C, Fregly BJ, Matsuda S, D'Lima DD. Patient-specific computer model of dynamic squatting after total knee arthroplasty. J Arthroplasty. 2015.

[7] Pàmies-Vilà R, Font-Llagunes JM, Cuadrado J, Alonso FJ. Analysis of different uncertainties in the inverse dynamic analysis of human gait. Mechanism and Machine Theory. 2012.

[8] M.P.T. Silva, J.A.C. Ambrosio. Kinematic Data Consistency in the Inverse Dynamic Analysis of Biomechanical Systems. Multibody System Dynamics 8: 219–239, 2002

[9] Smith S, Cockburn R, Hemmerich A, Li R, Wyss U. Tibiofemoral joint contact forces and knee kinematics during squatting. Gait & posture. 2008.

[10] A G Rothwell, G J Hooper, A Hobbs, C M Frampton. An analysis of the Oxford hip and knee scores and their relationship to early joint revision in the New Zealand Joint Registry. J Bone Joint Surg Br. 2010 Mar;92(3):413-8.

[11] Affatato S. 2 - Biomechanics of the knee. In: Affatato S, editor. Surgical Techniques in Total Knee Arthroplasty and Alternative Procedures. Oxford: Woodhead Publishing; 2015. p. 17-35.

[12] Shi J, editor Finite element analysis of total knee replacement considering gait cycle load and malalignment. University of Wolverhampton for the degree of Doctor of Philosophy, June 2007.

[13] Dumas R, Cheze L, Frossard L. Loading applied on prosthetic knee of transfemoral amputee: comparison of inverse dynamics and direct measurements. Gait Posture. 2009.

[14] Bergmann G, Bender A, Graichen F, Dymke J, Rohlmann A, Trepczynski A, et al. Standardized loads acting in knee implants. PLoS One. 2014.

[15] Singh Chauhan S. Kinematic and kinetic analysis of knee joint during squatting. IOP Conference Series: Materials Science and Engineering. 2019.

[16] H Farahini. Factors Influencing Range of Motion after Total Knee Arthroplasty. Iranian Red Crescent Medical Journal. Iran Red Crescent Med J 2012; 14(7):417-421
[17] I. Kutzner. Loading of the knee joint during activities of daily living measured in vivo in five subjects. Journal of Biomechanics 43 (2010) 2164–2173
[18] J. Ro, C. Kim. Contact mechanics and muscle stability of total knee arthroplasty during squatting and walking: a simulation study. Orthopaedic Proceedings Vol. 99-B, No. SUPP_5

BME0009

Effect of Insert Conformity to Contact Stress in Total Knee Replacement: Finite Element analysis

Techin Seechaipat[1], Supakit Rooppakhun[2,*], and Chotchuang Phombut[2]

[1]School of Biomedical Innovation Engineering, Institute of Engineering, Suranaree University of Technology 111 University Avenue, Muang, Nakhon Ratchasima 30000, Thailand
[2]School of Mechanical Engineering, Institute of Engineering, Suranaree University of Technology 111 University Avenue, Muang, Nakhon Ratchasima 30000, Thailand

* Corresponding Author: Supakit@sut.ac.th

Abstract. The conformity of insert component is one of the important geometric parameters in the design of total knee replacement (TKR) which must be considered for the biomechanics and wear performance. A changing of the insert conformity will result to contact stress between the tibiofemoral joint affected TKR performance. This study involved evaluating the effect of insert conformity in the posterior stabilized type of TKR to the contact stress using Finite Element (FE) Analysis. The three-level experimental designs for response surface of insert different curvature in the sagittal and coronal plane were analyzed. The FE model of femoral and insert components were created and analyzed under loading conditions based on the standard knee contact pressure test (PI-17). A total of nine design scenarios included the different insert conformity (curve, partial flat, and flat) in sagittal and coronal planes were analyzed in various knee flexion angles. According to the result, the insert conformity in the coronal and sagittal plane displayed the effect of the change on the contact stress and contact area in each flexion angle of the knee joint. While the flexion angle of knee joins raise, the magnitude of maximum contact stress increased however the contact area value decreased. The changing of insert conformity value in the sagittal plane displayed higher sensitivity to biomechanical contact than the changing of conformity in the coronal plane. The design of the insert component with low conformity will be benefited to decrease the contact area that affects to reduce wear volume in TKR. However, the decrease of insert conformity may affect the increase of contact stress included the limitation of the knee joint with low constraint. The study indicated that the geometric design of the insert conformity played a crucial role that influenced the contact stress as well as the biomechanical performance of TKR.

Keywords: Insert conformity, Total Knee Replacement, Contact stress, Finite Element Analysis

1. Introduction

Total Knee Replacement (TKR) is a medical device used in the orthopedic surgical procedure to replace the weight-bearing surfaces of the knee joint to relieve pain and commonly performed for osteoarthritis. However, there are currently still reports of complications from patients after surgery due to problems such as implant loosening, pain, and weight-bearing surfaces wear [1-3]. The surface wear of the insert component is an essential factor for the shortening lifetime included the loosening of TKR [4-7]. In severe cases, revision surgery may be required because of material damage, which generally uses Ultra-High Molecular Weight Polyethylene (UHMWPE). Biomechanically, the result of wear in TKR is caused by mechanical factors included material, geometry shape of insert design, and kinematics of daily activity. Insert conformity is one important parameter related in both the coronal and sagittal plane for the design of TKR s should be considered both of biomechanics contact and wear performance [4-8]. Normally, the conformity is the ratio between the curvature radius of the insert and the distal femoral component [3].

In previous studies showed that the design of TKR by a change in the insert conformity affects the contact mechanics distribution both of stress distribution as well as contact area [4-7]. The relation of UHMWPE volumetric wear is directly proportional to the wear coefficient and sliding distance included the contact area [4]. In addition, the mechanical contact between the tibiofemoral joint which related to the bearing-weight caused by the daily activity of the patient was an essential factor that leads to biomechanical wear [4-6]. The level of contact stress distribution correlated inversely with the contact area of the insert component in TKR with the various kinematics of the knee joint. In a previous study, the computational model using Finite Element (FE) analysis and experimental studies have shown that the effect of insert conformity is important in the determination of TKR wear included biomechanical performance [8-10]. Using FE analysis, the biomechanics contact between the articulating against of insert and a femoral component could be described which have reliable as the experimental study. In addition, in vitro study of contact pressure distribution in the tibiofemoral using Fujifilm technique or Tekscan pressure sensor was a common instrument, which helps to understand the impact of geometric design of TKR [11,12]. However, the experimental studies still have a limitation of the high cost and long-time. According to the standard knee contact pressure test (PI-17), the purpose of the test was to evaluate the pressure distribution and total contact area on the tibiofemoral joint of the TKR system based on the bodyweight load in each different flexion angle [13]. The bearing load in each flexion angle of 0 to 90 degree with the loading in the range of 4 to 5 times of body weight was used for determining the knee contact pressure. These results can be used to develop optimized geometries included the conformity of the insert component.

In the consideration of the main effect, the design of experiments (DOE) was used to evaluate the most important factor affecting the output, leading to the optimized output response and explanation of the interaction between the factors [14,15]. The purpose of responses surface methodology (RSM) was to determine the optimal condition of the system by analyzing multi-factor data included to evaluate the level of factors that optimize the response. In this study, we hypothesis that the various conformity ratio in TKR which the changing of insert curvature effect to the contact stress as well as the contact area. Therefore, this study aimed to investigate the main effect of insert conformity based on a curved, partial flat, and flat in the sagittal and coronal plane to the contact stress between the tibiofemoral joint of the TKR system. Using FE modeling and simulation, the main effect of insert conformity and surface response analysis to the contact stress was obtained. The results of this study provide essential information for the design of the insert component for the suitable biomechanical performance of TKR.

2. Materials and Methods

2.1 Computational Model

In this study, a 3D computational model that was the posterior-stabilized type of TKR was considered which consisted of the femoral component and insert component as shown in figure 1. The geometric parameter of the insert component was considered as the radius of curvature in the sagittal plane (Cs) and curvature radius in the coronal plane (Cc) as shown in figure 1(B). The insert conformity was defined by the ratio of curvature radius between the femoral component and insert component which in a range of 0 (flat) to 0.7 (curved) and 0 (flat) to 0.8 (curved) for the sagittal plane and coronal plane, respectively [16].

A total of 9 models varied conformity value with the maximum to minimum in the coronal and sagittal plane were analyzed by using computer simulation software (Abaqus Knee Simulator-SIMULIA, Johnston, USA) as shown in Table 1. The FE model of the femoral component was determined by a rigid body using the tetrahedron element type with a control element size of 1.0 mm. While the insert component was modeled as the deformed body using the hexahedron element type with a 1.0-mm element length. The mechanical properties of the insert component were considered with Young's modulus of 685 MPa, Poisson's ratio of 0.47, and the density of 0.94 g/cm^3 [17]. The coefficient of friction between the femoral component and the insert component was 0.04.

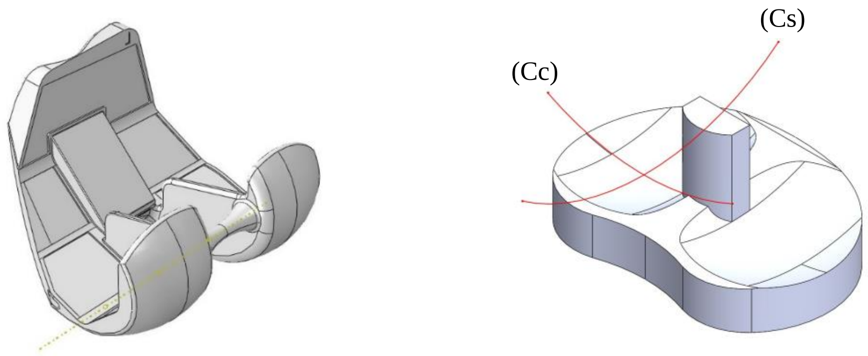

Figure 1. Posterior-stabilized TKR: (A) Femoral component, (B) Insert component.

Convergence testing was performed to verify that the solution did not exhibit any significant changes with mesh refinement as shown in figure 2. According to the testing, the element edge length was changed (in a range of 3.5 mm to 0.5 mm) until the percentage difference in the critical results of maximum contact stress between two consecutive mesh densities were less than 2% of the peak contact pressure during the knee flexion. The convergence study results indicated that the mesh density utilized for these insert components was an acceptable range relative to that obtained in a previous study [18, 19].

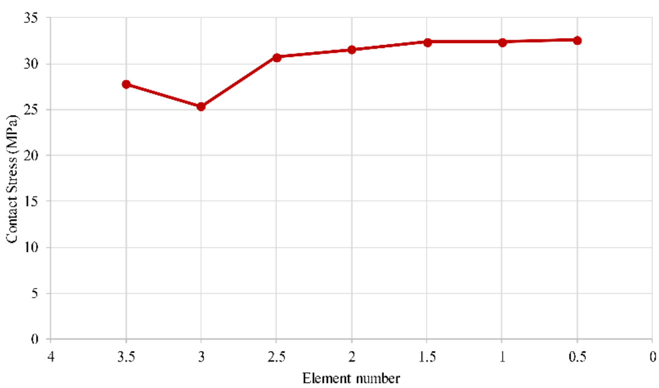

Figure 2. Convergence test for maximum contact stress.

Table 1. Different conformities of different insert components in the sagittal and coronal plane.

Parameters	Abbreviation	values
Coronal plane in curve conformity	Cc_{max}	0.80
in partial flat conformity	Cc_{mid}	0.40
in flat conformity	Cc_{min}	0.00
Sagittal plane in curve conformity	Cs_{max}	0.70
in partial flat conformity	Cs_{mid}	0.35
in flat conformity	Cs_{min}	0.00

2.2 Boundary and Loading Conditions

The FE models of TKR consisted of the femoral component and the tibial insert component was used to analyze the contact stress included the contact area on the insert component based on the standard knee contact pressure test (PI-17). For the boundary conditions, the vertical axial load under various flexion angle between the femoral components and insert was performed as displayed in Table 2. The bearing compressive load was considered as the bodyweight with equal distribution on the medial and lateral side of the femoral component. The bottom surface of the tibial insert component was considered fully constrained with no translation and rotation as shown in figure 3. The femoral component was allowed free moving in medial-lateral translation included the internal-external and varus-valgus rotations.

Table 2. The load and flexion angles according to standard knee contact pressure test (PI-17)

Flexion angle(°)	Load(kN)
0	2901
15	2901
30	3267
60	3626
90	3267

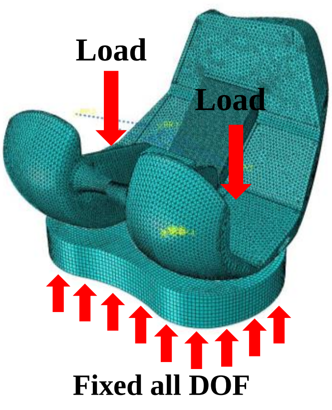

Figure 3. Boundary and Loading Conditions

2.3 Response Surface Methodology (RSM)
The design of experiment (DOE) was used to effectively statistical design and analysis process included the screening design and optimization [20, 21]. Generally, optimization design is mostly analyzed for finding a response optimizer to determine the optimum factor value. In this study, response surface methodology (RSM) was performed with a three-level (3^k) factorial experiment to evaluate the optimum conformity value of the insert component. All results were analyzed for determining the optimum value of the distribution of contact stress included the contact area.

3. Results
3.1 Effect of conformity to contact stress and contact area in various knee flexion angle
The typical FE result of contact stress distribution occurred on the contact surface of the insert component in each knee flexion angle (0º, 30º, 60º, and 90º) was displayed in figure 4. The magnitude of the contact stress is changed according to the knee flexion angle and occurred the high value of 43 MPa in the 90 degree of flexion angle. Also, the contact point displayed a change in the anterior-to-posterior direction as the increase of knee flexion angle.

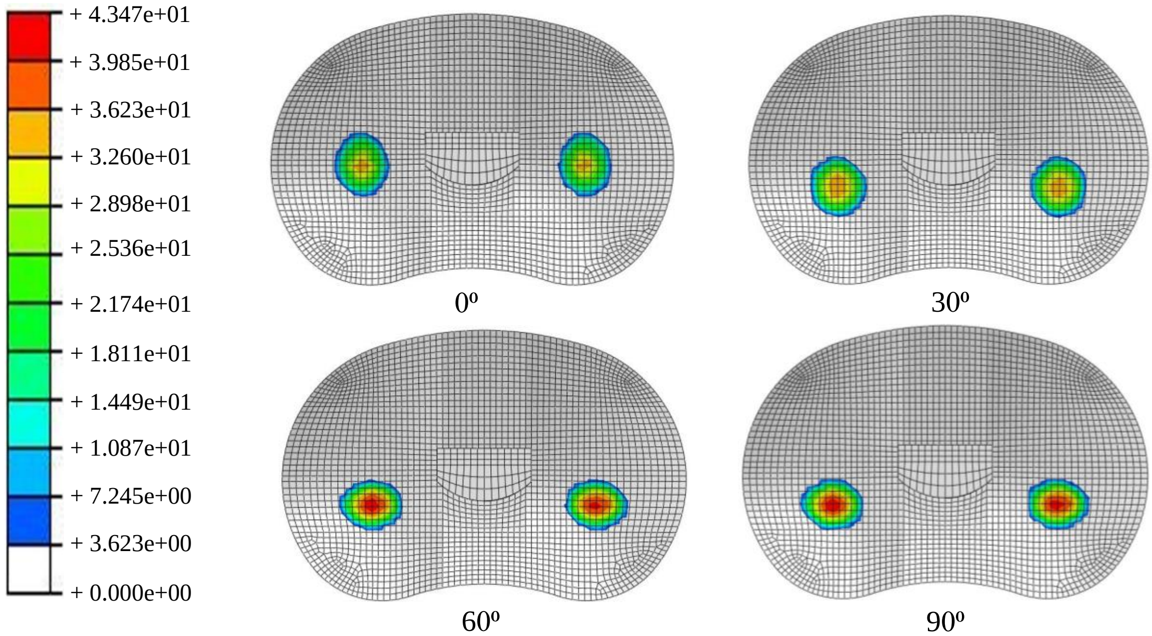

Figure 4. The typical contact stress distribution on the insert component in each flexion angle.

Figures 5 and 6 illustrated the result of contact area and the contact stress in various flexion angles which change with the conformity value of sagittal and coronal planes, respectively. The magnitude of contact stress tends to be clearly increased when conformity vale of both the sagittal and coronal planes was decreased included the increase of knee flexion angle. While the decrease in the contact area occurred in the case of low conformity at an increase in degree. The flat conformity in the sagittal plane exhibited the low contact area value as shown in figure 5(A). For example, the contact area of the curved, partial flat, and flat conformity was 292 mm^2, 178 mm^2, and 159 mm^2, respectively at the flexion angle of 0º. According to the result of contact stress, it was found that the flat conformity displayed the high contact stress, while the curved conformity revealed the low contact stress as shown in figure 5(B). In addition, the results showed that the tendency of changing contact stress following the conformity of the coronal plane displayed similar changes in the conformity of the sagittal plane.

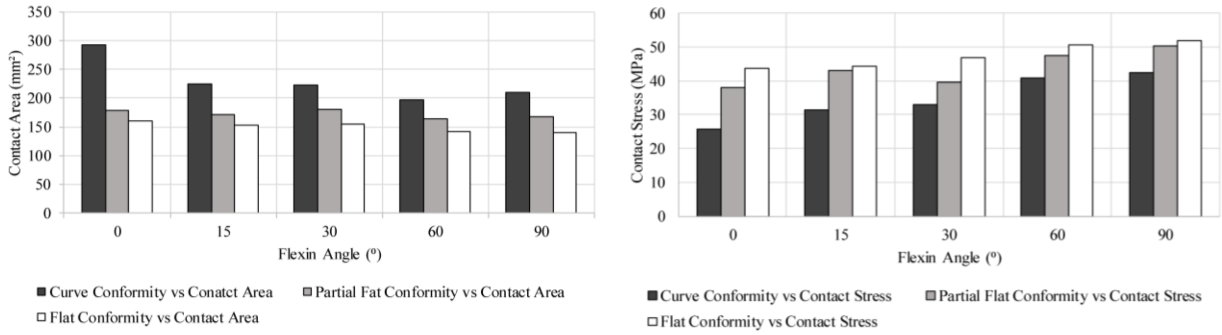

(A) (B)

Figure 5. The effects of sagittal conformity to contact area and contact stress in various flexion angles: (A) the contact area, (B) contact stress

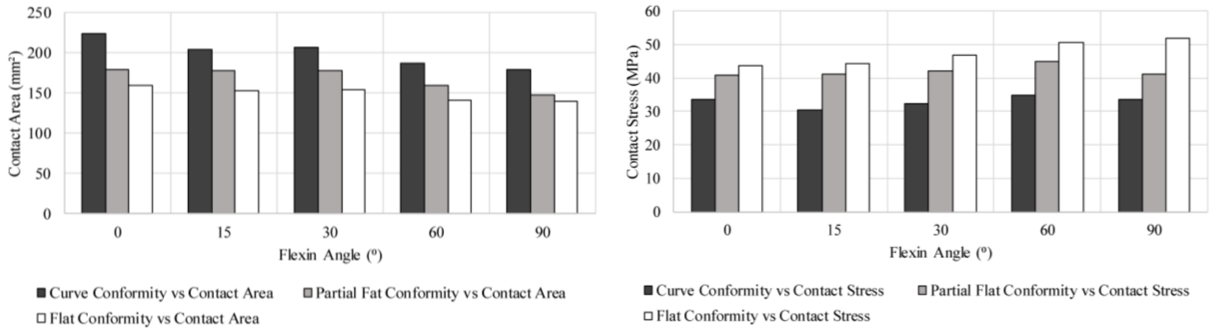

(A) (B)

Figure 6. The effects of coronal conformity to contact area and contact stress in various flexion angles: (A) the contact area, (B) contact stress.

3.2 Analysis of variance and response surface methodology of conformity

The analysis of the variance of insert conformity to the contact area and contact stress was shown in Tables 3 and Table 4, respectively. The value of R-square was 99.65 percent and 98.14 percent from the contact area and contact stress analysis, meaning if the variance of the data is 100 percent, then the variance of the results is 99.65 percent, which can be described by the regression equation. Also, the Adj-R-square value of the contact area and contact stress was similar to R-square, indicating that the studied data was sufficient for analysis of the experiment. The linear regression analysis for predicting contact area and contact stress showed in equations (1) and (2), respectively. The result of variance analysis of insert conformity (Table 3) found that the interaction between Cc and Cs had a significant statistical ($p < 0.05$) effect on the contact area. Likewise, Cc and Cs had a significant statistical ($p < 0.05$) effect to contact stress concerning contact stress, whereas the interaction between Cc and Cs was not statistically significant ($p < 0.05$). In addition, Tables 3 and 4 demonstrate that the conformity in the sagittal plane was the main effect to the contact stress included the contact area by considering the adjusted sums of squares (Adj SS) with the highest value.

Table 3. Analysis of variance of contact area

Source	DF	Adj SS	Adj MS	F-Value	P-Value
Model	5	36447.0	7289.4	172.81	0.001
Linear	2	32473.2	16236.6	384.92	0.000
Cc	1	7177.4	7177.4	170.15	0.001
Cs	1	25295.8	25295.8	599.69	0.000
Square	2	3969.6	1984.8	47.05	0.005
Cc*Cc	1	660.5	660.5	15.66	0.029
Cs*Cs	1	3309.1	3309.1	78.45	0.003
2-Way Interaction	1	4.2	4.2	0.10	0.772
Cc*Cs	1	4.2	4.2	0.10	0.772
Error	3	126.5	42.2		
Total	8	36573.5			
S = 6.49474 R-sq = 99.65% R-sq(adj) = 99.08% R-sq(pred) = 96.10%					

$$\text{Contact area} = 160.10 - 7.0\,Cc - 49.9\,Cs + 113.6\,Cc*Cc + 332.1\,Cs*Cs + 7.4\,Cc*Cs \quad (1)$$

Table 4. Analysis of Variance of contact stress

Source	DF	Adj SS	Adj MS	F-Value	P-Value
Model	5	525.358	105.072	31.64	0.008
Linear	2	505.650	252.825	76.14	0.003
Cc	1	143.164	143.164	43.12	0.007
Cs	1	362.486	362.486	109.17	0.002
Square	2	17.180	8.590	2.59	0.222
Cc*Cc	1	16.208	16.208	4.88	0.114
Cs*Cs	1	0.972	0.972	0.29	0.626
2-Way Interaction	1	2.528	2.528	0.76	0.447
Cc*Cs	1	2.528	2.528	0.76	0.447
Error	3	9.961	3.320		
Total	8	535.319			
S = 1.82221 R-sq = 98.14% R-sq(adj) = 95.04% R-sq(pred) = 79.63%					

$$\text{Contact Stress} = 44.12 + 0.03\,Cc - 20.50\,Cs - 17.79\,Cc*Cc - 5.7\,Cs*Cs + 5.68\,Cc*Cs \quad (2)$$

The surface response of contact stress and contact area was established from linear regression analysis as exhibited in equation (1) and equation (2). Figures (7A) and Figures (7B) showed the result of the response surface analysis of the contact area and the contact stress, respectively. The analysis results indicated that the contact area may be reduced by the decrease of Cs and Cc values, however, the decrease of Cs and Cc have increased contact stress. According to the optimal conformity, figure (8) showed optimum values of Cs and Cc for minimizing contact area and maximize contact stress. The results found that the Cc value of 0.0242 and Cs value of 0.0778 revealed the lower contact area as shown in figure (8A). For the contact stress, these results also showed that the use of low conformity in both Cs and Cc values exhibited the high contact stress as displayed in figure (8B).

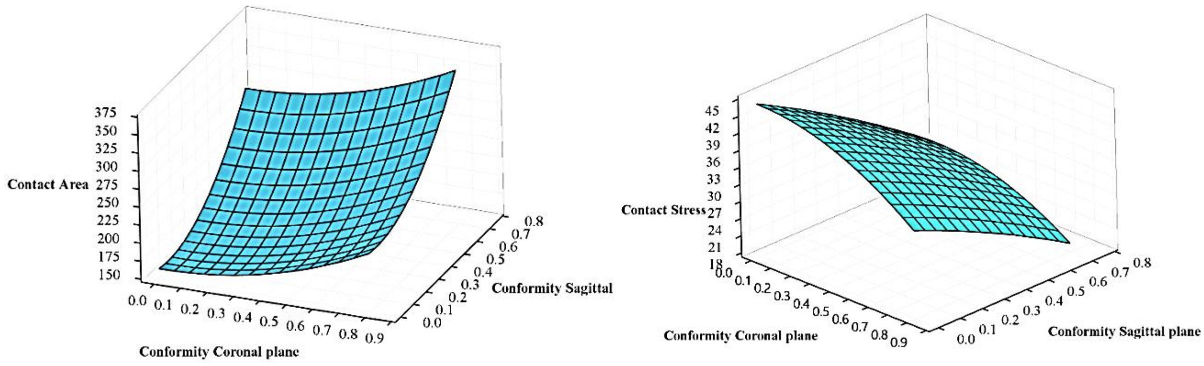

(A) (B)

Figure 7. The response 3D surface plots of contact mechanics: (A) Surface plots of the contact area to parameter conformity. (B) Surface plots of the contact stress to parameter conformity.

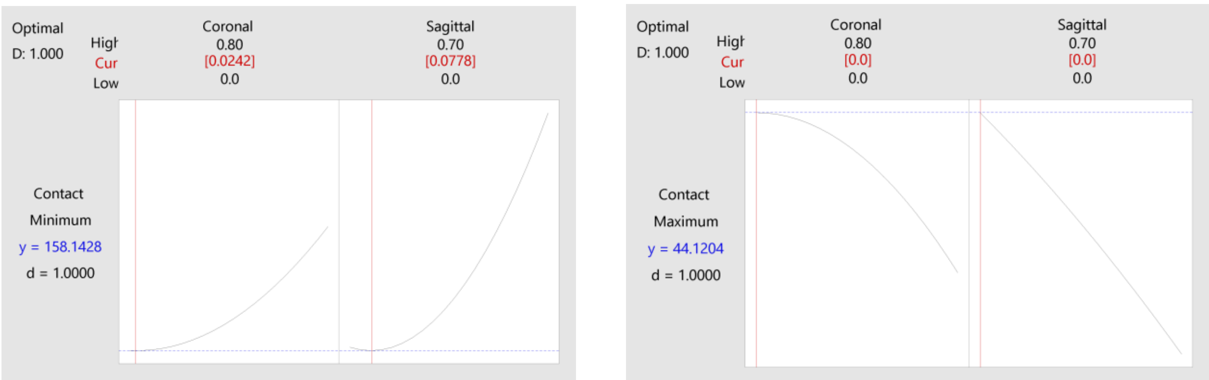

(A) (B)

Figure 8. Response optimization plot. (A) Main effects on the contact area. (B) Main effects on the contact stress.

4. Discussion

The effects of insert conformity on the biomechanics contact examined by using a computational model for the curve, partial flat, and flat insert conformity in the coronal and sagittal planes were investigated. The FE analysis was performed based on load and flexion angle following the standard PI-17. The results were analyzed for optimal values using the RSM method with three-level factorial designs. The results found that the contact stress has changed due to the variation of coronal and sagittal insert conformity design. By the insert component had low conformity demonstrates the highest contact stress and the lowest contact area than other insert conformity. Additionally, the factor of conformity in the sagittal plane displayed a higher effect to contact mechanics than the changing of conformity in the coronal plane that the significance level ($p < 0.05$). Moreover, the results of the optimization were analyzed that low conformity provides the optimal contact mechanism which will be benefited to decrease the contact area that affects to reduce wear volume in TKR.

The study showed that there was a difference in insert conformity in the coronal and sagittal planes, resulting in the distribution of the contact stress and the contact area in the flexion angle. Three different insert conformity were curve, partial flat, and flat showed an effect on contact stress that same both coronal and sagittal plane. The increase of flexion angle carries out the contact stress increases, whereas, the contact area decreases. The decrease of conformity value provides a high magnitude of contact stress but low contact area [4]. The volume wear loss was based on the contact area, sliding distance, and wear coefficient. Therefore, the low value of insert conformity will result in reducing the wear volume due to the contact area of the femoral component with the insert was narrower affecting the less contact dispersion [4,6]. In addition, the present study also showed the inversely preoperational relationship between contact stress and the conformity level. The low conformity value displayed the high magnitude of contact stress resulted in significantly low wear rates [5]. With higher contact stress on the low conformity, the insert will have smaller wear scars resulting in reduced wear. These results can be noticed that the insert conformity was significant for the contact stress and contact area, which affects the wear of the TKR.

According to the main effect analysis, the insert conformity value in the coronal and sagittal plane was carried by using variance and RSM in the analysis. The results of the analysis of variance in the significance level ($p < 0.05$) were shown in Table 3 and Table 4. The variance of insert conformity shown the value of R-square was 99.65 percent and 98.14 percent from the contact area and contact stress analysis, respectively. The result revealed that the validity of the regression equation described for approximately 99.65 and 98.14 percent in the contact area and contact stress, respectively. While the Adj-R-square of the contact area and contact stress analysis value displayed 99.08 and 95.04, respectively, which similar to R-square. From Table 3, the factors affecting the contact area were analyzed. It was analyzed that the interaction between Cc and Cs had a significant level in the contact area ($p< 0.05$). Likewise, factors of Cc and Cs were also effective in the contact area significantly. Table 4 showed the results of the analysis of factors affecting the contact stress. The results showed that the factor of Cc and Cs had a significant statistical effect on contact stress concerning contact stress ($p<0.05$), whereas the interaction between Cc and Cs was not statistically significant. When considering all factors, it could observe that values of the Adj SS in the factor of Cs were seen to be valued higher than the factor of Cc and factor interaction. This indicates that the factors of Cs were the main effect affecting contact stress and contact area. The study also found that the knee kinetics were significantly more affected by conformity insert design in the sagittal plane compared to the coronal plane [7]. Furthermore, most studies were likely to have similar results was that the insert conformity in the sagittal plane has a high effect on contact mechanical change than conformity in the coronal plane [4-7]. The results can be indicated that the insert conformity design in the sagittal plane was important for determining the TKR knee kinematics.

For the optimal conformity values using the RSM method, the results showed that the contact area was reduced when the conformity in the coronal and sagittal plane decreased from 0.8 to 0.0 and 0.7 to 0.0, respectively. The optimal value of insert conformity was performed. The optimal conformity values in the coronal and sagittal plane for the minimized contact area were 0.0242 and 0.0778, respectively. The optimal conformity coronal and sagittal planes for maximized values of contact stresses were 0.0 and 0.0 respectively. As a result, the low conformity tends to be well suited to contact mechanics that reduce wear that corresponds to the previous studies [4-6]. Although the low conformity was provided the decrease of contact area affecting wear volume reduction on insert component, however, there may be some limitations such as constraint or mobility of TKR. The constraint issue between insert components as articulated against the femoral component, such as a slide of the femoral component to enables femoral rollback with knee flexion [10]. In addition, the low conformity can be caused by unnatural femoral rollback that there may be no slide of the femoral component in anterior-posterior direction movement. For the design of TKR, it is necessary to consider other factors in order to complete the design of the TKR such as material, constraint, the volume of wear, etc.

Conclusion

This study evaluated the influence of insert geometric conformity in both of coronal and sagittal plane on biomechanical contact of TKR. Using a three-level factorial design of the experiment, the factor of three different curvatures included curved, partial flat, and flat insert shape was analyzed. The results showed that the variation of insert conformity has an impact on contact stress as well as the contact area during the flexion angle of the knee joint. The changing conformity in the sagittal planes displayed a significant effect to contact stress than the conformity in the coronal plane. The result of surface response analysis found that the low conformity provides a decrease of contact area but the increase of contact stress affecting wear performance of insert component. The geometric conformity design of the insert component played a crucial role influenced the contact stress as well as the biomechanical performance of TKR.

Acknowledgments

This research is partly supported and funded by the Health Systems Research Institute and Suranaree University of Technology. The authors also would like to acknowledge Dr. Sedthawatt Sucharitpwatskul (National Metal and Materials Technology Center-MTEC) for the suggestion of ABAQUS Knee Simulator software.

References

[1] M.M. Ardestani et al., 2015. Posterior stabilized versus cruciate retaining total knee arthroplasty designs: Conformity affects the performance reliability of the design over the patient population. *Medical Engineering and Physics*, 37(4), pp 350–360.
[2] Koh et al., 2018. Effect of geometric variations on tibiofemoral surface and post-cam design of normal knee kinematics restoration. *Journal of Experimental Orthopaedics*, 5(1), pp 53-65.
[3] Koh et al., 2019. Tibiofemoral conformity variation offers changed kinematics and wear performance of customized posterior-stabilized total knee arthroplasty. *Knee Surgery, Sports Traumatology, Arthroscopy*, 27(4), pp 1213–1223.
[4] Abdelgaied et al., 2014. The effect of insert conformity and material on total knee replacement wear. *Proc IMechE Part H: J Engineering in Medicine*, 228(1), pp 98-106.
[5] Galvin AL, Kang L, Udofia I, et al., 2009. Effect of conformity and contact stress on wear in fixed-bearing total knee prostheses. *J Biomech*, 42(12), pp 1898–1902.
[6] Brockett et al., 2018. Influence of conformity on the wear of total knee replacement: An experimental study. *Proc IMechE Part H: J Engineering in Medicine*, 232(2), pp 127-134.
[7] Q. Zhang, et al., 2019. Insert conformity variation affects kinematics and wear performance of total knee replacements. *Clinical Biomechanics*, 65, pp19–25.
[8] Usman and Shyh Chour Huang., 2017. Effect of Average Conformity on Contact Stresses in Total Knee Replacement: Finite Element Analysis. *MATEC Web of Conferences*, 108.
[9] Liming Shu et al., 2018. An in-vivo experimental evaluation of Abaqus Knee Simulator for Total Knee Replacement. Science in the Age of Experience. Retrieved May 16, 2019, from http://www.3ds.com/events/science-in-the-age-of-experience.
[10] S. Kuriyama et al., 2015. Posterior tibial slope and femoral sizing affect posterior cruciate ligament tension in posterior cruciate-retaining total knee arthroplasty. *Clinical Biomechanics*, 30(7), pp 676–681.
[11] R. Zdero et al., 2001. Fuji Film and Ultrasound Measurement of Total Knee Arthroplasty Contact Areas. *The Journal of Arthroplasty*, 16(3), pp 367-375.
[12] K.N. Bachus et al., 2006. Measuring contact area, force, and pressure for bioengineering applications: Using Fuji Film and TekScan systems. *Medical Engineering & Physics*, 28(5), pp 483–488.
[13] PI-17. Determination of Total Knee Implant Contact Pressure. Test instructions from Endolab® Mechanical Engineering GmbH from https://www.endolab.org/implant-testing.asp?topic=Knee%20contact%20pressure%20test%20PI-17&cat1=2&id=38.
[14] I. M. Fukuda et al., 2017. Design of Experiments (DoE) applied to Pharmaceutical and Analytical Quality by Design (QbD). *Braz. J. Pharm. Sci*, 54, pp 1-16.
[15] Montgomery, D.C., 2013. Design and Analysis of Experiments (John Wiley & Sons, Incorporated)
[16] C.W. Clary et al., 2013. The influence of total knee arthroplasty geometry on mid-flexion stability: An experimental and finite element study. *Journal of Biomechanics*, 46(7), pp 1351-1357.
[17] Koh Yong-Gon et al., 2019. Prediction of Wear on Tibial Inserts Made of UHMWPE, PEEK, and CFR-PEEK in Total Knee Arthroplasty Using Finite-Element Analysis. *Lubricants*, 7(4), pp 30.
[18] Alessandro Navacchia et al., 2016. Subject-Specific Modeling of Muscle Force and Knee Contact in Total Knee Arthroplasty. *J Orthop Res*, 34(9), pp 1576-1587.
[19] A.C. Godest et al., 2002. Simulation of a knee joint replacement during a gait cycle using explicit finite element analysis. *Journal of Biomechanics*, 35(2), pp 267–275.

CST0006

Computational Analysis of Directly Irradiated Annular Pressurized Receiver (DIAPR) for a Solar Tower

Pakpoom Nutthawaree[1], Supakorn Issarakul[2], and Wishsanuruk Wechsatol[1,*]

[1] Department of Mechanical Engineering, Faculty of Engineering, King Mongkut's University of Technology Thonburi, Bangkok, Thailand
* Pakpoom Nutthawaree : E-mail pakpoom.ruk@gmail.com
* Wishsanuruk Wechsatol : E-mail wishsanuruk.wec@kmutt.ac.th
[2] United Multidisciplinary Engineering Company Limited, Bangkok, Thailand
* Supakorn Issarakul: E-mail supakorn.is@gmail.com

Abstract. Energy harvesting from solar irradiation can be done by utilizing photovoltaic solar cells or direct heat absorption mediums. In this work, the high temperature solar concentrators which reflect and concentrate solar radiation onto flowing fluid mediums were investigated. The Directly Irradiated Annular Pressurized Receiver (DIAPR), which provides the high collection temperature of above 1,000 °C for solar concentrated towers was computationally investigated by utilizing finite element methods to observe the velocity flow field, temperature distribution throughout the DIAPR and heat collection efficiency. The standard air was selected as the heat collection medium. The computational results were validated with previous experiments from the literature. The results show that the highest temperature of 1,093°C can be obtained when the inlet air was fed to the DIAPR at 39.2 °C and 16.5 bar with the air flow rate of 100.5 kg/hr according to the literature. 30 kW of solar irradiation was applied to the DIAPR solar collector surface and yielded the solar heat collection efficiency of 85.40%
Keyword: Solar energy, Volumetric receiver, Direct Irradiated Annular Pressurized Receiver, DIAPR

1. Introduction

Sustainable energy is playing more roles in replacing the conventional fossil fuels. Solar power is ideally the largest energy source on earth and having tremendous potentials in heating and electricity generation. There are two common ways to harvest energy from solar radiation, -i.e. photovoltaic cells and direct heat adsorption. By utilizing semiconductor materials, Photovoltaic cells directly generate electricity from solar radiation with the electricity generation efficiency around 17% on average. In this work, the focus is on collecting heat from solar radiation at high temperature to serve as energy source in heat driven production processes. Solar concentrator devices are common equipment for harvesting solar heat energy. The most common solar concentrator type is the solar hot water heater on the household rooftops which can product hot water at the temperature as high as 95 °C at atmospheric pressure. For any heat driven production processes requiring heat supply above the standard atmospheric boiling point of water, the high temperature solar concentrators are required. The temperature at the focal points of solar radiation depends on the types of focal points and the concentration ratio. Table 1 is the common utilization temperature for each type and its concentration ratio. Fresnel concentrators, which has the lowest concentration ratio can provide lower temperature than other types, while solar tower with the highest concentration ratio can provide higher usage temperature of collected solar heat than other types. The highest temperature up to 3,500 °C was achieved at Odeillo solar furnace facility in Font-Romeu-Odeillo-Via, France [15].

Table 1 Common usage temperature of solar concentrators [6, 12, 14, 15, 16, 17, 19]

Concentrator types	Focal Types	Usage temperature [°C]	Concentration ratio	Common Application
Fresnel	Line	50 - 500	10 - 40	power generation, steam generation
Parabolic trough	Line	100 – 700	30 – 100	power generation, steam generation
Concentrated dish	Point	300-1,000	500-3,000	power generation, hydrogen production
Solar tower	Point	550 – 3,500	5,000 - 10,000	power generation, gas reforming, hydrogen production

The main equipment for high temperature solar heat collection are reflectors, receivers, and flow passages of heat absorption medium. The design of Direct Irradiated Annular Pressurized Receiver (DIAPR) was proposed by Karni J. [8]. Solar receivers for solar towers are divided into two types, the external receivers and the internal receivers. In the external receivers in Figure 1., the reflected heat from reflectors is directly focused onto the flow passages of the heat transfer medium, which are located in perimeter around the top of a solar tower. The configuration of external receivers allows the solar tower to receive the reflected heat in 360 degrees around the tower, thus minimize the reflector area and the effects of tower shade on the reflectors. However, such configuration, which is opened up to the surrounding air induces the natural convection of air drafting upward and the natural convective losses. DIAPR in Figure 2. is an internal volumetric cavity receiver which operates at pressurized condition of 10 bar – 20 bar in a closed volumetric space in order to direct the flow of heat adsorption medium, thus minimizing the convective losses. Since the convective loss is eliminated, the DIAPR can easily increase the temperature of flowing medium above 1,000 °C [8, 13], which is more than sufficient for power generation and hydrogen production by direct thermochemical water splitting processes. The common flowing medium for DIAPR are air and carbon dioxide. In this work, the focus is on creating computational model to study the flow phenomena and temperature distribution throughout the DIAPR.

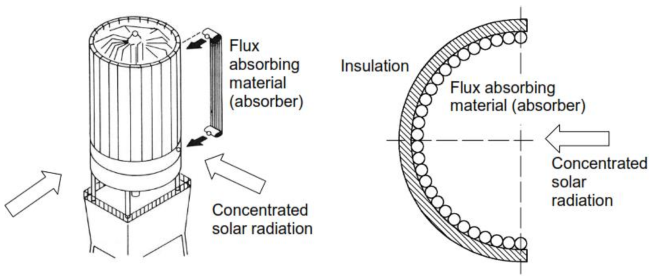

Figure 1. Solar receiver types external solar receiver (left) and cavity receiver (right) [2]

2. DIAPR configuration

The main components of DIAPR in Figure. 2 are composed of a compound parabolic concentrator (CPC), a KohinOr light extractors, a back reflector, a frustrum-like high pressure (FLHIP) window, porcupine absorbers, and flow passages. The compound parabolic concentrator (CPC) is typically made of high reflective mirror, which works as light tunnel to direct solar radiation received from the reflector field around the solar tower onto the KohinOr light extractors. The extractor acts as light distributor onto the porcupine absorbers, which are normally made of alumina ceramic. Typically, the intensity rate of concentrated solar energy on the surface of porcupine absorbers is larger than 100,000 W/m^2 and maybe up to 10 MW/m^2 [8]. The frustrum-like high pressure (FLHIP) window allows intense light to pass through and acts as the transparent wall of heat transfer chamber to seal off any heat convective loss. The frustrum-like high pressure (FLHIP) window must be made of fused silica (fused quartz) to endure heat at high temperature. The flowing medium which is standard air in this study is pumped though the chamber and exchange heat with the porcupine fins of the absorber.

The development phase based on experimental trial started in the year 1992. The first DIAPR with volumetric absorber was developed at WIS Solar Furnace. It produced power input of only 11 kW of heat under low operating temperature [11]. In 1996, porcupine absorber was introduced causing DIAPR to be able to operate at 1200 °C [13]. The concept of CPC was first introduced in 1974 [CPC] and was installed in combination with the extractor. The extractor was developed by taking reflection index of each geometry into account obtaining its most suitable geometry, the regular hexagonal prism. The 1996 version of DIAPR had 2 inlet tubes with close ends at upper cavity and 3 exit tubes with close end similar to the 1992 version. Its air exit temperature was approximately 1000 °C [13]. In order to be able to operate under high pressure, window was also installed into the 1996 version to withstand operating pressure of over 50 bar [9]. In 1998, another version of DIAPR was developed, the second flow inlet tube at the upper part of the cavity and 2 exit tubes were eliminated. Its air exit temperature was 1089 °C [13].

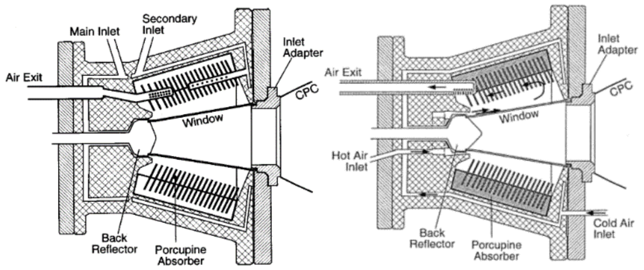

Figure 2. Schematic cross-section of the DIAPR (a) 1996 version and (b) 1998 version [13]

In this work, 30 kW DIAPR with component and dimension as specified in Figure 3 was computationally investigated to observe the flow field and heat transfer phenomena of air flowing through the heat exchanging chamber of the DIAPR. The Frustum-like High Pressure (FLHIP) has the front and back cavities with diameter of 125.5 mm and 65 mm, respectively and slope angle of 10°. To withstand high pressure and temperature, the FLHIP is typically made of fused silica (fused quartz) with thickness of 2 mm. CPC and KohinOr light extractor is installed at the front end to direct and reflect solar radiation through the FLHIP window onto the porcupine absorbers.

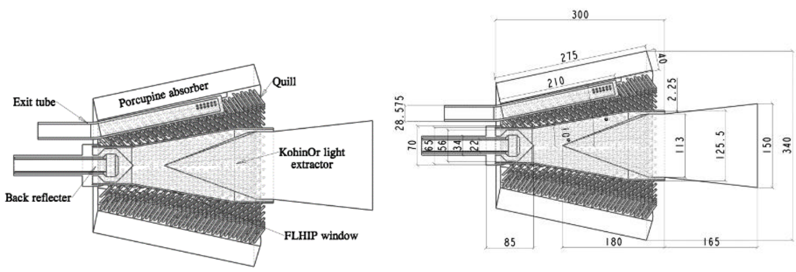

Figure 3. Component and dimension of 30 kW DIAPR

The main function of the absorber in Figure 4 is absorbing solar heat irradiation and transferring heat to working fluid. The absorber also has frustum pyramid shape equipped with its heat transfer elements (the porcupine quills or the porcupine pin fin) facing the axis. The 12 base plates are made from 40 mm alumina plate with 100 mm width and 300 mm length each. The material of 1308 porcupine quills are Alumina-silica tube with outer and inner diameter of 3 mm and 2 mm respectively, with the length of 100 mm.

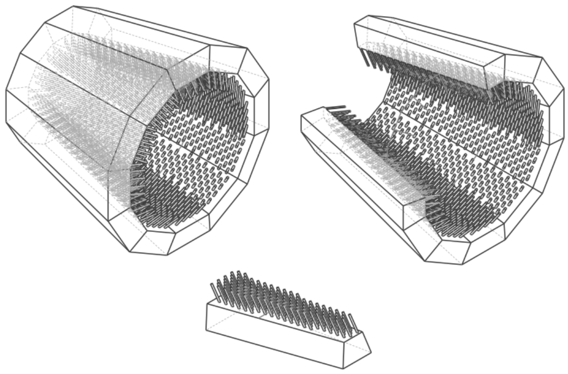

Figure 4. Porcupine Absorber

3. Computational Model of DIAPR

The steady state computational model of air flowing through DIAPR was developed based on the continuity relation of incompressible flow, k-ε turbulent momentum equations, thermal energy balance and non-isothermal flow relation.

- Continuity Equation

$$\nabla\cdot(\rho u) = 0 \qquad (1)$$

- Navier Stoke Equation (k-ε Model)

$$\rho(u\cdot\nabla)u = \nabla\cdot\left[-p\boldsymbol{I} + (\mu+\mu_T)(\nabla u + (\nabla u)^T) - \frac{2}{3}(\mu+\mu_T)(\nabla\cdot u)\boldsymbol{I} - \frac{2}{3}\rho k\boldsymbol{I}\right] + F + \rho g \qquad (2)$$

$$\rho(u\cdot\nabla)k = \nabla\cdot\left[\left(\mu+\frac{\mu_T}{\sigma_k}\right)\nabla k\right] + P_k + \rho\epsilon \qquad (3)$$

$$\rho(u\cdot\nabla)\epsilon = \nabla\cdot\left[\left(\mu+\frac{\mu_T}{\sigma_\epsilon}\right)\nabla\epsilon\right] + C_{\epsilon 1}\frac{\epsilon}{k}P_k - C_{\epsilon 2}\rho\frac{\epsilon^2}{k} \qquad (4)$$

$$P_k = \mu_T\left[\nabla u : (\nabla u + \nabla u^T) - \frac{2}{3}(\nabla\cdot u)^2\right] - \frac{2}{3}\rho k\nabla\cdot u \qquad (5)$$

$$\mu_T = \rho C_\mu\frac{k^2}{\epsilon}\ ,\ k = \frac{1}{2}(\nabla\cdot u'^2) \qquad (6)$$

- Thermal energy balance in fluid domain

$$\rho c_p(u\cdot\nabla T) - \nabla\cdot(k\nabla T) = Q \qquad (7)$$

- Non-isothermal flow relation

$$-n\cdot q = \rho c_p u_t\left(\frac{T_w - T}{T^+}\right) \qquad (8)$$

where $T^+ = \begin{cases} Pr\delta_w^+ & for\ \delta_w^+ < \delta_{w1}^+ \\ 15Pr^{\frac{2}{3}} - \frac{500}{{\delta_w^+}^2} & for\ \delta_{w1}^+ \le \delta_w^+ \le \delta_{w2}^+ \\ \frac{Pr_T}{\kappa_v}\ln\delta_w^+ + \beta & for\ \delta_w^+ \le \delta_w^+ \end{cases}$

and $\delta_w^+ = \frac{\delta_w\rho\sqrt{C_\mu^{\frac{1}{2}}k}}{\mu}\ ,\ \delta_{w1}^+ = \frac{10}{Pr^{\frac{1}{3}}}\ ,\ \delta_{w2}^+ = 10\sqrt{10\frac{\kappa}{Pr_T}}\ ,\ Pr = \frac{c_p\mu}{\lambda}\ ,$

$\beta = 15Pr^{\frac{2}{3}} - \frac{Pr_T}{2\kappa_v}(1 + \ln 1000\frac{\kappa}{Pr_T})$

Standard air at the inlet temperature T_i of 39.2 °C enters the heat transfer chamber through the inlet port in Figure 5 with uniform inlet velocity u_i and the mass flow rate of 100.5 kg/s at the operating pressure of 16.5 bar. The cross-sectional area of the inlet port is 452 mm^2. Air flows through the heat transfer chamber, while exchanging heat with the porcupine quills and leaves the DIAPR receiver at the reference ambient pressure. The air/quill contact surface has the effect of convective heat transfer with buck heat transfer coefficient h of equal to 210 W/m^2 and the porcupine absorber surface temperature T_S in the range of 1,380 °C – 1,550 °C [8] as reported in Figure 6. Figure 6 shows the applied temperature variation along the axial direction of the porcupine absorber. The air/quill contact surface transfers constant heat flux at the rate of 38.2 kW [13]. All surfaces except the inlet and outlet ports can be applied the no-slip turbulent flow conditions. The remaining surfaces other than air/quill surface, inlet and outlet planes are well-insulated. The outlet plane is assumed to have zero heat flux.

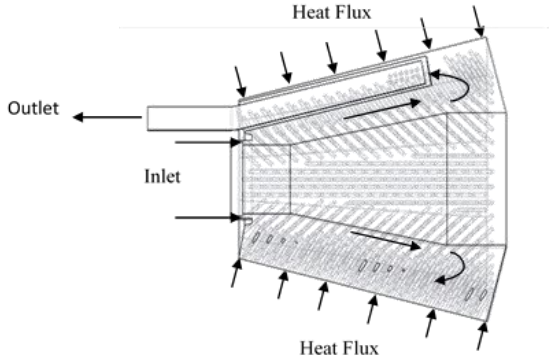

Figure 5. Boundary Condition for this DIAPR Mathematical Model

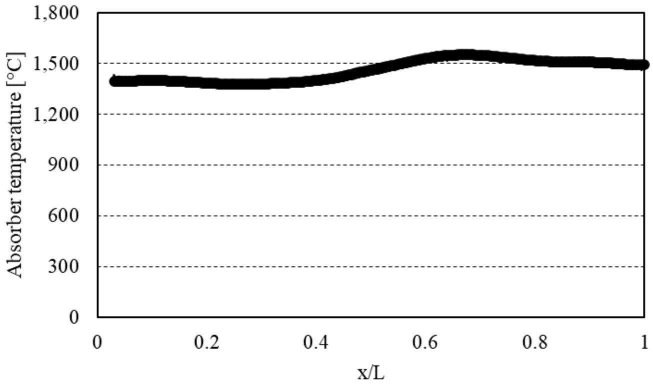

Figure 6. Absorption surface temperature

The commercial finite element package Comsol Multiphysics was used to perform the computational analysis. Grid generation study was performed to confirm the minimum effects of truncation errors on computational results and reported in Figure. 7, where the number of elements was increased from 1,253,325, to 3,323,604, and to 6,939,863, respectively. The outlet target temperature varied with the number of elements, but at the element number of 6,939,863, the outlet target temperature was almost insensitive to the refinement of element sizes. The number of elements at 6,939,863 seems appropriate and is further used in this study.

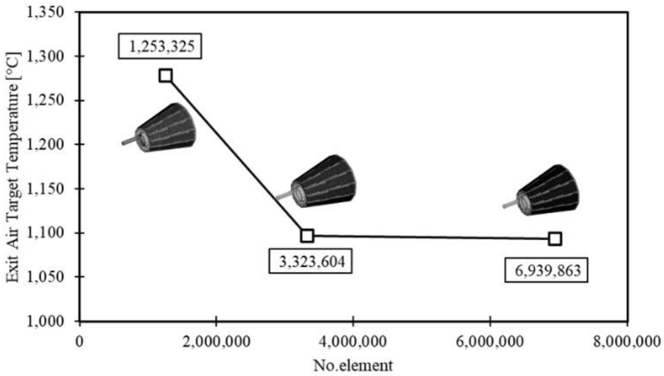

Figure 7 Effects of Computational Mesh on DIAPR computational results

4. Results

In order to confirm the accuracy of computational scheme, the simulation results were compared with the experimental results by Karni J. [13] at the same operating condition as reported in Table 2. The computational results agree within 0.47% of the experimental results. This study confirms the performance of DIAPR to deliver hot gas at the temperature above 1,000 °C, which is sufficient for high temperature driven production process such as H_2 generation by steam reforming of methane or by the direct thermochemical water splitting processes.

Table 2. Result comparison with experimental data by Karni J. [13]

Parameter	Karni J. 2001	This Study	Value Difference (%)
Power Input, Q_{in} (kW)	38.20	38.20	-
Working Pressure, P (bar)	16.50	16.50	-
Mass Flow Rate, m (kg/h)	100.50	100.50	-
Air Inlet Temperature, T_i (°C)	39.20	39.20	-
Air Exit Temperature, T_o (°C)	1089.00	1093.40	0.40%
Power Output, Q_{out} (kW)	32.47	32.62	0.47%
Thermal Efficiency, η_{th} (%)	85.0%	85.4%	0.47%

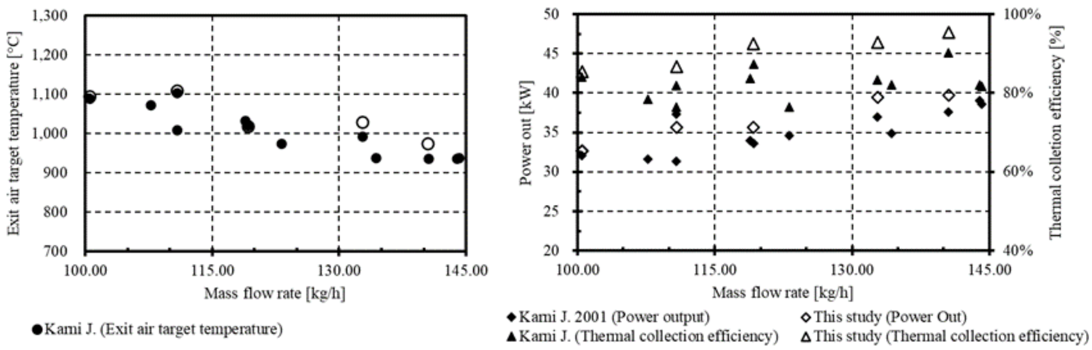

Figure 8 Power output, thermal collection efficiency and exit temperature from this simulation and experimental data [13]

Further comparisons to validate accuracy of this proposed computational scheme were reported in Figure 8. The air exit temperature, power output and thermal collection efficiency at different air supplied flow rate are reported, where the trends of simulation results agree with the experimental results. The exit temperature decreases, while both thermal collection efficiency and power output increase with the air flow rate at the fixed value of applied solar radiation. The thermal collection efficiency of DIAPR is around 80%.

To understand the flow phenomena and heat transfer behavior inside the DIAPR, the velocity profile and temperature distribution on cross-sectional plane A-A and B-B in Figure 9 is reported in Figure 10 and 11, respectively. Cross-section B-B shows the flow and temperature distribution at the section cutting through porcupine quills, while cross-section A-A shows the flow phenomena and temperature distribution in the straight flow channel without a blocking quill. The velocity profile shows that when air receives heat from the quills, air would move away from the quills and create air circulation, thus enhancing the heat transfer performance. Figure 11 confirms that the highest temperature region situates among the space between each quill.

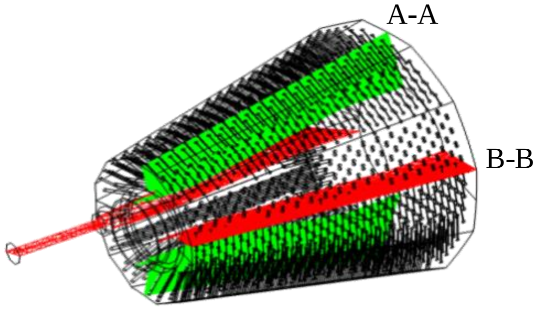

Figure 9 Section plane A-A (green plane) and section B-B (Red plane)

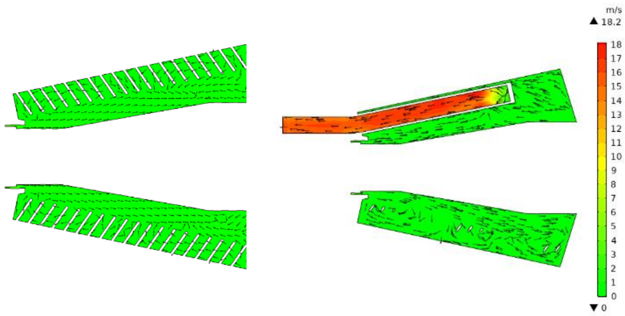

Figure 10 Velocity profile of air flowing through DIAPR at Section A-A and B-B

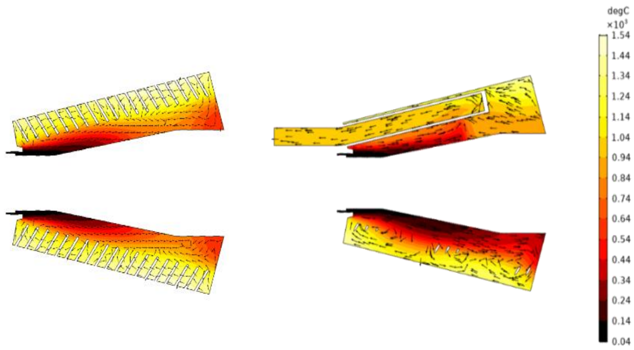

Figure 11 Temperature distribution of air flowing through DIAPR at Section A-A and B-B

5. Conclusion

The computational scheme for analyzing and designing a Directly Irradiated Annular Pressurized Receiver (DIAPR) was proposed and could provide adequate accuracy in prediction of heat transfer performance and target temperature. DIAPR design can eliminates the natural convective losses, thus allowing the possibility to collect heat from solar radiation at high temperature. The high temperature hot gas of above 1,000 °C from DIAPR can provide competitiveness in the energy markets and has possible wide range of applications such as power generation, high temperature solar furnace and hydrogen production utilizing direct thermochemical water splitting processes. Further study could be done on optimizing porcupine fin arrangement and geometry for thermal performance improvement, while providing competitive fabrication cost.

6. Acknowledgments

Authors would like to play gratitude to the Thailand Research Fund (TRF) and ATE company for financial support of this project. Authors are also thankful for technical recommendation from technical staff of the United Multidisciplinary Engineering. Lastly, without support and excellent facility at the department of mechanical engineering, Faculty of Engineering, King Mongkut's University of Technology Thonburi, this project would not be as productive as the work presented here.

Reference

[1] Ahed J, Husam H, Kamaruzzaman S, Nohd R, Saleem Z 2017 "Design and development of compound parabolic concentrating for photovoltaic solar collector" Renewable and Sustainable Energy Reviews, p 1108-1121
[2] Aichmayer L 2011 "Solar Receiver Design and Verification for Small Scale Polygeneration Unit" Graz University of Technology. Austria. Institute for Thermal Turbomachinery and Machine Dynamics
[3] Akiba S 2016 "Solar energy at high temperature; researches at the Weizmann Institute of Science, Israel; 25 years of success" Renew Energy Environ Sustain 1.
[4] Bernhard H 2014 Receiver for Solar Tower Systems (France-Font Romeu)
[5] Craig G, Oomman V, Sudhir R 2008 Light, Water, Hydrogen The Solar Generation of Hydrogen by Water Photo electrolysis HYDROGEN GENERATION BY WATER SPLITTING Hydrogen Production by Thermochemical Water-Splitting Spring chapter 2 pp 55
[6] Ennio M and Macro A 2017 Organic Rankine Cycle (ORC) Power System Solar thermal powered Organic Rankine Cycles Parabolic dish reflector Woodhead Publishing chapter 16 pp 585 – 586
[7] Joao F. and Mauro G. 2014 GREEN POWER PERSPECTIVE ON SUSTAINABLE ELECTRICITY GENERATION An Overview of Electricity Generation Source solar CRC Press chapter 2 pp39
[8] Karni J, Kribus A, Doron P, Rubin R, Fiterman A and Sagie D 1997 "The DIAPR: a high-pressure, high-temperature solar receiver" ASME J. Sol. Energy Eng, February Vol 119, p 74-78
[9] Karni J, Kribus A, Ostraich B and Kochavi E 1998 "A High-Pressure Window for Volumetric Solar Receivers" J. Sol Energy Eng. Vol 120, p 101-107
[10] Karni J, Kribus A, Rubin R and Doron P 1998 "The "Porcupine": A Novel High-Flux Absorber For Volumetric Solar Receiver" J. Sol Energy Eng. Vol 120, p 85-95
[11] Karni J, Rubin R and Kribus A 1992 "DEVELOPMENT OF THE KIPPOD-IN-DIAPR SOLAR THERMAL RECEIVER" *Solar Research Facilities Unit The Weizman Institute of Science Rehovot 76100,* RD-05-93
[12] Keith L and Wes S 2012 Concentrating solar power technology Introduction to concentrating solar power (CSP) technology Linear Fresnel reflectors Woodhead Publishing chapter 1 pp 8 - 61
[13] Kribus A, Doron P, Rubin R, Reuven R, Taragan E, Duchan S and Karni J2001 "Perfoemance of Directly-Irradiated Annular Pressurized Receiver (DIAPR) Operating at 20 Bar and 1,200 ˚C" ASME J. Sol Energy Eng, February Vol 123, p 10-17.
[14] Mohammud R, Abul A and Subhash S 2017 CLEAN ENERGY FOR SUSTAINABLE DEVELOPMENT Solar Pyrolysis: Converting Waste Into Asset Using Solar Energy Parabolic-Trough Solar Concentrator Academic Press chapter 8 pp 224
[15] Piegari A and Flory F 2018 Optical Thin Films and Coatings 2ed *Optical coating for large facilities SOLAR PLANTS* chapter 19 pp 702-703
[16] Rubin R and Karni J2011 "Carbon Dioxide Reforming of Methane in Directly Irradiated Solar Reactor With Porcupine Absorber" J. Sol Energy Eng Vol 133, p 021008-1-021008-5
[17] Zhifeng W 2019 DESIGN OF SOLAR THERMAL POWER PLANTS BRIEF INTRODUCTION TO SOLAR THERMAL POWER GENERATION Linear Fresnel Reflector Solar Power Generation Chapter 1 pp 27 - 28
[18] Zikauskas A "Heat transfer from tube in cross flow" Advance in Heat Transfer" *J.P. Hartnett and T.F. Irvine, eds, Academic Press,* New York, Vol 18, p 87-159
[19] Ziyad S 2014 Renewable Energy System Design *Emerging Renewable Energy Sources Emerging Renewable Energy Sources Large-scale STECS academic Press* chapter 5 pp 350-352
[20] Haraid R, Akiba S and Karni J 1997 "Extractor concentrated guide light" Optical Society of America Vol 36, p 2869-2874

CST0011

Motion Analysis Method of Mechanical System with Contact and Plastic Deformation

Shun YAMAGUCHI[1,*], Yoshiki SUGAWARA[1], and Masakazu TAKEDA[1]

[1]Aoyama Gakuin University, 5-10-1, Fuchinobe, Chuo-Ku, Sagamihara, Kanagawa, 252-5258, Japan

* Corresponding Author: c5619131@aoyama.jp

Abstract. Currently, a simple and small planetary landers exploration project are planned. The landing system for this project needs to absorb landing shocks while being a small and simple mechanism. Porous metal has shock absorption, and it is expected to be used for the landing system of small landers. Porous metal is one of the cellular solids and has energy absorption during compression plastic deformation. To develop this landing system, it is necessary to understand effects of large plastic deformation of porous metal and collision with the ground on the motion of the lander. This study proposes a motion analysis method that models non-smooth phenomenon of plastic deformation. As a result, it is possible to analyze the motion of mechanical system with large plastic deformation such porous metal, and to utilize the analysis results for design of planetary lander.

1. Introduction

In recent years, a plan to explore the lunar and planetary exploration using small landers has been promoted. Conventional landers have achieved planetary landing by using a large and advanced mechanical system. For example, the Mars rover Curiosity (NASA) successfully made a soft landing using an aeroshell, a parachute, thrusters, and a technique called a sky crane. The weight of the lander was about 900 kg [1]. The soft landing on a planet has been realized by using a complex system consisting of many mechanical elements. However, the development and operation of these systems require a huge budget and a long development period. Therefore, the exploration of the lunar and planetary exploration has been carried out only by a limited number of agencies with huge resources and mature technology.

On the other hand, small landers can be developed and operated by small organizations such as universities and emerging countries because they can be developed on a low cost by simplifying the system. In addition, although the payload per exploration is reduced, the development of a successor is facilitated because of the short development period. As a result, the frequency of exploration will be increased and continuous planetary exploration will be possible. Currently, small landers are being considered for use on the lunar and Mars. SLIM (JAXA), a small lunar lander, is currently undergoing a plan to realize an autonomous, high-precision landing at a landing site using a small lander [2]. In addition, the Mars exploration plan using a small and simple lander aims to realize landing with minimal active control [3].

For such a small lander, the landing system should be small, light, and simple. Porous metals are attracting attention as a lightweight shock-absorbing material [4]. Porous metal is a metallic material with a large number of internal pores and a porosity of more than 70 %, which makes it light in weight. In addition, it has a plateau region where plastic deformation continues at a constant stress, and thus has excellent energy absorption properties. Because of these characteristics, it is expected to be used for small landers. This paper proposes a landing system for a small lander using porous metal as a shock absorber. We also derive a mathematical model of the system and evaluate its effectiveness by numerical analysis.

2. Proposal method

2.1. Porous metal

The porous metal used as a shock absorber is a metallic material with many porosities inside. Because of porosity, it has sound absorption, thermal insulation, and energy absorption properties. Figure 1 illustrates a photo of the porous metal and a stress-strain curve when compressive stress is applied. As the strain develops, it can be divided into three characteristic regions [4].

(I) Elastic region: Region in which Hooke's law of proportionality between stress and strain holds.
(II) Plateau region: Region of continuous plastic deformation due to bending and buckling of a porous wall. The strain develops under constant stress.
(III) Densification region: Region of increased stress as the porosity decreases due to progressive fracture of the pore wall, which approaches the mechanical properties of the dense material.

The constant stress in the plateau region is called the plateau stress σ_{pl} [4]. The strain where the plateau region ends and the densification region begins is called the plateau strain ε_{pl}, which is known to be about 0.5 [5, 6]. The plateau stress is determined by the mechanical properties and porosity of the base metal. Therefore, the stress generated during energy absorption can be designed [7].

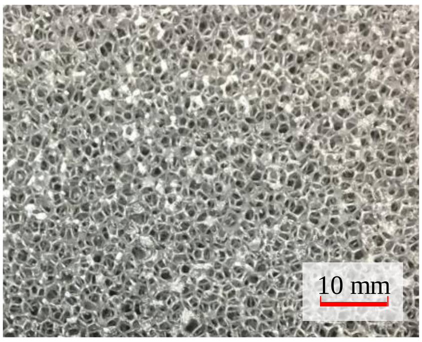

(a) Image of porous metal.

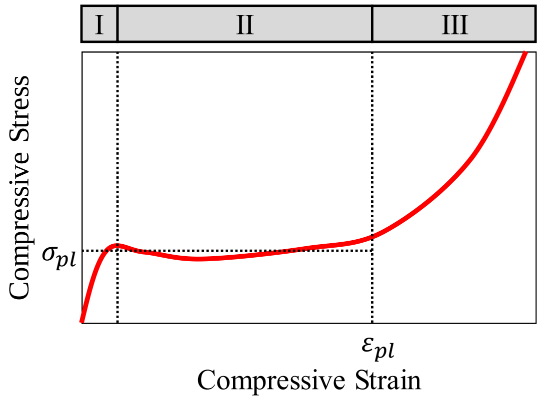

(b) Compressive strass-strain curve.

Figure 1. Features of porous metal.

2.2. Multi-stage landing legs

It is necessary for a small lander to absorb enough kinetic energy during landing by the porous metal to keep the impact small. Also, since the deceleration system is limited, landing speeds are expected to be high. Therefore, the volume of the porous metal required is large. Furthermore, the larger the cross-sectional area of the porous metal subjected to impact loading, the greater the proportional load. Therefore, it is necessary to reduce the cross-sectional area. From the above, it can be said that a long and thin shape of the porous metal is suitable for this purpose. However, there is a high possibility that buckling may occur in such a shape, and sufficient energy absorption may not be achieved. Therefore, this problem is avoided by filling the guide case with porous metal and compressing it like a piston.

As described above, the landing legs are required to be small. Therefore, we designed a multi-stage nested landing leg structure that is small enough to be stored at launch and deployed at landing. A schematic diagram of the proposed landing leg is illustrated in Figure 3. Legs 1, 2 and 3 have a nested structure, and the inside of legs 1 and 2 is filled with porous metal. Leg 2 compresses the porous metal inside leg 1, and leg 3 compresses the porous metal inside leg 2 to absorb energy.

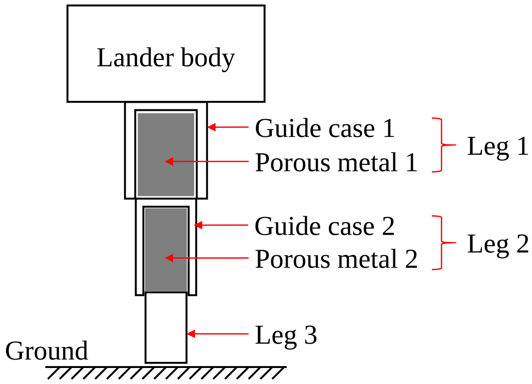

Figure 2. Proposed landing system.

3. Mathematical models

3.1. Mathematical model of porous metals

As described in the previous section, porous metals have characteristic regions of elastic, plateau, and densification regions during compressive deformation. In addition, when the strain rate is high, a large amount of stress is generated instantaneously, and the plateau stress increases. To simplify these mechanical properties, the elastic and plateau regions are represented by the step response of second-order delay elements, and the densification region is represented by quadratic functions. The mathematical model for porous metals is shown in the following equation.

$$\begin{cases} \sigma(\varepsilon) = \sigma_{pl}\{1 - \alpha_1 e^{-\alpha_2 \varepsilon} \sin(\alpha_3 \varepsilon + \alpha_4)\} & (0 \leq \varepsilon \leq \varepsilon_{pl}) \\ \sigma(\varepsilon) = \alpha_5 (\varepsilon - \varepsilon_{pl})^2 + \sigma_{pl} & (\varepsilon_{pl} < \varepsilon) \end{cases} \tag{1}$$

Here, $\alpha_1 \sim \alpha_5$ are constants, and by changing these constants, the above mechanical properties can be expressed.

3.2. Switching the equation of state considering the deformation states

A mathematical model of the landing legs for numerical analysis is illustrated in Figure 3. Since the purpose of this study is to confirm the basic function of the landing leg, the motion and deformation are limited to one axis only. Let y_i be the generalized coordinate of the guide case for leg $i(= 1, 2, 3)$. The masses of the legs 1 and 2, m_1 and m_2, are the sum of the guide cases and the porous metals, respectively. The compressive strain ε_j of the porous metal $j(= 1, 2)$ is expressed in the following equation using the pre-deformation length of the porous metal H_{orgj} and the generalized coordinates.

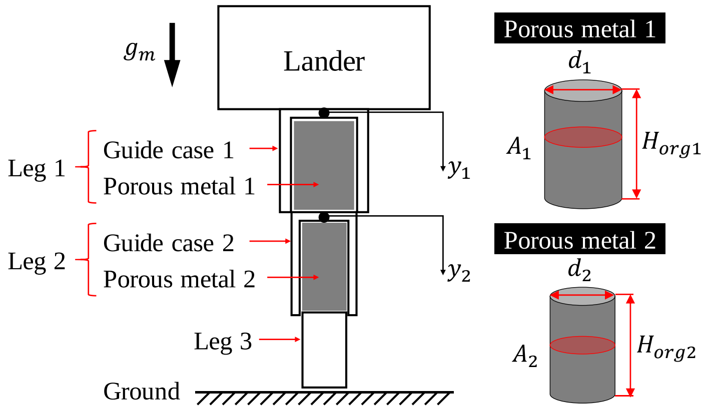

Figure 3. Analysis model.

$$\varepsilon_1 = \frac{y_1 - y_2}{H_{org1}} \tag{2}$$

$$\varepsilon_2 = \frac{y_2 - y_3}{H_{org2}} \tag{3}$$

The reaction force F_j under compressive deformation of a porous metal is expressed by the stress-strain model of equation (1) as

$$F_j = \sigma_j(\varepsilon_j)A_j \tag{4}$$

where A_j is the cross-sectional area of the porous metal j in the axial direction of compression. Free body diagram of the analysis model is illustrated in Figure 4. N_α and N_β are reaction force due to the deformation of the porous metal, and $N_\alpha = F_1$ and $N_\gamma = F_2$ during deformation. Therefore, the equation of state when porous metals are deformed is given by the following equation.

$$\frac{d}{dt}\begin{bmatrix} y_1 \\ y_2 \\ \dot{y}_1 \\ \dot{y}_2 \end{bmatrix} = \begin{bmatrix} \dot{y}_1 \\ \dot{y}_2 \\ g_m - \dfrac{F_1(\varepsilon_1)}{M + m_1} \\ g_m + \dfrac{F_1(\varepsilon_1) - F_2(\varepsilon_2)}{m_2} \end{bmatrix} \tag{5}$$

The equation of state in equation (5) is based on the reaction force F_j when the porous metal is subjected to compressive deformation. Therefore, it is not applicable when the porous metal does not undergo compressive deformation or when displacement occurs in the tensile direction. In addition, since the porous metal absorbs energy by means of plastic deformation, it does not return to its original length once it is subjected to compressive deformation. Therefore, it is necessary to represent non-smooth behavior of plastic deformation for numerical analysis. In this study, this non-smooth behavior is simplified by detecting the state of deformation of a porous metal and switching the equation of state to enable the numerical analysis. For the model in Figure 3, the deformation of the porous metal can be in the following cases.

(i) Compressive deformation of both porous metals 1 and 2
(ii) Porous metal 1 is not deformed, only porous metal 2 is deformed by compression
(iii) Only porous metal 1 is compressively deformed, but porous metal 2 is not.
(iv) Neither of the porous metals 1 and 2 are subject to compressive deformation.

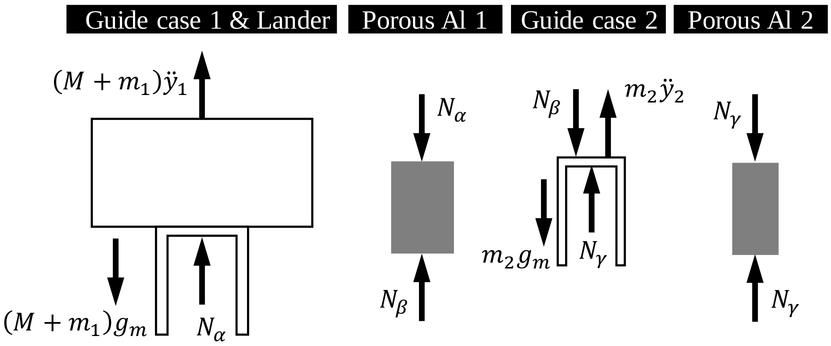

Figure 4. Free body diagram for deformation determination.

We describe the detection of the deformation state of the porous metal. When a compressive force is applied to the porous metal and it reaches the yield stress, it deforms plastically. When an object is given work by collision, it is deformed and converted into strain energy. The porous metal in these states is judged to be in a deformed state.

First, consider the deformation caused by compressive forces. Figure 4 illustrates the relationship between the forces applied to each member when the porous metal is not deformed. From this, the external force N_α and N_β applied to the porous metal 1 is expressed by the following equations

$$N_\alpha = (M + m_1)(g_m - \ddot{y}_1) \tag{6}$$

$$N_\beta = N_\gamma - m_2(g_m - \ddot{y}_2) \tag{7}$$

Here, N_γ is an external force applied to the porous metal 2. The difference between N_α and N_β is the force that gives the acceleration to the porous metal 1, and the other forces, i.e., the forces in equilibrium, are the internal forces. In other words, the smaller of N_α and N_β is equal to the value of the internal force. This internal force is the compression force N_D. The porous metal 1 is deformed when the stress due to N_D is greater than the yield stress.

The deformation caused by the collision of an object is caused when kinetic energy is given to the porous metal. Therefore, it is judged that deformation occurs when the porous metal has velocity in the compression direction. In this way, a numerical analysis is performed by switching the equation of state by detecting the deformation state based on the values of acceleration and velocity. In this way, the deformation state of porous metals due to contact force is expressed by switching the equation of state.

4. Numerical analysis

The effectiveness of the proposed landing leg is evaluated by numerical analysis. In order to evaluate the shock-absorbing behavior of the deformed porous metal at the time of landing, the moment when the landing legs touched the ground was used as the initial condition. The accelerating speed of the internal equipment was set to 100 G. The code to perform numerical integration of the derived equations based on the Runge-Kutta method was created in MATLAB. Figure 5 illustrates the results of the analysis. Figure 5(a) shows the time history response of the compression strain of the porous metals, and Figure 5(b) shows the time history response of the acceleration of the lander body (leg 1) and leg 2. In addition, Figure 5(c) shows the time history response of the kinetic energy of the system. As shown in Figure 5(a), the deformation of both porous metals 1 and 2 immediately after impact, but then the deformation of porous metal 1 stopped and only porous metal 2 was found to be deformed significantly. When the strain of porous metal 2 exceeded the plateau strain $\varepsilon_{pl}(= 0.5)$, it entered the densification region and the deformation of porous metal 1 resumed due to the increased stress. The final strains of porous metals 1 and 2 were 0.379 and 0.530, respectively. From the results in Figure 5(b), it can be seen that there is an instantaneous large acceleration in leg 2 immediately after ground contact and just before the deformation of the porous metal 2 stops. However, the acceleration of the lander body is always kept below 100 G, which indicates that the equipment is protected from landing impacts. Furthermore, the results in Figure 5(c) show that the kinetic energy of the system is absorbed by plastic deformation of the porous metal. From the above, it can be said that the proposal system is effective.

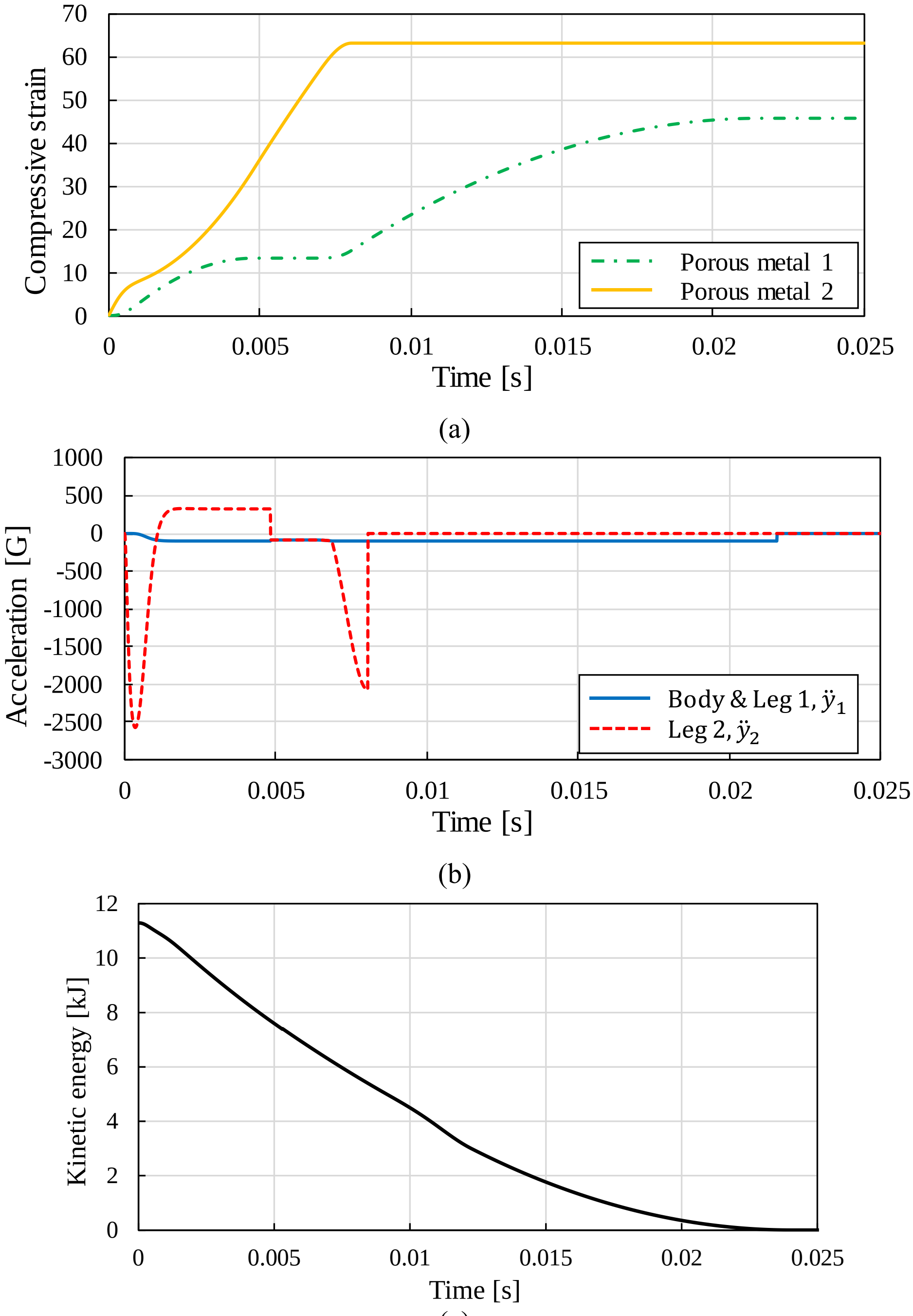

(c)

Figure 6. Analysis results: (a) Compressive strain of porous metal; (b) Acceleration; (c) Energy

Conclusion

In this study, we proposed a landing leg made of porous metal as a shock absorber to realize a small and simple landing on a planet. A stress-strain model of the porous metal and a mathematical model of the landing legs were derived for validation by numerical analysis. In order to describe non-smooth behavior of a porous metal, we proposed a numerical analysis method to detect the deformation state and switch the equation of state. This method expresses the deformation phenomenon of porous metal due to contact force. The result of the numerical analysis show that the impact acceleration is within the required range. Furthermore, it is shown that the kinetic energy is sufficiently absorbed. From these result, it is shown that the proposed system is effective. In the future, it is necessary to verify the validity of the proposed analysis method by experiments.

References

[1] Way D W, Davis J L and Shidner J D 2013 *NASA Tech. Rep.* AAS **13-420** 1
[2] Kuga T, Kojima H and Fukuda S 2016 *J. Japan Soc. Aeronautical Space Sci.* **64** 303
[3] Sakagami R, Takahashi R, Wachi A, Koshiro Y, Maezawa H, Kasai Y and Nakasuka S 2018 *Acta Astronaut.* **144** 103
[4] Gipson L J and Ashby M F 1988 *Cellular Sorids: Structure and Properties* (Oxford: Pergamon Press)
[5] Barnes A T, Ravi-Chandar K, Kyriakides S and Gaitanaros S 2014 *Int. J. Solids Struct.* **51** 1631-1645
[6] Gaitanaros S and Kyriakides S 2014 *Int. J. Solids Struct.* **51** 1646-1661
[7] Avvalle M, Belingardi G and Ibba A 2007 *Int. J. Impact Eng.* **34** 3

CST0013

Numerical Study on Heat Transfer and Entropy Generation of Nanofluid Flow in Round Tube with Inclined Ring Ribs

Somchai Sripattanapipat[1,*], Watcharin Noothong[2], and Pongjet Promvonge[3]

[1]Department of Mechanical Engineering, Faculty of Engineering, Mahanakorn University of Technology, Bangkok, 10530, Thailand
[2]Factory of Engineering, Thai-Nichi Institue of Technology, Bangkok, 10250, Thailand
[3]Department of Mechanical Engineering, School of Engineering, King Mongkut's Institute of Technology Ladkrabang, Bangkok, 10520, Thailand

* Corresponding Author: ssomchai@mut.ac.th

Abstract. A numerical investigation on turbulent nanofluid flow, heat transfer and entropy generation behaviours in a constant heat-fluxed tube with inclined ring ribs (IRR) has been performed. The computations are performed using a finite volume approach with the couple algorithm for the mass flow rate of nanofluid (Al_2O_3-water) in the form of Reynolds number between 4000 and 12,000. Effects of nanofluid with 1%, 2%, and 3% volume fraction (vf) on the rate of heat transfer, friction loss and entropy generation are examined. The numerical result reveals that a pair of counter-rotating vortices produced by the IRR can induce impingement flows on the wall region resulting in greater increase of the heat transfer above the plain tube alone, apart from the nanofluid effect. The maximum thermal performance occurring at PR = 0.5, Re = 4000, and vf = 3% is about 2.03 and the entropy generation was lowest at this condition.

1. Introduction

The utilization of rib/baffle turbulators by placing them in the heating/cooling tube of a heat exchanger is taken to account as one of the most popularly employed passive technique for the duct/tube flow because repeatedly located ribs in a tube help to disrupt the thermal and hydrodynamic boundary layers, aside from inducing swirling flow. For a ribbed tube, the downstream flow phenomenon of each rib is that there are flow separation, recirculation, and impingement over the tube wall and those effects are considered to be the key reasons to support the augmenting convection heat transfer inside the tube. Patankar et al. [1] initially offered a fully-developed periodical flow concept to explore numerically the fluid friction and thermal behaviors in a circular tube. Thus, several researches on numerical simulations of a periodic flow model based on this concept have been rich. For instance, Promvonge et al. [2] performed a numerical simulation of flow and thermal behaviors in a square channel with 45° inclined baffles on a lower wall and showed that there was a single longitudinal vortex-flow appearing along the duct that assists to induce impinging jets on the lower, upper and side walls.

Nanofluids are denoted as a colloidal mixture of a nanoparticle group whose size is smaller than 100 nm, which is a term introduced by Choi [3]. The conventional heat transfer fluids such as oil, water, and ethylene glycol are very popular for use in cooling/heating of thermal systems. In general, thermophysical properties of nanofluids have superiority over base fluids [4]. Maxwell [5] initially put forward a theoretical report to point out the feasibility of augmenting thermal conductivity by mixing liquids with micron-sized solid particles. Nonetheless, there have been several problems i.e. clogging, rapid sedimentation, large pressure loss, and erosion resulted from using the solid nanoparticles and thus, it has made this technology unsuitable for use in practice.

An analysis technique of entropy generation obtained from the 2nd law of thermodynamics is used effectively in estimating the useful energy disruption resulted from the pressure drop and the convection heat transfer by considering the viewpoint of energy utilization. An investigation on the irreversibility in a counter-flow concentric tube heat exchanger using air was conducted by Mohamed et al. [6] using the test fluid. They reported that the influence of pressure loss on the entropy generation was found to be very small while the temperature difference had a significant effect. Thus, the entropy generation from the pressure drop was marginal. Wang et al. [7] numerically studied entropy generation in the outward transverse and helical corrugated tubes. The results showed that the corrugation induced detached vortex and spiral flows that have significantly affected the local entropy generation. The swirl flow in the helical corrugated tube contributed to the irreversibility was lower than those in the transverse corrugated tube.

Most numerical studies have emphasized on thermal behaviors in a general tube flow. Hence, the investigation on turbulent flow of nanofluids through a round tube with multiple inclined ring ribs (IRR) has never been reported in the literature. In the current work, the computation on a 3D turbulent nanofluid tube flow through 45° IRRs is carried out numerically with the key purpose being to investigate the structure of nanofluid flow and thermal behaviors. The variations of local entropy generation and mean entropy generation number are examined to find out the optimal geometry of the IRR.

2. Mathematical Foundation

2.1. Governing equations

The numerical heat transfer and tube flow model is simulated through the following assumptions: steady, turbulent, incompressible and 3-dimensional flow; and neglecting the body forces, viscous dissipation and radiation effect. From the mentioned strategy, the model of flow is governed via the equations of continuity, Navier-Stokes and energy. By a cartesian tensor notation, all equations are expressed via

Continuity equation:

$$\frac{\partial(\rho u_i)}{\partial x_i} = 0 \tag{1}$$

Momentum equation:

$$\frac{\partial\left(\rho u_i u_j\right)}{\partial x_j} = -\frac{\partial p}{\partial x_i} + \frac{\partial}{\partial x_j}\left((\mu + \mu_t)\left(\frac{\partial u_j}{\partial x_i} + \frac{\partial u_i}{\partial x_j}\right)\right) \tag{2}$$

Energy equation:

$$\frac{\partial(\rho u_i T)}{\partial x_i} = \frac{\partial}{\partial x_i}\left(\left(\frac{\mu}{Pr} + \frac{\mu_t}{Pr_t}\right)\frac{\partial T}{\partial x_i}\right) \tag{3}$$

In the current investigation, the GEKO k-ω turbulence model is utilized to show the quantities of turbulence stresses and heat-flux of the pertinent physical phenomena. The above equations are discretized using the second-order upwind (SOU) scheme whereas the coupling of velocity-pressure terms is coped using the Couple algorithm and all are simultaneously solved by a finite volume method [8]. The numerical solutions are to be converged as the values of their residuals are under 10^{-5} for all variables except for the energy equation below 10^{-9}.

2.2. Entropy generation

The rate of local entropy generation in a flow model is written as [9,10]:

$$\dot{S}'''_{ht} = \frac{\lambda}{T_f^2}\left[\left(\frac{\partial T}{\partial x}\right)^2 + \left(\frac{\partial T}{\partial y}\right)^2 + \left(\frac{\partial T}{\partial z}\right)^2\right] \tag{4}$$

$$\dot{S}'''_{fr} = \frac{\mu}{T_f}\left\{2\left[\left(\frac{\partial u}{\partial x}\right)^2 + \left(\frac{\partial v}{\partial y}\right)^2 + \left(\frac{\partial w}{\partial z}\right)^2\right] + \left(\frac{\partial u}{\partial y} + \frac{\partial v}{\partial x}\right)^2 + \left(\frac{\partial u}{\partial z} + \frac{\partial w}{\partial x}\right)^2 + \left(\frac{\partial v}{\partial z} + \frac{\partial w}{\partial y}\right)^2\right\} \tag{5}$$

$$\dot{S}_{tot} = \int \dot{S}'''_{tot}\, dV = \int \left(\dot{S}'''_{ht} + \dot{S}'''_{fr}\right) dV \tag{6}$$

where λ, μ, and T_f are, respectively, fluid thermal conductivity, absolute viscosity, and overall bulk mean temperature in the form of average values at the entrance and exit. The total rate of entropy generation ($\dot{S}_{tot}$) is obtained by the summation of the local total entropy generation ($\dot{S}'''_{tot}$) around the domain, identical to the average heat transfer and friction entropy generation ($\dot{S}_{fr}$ and $\dot{S}_{ht}$).

Four pertinent parameters are of interest: friction factor (f), Reynolds number (Re), Nusselt number (Nu) and thermal enhancement factor (TEF). The f calculated from the pressure drop, Δp of the periodic tube length, L is defined by

$$f = \frac{(\Delta p/L)D}{(1/2)\rho\bar{u}^2} \tag{7}$$

The Reynolds number is denoted as

$$Re = \frac{\rho\bar{u}D}{\mu} \tag{8}$$

The rate of heat transfer is achieved from local Nusselt number which is written by

$$Nu_x = \frac{h_x D}{k} \tag{9}$$

The average Nu is obtained by

$$Nu = \frac{1}{A}\int Nu_x\, dA \tag{10}$$

TEF denoted as the ratio of the convection coefficient of the enhanced tube, h to that of the plain tube, h_0, at identical pumping/blowing power is prescribed as [11]

$$TEF = \frac{h}{h_0} = \frac{(Nu/Nu_0)}{(f/f_0)^{16/55}} \tag{11}$$

where the subscript "0" is for the plain tube only.

The total entropy generation number (N_{s-tot}) is denoted as the ratio of total entropy generation of the enhanced tube to that of the smooth tube [9]. Similarly, the friction and heat transfer entropy generation numbers (N_{s-f} and N_{s-ht}) are declared. As N_s< 1, it means that the irreversibility degree is declined while the ratio of useful energy is raised in comparison with the plain tube case.

$$N_{s-ht} = \dot{S}_{ht-ring\,rib\,tube}/\dot{S}_{ht-smoot\,tube} \tag{12}$$

$$N_{s-fr} = \dot{S}_{fr-ring\,rib\,tube}/\dot{S}_{fr-smoot\,tube} \tag{13}$$

$$N_{s-tot} = \dot{S}_{tot-ring\,rib\,tube}/\dot{S}_{tot-smoot\,tube} \tag{14}$$

To determine the thermo-physical properties of nanofluid, the proposed equations are as follows:
Density [12]:

$$\rho_{nf} = (1-\varphi)\rho_{bf} + \varphi\rho_{np} \tag{15}$$

Heat capacity [12]:

$$\left(C_p\right)_{nf} = \frac{\left[(1-\varphi)\left(\rho C_p\right)_{bf} + \varphi\left(\rho C_p\right)_{np}\right]}{\rho_{nf}} \tag{16}$$

Effective thermal conductivity [13]:

$$k_{nf} = \frac{k_p + 2k_{bf} - 2(k_{bf} - k_p)\varphi}{k_p + 2k_{bf} + (k_{bf} - k_p)\varphi} k_{bf} + 5 \times 10^4 \beta\varphi\rho_{bf}(C_p)_{bf}\sqrt{\frac{\kappa T}{\rho_{np} d_{np}}} f(T, \varphi) \tag{17}$$

Dynamic viscosity [16]:

$$\mu_{nf} = \mu_{bf} / \left(1 - 34.87 \left(\frac{d_p}{d_f}\right)^{-0.3} \varphi^{1.03}\right) \tag{18}$$

Thermo-physical properties of water and Al_2O_3 nanoparticles are given in Table 1.

Table 1. Thermophysical properties of water and Al_2O_3 at T=300 K

Thermo-physical properties	Water	Al_2O_3
ρ (kg/m^3)	998.2	3970
C_p (J/kg K)	4182	765
k (W/m K)	0.6	40
μ (N s/m^2)	0.001003	-

3. Configuration of Tube Flow Model

3.1. Geometry and arrangement of IRR

The flow model in the present computation is a round tube with 45° (θ) IRRs as shown in Figure 1. The periodic flow model concept is that the flow attains a periodical flow condition where the variables of velocities and temperatures are set to repeat themself from a single cell/module to another. The concept of fully-developed periodical flow and the solution procedure were explained in Ref. [1]. The nanofluid flows into the flow model with the inlet temperature, T_{in}, before flowing through the IRR where d/2 (d=0.0075 m) is the ring rib height. D = 0.05 m, is the diameter of tube while P is a pitch length of the rib module, P/D is denoted as the pith ratio, PR whose value is between 0.05 and 1.5.

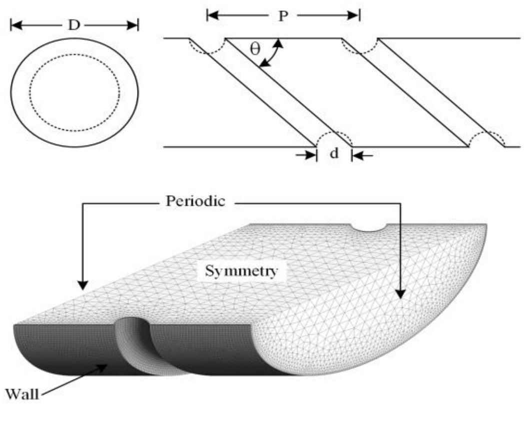

Figure 1. Computational domain of the periodic flow model.

3.2. Boundary conditions and grid independence test

Owing to the model assumption, the periodical boundaries are applied at the flow outlet and inlet. Also, a mass flow rate of nanofluid at 300 K is presumed constant obtained from each given Re. All nanofluid properties are set to constant at overall bulk mean fluid temperature. The surfaces of the tube and IRR are set to no-slip wall and impermeable boundary conditions. A constant wall heat flux is maintained at 5000 W/m^2. The number of grids around 325,000 was tested and found to be independent of its solution.

4. Results and Discussion

4.1 Validation

A comparison of the numerical Nusselt number and friction factor results with measured data from Ref. [15] is depicted in Figure 2(a). It is evident that the numerical results are in favourable agreement with the measured results. Quantitatively, the maximum discrepancies between both the results are about 5% for Nusselt number and 15% for friction factor. The result of the plain tube with a fixed heat-flux value by the model of local entropy generation and the Bejan's formula [16] as per equation (19) below is displayed in Figure 2(b). It is noticeable that both the results exhibit the excellent agreement. The deviations of the heat transfer and the friction entropy generations are, respectively, within 1.8% and 8.3%. Thus, the simulation model adopted in the current investigation for the heat transfer, pressure drop and entropy generation predictions can be reliable.

$$\dot{S}'_{tot} = \frac{q'^2}{\pi\lambda T^2 Nu} + \frac{8\dot{m}^3 f}{\pi^2\rho^2 T D^5} \tag{19}$$

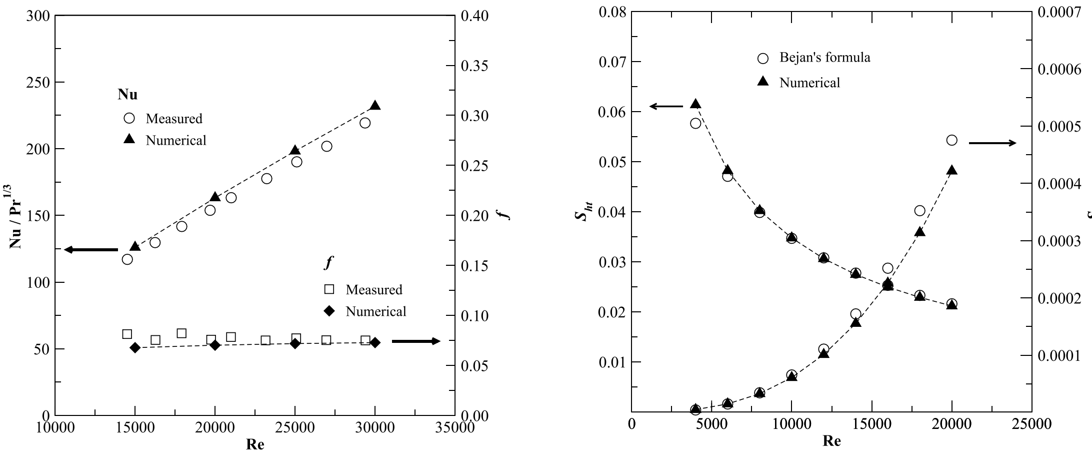

(a) (b)

Figure 2. Validation of (a) Nu and *f*, and (b) heat transfer and friction entropy generation of smooth tube.

4.2 Flow structure, Heat transfer and Entropy generation

The structure of flow and vortex coherent for the IRR tube is presented in the form of streamlines and pressure contours at Re=10000, PR=1.0 as portrayed in Figure 3. In the figure, it is seen that the existence of the IRR causes the flow to become a pair of main counter-rotating vortices throughout due to different pressure field. The pair of the main vortices can help induce the impinging jets on the tube surface resulting in the greater increase of the rate of heat transfer. Local Nu_x contour plots of the IRR tube at PR = 0.5-1.5, Re = 10000 are depicted in Figure 4. As found in the figure, the high Nu_x value for the IRR tube is in a large region on the front surface of the IRR owing to the more fluid impingement for decreasing PR. Figure 5 depicts the $\dot{S}'''_{tot}$ contours and streamlines at Re=10000, PR=1.0. As shown in the figure, the total entropy generation mainly occurs at the wall area at which the temperature gradient is very high. In the vicinity of IRR, the total entropy generation is somewhat large since the fluid in that region has nearly less motion compared to the axial flow.

4.3. Performance comparison

The distribution of the Nusselt number ratio, Nu/Nu_0 with Reynolds number for various BRs and nanofluid volume fractions is portrayed in Figure 6(a). It is visible that Nu/Nu_0 has the decreasing tendency with rising Re for all the PRs and nanofluid volume fractions. The results reveal that Nu/Nu_0 rises with decreasing PR and using the higher nanofluid volume fraction leads to the rise in Nu/Nu_0. The highest Nu/Nu_0 at PR = 0.5 and vf = 3% is about 3.52 times. The use of IRR with nanofluid results in the rise of heat transfer rate around 2.34–3.52 times the plain tube alone. Figure 6(b) shows the profile of the friction factor ratio, f/f_0 with Re for various volume fractions of nanofluid and PRs. In the figure, it is seen that f/f_0 has the increasing tendency with rising Re. It is interesting to note that the influence of the nanofluid volume fraction value on f/f_0 is not significant. The IRR tube gives the greater increase in friction factor compared with the plain tube. The rise in PR leads to the decline in friction factor. The f/f_0 of the IRR tube is about 4.57 – 8.88 times depending on the volume fraction and PR.

Figure 6(c) exhibits the distribution of thermal enhancement factor (TEF) with Re for different nanofluid volume fraction and PR values. It is seen that TEF has the declining tendency with rising Re and PR. TEF of the IRR tube is varied in a range of 1.43-2.03, depending on PR, Al_2O_3 volume fraction and Re values. It is noticeable that TEF rises with the increment of the volume fraction. This points out the advantage of the IRR and nanofluid for enhancing thermal-hydraulic performance in a tubular heat exchanger system.

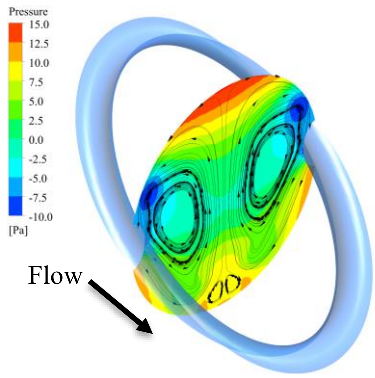

Figure 3. Pressure contours and streamlines in frontal plane.

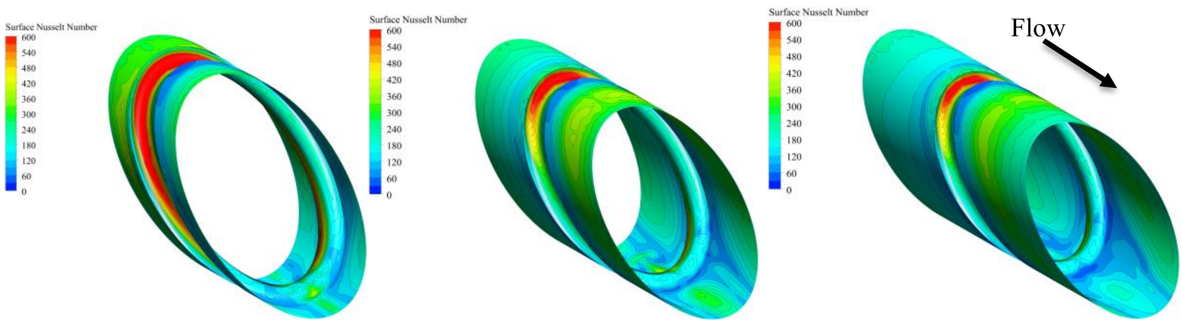

(a) (b) (c)

Figure 4. Nu$_x$ contours for (a) PR=0.5, (b) PR=1.0, and (c) PR=1.5 at Re=10000 and $\varphi = 2\%$

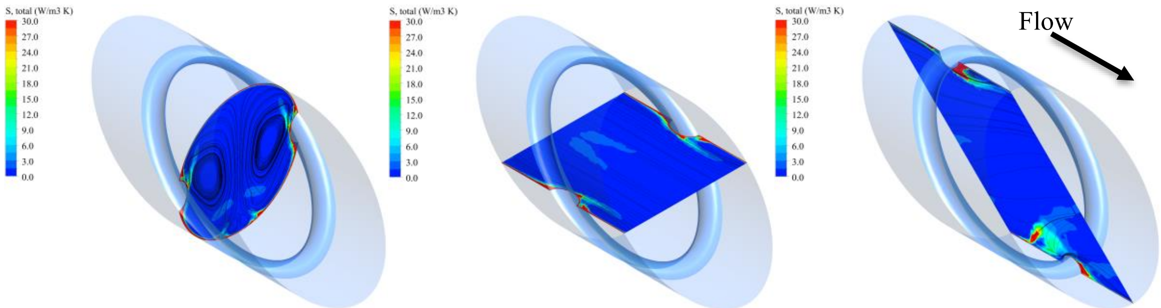

(a) (b) (c)

Figure 5. $\dot{S}'''_{tot}$ contours and streamlines in (a) frontal plane, (b) transverse plane and (c) longitudinal plane at PR=1.0, Re=10000 and $\varphi = 2\%$.

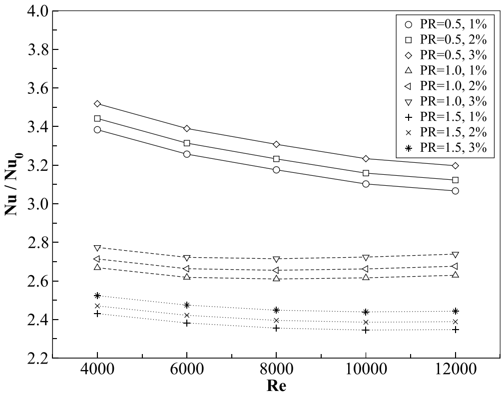

(a)

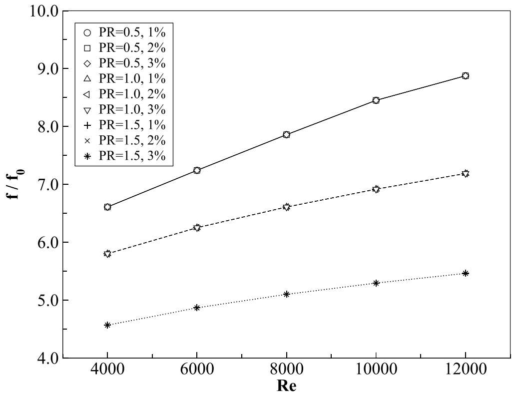

(b)

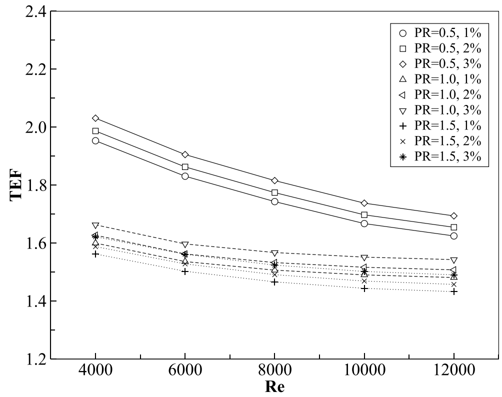

(c)

Figure 6. Influence of PRs and Al_2O_3 volume fractions with Re on (a) Nu/Nu_0, (b) f/f_0, and (c) TEF.

4.4. Thermodynamic irreversibility

The variations of the fluid friction, heat transfer and total entropy generation numbers (N_{s-ht} , N_{s-fr} and N_{s-tot}) with Re for various PR and vf values are, respectively, depicted in Figure 7(a), 7(b) and 7(c). It is noted that the irreversibility is improved with using the IRR. The N_{s-ht} decreases with Re for PR=0.5 and 1.0 and slightly increases with Re for PR=1.5. The heat transfer irreversibility of the IRR tube is clearly smaller than the smooth tube, which is contributed to the vortex flow. The friction entropy generation for all cases is greater than the smooth tube as a result of the friction losses increasing for using the IRRs. The total entropy generation, N_{s-tot}, tends to decline for decreasing PR and increasing the volume fraction. However, the lowest total entropy generation is found at PR=0.5 and vf = 3% which is consistent with the maximum TEF.

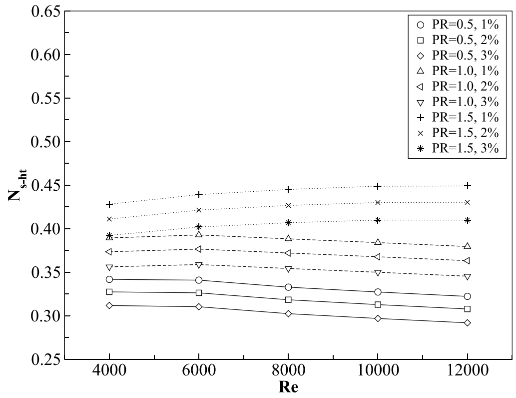

(a)

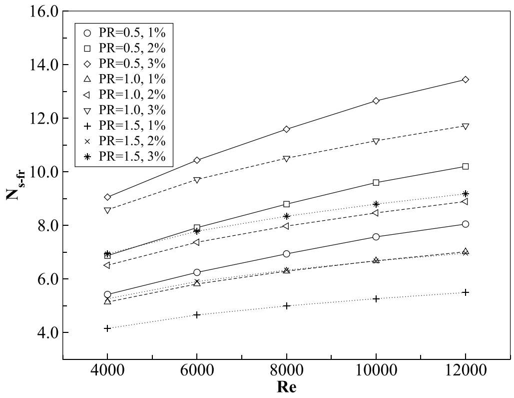

(b)

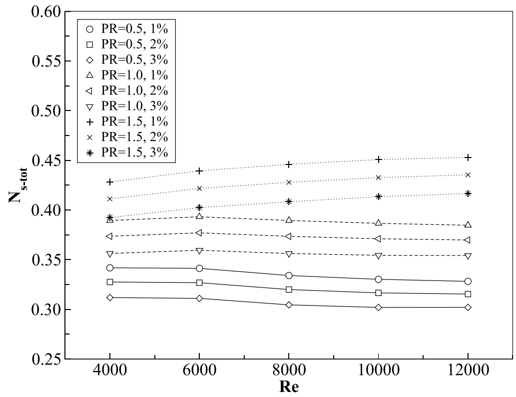

(c)

Figure 7. Effect of PR and Al_2O_3 volume concentrations with Re on (a) N_{s-ht}, (b) N_{s-fr}, and (c) N_{s-tot}.

5. Conclusions

A numerical simulation of turbulent nanofluid flow to examine the heat transfer and entropy generation in a tube fitted with inclined ring ribs (IRR) has been performed. The use of IRR can help produce two main counter-rotating vortices flowing throughout the tube. This vortex flow phenomenon can induce the flow impingements on the tube surface leading to the greater rise in the heat transfer. The augmentation of Nu/Nu_0 is around 2.34-3.52 times at PR=0.5-1.5 and vf = 1 - 3% whereas the friction loss, f/f_0 is enlarged around 4.57-8.88 times. The highest thermal performance (TEF) around 2.03 is seen at PR = 0.5, Re = 4000, and vf = 3% while the entropy generation is lowest at this condition.

References

[1] Patankar S V, Liu C H and Sparrow E M 1998 *ASME J. Heat Transf.* **98** 1109-1151
[2] Promvonge P et al. 2010 *Int. Commun. Heat Mass Transf.* **37** 170-177
[3] Choi S U S and Eastman J A 1995 *Enhancing thermal conductivity of fluids with nanoparticles*
[4] Wen D, Lin G, Vafaei S and Zhang K 2009 *Particuology* **7(2)** 141-150
[5] Maxwell J C 1873 *A treatise on electricity and magnetism* (Oxford: Clarendon Press)
[6] Mohamed H A 2005 *J. Heat Transf.* **128** 87–92
[7] Wang W et al. 2018 *Int. Journal of Heat and Mass Transfer* **128** 836-847
[8] Versteeg H K and Malalasekera W 1995 *An Introduction to Computational Fluid Dynamics: The Finite Volume Method* (England: Longman Group Limited)
[9] Bejan A 1979 *J. Heat Transf.* **101** 718–725
[10] Bhardwaj S, Dalal A and Pati S 2015 *Energy* **79** 467–481
[11] Promvonge P and Skullong S 2020 *Applied Thermal Engineering* **164**
[12] Ghasemi B and Aminossadati S 2010 *Int. Journal of Thermal Sciences* **49(6)** 931-940
[13] Vajjha R S, Das D K and Kulkarni D P 2010 *Int. Journal of Heat and Mass Transfer* **53(21)** 4607-4618
[14] Corcione M 2010 *Int. Journal of Thermal Sciences* **49(9)** 1536-1546
[15] Li X W, Meng J A and Guo Z Y 2009 *Int. J. Heat and Mass Transfer* **52** 962-970
[16] Bejan A 1996 *Appl. Phys. Rev.* **19** 1191-1218

CST0016

System Identification Approach for Autoregressive Exogenous Model on Small Unmanned Surface Vehicle

Surasak Timpitak[1,*], and Eakkachai Pengwang[1]

[1]Intitute of Field roBOtics, King Mongkut's University of Technology Thonburi, 126 Pracha Uthit Rd., Bangmod, Thung Khru, Bangkok, 10140, Thailand

* Corresponding Author: E-mail : surasakk16@gmail.com

Abstract. The system identification of small unmanned surface vehicle (USV) is proposed in order to predict parameters based on autoregressive exogenous (ARX) model. The simulated system of USV master with autonomous control coordinates point to point and data collection system measuring the output data and input data of USV master to compare parameters between model master and model predict. In this research, the experiment model comparing the predictive model in two aspects; 1) analyze and find the values of variables by using parameter predictions with autoregressive exogenous (ARX) method, and 2) predict a USV model with autonomous control system in order to achieve the movement along with a desired position. These experimental data can help for validation based on predictive model. This method can also describe the position of the predict model accurately and can be applied to identify other model of USV.

1. Introduction

The development of robotic has been consistently developed and gradually become a part of human daily lives. For increasing productivity at the manufacturing facility, productivity in the production process, improving quality of life, and creating convenience to improve human experiences. Moreover, the robotic and autonomic machine consists of a programming controller become increasingly complex and existence a high-performance computer for calculation of the complicated formula of mathematic. The mathematical models were used for investigation and testing the simulated, which can examine for control design, shows the response of the dynamic model.

The corrective dynamic model is the most important factor in ensuring good performance. The differential thrust DW-uBoat [1,2] is research by the Institute of Marine Vehicle and Underwater Technology, which zigzag experimental carried to real environment obtain data to system identification enhance by cuckoo search algorithm and ensemble learning of stacking method for faster convergence and high correctness. In Germany, dynamic model without disturbances surrounding and experiment low speed of reflecting the actuator force was use in the research. For parameters analysis and based identification process of unknown hydrodynamic in SonoBot USV [5]. Unstructured uncertainties of vessel steering were modified second-order Nomoto model [6] (full state model) and reduced order state model. Both of them were referring to system identification an extended Kalman filter (EKF).The twin hull catamaran CaRoLIME [7] design hull, differential propulsion, navigation and control system, these spiral maneuvers collect data to least square estimation parameters in Matlab/Simulink and plot particle swarm convergence algorithm.

The structure of this paper present follows to. Section 2 dynamic equations of motion and vector of control inputs with the unmanned surface vehicle. Section 3 parameter predictions with system identification the autoregressive exogenous method on discrete-time. Autonomous control system with PID control and the movement along with simulate position in Section 4. Finally, evaluate of tracking master model and compare tracking-error for the straight path in Section 5.

2. Dynamic Model of Small USV

For the mathematical model in simulation, dynamic and kinematic models the equation of motion in the dynamic non-linear. Six degrees of freedom (6-DOF) by applying Newton's second law, the linear and angular velocity of the vehicle should be expressed in the body frame coordinate system can be written as in equation (1)

$$\mathbf{M}\dot{\mathbf{v}} + \mathbf{C}(\mathbf{v})\mathbf{v} + \mathbf{D}\mathbf{v} = \boldsymbol{\tau} \tag{1}$$

The vector denotes $\mathbf{v} = [u, r]^T$ is linear velocity motion in the x direction (surge) and angular velocity about the z axis (yaw). Vehicle in thrust vector describe $\boldsymbol{\tau} = [X, N]^T$ force motion in the x direction and moment about the z axis. Inertia matrix including added mass denotes $\mathbf{M}$, the coriolis and centripetal including added mass denotes $\mathbf{C}$ and where $\mathbf{D}$ hydrodynamic damping matrix.

$$\boldsymbol{\tau} = \boldsymbol{B}\boldsymbol{u} \tag{2}$$

This has to be considered the matrix control inputs $\boldsymbol{\tau}$ as in equation (2), where $\boldsymbol{B}$ is the control matrix described as the thruster configuration [8]. The unmanned surface vessel is not assumed to as sway and heave motions, roll and pitch rotation in this dynamic model. The propeller matrix input $\boldsymbol{u} = [u_{TL}, u_{TR}]^T$ of thrust propeller left and propeller right respectively is shown in Figure 1.

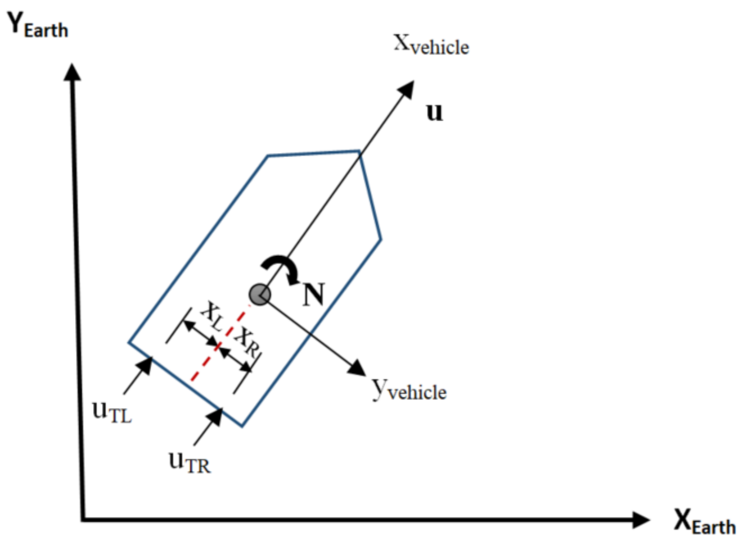

Figure 1. Coordinate of unmanned surface vehicle with differential propeller.

Therefore centers of mass (CM) of USV distance along the y-axis are x_L and x_R, which forward force is a sum left and right propeller $(X = u_{TL} + u_{TR})$ and moment append to distance between CM and propeller $(N = x_L u_{TL} - x_R u_{TR})$ force and moment respectively.

3. AutoRegressive eXogenous (ARX) with Parameter System Identification

This section explains for prediction unknown parameters of the vessel by the system identification algorithm. The dynamic equation of motion continuous time can be evaluated into 2 DOF as in equation (3), therefore a process system identification model transforms to transfer function on the discrete-time domain.

$$\begin{aligned}\dot{u} &= \left(\frac{X_u}{m - X_{\dot{u}}}\right)u + \left(\frac{1}{m - X_{\dot{u}}}\right)u_{TL} + \left(\frac{1}{m - X_{\dot{u}}}\right)u_{TR} \\ \dot{r} &= \left(\frac{N_r}{I_z - N_{\dot{r}}}\right)r + \left(\frac{X_L}{I_z - N_{\dot{r}}}\right)u_{TL} - \left(\frac{X_R}{I_z - N_{\dot{r}}}\right)u_{TR}\end{aligned} \tag{3}$$

The AutoRegressive eXogenous (ARX) model structures describing the dynamic system in discrete time, this represents between Autoregressive part $A(q)y(t)$ and eXogenous part $B(q)u(t)$. Where $y(t-i)$ delay output and $u(t-i)$ delay input by i time step, denotes $e(t)$ with noise disturbance model as in equation (4) and Simplify in transfer-function from gives as in equation (5)

$$y(t) + a_1 y(t-1) + ... + a_{n_a} y(t-n_a) = b_1 u(t-1) + ... + b_{n_b} u(t-n_b) + e(t) \tag{4}$$

$$y(t) = \frac{B(q)}{A(q)}u(t) + \frac{1}{A(q)}e(t) \tag{5}$$

Model structure ARX are denoted as (n_a, n_b, n_k) describe n_k the number of sampling time, n_a are number of poles and n_b are number of zeros plus one. Polynomial shifts operate backward q^{-1} with $A(q)$ and $B(q)$ as in equation (6) and equation (7)

$$A(q) = \sum_{k=0}^{n_a} a_k q^{-k} = 1 + a_1 q^{-1} + a_2 q^{-2} + ... + a_{n_a} q^{-n_a} \tag{6}$$

$$B(q) = \sum_{k=1}^{n_b} b_k q^{-k} = b_1 q^{-1} + b_2 q^{-2} + ... + b_{n_b} q^{-n_b} \tag{7}$$

The vector matrix notation the output vector $\boldsymbol{\hat{y}(t)}$ and $\vartheta(t)^T$ is discrete time unknown parameter can rewrite as in equation (8) and describe ϕ regression matrix in equation (9)

$$\boldsymbol{\hat{y}}(t, \vartheta) = \boldsymbol{\phi}(t)^T \boldsymbol{\vartheta} \tag{8}$$

$$\phi = \begin{bmatrix} -y(n_a - 1) & \cdots & -y(0) & u(n_a - 1) & \cdots & u(n_a - n_b) \\ -y(n_a) & & -y(1) & u(n_a) & \cdots & u(n_a - n_b + 1) \\ -y(n_a + 1) & & \vdots & & \vdots & \\ \vdots & & & & & \\ -y(N-1) & \cdots & -y(N - n_a) & u(N-1) & \cdots & u(N - n_b) \end{bmatrix} \tag{9}$$

The unknown parameter AutoRegressive eXogenous method cans prediction in equation (10)

$$\boldsymbol{\hat{\vartheta}} = (\boldsymbol{\phi}^T \boldsymbol{\phi})^{-1} \boldsymbol{\phi}^T \boldsymbol{\hat{y}} \tag{10}$$

4. Autonomous Feedback PID Control System

A proportional integral derivative (PID) controller is a control loop vehicle model. The propose is to feedback value of the vehicle model to reference command. Matlab and Simulink program unmanned surface vehicle simulation of feedback control with heading error and distance error. Model master and model predict of USV control coordinate point to point.

4.1. Heading Error Response

The simulated system of USV master model with autonomous control heading error and USV predict model by ARX method with a similar gain of PID controller. The result heading error response improve to master output is shown in Figure 2.

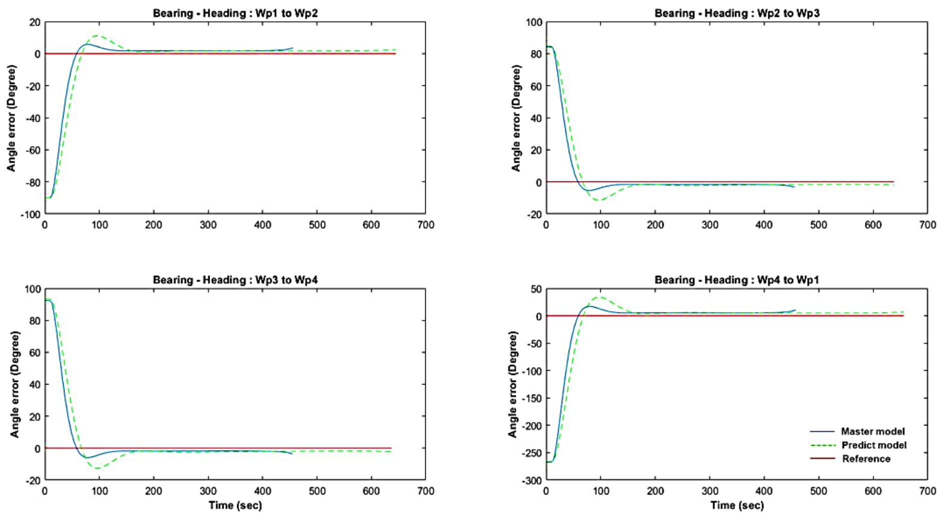

Figure 2. A heading error in MATLAB simulation results used for the autonomous motion USV between master model and predict model.

4.2. Positioning Feedback

These experiments describe an autonomous 4 waypoint able to achieve the position movement to target a waypoint radius of 1 meter. The result in order to explain the predict model position have converge to path following shown in Figure 3.

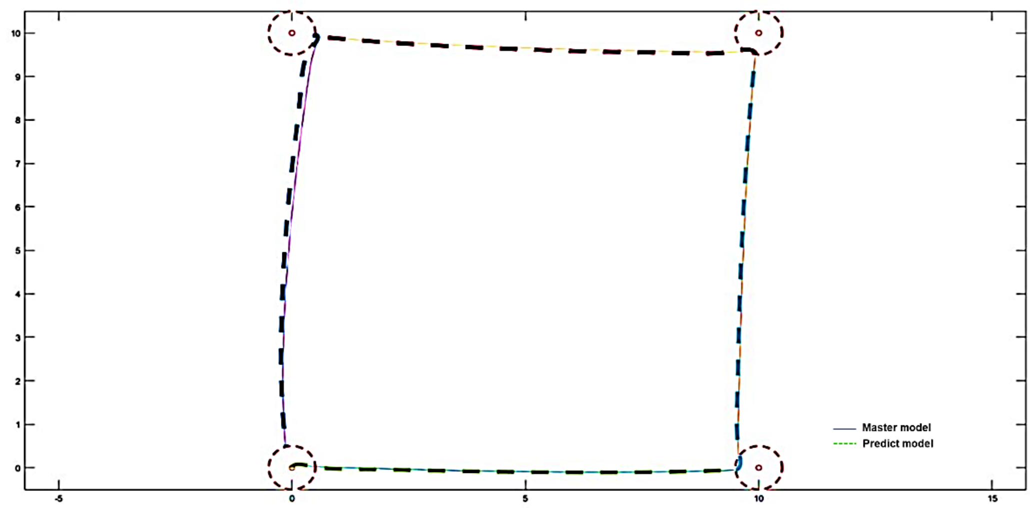

Figure 3. A waypoint autonomous position USV between master model and predict model.

5. Validation Straight-Path Vehicle Tracking-Error

The vehicle path following compare tracking error by perpendicular straight line [10] between vehicle position and reference line trajectory. As a result of positive and negative value present a point to reference point shown in Figure 4.

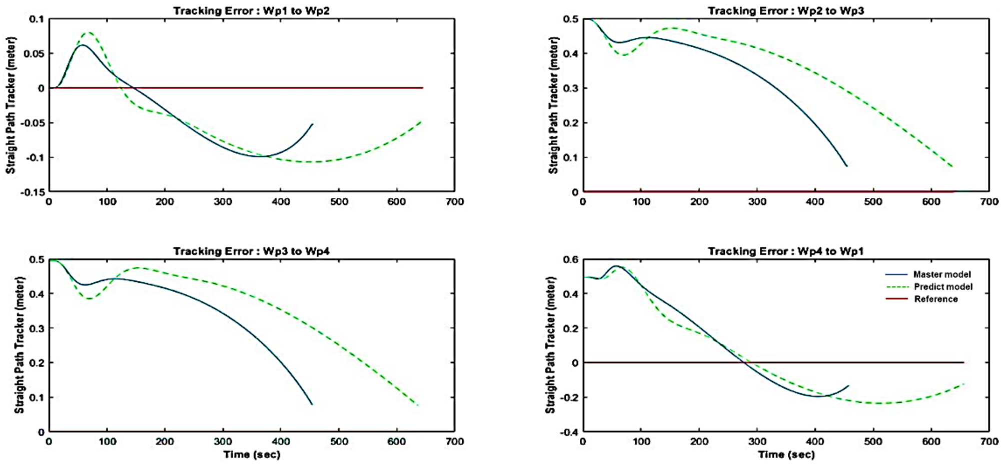

Figure 4 A waypoint in MATLAB simulation results used for the autonomous motion USV between master model and predict model.

However, the tracking error indicated the error values for a group error are converging. The autonomous result for vehicle in straight path tracker is can use parameter predict model for use same controller of master model.

Conclusion

In this paper, the system identification (SI) was presented based on the simulated input and output from a small USV master model with PID control autonomous waypoint. The result has shown that the AutoRegressive eXogenous (ARX) is an effective method for parameter prediction. The movement along with the desire position was achieved by predicting a USV model with an autonomous control system. This SI experiment can be applied with real implement mobile robot future work

Acknowledgments

This research was supported by King Mongkut's University of Technology Thonburi. The authors were grateful for the kind support from associate professor Pradya Prempraneerach from Tammasat University and associate professor Manusak Janthong from Rajamagala University of Technology Thunyaburi department of mechanical engineering.

References

[1] Peng-Fei X, Chen C, Hong-Xia C, Ya-Lin S and Yan-Xu D 2020 *J.Ocean Engineering* Volume 197, DOI: 10.1016/j.oceaneng.2019.106898.
[2] Chen C, Peng-Fei X, Hongxia C, Yanxu D, Jinhai Z, Tong G, Dianhong S and Jin X, 2020 *J.Ocean Engineering* Volume 207, DOI: 10.1016/j.oceaneng.2020.107388.
[3] Earle W. Isibue and Thomas J. Pingel 2020 *J. Urban Forestry & Urban Greening* Volume 48, DOI: 10.1016/j.ufug.2019.126574.
[4] Rolf John B and Petter G. Almklov 2019 *J.Marine Policy* Volume 109, DOI:10.1016/j.marpol.2019.103675.

[5] Stefan W, Hanna W, Thomas. T and Johannes R, 2015, *20th International Conference on Methods and Models in Automation and Robotics (MMAR)*, Miedzyzdroje, Germany, pp. 701-706, DOI: 10.1109/MMAR.2015.7283960
[6] Lokukaluge Prasad P, Paulo O and Carlos Guedes S, 2016 *IEEE Journal of Oceanic Engineering*, vol. 41, no. 3, pp. 515-528 DOI: 10.1109/JOE.2015.2460871.
[7] Michael B, Stefan W, Markus O, Oliver H and Johannes R, 2013 *9th IFAC Conference on Control Applications in Marine Systems*, DOI: 10.3182/20130918-4-JP-3022.00056.
[8] Thor I F, 1994, *Guidance and Control of Ocean Vehicle* (NewYork: John Wiley & Sons)
[9] Keesman K J 2011 *System Identification* (New York: Springer-Verlag) chaprer 6 pp 113-152
[10] Sherman K S and Anthony B, 1992, *Calculas and Analytic Geometry* (New York: McGraw-Hill)

CST0017

Assessment of rice production of Malaysia using Remote Sensing

Emaad Ansari[1], Mohammed Nishat Akhtar[1], Ahmad Faizul Hawary[1], Mohamad Khairi Ishak[2] and Elmi Abu Bakar[1,*]

[1]School of Aerospace Engineering, Universiti Sains Malaysia, 14300 Nibong Tebal, Penang, Malaysia
[1]School of Electrical and Electronic Engineering, Universiti Sains Malaysia, 14300 Nibong Tebal, Penang, Malaysia

* Corresponding Author: meelmi@usm.my

Abstract. Rice is the basic staple food in the Malaysian diet. Although rice being a vital diet component, Malaysia produces only 70% rice and imports 30% rice from its neighbours. Remotely sensed data captured through satellite shows that although Malaysia having similar suitable climatic conditions for rice production as compared to other South East Asian countries, still it produces very small amount of rice compared to its neighbours. The current study compares the climatic conditions of Malaysia and its neighbouring countries and focusses on the scope of using satellite data and images for sensing out the lands and agricultural fields suitable for producing rice. Attention is given on using weather satellites for sensing suitable temperature and average rainfall necessary for rice production. The focal point of the current study is on the simplicity of using satellite images such as LANDSAT images for determining the paddy fields. Ease of using remote sensing technology is elaborated in the present work.

Keywords: Rice, Remote Sensing, Satellites, Temperature, Rainfall.

1. Introduction

Malaysian food always constitutes of rice in the diet, which is known as *Nasi* in the Bahasa Melayu language. Still the rice production of Malaysia is very low as compared to the rice consumed by its inhabitants. Only 70 % of the total rice consumed in Malaysia is produced in Malaysia and the rest is imported from other countries such as Thailand, Vietnam, India, etc. Najim et al. [1] focused on the impact of rice production in Malaysia, which leads to a healthy sustenance. Importance of policy changes and private sector investments are studied. Vaghefi et al. [2] listed out the adverse effect of climate change on rice production in Malaysia. The climate change also leads to economic losses which can be controlled by the adaptation policies listed in the study. Akinbile et al. [3] suggested the rice production techniques and efficient use of water for self-sustenance. The change in eating habits is also suggested for independency on other countries. Sarwar and Khanif [4] conducted an experiment to investigate the change in soil properties by saving water in rice fields. Rajamoorthy et al. [5] enlisted the limitations coming in the way of rice production due to government policies and their implications. Fatimah et al. [6] conducted policy analysis of food security. System dynamics is required for better rice management. Azman et al. [7] paved a way of increase in rice production by using lime sources in acid sulphate soil in Malaysia. Thus, a change in policy, better use of water and proper investigation is suggested in previous studies for increase in rice production in Malaysia.

Previous studies exhibits multiple applications of remote sensing [8-18]. This includes agricultural studies, oil palm investigation, municipal waste management, vegetation indices, forest studies, fisheries, etc.

2. Current Rice Production Scenario

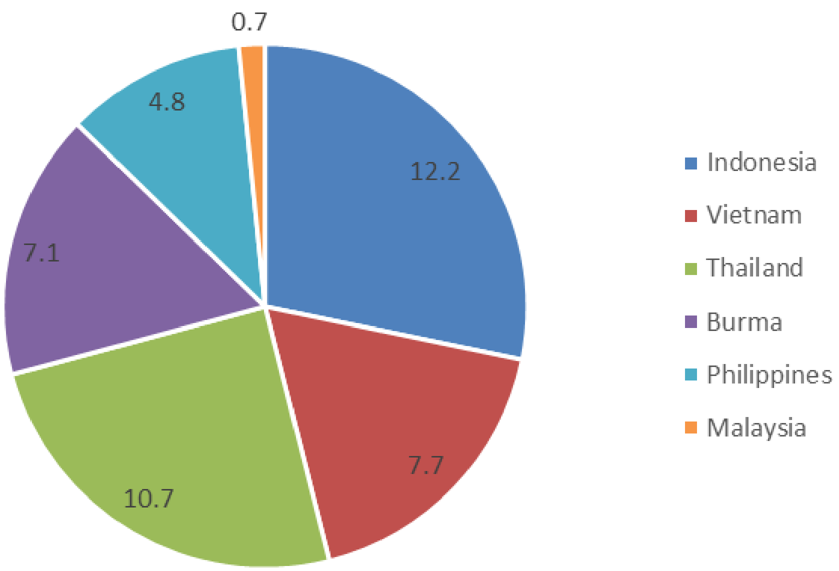

Figure 1. Rice production in South East Asian countries (In million Hectares) (Image Courtesy: USDA)

Figure 1 shows the rice cultivation in some of the South East Asian countries in million hectares. Maximum rice is cultivated in Indonesia which itself consumes the production and becomes a good exporter of rice. Vietnam and Thailand too produces a good amount and both of them exports to Malaysia as well. Having similar climatic conditions as that of Malaysia, countries of Burma and Philippines produce more rice as compared to Malaysia. Malaysia only produces 0.7 million hectares of rice which leads to its dependency on other countries.

3. Climatic Conditions

The two vital climatic requirements for rice production is a suitable amount of rainfall and average temperature range. Malaysian climate has both requirements fulfilled. A detailed analysis of climate using satellite data is elaborated.

3.1. Average Rainfall

Figure 2 shows the minimum and maximum amount of rainfall received in South East Asian countries such as Indonesia, Vietnam, Thailand, Burma, Philippines and Malaysia. The rainfall is calculated by measuring precipitation with the help of earth observing satellites. For better rice production and good paddy fields, minimum rainfall of 115 cm is required [3]. Also, best suited rainfall for rice production is 175 cm to 300 cm [3]. These criteria is fulfilled by Malaysian climatic conditions. Although maximum rainfall received in Malaysia is less as compared to its neighbors, still the condition is well suited for rice production. And the minimum rainfall received in Malaysia is well above the minimum requirement of 115 cm.

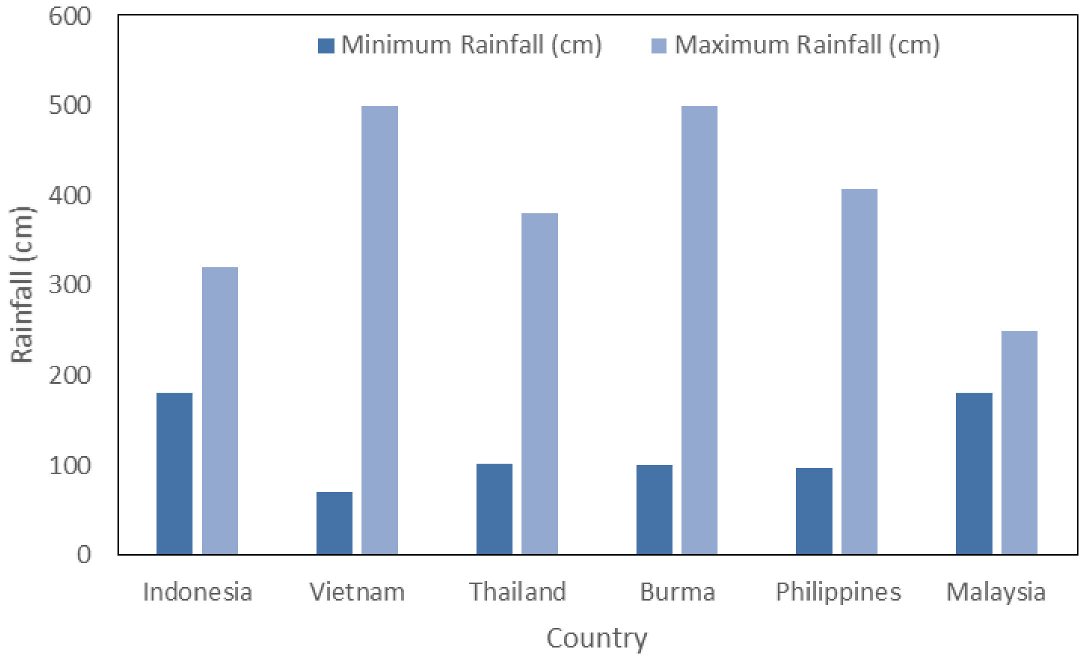

Figure 2. Rainfall received in Malaysia and its neighbouring countries

3.2. Temperature

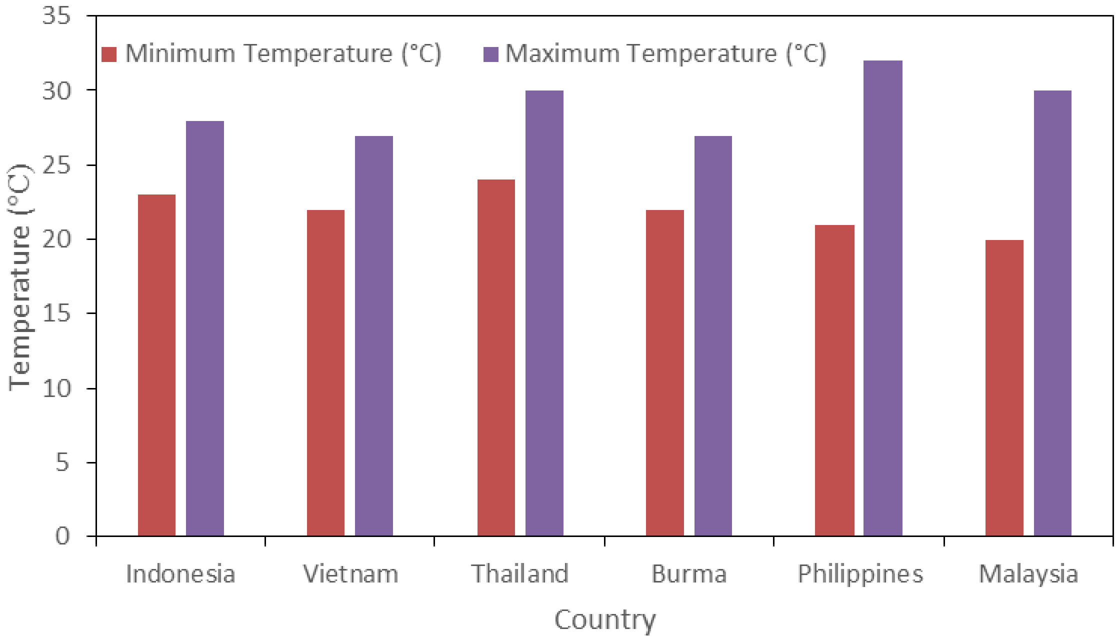

Figure 3. Temperature range in Malaysia and its neighbouring countries

Figure 3 shows the minimum and maximum temperature recorded in the countries of Indonesia, Vietnam, Thailand, Burma, Philippines and Malaysia. Temperature of earth can be measured using GISS

Surface Temperature Analysis (GISTEMP) satellites as well as atmospheric infrared sounder (AIRS) satellites. Malaysian temperature is well fitted in the range of 20 ℃ to 30 ℃ which falls in the range of better rice production. Also the temperature of Malaysia does not falls below 15 ℃ which makes it more suitable for rice production. Thus Malaysia has both good amount of rainfall and suitable range of temperature suited for rice production.

4. Methodology to investigate the Paddy fields

A two-step methodology is used in the present study to determine the land suitable to be used as paddy fields. First the Soil Adjusted Vegetation Index (SAVI) is calculated for the images captured using LANDSAT 8 using the ArcGIS software to compare soil colour and soil moisture of paddy fields and probable land. Secondly, colour histogram is analysed to compare the Red, Green, and Blue (RGB) colour model using Fiji software. A brief study of these two steps is very helpful in determining probable land that can be used as paddy fields for rice cultivation.

4.1. Soil Adjusted Vegetation Index (SAVI)

Soil Adjusted Vegetation Index can be calculated using Equation 1 in the ArcGIS software

$$SAVI = \frac{NIR - Red}{NIR + Red + L}(1 + L) \quad (1)$$

Where NIR is the Near Infrared Band (Band 5), Red band is band 4 and L is canopy background adjustment factor which is usually taken 0.5 for better calibration.

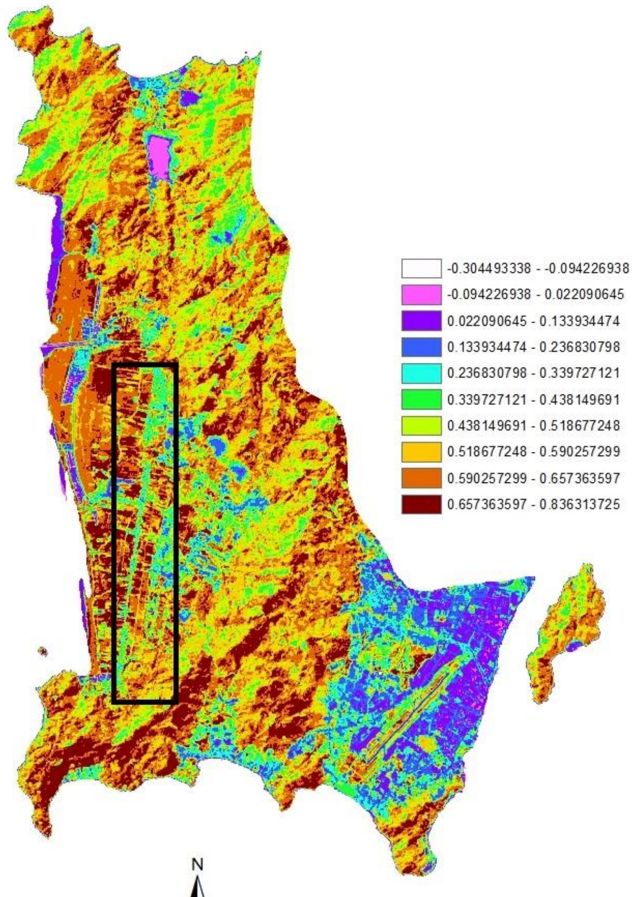

Figure 4. SAVI of Barat Daya, Penang, Malaysia

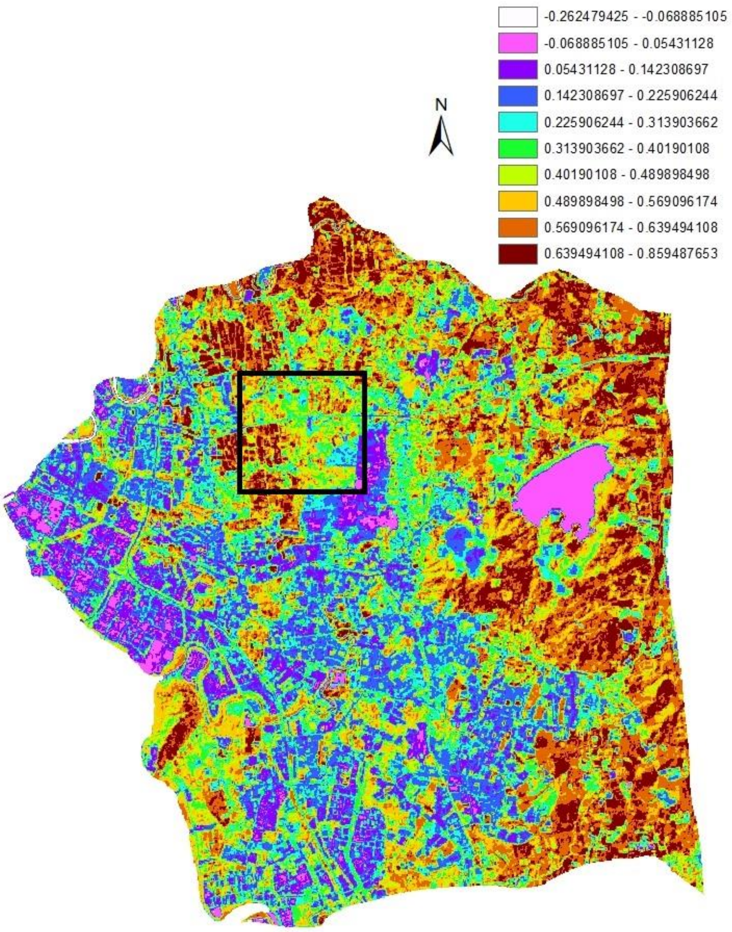

Figure 5. SAVI of Seberang Perai Tengah, Penang, Malaysia

Figure 4 and Figure 5 shows the Soil Adjusted Vegetation Index (SAVI) of Barat Daya district and Seberang Perai Tengah district respectively. Both the districts lies in the northern Malaysian state of Penang. There are presence of paddy fields in the Barat Daya district which is highlighted in Figure 4. The SAVI index of these paddy fields in Barat Daya district is 0.43 to 0.52. Similar quality lands are available in Seberang Perai Tengah district. These have SAVI index of 0.4 to 0.5 as seen in Figure 5. Thus, these barren land of Seberang Perai Tengah district can be used as paddy fields for rice cultivation. Thus it can be concluded that the SAVI criteria for paddy fields lies in the range of 0.4 to 0.5.

4.2. Red, Green, Blue (RGB) Colour Histogram

Figure 6 and Figure 7 shows the color histogram of a paddy field and barren land respectively. The images are captured using Google Earth Pro and analyzed in Fiji software. The scale of both the images is fixed. The average value of RGB from both the histogram is almost similar. The green color difference in the image is due to the grasses that has come up in Figure 7. Apart from that, the natural color visibility of both land are almost similar. Thus showing the similar qualities among both the land. Also it is evitable that the mean values of RGB for paddy fields is in the range of 105-115, 95-120 and 85-100 respectively.

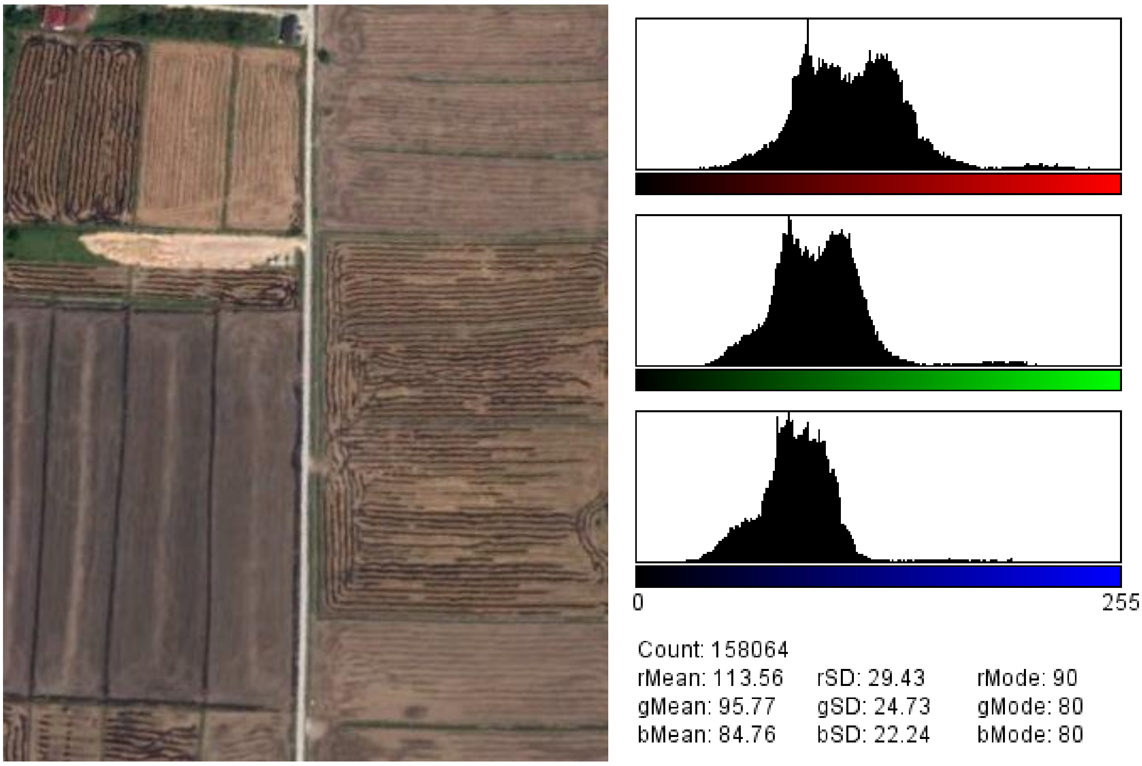

Figure 6. Colour histogram of paddy field in Barat Daya, Penang

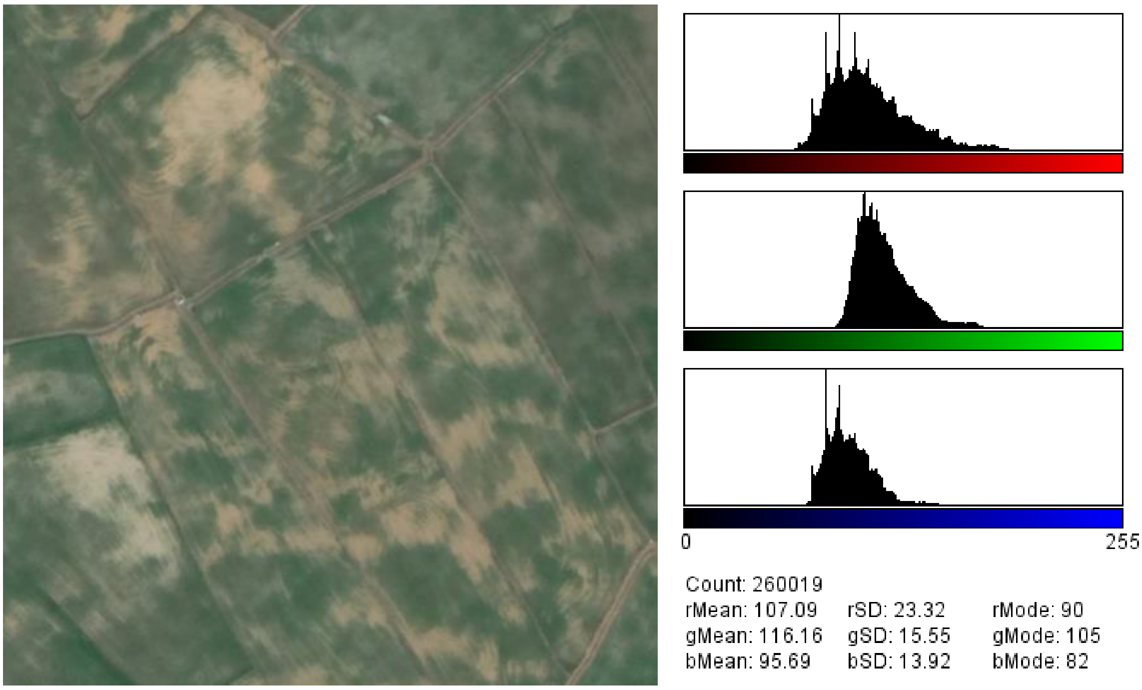

Figure 7. Colour Histogram of barren land in Seberang Perai Tengah, Penang

Conclusion

The use of satellite data and satellite images for sustainable agricultural activities is studied effectively. Average rainfall, suitable temperature range and land details using satellites is used to determine the conditions for farming. The SAVI index and RGB colour histogram is analysed for comparing soil properties. Many more index can be calculated for further analysis of soil. The objective of studying the climatic conditions and soil conditions are successfully achieved in the present work. Image processing algorithm can also be developed for future study for better analysis of images captured using satellites.

Acknowledgments

The authors would like to acknowledge the Research University Internal grant (RUI1001/PAERO/8014035) provided by the Research Creativity and Management Office (RCMO), Universiti Saint Malaysia to support this research.

References

[1] Najim M M M, Lee T S, Haque M A and Esham M 2007 Sustainability of Rice Production: a Malaysian Perspective *J. Agric. Sci.* **3** 1–12
[2] Vaghefi N, Nasir Shamsudin M, Makmom A and Bagheri M 2011 The economic impacts of climate change on the rice production in Malaysia *Int. J. Agric. Res.* **6** 67–74
[3] Akinbile C O, Abd El-Lat K M, Abdullah R and Yusoff M S 2011 Rice Production and Water use Efficiency for Self-Sufficiency in Malaysia: A Review *Trends Appl. Sci. Res.* **6** 1127–40
[4] Sarwar M J and Khanif Y M 2005 Techniques of Water Saving in Rice Production in Malaysia *Asian J Plant Sci* **4** 83–4
[5] Rajamoorthy Y, Rahim K b A and Munusamy S 2015 Rice Industry in Malaysia: Challenges, Policies and Implications *Procedia Econ. Financ.* **31** 861–7
[6] Fatimah M A, Emmy F A, Kusairi M N and Tasrif M 2015 Food security: self–sufficiency of rice in Malaysia **18** 83–100
[7] Azman E A, Shamshuddin J, Che F I, and Roslan I 2014 Increasing Rice Production Using Different Lime Sources on an Acid Sulphate Soil in Merbok, Malaysia *Pertanika J. Trop. Agric. Sci.* **37** 223–47
[8] Weiss M, Jacob F and Duveiller G 2020 Remote Sensing of Environment Remote sensing for agricultural applications : A meta-review *Remote Sens. Environ.* **236** 111402
[9] Singh A 2019 Remote sensing and GIS applications for municipal waste management Collection & Transport *J. Environ. Manage.* **243** 22–9
[10] Belgiu M and Dragut L 2016 Random forest in remote sensing : A review of applications and future directions *ISPRS J. Photogramm. Remote Sens.* **114** 24–31
[11] Ma L, Liu Y, Zhang X, Ye Y, Yin G and Johnson B A 2019 Deep learning in remote sensing applications : A meta-analysis and review *ISPRS J. Photogramm. Remote Sens.* **152** 166–77
[12] Xue J and Su B 2017 Significant Remote Sensing Vegetation Indices : A Review of Developments and Applications *J. Sens.* **2017** 1-17
[13] Chong K L, Kanniah K D, Pohl C, Tan K P and Group F 2017 Geo-spatial Information Science A review of remote sensing applications for oil palm studies *Geo-spatial Inf. Sci.* **5020** 1–17
[14] Mhawish A, Kumar M, Mishra A K, Srivastava P K and Banerjee T 2018 *Remote Sensing of Aerosols From Space : Retrieval of Properties and Applications* (Elsevier Inc.)
[15] Fesenmyer K A and Leasure D R 2017 Satellite and Airborne Remote Sensing Applications for Freshwater Fisheries *Fisheries* **42** 526–37
[16] Yao H and Qin R 2019 Unmanned Aerial Vehicle for Remote Sensing Applications — A Review *Remote Sens.* **2019** 1443
[17] Talbot B, Pierzchała M and Astrup R 2016 Applications of Remote and Proximal Sensing for Improved Precision in Forest Operations *Crot. J. for Eng.* **38** 327–36
[18] Management F R 2018 A Review on Applications of Remote Sensing and Geographic Information Systems (GIS) in Water Resources and Flood Risk Management *Water* **2018** 608

DRC0001

Concept and Prototype of the Pure Intonation Ensemble System

Ryusuke Ishikawa[1,*], Kazuteru Tobita[2]

[1]Graduate School of Shizuoka Institute of Science and Technology, 2200-2 Toyosawa, Fukuroi, Shizuoka, 437-8555, Japan
[2]Shizuoka Institute of Science and Technology, 2200-2 Toyosawa, Fukuroi, Shizuoka, 437-8555, Japan

* Corresponding Author: 2021001.ir@sist.ac.jp

Abstract. Automatic performance of music instruments has been existing since many years ago. Today, an automatic performance system that can cooperate with a player by using machine learning is developed. We are making such system that we call it "Pure Intonation Ensemble System" and even planning to applicate it to the field of industry. We planned and are making two sub-systems of Pure Intonation Ensemble System and conducting some basic experiments. We are going to install detection system of player's motion, audio input and machine learning for conducting proper accompaniment data and improve the automatic performance that can make pure intonation ensemble with a reference tone.

1. Introduction

Some cooperation robots that cooperate with human are researched, developed and implemented to the field of industry these days. This movement will continue under the background of labor shortage of Japanese society and more-advanced cooperation robots are demanded. Here, we are assuming that ensemble of instruments is one of the most-advanced cooperation between humans, as the players need to not only follow their score but also feel their breath each other. Therefore, it can be thought that researching about ensemble between human and robot will promote the development of cooperation robots.

Automatic performance of music instruments has been existing since many years ago, from mechanical instrument such as automatic piano, electrical instrument such as synthesizer to the robot that performs an instrument like a human player[1]. Generally, their performance is fixed by its mechanism or synchronizing signals so that it was difficult to ensemble with human player in the same breath. However, thanks to development of machine learning, automatic performance system that learns human player's performance such as tempo and performs an accompaniment matches it is making an appearance today[2]. The anticipation for more-advanced automatic performance system is glowing.

In our research we are making such system that we call it "Pure Intonation Ensemble System". Its goal is to ensemble pure intonationally with a human player by learning and predicting their performance. Here, we are focusing on not only ensemble with human player in the same tempo but also control timing, volume, pitch and so on to make a beautiful harmony. In this paper, we will describe the concept and prototype of the Pure Intonation Ensemble System and conduction of some basic experiments of it.

2. Concept of the Pure Intonation Ensemble System

The Pure Intonation Ensemble System can be separated into two sub-systems by its function; "Player Movement Detection System", that detects, learns and predicts a human player's performance, and "Realtime Volume Pitch Control System", that makes accompaniment by performing a string instrument.

The complete concept image of Pure Intonation Ensemble System is shown in figure 1. Left half is Player Movement Detection System that consists of a camera, a 3D TOF camera, a contact mic, acceleration/gyro sensors and a computer. Right half is Realtime Volume Pitch Control System that consists of a violin-like instrument with one string that tensioned by String Tensioner, a bow that bowed by Bow Linear Mover and Bow Presser, motor drivers and a contact mic.

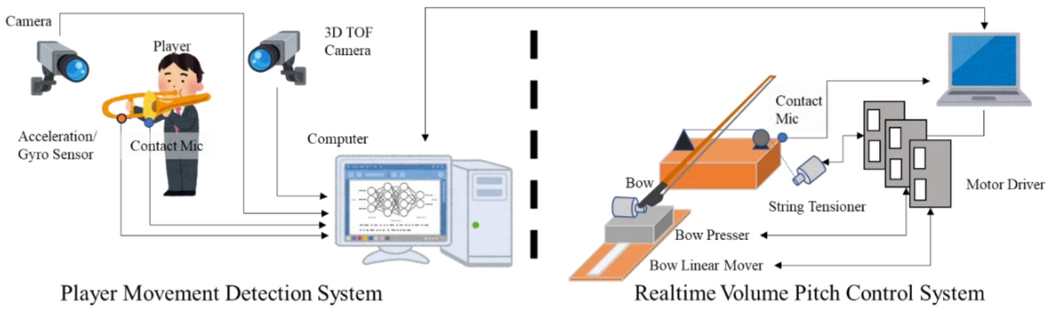

Figure 1. Complete Concept Image of the Pure Intonation Ensemble System.

3. Design and Prototype

We made very first prototype of Pure Intonation Ensemble System in 2019[3]. At that time, we implemented audio-process-system and Realtime Volume Pitch Control System with limited functions. This time, we designed and made a new prototype with additions of video-process-system and some improvements of actuators and so on, shown in figure 2.

The prototype of Player Movement Detection System consists of a computer with built-in camera, mic and some programs that processes the data from them. 3D TOF camera and sensors are not attached yet. This time, the player plays a recorder as it makes clear sound (its waveform is similar to sine wave) so that detecting its sound is easier than the other instruments we had. The detail of this sub-system is described in section 3.1. Also, the prototype of Realtime Volume Pitch Control System is assembled as same as concept, without the contact mic. The detail of this sub-system is described in section 3.2.

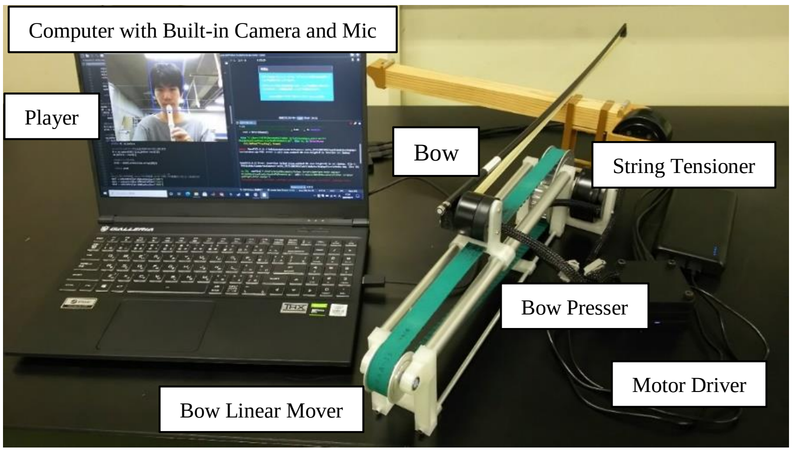

Figure 2. Prototype of the Pure Intonation Ensemble System.

3.1. Player Movement Detection System

This sub-system gathers the player’s performance data such as video image from camera and audio input from mic. There are multiple ways to detect and use of these data. For example, a research uses virtual buttons or faders on the video image to interact with a automatic performance robot[4]. However, we are focusing on more-advanced interactive/cooperative system. To achieve that, we introduce machine learning that processes and learns these data to predict player’s performance such as emit-timing of their sound, tempo, volume, pitch and so on.

The hardware of prototype of this sub-system consists of a computer (Galleria GCL1650TGF Intel®Core™ i5-10300H CPU @ 2.50GHz 2.50 GHz) with built-in camera and mic. Also, Python3.8 is used as software. The flowchart of the prototype is shown in figure 3.

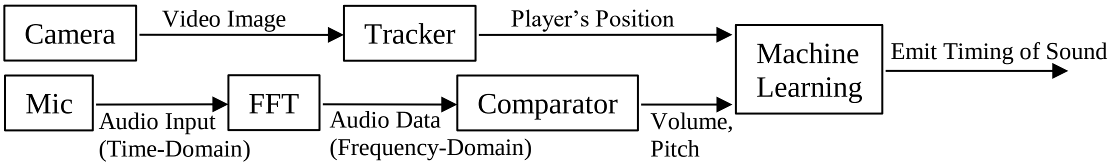

Figure 3. Flowchart of Prototype of Player Movement Detection System.

By using a tracker, KCF (Kernelized Correlation Filter, one of the kinds of motion track algorithm[5]), it gains player’s position data from the video image. Also, by using FFT, it gains volume and pitch data from the audio input. From these data, the machine learning detects/predicts emit-timing of the player’s sound. The image of this function is shown in figure 4.

First, the player emits a sound after they seesawed their face. Its relative displacement dy[px] (the displacement of the position of the player’s face between current flame and last flame, along the vertical axis. That means dy(i)=y(i)-y(i-1), where y(i) and y(i-1) are current and last position of the player’s face detected by the tracker respecively, i is the number of times of the process.) and audio data are detected as time-chart, then the emit-timing is recorded as label 1 and others are 0.

Second, these data are learned by the machine learning, MLP Classifier (Multilayer Perceptron, one of the kinds of neural network[6]), and it predicts next emit-timing.

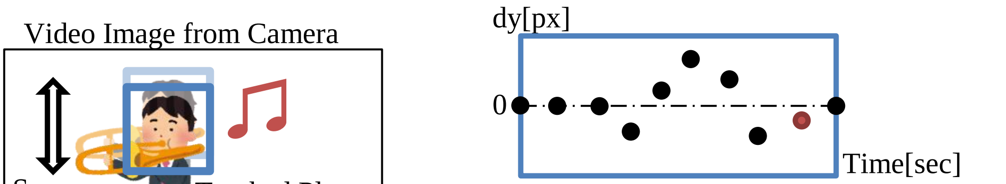

dy[px]	0	0	0	-3	1	3	2	-3	-1	0
Detect/Predict	Emit-Timing? --- YES:1 / NO:0									

Figure 4. Image of Detection/Prediction of Emit-Timing.

3.2. Realtime Volume Pitch Control System

This sub-system has a string instrument consists of three mechanisms; String Tensioner, Bow Linear Mover and Bow Presser. Like a violin, it emits sound by rubbing a string using a bow. Also, there will be a contact mic for monitoring the condition of its sound.

3.2.1. String Tensioner/Instrument

The image of String Tensioner/Instrument is shown in figure 5. It has a string, its one end is fixed on a tail piece and another end is tied around a peg that fixed with a torque-controlled motor. Also, the vibration length of the string is fixed by the distance between the bridge and the nut.

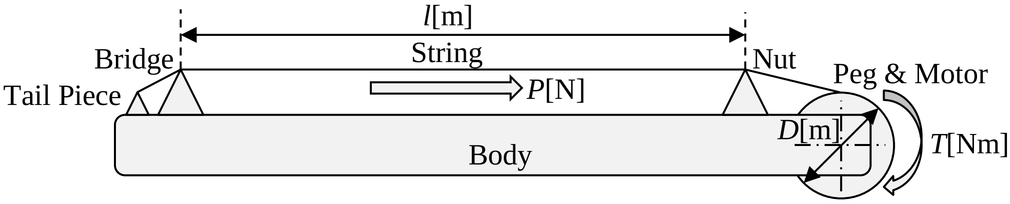

Figure 5. Image of String Tensioner/Instrument.

The purpose of String Tensioner is to control the pitch (frequency of sound) made by transverse vibration of the string. Its natural frequency f_n[Hz](n=1, 2, 3, …) is determined theoretically as

$$f_n = \frac{n}{2l}\sqrt{\frac{P}{\mu}} \tag{1}$$

where l is vibration length of the string (approximately 0.384[m]), μ is mass per unit length of the string (approximately 0.000985[kg/m]) and P[N] is tension of the string[7]. The main audible natural frequency is considered to be f_1 (written as f below) so that transform equation (1) into

$$f = \frac{1}{2l}\sqrt{\frac{P}{\mu}} \tag{2}$$

The tension P is controlled by the peg, its outer diameter is D (approximately 0.012[m]), and the motor, that drives torque T[Nm]. When motor is not rotating, $P=2T/D$ so that equation (2) can be transformed into

$$f = \frac{1}{l}\sqrt{\frac{T}{2\mu D}} \tag{3}$$

From equation (3), theoretical-torque T_{th}[Nm] is lead as below when referenced-frequency/pitch is f_{ref}[Hz].

$$T_{th} = 2\mu D l^2 {f_{ref}}^2 \tag{4}$$

However, there could be disturbance such as friction so that the pitch will not be as same as f_{ref} even String Tensioner drives T_{th}. To compensate this, we introduce PID controller shown in figure 6 as block diagram.

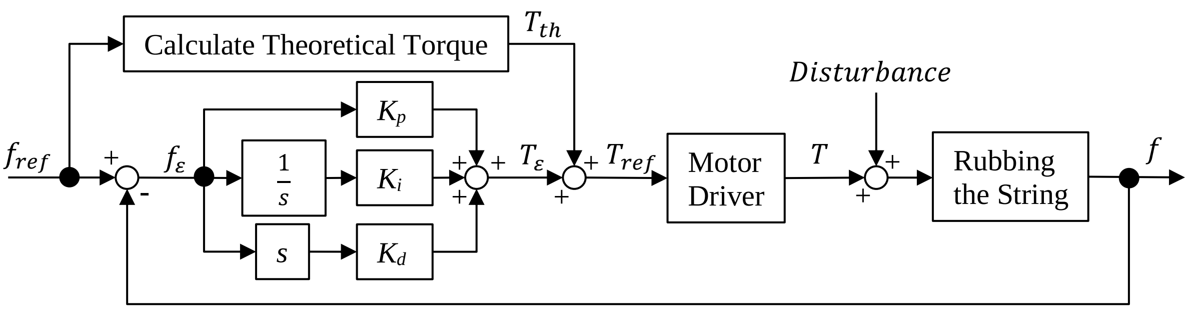

Figure 6. Block Diagram of PID Controller for Pitch Control.

First, f_{ref}[Hz] is added as input and calculate theoretical-torque T_{th}[Nm] and compensate-torque T_ε[Nm], that lead as below.

$$T_\varepsilon = K_p f_\varepsilon + K_i \int_0^t f_\varepsilon d\tau + K_d \frac{df_\varepsilon}{dt} \tag{5}$$

where f_ε[Hz] is error of pitch, the difference between f_{ref} and emitted-pitch f[Hz]. K_p, K_i and K_d are gains.

Second, run the motor with T_{ref}, sum of T_{th} and T_ε, producing actual-torque T[Nm] via motor driver.

Third, the system emits sound of pitch f by rubbing the string. This f will be feedbacked.

3.2.2. Bow Linear Mover and Bow Presser

The images of Bow Linear Mover, that moves a bow forth and back, and Bow Presser, that presses down the bow on the string, are shown in figure 7. Bow Linear Mover consists of a pair of pulleys, a timing belt and a motor. The rotation of the motor is converted into linear movement. Bow Presser consists of a support part that fixed on the timing belt, a motor and the bow. The torque of the motor is converted into the force that presses down the bow on the string.

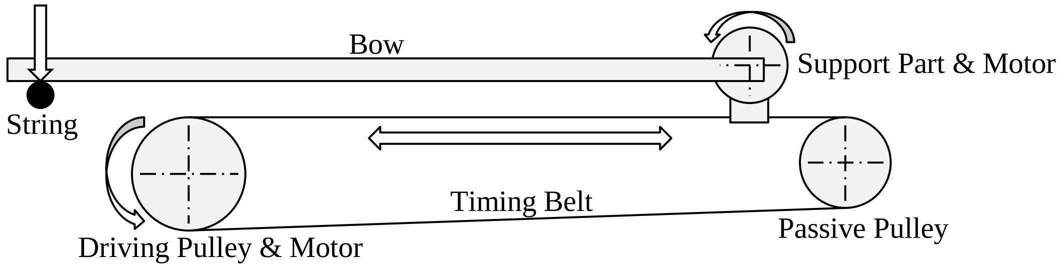

Figure 7. Image of Bow Linear Mover and Bow Presser.

4. Basic Experiments

To check the functions of the two sub-systems, we conducted some basic experiments as below.

4.1. *Detection and Prediction of Emit-Timing Experiment*

To evaluate the efficiency of machine learning that detects/predicts emit-timing of the player, we obtain time-charts of the player's relative displacement dy[px] and detected/predicted emit-timing.

First, we set three MLP Classifiers with one hidden layer of 1000, 2000 and 3000 neurons, activation function of relu and solver of adam.

Second, we made training data shown in figure 8 by detecting the emit-timing while tracking the motion of a player's face, just like shown in figure 4. In figure 8, the top line is relative displacement dy[px] of the player's face and the bottom line is the detected emit-timing.

Third, we let the MLP Classifiers learn the training data, that separated into the sets of 10 dy[px] and one emit-timing label as shown in figure 4. After that, did detecting and predicting of the emit-timing at same time.

The result is shown in figure 9, the order of the lines from the top is dy, detected emit-timing, predicted emit-timing using 1000, 2000 and 3000 neurons. By the result, it is shown that predicted emit-timing using 2000 and 3000 neurons are very close to detected emit-timing, in contrast to 1000 neurons that has a lot of errors.

Thus, we suggest that it is sufficient to predict the emit-timing by using MLP Classifier of 2000 or more neurons.

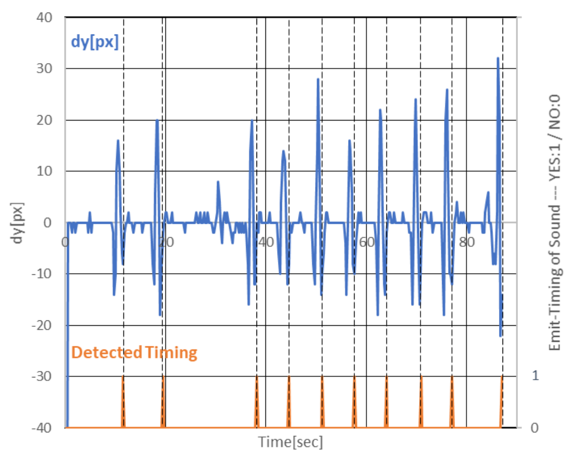

Figure 8. Time-Chart of Training Data.

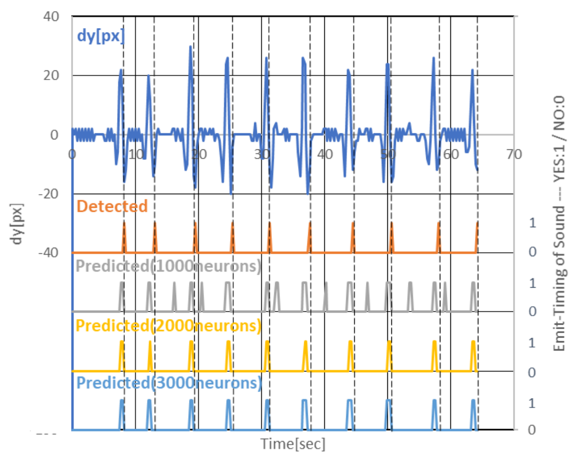

Figure 9. Time-Chart of Detected/Predicted Timing.

4.2. Torque Control Experiment

The motors that used in String tensioner, Bow Linear Mover and Bow Presser, can control and monitor their angle position, speed and torque by command them. To evaluate the controllability of them, especially torque, we conducted torque control experiment with the device shown in figure 10, consists of a electric scale “WeiHeng (Range: 0~10[kgf], Resolution: 5[gf])”, the motor “KeiganMotor KM-1S-M6829 (Max Torque: 0.5[Nm])” and a tape that connects the scale and the motor.

First, run the motor with stational torque command, and record the force that measured by the scale *P*[kgf] and the torque that monitored by the motor itself T_m[Nm]. We did this repeatedly changing torque command three rounds.

Second, compare T_m and *T*[Nm] that calculated as below.

$$T = \frac{D_m}{2} Pg \tag{6}$$

where D_m is outer diameter of the motor (approximately 0.0693[m]) and *g* is gravitational acceleration.

The result is shown in figure 11. If measured-torque T_m = calculated-torque *T*, it was ideal because that means the motor senses its torque correctly. However, there is gap around ±0.05[Nm] at most. This means the motor does NOT senses its torque correctly, that could make errors at pitch control of the String Tensioner. To evaluate this, PID controller described next section is considered to be needed.

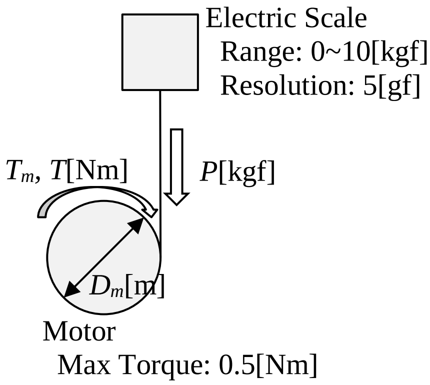

Figure 10. Torque Control Experiment Device.

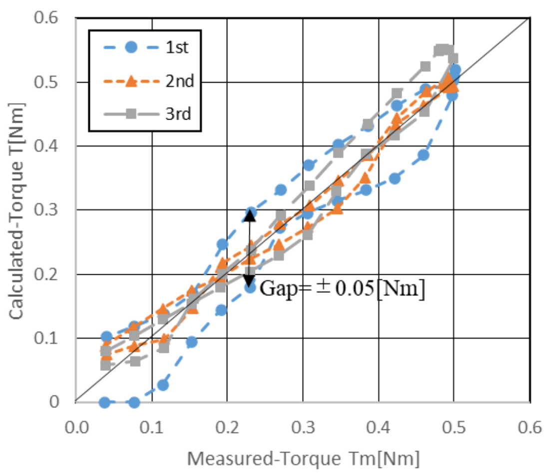

Figure 11. Measured-Torque and Calculated-Torque.

4.3. Pitch Control Using PID Controller Experiment

To evaluate the PID controller that compensate the pitch of String Tensioner, we gain time-charts of pitch and torque while Realtime Volume Pitch Control System performs. This time, we set PID gains K_p = 0.0001, K_i = 0.0001 and K_d = 0.0001.

First, input referenced-frequency/pitch f_{ref} = 250, 300, 350[Hz] to Realtime Volume Pitch Control System one by one and let the sub-system emit sound.

Second, detect the emitted-pitch *f*[Hz] of the sound and compare it with f_{ref}. Also compare the measured-torque T_m[Nm] with theoretical-torque T_{th}[Nm].

As a result, we obtained time-chart of pitch shown in figure 12. There are noises but still can be seen that emitted-pitch *f*[Hz] is controlled around f_{ref} = 300 and 350[Hz] with errors of just ±few Hz. However, there is large error where f_{ref} = 250[Hz], that could not be compensated. Also, we obtained time-chart of torque shown in figure 13. It can be seen that measured-torque T_m is changing continually, to compensate the pitch error between f_{ref} and *f*.

From this, it is shown that PID controller works but also needs more improvement. As its solution we suggest optimization of PID gains to make the controllability of the PID controller quicker and more accurate. However, increasing PID gains may cause divergence so that we must be careful about that.

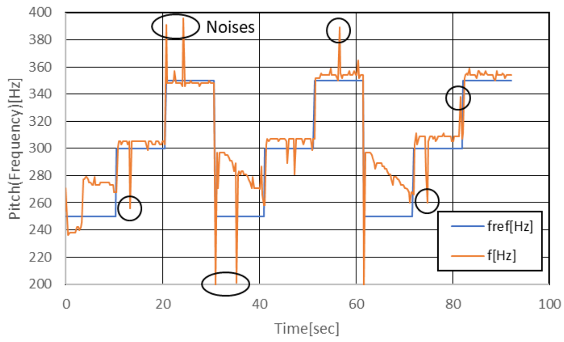

Figure 12. Time-Chart of Pitch.

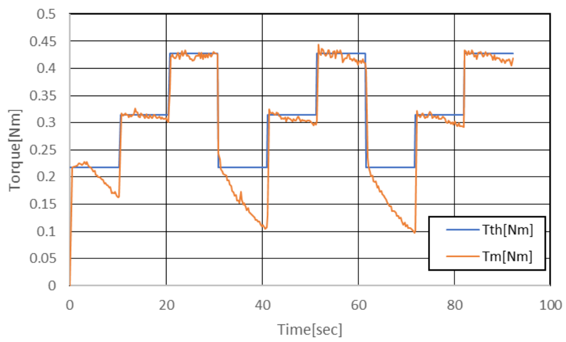

Figure 13. Time-Chart of Torque.

5. Summerly and Conclusion

We introduced concept and prototype of the Pure Intonation Ensemble System and conducted some basic experiments.

According to their results, they are indicated that detection/prediction of the player's emit-timing of sound by using video image from camera, audio input from mic and machine learning is attached to the sub-system, Player Movement Detection System. This function will help the sub-system to make proper accompaniment data better. Also, PID controller for pitch control is attached to another sub-system, Realtime Volume Pitch Control System. This will help the sub-system more accurate pitch control. However, this function needs improvements such as optimization of the PID controller.

A further direction of this study will be to improve these functions by attaching 3D TOF camera and acceleration/gyro sensors to gather more-detailed movement data of the player, training our machine learning by using professional player's performance data, combining two sub-systems to make one Pure Intonation Ensemble System and conducting some ensemble experiments.

Acknowledgments

This work was supported by JSPS Grants-in-Aid for Scientific Research Grant Number JP19K04300.

References

[1] Makoto K 1996 *Automatic or Robotic Stringed Instrument Player* Journal of The Robotic Society of Japan Vol 14 No 2 pp 168~171

[2] Akira M 2016 *Coupled Timing Model for Automatic Music Accompaniment* IPSJ SIG Technical Report Vol 2016-MUS-112 No 19

[3] Ryusuke I and Kazuteru T 2020 *Reserch about Cooperation of Human and Robot -Plan and Trial of Pure Intonation Ensemble System-* Proceedings of the 2019 JSME Conference on Robotics and Mechatronics 2A1-D02

[4] Klaus P, Jorge S and Atsuo T 2010 *Musical-based interaction system for the Waseda Flutist Robot* Auton Robot (2010) 28: 471–488

[5] Joao F. H, Rui C, Pedro M and Jorge B 2014 *High-Speed Tracking with Kernelized Correlation Filters* IEEE TPAMI vol.37 no 3 pp 583-596

[6] scikit-learn *https://scikit-learn.org/stable/modules/neural_networks_supervised.html* [Accessed Sep 8, 2020]

[7] Alok S 2014 *Vibration of Mechanical Systems* (Cambridge University Press) p 254

DRC0005

Self-Making of Wind Tunnel with Lowing Noise and Consideration of Aerodynamic Noise Generation Mechanism in Wind Tunnel Experiments

Hikaru Yamaguchi[1*], Yoshiki Sugawara[2], and Masakazu Takeda[2]

[1*] Aoyama Gakuin University Graduate School, 5-10-1, Fuchinobe, Chuo-ku, Sagamihara-shi, Kanagawa-ken, 252-5258, Japan
[2] Aoyama Gakuin University, 5-10-1, Fuchinobe, Chuo-ku, Sagamihara-shi, Kanagawa-ken, 252-5258, Japan

* Corresponding Author: c5620153@aoyama.jp

Abstract. This investigation indicates the details of a wind tunnel with lower noise and measurement of aerodynamic noise in wind tunnel experiments to consider its generation mechanism. Recent years, high speed running machines, for instance bullet train, aircraft, and so on, generate the sound which is called wind noise caused by air flows. This noise makes us uncomfortable and causes environmental problems. There are a lot of ways trying to reduce the noise but still haven`t established enough yet. Therefore, the small wind tunnel would be made to determine the aerodynamic noise and consider the generation mechanism. This study will help to find the new method of sound reduction system.

1. Introduction

Bullet train sounds are classified in collector system noise, upper part aerodynamic noise, lower part cars noise and concrete bridge structure noise, and one of the biggest contribution are collector system noise, especially the sound which is caused by the pantograph[1][2]. Also, the pantograph sound is divided into aerodynamic sound, rubbing sound and electric arc sound[3]. Focusing on the aerodynamic sound, the sound level increases in proportion to running speed to the six power[1]. It means that making the bullet train's speed faster, the noise will get bigger. Thus, the contribution of aerodynamic sound is high comparing to the others when the bullet train's speed is fast, and this noise makes us uncomfortable and causes environmental problems. Therefore, the method of sound reduction system must be created.

In previous works, they are indicated to make it possible to decrease sound with improving pantograph's configuration[4][5]. Furthermore, it is possible to reduce sound with controlling the running speed, though this will also decrease the transportation efficiency and causes a huge economic loss. Therefore, it is necessary to develop a drastic system of sound reduction for the pantograph. To establish the system, the details of aerodynamic noise generation mechanism which caused by air flows also have to be elucidated.

In general, regarding the method of wind tunnel experiment or measurement procedure of the aerodynamic sound, the dimensionless number such as Reynolds number or Strouhal number must usually be corresponded so that it is possible to estimate the sound of real machine from model experiment[6]. Moreover, it is clarified the significant influence if the Reynolds number of model goes below the critical Reynolds number($Re = 2 \times 10^5$) when the Reynolds number of real machine is surpassed by the critical Reynolds number. In addition, it is indicated that the background noise has to be 60~65 dB when the flow velocity of wind tunnel is 50 m/s, and the influence of pseudo-acoustic wave, indirect sound and reflected sound[7]. However, it is hard to manufacture such a high specification wind tunnel to achieve those items because it is expensive and necessary to have a big space to put the equipment. It is also difficult to eliminate the influence of difference with the dimensionless number using a versatile facility. Though, in case to examine the sound reduction system, it seems that the effect of reduction could be seen similar to the real from the result of model[6].

Therefore, this study focused on proposing a new aerodynamic sound reduction system. This investigation indicates the details of a wind tunnel with lowing noise and measurement of aerodynamic noise in wind tunnel experiments to consider its generation mechanism. In the general wind tunnel, blower has an influence on the acoustic measurement. Thus, this study verified to put silencer and sound absorbing material with the efficient place so that we could reduce the blower sound to level[8] which was able to measure acoustic. Also, some structures which imitating bullet train’s pantograph are made using 3D printer and aerodynamic noise generated from the structures is measured by wind tunnel experiments. Especially, insulator, collector shoe, and so on, the parts that constitute a pantograph, are researched for how they influence the sound generation. Furthermore, evaluating the sound pressure level and the result of FFT analysis which analyzed the acoustic wave, it aimed to consider the basic generation mechanism of aerodynamic noise.

2. Details of wind tunnel

2.1. Constitution of wind tunnel

In this study, author made a discharge-type compact wind tunnel with lower noise to measure the acoustic sound. Schematic chart is shown in figure 1. It composes of blower, silencer, diffusion barrel, rectification barrel, nozzle barrel and test section. Blower is a part to make the fluid field but it creates a turbulence. Diffusion barrel effects to make the flow slowly so that it can be rectified as it goes through to the rectification barrel. Nozzle barrel is able to increase the flow velocity which is rectified. The test section is a place to measure the acoustic sound.

Furthermore, the main sound source, blower should be reduced to make it possible of acoustic observation for the wind tunnel because the sound level was 95.7 dB. From this, discharge silencer and suction silencer were used to reduce the wind noise generated from blower to 82.8 dB. Also, sound insulating board which installed the sound absorbing material was used around blower to have a big effect of reduction (figure 2). From these effect, sound level was 76.0 dB and able to reduce the blower sound to level[8] which was able to measure acoustic.

For the acoustic observation, test section should be opened-anechoic room so that it can eliminate the reflected sound. In this study, a large board with sound absorbing material was used against to the nozzle barrel’s discharge opening.

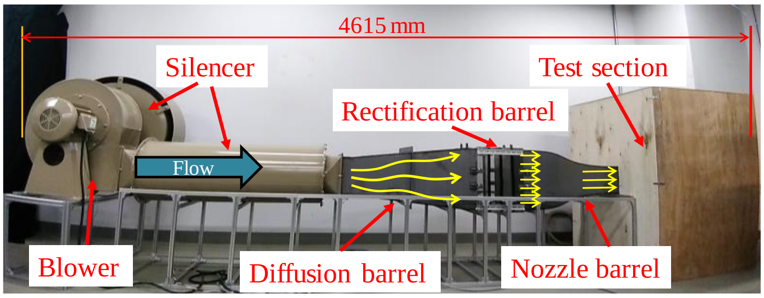

Figure 1. Constitution of wind tunnel.

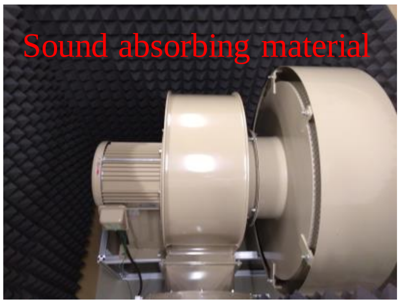

Figure 2. Blower.

2.2. Test section

In test section, velocity and aerodynamic sound would be measured. In case of acoustic observation, reflected sound must be taken off. Only covering the fluid field with a flat plate allows the noise that is produced from the test specimen to reflect to the plate and interfere with sound of generation and reflection. Therefore, a big veneer was covered compared to the air duct and specimen. Sound absorbing material was put it on inside and it will absorb and reduce the reflection sound from the wall. Figure 3 shows the internal of test section. The dimension would be $915\ \text{mm} \times 915\ \text{mm} \times 745\ \text{mm}$ and thickness would be 5 mm. Sound absorbing material would be urethane foam and configuration would be pyramid type.

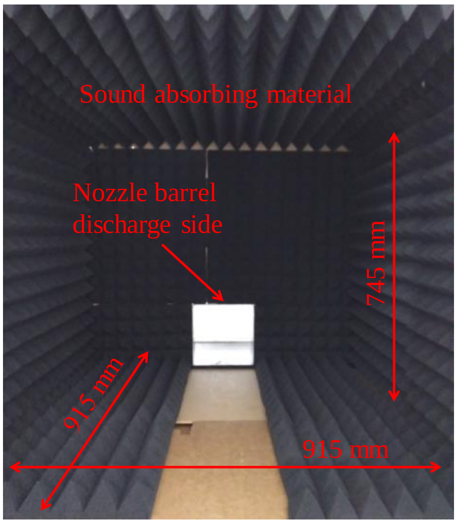

Figure 3. Test section.

3. Wind tunnel experiment

3.1. Model of pantograph

Schematic chart of test specimen is shown in figure 4. The test model was simulated with bullet train's single-arm type pantograph (PS208). In this study, it was made with 3D printer and size is a one-sixth scale of pantograph. The specimen composes of collector shoe, upper arm, lower arm and insulator. To consider the aerodynamic sound generation mechanism, the existence of collector shoe or differences of arm angle were researched.

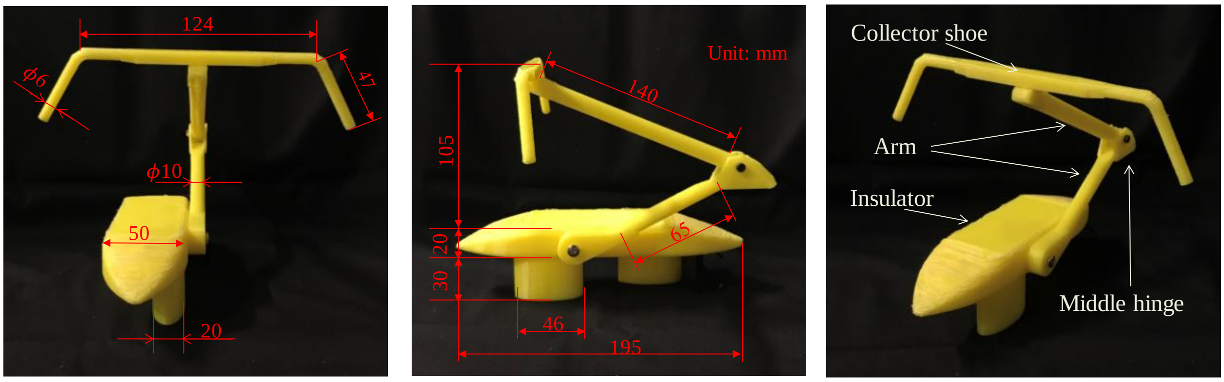

(a) Front view. (b) Side view. (c) Parts' name.

Figure 4. Model of single arm pantograph.

3.2. Experimental method

In this experiment, some holes were opened on the veneer's surface for putting the measuring instrument. The positional relation of test model, inlet of nozzle barrel and measuring points are shown in figure 5. The holes were opened every 100 mm, 5 points on the upper, 7 points on the side to make it possible of measuring some directions. The preliminary experiment was done, using some size of cylinders to research which holes were better to measure the acoustic. It is easy to calculate the theoretical value using the Strouhal number, and comparing with results, it helped to find which holes were excited stronger and measured accurately. From this result, it found suitable to put the measuring instrument in 11th hole. The condition of flow velocity was the maximum of U =32.7 m/s.

To consider the sound generation mechanism, sound pressure, level or frequency should be measured. Sound pressure is a fluctuation of atmospheric pressure which generated from the sound wave. Sound level is a quantified value of sound pressure. In this investigation, sound pressure[Pa] or sound level[dB] were measured by sound level meter (RION:NL-42)[9] shown in figure 6. Also, wave of pressure fluctuation was recorded and was analysed the FFT to evaluate the dominant frequency. The frequency weighting was A-weighting, the sampling frequency was 48000 Hz, the frequency resolving power was 2.390 Hz and the sampling time was 10 seconds.

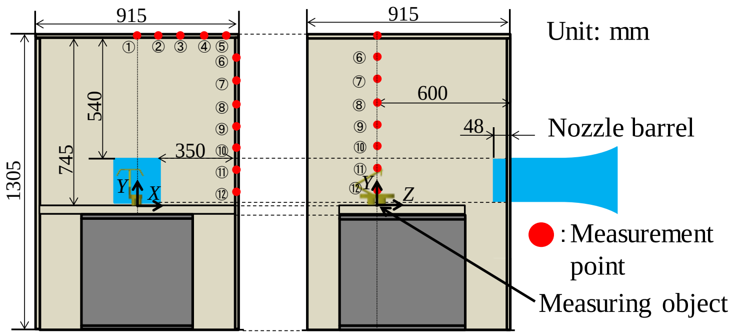

Figure 5. Measurement position.

Figure 6. Sound level meter.

4. Experimental results

Figure 7 shows the result of FFT analysis which was performed the experiment with only the insulator. At that time, the sound level was 84.0 dB. Figure 8, 9, 10 show the results of FFT analysis when arm angle θ_{arm} was 30°, 60°, 90° and the existence of collector shoe. (a) shows the result when the air flows bump to the front side and (b) shows the back side. Table 1 shows each condition's sound level. Also, the background sound was 82.2 dB.

In figure 7, frequency of 550~640 Hz was excited and this is guessed because of the leg part. Without that, there was no big difference between the background, so it could be said that influence of insulator is small.

From table 1, it could be said that the sound level decreases when collector shoe wasn't used. This will argue that collector shoe is one of biggest sound source. Also, back side is bigger than front side. It is thinkable that contribution of middle hinge is bigger than the front side because flow bumped to it first and made the slipstream disturbed when the condition was back side.

In figure 8 to 10, dominant frequency of almost 780, 860, 900 Hz was excited but it decreased when the collector shoe didn't exist. This indicates that these frequencies were caused by the collector shoe. Moreover, frequency of 580 Hz was excited and it seems that there is a relation between the frequency spectrum and the sound level because both are bigger when the air flows bump to the back side. Also, it is big when the arm angle was 60° and small when it was 30°. This result could be said that dominant frequency of 580 Hz is caused by the arm angle or middle hinge. Furthermore, frequency band of almost 550 to 650 Hz is narrowed when the arm angle gets smaller. It is thought that exposed surface area is large and make it easier to disturb the flow so the wide range of frequency band was excited. However, when the angle gets smaller, the surface area will also become smaller so the flow doesn't bump to arm very much and make less turbulence. This causes a narrow frequency band of exciting.

From this consideration, it could be said that collector shoe is one of the sound source and the noise was bigger when flow bumped to the back side but it would decrease when the arm angle was 30°.

Table 1. Measurement value of the sound level.

	Single arm pantograph		Without collector shoe	
	Front [dB]	Back [dB]	Front [dB]	Back [dB]
θ_{arm}=90°	85.5	85.6	84.9	85.3
θ_{arm}=60°	85.8	86.2	84.2	84.9
θ_{arm}=30°	84.8	85.0	83.9	84.1

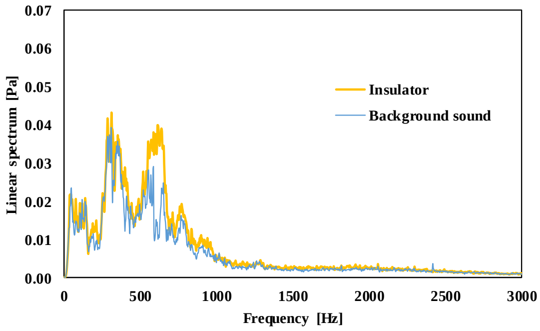

Figure 7. FFT analysis results of the insulator.

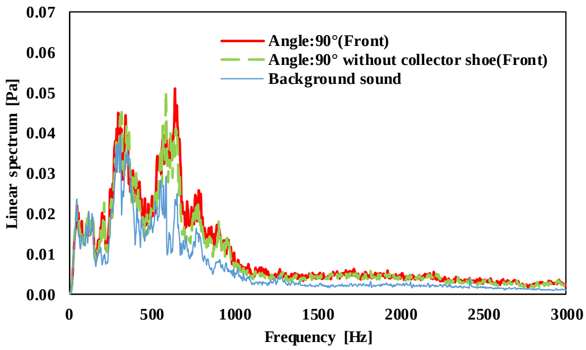

(a) Front side.

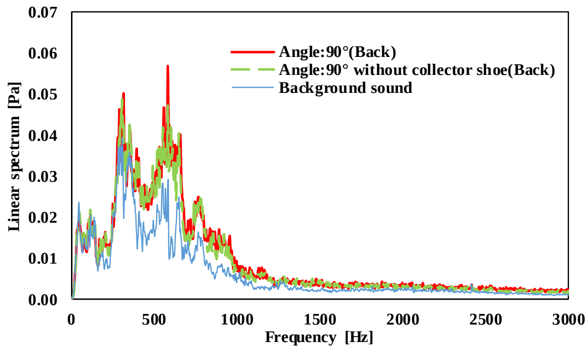

(b) Back side.

Figure 8. FFT analysis results when the arm angle is $\theta_{arm} = 90°$.

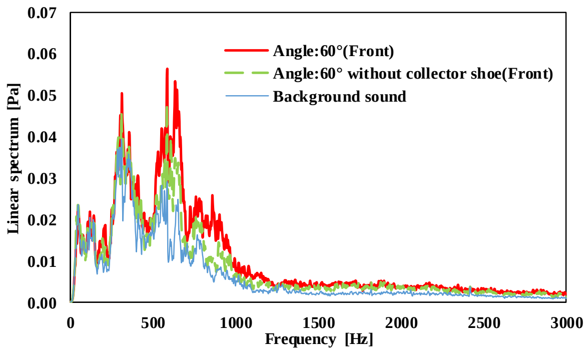

(a) Front side.

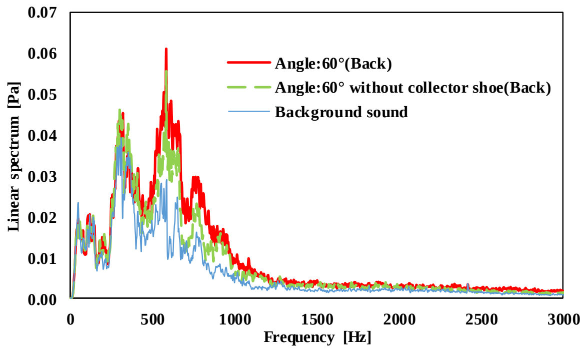

(b) Back side.

Figure 9. FFT analysis results when the arm angle is $\theta_{arm} = 60°$.

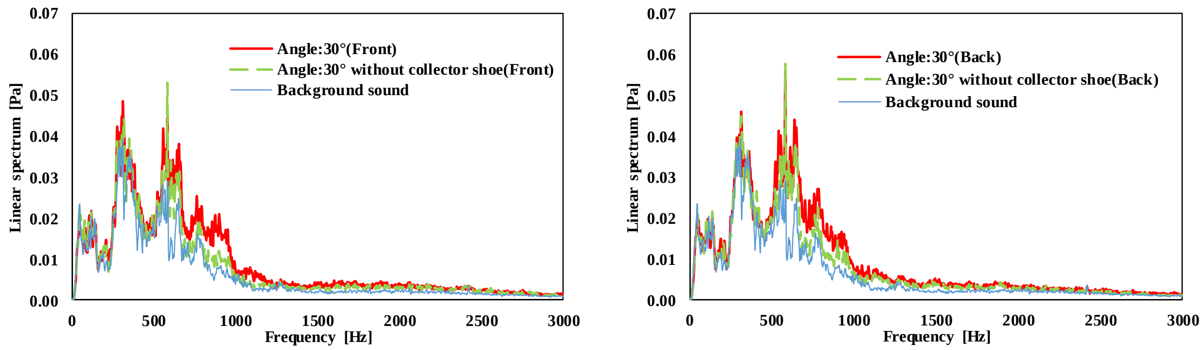

(a) Front side. (b) Back side.

Figure 10. FFT analysis results when the arm angle is $\theta_{arm} = 30°$.

Conclusion

In this study, a compact wind tunnel with lower noise which was able to measure the aeroacoustics was made. Also, the 3D printer which imitating the single-arm pantograph was measured of aerodynamic noise. Especially, the sound generation mechanism and the differences of frequency spectrum was considered when arm angle changed and collector shoe existed or not.

In future's issue, it is necessary to use the numerical simulation and compare with experimental result to help to consider the mechanism. Furthermore, a new sound reduction system should propose and establish from those results.

References

[1] Toshiki KITAGAWA, Kiyoshi NAGAKURA, Takeshi KURITA 2012 "The Noise Generated from the Lower Part of Shinkansen Cars Running at High-Speed" *Journal of Environment and Engineering* vol.7 no.1 pp.66-75

[2] Takeshi KURITA, Yuusuke WAKABAYASHI, Haruo YAMADA, Masahiko HORIUCHI 2011 "Reduction of Wayside Noise from Shinkansen High-Speed Trains" *Journal of Mechanical Systems for Transportation and Logistics* vol.4 no.1 pp.1-12

[3] Kiyoshi NAGAKURA 2008 "Present situation and future prospects of railway noise problem" *The Acoustical Society of Japan* vol.64 no.10 pp.624-628 (in Japanese)

[4] Takeshi SUEKI, Mitsuru IKEDA, Takehisa TAKAHASHI, Takeshi KURITA, Haruo YAMADA 2010 "Reduction of aerodynamic noise from high-speed pantograph using porous materials" *Journal of Environment and Engineering* vol. 5 no.3 pp.469-484

[5] Kaoru MURATA, Takeshi KURITA 2003 "Countermeasures for Aeroacoustic Noise from Pantographs" *The Institute of Noise Control Engineering of Japan* vol.27 no.5 pp.337-342 (in Japanese)

[6] Akiyoshi IIDA 2007 "Similarity of scale model experiments on aeroacoustics" *The Acoustical Society of Japan* vol.63 no.9 pp.549-554 (in Japanese)

[7] Akiyoshi IIDA 2003 "Aeroacoustic measurements" *The Acoustical Society of Japan* vol.59 no.9 pp.282-287 (in Japanese)

[8] Hajime FUJITA 2002 "Low Noise Wind Tunnel" *Journal of Japan Society of Fluid Mechanics [Nagare]* vol.21 no.5 pp.394-399 (in Japanese)

[9] Kazuo SHIBATA, Yukihito ISEKI 2011 "Correct operation and usage of sound level meter" *The Acoustical Society of Japan* vol.67 no.12 pp.576-581 (in Japanese)

[10] Ichiro YAMADA, Kyouji YOSHIKAWA 1999 "Suggestions for noise measurement using sound level meters" *The Acoustical Society of Japan* vol.55 no.5 pp.382-385 (in Japanese)

DRC0006

Study of Passive Damping Systems Using Giant Magnetostrictive Materials by Collision Mechanism

Hiroki Kudo[1,*], Yoshiki Sugawara[2], and Masakazu Takeda[2]

[1]Aoyama Gakuin University Graduate School, 5-10-1, Fuchinobe, Chuo-ku, Sagamihara-shi, Kanagawa-ken, 252-5258, Japan
[2]Aoyama Gakuin University, 5-10-1, Fuchinobe, Chuo-ku, Sagamihara-shi, Kanagawa-ken, 252-5258, Japan

* Corresponding Author: c5620137@aoyama.jp

Abstract. A passive damping system using giant magnetostrictive materials (GMM) converts mechanical energy of vibration into thermal energy by Villari effect of the GMM, electromagnetic induction of a coil and Joule heat of a resistor. The system's vibration control performance is better as the deformation speed of GMM becomes faster. However, natural frequency of a flexible structure is usually low. In this research, the paper proposed a passive damping system with collision mechanism to convert vibration frequency from low into high so as to improve control performance. A numerical analysis model using finite element method is constructed to demonstrate the damping effect of the proposed system. Moreover, an experimental equipment is built to evaluate the validity of the proposed method. The results of the numerical analysis and the experiment show that high frequency vibration is excited by the collision mechanism. Furthermore, the numerical analysis results show damping effect of the proposed method. The experimental results reveal necessity for further improvement in damping effect.

1. Introduction

In recent years, a spacecraft is increasing in size and lightening caused by advancement of missions and a limitation on load of a rocket. As a result, a development structure is employed, and a flexible structure that is low rigidity come to be used. However, there is a possibility of various problems such as a bad influence on control because the flexible structure is easy to vibrate. In outer space, passive damping systems are desirable because of a limitation on energy supply.

There are methods that piezoelectric materials, which are smart materials, are used as passive damping systems. N. W, Hagood et al. [1] did research that is used piezoelectric materials and RL circuits as damping systems. However, there is a problem in practically because a large-scale inductor is required for efficient damping. Therefore, this study focuses on giant magnetostrictive materials (GMM) that can transform mechanical energy into electrical energy as well as piezoelectric materials. The GMM is better than the piezoelectric material in term of energy density and electromechanical coupling.

As previous studies, Ralph C. Fenn et al. [2] studied about passive damping systems using properties of GMMs. After that, Hatakeyama et al. [3] conducted a study to apply the passive damping systems using GMMs to flexible structures. In that study, Hatakeyama et al. proposed passive damping systems that are used spacers to vibrate the GMM. Furthermore, Syoji et al. [4] optimized parameters in the passive damping systems that are used for flexible structures for efficient vibration control performance based on the study of Hatakeyama et al. Although the system's vibration control performance is better as the deformation speed of GMM becomes faster, the speed depends on low frequency vibrations of a flexible structure in previous studies. Accordingly, the vibration control performance is low. Hence, it is possible to improve the control performance by exciting high frequency vibrations in the GMM.

In this research, the paper proposed a passive damping system with collision mechanism to convert vibration frequency from low into high so as to improve control performance. Numerical analysis demonstrates the damping effect of the proposed system. Moreover, an experimental equipment is built to evaluate the validity of the proposed method.

2. Proposed Method

In this research, Villari effect of the GMM is used for passive damping systems. When a coil is wound around the GMM, magnetic flux in the coil is changed by Villari effect. After that, voltage is generated by electromagnetic induction. It is possible to dissipate the generated electrical energy as Joule heat when a resistor is connected to the coil. Therefore, vibration is damped passively because the GMM converts mechanical energy of vibration into electrical energy and the electrical energy is dissipated as thermal energy. When magnetostrictive property of GMM is used in linear range [5], the thermal energy P_m that is generated in a resistor by voltage which is generated from the passive damping system can be expressed as

$$P_m = \frac{1}{2}\frac{N_m^2 A_m^2 R}{R^2 + R_w^2 + \left(L\omega\right)^2}\left(\frac{d^*}{s^H l_m}\right)^2 \dot{z}^2 \tag{1}$$

where N_m is number of coil turns, A_m is cross section of the GMM, R is resistance value of the resistor, R_w is internal resistance, L is self-inductance, ω is angular frequency of the vibration, s^H is elastic compliance of the GMM, l_m is length of the GMM, d^* is magnetostriction constant, and z is deformation of the GMM.

The thermal energy is proportional to the square of the deformation velocity of the GMM. Therefore, equation (1) indicates that the system's vibration control performance is better as the deformation velocity of the GMM becomes faster. This paper proposes a collision mechanism to convert vibration frequency from low into high. Impulse is added to the GMM by using collision mechanism, and high frequency free vibration occurs in the GMM to axial direction. Spacers are used as collision mechanism for a flexible structure.

3. An Analysis Model and Numerical Analysis

3.1. A model using finite element method

An object of the model is shown in Figure 1. The flexible structure that is the target of control is assumed as a cantilever. Passive damping units using GMMs are fixed on both side of the cantilever by spacers.

When spacers move associated with vibration of the beam, spacers collide with passive damping units. The cantilever, spacers, and GMMs are modeled using finite element method. The cantilever and spacers are assumed as linear beam elements that are deformable in bending and axial directions [6]. GMMs are assumed as elastic bodies that are deformable in axial direction [7]. Moreover, gravity acceleration, air resistance, and internal viscous damping are ignored. A whole model is shown in Figure 2 where i is number of elements of the cantilever and j is number of elements of spacers.

Spacers are connected vertically to the cantilever and GMMs are connected to the end of spacers. GMMs and the end of spacers are assumed to collide. A collision model is explained later.

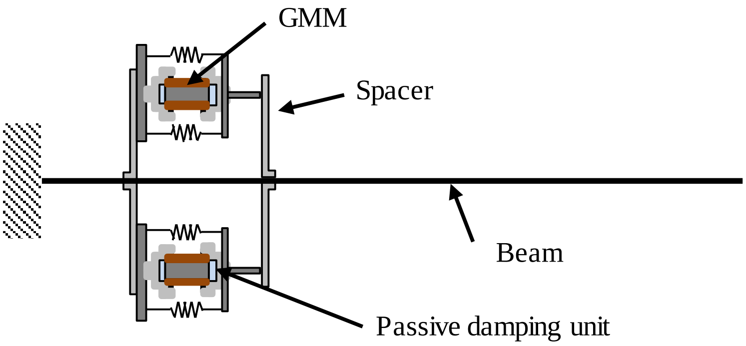

Figure 1. Target of model.

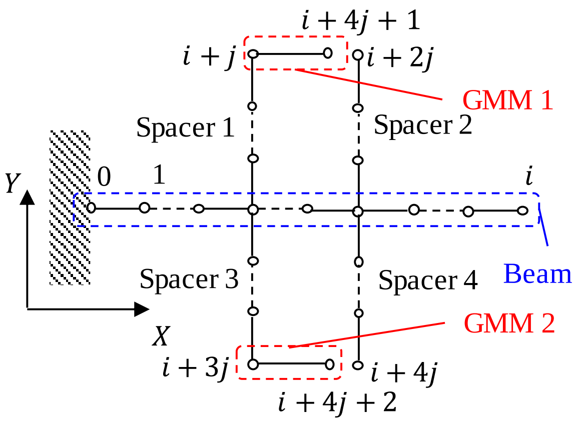

Figure 2. FEM model of a beam, spacers, and GMMs.

3.2. Derivation of equation of motion

Generalized coordinates to express the equation of motion can be expressed as

$$\mathbf{q} = [\mathbf{q_e} \quad \mathbf{q_m}]^T \tag{2}$$

$$\mathbf{q_e} = [u_n \quad v_n \quad \theta_n]^T \tag{3}$$

$$\mathbf{q_m} = [z_1 \quad z_2]^T \tag{4}$$

where $\mathbf{q_e}$ is nodal coordinate vector of beam elements in finite element method, u_n is deformation of axial direction of n-th node, v_n is deformation of bending direction, θ_n is deflection angle, $\mathbf{q_m}$ is vector about deformations of GMMs, and z_1 and z_2 are displacement of the tip of GMMs.

The equation of motion shown equation (5) is derived using Lagrange equations after deriving kinetic energy of the cantilever, spacers, and GMMs, potential energy of the cantilever, spacers, GMMs, and prestress springs, and dissipation energy of passive damping units.

$$\mathbf{M\ddot{q}} + \mathbf{C\dot{q}} + \mathbf{Kq} = \mathbf{F} \tag{5}$$

M is mass matrix, **C** is damping matrix, **K** is stiffness matrix, and **F** is external forces.

3.3. A collision model using the equation of motion

This paper proposed a simplified model that simulates collision because collision of flexible bodies is complicated. A model of passive damping unit to simulate collision is shown in Figure 3 where m_m is a mass that is added to the GMM and m_s is a mass that is added to the spacer. First, masses are added to spacers and GMMs in the FEM model. The collision is assumed to occur when a distance between a spacer that hold the GMM and a spacer that collides with the GMM becomes less than a certain amount. Change in momentum before and after the collision is calculated using the masses and velocity before and after the collision as collision of point mass. A fact that the change in momentum is equal to impulse is used. A force given by a step time can be calculated by dividing the change in momentum by the step time. The simulation of collision is completed by applying the forces at the tip of the spacer and the GMM to the external forces term in the equation of motion.

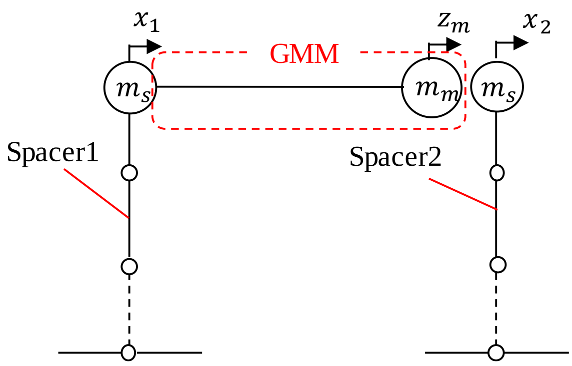

Figure 3. Model of collision.

3.4. Numerical analysis results

Parameters of numerical analysis is shown in Table 1. Material of the beam is A6063, material of the spacers is A5052, and the GMM is Terfenol-D. A result of Fast Fourier Transform analysis of time history response of the GMM's deformation is shown in Figure 4. Figure 4 indicates that high frequency vibrations are included because a peak in amplitude is seen in high frequency. Therefore, it suggests that collision mechanism works because vibrations of high frequency is generated in the GMM. Displacement of the beam in bending direction id shown in Figure 5. In Figure 5, "inf" refers to a case without resisters. Power spectral density is calculated for Figure 5. Peak energy of primary mode decreased by 10.7%. Then, damping effect is confirmed.

The proposed model is used in this numerical analysis. However, it is not clear whether the proposed collision model adequately represents the phenomenon of collision or not. Therefore, it is necessary to validate the model of collision as a future task.

Table 1. Parameters of simulation.

Diameter (GMM)	6mm	Width (Spacer)	16 mm	Coefficient of restitution	0.3
Length (GMM)	25 mm	Length (Spacer)	40 mm	Additional mass (GMM)	0.0065 kg
Width (Beam)	30 mm	Thickness (Spacer)	4 mm	Additional mass (Spacer)	0.0073 kg
Length (Beam)	500 mm	Spring constant	0.103 N/mm	Moment of inertia (Spacer)	3.61×10^{-6} kg/m^2
Thickness (Beam)	2 mm	Coil turns	200 Turns	Distance between tips of spacers on collision	99 mm

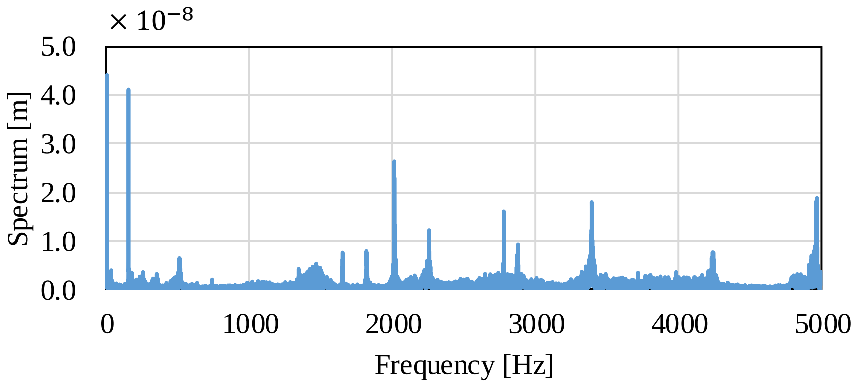

Figure 4. An FFT analysis result of GMM.

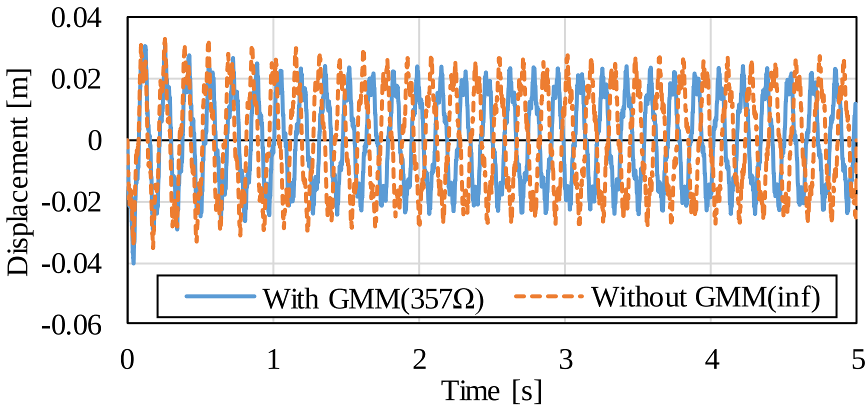

Figure 5. Bending deformation of the beam (simulation).

4. Verification experiment

4.1. Purposes of experiment

This verification experiments focus on two point. The first is to verify whether low frequency vibration of a flexible structure is converted into high frequency voltage by using the collision mechanism. The second is to verify whether the passive damping system using the collision mechanism can damp the flexible structure that is target of control. The purpose of the experiments is to evaluate the passive damping system using GMMs and the collision mechanism by result of the experiments. In the verification experiments, free vibration experiments are conducted assuming that the free vibration is generated in a flexible structure due to external disturbances.

4.2. Experimental equipment

An overview of the experimental equipment is shown in Figure 6. Furthermore, mechanism of the passive damping unit in the experimental equipment is shown in Figure 7. The experimental equipment consists of passive damping units, a beam, a laser displacement sensor, resistors, and a string. Two passive damping units are fixed on both sides of the beam for efficient damping like as the analytical model. Magnets and springs are incorporated into the passive damping units to use the GMMs to extent that properties of GMM exhibit linearity. Because of experimental purposes, time history of displacement in bending direction of the beam is obtained using the laser displacement sensor and time history of generated voltage is obtained using an oscilloscope.

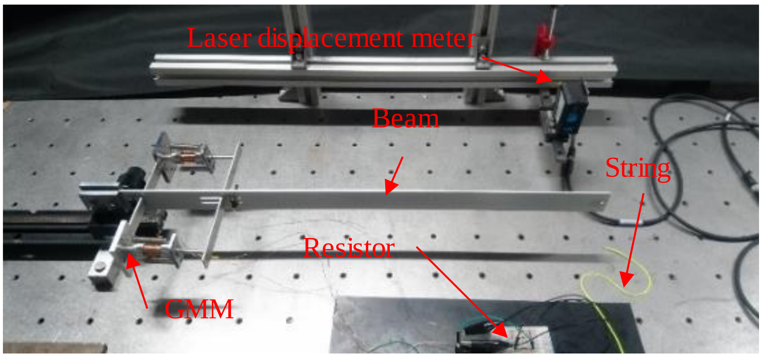

Figure 6. Experimental equipment.

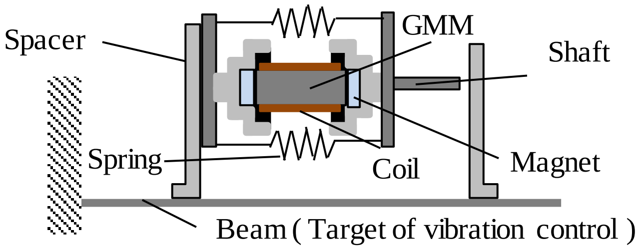

Figure 7. Passive damping unit.

4.3. Results of experiments

Experimental conditions are same as the condition of numerical analysis. A time history of generated voltage by the GMM using the oscilloscope is shown in Figure 8. A result of FFT analysis to Figure 8 indicates dominant frequency of the generated voltage is about 8330 Hz. On the other hand, dominant frequency of vibration in bending direction of the beam is about 8.36 Hz. It is thought that the voltage is generated by electromagnetic induction that caused by high frequency vibration excited in the GMM by the collision. Therefore, it is shown experimentally that the proposed method can excite high frequency in the GMMs. A time history of displacement in bending direction at the tip of the beam obtained by the laser displacement sensor is shown in Figure 9. Damping ratio derived using logarithmic decrement is 0.00969 when the passive damping function using the GMMs is enabled and 0.0101 when it is not. There is no significant difference in damping effect due to the GMMs, and this is a future task. It is thought that the causes are low rigidity of the spacers and dominance of internal damping and damping caused by collision.

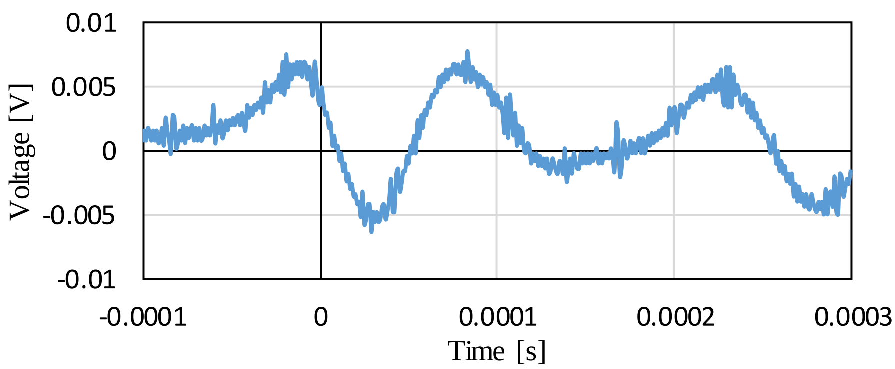

Figure 8. Voltage generated by the GMM.

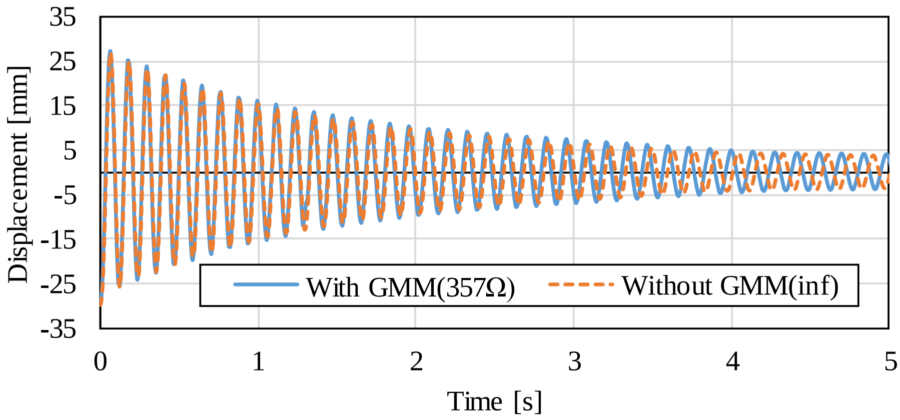

Figure 9. Bending deformation of the beam (experiment).

Conclusion

This paper proposes a passive damping system using a collision mechanism that can excite high frequency vibration on GMMs to improve damping performance. The passive damping system that is incorporated in target of vibration control is modeled using finite element method, and a model that simulates a collision is proposed. Damping by GMMs is confirmed from results of numerical analysis. Experiments that free vibration is excited on a beam are conducted and obtain time history of generated voltage and displacement of the tip of the beam. Generation of high frequency voltage is confirmed from result of the experiment. Future tasks include reviewing and modifying the numerical analysis method and improving the experimental equipment to improve the damping effect.

References

[1] N. W. Hagood, Knapp, and A. V. Flotow 1991 "Damping of structure vibration with piezoelectric materials and passive electrical networks" *Journal of Sound and vibration.* Vol 146 No. 2 pp 243-268

[2] Ralph C. Fenn and Michael J. Gercver 1994 "Passive damping and velocity sensing using magnetostrictive transduction" *Proceeding of SPIE 2190, Smart Structures and Materials 1994: Smart Structures and Intelligent Systems* pp 216-227

[3] Shu HATAKEYAMA and Yoshiki SUGAWARA 2015 "Passive control for flexible structure using magnetostrictive material" *JSME Dynamics, Measurement and Control Division Proceedings of Dynamics & Design Conference 2015* No. 703 (in Japanese)

[4] Syoji IORI, Syoya KINOSHITA, Yoshiki SUGAWARA, and Kiyoko SAKAMA 2017 "Optimization of Vibration Absorber Using Giant Magnetostrictive Material for Flexible Structure" *Proceeding of The Society of Instrument and Control Engineers System Integration Division Conference 2017 (SI2017)* No. 1C4-09 (in Japanese)

[5] F. Braghin, S. Cinquemani, F. Resta 2011 "A model of magnetostrictive actuators for active vibration control" *Sensors and actuators A: Physical* vol 165 pp 342-350

[6] Nobuyuki KOBAYASHI, Hiroyuki SUGIYAMA 2008 "Vibration engineering using Matlab from basics to multibody dynamics" Tokyo Denki University Press pp 183-199 (in Japanese)

[7] Singiresu S. Rao 2004 "Mechanical Vibration Fourth Edition" Pearson Prentice Hall pp 858-860

DRC0007

A Behavior Analysis of a Flexible Payload Constrained to Trajectory using Feedforward Anti-Sway Control Method

Masaki Uehara[1,*], Sotaro Furuta[1], Yoshiki Sugawara[1], and Masakazu Takeda[1]

[1]Aoyama Gakuin University, 5-10-1, Fuchinobe, Chuo-ku, Sagamihara-shi, Kanagawa-ken, 252-5258, Japan

* c5619113@aoyama.jp

Abstract. A fusion power generation is being advanced to the engineering design stage in order to secure safe and stable next energy. It is essential to develop maintenance technology in the reactor for continuous operation. The environment inside the reactor damages internal components. However, in the helical fusion reactor dealt with in this research, no effective method for maintenance has been established. In the helical type, a spiral coil is used for the internal structure, which results in very severe structural constraints and is a major obstacle to the maintenance systems. Considering this structure, CARDISTRY-B2 is currently proposed to replace the internal parts. Due to structural restrictions, it is necessary to perform replacement work using an overhead crane while control vibration and interference with other parts. This research is studying feedforward anti-sway control method that is constrained to the target trajectory by combining input shaping and nonlinear optimization calculation. Furthermore, the payload has this structure, then the deterioration of control performance is expected due to the influence of shape and flexibility. Therefore, the influence of the deterioration should be evaluated for efficient maintenance operation. The control method is applied to the two-dimensional payload with two-point suspension, the influence of the control when the payload is flexible body is confirmed, and the control system is examined. Numerical analysis showed that the control objective of a two-point suspension is feasible. In addition, numerical analysis demonstrated the validity of applying the control method to the system with flexibility.

1. Introduction

Nuclear fusion generation is being advanced to the engineering design stage to secure safe and stable next-generation energy. Maintenance and maintenance technology in the reactor are indispensable to realize continuous fusion power generation. It is necessary to confine the substance in the reactor at a high temperature and high density for a certain period to cause a fusion reaction. It is known that the inside of the operating furnace is in an extreme environment such as strong radiation, high vacuum, strong magnetic field, and high-temperature environment. This environment is not desirable for mechanical systems and damages internal components. The helical fusion reactor treated in this research is a method of forming a confined magnetic field of plasma by using a spiral coil.

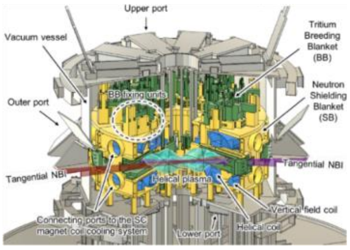

Figure 1. Schematic view of the CARDISTRY-B2 [1]

Considering this complicated structure, CARDISTRY-B2 [1] for replacing the internal parts shown in Figure 1 have been proposed. This realizes replacement by an overhead crane from a structurally limited maintenance port by dividing the replacement part into multiple parts. Due to structural constraints, when replacing parts, it is possible to avoid interference with other parts and to perform work that involves withdrawal and insertion. For that purpose, it is necessary to control the vibration in addition to restraining the rope length and the crane truck to the target track. In the extreme environment of the reactor, the sensor for obtaining the state quantity may be damaged, leading to a decrease in the reliability of the entire system. Therefore, we consider using Input Shaping [2], which is a feed-forward type compensator, for the steady rest control of the crane. Various studies have been conducted on the simultaneous operation of rope length and bogie position [3-5], but none of them deal independently with the trajectory planning problem and the vibration suppression problem of suspended objects. In the previous research, open-loop steady rest control [6] of the suspended object constrained to the target trajectory is performed by combining Input Shaping and nonlinear optimization calculation. Furthermore, since the replacement parts are of thin plate structure, the control performance is expected to deteriorate due to the shape and flexibility. In this study, we verify a two-point suspended rigid object to handle extraction and insertion using this control method, confirm the influence on the control when considering flexibility and examine the control system.

2. Formulation of 2-point suspension model

This section describes a method for handling the pulling and inserting of suspended objects. The suspended object is a quadrangle with mass m and moment of inertia *I*, and various parameters are set as shown in Figure 2(a). Rope mass and deformation can be ignored. If the rope length and the bogie position can be arbitrarily determined and, $\ddot{L}_1$, $\ddot{L}_2$, $\ddot{x}_u$is treated as a time-varying parameter, the following nonlinear state equation can be obtained with the state quantity being $\mathbf{x} = [\theta \quad \dot{\theta} \quad L_1 \quad \dot{L}_1 \quad L_2 \quad \dot{L}_2 \quad x_u \quad \dot{x}_u]^{\mathrm{T}}$.

$$\dot{\mathbf{x}} = \mathbf{f}\left(\mathbf{x}, \ddot{L}_1, \ddot{L}_2, \ddot{x}_u\right) \tag{1}$$

Input Shaping design requires an approximation to a linear time-varying system, and it has been reported [3] that the conventional two-point suspension container crane model can be approximated to the rigid pendulum model shown in Figure 2(b). In this research, we apply this method and express a linear time-varying system using an approximate model. Under the assumption that the swing angle is always controlled minutely, it is assumed that the left and right rope lengths can always be considered equal, and the following relationship is assumed.

$$L = (L_1 + L_2)/2 \tag{2}$$

From these conditions, the following equation is obtained as the correlation in Figures 2(a) and 2(b).

$$\theta = -\phi + \sin^{-1}\left(\frac{d}{w}\sin\phi\right) \tag{3}$$

$$l = \sqrt{L^2 - d^2 - w^2 + 2dw\cos\theta} \tag{4}$$

Therefore, the following equation is obtained by deriving the equation of motion using the Euler–Lagrange equation and then linearizing it assuming that ϕ is a small angle.

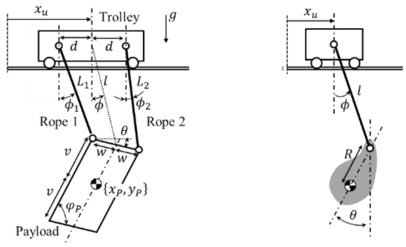

(a) 2-point suspended (b) Rigid pendulum

Figure 2. Crane model approximation.

However, since the suspended object is rectangular, it is assumed that $R = v$.

$$\ddot{\phi} + 2\mu\dot{\phi} + \omega^2\phi + \frac{\mu}{\dot{L}}\ddot{x}_u = 0 \tag{5}$$

Here,

$$\begin{aligned} \omega &= \sqrt{\frac{g(L + \bar{a}^2 R) - \bar{a}\dfrac{dR\ddot{L}}{w}}{L^2 - 2\bar{a}RL + \bar{a}^2\left(\dfrac{I}{m} + R^2\right)}} \\ \mu &= \frac{\dot{L}(L - \bar{a}^2 R)}{L^2 - 2\bar{a}RL + \bar{a}^2\left(\dfrac{I}{m} + R^2\right)} \\ \bar{a} &= \frac{d - w}{w} \end{aligned} \tag{6}$$

This model can be expressed as a general linear time-varying system if the rope length change profile is given in advance.

$$\dot{\bar{\mathbf{x}}} = \mathbf{A}(t)\bar{\mathbf{x}}(t) + \mathbf{b}(t)\bar{u}(t) \tag{7}$$

Here, the state quantity $\bar{\mathbf{x}}$, the input $\bar{u}$, the matrix $\mathbf{A}$, and the vector $\mathbf{b}$ are as follows.

$$\begin{aligned} \bar{\mathbf{x}} &= \begin{bmatrix} \phi \\ \dot{\phi} \end{bmatrix} \\ \bar{u} &= \ddot{x}_u \\ \mathbf{A}(t) &= \begin{bmatrix} 0 & 1 \\ -\omega^2 & -2\mu \end{bmatrix} \\ \mathbf{b}(t) &= \begin{bmatrix} 0 \\ -\mu/\dot{L} \end{bmatrix} \end{aligned} \tag{8}$$

This model holds only if the left and right rope lengths are always the same. If this condition can be eliminated, a wider range of problem settings can be dealt with, such as operating the suspended object at an angle.

3. Control method

3.1. Input Shaping damping principle

In a general mechanical system, when a feedback control system for velocity and position is designed the input profile to achieve the designed control law is given by the host controller. Input shaping shapes the input profile in an open loop so as to implement a vibration isolation effect. We consider the combination of impulse inputs so that the response of the system become zero, and finally, realize the operation without residual vibration. It is possible to prevent the occurrence of residual vibration by inputting a secondary impulse to the impulse response of an undamped linear time-invariant system when half of its natural period has elapsed. Also, by normalizing the integral value of the impulse group to be 1 and calculating the composite product with arbitrary inputs, it is possible to obtain input with a vibration isolation effect. In this way, the anti-swing effect is obtained by delaying the input time and determining the delay time. In this research, Lee's method [6] is applied as a shaping method for linear time-varying systems. In this method, the solution of the linear time-varying system is represented by the state transition matrix $\boldsymbol{\phi}$, the left eigenvalue matrix $\mathbf{U}(T)$ for $\mathbf{A}(T)$ is introduced, and the modal response $\boldsymbol{\eta}(T)$ is derived as,

$$\boldsymbol{\eta}(T) = \mathbf{U}^{\mathrm{T}}(T)\boldsymbol{\phi}(T, t_1)\mathbf{b}(t_1) + \mathbf{U}^{\mathrm{T}}(T)\boldsymbol{\phi}(T, t_2)\mathbf{b}(t_2)\alpha(t_2) \tag{9}$$

The vibration isolation effect can be added by determining the time t_2 and magnitude of the secondary impulse input α that satisfies this equation and taking the composite product with the arbitrary input. For details, refer to Reference [6].

3.2. Restraining the suspended target trajectory

The purpose of control in this research is to move the whole system from stationary to stationary and follow the target trajectory by using Input Shaping for feedforward input. In this study, we assume a linear trajectory $aP_x + bP_y + c$ as the target trajectory. The suspended object trajectory does not always satisfy an arbitrary desired trajectory because the suspended object trajectory depends on the profile of bogie acceleration and rope length change even if a trajectory with an anti-swing effect is generated by this method. It is necessary that the center of gravity of the suspended object satisfies the target trajectory and that the swing angle of the suspended object is always kept at zero to handle the problem of pulling out and inserting the suspended object. Since it is difficult to find the solution of the constraint equation under this condition, the deviation from the target trajectory of the center of gravity is set as the evaluation function and the input profile that satisfies the target trajectory is obtained using the nonlinear optimization method. Therefore, the evaluation function is defined as shown below.

$$J = \frac{1}{2}\int_0^{t_f} \left\{\theta^2 + \left(ax_p + by_p + c\right)^2\right\} dt \tag{10}$$

It is difficult to design the Input Shaper and solve the optimization problem simultaneously. Therefore, a truck acceleration input and rope length variation profile that satisfies both Input Shaping and track constraint is derived by ignoring the influence of the rope length change and speed on the truck acceleration input by repeating the optimization calculation and shaping process. Figure 3 shows the concept. The steepest descent method is used for the optimization algorithm, and the optimization variable is the rope length variation profile. Even if a profile that satisfies the target trajectory is obtained by the optimization calculation, residual vibration occurs because it is difficult to implement the design procedure of the Input Shaping in the optimization calculation. However, the trajectory obtained when reshaping is performed using this rope length variation profile generally does not significantly affect the dynamics of the system. Therefore, the orbit after reshaping is closer to the target orbit than the orbit by the first shaping, and the residual vibration is suppressed. By this, it is thought that the orbits will converge. For details, refer to Reference [7].

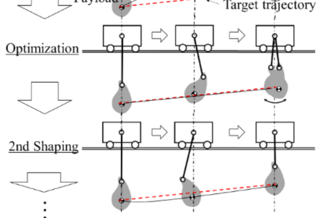

Figure 3. Trajectory constraint calculation.

4. Analysis result

The two-point suspension model in Section 2 is targeted, and the results of numerical analysis using the trajectory constraint algorithm described in Section 3 are compared with the conventional method [6] described in Section 3.1. The analysis time is 20 s, the step size is 0.01s, the travel distance is 8 m, and the rope length changes linearly from 10m to 9m. As the model parameters, the mass of suspended object is 100 kg, the height is 2 m, the width is 0.4 m, and the distance between the rope fulcrums is 1 m. Figure 4 is a comparative diagram regarding the position of the bogie. The convergence time of the trolley movement due to the input after shaping is extended, and the difference due to the shaping method is small. This is due to the extension of input time inherent to Input Shaping, not the trajectory constraint. Also, the drifts of the truck in the steady state is due to the error in the integral calculation. Figure 5 shows the variation of rope length. Due to the trajectory constraint, the change in rope length is corrected so that it follows the trajectory. The convergence time of the rope length is slightly extended, which is due to the constraint of the track, but this is due to the extension of the input time of the bogie position. It can be said that the target track is not followed because the rope length convergence time is not extended in accordance with the extension of the input time in the trolley and the winding of the rope is completed during the transportation. Figure 6 is a comparison diagram of the swing angle θ. Compared to the case without shaping, the total amplitude of the residual vibration of the conventional method is reduced by 96.3%, and the total amplitude of the residual vibration of this method is reduced by 96.2%, which shows that a good vibration suppression effect is obtained. Figure 7 is a drawing of the suspended object trajectory of the crane every 1 second. It is found that the trajectory of the suspended object is in good agreement with the target trajectory in this method considering the trajectory constraint. On the other hand, the conventional method suppresses residual vibration, but does not follow the target trajectory. In this method, the constraint to the suspended object trajectory and the suppression of residual vibration are sufficiently performed even with two-point suspension, and it can be said that this method is effective.

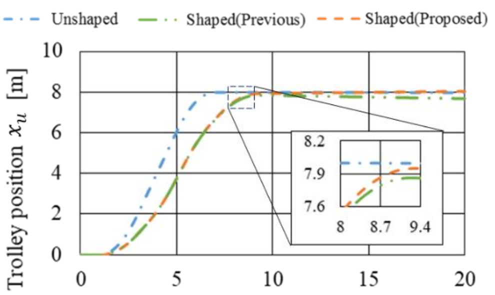

Figure 4. Trolley Position.

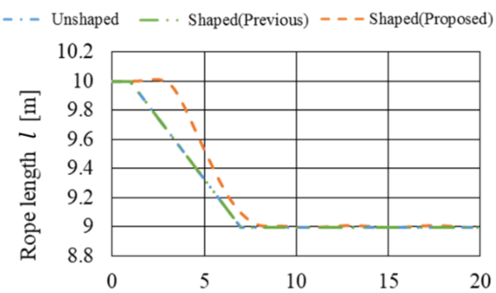

Figure 5. Rope length.

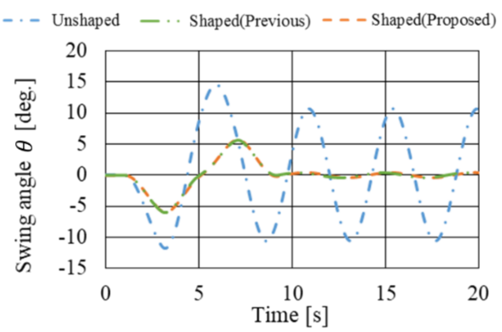

Figure 6. Swing angle of payload.

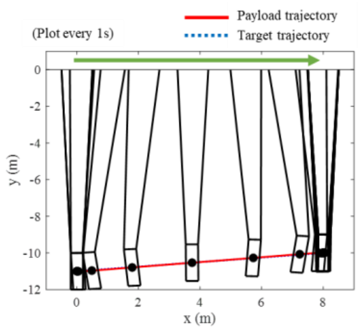

Figure 7. Payload trajectory [Proposed].

5. The impact of flexibility on control

In Section 4, the control effect of the two-point suspended rigid body model was confirmed. Since the suspended object in the actual system has flexibility, its influence needs to be confirmed. This section describes the influence on the control when an input profile for a rigid body model is directly applied to a flexible body model. The T-shaped suspension as a flexible body model shown in Figure 8(a) is introduced. The analysis time is 20 s, the step size is 0.01 s, the movement distance is 2 m, and the rope length changes from 1 m to 0.8 m at a constant speed. As model parameters, mass of the suspended object is 0.0874 kg, the upper height is 0.002 m, the upper width is 0.2 m, the lower height is 0.5 m, the lower width is 0.002 m, and the distance between rope fulcrums is 0.225 m. As shown in Figure 8(b), the lower part is divided into 3 links to simulate flexibility.

Figure 9 shows the locus of the center of gravity of the suspended object. The difference between the flexible body and the target trajectory at the beginning of the movement and near the target position is confirmed compared to the rigid body. There is no large error near the center of transportation. Therefore, this is considered to be due to the sudden acceleration and deceleration of the transport operation. Figure 10 shows the swing angle of the suspended object with respect to the vertical direction. The total amplitude of the flexible body does not show the swing suppression effect compared with the rigid body, and multiple modes of vibrations can be confirmed from the swing angle after 10 s. Originally, the vibration of the rope length due to transportation is suppressed by the design of Input Shaping. However, it is considered that the vibration of the rope length is generated by the vibration due to the flexibility of the structure. Moreover, the swing angle of the rope length and the swing angle of the upper part of the T-shape of the flexible body are linked by a geometric correlation. Furthermore, the deflection angle of the upper part of the T-shape of the flexible body is the same as the waveform of the deflection angle of the rigid body. From this, the structural flexibility of the flexible suspension is the primary mode vibration of the beam. Figure 11 shows the frequency analysis of the results from 10s to 20s at the swing angle in Figure 10. The frequency domain is 50Hz and the resolution is 0.1Hz. It can be said that the other frequency component in the response of the flexible body model are due to structural flexibility since it is clear that the frequency component in the response of the rigid body model is the natural frequency due to the two-point suspension rope. The frequency due to the rope may differ between the rigid body model and the flexible body model since the position of the center of gravity changes due to deformation during transport. However, there was no difference in the first-order mode due to the frequency components between the cases of rigid body model and the flexible body model. Since the movement of the center of gravity is small due to structural flexibility, the frequency change is also small. So, it was not displayed in the analysis result. Therefore, it is not necessary to consider the flexibility with respect to the frequency of the primary mode if the effect of the movement of the center of gravity due to structural flexibility is small.

From the above, since the deviation from the trajectory constraint due to the movement of the center of gravity and the residual vibration suppression effect are small, the influence of the flexibility on the vibration isolation effect and the trajectory constraint cannot be ignored. In addition, the change in frequency with rope length is small, and the effect of frequency due to structural flexibility is large. This will be solved by expanding Input Shaping for multiple modes.

Conclusion

In this study, a two-point suspension crane model was drove and approximated to a rigid pendulum in order to simulate operations such as pulling out and inserting parts by a crane. We proposed a control that combines Input Shaping and optimization. And numerical analysis was used to show that the control objective of a two-point suspension is feasible. In addition, numerical analysis confirmed the effect of applying the control method to flexibility. A future task is to perform numerical analysis assuming simple extraction and insertion work. In addition, we will search for conditional expression of an approximate model when the two rope lengths are different. Then, an experiment of pulling out and inserting work using an actual machine will be performed.

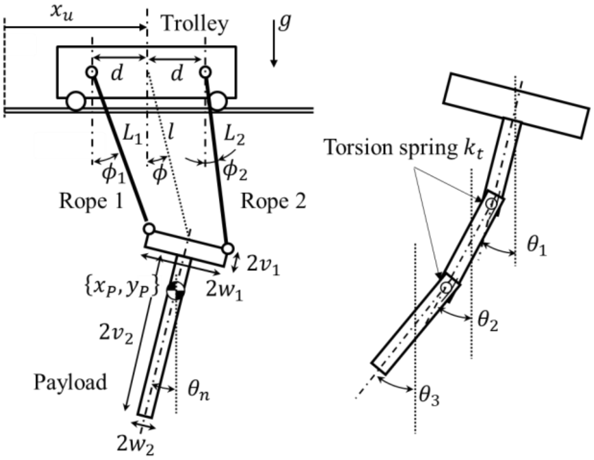

(a) T-shaped model. (b) Flexible model.

Figure 8. Crane model approximation.

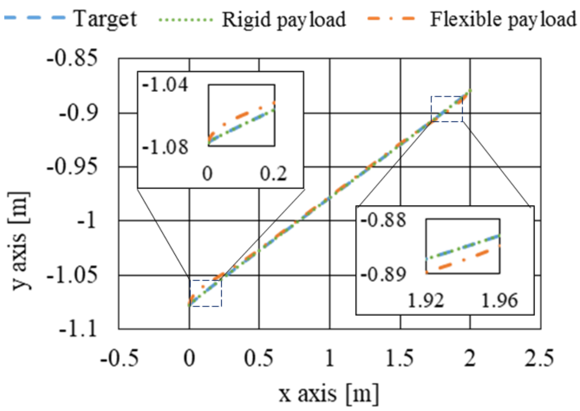

Figure 9. Payload trajectory in of flexible.

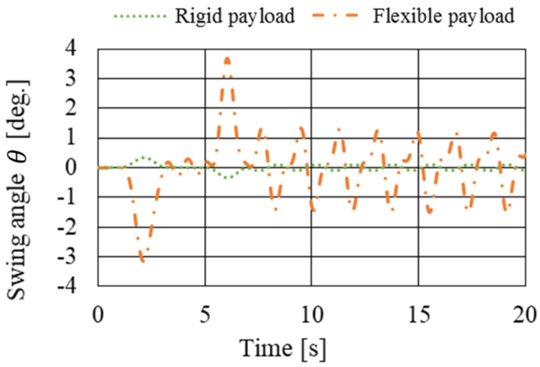

Figure 10. Swing angle in result of flexible.

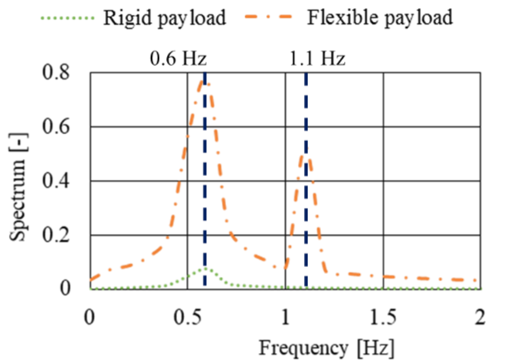

Figure 11. Frequency component of flexible.

References

[1] Junichi MIYAZAWA and others, Plasma and Fusion Research, Vol.14, 1405163 (2019).
[2] N. C. Singer and W. P. Seering, ASME, Journal of Dynamic Systems, Measurement and Control, Vol.112, Issue 1 (1990), pp.76-82.
[3] Z. N. Masoud and M. F. Daqaq, IEEE Transactions on Control Systems Technology, Vol.14, No.6 (2006), pp.1070-1077.
[4] Singhose, W., Porter, L. and Seering, W., Proceedings of American Control Conference, Vol.1 (1997), pp.97-100.
[5] Kress, R., Jansen, J. F. and Noakes, N. W., two-DOF, AC induction motor-driven crane, Fifth International Symposium on Robotics and Manufacturing, (1994), pp. 585-592.
[6] K. Lee and Y. Park, Robotica, Vol.20, Issue 6 (2002), pp.553-561.
[7] Sotaro FURUTA, Yoshiki Sugawara and Masakazu Takeda, The Japan Society of Mechanical Engineers, Dynamics, Measurement and Control Division, Dynamics and Design Conference 2020, (2020), 546

DRC0009

Real-time Feedback Control during Fiber Laser Welding of Low Carbon Steel Sheets

Boonrit Kaewprachum [1] and Pornsak Srisungsitthisunti [1,*]

[1]Production Engineering Department, Faculty of Engineering, King Mongkut's University of Technology North Bangkok, 1518 Pracharat 1 Road, Wongsawang, Bangsue, Bangkok 10800, THAILAND

* Corresponding Author: pornsak.s@eng.kmutnb.ac.th

Abstract. Real-time quality control of laser welding of steel sheets was studied by using feedback information taken by an infrared camera. This method analyzed infrared images during welding to directly determine the quality of welding using the average temperature (Avg.Temp) and the size of the molten pool. The Avg.Temp and the size of the molten pool depended on laser power, laser welding speed, materials, thickness, and so on. In this experiment, we fixed all the welding parameters except the laser welding power and the steel sheet thickness. The feedback control system was able to adjust the laser power to maintain the welding temperature within ±50 ºC accuracy. By monitoring and controlling the Avg.Temp of the molten pool, the low carbon steel sheets with varying thicknesses (0.5-1.0 mm) could be welded together with the optimum laser power. The welded specimens were characterized on welding appearance and full penetration depth. Our feedback control technique was suitable for the automatic laser welding system of metal sheets with unknown thickness and varying thickness.

Keywords: Feedback control, Molten pool, IR camera, Low carbon steel, Laser welding

1. Introduction

In recent years, fiber lasers have been developed rapidly due to their advantages in high welding power, good beam quality, and high flexibility. Laser welding has been widely used especially in the industrial field of automobile and shipbuilding [1]. Monitoring and control system being more important for quality and cost management for welding. Online monitoring of laser welding quality inspection has been developed to improve weld quality, eliminate defect in welding process and reduce overall costs [2, 5].

One of the most important parameters in welding process is thermal distribution which has the direct effect on microstructure of welding products especially in welding products which have thickness less than 1 mm thickness [6-8]. Welding temperature and thermal distribution can be monitored using non-contact sensors such as pyrometers, infrared camera, multi sensor or CCD high speed camera [3, 4, 11]

In this paper we propose the design and development of a feedback control system of laser welding that maintained the Avg.Temp by automatically adjusting the laser power. The monitoring system used the IR camera to determine the average temperature of the molten pool area. The reference temperature area was carefully determined to effectively represent the welding spot. An automatic setup routine and a digital gain controlling were used to control the laser unit. The quality of the laser welding process was controlled in term of Avg.Temp value and its fluctuation. The PID controlling algorithm was tested to maintain the laser welding temperature during welding of varying steel sheet thickness.

2. Experiment setup

Table 1 describes the laser welding parameters used in the experiment. A laser welding JenLas CW500 with maximum power 500W was used to weld low carbon steel sheets (JIS G3101 SS400) plates with variable thickness between 0.5 - 1.0 mm. All experiments were realized at a constant speed of 3 mm/s and are butt-joint type weld. During welding process, the weld seam was shielded by high purity argon gas supplied at 15 liters/min to prevent oxidation effect.

The laser welding head was positioned at a defocus distance of +20 mm above workpiece. The laser beam incident angle was 10 degree to avoid the radiation reflection to the fiber laser. The IR camera (Optris PI 1M) was setup 400 mm above workpiece at a viewing angle of 15 degree in order to obtain the weld seam and avoid obstruction of laser head. The actual known scale was used to calibrate and distortion recovery of the images and average temperature of molten pool.

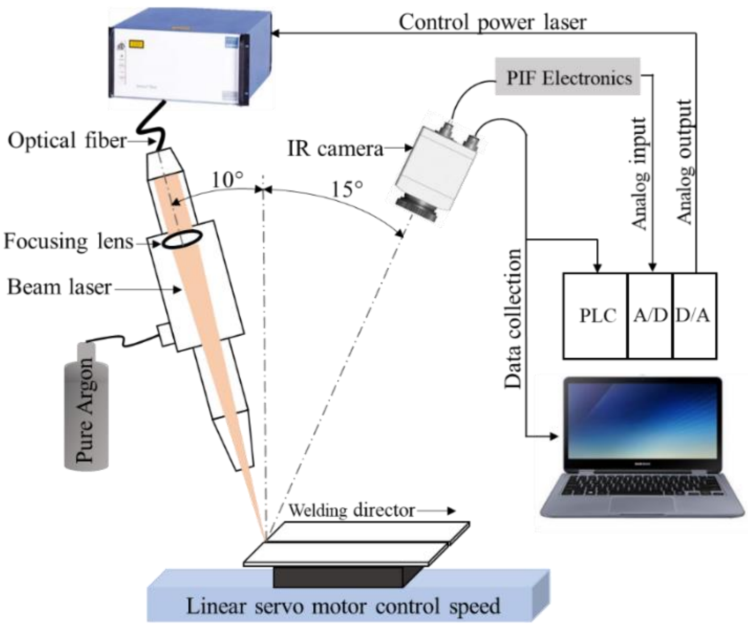

Figure 1. Schematic of the experimental laser welding setup.

Table 1. Experiment setup parameter.

No.	Experiment parameters	Values
1	Laser power	100-500W
2	Speed	3 mm/s
3	Work piece thickness	0.5-1.0 mm
4	Angle of Laser beam	10 degree
5	Defocusing	+20 mm
6	Argon flow rate	15 l/min
7	Angle of IR Camera	15 degree
8	Distance from work piece to IR camera	400 mm

The experimental setup is shown in figure 1. The real-time feedback control system started simultaneously with the welding operation. IR camera captured welding images and the software determined the real-time average temperature (Avg.Temp) of the welding area. The temperature was sent as analog signal to PLC that used PID controller to calculate the desire laser power. Then the PLC sent out the analog signal to increase or decrease power of fiber laser in order to optimize the welding process.

3. Feedback control design

3.1. IR camera and PLC control

IR camera can access radiation in infrared wavelength (1150-1800 nm) due to temperature of radiated object. Temperature monitoring was converted in real-time by IR camera in a capable range from 450 to 1800 ºC. IR camera also provided real-time infrared thermography as shown in the figure 2. The IR camera was communicated to a computer by using PIF (Process Interface) connector.

The overall quality of the welding can be assessed from the infrared image inside the reference area around the welding spot (hot spot). In this experiment, the elliptical shape of 26 × 32 pixels was created around the welding spot to be the reference area as shown in figure 2. This size of reference area was designed to cover the maximum size of molten pool in case of using the maximum power.

The Avg.Temp was obtained from the reference area and has been converted to an analog signal 0-10 volts then transferred via PIF connection to a PLC unit. As a result, the analog signal from the IR camera directly sent to the PLC. The PID algorithm determined the appropriate laser power to be used and then the PLC sent out the analog signal to the power control unit. Therefore, the laser power (100-500W) was continuously adjusted with feedback parameters to maintain the Avg.Temp and laser welding process.

3.2. Optimized laser powers for different sheet thicknesses

The relationship between laser power and thickness of low carbon steel has been studied. Steel sheet specimen size 38mm × 150mm and uniform thickness of 0.5, 0.8 and 1.0 mm were used in this experiment. We used different laser power of 100, 200, 300, 400 and 500W to find out the welding temperature (Avg.Temp) from the IR camera for each condition.

Figure 3 shows the Avg.Temp and standard deviation (S.D.) of thickness 0.5, 0.8 and 1.0 mm at different laser power conditions. There were cases of insufficient welding power where the laser did not fully weld the steel sheet. Only full welding penetration work pieces were selected to consider proper Avg.Temp set point for feedback control. The results showed that full penetration for work piece thickness 0.5 mm required laser power 200-300W (Avg.Temp range 968-1,146 ºC). Steel sheet thickness 0.8 mm required power 300-400W (Avg.Temp range 995-1,114 ºC) and steel sheet of 1.0 mm required power range between 400-500W (Avg.Temp range 1,000-1,140 ºC). As shown in figure 3(d), the temperature of 1000 ºC (dash line) which intersected all the three thicknesses was suitable for using as Avg.Temp for feedback control. Therefore, the set point of Avg.Temp of 1000 ºC can be used to feedback control steel sheet within thickness range 0.5-1.0 mm (for a given laser power range of 100-500W).

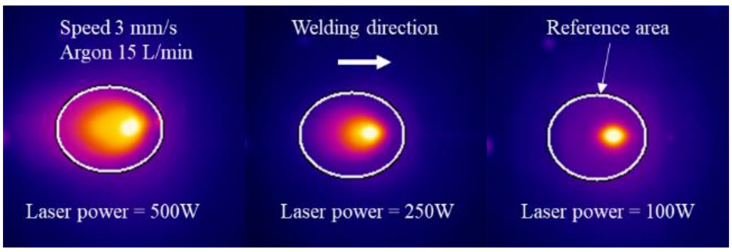

Figure 2. Infrared images of the molten area during laser welding from IR camera and their corresponding intensity profile.

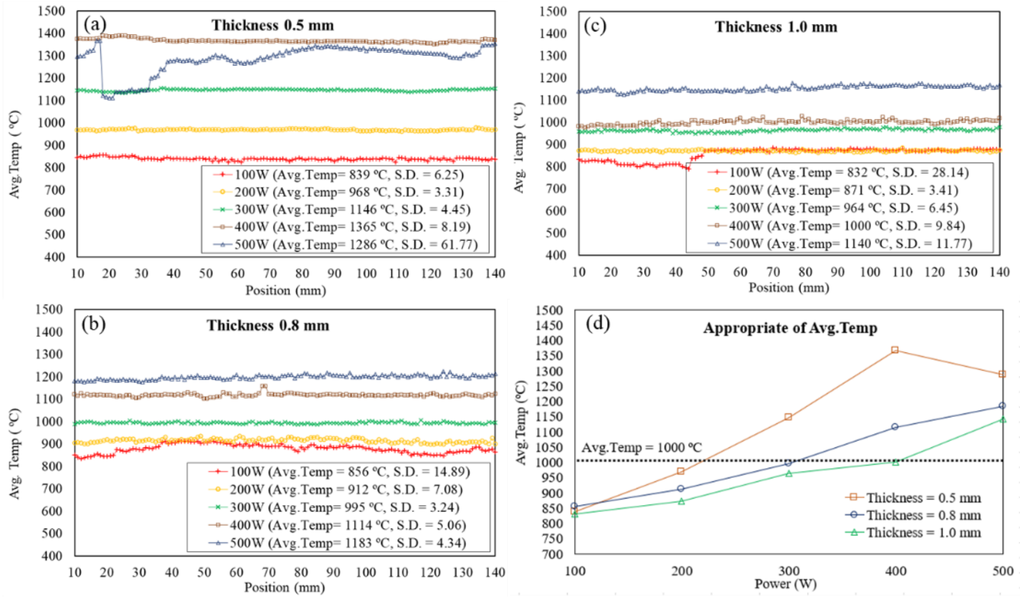

Figure 3. The Avg.Temp of laser welding process of low carbon steel sheet with power 100, 200, 300, 400 and 500W (a) Thickness 0.5 mm, (b) Thickness 0.8 mm, (c) Thickness 1.0 mm and (d) Avg.Temp of laser welding for different sheet thicknesses and laser powers.

3.3. Laser power feedback control

A PID controller is commonly used as a controller in industrial feedback control applications. The controller compared the measured process output value with the reference set point value. The difference or an error signal (welding temperature) was then process for calculation the control signal to manipulated process input so the system output (laser power) reached the desired reference value. Unlike simple control algorithms, the PID controller adjusted process inputs based on the history and rate of change of the error signal, which gave more accurate and stable control.

The schematic of the laser power controller architecture are shown in the figure 4. Adjusting the gain of the PID controller to make the system has the desired response by using the method of Ziegler and Nichols method [9, 10] was the PID tuning techniques based on the certain controller assumptions. Hence, there was always a requirement of further tuning; because the controller settings derived were rather aggressive and thus result in excessive overshoot and oscillatory response. Therefore, the above method has been applied to control laser power for stability and good performance.

When K_p, K_i And K_d was obtained from Ziegler and Nichols method, the results were used to control this research. By the feedback control with set point Avg.Temp of 1000 °C was conducted to weld and use the IR camera to receive the Avg.Temp on molten pool as a feedback signal for adjusting the power of the laser welding. However, in practice it may be necessary to adjust the K_p, K_i And K_d further to achieve the desired stability control.

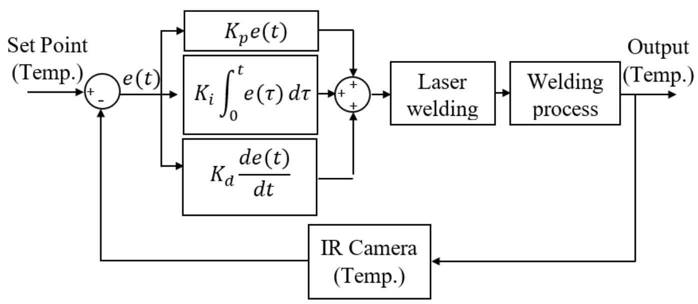

Figure 4. PID algorithm of automatic controlling system for laser welding process.

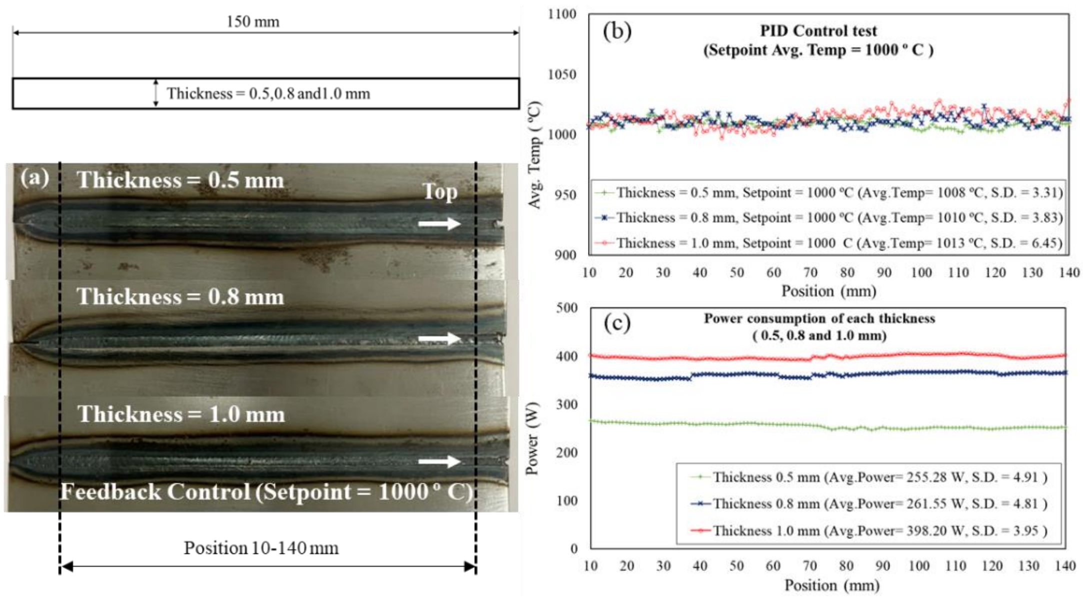

Figure 5. Welding of uniform sheet with feedback control setpoint Avg.Temp = 1,000 ºC (a) Welded steel sheets with uniform thickness of 0.5, 0.8 and 1.0 mm, (b) Avg.Temp and standard deviation (S.D.) of welding temperature and (c) Laser power used for each condition.

In figure 5, the feedback control with set point Avg.Temp of 1000 ºC was conducted to weld the three thicknesses. In figure 5(a) was a photograph welded sheets with feedback control, which revealed that all welds exhibited complete penetration and relatively uniform heat distribution. (Notice the black edge on the side of the weld). In figure 5(b) shows the Avg.Temp that occurs during welding (by collecting data every 1 second) of the weld for all three thicknesses, the results showed that the welding temperature was maintained within ±6.45 ºC (SD = 6.45). In figure 5(c) showed the graph of laser power that was retrieved from the feedback control unit (PLC) in each condition. The laser powers were adjusted about 1-2% during welding to compensate heat and maintain the welding temperature.

4. Result and discussion

4.1. Feedback control of welding sheet with step-change thickness

The experiment compared the laser welding of steel sheet with step-changes thickness with feedback control and without feedback control. Steel sheet specimens were machine to have thickness of 0.5 mm in the first half and 1.0 mm in the second half. The laser power was setup to 250W and 400W for no feedback control tests. The feedback control test used optimize power depending on the feedback Avg.Temp. The result showed that the constant power 250W provided good welding quality for only 0.5 thickness but insufficient power for melting to weld a work piece with a thickness of 1.0 mm. as shown in figure 6(a). In the case of constant power 400W, 1.0 mm thickness area showed good welding quality but at 0.5 mm thickness, the power was too high such that it cut through the steel as shown in the figure 6(b). Using Avg.Temp as a feedback control signal of the PID control resulted in good weld quality throughout the entire length, even with step changes in thickness as shown in figure 6(c).

The Avg.Temp form the IR camera were largely unstable and jump lower when experiencing with change in sheet thickness from 0.5 mm to 1.0 mm. as shown in the figure 6(d). The feedback control smoothly increased the laser power to maintain the Avg.Temp resulting in good welding quality as shown in the figure 6(e).

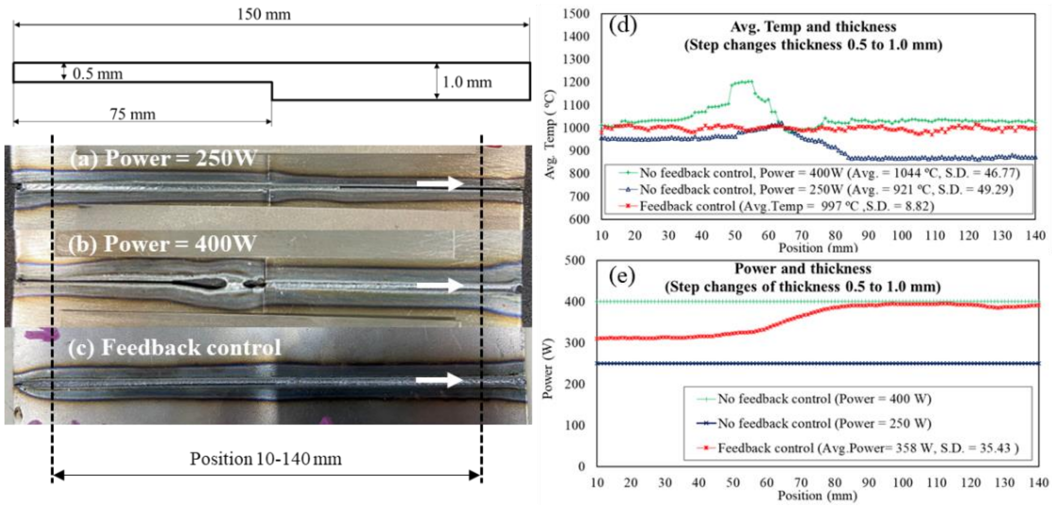

Figure 6. Welding of step changes sheets with thickness 0.5 - 1.0 mm for feedback control set point = 1,000 ºC (a) Welded steel sheet by a constant power of 250W, (b) Welded steel sheet by a constant power of 400W, (c) Welded steel sheet by feedback controlling laser power, (d) Avg.Temp and standard deviation (S.D.) of welding temperature and (e) Laser power used for each condition.

4.2. Feedback control of welding sheet with linear-change thickness

The experiment compared the laser welding of steel sheet with linear-changes thickness with feedback control and without feedback control. Steel sheet specimens were machine to have thickness increasing from 0.5 mm to 1.0 mm along the length as shown in figure 7(a). The laser power was setup to 400W for no feedback control tests. The feedback control test used optimize power depending on the feedback Avg.Temp. Without feedback control, the constant laser power of 400W was not able to weld nonuniform sheet and caused holes insides welding area. On the other hand, the quality of welding line from feedback control system experiments were constant and stable as shown in the figure 7(a) and figure 7(b). The feedback control system has been successfully maintained quality of welding process that reflect to uniform welding line and provided stable thermal distribution throughout welding process.

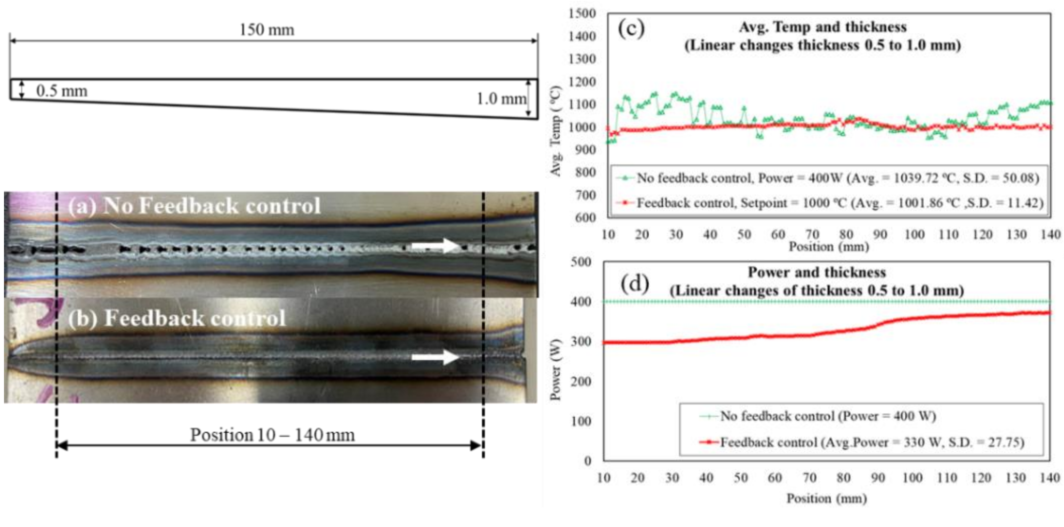

Figure 7. Welding of linear changes sheets with thickness 0.5 - 1.0 mm for feedback control set point = 1,000 ºC (a) Welded steel sheet without feedback control, (b) Welded steel sheet with feedback control, (c) Avg.Temp and standard deviation (S.D.) of welding temperature and (d) Laser power used for each condition.

The result of both linear-change of thickness and step-change of thickness experiment showed that feedback control can solve problem when welding unknown thickness steel sheet and achieved uniform welding quality. The Avg.Temp of the feedback control were maintained within ±8.8 ºC and ±11.4 ºC which were around 1% as shown in the figure 6(d) and the figure 7(c).

5. Conclusion

Real-time feedback control system for laser welding with a fiber laser has been successfully demonstrated to control Avg.Temp of molten pool. Feedback control system consisted of IR camera, PLC unit with PID controller and laser power control unit. The controlling parameter was based on the average temperature of the welding area (Avg.Temp) obtained from the IR image. The feedback control system in this study was able to weld steel sheets with 0.5 – 1.0 mm thickness in both step-change thickness and linear-change thickness with only 1% fluctuation in welding temperature. More study should be conducted in finding relationship between infrared imaging and the welding quality in microstructure in order to apply the feedback control technique more accurately.

Acknowledgments

This research was funded by King Mongkut's University of Technology North Bangkok. Contract no. KMUTNB-61-GOV-01-12 to support the equipment**.**

References

[1] D. Y. You1, X. D. Gao and S. Katayama., 2014. Review of laser welding monitoring. Science and Technology of Welding and Joining. J. 0, 1-21.

[2] John Stavridis1, Alexios Papacharalampopoulos1 and Panagiotis Stavropoulos., 2018. Quality assessment in laser welding: a critical review. Int J Adv Manuf Technol. J. 94, 1825–1847.

[3] W Huang and R Kovacevic., 2009. Feasibility study of using acoustic signals for online monitoring of the depth of weld in the laser welding of high-strength steels. Proc. Inst. Mech. Eng. B: J. Eng. Manuf. J. 223, 343-361.

[4] Pu Zhang, Li Kong, Wenzhong Liu, Jingjing Chen and Kaibo Zhou., 2008. Real-time Monitoring of Laser Welding Based on Multiple Sensors. In: Chinese Control and Decision Conference p 1746

[5] A.R. Konuk, R.G.K.M. Aarts, A.J. Huis in 't Veld, T. Sibillano, D. Rizzi,A.and Ancona., 2011. Process Control of Stainless Steel Laser Welding using an Optical Spectroscopic Sensor. Physics Procedia. J. 12, 744–751.

[6] Mingsheng XIA,Elliot BIRO, Zhiling TIAN and Y. Norman ZHOU., 2008. Effects of Heat Input and Martensite on HAZ Softening in Laser Welding of Dual Phase Steel. ISIJ International. J. 48, 809–814.

[7] Mingsheng Xia, Zhiling Tian, Lin Zhao and Y. Norman. Zhou., 2008. Fusion Zone Microstructure Evolution of Al-Alloyed TRIP Steel in Diode Laser Welding. Materials Transactions. J. 49, 746-753.

[8] Zhengwei GU, Sibin YU, Lijun HAN, Xin LI and Hong XU., 2012. Influence of Welding Speed on Microstructures and Properties of Ultra-high Strength Steel Sheets in Laser Welding. ISIJ International. J. 52, 483-487.

[9] Hari Om Bansal, Rajamayyoor Sharma and P. R. Shreeraman., 2012. PID Controller Tuning Techniques. A Review Journal of Control Engineering and Technology (JCET). J. 2, 168-176.

[10] Manoj Kushwah and Ashish Patra., 2014. PID Controller Tuning using Ziegler-Nichols Method for Speed Control of DC Motor. International Journal of Scientific Engineering and Technology Research. J. 3, 2924-2929.

[11] Boonrit Keawprachum and Pornsak Srisungsitthisunti., 2014. Real-Time Process Monitoring of Laser Welding by Infrared Camera and Image Processing. Key Engineering Materials. J. 856, 160-168.

EDU0001

The Development of Orthographic Projection Worksheet based on 5E Learning Model and Augmented Reality

Chotiwut Prasopsuk[1,*]

[1]Department of Mechanical Technology, Faculty of Industrial Technology, Thepsatri Rajabhat University, 321 Naraimaharat Rd, Talaychubsorn, Lopburi 15000, Thailand.

* chotiwut.p@lawasri.tru.ac.th

Abstract. Nowadays technology plays an important role in supporting pedagogical training and learning such as Computer-assisted instruction, Web-based Training, Virtual Reality (VR) and Augmented Reality (AR). The objective of this article is to develop an Orthographic worksheet for Engineering Drawing I course. The development of worksheet was done based on the 5E Learning Model and Augmented Reality (AR) technology used to supplement student self-learning. The sample used in this study consisted of three educational specialists, five engineering drawing instructors in university and a teacher in college. The consideration of specialists and teacher opinions were employed as a result were obtained by materials evaluation scale and interviews. The main conclusion drawn from this study is that the opinions of the specialists and teachers are positive.

1. Introduction

Engineering Drawing is very important and useful for learning in mechanical technology. The graphics are written in the form of drawing presenting shape, size, and specification of objects. The product drawing must be intentionally designed before manufacturing and assembling. Therefore, the students who are studying engineering drawing must have an ample knowledge and imagination. Orthographic projection is a part of engineering drawing which represents different views and reference level of perpendicular to respective reference of the target object which requires an engineering sense to transfer 3-D modeling to 2-D drawing. The traditional teaching used 3-D model as an instructional material to explain the structural view of orthographic projection. In the present epidemic, many countries are struggling from the coronavirus. Educational places were temporary closed, but the instruction is switched to online based learning. Therefore, it is necessary to find effective methods in order to serve as the most supportive teaching material in online classroom.

In this paper, a new worksheet of orthographic projection using the 5E learning model was developed through AR application supported by smartphone for easy usage which was suitable for motivating students' learning.

1.1. 5E learning model.

Constructive learning approaches is a one of the learning methods which can be employed to improve students' understanding and their learning achievement where the learning process is not centred by teachers, the students inquire the knowledge to solve the problems, as written in the Taxonomy Revision [1] supporting that students can construct knowledge by themselves with the help of teachers

5E Learning Cycle is a part of constructive learning approaches, the process is consisting of 5 phase – engage, explore, explain, elaborate, and evaluate.

Table 1. Teaching stages and learning activates for the 5E learning model [2]

Teaching Stages	Learning Activities
1. Engage	This stage is attempted to mentally increase students' interest and motivation which focus on a problem and situation.
2. Explore	This stage is engaged in self-exploration activities, proposing and testing hypotheses, exploring problem-solving concept and discussing the rationale of proposed concepts under teacher guidance.
3. Explain	Students are supported by teacher guidance, clarifying their concepts and explanations, and sharing their findings.
4. Elaborate	Students expand their new mentality and apply their constructed knowledge in new contexts
5. Evaluate	In the last stage, students and teacher reviewed their learning achievement and understanding for improving the next developed instruction.

1.2 Augmented reality (AR)
Augmented reality is a technology-assisted learning that combines the real-world environment and multiple sensory modalities. In the recent years, AR technology has increasingly become the effective tool suitable for enhancing students' motivation and participation in the classroom. [3, 4] Moreover, the AR is often used in the classroom for attracting students' attention in the classroom by entertaining [5], from the mentioned point of view, AR technology is inevitably useful for supporting the constructivism approaches which intentionally activate students' motivation in the appropriate learning environment.

There are numerous researches conducting on augmented reality used in teaching context. It has been appeared to promote higher learning achievement. Augmented reality could help both talented learners and those with low motivation, as well as students with special needs could gain more benefits from the use of AR

2. Purpose
The purpose of the present study was to develop the orthographic projection AR worksheet based on the 5E learning model in order to support the learning in the Engineering Drawing I course for the first-year students majoring in Mechanical Engineering.

3. Method
Firstly, the researcher employed AR application for teaching in Engineering Drawing I course based on the 5E learning model. Then, the orthographic projection worksheet was designed, then the worksheet was rated based on the opinions and recommendation of educational specialists who are specialized in teaching engineering in a university and college. The opinions and recommendation were conducted by semi-structured interviews [6] and a material evaluation scale [7] which validity and reliability were already confirmed.

3.1 Sample
The sample of this study was composed of three educational specialists who are holding PhD degree in field of Engineer, Engineering Education and Education, five engineering instructors in University, who are responsible for teaching engineering drawing course in a university of technology. General information of the participants in this study, are presented in Table 2 and Table 3.

Table 2. General information of the specialists.

Specialists	Gender	Academic title	Qualification
S1	Male	Assoc.Prof.Dr.	Ph.D. in Curriculum and Instruction
S2	Male	Assoc.Prof.Dr.	Ph.D. in Electrical Education
S3	Male	Asst.Prof.Dr.	D.Eng. (Mechanical Engineering)

Table 3. General information of the university instructors.

Participants	Academic title	Department	Tenure of office
U1	Asst.Prof.Dr	Mechanical Technology Education	16
U2	Asst.Prof.Dr	Machine Design and Manufacturing Engineering Technology	18
U3	Asst.Prof.	Mechanical Technology	22
U4	-	Industrial Technology	13
U5	-	Mechanical and Automotive Engineering Technology	7

3.2 The AR application used in the study

The constructed an AR application for supporting online learning, recognizes a square AR marker and overlays a virtual mechanical parts made by 3D-CAD. A virtual object is overlaid on an AR marker taken by the smartphone camera. Position and orientation of the virtual object is defined by recognizing the position and the orientation of the AR marker. The virtual object can be rotated in all directions which are able to see the shape on each side.

In this research, the AR was built from an open-source AR creation platform called AR.js Studio. Black and white image was employed to create the AR marker which was used to anchor the content. Then, the researcher uploaded the developed contents and 3-D object in the AR marker. Once the process was done, the researcher exported the content out of the AR.js and uploaded to the sever.

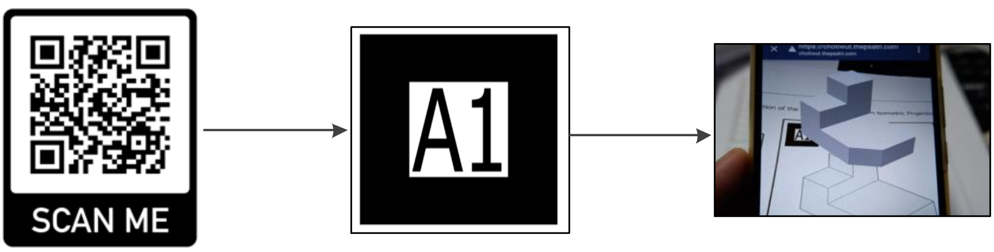

Scan QR code or visit https://chotiwut.thepsatri.com

AR Marker for 3D object

Scan marker for overlay a virtual object on worksheet

Figure 1. How to overlay a virtual object on an AR marker by AR.js Studio.

3.3 Process of development of worksheet with 5E learning cycle

The orthographic projection lesson was used in the target course for the first-year students. Also, the worksheet was developed in order to facilitate the students' self-learning process or online learning. The researcher studied the involved academic sources on the 5E learning model for adapting its theoretical framework to the present objective of the study as presented in the table 4.

Table 4. Characteristics of the activities developed based on stages of the 5E learning model

Stage of the 5E learning Model	Activities for online-learning	Used of time in the stage
Engage	▪ Questions based on texts or pictures that enable the students to think of their surrounded object and its phenomena in daily life e.g. "How is the shadow of the object in the morning and evening different, if it faces to the north? ▪ Teacher asked and recorded deficient or incorrect answers of students	20 minutes
Explore	▪ Students explored the orthographic projection models through the use of AR application to displays virtual objects by using their own smartphone. Then they sketched the third angle view of object component on the space provided in the paper sheet.	40 minutes
Explain	▪ Students shared and explained the results of their exploration. ▪ Teacher provided the explanation.	20 minutes
Elaborate	▪ Students extended and applied the learned knowledge and skill to further figure out other object	20 minutes
Evaluate	▪ The researcher interviewed the students using open-ended question asking about what they had learned so far.	20 minutes

3.4 Data collection

A material evaluation scale consisted of two main parts: 1) structural evaluation 2) contextual evaluation evaluated by specialists and instructors. The specialists evaluated by rating their opinions with positive and negative. The instructor evaluation score was determined as follows: "Yes" is 1 point, "No" is -1 point and "Partial" is 0 point. The content validity of the item was confirmed by using the Index of Item Objective Congruence (IOC) [8]. The overall value from the IOC must be higher than 0.5 which indicates that the specialists and instructors' opinions are consistent to the research objective.

The qualitative data was conducted by using semi-structured interviews with specialists and instructors. Topics and questions were used to elicit their opinion about orthographic worksheet development.

4. Result

The results of this research were analyzed by the opinions of specialists and instructors through a course material evaluation scale and semi-structured interviews and presented as follows:

4.1. The opinions of the specialists and the instructors through a material evaluation scale.

Table 5. The evaluation criteria, opinion from the specialists and IOC mean score from the instructors

Structural Evaluation

Evaluation criteria	Opinions from the specialists	IOC score from the instructors
1. The congruence with curriculum.	Positive	0.6
2. The congruence with subject.	Positive	0.6
3. The congruence with the age of students.	Positive	0.6
4. The congruence with the research problem.	Positive	1

5. The congruence with the student's development process.	Positive	0.8
6. The suitability of the content.	Positive	0.6
7. The suitability between the activities and the 5E learning model.	Positive	0.8
8. The suitability for studying in 2 hours	Positive	0.4
9. The suitability of learning activities assignments.	Positive	0.6
10. The suitability of worksheet such as language, layout.	Positive	0.6
11. The suitability between worksheet and students level.	Positive	0.4
12. The suitability between AR application and learning model.	Positive	1
Total	Positive	0.67

The results of the structural evaluation are presented in Table 5. According to the specialists, the overall opinion was positive.

The opinions of the instructors were calculated by the IOC method with structural content. The overall average of all criteria was 0.67 (maximum 1.0). The evaluation criteria item.8 and item.11 were ranked at the lowest (0.4). For item.8, the U1 and U2 rated their opinion with "Partial" (zero point) and "No" (minus one point) respectively. For item.11, the U2 and U5 rated their opinion with "No" and "Partial" respectively, but the overall point of view was acceptable. However, all instructors rated "Yes" in three evaluation criteria, namely the congruence with the research problem, the student's development process and the suitability between AR application and learning model. Furthermore, the U2 rated "No' and "Partially" which were 0.6 and 0.8 points respectively.

Table 6 The evaluation criteria, opinion from the specialists and IOC mean score from the instructors

Contextual Evaluation

Evaluation criteria	Opinions from the specialists	IOC score from the instructors
1. Students are motivated to study.	Positive	1
2. Enough to activate prior knowledge.	Positive	0.6
3. Worksheet activities can be used to encourage the skill of students.	Positive	0.6
4. Worksheet activities are congruent with student's level.	Positive	0.6
5. Worksheet activities can be used to apply to use in real life.	Positive	0.6
6. Worksheet activities can be used to instruct to critical thinking.	Positive	0.8
7. Worksheet activities can be used to instruct to self-exploration.	Positive	0.8
8. Worksheet activities can be used to instruct to self-evaluation.	Positive	0.4
9. The first section is in-line to engage phase of 5E learning.	Positive	0.8
10. The second section is in-line to explore phase of 5E learning.	Positive	1
11. The third section is in-line to explain phase of 5E learning.	Positive	0.6
12. The fourth section is in-line to elaborate phase of 5E learning.	Positive	0.6
13. The fifth section is in-line to evaluate phase of 5E learning.	Positive	0.8
Total	Positive	0.70

The results of the contextual evaluation are presented in Table 5. According to the specialists, the overall opinion was positive even though the S2 rated "Negative" in item 8.

According to the instructors, the evaluation criteria as shown from item 1 and 10 which were rated as 1 point. The U2 commented "No" on worksheet activities in terms of activating prior knowledge, encouraging the skill of students, congruent with student's level, and applying to use in real life. Moreover, the U1, U2 and U5 agreed that the self-evaluation criteria were rated on "Partial" and only the U5 commented "Partial" in item 9. Accordingly, other participants expressed "Yes" of all criteria.

That is to say, the IOC score of instructors' opinions about contextual evaluation of all criteria was 0.70 (maximum 1.0) which is higher than 0.5. It indicated that the material was effective.

4.2. The results obtained from semi-structural interviews.
There are insightful suggestions on how to further develop the worksheet as the followings. The specialist code S1 who is teaching in faculty of education commented that "*The worksheet alone is not enough to foster the students understanding, it should be developed into the teaching modules including other several parts of teaching*". Next, the specialist code S2 who is teaching in faculty of technical education stated that "*The warm-up questions in the engage phase should be included the closed-ended questions and the question should be narrowed down to the scope of the research, for easier evaluation*". The last specialist code S3 suggested that "*the 3-D objects in the AR should be added a different color texture to the plane to increase the understanding of students*"

The results from the interview session with the instructors were in the same direction to the specialists. The researcher began the question with the strengths of the worksheet. All instructors commented that the lesson could facilitate students' motivation and understanding. Interestingly, the U4 therefore, made engaging comment that "*It is recommended that the developed instruction should be further buried in online learning platform ie. Thai MOOC*". However, when considering the results in more details about the weakness, the instructor code P1 commented that "*The activity in the explore phase seems too difficult, the exercise should be focusing only on orthographic projection analyzing".* The instructor code P2 commented that "*Firstly, the objectives of worksheet should be clear about the instruction of the third angle projection. Next, the activities on the explore phase should be arranged based on its difficulty. Also, the activity in the elaborate phase should be specified a scope of the 3-D object clearly in order to be consistent with the learning objective*". The instructor code U3 shared his experience of teaching. He said "*Many students cannot separate each plane of 3-D objects, so the lesson should include more exercises such as pictorial and orthographic matching before starting drawing the orthographic projection*". The instructor code U5 commented that time required for activity in the explore phase is too long (40 minutes). It should be reduced and add more time on practices.

5. Conclusion
In conclusion, the opinion of the specialists and instructors are positive and the average of IOC were passed which indicated that the lesson was effective for teaching engineering drawing. However, the worksheet still needs to be revised according to the comments, especially, the time management of 5E activities in worksheet.

Moreover, it should be clear if the lesson is employed to teaching in the classroom to see whether or not the lesson is effective. In addition, the comparison of the students' achievement from the control and experimental group after using lesson should be further investigated in order to determine the effectiveness for the future work.

References
[1] Marj J 2007 *Journal of Family and Consumer Sciences Education.* vol 25 p 45
[2] Ping-Han Cheng, Ya-Ting Carolyn Yang, Shih-Hui Gilbert Chang and Fan-Ray Revon Kuo 2016 *IEEE Transactions on Education* vol 59(2) 147
[3] Su Cai et al 2013 *International Journal of Engineering Education.* vol 29 p 856
[4] Wojciechowski R. and Cellary W 2013 *Computers & Education.* vol 68 p 570
[5] Yoon S A, Elinich K, Wang J, Steinmeier C, and Tucker S. 2012 *International Journal of Computer-Suported Collaborative Learning.* vol 7 p 519
[6] R. Longhurst. 2009 *International Encyclopedia of Human Geography.* p 580
[7] Kaleli-Yilmaz, G., Ertem, E. and Cepni, S. 2010 *Procedia Social and Behavioral Sciences.* 2 p 1405
[8] Ronna C. Turner and Laurie Carlson. 2003 *International Journal of Testing.* 3(2) p 163

ETM0002

The Effect of the Number of Blades on the Characteristics of Compressed Air Wind Turbines Using R1235 Airfoil Blade Profile

Wirachai Roynarin[1,*], Wongsakorn Wisatesajja[1], and Gerald Aguila[2]

[1]Engineering Faculty, Rajamangala University of Technology Thanyaburi (RMUTT), Pathum Thani, 12110 Thailand
[2]Mechanical Engineering Department, Batangas State University, Philippines

* Corresponding Author: wirachai_r@rmutt.ac.th

Abstract. Renewable energy is an eco-friendly, economical, and unlimited source of energy. There are several applications that have been applied in human activities using wind energy to replace fossil fuel consumption. Since most Asian countries have low wind speed areas, the design of turbine blades must be applied to generate power at lower wind speed and in unsteady conditions. Wind speed is associated with selecting the tip speed ratio (TSR), which is an important parameter in the initial design phase of wind turbines. Generally, the TSR depends on the airfoil blade profile type used, the number of blades, and other parameters. This paper aimed to study the influence of the number of blades on the performance of the compressed air application. Two-blade and three-blade wind turbines with an R1235 airfoil blade profile equipped were tested in a wind tunnel at the Research and Service Energy Center (RSEC), Rajamangala University of Technology Thanyaburi (RMUTT). The results showed that the two-blade wind turbine could perform at a higher rotational speed of 1543 rpm and maximum TSR of 10.11 at a wind speed of 6 m/s, while the three-blade wind turbine performed at a rotational speed of 1231 rpm with a maximum TSR of 9.08 at a wind speed of 5 m/s. However, the three-blade wind turbine is more appropriate to be applied for wind turbine compressed air application due to the lower cut-in speed of 3 m/s and the ability to reach maximum TSR at a lower wind speed than the two-blade wind turbine. Also, it is more suitable for operation in low-wind speed areas.

1. Introduction

Wind energy has been applied in human activities for many years. There are several applications implemented from wind energy such as pumping water, grinding grain, compressing air, and generating electricity to reduce fossil fuel consumption [1]. However, the global average on-land wind speed at 80 meters is 4.54 m/s; most wind turbines are designed to generate rated output power at wind speeds of around 10-15 m/s [2]. Therefore, low-speed wind turbines are a potential solution to operate mechanical power at low-wind energy with careful design of the airfoil blade and wind turbine characteristics, which could be expanded for the benefit of low-speed wind turbines in terms of commercial applications [3]. Hence, the low-speed airfoil blade profile, called "R1235", has been developed by Research and Service Energy Center (RSEC) at Rajamangala University of Technology Thanyaburi (RMUTT) for wind turbines operating specifically in low-wind speed areas [4]. Also, the number of wind turbine blades could influence the performance of wind turbines, in which the most common wind turbine design is equipped with three-blade rotors. Nevertheless, the number of wind turbine blades should be designed by understanding the characteristics and application of the wind turbine for analysis in terms of performance and economics [5].

This paper aimed to investigate the influence of the number of blades on the performance of the compressed air wind turbine. Experimentation in the wind tunnel between two-blade and three-blade horizontal axis wind turbines was performed to obtain the data. The results were analyzed and compared for wind speeds of 3.5 – 7 m/s.

2. Theory

2.1. Wind Energy

Wind energy occurs from absorbing solar radiation on the earth's surface, which causes differences in temperature and pressure, thus creating moving air. Wind energy can be converted into electricity using an energy-converting machine called a "wind turbine", which harnesses the wind energy from wind flow turning the blade rotors to drive the generator and produce electricity. Wind turbines can be classified into two kinds including horizontal axis wind turbines (HAWTs) and vertical axis wind turbines (VAWTs), as shown in Figure 1. HAWTs operate as wind flows parallel to the rotating axis of the blade rotors. The benefits of these wind turbines are high power efficiency, low cut-in wind speeds, high turbine efficiency, and more economical per unit power output. The VAWTs operate as the blade rotors rotate perpendicular to the wind direction. The main advantage of this wind turbine is that the blade rotors can be operated in any wind direction, meaning yaw control would not be required. Also, it is simple for maintenance since the generator and gearbox are installed on the ground. [6].

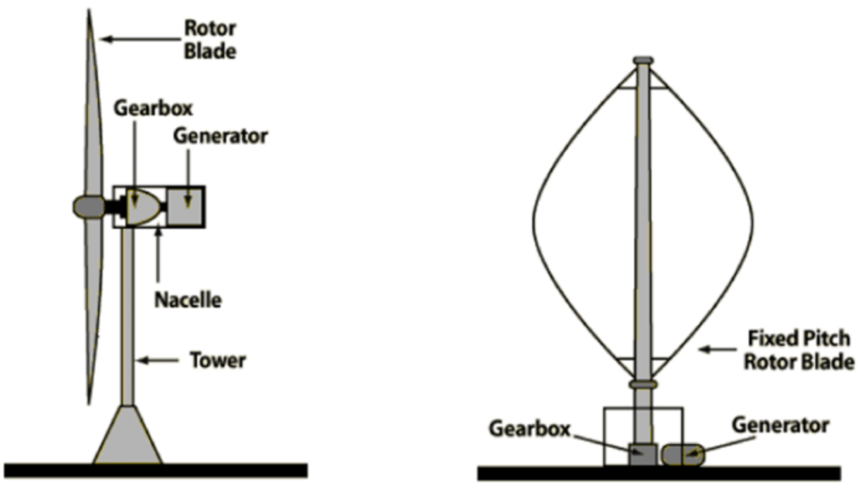

Figure 1. Left: Horizontal axis wind turbines. Right: Vertical axis wind turbines [7]

2.2. Betz's Law and Power Coefficient (Cp)

In 1919, Albert Betz discovered the "Betz limit" to explain the ideal value of wind turbine performance that extracted kinetic energy from the wind into mechanical energy. The concept could explain that the wind flow at the backside of the rotor could be restrained if all energy from the incoming wind flow were extracted to useful energy. Hence, the wind speed would reduce to zero and it would obstruct the wind movement. Therefore, the wind on the backside of the rotor must have enough wind speed to move away and allow more wind flow through the rotor. The Betz limit describes the maximum extraction of wind energy at 59% due to the wind flow through the rotor, which is reduced to the wind speed from losing energy to extraction from a turbine; the airflow requires distribution to a wider area. Also, the power coefficient is defined as being related to the Betz limit to the optimal rotor tip speed ratio of wind turbines [8]. The power coefficient could be defined as the ratio of power extracted by the turbine to the available wind power, which is given as follows [9].

$$C_P = \frac{P_T}{P_A} = \frac{Power\ output\ from\ wind\ turbine}{Power\ available\ in\ wind} \tag{1}$$

2.3. Tip Speed Ratio (TSR)

TSR is the ratio of rotor tip speed over wind speed. It is important to design the wind turbines with an optimal tip speed ratio in order to extract as much power as possible from wind energy. If the rotor rotates too slowly, it causes the undisturbed to the rotor, in which the wind flows through the space between the blades and reduces power extraction. In another way, the rotor spins too rapidly, which would appear as a solid wall, causing obstruction to the wind flow and reducing power extraction. The TSR equation could be written as follows [10]:

$$TSR = \frac{U}{V} = \frac{\omega r}{V} = \frac{2\pi r N}{60V} \tag{2}$$

Where U is rotor tip speed (m/s), V is wind speed (m/s), ω is the angular velocity (rad/s), r is the rotor radius (m), and N is the rotational speed (rpm).

A graph of power coefficient and TSR for each type of wind turbines is shown in Figure 2. Typical three-blade wind turbines contain TSR of 6-8, which provides a power coefficient of around 45%. Also, the typical small wind turbines power coefficient is around 10 – 25% [11].

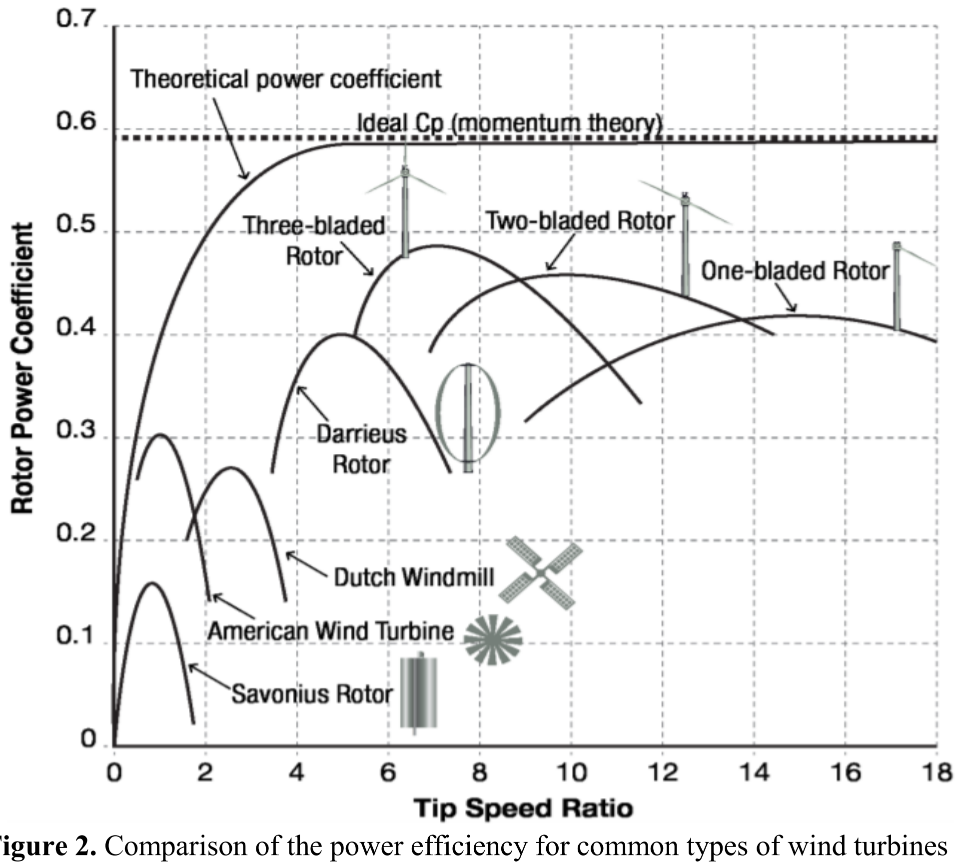

Figure 2. Comparison of the power efficiency for common types of wind turbines [11]

2.4. Wind Turbine Power Output

The power from wind energy could be captured from the effective rotor blade area of the wind turbine, given as:

$$P_A = \frac{1}{2}\rho A V^3 \tag{3}$$

Where ρ is air density (1.225 kg/m^3), A is blade swept area (m^2), and V is wind speed (m/s)
The wind turbine could not extract all the energy from wind flow as the Betz limit explains that the theoretical maximum kinetic energy of the wind could be converted into mechanical energy at 59%. The common power coefficient of the wind turbine design is around 0.35 – 0.45. The total power output from the wind turbine could be derived from equation (1), which is given as [12]:

$$P_T = \frac{1}{2}\rho A V^3 C_P \tag{4}$$

2.5. Effect of Blade Numbers

The number of rotor blades is another essential parameter that affects wind turbine performance. TSR could be optimal depending on the rotor blade numbers; a fewer number of rotor blades would provide faster wind turbine rotation. However, the power coefficient is decreased due to the rotor blades rotating too fast. [10]. Figure 3 shows a comparison between one, two and three rotor blades with respect to power coefficient and TSR. It provided that the power coefficient would be decreased as the smaller number of rotor blades at the same TSR. Most commercial wind turbines consist of two or three rotor blades, though most of the two-blade wind turbines provide higher TSR than the three-blade wind turbines [13].

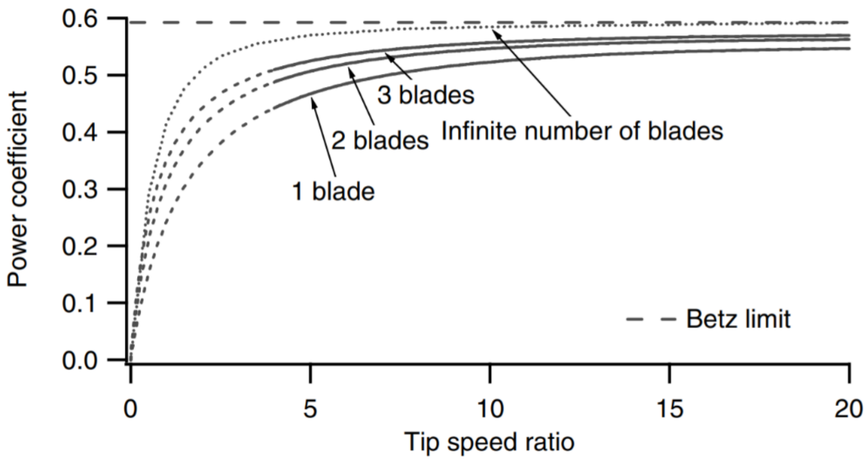

Figure 3. Optimum power coefficient for several numbers of rotor blades [13]

2.6. Compressed Air Systems

Compressed air is a form of energy storage that is integrated into several manufacturing purposes such as machinery, equipment, and processes. There are two compressed air systems, including positive displacement compressors and dynamic compressors. Positive displacement compressors could be operated based on storing the air inside the compression chamber and existing volume mechanically decreased, creating a corresponding increase in pressure prior to discharge. This system could be operated by using a reciprocating piston and rotary screws, as shown in Figure 4 [14]. The dynamic compressor's basic operation is to increase air velocity by using axial and centrifugal impeller, which is then converted to pressure at the outlet. Further classification of dynamic compressor types is radial and axial flow types, as shown in Figure 4 [15].

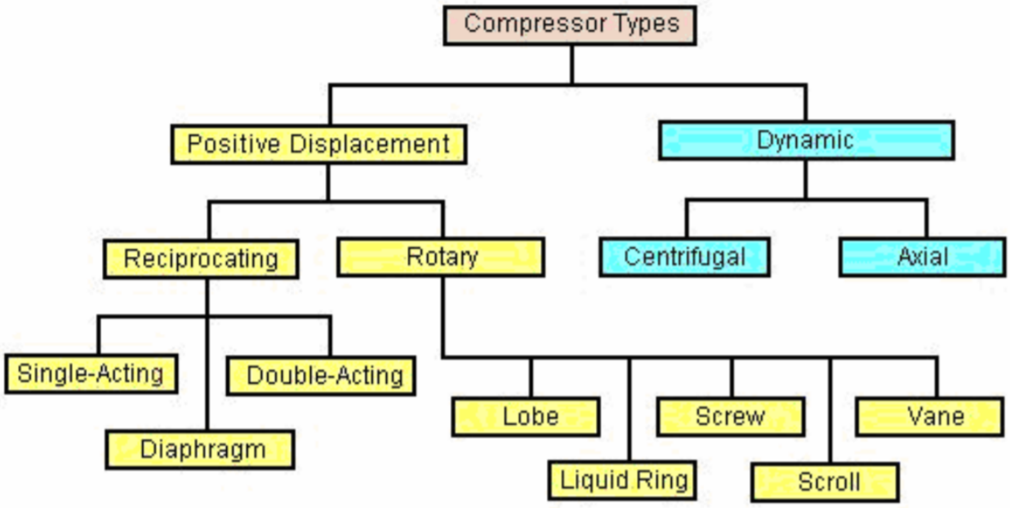

Figure 4. Compressor chart [15]

3. Materials and Methods

3.1. Experimental Setup

The aerodynamic experiments would be performed in a wind tunnel at the Research and Service Energy Center (RSEC) at Rajamangala University of Technology Thanyaburi (RMUTT). The wind tunnel contains a 20,000 CFM centrifugal fan with a wind speed controller. There are two experimental models to be tested, including two-bladed wind turbines and three-bladed wind turbines. Also, the compressed air torque load is applied to the wind turbines. The experiment investigates the wind turbine performance including rotational speed, TSR and power output between the two experimental models at 0 – 7 m/s. A schematic diagram of the wind tunnel is shown in Figure 5.

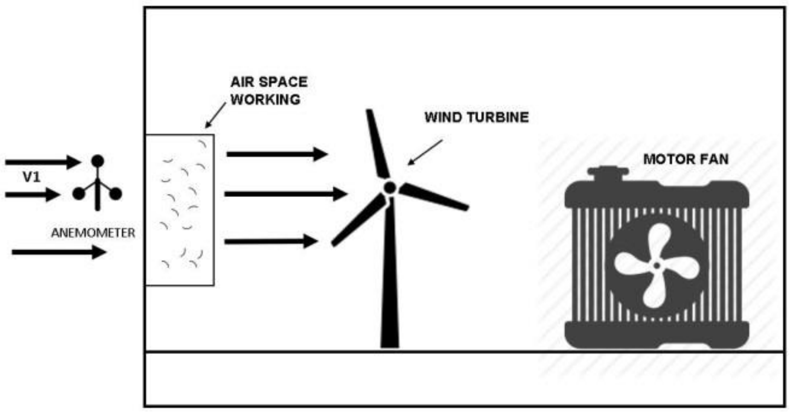

Figure 5. Schematic diagram of a wind tunnel

The wind turbines in this experiment have a blade diameter of 84 cm with a 105 cm tower height. The airfoil blade profile R1235 is specifically designed to create high lift force, which would make wind turbine to operate better in low-wind speed areas. The small-scale air compressor is mounted on top of the wind turbine to produce air pressure directly when the rotor blades are rotated. The experimental model configurations with the R1235 airfoil blade profile are shown in Figure 6.

Figure 6. Experimental models in the wind tunnel. Left: Two-blade wind turbine. Right: three-blade wind turbine.

3.2. Measurement Methods

The experimental data could be gathered by using measurement tools including an anemometer for measuring wind speed and a tachometer for measuring the rotational speed of the wind turbines, as shown in Figure 7. The wind speed could be adjusted by using the variable frequency drive of the fan motor. The tests were performed several times for measuring blade rotational speeds at different wind speeds.

Figure 7. Measurement methods

4. Results and Discussion

4.1. Variation of Power Production at Different Wind Speeds

Table 1 shows the theoretical calculations of available wind power, total power output and power output with compressed air loads. The power could be determined by using equations (3) and (4). The capacity of the power from the wind turbine used a power coefficient of 0.35. Also, the developed power of compressed air was determined by using efficient of 0.75.

Table 1. Variation of Power Production at Different Wind Speeds

Wind Speed (m/s)	Available Wind Power (Watt)	Power from Wind Turbine (Watt)	Compressed Air Power (Watt)
1	0.3394	0.1188	0.0831
2	2.7154	0.9504	0.6652
3	9.1647	3.2076	2.2453
4	21.7237	7.6033	5.3223
5	42.4291	14.8502	10.3951
6	73.3176	25.6611	17.9628
7	116.4256	40.7489	28.5242
8	173.7898	60.8264	42.5785
9	247.4469	86.6064	60.6244
10	339.4333	118.8016	83.1611

Figure 8 shows the different power production between available wind power, wind turbine power and compressed air power determined by using a theoretical equation. The available power in wind consists of higher power due to the power coefficient being neglected. However, it is impossible that the wind turbine would convert all the energy from the wind. Therefore, the wind turbine power showed that the power output results were decreased from the available wind due to the power coefficient of 0.35, which was applied in the equation to determine the actual power output of the wind turbines. Also, the compressed air load efficiency of 0.7 was applied, for which the power output from the compressed air would be decreased as an additional mechanical load was applied.

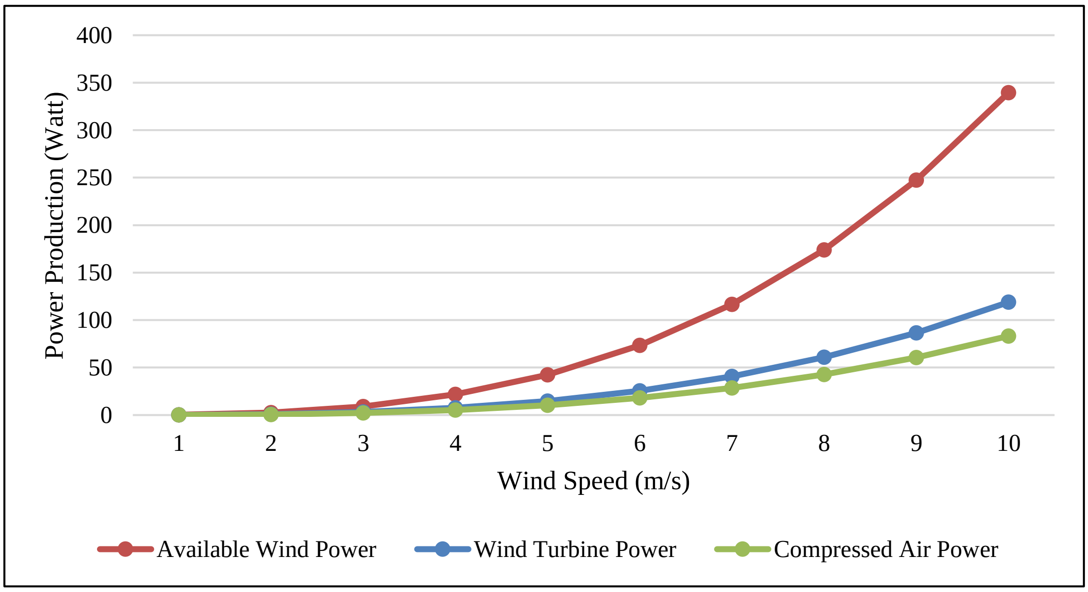

Figure 8. Power production vs. wind speed

4.2. Characteristics of R1235 Wind Turbine Blades

An R1235 airfoil blade profile was designed by Asst. Prof. Dr. Wirachai Roynarin specifically to operate in a low-wind speed area, in which the characteristics of the wind turbines are performed for high lift force with low Reynolds numbers. Figure 9 shows the comparison of C_P – TSR curve between the theoretical blade profile and the R1235 airfoil blade profile [13]. At point b to c of the curve, the data were obtained by experiment with the R1235 airfoil blade profile in the wind tunnel, while point a to b was estimated due to the incoming wind speeds being very low. Similarly, point c to d at the curve was estimated due to the limitation of the wind speeds being very high and the fixed load of compressed air load. The curve shows that theoretical airfoil blade performance dropped to zero at a TSR value of 10, while the R1235 airfoil blade profile was still operated due to the characteristics of the airfoil, which could extend the performance to a TSR value of 14 to reach zero C_P value.

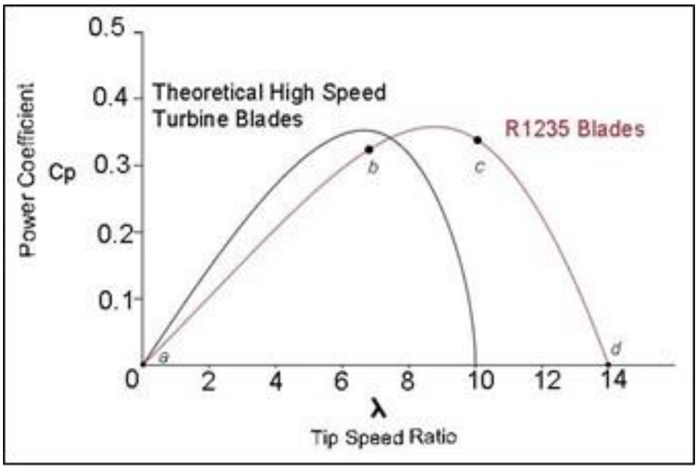

Figure 9. Comparison of the tip speed ratio between the theoretical and R1235 airfoil blade profiles

4.3. Two-Blade and Three-Blade Wind Turbine Experiment Results

The blade number of the wind turbines is a parameter to be considered for optimizing the performance of the wind turbines. The following tables represent the results obtained from the experiment in a wind tunnel with compressed air installed in the wind turbine.

Table 2 presents the two-blade wind turbine data. The wind turbine started to rotate at a wind speed of 5 m/s. The wind speed was increased gradually until it reached the maximum wind speed of 7 m/s due to the limitations and protecting the equipment from damage. The rotational speeds were increased as the wind speed increased with the maximum rotational speed of 1543 rpm achieved at 7 m/s. Also, the optimum TSR value of 10.11 occurred at 6 m/s.

Table 2. Two-blade wind turbine data

Wind Speed (m/s)	Rotational Speed (rpm)	Tip Speed Ratio
0	0	0
5	1006	8.86
5.5	1206	9.64
6	1380	10.11
7	1543	9.70

Table 3 presents the three-blade wind turbine data. The cut-in speed for the three-blade wind turbine was 3.5 m/s due to the higher blade number decreasing the wind speed to start rotating the rotor blades. The optimum TSR of 9.08 was reached at a wind speed of 5 m/s. The maximum rotational speed at 7 m/s was 1231, which was slower than the two-blade wind turbine. The results were obtained up to a maximum wind speed of 7 m/s to avoid risk to the equipment.

Table 3. Three-blade wind turbine data

Wind Speed (m/s)	Rotational Speed (rpm)	Tip Speed Ratio
0	0	0
3.5	576	7.24
4	714	7.85
5	1032	9.08
6	1086	7.96
7	1231	7.73

Figure 10 shows the comparison of C_P – TSR curve between two-blade and three-blade wind turbines. The two-blade wind turbine could reach higher TSR due to the rotational speed being faster than that of the three-blade wind turbine. However, the three-blade wind turbine could achieve the maximum TSR faster than the two-blade wind turbine, which is suitable for small wind turbines compressed air applications in low-wind speed areas.

From point *a* to *a'* and *b* to *b'*, both curves were plotted from the results obtained from the experiment in the wind tunnel. The remaining points such as *o* to *a* and *o* to *b* were estimated due to the low wind speed problems, so the points *a'* to *e* and *b'* to *f* were also estimated due to the higher wind speed and a fixed load of compressed air load.

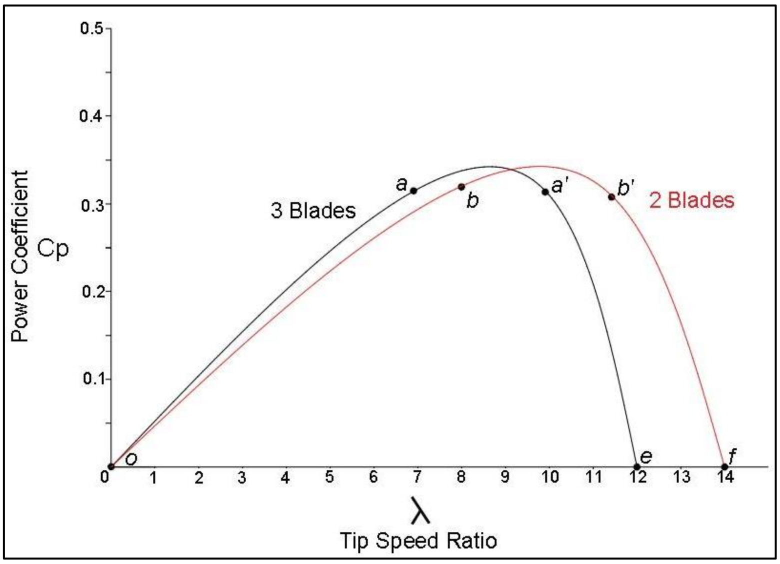

Figure 10. Two-blade and three-blade wind turbine curve performance

Conclusion

This paper aimed to investigate the influence of the number of blades on the performance of the compressed air wind turbine application. The two models of two-blade and three-blade wind turbines were tested in a wind tunnel with an R1235 airfoil blade profile equipped. The results showed that the blade numbers of the wind turbines influenced the performance of both wind turbine models. Two-blade wind turbine performance is higher than three-blade wind turbine performance in terms of rotational speed and TSR. However, the three-blade wind turbine is suitable for use in wind turbine compressed air applications in low-speed areas due to the lower cut-in speed at 3.5 m/s and lower wind speed reaching maximum TSR.

Further studies could be applied to the experimental models in a computational fluid dynamics (CFD) program to compare the results in the wind tunnel for more precise research. Also, more blades could be added to the wind turbine to investigate performance.

Acknowledgments
I would like to thank my team for supporting me and sharing his knowledge with me for this research. I would also like to thank Mr. Gerald Aguila for the laboratory results. I am deeply grateful to the team at the Energy Research and Service Center (ERSC) of the Engineering Faculty, RMUTT for providing the laboratory for the experiment. Finally, I would like to give all credit to my family who always supports me.

References

[1] Pasqualetti M and Gipe P 2004 History of Wind Energy. *Encyclopedia of Energy* ed C Cleveland (Amsterdam: Elsevier) pp 419-433
[2] Archer C and Jacobson M 2005 *Journal of Geophysical Research* **110** D12110
[3] Briggs H 2012 Low Wind Speed Design. *Advances in Wind Power* ed R Carriveau (London: IntechOpen Limited) chapter 11
[4] Intholo D 2012 *Study of Blade Efficiency Wind Turbine 10 kW Using Computational Fluid Dynamics Method* (Rajamangala University of Technology Thayaburi)
[5] Mühle F, Adaramola M and Sætran L 2016 *Journal of Physics Conference Series* **753** 032017
[6] Tong W 2010 Fundamentals of Wind Energy. WIT Transactions on State of the Art in Science and Engineering Vol 44 (Southampton: WIT Press) chapter 1 pp 3-48
[7] Ebeed M 2012 *Enhancement Protection and Operation of The Doubly Fed Induction Generator During Grid* Fault (South Valley University)
[8] Wagner HJ 2015 EPJ Web of Conferences **98** 04002
[9] Kalmikov A 2017 Wind Turbine Fundamentals. *Wind Energy Engineering* ed T Letcher (London: Elsevier) chapter 2 pp 17-24
[10] Ragheb M and Ragheb AM 2011Wind Turbines Theory – The Betz Equation and Optimal Rotor Tip Speed Ratio. *Fundamental and Advanced Topics in Wind Power* ed R Carriveau (London: IntechOpen Limited) chapter 2
[11] Dean J, Hotchkiss E, Kandt A and Robichaud R 2011 *Broad Overview of Energy Efficiency and Renewable Energy Opportunities for Department of Defense Installations* (Colorado: National Renewable Energy Laboratory)
[12] Aho J, Buckspan A, Laks J, Jeong Y, Dunne F and Pao L 2012 *the 2012 American Control Conference (Montreal)* (Tennessee: National Renewable Energy Laboratory)
[13] Manwell JF, McGowan JG and Rogers AL 2009 *Wind Energy Explained: Theory, Design and Application* (West Sussex: John Wiley & Sons Ltd)
[14] Natural Resources Canada 2016 *Compressed Air: Energy Efficiency Reference Guide* (Ottawa: Government of Canada)
[15] Bhatia A 2020 *Compressors and Compressed Air* (New York: Continuing Education and Development, Inc.)

ETM0003

Availability and Reliability Evaluation of Cooling System in Data Center: A Case Study of International Standard

S Koksungnoen[1], M Wiboonrat[2], and M Pimsarn[1,*]

[1, 2] King Mongkut's Institute of Technology Ladkrabang, 1 Soi Chalong Krung 1, Ladkrabang Subdistrict, Ladkrabang District, Bangkok, 10520, Thailand

* Corresponding Author: monsak.pi@kmitl.ac.th

Abstract. Technology growth, the internet of things, and the cloud systems has caused information use demand has been being to increase dramatically. The data center, then, has an important role to support and secure that data. When comparing the relative importance of the system components, the cooling system is a key infrastructure. Its availability is standardized by the various organizations - ANSI/BICSI 002, Uptime Institute, TIA-942, and ISO 22237. The standard recommendations show that when the system has more redundant components and distribution paths, which result in higher construction and maintenance expenses, availability can be increased. However, there is little evidence supporting those suggestions. To show the validity of these standards, we simulated efficiencies of cooling system models, based on the topology of ANSI/BICSI 002-2019, and the Uptime Institute criteria was used as a guideline. Data from IEEE Recommended Practice were adapted. Our simulations, consistent with extant published word, show that the cooling system factors, such as availability, reliability and downtime per year, can be improved by adding alternative components and paths as recommended.

1. Introduction

The emergence of various technologies, for example, data analytics, internet of things and mobile applications, has caused the amount of data usage to increase rapidly. Thus, many organizations have focused on places to manage this data, which results in an important role for data centers. The data center, therefore, is crucial for every sector operated to drive the societies, for example, e-commerce, financial services, education, and retail [1-4]. The electricity consumed by data centers was estimated at 7% in 2017, and to rise to 13% in 2030. In 2012, the annual growth rate of data centers was already 2.3% higher than the growth rate estimated for 2040 [4, 5]. From 2010 to 2016, the average outage cost of a data center increased by around 38%, or from $505,500 to $740,400 [1, 2] Historical data shows that a data center can significantly disrupt the revenue and reputation of various organizations if its performance is low [1, 2]. To efficiently construct and operate a data center, key factors, including availability, reliability and system topology, must be evaluated by effective criteria. Therefore, international standards, for example ANSI/BICSI 002 [6], Uptime Institute [7, 8], TIA-942 [9], and ISO 22237 [10], were written as guidelines and certifications for data center providers. For the importance of data center, which has various components, several researchers focused on its three main infrastructures, namely, information technology (IT), electrical, and cooling systems. For example, the reliability of IT topologies is studied in Couto RS et al. [11] and Ma X et al. [12]. For electrical infrastructure, Wiboonrat M [13] analyzed the trade-off between system reliability and costs following four tier criteria (from I to IV) by using data from IEEE Recommended Practice [14]. The electrical equipment arrangements between parallel and load-sharing system were demonstrated in Wiboonrat M [15], and rink anatomy was also demonstrated in Wiboonrat M [16].

The cooling system consumed about 40% of the energy for the whole system [4, 17]. In Capozzoli et al. and Anandan SS et al. research [18, 19], they showed that 55% of the electrical component failures were caused by high temperature. Consequently, the cooling system needs to be designed, operated, and maintained optimally to maintain acceptable temperatures. Therefore, Callou G et al. [20] examined five cooling architectures and discovered that the system can achieve suitable availability and downtime, by adding redundant components. However, the international criteria were not considered. Gomes DM el al. [21] evaluated the cooling system efficiencies based on TIA-942 standard in Tier I and Tier II. In Cheung H and Wang S research [22], they analysed the effects of different numbers in headers and redundant equipment arranged in cooling system. The four-tier cooling system standard and on-site components data were used for simulation. Results showed that redundant component could not be replaced with the additional headers and in Tier IV, the availability of configurations that have the number of main components or paths used to support a maximum load (N) in form of N+2 and 2(N+1) had insignificant value compared with a 2N and N+1 configuration. However, other system indices, for example, mean time to failure (*MTTF*) and mean time to repair (*MTTR*) were not considered.

As mentioned above, there has no research that evaluates the important indexes of the DC cooling system, such as availability, reliability, downtime, *MTTF*, and *MTTR*, in four tiers topologies, which are affected by the cooling components arrangements. Also, few numerical confirmations support the international standard suggestions for the system design. Therefore, this research studies the efficiencies of the cooling system models based on the topology of ANSI/BICSI 002-2019 [6] by using a guideline from the Uptime Institute criteria [7, 8]. The input data were extracted from IEEE Recommended Practice [14]. Our model was validated against previous work and can be used as a guide for designing cooling systems.

2. Problem Definition and Procedure

The details of data center cooling systems, including system index definitions, topologies, standards and numerical procedures, used here are described next.

2.1. Availability and Reliability Definition

We systematically investigated the availability, reliability and other indices for cooling systems. The performance must be investigated in the design phase, to assure that the system will operate continuously without any failures or the system can quickly recover when failures occur. The prediction of failures, for example failure frequencies, time to system failure and time to recover, help to achieve maximum system performance and minimum total product cost. Reliability is an attribute of a component or system working continuously, without damage under specified conditions, for example to a service life or lifecycle.

In general, the reliability, R, is involved with failure rate, λ and operating time, t, of the component. It can be expressed in exponential distribution as:

$$R(t) = e^{-\lambda t} \tag{1}$$

The failure rate, λ, is the inverse of the mean time to failure (*MTTF*) and can be calculated:

$$\lambda = \frac{1}{MTTF} \tag{2}$$

However, for a component with can be maintained or restored, when it fails, as the cooling systems here, the speed of system restoration to its operational status after failure measured in terms of availability.

The availability, *A*, and unavailability, *UA*, of a component can be calculated:

$$A(t) = \frac{UPTIME}{UPTIME+DOWNTIME} = \frac{MTTF}{MTTF+MTTR} = \frac{\mu}{\mu+\lambda} = 1 - UA \quad (3)$$

where *MTTR* is mean time to repair and μ is the repair rate:

$$\mu = \frac{1}{MTTR} \quad (4)$$

For a system linked by multiple components and operating together with some working function, the availability and reliability estimation for such a system depends on how components are connected.

In a series arrangement, the system becomes unavailable, when any component fails. The reliability, *R(t)*, and availability, *A(t)*, can be defined by:

$$R(t)_{series} = e^{-(\sum_{i=1}^{n} \lambda_i)t} \quad (5)$$

$$A(t)_{series} = \prod_{i=1}^{n} (\frac{\mu_i}{\lambda_i+\mu_i}) \quad (6)$$

In a parallel arrangement, the system can operate even if some components are unavailable. The overall reliability and availability are:

$$R(t)_{parallel} = 1 - \prod_{i=1}^{n} (1 - e^{-\lambda_i t}) \quad (7)$$

$$A(t)_{parallel} = 1 - \prod_{i=1}^{n} (\frac{\lambda_i}{\lambda_i+\mu_i}) \quad (8)$$

In a partial system, if the system consists of *n* parallel components, where at least *r* out of the *n* components are operating. The entire reliability and availability can be estimated by binomial distribution [23, 24]:

$$R(t)_{r\ out\ of\ n} = \sum_{i=r}^{n} C_n^i\ R(t)^i\ (1 - R(t))^{n-i} \quad (9)$$

$$A(t)_{r\ out\ of\ n} = \sum_{i=r}^{n}\ C_n^i\ \frac{\mu^i\ \lambda^{n-i}}{(\lambda+\mu)^n} \quad (10)$$

2.2. International Standards for Data Centers

The industry widespread standards, *i.e.* ANSI/BICSI and Uptime Institute, which are used for assuring a design, construction and operation, were applied here. The Uptime Institute divides the infrastructure into site levels, called “tier classification”, by specifying performance and topology criteria. The higher tier levels, from I to IV, have more redundant components and distribution paths [7, 8]. ANSI/BICSI defines the site level into classes F0 to F5. A system, that works, with a single loading path, without UPS, is classed as class F0, while classes F1 to F5 have similar characteristics to tier I to IV. The ANSI/BICSI standard also covers other sections in data centers, for example, space planning, site selection, architecture, *etc.* [6]

2.3. Cooling System Topologies

In general, a water-cooled system consists of a cooling tower, cooling water pump, chiller, chilled water pump and Computer Room Air Handler (CRAH). Here, an *N*=1 system was assumed to support cooling demand, using one unit of cooling tower, cooling water pump, chiller, chilled water pump and two units of CRAH. For temperature and humidity control, the hot air produced by the IT equipment in the server room was absorbed by the cold air blown from cool water in the CRAH. Then, the water remaining after the absorption was then sent to the chiller and cooling tower to discharge the heat into the atmosphere. In the cycle, the water was sent back to chiller, using the cooling water pump, and to the CRAH, using the chilled water pump. The models for the cooling system configurations, followed ANSI/BICSI 002-2019 [6], and are presented in Figure 1, where the numbers in each box refer to the numbers of sub-components in Table 1.

2.4. Typical Data and Procedure for System Assessment

To calculate the entire cooling system efficiency, the failure and repair factors of sub-components are needed. The *MTTF* and *MTTR* of sub-components were obtained from the IEEE Recommended Practice [14] and Cheung H and Wang S [22] and the failure and repair rates, solved using Equation (2) and (4), are set out in Table 1. Table 2 presents the numbers of sub-component in each main component.

Simulation randomized the component failure probability. There were *N* system components, and each one was randomly chosen to fail. The simulation was run until the outcomes converged. Then, we inferred the system failure probability, *i.e.* the unavailability. The availability was 1-unavailability, as in equation (3).

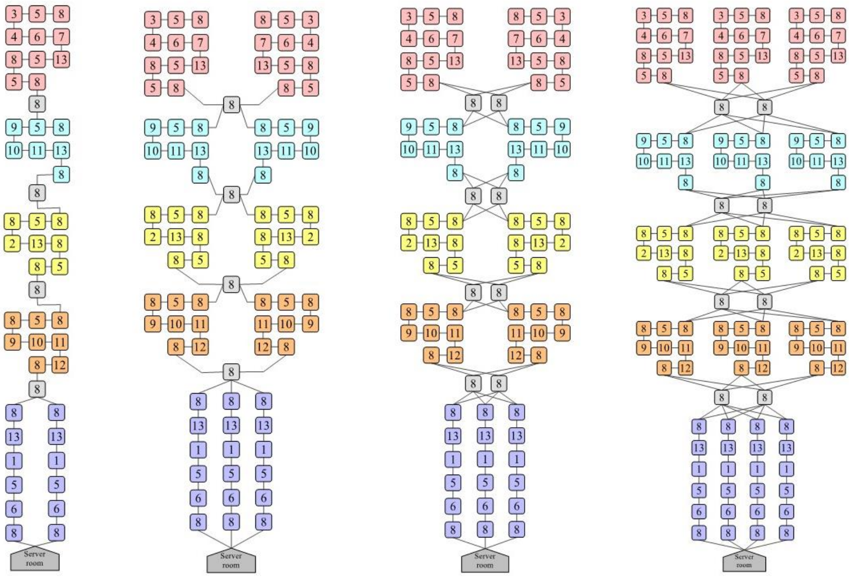

(a) Tier I (b) Tier II (c) Tier III (d) Tier IV

Figure 1. Models for data center cooling system configurations

Table 1. The *MTTF*, *MTTR*, failure rate (λ) and repair rate (μ) of sub-component.

No.	Sub-component		MTBF (hr)	MTTR (hr)	Failure rate (λ)	Repair rate (μ)
	Name	Description				
1	Air handling unit	Air-handling unit, non-humid wo/drive	796,075.20	2.360	1.256×10^{-6}	0.424
2	Chiller machinery	Chiller, centrifugal, 600 tons to 1000 tons	190,872.10	14.520	5.239×10^{-6}	0.069
3	Cooling tower fan blades	Fan tube axial	866,290.90	7.910	1.154×10^{-6}	0.126
4	Cooling tower housing	Cooling tower evaporative type	1,504,800.00	16.670	6.645×10^{-7}	0.060
5	Electric control valve	Valve operator, electric	885,794.00	18.420	1.129×10^{-6}	0.054
6	Fan motor	Motor, electric, induction, <=600 V	791,448.00	1.000	1.264×10^{-6}	1.000
7	Fan variable-speed drive	Drive, adjustable speed	396,929.09	16.550	2.519×10^{-6}	0.060
8	Piping	Piping, refrigerant, 1 in to 3 in, per 100 ft	3,104,080.00	10.670	3.222×10^{-7}	0.094
9	Pump housing	Pump Centrifugal	1,507,638.00	6.750	6.633×10^{-7}	0.148
10	Pump inverter	Inverters, all types	1,817,016.00	26.000	5.504×10^{-7}	0.038
11	Pump motor	Motor, electric, single phase, >5 A	6,037,872.00	3.000	2.656×10^{-7}	0.333
12	Pump variable-speed drive	Drive, adjustable speed	396,929.09	16.550	2.519×10^{-6}	0.060
13	Switchgear control panel	Control panel, switchgear controls	446,426.20	1.270	2.240×10^{-6}	0.787

Table 2. Main and sub-components.

Components	Sub-component
Cooling tower	Cooling tower housing×1, Fan motor×1, Fan variable-speed drive×1, Electric control valve×3, Switchgear control panel×1, Piping×3
Cooling water pump	Electric control valve×1, Piping×2, Pump housing×1, Pump inverter×1, Pump motor×1, Switchgear control panel×1
Chiller	Chiller machinery×1, Electric control valve×2, Piping×4, Switchgear control panel×1
Chilled water pump	Electric control valve×1, Piping×2, Pump housing×1, Pump inverter×1, Pump motor×1, Pump variable-speed drive×1, Switchgear control panel×1
CRAH	Air handling unit×1, Electric control valve×1, Fan motor×1, Piping×2, Switchgear control panel×1

The cooling system were studied assuming:

i. In the beginning, all components were new.
ii. For the active alternative system, one was in active state while the other was in standby state. when the active component/path failed, it was repaired immediately, while the standby component or path was swapped into the active state by switching within 60 seconds and probability of 0.9. After the failed component or path was repaired, it turned into the active component or path again. Component or path 1 had a higher repair precedence, than other when both components or paths failed.
iii. For simultaneously active or load-sharing systems, both components or paths will work simultaneously. When the work load changed, both components or paths shared the load so that they could handle the total load, for example, 50%-50% or 70%-30%. When one component or path failed, the other handled the total load.
iv. The failure and repair rates were constant, the reliability was an exponential distribution and sub-components were connected in series for each major component.
v. Efficiencies were calculated at a resolution at 0.0001, the number of iterations was 5000, simulations covered 8760 hours at 1 hour time steps.

3. Results and Discussion

To evaluate the cooling system efficiency, their sub-component factors in Table 1 were used.

3.1. Model Verification

Our study was validated against the system of Cheung H and Wang S [22], the *N* cooling system (*N*=4), see Table 3, with consistent system indices, differing by 1.7% in reliability and 0.03% in availability due to some errors that may generate from the numerical scheme differences. From this relation, it is worth noting that the models employed in this paper are stable and reliable.

Table 3. Model verification.

System indexes	Previous work [22]	This research	Percentage Difference
Reliability	4.426%	4.500%	1.658%
Availability	99.679%	99.709%	0.030%

3.2. Effects of Redundancy and Distribution Path

We simulated cooling systems modelled as *N*, *N*+1, *N*+2, and *N*+3 following recommendations [6-8] to study the effect of the increase in alternative components and paths. The results for a one-year system operation are shown in Table 4. The output indices show that when the system had more components to carry the cooling load from *N* to *N*+1, the overall system performance improved. The system reliability and availability increased, while the downtime and *MTTF* decreased. Adding more redundant components from the *N*+1 to *N*+2 system, all index values remained constant, consistent with the work of Cheung H and Wang S [22].

Table 4. Effects of increasing the number of redundant component and distribution paths.

	N	***N*+1**	***N*+1**	***N*+2**	***N*+2**	***N*+3**
Capacity components	*N*	*N*+1	*N*+1	*N*+2	*N* after any failure	*N* after any failure
Distribution paths	*N*	*N*	1 Active – 1 Alternate	1 Active- 2 Alternate	2 simultaneously active	3 simultaneously active
Availability (%)	99.958	99.996	99.996	99.996	99.999	99.999
Reliability (%)	73.940	74.820	75.360	75.360	99.960	99.960
Total Downtime (hr)	3.657	0.371	0.360	0.360	0.003	0.003
MTBF (Uptime) (hr)	29,129.550	30,670.970	30,843.801	30,843.801	21,899,992.270	21,899,992.270
MTTR (hr)	12.166	1.285	1.256	1.256	7.728	7.728

Remark: *N* is the number of main components or paths used to support a maximum load.

When adding distribution paths, the *N*+1 system with and without an alternative path, it can be seen that the system, with an alternative path, gains in *MTBF* by 172.8 hrs, while other values were slightly changed. Further, the index values remained unchanged, even after adding more alternative paths from *N*+1 to *N*+2 systems.

For simultaneously active or load-sharing in the *N*+2 system, it achieved the highest availability (99.999%), reliability (99.960%) and lowest downtime (0.0031 hrs). *MTTR* was slightly higher than in the active-alternative system, while significantly increasing *MTBF*, after joining more sharing paths, to become the *N*+3 system, all indices were unchanged. It can be seen that all indices in the simultaneously active system had better efficiency.

3.3. *Availability and Reliability Compare to Standard*

To validate the Uptime Institute criteria [7, 8], the indices of system efficiency from varying cooling component arrangements, recommended by ANSI/BICSI 002-2019 [6] were investigated -see Table 5, which demonstrates that the availability and downtime computed here were closely consistent with values from the Uptime Institution.

Table 5. Comparison with Uptime Institute criteria.

Tier		**Description**	**Availability (%)**		**Downtime (hrs.)**	
			The criteria [7, 8]	**This research**	**The criteria** [7, 8]	**This research**
I	*N*	Capacity components: *N* Distribution paths: *N*	99.671	99.958	28.800	3.657
II	*N*+1	Capacity components: *N*+1 Distribution paths: *N*	99.749	99.996	22.700	0.371
III	*N*+1	Capacity components: *N*+1 Distribution paths: 1 Active - 1 Alternate	99.982	99.996	1.600	0.360
IV	*N*+2	Capacity components: N after any failure Distribution paths: 2 simultaneously active	99.995	99.999	0.417	0.003

Conclusion

A data center cooling system design, that complies with international standards, is essential to satisfy users. We found that by increasing the number of redundant components and distribution paths according to the recommendations of the ANSI/BICSI 002-2019 topologies and using sub-component data in IEEE Recommended Practice, system performance was improved to meet all four tier criteria of the Uptime Institute standards, both for availability and downtime. However, in practical situations, the cooling system consists of various components, complex arrangement and several operations. For future research, the trade-offs between cooling system reliability and cost, complexity of the system, and the different cooling technologies will be considered.

Acknowledgments

This work was supported by King Mongkut’s Institute of Technology Ladkrabang, Thailand.

References

[1] Institute P 2016 Cost of data center outages. *Data Center Performance Benchmark Series*.
[2] Wiboonrat M 2020 Human Factors Psychology of Data Center Operations and Maintenance 2020 6th *Int. Conf. on Information Management (ICIM)*. p 167-71
[3] Jones P, Hillier D, Comfort D 2013 Data centres in the UK: property and planning issues. *Property Managemen*t.
[4] Avgerinou M, Bertoldi P, Castellazzi L 2017 Trends in data centre energy consumption under the european code of conduct for data centre energy efficiency. *J. Energies*.10(10):1470.
[5] Andrae AS, Edler T 2015 On global electricity usage of communication technology: trends to 2030. *Challenges*.6(1):117-57.
[6] Standards BI 2019 ANSI/BICSI 002-2019 Data Center Design and Implementation Best Practices BICSI
[7] Institute U 2018 Data Center Site Infrastructure Tier standard: Topology The Uptime Institute, LLC
[8] Turner WP, Seader JH, Brill KG. Industry standard tier classifications define site infrastructure performance. Santa Fe, NM: *Uptime Institute*; 2005.
[9] Association TI 2010 TIA-942 Telecommunications Infrastructure Standard For Data Centers. Arlington Virginia: Telecommunications Industry Assn.
[10] Infrastructures IT-DCFa 2018 ISO/IEC TS 22237-7:2018
[11] Couto RS, Campista MEM, Costa LHM 2012 A reliability analysis of datacenter topologies 2012 *IEEE Global Communications Conference (GLOBECOM)*. vol p 1890-95
[12] Ma X, Liu B, Yang L, Peng R, Zhang X 2020 Reliability analysis and condition-based maintenance optimization for a warm standby cooling system. *J. Reliab. Eng. Syst. Saf*.193:106588.
[13] Wiboonrat M 2019 Data Center Investment vs. System Reliability in Power Distribution Systems *Conf. on SoSE*. vol p 146-51
[14] Heising C IEEE recommended practice for the design of reliable industrial and commercial power systems.
[15] Wiboonrat M 2012 System reliability of fault tolerant data center *The 5th Int. Conf. on Communication Theory, Reliability, and Quality of Service*. vol p 19-25
[16] Wiboonrat M 2008 Risk anatomy of data center power distribution systems 2008 *IEEE Int. Conf. on Sustainable Energy Technologies*. vol p 674-79
[17] Ni J, Bai X 2017 A review of air conditioning energy performance in data centers. *Renewable Sustainable Energy Rev*.67:625-40.
[18] Capozzoli A, Primiceri G 2015 Cooling systems in data centers: state of art and emerging technologies. *J. Energy Procedia*.83:484-93.
[19] Anandan SS, Ramalingam V 2008 Thermal management of electronics: A review of literature. *J. Therm. Sci*.12(2):5-26.
[20] Callou G, Maciel P, Tutsch D, Araújo J 2012 Models for dependability and sustainability analysis of data center cooling architectures *IEEE/IFIP Int. Conf. on Dependable Systems and Networks Workshops (DSN 2012)*. p 1-6
[21] Gomes DM, Endo PT, Gonçalves G, Rosendo D, Santos GL, Kelner J, et al. 2017 Evaluating the cooling subsystem availability on a cloud data center 2017 *IEEE Symposium on Computers and Communications (ISCC).* p 736-41
[22] Cheung H, Wang S 2019 Reliability and availability assessment and enhancement of water-cooled multi-chiller cooling systems for data centers. *J. Reliab. Eng. Syst. Saf.*191:106573.
[23] Smith DJ. *Reliability, maintainability and risk: practical methods for engineers*: Butterworth-Heinemann; 2017.
[24] Bourouni K 2013 Availability assessment of a reverse osmosis plant: comparison between reliability block diagram and fault tree analysis methods. *J. Desalination*.313:66-76.

ETM0008

Development of Must Flow Dryer for shallot (Allium ascalonicum) Processing

Arnon Amornnantasiri[1], Duangrat Shuwisitkul[2] ,Pracha Bunyawanichakul[3]*

[1,3]Research Center of Agricultural Engineering and Product Design, Department of Mechanical Engineering, Faculty of Engineering, Srinakharinwirot University, Ongkharak District, Nakornnayok Province 26120

[2]Department of Pharmaceutical Technology, Faculty of Pharmacy, Srinakharinwirot University, Ongkharak District, Nakornnayok Province 26120

* Corresponding Author : prachabu@g.swu.ac.th

Abstract. Today several drying methods are used in agricultural production. In present, they cannot reduce moisture content at the same level for all and use the long time for batch type dryer. Then shallot have moisture at the level for growth of bacteria, fungi and yeast. Therefore, this research aims to develop Must Flow Dryer for shallot. This type of dryer is able to reduce the moisture content at the same level in the short time. Shallot sliced 1-3 mm thickness are the raw material for the drying test with Must Flow Dryer. The present work aimed on one hand to study of the drying of shallot which was evaluated variable temperature at 50 ˚C, 60 ˚C and 70 ˚C and air flow rate of 0.30, 0.35 and0.40 m^3/s is used to remove the water evaporated from fresh shallot to the final moisture content of <10 %db. As a result of the shallot slices dried under different air temperature and air flow rate at the best condition at temperature 70 ˚C and air flow rate 0.30 m^3/s final moisture content at 5.2%db. The drying of shallot slices exhibited drying to have taken place in falling drying rate period. The drying rate was significantly influenced by air temperature and air flow rate. The drying time increased with increases in air velocity at all air temperature applied, however it decreases with increase in air temperature. Must Flow Dryer had better drying rate and shorter drying period. Dried sample, that means the product was superior in quality. There is good scope of producing a good quality dried shallot slices suitable for preparing essential extracts for acne treatment product.

1. Introduction

Shallot is normally used as food and medicine products. Shallot extract can anti bacteria that cause of acne. An important substance is quercetin that can reduce inflammation. Therefore, shallots are able to development into acne treatment drug. The development of shallot extract required appropriate drying process to maintain the essence substance. As well as the storage period of raw materials. The drying process is an important step in the preparation of the extraction of shallot essential extract. Must flow dryer had been developed for fast drying of paddy[7,8]and it suitable for herbal drying applications that require to maintain an essence substance that not to be lost during drying.

To reduce operating cost and drying time, and increase drying capacity, therefore, Must Flow Dryer would be proposed in this study. The objectives were to investigate parameters affecting the drying characteristics of shallot slices. Thus, Must Flow Dryer for paddy drying was developed to be able to dry shallot slices for essential extraction.

Drying experiments of shallot slices at different inlet air temperature and air flow rate was conducted to investigate its drying rate for the lowest final moisture content and longer storage period.

2. Material and method

Shallot are tubers from the bulb of monocotyledons. Scientific name is Allium ascalonicum L. in the family Alliaceae. Shallots are formed from leaf sheaths arranged layers (layer bulb) is the storage area for food and is the place where the roots. Fresh shallot slices thickness 1-3 mm were used as an experimental feed material. Shallot slices with initial moisture contents of 80-90 % wb. was dried at different inlet drying air temperatures of 50 ˚C, 60 ˚C and 70 ˚C and specific air flow rate of 0.30, 0.35 and 0.40 m^3/s [2]in order to study the effect of inlet drying air temperature, effect of air flow rate on drying rate.[3]

Must Flow dryer is a continuous system used in this study[6-8] consists of a rectangle drying chamber in 20 cm width 100 cm length and 30 cm height and grate drilling hole of 2 mm diameter. LPG burn is used as heat source. Components of Must flow Dryer shown in Figure.1. The hot air was supplied into the drying chamber to mix with an ambient air and then suck through the layer of shallot slices by blower on the top of drying chamber. The drying temperature and air flow rate will be adjusted during drying experiments. The shallot slices fall from the hopper vertically and move horizontally on the air distributor plate to exchange heat and transfer mass to hot air. Suction blower will pull hot air and moisture away from the drying chamber during shallot slices travelling along the surface of air distributor plate in the drying with cross flow movement. A falling-rate period where moisture movement is controlled by internal resistances.[1] Finally, dried shallot slices with low moisture will skips over the weir and fall into the drying chamber discharge port.

Schematic diagram of the overall experimental apparatus is shown in Figure 1 are 1) Heat Source 2) Distributer Plane 3) Drying Chamber 4) Feed valve 5) Hopper 6) Hot Air Chamber 7) Weir 8) Port 9) Cover Chamber 10) Suction Blower.

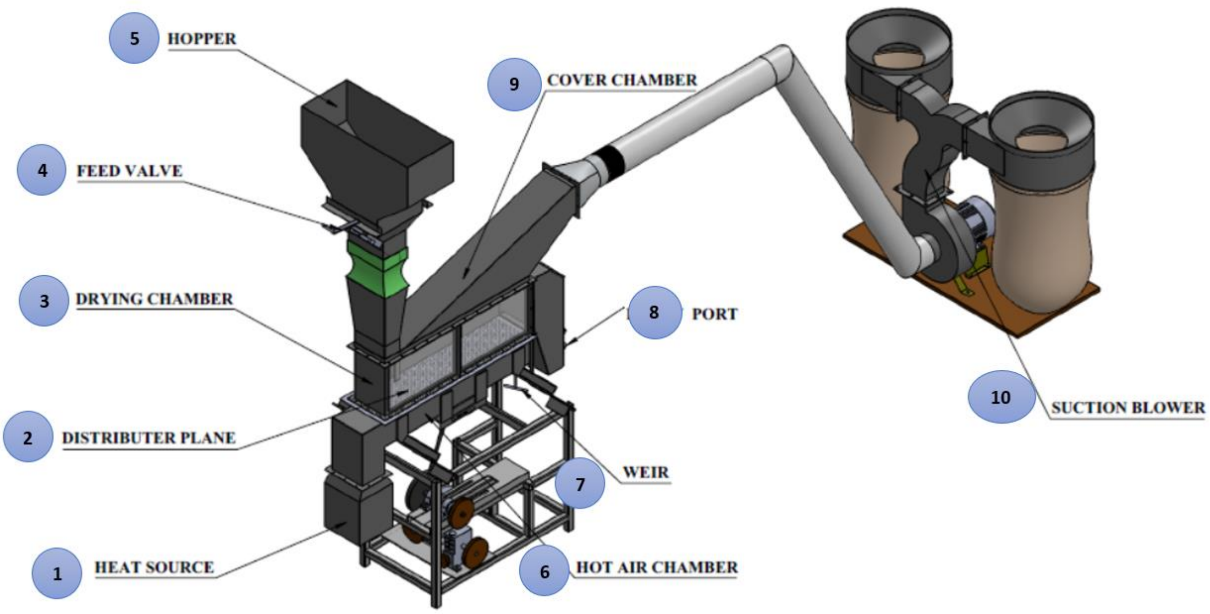

Figure 1. Schematic diagram of Must Flow Dryer.

During drying process is keep sampling every 15 minutes from port of drying chamber to investigate their moisture content. The inlet air temperature measuring are were shown in Figure.2, temperatures were measured 10 position (A,B,C,D,E,F,G,H,I,J) by a thermocouple type K connected to a data logger (accuracy ±1 ˚C). Air Flow Rate were measuring are were shown in Figure.2, air flow rate 1 position (K) by a hot wire anemometer (accuracy ±5%) in center of air duct outlet. Drive unit and suction blower motors was control by inverter. An electrical power was measured by electrical power meter.

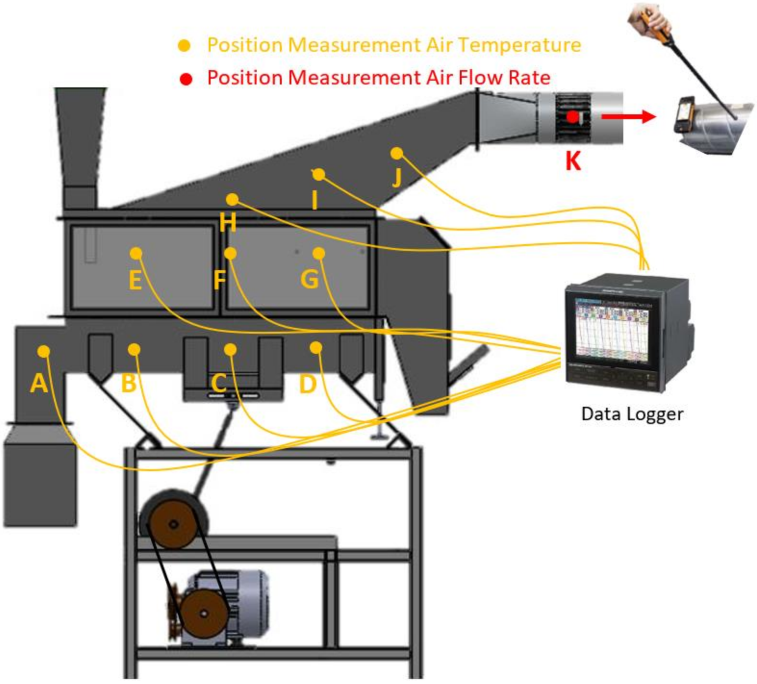

Figure 2. Measurement the air flow rate and air temperature in the chamber of Must Flow Dryer.

The proposed process is Must Flow dryer is expected to dry of fresh shallot in short time period without damage. The advantage of this process are able to reduce the energy consumption. It also concern the quality of shallot. Feature of Must Flow dryer. The hot air flow from LPG burner through the shallot layer and leaves at the top of chamber through the hopper unit. The high moisture content shallot fed into the drying chamber and controlled by feed valve. The dried shallot is fed from the chamber by discharge valve. The beginning stage of drying process is mainly involved in heat transfer which is able to separate into 3 phases namely preheat, moisture content discharge, and moisture content blowout. The overall process takes time 90 second. The heat transfer process is derived from the thin layer theory. The hot air vertical flow is force to flow through the layer of shallot. Fresh shallot is slowly fed forward and be sorted by density and porosity of shallot layer. Heat transfer and moisture releasing are appearance completed vertically. Relative velocity between hot air and shallot inside Must Flow dryer is very high so that moisture content is removed continuously at very high rate in the chamber while the hot air as well as moisture content flow throughout the chamber's section. Shallot is lifted and dropped in relative to the moving forward direction because the moisture shallot will drop to the below of grill. The relative velocity drop is very high in short residence time. All is forced to move forward by the particular temperature strictly control at mention above. The hot spot phenomenon is rarely occurring. The moisture content is controlled well then the growth of micro-organism, fungus and bacteria is limited.

3. Result and discussion

The data collected on loss in the moisture content with elapsed time were analyzed to study the drying behavior of the product and also the effect of operational parameters on the drying characteristics was analyzed and presented below.[4,5]

3.1. Effect of air temperature

The drying curves of shallot slices at air flow rate of 0.30 m^3/s air temperatures of 50, 60 and 70 ˚C are shown in Figure3. The drying curves are typical to ones for food stuffs, i.e. moisture content of shallot slices decreased exponentially with elapsed drying time. As the air temperature increased, other drying conditions being same, the drying curves became steeper indicating higher moisture removal rates thus resulted into substantial decrease in drying time (t). Due to shallot is forced to move forward by principle of Must Flow Dryer is very high so that moisture content is removed continuously at very high rate in the drying chamber while the hot air as well as moisture content flow throughout the chamber's section. The hot spot phenomenon is rarely occurring. At air flow rate of 0.30 m^3/s, drying time for the shallot slices at air temperature of 50, 60 and 70 ˚C were about 15,30,45,60 and 90min, respectively. Similar drying trends were observed at air flow rate of 0.35 and 0.4 m^3/s. The testing conditions of the Must Flow dryer shows in Table1.

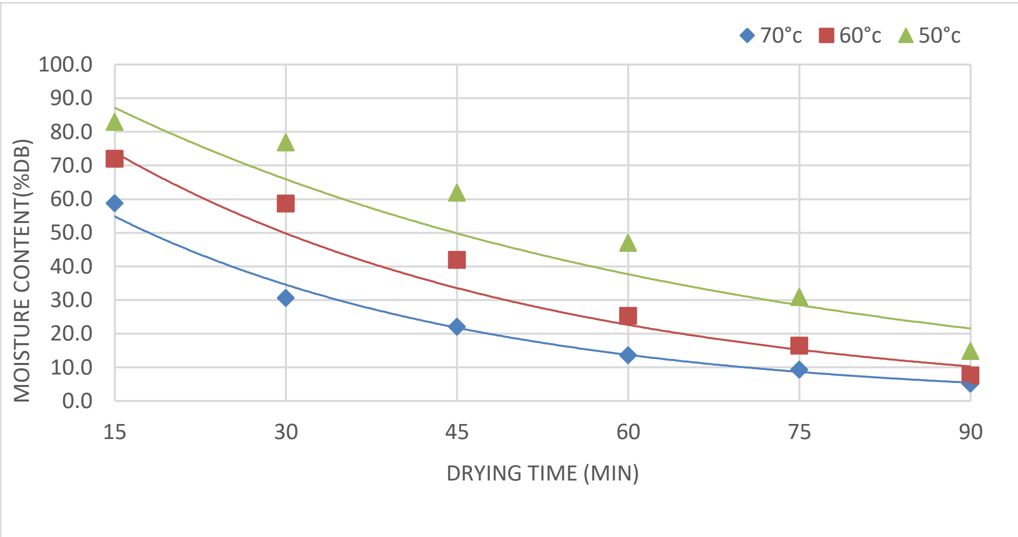

Figure 3. Drying curves for shallot slices at various air temperatures at air flow rate 0.30 m^3/s.

3.2. Effect of air flow rate

The air flow rate also influenced the drying time of the shallot slices as shown in Figure.4 At a given air temperature an increase in air flow rate increased the drying time i.e. and decreased the moisture removal rate. The moisture content at any time was found to be a little higher with higher velocity. Due to principle of Must Flow Dryer is use low air flow rate that can carry heat and moisture to outside of the drying chamber which is an advantage thus saving energy. But if using a high air flow rate the air flow carries the heat inside the drying chamber while the heat and mass transfer between hot air and shallot. As a result it takes more time for drying.The drying time for the shallot slices at air flow rate of 0.30 m^3/s, air temperature of 60 ˚C when air flow rate was increased to 0.35 m^3/s, the other parameters being unchanged. The increase in air flow rate accelerated the cooling effect, reducing the temperature at the surface of product thus the water vapor pressure or the moisture driving force. Carried out to see the effect of process variables on the drying time of shallot slices revealed that air flow rate and air temperature had a significant effect on the drying time a result of drying. The testing conditions of the Must Flow dryer shows in Table1.

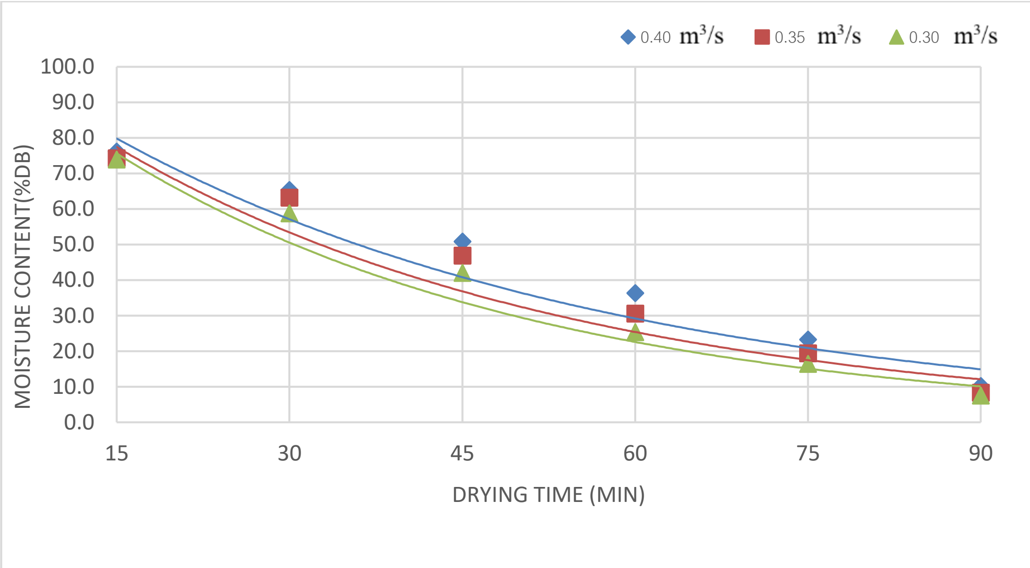

Figure 4. Drying curves for shallot slices at various air flow rate at air temperature 60°C.

Figure 5. Sliced shallot after the drying
at condition temperature 70 ◦C and air flow rate 0.30 m^3/s by Must Flow Dryer

Table 1. A Result of drying condition.

Drying Condition		Moisture Content	
Temperature(°C)	Air flow rate(m^3/s)	Initial Moisture (%db.)	Final Moisture (%db.)
50	0.30	89.0	14.9
	0.35	87.3	15.2
	0.40	88.8	16.1
60	0.30	85.3	7.6
	0.35	85.3	8.3
	0.40	87.0	10.2
70	0.30	89.0	5.2
	0.35	87.9	5.5
	0.40	85.1	5.7

From Table1. Shows a result of moisture content separate by each test condition for the Must Flow Dryer drying test the shallot 1 kg takes 90 min of drying time per condition. According to the data found it can be seen that temperature is 70 °C reduce moisture better at all levels and air flow rate 0.30 m^3/s reduce moisture better at all levels. So, The best condition at temperature 70 °C and air flow rate 0.30 m^3/s and final moisture content at 5.2%db. Can reduce moisture up to 83.8 %db within 90 min.

4. Conclusion

The drying of shallot slices exhibited drying to have taken place in falling drying rate period. The drying rate was significantly influenced by air temperature and air flow rate. The drying time increased with increases in air velocity at all air temperature applied, however it decreases with increase in air temperature. The shallot slices dried under different air temperature and air flow rate at the best condition at temperature 70 °C and air flow rate 0.30 m^3/s and final moisture content at 5.2%db. using Must Flow Dryer had better drying rate and shorter drying period compare to batch tray dryer dried sample, that means the product was superior in quality. There is good scope of producing a good quality dried shallot slices suitable for preparing essential extracts for acne treatment product.

Acknowledgments

This research received a scholarship. 70 Years 70 scholarship return to society scholarship from Graduate School Srinakharinwirot University of the year 2019 and a research grant from the National Higher Education Science Research and Innovation Policy Council (NXPO) Contract No.C10F630025 Project Code. 10040 Thank the Department of Mechanical Engineering Faculty of Engineering Srinakharinwirot University and Department of Pharmaceutical Technology, Faculty of Pharmacy, Srinakharinwirot University for support the implementation of this research.

References

[1] Han, W., B. Mai, and T. Gu.1991 "*Residence time distribution and drying characteristics of a continuous vibro-fluidized bed*. *Drying Technology*", Vol. 9(1),p159–181.
[2] P.N. Sarsavadia. 1999 "*Drying behaviour of brined onion slices," Journal of Food Engineering*, vol. 40, p. 219-226.

[3] M. K. Krokida. 2003 "*Drying kinetics of some vegetables," Journal of Food Engineering*, vol. 59, p. 391-403.
[4] G.P. Sharma, R.C. Verma, Pankaj Pathare. 2005 *"Mathematical modeling of infrared radiation thin layer drying of onion slices," Journal of Food Engineering*, vol. 71, p. 282–286.
[5] G.P. Sharma a, R.C. Verma a, P.B. Pathare. 2005 "*Thin-layer infrared radiation drying of onion slices," Journal of Food Engineering*, vol. 67, p. 361-366.
[6] Tuynaak P., Chuchonaak M., Yapha M. and BunyawanichakulP.2013 "*Influence of flow rate and temperature of hot air to moisture content reduction of paddy (case study of Must Flow paddy dryer)*", MEnett 27th DhusitThani, PattayaChonburi, October 16-18.
[7] Yapha M. and Bunyawanichakul P 2014 "*Must Flow Dryer for coarse Rice*", the 13th conference an energy heat and muss thermal equipment and process ChaolaoCabana, Chenthaburi, March 13-14.
[8] Yapha M. and Bunyawamchakul P 2014 "*Must Flow Dryer for Rough Rice*", The second International conference on Green computing Technology and Innovation, Asia Pacific University of technology and Innovation, p. 26-30.

ETM0017

Study on Influence of Wire Mesh Stainless Porous Material for Lingzhi Mushroom Hot Air Drying

Kompet inla[1], Bundit krittacom[2], Pathiwat Waramit[2] and Ratinun Luampon[2,*]

[1] Mechanical engineering Faculty of Agriculture and Technology
[2] Mechanical engineering Faculty of Engineering and Architecture
Rajamangala University of Technology Isan 744 Suranarai Road, Muang,
Nakhon Ratchasima 30000, Thailand

* Corresponding Author: E-mail: ratinun.lu@rmuti.ac.th

Abstract.The objective of this research is to study the influence of wire mesh stainless porous material for Lingzhi mushroom (Ganoderma Lucidum) with hot air drying. Lingzhi mushroom is a drying product and slice at 3 mm thickness. In the experiment LPG burner is a heat source for maintaining hot air temperature at 70 °C, hot air is flowing through wire mesh stainless porous material at a velocity of 2 m/s before flow into the drying chamber with Pores Per Inch (PPI) is 6, 8 and 12 PPI and wire mesh stainless porous material layer is (W_L) 4, 8 and 12 layers. The results are collected in a data logger at intervals of 5 minutes until the final moisture content reaches 12 %w.b. The variables use in this study are consist of Wet basis moisture content (M_w), Drying rate (R), and Specific energy consumption (SEC). From experimental results, there are shown that the moisture content is decreased, and the drying rate increases with increase PPI and W_L and decreases SEC. Drying time is shortest and SEC was lowest at PPI = 8 and W_L = 12. The SEC can reduce to 26.18% when compared with the drying without wire mesh stainless porous material.

Keywords: Lingzhi mushroom, Wire mesh stainless porous material, Moisture content, Drying rate, Specific energy consumption

1. Introduction

The problem of shortage and rising energy prices are important for the economy has one of the main mechanisms for national development in various fields of the country because of the amount of energy demand in various fields. An increase every year by the agricultural is the drying industry group. To process and increase product value has one group that should promote energy conservation in the production process to reduce energy costs. Lingzhi mushroom (Ganoderma Lucidum) is a popular agricultural product with high value because Lingzhi mushroom contains many nutrients that may be beneficial to health such as various fibers, proteins, carbohydrates, fats, vitamins, and certain minerals such as calcium, potassium, phosphorus, magnesium, selenium, iron, zinc, copper, important biological molecules such as Stearate, Steroids, Terpenoids, Phenols, Nucleotides, Glycoproteins, Polysaccharides and other derivatives, especially Amino acids, Lysine and Leucine suitable for the production of tonic or medicine. Due to its high nutritional value and contains antioxidants. The packaging is a very important factor that should be a package that can prevent moisture well because moisture can cause the fungus to grow and Lingzhi mushroom is quite sensitive to moisture. Currently, the rate of cultivating by Lingzhi mushroom is higher, therefore causing some mushrooms to spoil due to improper storage. In most cases, each type of mushroom will rot in 24 hours at room temperature and 5-7 days when stored in the cold. Motevali et al. [1] Most farmers are storing agri-product with drying to increase benefits and prevent nutritious to have a high market value. Singh at al. [2] The packaging is one factor that should be a package that can prevent moisture because fungus and bacteria can grow up if high moisture and the Lingzhi mushroom is quite moisture-sensitive. Olufayo et al. [3] Therefore, drying to a safe moisture level before packaging is an important way to extend shelf life and increase the value of Lingzhi mushroom.

Currently, there are many drying methods that drying products have high efficiency but also have a high energy consumption rate. Camila et al. [4] The principle of drying agricultural products is to reduce the moisture content of the product to a level that can be stored for a long time. Huang et al. [5] Drying is a process that requires heat has a relatively high-power consumption. There are many methods of agricultural product rehydration such as sun drying, hot air drying, superheated steam drying, Infrared radiation drying, and heat pump drying. Ausra et al. [6] The drying method that most people use is sun drying because it is heat energy derived from nature, no charge, and can be used for a long time. Kuanpradit et al. [7] but the current environment of Thailand found that it is very different from the past. The hot weather has a rather long period. The rainy season and winter have changed a lot. Observed from the occurrence of drought that is faster and longer. Coupled with the uncertainty of weather conditions is during the rainy season in Thailand that will directly affect the sunlight used for drying each day because the sunlight may not be enough to reduce the production and drying quality, and the sun drying, animals and insects are disturbed. Makes it unclean, which may be at risk of germs from contaminated organisms and pollution around the drying terrace, such as dust, these things may cause consumers who use products to negatively affect the digestive system. VijayaVenkataRaman et al. [8]. Also, hot air drying from heating coils is one of the most widely used methods because of the low cost for constructing the machine compared to other methods but these methods will have high power consumption. Swasdisevi et al. [9] To decrease energy consumption from heating coils, drying with hot air from LPG, and use of porous materials is an interesting method to study and to reduce the energy consumption because porous materials can absorb heat and radiate heat, it promotes and enhances the heat transfer to the drying products. From past research, researchers have developed a fire nozzle together with many porous materials. The result of the development of the combustion torch with porous material appears to be more efficient than the flame nozzle without installing the porous material. That means is having a higher temperature uses less fuel, since porous materials have to absorb and radiating heat. Krittacom & Kamiuto [10] and Mital et al. [11] And from past drying research, hot air drying combined with wire mesh stainless porous materials it was found that specific energy consumption (SEC) is less than conventional drying. Luampon & Krittakom [12] Therefore, this study is the focus to decrease energy consumption by installing wire mesh stainless porous materials to enhance heat transfer in the dryer by using hot air from the gas stove. The experimental results will be useful and can be used as a guideline for further develop drying processes who interest to save energy for other foods or agri-product drying.

2. Nomenclature

PPI	Pores per inch (PPI)
W_L	Number of wire mesh stainless porous material layer (Layer)
M_w	Wet basis moisture content (%w.b.)
SEC	Specific energy consumption (kJ/kg water)
v	Hot air velocity (m/s)
T	Hot air temperature (°C)
W	Mass of wet product (kg)

d Mass of dry product (kg)
$m_{water,evap}$ Amount of water evaporated from the drying product (kg water)
Q_{all} Total energy use of dryer (MJ)
R Drying rate (kg water/min)
W_t Mass of product at any time t (kg)
W_{t-1} Mass of product at time t-*1 (*kg)

3. Materials and Methods

3.1 Experimental equipment

The drying chamber is made from a steel frame and galvanized sheet and covered with a fiberglass insulator. The drying room consists of a drying tray made of stainless-steel sieve that hung with a load cell to collect drying product mass. The blower is using to blow hot air and moisture out of the drying chamber. The heat source is an infrared LPG burner with locating at before the wire meshes stainless porous material section and hot air is flowing through the wire mesh stainless porous material to enhance heat transfer before flow into the drying chamber. Experimental equipment is shown in Figure 1.

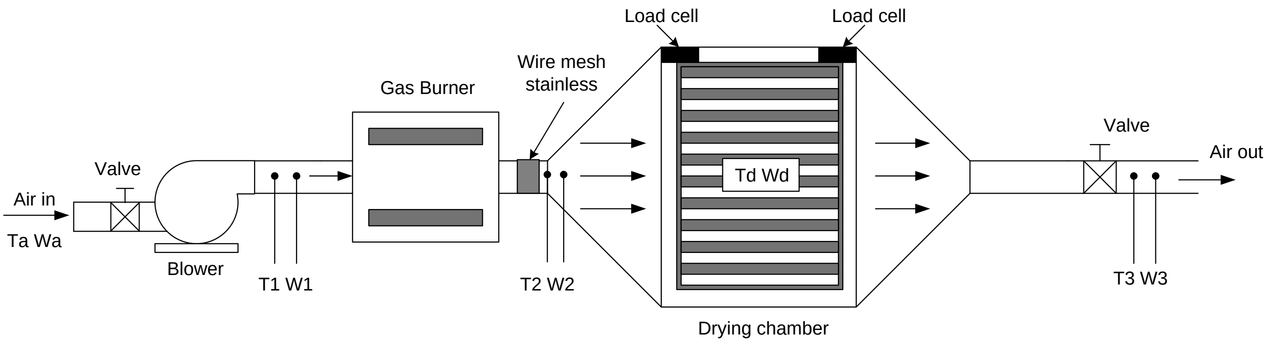

Figure 1. Hot air dryer using a flame nozzle with a stainless-steel mesh porous material

3.2 Method of experiment

In the experiment, the temperature is measure by type K thermocouples and relative humidity is measure by relative humidity sensors at 3 positions. In the experiment, the drying products are preparing to the same size, the porous materials are preparing to the desired size, and place at the inlet of the drying chamber. The porous materials are wire mesh stainless No. 304 with porosity (Pore per inch, PPI) 6, 8, and 12 PPI and are wire mesh stainless layer (W_L) 4, 8, and 12 layers. The drying temperature and hot air velocity will adjust according to the drying conditions at a hot air temperature are 70 ^{o}C and hot air velocity is 2 m/s. The drying products will be placed on the drying tray when the drying condition is reached to set point and collect initial values such as the air temperature, relative humidity, initial moisture content, and initial drying mass. And then the drying process is run continuity until the moisture content reaches to final moisture at 12 %w.b. calculate with Eq.1 by measuring the mass of the drying product from digital weighing DM.3 resolution 0.01 g. During the drying process, the parameter values will record into the data logger (Graphtec brand GL820) at intervals every 5 minutes and the experiment is repeated 3 times in all conditions.

3.3 Lingzhi mushrooms preparation

In this experiment, Lingzhi mushrooms are used from the same market and select at the same size and slice at 3 mm thickness. Lingzhi mushrooms are weighed to 500 g before drying. Then the initial moisture content of Lingzhi mushrooms was determined by AOAC 2003. From the AOAC 2003 result, Lingzhi mushroom has an average initial moisture content is 68% w.b.

4. Drying analysis

4.1. Wet basis moisture content (M_W)

The wet basis moisture content is a value indicating the amount of water in the drying product with the mass of the wet product at any time. Moisture content on a wet basis can be calculated with Eq.1. Wu et al. [13]

Wet basis moisture content (M_W)

$$M_w = \frac{w - d}{w} \times 100 \tag{1}$$

4.2. Drying rate (R)

The drying rate is the rate of evaporation of water from the drying product per interval drying time. The drying rate can be calculated with Eq. 2. Hakan et al. [14] and Ratanadecho et al. [15]

$$R = \frac{W}{t} = \frac{W_t - W_{t-1}}{\Delta t} \tag{2}$$

4.3. Specific energy consumption (SEC)

Specific energy consumption is used to measure drying efficiency in MJ/kg of water evaporated. Luampon & Krittacom [12]

$$SEC = \frac{Q_{all}}{m_{water,evap}} \tag{3}$$

5. Results and Discussion

Experimental results in Figure 2 are the influence of pores per inch (PPI) and wire mesh stainless layer (W_L) on moisture content. In the experiment use drying condition as, size of wire mesh stainless porous material is PPI = 0 (without wire mesh), 6, 8 and 12, W_L = 0, 4, 8, and 12 layers, hot air temperature, and hot air velocity are constant 70 °C and 2 m/s, respectively. From the experiment results, there are shown that drying time is between 0–241 minutes and moisture content decreases with increase drying time. A drying with wire mesh stainless porous material is better than without if compare a dryer with and without wire mesh stainless porous material at between PPI = 8, W_L = 12 and PPI = 0, W_L = 0 the drying time of both porous material size is 200 minutes and 241 minutes, respectively it is found that dryer with installing wire mesh stainless porous material can reduce drying time to 41 minutes.

Figure 3 is the influence of PPI and W_L on the drying rate. The drying rate is the rate of evaporation of water from the drying product per interval drying time, it is found that the drying rate is between 0.40-2.52 kg water/min and increase with increase PPI and W_L so if drying is a rate increase, drying time is decreased. Drying time is fastest and the drying rate is highest with PPI = 8, W_L = 12 layers at 195 minutes and 1.39 kg water/min, respectively but if increase PPI = 12 and W_L = 12 layers the drying time is increase 10 minutes because the properties of porous material are when increasing size of a porous material or increase porous material volume cause to the energy or heat are more absorb in porous material so that the heat enhancement effective (heat radiation or emission) is decreased and drying time increases more than drying condition at PPI = 8, W_L = 12 layers.

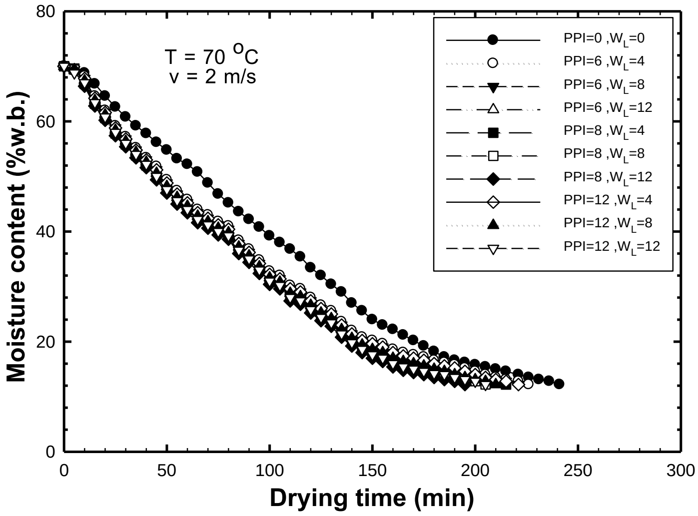

Figure 2. The influence of pores per inch (PPI) and wire mesh stainless layer (W_L) on moisture content.

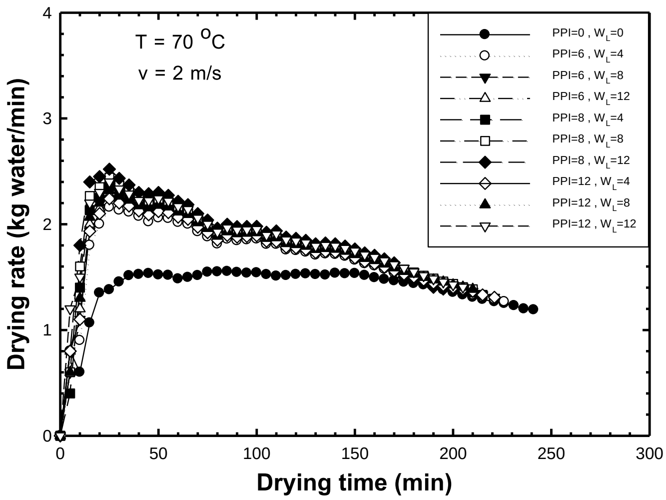

Figure 3. The influence of PPI and W_L on the drying rate.

Figure 4 shows the influence of PPI and W_L on the specific energy consumption (SEC) it is found that SEC is between 0.79 - 0.98 MJ/kg water. A drying with installing wire mesh stainless porous material can reduce the SEC and the SEC is decrease with increase PPI and W_L, at PPI = 8, W_L = 12 layers has the lowest SEC at 0.68 MJ/kg which can reduce energy consumption by 26.18% compared with dryer without installing wire mesh stainless porous material (PPI=0, W_L=0) because drying time is shortest and when considering SEC in case PPI = 12, W_L = 12 layers the SEC is higher than PPI = 8, W_L = 12 layers because if PPI increases, it causes to porous material volume is increased, so the energy and heat that flow through porous material are absorbed in porous material more than emitting and if porous material volume increase, the space in the porous material is decrease cause to pressure drop is an increase, so the energy consumption in blower is the increase (Luampon and et al., 2017).

From figure 4, the SEC is lowest at PPI = 8, W_L = 12 layers with SEC = 0.79 MJ/kg water. and SEC is highest at PPI = 0, W_L = 0 layers (without porous material) with SEC = 0.98 MJ/kg water.

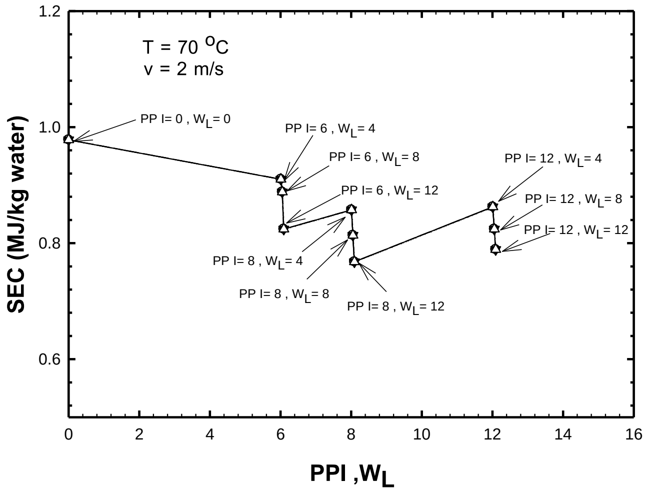

Figure 4. shows the influence of PPI and W_L on the specific energy consumption (SEC)

6. Conclusion

This This research is a study on the influence of wire mesh stainless porous material for Lingzhi mushrooms with hot air drying. In experimental, hot air temperature and hot air velocity are constant at 70 ^{o}C and 2 m/s, respectively and wire mesh stainless porous material is a varied size at PPI = 0, 6, 8, and 12, W_L = 0, 4, 8, and 12 layers. Lingzhi mushroom slice at size 3 mm thickness is a drying product. From the experimental result, it is found that moisture content decreases with increase drying time, drying time is decreased, the drying rate increases, and SEC is decreased with increase PPI and W_L. At PPI = 8, W_L = 12 layers have the shortest drying time, highest drying rate, and lowest SEC and when compare with dryer is not install wire net stainless porous material, the SEC can reduce to 26.18%.

7. Acknowledgments

The author of the article wishes to thank the Energy Policy and Planning Office (EPPO), the Ministry of Energy for funding student research. Annual budget year 2019 and thanks to the Department of Mechanical Engineering, Rajamangala University of Technology Isan, and mechanical engineering Rajamangala University of Technology Isan Surin Campus. That has supported experimental equipment and the location of the experiment to be used in this research until accomplished.

8. References

[1] Motevali, A., Minaei, S., Khoshtaghaza, M.H. and Amirnejat. H. 2011. Comparison of energy consumption and specific energy requirements of different methods for drying mushroom slices, Energy, 36, pp. 6433-6441

[2] Singh, U. Jain, S.K. Doshiz, A. Jain, H.K. and Chahar, V.K. 2008. Effects of pretreatments on drying characteristics of button mushroom, Journal of Food Engineering, 223, pp. 208-219.

[3] Olufayo, A.A. and Ogunkunle, O.J. 1996. Natural Drying of Cassava Chips in the Humid Zone of Nigeria. Bioresource Technology 58:pp. 89-91.

[4] Camila, AP. Chandan, K. Fernanda, DC. Karim MA. 2014. Heat and mass transfer modeling of the osmo-convective drying of yacon roots (Smallanthus sonchifolius). Appl Therm Eng. 2014; 63: 23-32.

[5] Huang, J. and Zhang, M. 2016. Effect of three drying methods on the drying characteristics and quality of okra. Drying Technology, 34(8), 900-911.

[6] Ausra, C. Henrikas, N. Algirdas, R. and Egidijus, Z. 2015. Usage of hybrid solar collector system in drying technologies of medical plants. Energy conversion and management, 93, 399-405.

[7] Kuanpradit, H. Kunchornrat, A. and Tavattana, T. 2012. The Development of solar parabolic concentrators in drying process for agricultural products. Journal of Industrial Education. 7(2), 81-90.

[8] VijayaVenkataRaman, S., Iniyan, S. and Goic, R. 2012. A review of solar drying technologies. Renewable Sustainable Energy Rev, 1, 2652–2670.

[9] Swasdisevi, T. Devahastin, S. Sa-Adchom, P. and Soponronnarit, S. 2009. Mathematical modeling of combined far-infrared and vacuum drying banana slice. J. Food Eng. 92, 100-106.

[10] Krittacom, B. and Kamiuto, K. 2009. Radiation emission characteristics of an open-cellular porous burner. J. Therm. Sci. Tech-JPN., Vol 4, Pp 13-24.

[11] Mital, R. Gore, J.P. and Viskanta, R. 1997. A study of the structure of submerged reaction zone in porous ceramic radiant burners, Combustion and flame, Vol. 111, pp. 175-184.

[12] Luampon, R. and Krittacom, B. 2016. Study Drying Kinetic of Tilapia using Hot Air Flowing through the Porous Media, 13th Eco-Energy and Materials Science and Engineering Symposium, 1-4 December 2016, Udonthani, Thailand.

[13] Wu, L. Orikasa, T. Ogawa, Y. and Tagawa, A. 2007. Vacuum drying characteristics of eggplants. Journal of Food Engineering 83 : 422–429

[14] Hakan, Ebru and Akpinar 2008. Numerical and experimental analysis of moisture transfer for convective drying of some products. International Communications in Heat and Mass Transfer: Volume 35, Issue 2, February 2008, Pages 169-177.

[15] Ratanadecho, P. Aoki, K. and Akahori, M. A 2001. Numerical and experimental study of microwave drying using a rectangular waveguide. Drying Technology International Journal 19, 2209–2234.

TSF0001

Coupling of 1D Simulation Model and CFD Model for the Pressure Relief Valve in the High-Pressure Pump

Warodom Phungjununt[1], Jeerasit Bumrungpetch[2], Naphat Chaiprasop[2], and Ekachai Juntasaro[1,*]

[1]Department of Mechanical and Process Engineering, The Sirindhorn International Thai-German Graduate School of Engineering (TGGS), King Mongkut's University of Technology North Bangkok, Bangkok 10800, Thailand.

[2]Department of Research and Development, Robert Bosch Automotive Technologies (Thailand) Co., Ltd., Hemaraj Eastern Seaboard Industrial Estate (Rayong), 500/92 Moo3, Tambol Tasith, Amphur Pluak Daeng, Rayong 21140, Thailand.

* Corresponding Author: ekachai.j@tggs.kmutnb.ac.th

Abstract. High-pressure pump is one of the main components of the gasoline direct injection system which is used to increase the fuel pressure by the plunger reciprocation inside the high-pressure pump. To control the high pressure of the fuel not to exceed the limit, the pressure relief valve is required to be installed in the pump. This paper is aimed to improve the one-dimensional model of the high-pressure pump by modifying the one-dimensional model with the aid of CFD simulation and also to improve the accuracy and precision of the one-dimensional model of the high-pressure pump. This study can be divided into two sections. The first section is the generation of the lookup tables with CFD analysis using the CFD++ software. In this section, CFD simulation is used to analyse the flow behaviour in the pressure relief valve when it is opened by employing the Zwart-Gerber-Belamri cavitation model and the Reynolds-Averaged Navier-Stokes (RANS) realizable k-ε turbulence model. The averaged force result table and the averaged inlet mass flow rate result table are created by varying the valve lift displacement and the total pressure difference. The second section is the one-dimensional simulation using the LMS Imagine.Lab AMESIM software. One-dimensional simulation is used to create the pressure relief valve component in the high-pressure pump model and assess the potential of the system. The CFD lookup tables are implemented into the one-dimensional model to fulfill the high-pressure pump model. It is found that when the CFD lookup tables obtained from the first section are implemented into the one-dimensional model, the results from the one-dimensional model are in good agreement with the measurement data and better than the previous work.

1. Introduction

Gasoline Direct Injection (GDI) system is the engine system that is developed to directly inject the fuel for compressing the fuel until it becomes the mixture and running the engine [1]. There are several components in the GDI system, e.g. electric fuel pump, high-pressure pump, fuel rail, fuel injectors, etc. The high-pressure pump is one of the main components of the GDI system. Increasing the fuel pressure is the main function of the high-pressure pump in this system. The high-pressure pump compresses the fuel (delivered from the fuel tank by the low-pressure lift pump) using the piston in the high-pressure pump driven by cam. After being compressed, fuel flows to the rail and finally is injected. To control the high pressure of the fuel not to exceed the limit, the pressure relief valve is required to be installed in the pump. The pressure relief valve (PRV) or the pressure-limiting valve is used to prevent the fuel pressure not to exceed the high-pressure limit of the pump and separates the low-pressure fuel from the high-pressure fuel [2]. The pressure relief valve limits the fuel pressure by using the ball valve to separate the low-pressure fuel from the high-pressure fuel and using the spring force to push the ball for closing the valve.

Previously, the one-dimensional model of the high-pressure pump, which was developed by researchers at Robert Bosch, was used to evaluate the performance of the high-pressure pump at various conditions. However, the one-dimensional model of Robert Bosch high-pressure pump (HDP6) was still incomplete due to an inaccuracy in the simulation results. Therefore, the further development of the one-dimensional model of the high-pressure pump should be performed. From the literature survey, the one-dimensional model was generally considered together with the CFD simulation. One-dimensional simulation and CFD simulation can also be separately used for different considerations [3-6]. Over the past decade, there were several researchers attempting to develop and improve the coupling of the one-dimensional simulation with the CFD simulation. For instance, previous research studies [7-13] put the results from one simulation to another to increase the precision and accuracy of the simulation. Timothy et al [7] improved the one-dimensional model of an inlet valve of the high-pressure pump by generating the CFD lookup tables. In addition, for the CFD simulation, multiphase-flow modeling is significantly valuable for the flow simulation to observe the occurrence of this physical phenomena. This modeling can be achieved by using the cavitation model, e.g. the cavitation models of Zwart-Gerber-Belemri [14], Schnerr-Sauer-Yuan [15], Singhal et al [16], etc. Based on the previous works, it was found that separate simulations of one-dimensional model and CFD model cannot improve an accuracy of the one-dimensional model and consume time. Inserting CFD simulation results into the one-dimensional model was able to improve the one-dimensional model. From the preliminary study, CFD lookup table generation approach was adopted for this study to improve the one-dimensional model.

The present work is aimed to improve an accuracy and precision of one-dimensional model of the high-pressure pump by modifying the one-dimensional model with the aid of CFD simulation by generating CFD lookup tables of the averaged force and the averaged inlet mass flow rate. In this research, the latest generation of Robert Bosch high-pressure pump (HDP6), which was developed from HDP5evo by increasing the high-pressure value of the fuel in the pump from 250 to 350 bar, is used. The work of this research can be divided into two sections. The first section is the generation of the lookup tables with CFD analysis using the CFD++ software. In this section, CFD simulation is used to analyse the flow behaviour in the pressure relief valve. In the second section, the one-dimensional simulation is used to create the pressure relief valve component in the high-pressure pump model and assess the performance of the system. The modified model obtained from this research will improve the one-dimensional model of the high-pressure pump.

2. CFD simulation approach

2.1 Cavitation model

For the CFD simulation, the CFD ++ software is used to study the fluid flow behaviour and to generate the CFD lookup tables. In this work, the flow is set to be two-phase and compressible. The steady flow is simulated by employing the RANS realizable k-ε turbulence model at various valve lift displacement positions and the total pressure difference. For the two-phase flow modelling, the Zwart-Gerber-Belemri cavitation model is used to simulate the two-phase flow. This cavitation model was created based on the bubble dynamics equation for which the Rayleigh-Plesset equation is required as shown in equation (1).

$$R_B\frac{d^2R_B}{dt^2}+\frac{3}{2}(\frac{dR_B}{dt})^2=\frac{P_B-P}{\rho_l}-4\vartheta_l\frac{dR_B}{dt}-\frac{2S}{\rho_l R_B} \tag{1}$$

where R_B is the bubble radius, P_B is the bubble surface pressure, P is the liquid pressure, ρ_l is the liquid density, ϑ_l is the kinematic viscosity of liquid and S is the surface tension of bubble. For the bubble dynamics considered, it is assumed that the second-order term ($\frac{d^2R_B}{dt^2}$) is neglected and the effect of surface tension (S) is neglected. The bubble growth rate can be expressed as equation (2).

$$\frac{dR_B}{dt} = \frac{2}{3}\sqrt{\frac{P_B - P}{\rho_l}} \tag{2}$$

For the multiphase flow modelling, the liquid phase and the vapour phase which represents the growth of bubble (evaporation) and the bubble collapse (condensation) can be governed and predicted by the flow behaviour using the vapour transport equation in equation (3).

$$\frac{\partial \rho_v}{\partial t} + \nabla(\rho_v \vec{V_v}) = R_e - R_c \tag{3}$$

where ρ_v is the vapour density, $\vec{V_v}$ is the vapour velocity, R_e is the growth rate of bubble or the evaporation rate, and R_c is the collapse rate of bubble or the condensation rate. Both R_e and R_c are the source terms of the vapour transport equation. This cavitation model accounts for the growth rate and the collapse rate of bubble in the vapour transport equation by assuming that all bubbles are perfectly spherical and have the same size in the cavitation. In the bubble growth process (evaporation), there is a hypothesis for generalizing the evaporation rate, i.e. the bubble growth starts from the nucleation site at the initial stage. Once the volume fraction of vapour (α_v) increases, the nucleation density accordingly decreases. Therefore, the volume fraction of vapour in the evaporation process can be written in terms of the nucleation site volume fraction (α_{nuc}). Finally, the Zwart-Gerber-Belemri cavitation model is given in equations (4) and (5).

Rate of evaporation (Bubble growth; $P < P_v$):

$$R_e = F_{evap}\frac{3\alpha_{nuc}(1-\alpha_v)\rho_v}{R_B}\sqrt{\frac{2}{3}\frac{P_v - P}{\rho_l}} \tag{4}$$

Rate of condensation (Bubble collapse; $P > P_v$):

$$R_e = F_{cond}\frac{3\alpha_v\rho_v}{R_B}\sqrt{\frac{2}{3}\frac{P_v - P}{\rho_l}} \tag{5}$$

where F_{evap} is the evaporation coefficient which is equal to 50, F_{cond} is the condensation coefficient which is equal to 0.001, and the nucleation site volume fraction (α_{nuc}) is equal to 5×10^{-4}.

2.2 CFD simulation setup

CFD simulation of the pressure relief valve is carried out by employing the Zwart-Gerber-Belemri cavitation model and the RANS realizable k-ε turbulence model to generate the CFD lookup tables. The total pressure difference between the high-pressure side and the low-pressure side in the chamber and the ball valve lift displacement are set to be the boundary conditions for the simulation as displayed in figure 1 (a) and 1 (b) respectively. The CFD lookup tables, which are the results from the CFD simulation, are generated from 38 cases of the valve lift displacement and 32 cases of the total pressure difference. The CFD lookup tables of both the averaged force and the averaged inlet mass flow rate are generated before creating the one-dimensional model of the pressure relief valve component.

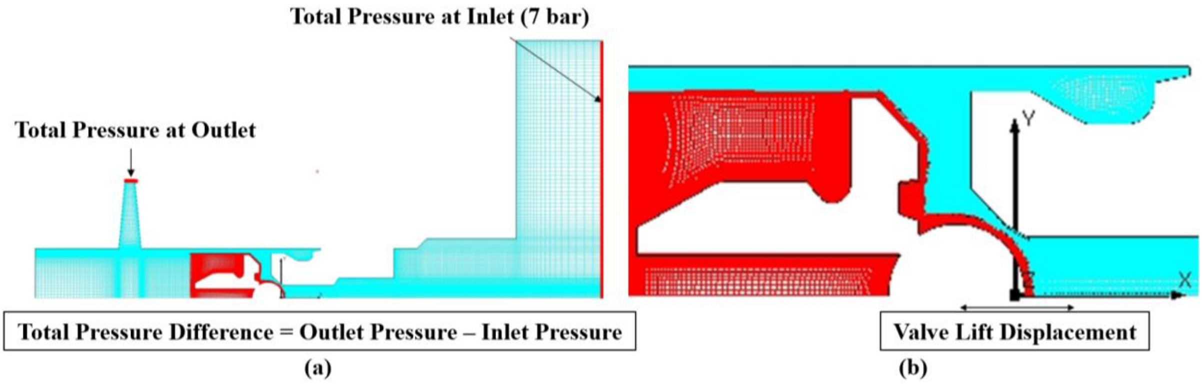

Figure 1 *Boundary conditions for (a) the total pressure difference and (b) the valve lift displacement.*

2.3 CFD lookup table generation from the CFD simulation

The CFD lookup table of the averaged inlet mass flow rate, as shown in figure 2 (b), reveals that increasing the valve lift displacement can gradually increase the averaged inlet mass flow rate up to 500 micron of valve lift displacement. In addition, the averaged inlet mass flow rate increases linearly when the total pressure difference increases as a result of the averaged inlet mass flow rate CFD lookup table. The CFD lookup table of the averaged force which exerts on the ball valve in the direction of negative x-axis is generated and shown in figure 2 (a). Basically,the averaged force is increased when the total pressure difference is increased. In the CFD lookup table of the averaged force, it is found that the higher valve lift displacement can cause the higher averaged force when the valve lift displacement is higher than 30 micron.

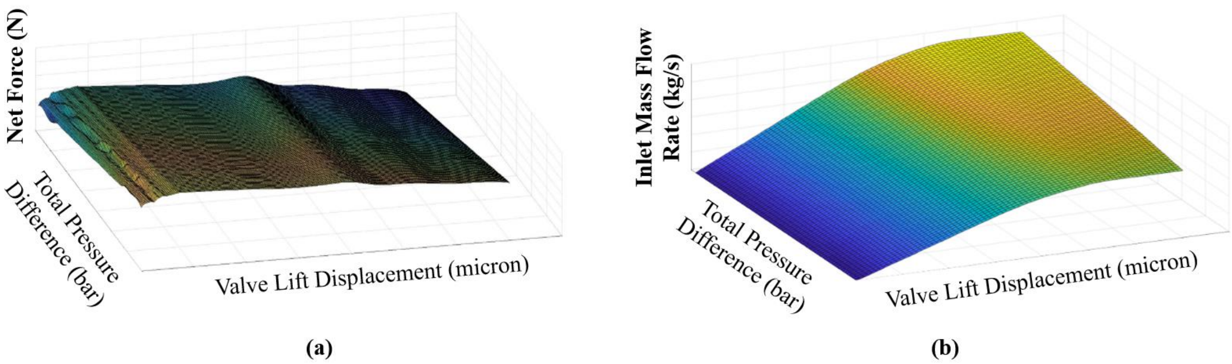

Figure 2 *CFD lookup tables of (a) the averged force and (b) the averaged inlet mass flow rate.*

3. One-dimensional model of the pressure relief valve generation

For the one-dimensional simulation, the one-dimensional model of the pressure relief valve is based on the working principle of the pressure relief valve [17]. The ball valve relies on the spring force which is balanced with the fluid force to prevent the pressure exceeding its limits. To create the one-dimensional model of the pressure relief valve with the CFD lookup tables, the valve lift displacement and the total pressure difference are the inputs of both the CFD lookup table of the averaged force and the averaged inlet mass flow rate. At the initial stage, the averaged force from the CFD lookup table is lower than the spring force. Therefore, the valve lift displacement is initially equal to zero. Once the averaged force from the CFD lookup table is higher than the spring force, the ball valve starts opening and there is some mass flow rate, which is extracted from the CFD lookup table of the averaged inlet mass flow rate, from the high-pressure side to the low-pressure side. Furthermore, the fluid volume at the throat should be calculate due to the ball valve movement. Finally, the one-dimensional model of the pressure relief valve is created as shown in figure 3.

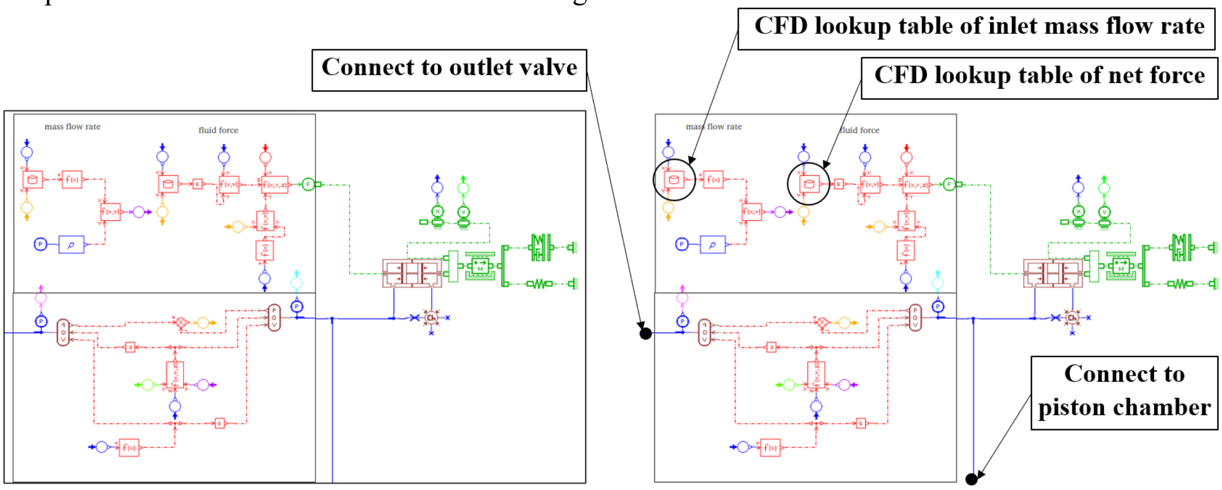

Figure 3 *One-dimensional model of the pressure relief valve with CFD lookup tables.*

4. Results and discussion

4.1 Simulation results of the pressure in rail and the pressure after the high-pressure pump under the different pump speeds

For the validation, the one-dimensional model of the pressure relief valve is applied in the one-dimensional model of the high-pressure pump (HDP6 AMESIM model). In this paper, the simulation results from the HDP6 AMESIM model which is connected to the pressure relief valve AMESIM model with and without CFD lookup tables are compared with the measurement data. The 10-mm piston diameter pump model driven by cam shaft number N458 which is the 3-lobe cam and 5.5-mm stroke lift is used. There are two parameters that are used for the validation: the pressure in rail of the high-pressure pump and the pressure after the high-pressure pump at various pump speeds from low pump speed (500 rpm) to high pump speed (3500 rpm). Finally, both parameters are calculated by varying with the pump speeds and evaluated by finding the maximum of the averaged values from all simulation cycles (Max – Mean Evaluation) and the maximum of the maximum values from all simulation cycles (Max – Max Evaluation). There are 4 results: the red line which represents the result from the measurement data by testing from the low pump speed to the high pump speed, the blue line which represents the result from the measurement data by testing from the high pump speed to the low pump speed, the dot blue line which represents the result from the simulation using the one-dimensional model of the pressure relief valve component without the CFD lookup tables, and the dash green line which represents the result from the simulation using the one-dimensional model of the pressure relief valve component with the CFD lookup tables of the averaged force and the averaged inlet mass flow rate.

For the pressure in rail, the simulation results with the CFD lookup tables at the steady state is close to the measurement data compared with the simulation results without the CFD lookup tables. Although the simulation results of the pressure in rail are built up faster than the measurement data at the low pump speed, the pressure built-up from the simulation results are similar to the measurement data as the pump speed increases.

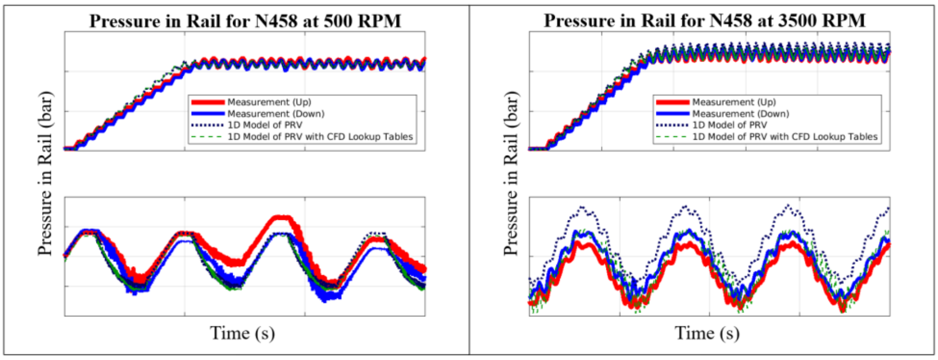

(a) (b)

Figure 4 *Simulation results of the pressure in rail under different pump speed*

For the results of the pressure after the high-pressure pump, the pressure built-up is still faster than the measurement data at the low pump speed while the simulation result with the CFD lookup tables at the steady state is in good agreement with the measurement data, similar to the result of pressure in rail. There appears the fluctuation in the simulation result which causes the maximum peak in the result higher than the measurement data at the high pump speed.

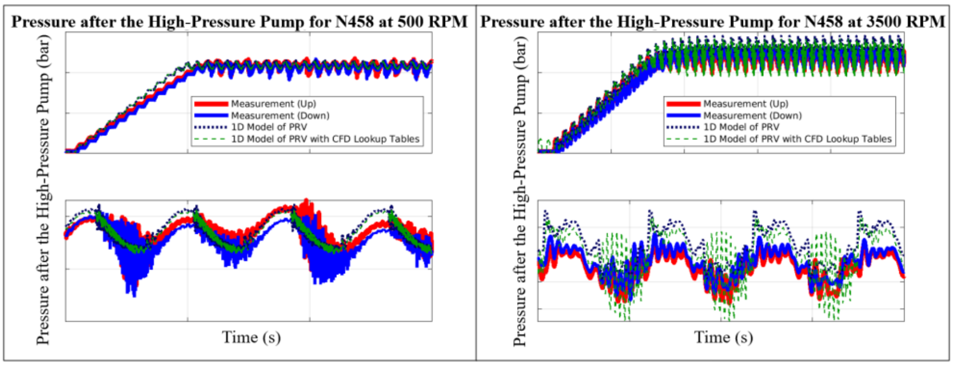

(a) (b)

Figure 5 *Simulation results of the pressure after the high-pressure pump under different pump speeds*

Although the simulation result with the CFD lookup tables at the pump speed of 1000 rpm at the steady state is higher than the simulation result without the CFD lookup tables, it is in better agreement with the measurement data.

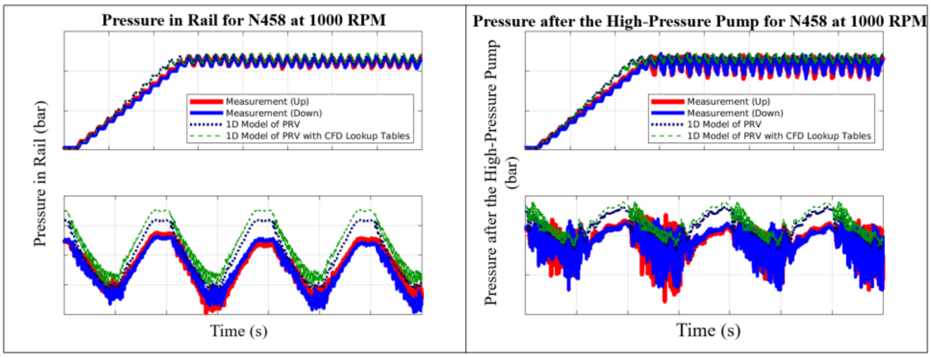

(a) (b)

Figure 6 *Simulation results of (a) the pressure in rail and (b) the pressure after the high-pressure pump at 1000 rpm*

4.2 Max – Mean Evaluation of the pressure in rail and the pressure after the high-pressure pump

In figure 7, the accuracy at the high pump speed is higher than the accuracy at the low pump speed for the Max – Mean Evaluation of the pressure in rail and the pressure after the high-pressure pump because the simulation results with the CFD lookup tables agree well with the measurement data at the steady state.

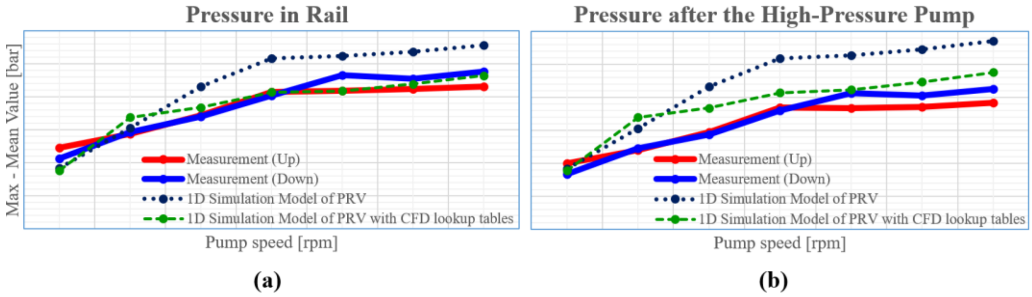

Figure 7 *Max – Mean Evaluation of (a) the pressure in rail and (b) the pressure after the high-pressure pump*

4.3 Max – Max Evaluation of the pressure in rail and the pressure after the high-pressure pump

As shown in figure 8, the result of Max – Max Evaluation of the pressure in rail from the simulation result with the CFD lookup tables is more accurate than the simulation result without the CFD lookup tables. Although the Max – Max value of the pressure in rail is more accurate at the low speed pump, the Max – Max value of the pressure after the high-pressure pump at the highest speed is not quite accurate due to the fluctuation of fluid in the pressure relief valve and the outlet valve.

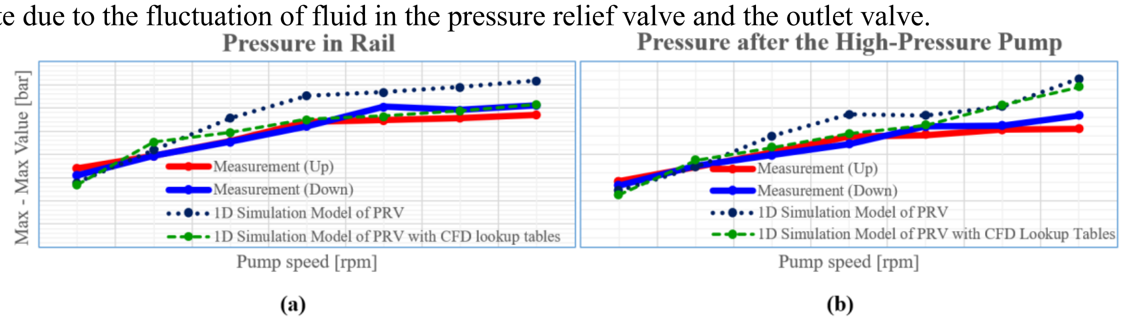

Figure 8 *Max – Max Evaluation of (a) the pressure in rail and (b) the pressure after the high-pressure pump*

5. Conclusion

In this work, the one-dimensional model of the high-pressure pump is improved by modifying the one-dimensional model with the aid of CFD simulation and hence more accurate and precise.

The results demonstrate that the AMESIM model of the pressure relief valve component with the CFD lookup tables is able to work with the one-dimensional simulation model of HDP6 from the AMESIM. In general, the results from the simulation agree well with the measurement data. However, the pressure built-up for the HDP6 simulation model C3.4 (10-mm diameter piston) is currently faster than the measurement data.

Although the results from the simulation acceptably correlate with the measurement data, further improvement should be carried out for more accurate results. There are two hypotheses on the problem of pressure built-up in case of the 10-mm diameter piston. First, this piston diameter is larger than the others. This can cause the higher piston leakage from the chamber. When there is the leakage in the chamber, the pressure in the chamber would be increased due to the decrease in the volume of fuel in the chamber. The other possibility is about the data of fluid properties. At the low pump speed, since there is the small change in temperature, the fluid properties become isothermal. At the high pump speed, the higher speed can cause the higher temperature change so that the fluid properties become isentropic. The current fluid considered is an isentropic CEC at 20 degree Celsius.

6. Acknowledgements

The first author (Warodom Phungjununt) would like to gratefully thank Robert Bosch Automotive Technologies (Thailand) Co., Ltd. for the scholarship during his Master-Degree study at TGGS, KMUTNB, and also for the high-performance computer to run the simulation.

7. References

[1] Wikipedia 2019, *Gasoline direct injection*, https://en.wikipedia.org/wiki/Gasoline_direct_injection [Assessed on 2019, Dec 23]
[2] Konrad R 2015, *Gasoline Engine Management* (Wiesbaden: Springer Vieweg)
[3] Saha R, Mahesh M K, Long-Kung H, Xingshi W, Fengchao Zh, Xiaodan Zh, Liu Y, Weiqing S, Yan W, Wei Ch, and Mingjin L 2016, SAE Technical Paper 2016-01-8073, p 8
[4] Xiaoyan J, Baigang S, Dongwei W, Dan X, Wei Z, Wei Sh and Jie W 2017, SAE Technical Paper 2017-01-2310, page 11
[5] Alessandro C and Massimo R 2018 *Proc. Conf. on Energy (Pisa)* vol 81 pp 114-121
[6] Yang H, Wang W and Lu K 2019 *IEEE Access (vol 7)* pp 28001-28010
[7] Timothy D S, Shi-Ing Ch, Sudhakar D, Eugene N and Robert L 2009, SAE Technical Paper 2009-01-1504, p 11
[8] Falfari S, Brusiani F and Pelloni P 2010 *SAE Int. J. Engines 2(2)* pp 105-118
[9] Marco A, Andrea B and Marco F 2014 Proc. Conf. on Energy vol 45 pp 1077-1086
[10] Emma F, Adolfo S, Dario B and Luigi A 2015 Proc. Conf. on Energy vol 81 pp 794-804
[11] Xiyuan C, Jianzhong Y, Tianpeng Y and Shibin Y 2016, Int. J. of Sim. Sys. Sci. and Tech. vol 17 pp 11.1-11.7.
[12] Salvador FJ, De La Morena J, Crialesi E M, Martínez L J 2017 *Proc IMechE Part D: J Automobile Engineering* pp 1-19
[13] Chen Q, Ji H, Zhu Y and Yang X 2018 IEEE Access (vol 6) pp 33148–33158
[14] Philips J Z, Andrew G G, and Thabet B 2004, *5th Int. Conf. on Multiphase Flow*, Yokohama, Japan, 2004.
[15] Weixing Y, Jürgen S, and Günter H S 2001: *Proc. 1st Int. Colloquium on Microhydrodynamic* pp 383–394
[16] Ashok K S, Mahesh M A, Huiying L and Yu J 2002 *J. of fluids engineering* pp 617-624
[17] Antoine V 2011 *Proc. of the 8th Int. Modelica Conf.*, Dresden, German pp 256-265

TSF0002

High Efficiency Solar Panel with Heat Pipe

Chirdpun Vitooraporn*[1], Ultimate Tiamsa-ad[1], and Tithit Surakampontorn[2]

[1]Mechanical Engineering Department, Chulalongkorn University, Bangkok, 10330, Thailand
[2]Environmental Engineering Department, Chulalongkorn University, Bangkok, 10330 Thailand

* chirdpun@hotmail.com

Abstract. Solar energy is becoming one of major energy sources that being used worldwide. Solar panel system is a system that used mostly to convert solar energy into electric energy. However, due to its efficiency drops as its surface temperature rises which leads to system output reduction, there is a need to find out how to avoid this energy loss in a system. The objective of this research is to design and manufacture a heat pipe to apply with solar panel which can enhance heat transfer of the panel and hence reduce the energy loss. The heat pipe is tested to verify its potential in reducing the panel's surface temperature. Benefit of applying heat pipe to solar panel is analysed in order to quantify the increase in electric power production, feasibility of investment in the heat pipe-combined solar panel as well as the amount of carbon dioxide that can be reduced. The designed heat pipe has a rectangular-shape cross section. It is made of aluminium and uses water as a working fluid. The heat pipe is manufactured to form as a sleeping chair-liked shape. Water is filled over evaporator section of the heat pipe and vacuumed until the water is in saturated state. An experiment is conducted to test its potential by projecting light from a halogen lamp on 2 samples, the first one is on a plain solar panel and the other is on a solar panel attached with the heat pipe. Results show that heat pipe is capable of reducing panel's surface temperature by 11.7 ºC under 26 ºC ambient temperature which results in 5.22% increase of average electric power production. The amount of carbon dioxide reduction is approximately 10.15 kg per year and the breakeven point for the system is about 6.67 years.

Keywords: Solar Panel, Efficiency, Heat pipe, Heat transfer, Two-phase liquid**.**

1. Introduction

Solar energy become one of the most attractive energies especially in Thailand in which the country enjoys this energy from moderate to high level throughout the year. The conventional method to use solar energy from the sun is by using solar panels. Unfortunately that the efficiency of solar panel reduces as its surface temperature increases. This characteristic has been verified by several researches as well as information obtained from solar panel manufacturers. In average, for every 1ºC increase in panel's surface temperature, the efficiency in producing electric power is reduced by 0.5%.

There are many methods in reducing panel's surface temperature such as by using extended surface to increase heat transfer area [1] or using force convection. However these methods are considered to be active cooling methods where additional energy must be used to cool down the panel. Another method is called passive cooling method in which no energy usage is required. In fact this method could be more feasible in lowering panel's surface temperature than using the extended surface principle [2]. Moreover the heat carried out from the panel could be used for other purposes as well.
In this research, heat pipe, as one of passive methods, is used to reduce panel's surface temperature. The heat pipe is designed to be suitable to attach and apply with the solar panel. The effectiveness in reducing panel's surface temperature of this designed heat pipe is evaluated in term of increase in electric energy production, breakeven point as well as carbon dioxide reduction.

2. Literature Reviews

Supavit V. & Chanin S. [1] studied surface temperature reduction on mono crystalline silicon solar panel by attaching aluminum fins at the back of the panel. They found that reducing panel's surface temperature helps increasing electric power produced by the panel as shown in Fig. 1

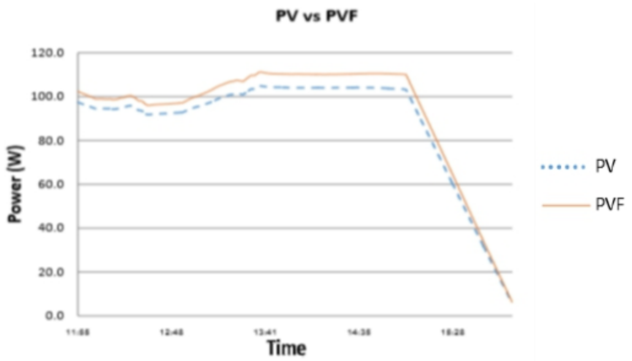

a. Electric Power Produced vs. Time

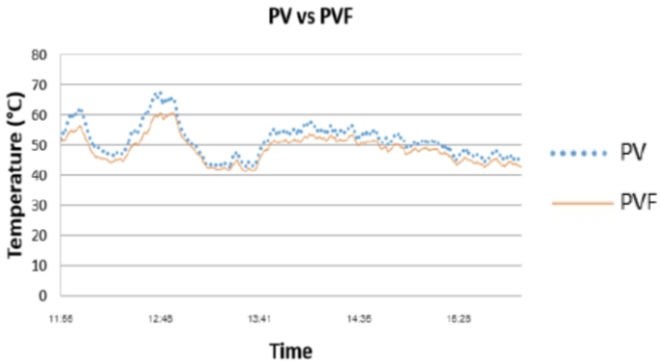

b. Panel Surface's Temperature .vs. Time

Figure 1 Electric Power and Panel's Surface Temperature versus Time on PV (panel without fin) and PVF (panel with fin) [1]

Results obtained from field experiment is shown in Table 1. The average panel's surface temperature reduction was 5.2°C which results in average increase of 5.5 watt in electric power produced at about 35°C ambient temperature.
A.K. Mozumder, A.F. Akon, M.S.H. Chowdhury and S.C. Banik [2] studied on the effect of using different working fluids, i.e. water, acetone and methanol, and different fill ratios in a miniature heat pipe which is 150 mm long and 5 mm inside diameter. The pipe is divided into 3 parts, i.e. condensing

part, adiabatic part and evaporator part, as shown in Fig. 2. The evaporator part is filled with fluid at 0, 35, 55, 85 and 100% by volume. Heat loads supplied to the evaporator part were 2, 4, 6, 8 and 10 watt. Experiments were done with and without fluid in order to compare heat pipe performance. By using 55% of methanol by volume with heat load equal to 4 watt, heat pipe's temperature could be reduced from 73ºC to 53ºC or 20ºC temperature reduction when compared with heat pipe that without working fluid. The same trend was happened with other working fluids as shown in Fig. 3

Table 1 Results on Panel's Surface Temperature Reduction and Increase in Electric Power Produced from Field Experiment [1]

Date	Panel's Surface Temperature Reduction (ºC)		Increase in Electric Power Produced (Watt)	
	Minimum	Maximum	Minimum	Maximum
20/04/2017	1.2	4.8	0.5	5.3
21/04/2017	0.3	5.1	0.8	6.7
23/04/2017	0.5	3.8	0.8	7.2
24/04/2017	0.7	7.6	0.4	6.8
25/04/2017	0.2	2.8	0.1	5.5
02/04/2017	0.3	4.7	0.7	4.4
03/04/2017	0.4	4.3	0.3	6.5
04/04/2017	0.3	5.8	0.7	1.5
06/04/2017	0.4	6.0	0.9	4.3
07/04/2017	0.4	6.9	0.8	6.5
Average	0.5	5.2	0.6	5.5

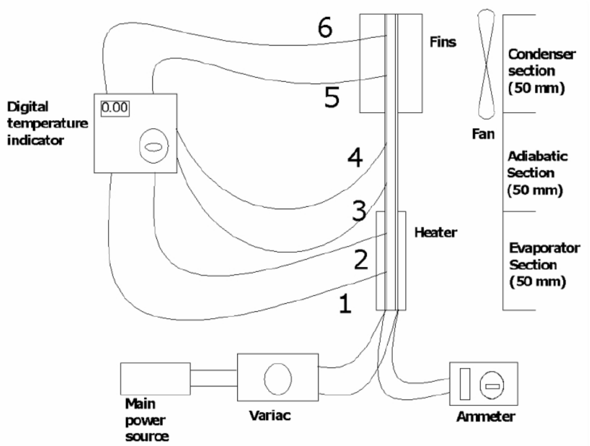

Figure 2 Schematic Arrangement of Experimental Setup [2]

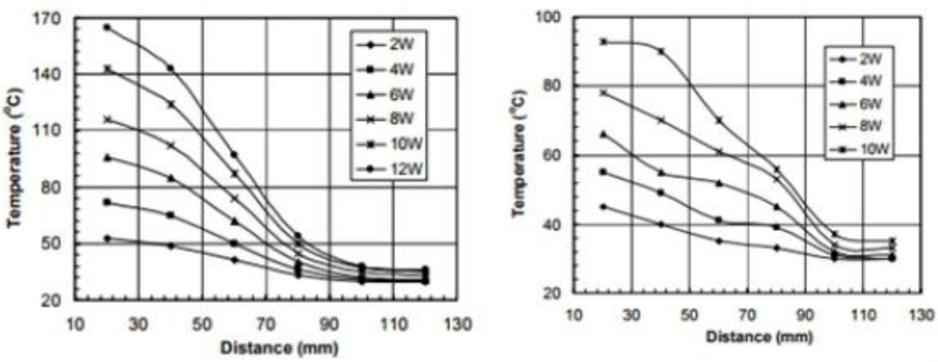

a. Temperature Profile for DRY RUN   b. Temperature Profile for Water, 55% Fill Ratio

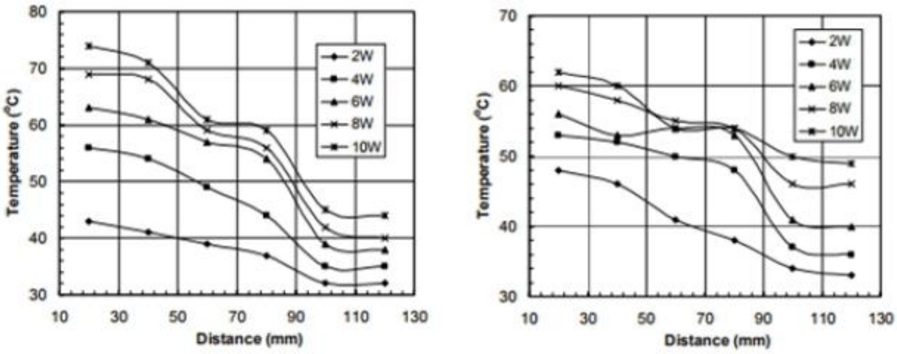

c. Temperature Profile for Methanol, 55% Fill Ratio d. Temperature Profile for Acetone, 55% Fill Ratio

Figure 3 Effect of Different Working Fluids on Heat Pipe Temperature for Different Fill Ratios [2]

It was also found that the best heat pipe performance is at 100% fill up by volume of the evaporator part.

3. Heat Pipe Design Consideration and Calculation

In this study, heat pipe is designed in 2 parts, i.e. part that can be assembled and worked with solar panel which is called the main part and part that helps facilitating the test which is called the test part.

3.1. Main Part Design Consideration

For this main part, the heat pipe is divided into 3 sections. The first section is the heat transfer area between the solar panel and the heat pipe, i.e. evaporator section, which is intended to gain maximum heat exchange between these two areas. The middle section, i.e. adiabatic section, is the flow area of working fluid which flows from heat transfer area to heat release area or vice versa. The last section is the heat release area from the heat pipe to atmosphere, i.e. condensing section, These 3 sections when assembled together have to be able to attach to the solar panel. The working fluid used is selected based on working temperature range of solar panel in which the saturated pressure of working fluid is then determined.

3.2. Test Part Design Consideration

To measure heat pipe condition during the test, test part has to allow for internal pressure measurement, working fluid filling and air venting. This can be done either by boiling the working fluid in the heat pipe and then evaporate some portion out or by vacuuming the heat pipe with vacuum pump until some working fluid is evaporated before closing the valve.

Hollow rectangular section aluminium tube size 180 mm x 12 mm with 4 mm thick is used for manufacturing heat pipe due to its good heat transfer characteristic. The heat pipe's shape looks like a sleeping chair with all dimensions as shown in Fig. 4. To determine the working fluid used, the solar panel's surface temperature is first measured throughout the day and temperatures are found in the range between 30°C to 60°C with the average temperature at 50°C while the ambient temperature is at 32°C as shown in Fig. 5. Therefore the working fluid selected is water as the saturated pressure within the range of panel's surface temperature is not too high and too low.

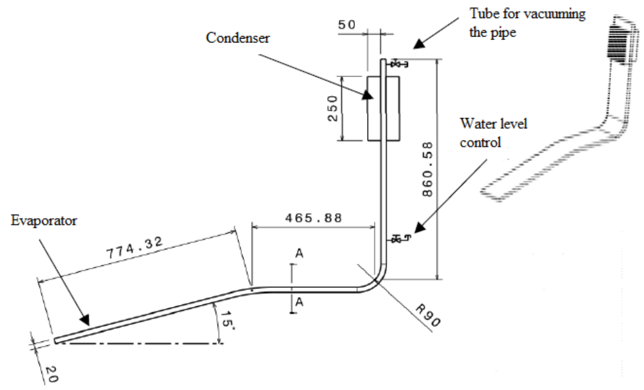

Figure 4 Designed Heat Pipe

.

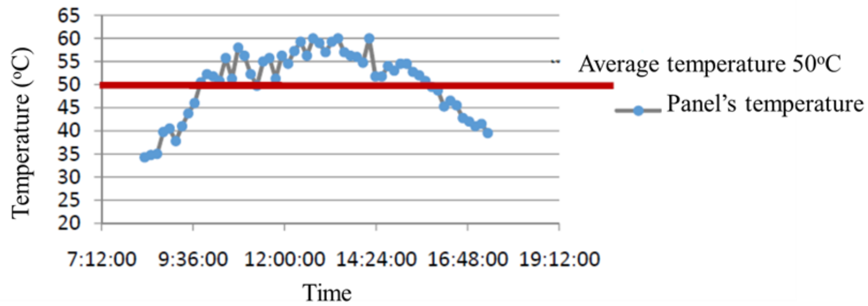

Figure 5 Solar Panel's Surface Temperature throughout the day on 22nd March 2017

3.3. Calculation on Panel's Surface Temperature Reduction Capacity of Heat Pipe

The heat transfer characteristic to atmosphere between solar panel with and without heat pipe attachment is different as shown in Fig. 6.

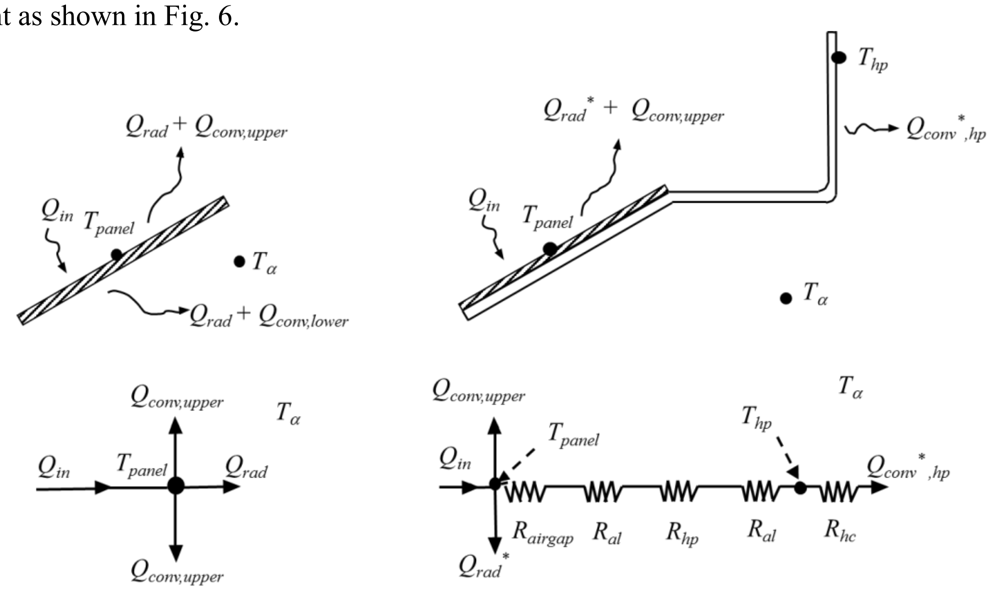

a. Solar Panel without Heat Pipe b. Solar Panel with Heat Pipe

Figure 6 Heat Transfer and Thermal Resistance Diagram on Solar Panel

On solar panel without heat pipe, natural convection, $Q_{conv,upper}$ and $Q_{conv,lower}$, and radiation, Q_{rad}, occur on both upper and lower surface of solar panel while on solar panel with heat pipe, natural convection,

$Q_{conv,upper}$, occurs on the upper surface, natural convection, $Q_{conv^*,hp}$, occurs throughout heat pipe and radiation, Q_{rad^*}, throughout solar panel and heat pipe. The amount of heat transfer to the solar panel depends on both the atmospheric temperature and solar panel's surface temperature as shown in Eq. (2) for solar panel attached with heat pipe.

$$Q_{in} = Q_{rad^*} + Q_{conv,upper} + Q_{conv^*,hp} \tag{1}$$

$$Q_{in} = Q_{rad^*} + Q_{conv,upper} + (T_{panel} - T_{\alpha}) / (R_{airgap} + 2R_{al} + R_{hp} + R_{hc}) \tag{2}$$

$$Q_{rad^*} = \frac{\varepsilon_{si} A_p \sigma (T_{panel}^4 - T_{\alpha}^4)}{2} \tag{3}$$

$$Q_{conv,upper} = \frac{h_u A_p (T_{panel} - T_{\alpha})}{2} \tag{4}$$

Where Q_{in} = Rate of heat transfer to solar panel, *watt*
Q_{rad^*} = Rate of radiation heat from solar panel and heat pipe, *watt*
$Q_{conv,upper}$ = Rate of convection heat from solar panel, *watt*
$Q_{conv^*, hp}$ = Rate of convection heat from heat pipe, *watt*
R_{airgap} = Contact thermal resistance, *K/watt*
R_{al} = Thermal resistance of aluminium, *K/watt*
R_{hp} = Thermal resistance of heat pipe, *K/watt*
R_{hc} = Convective thermal resistance, *K/watt*
ε_{si} = Emissivity coefficient of silicon
σ = Stefan-Boltzmann constant, $W/(m^2K^4)$
A_p = Solar panel's surface area (2 sides), m^2
h_u = Convective heat transfer coefficient at upper part of solar panel, $watt/(m^2K)$
T_{panel} = Solar panel's surface temperature, *K*
T_{α} = Ambient temperature, *K*

Since all terms in above equations are involved with solar panel's surface temperature, T_{panel}, an iteration process is needed to solve for the solar panel's surface temperature for certain amounts of heat transfer to the panel. Figure 7 show results obtained from calculation for different amounts of heat transfer to the solar panel and the panel's surface temperature for both with and without heat pipe. The panel's surface temperature can be reduced as high as 8.81°C.

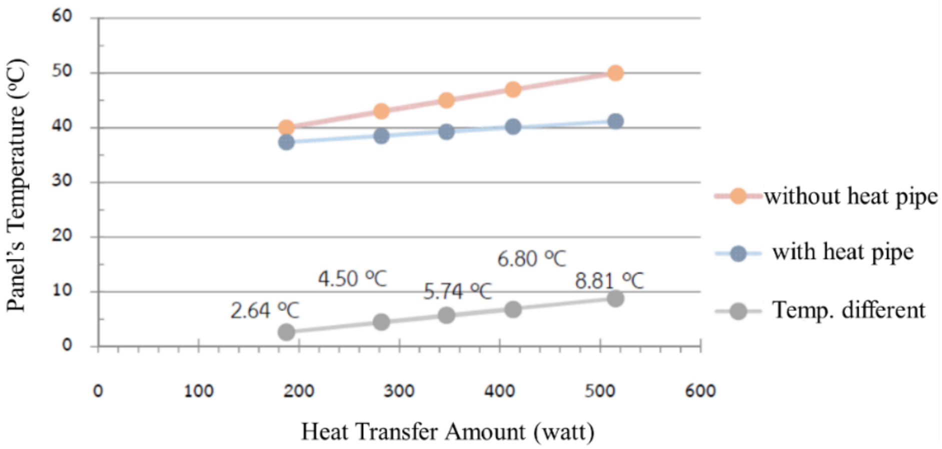

Figure 7 Relation between Heat Transfer Amount and Solar Panel's Surface Temperature on both with and without Heat Pipe

4. Experiment Setup

The test apparatus is set up as shown in Fig.8. Halogen lamp is set at 0.5 m. away from the panel and radiates heat in the perpendicular direction to the panel. The panel used is 0.7x0.16 m. mono crystalline silicon solar panel. The electric power supply to Halogen lamp is varied at different time of the day to simulate the sunlight to the panel throughout the day. This is done by using adjustable transformer. Thermocouple type K is used to measured heat pipe temperature at 2 different points while panel's surface temperature is measured by using infrared temperature gun as shown in Fig 9.

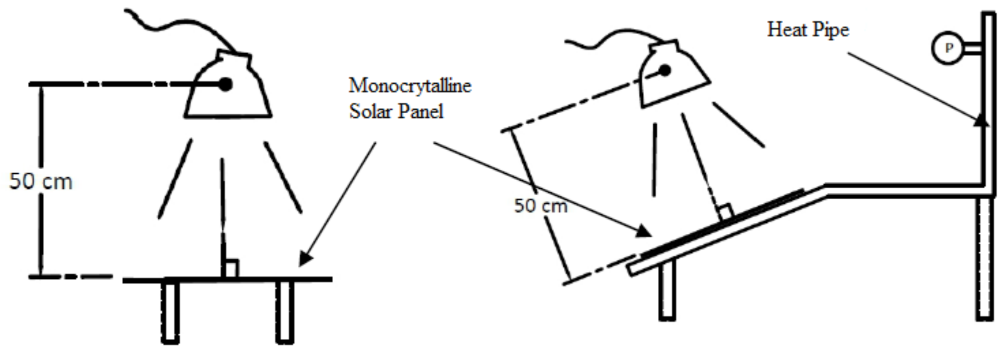

(a) Solar Panel (b) Solar Panel with Heat Pipe

Figure 8 Test Apparatus on Solar Panel with and without Heat Pipe

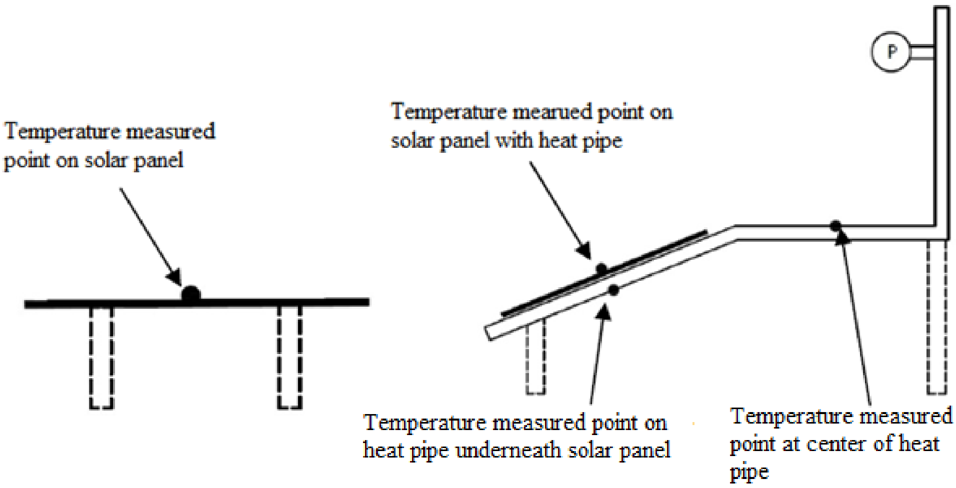

Figure 9 Temperature Measured Points on Solar Panel and Heat Pipe

The test is done by first measuring temperature and then providing electric power to the Halogen lamp. The electric power is varied from 0 to 500 watt at 50 watt step. For each step, the panel has to reach equilibrium before taking temperature measurement. This takes about 20 minutes to 1 hour. The test is repeated twice by varying electric power downward and upward so that each measuring point has 2 temperature measuring values. This is to ensure the test reliability.

5. Result Analysis

Figure 10 show solar panel's surface temperature and electric power supplied to halogen lamp for solar panel under 26°C ambient temperature. With solar panel's surface temperature at about 58.9°C, solar panel's surface temperature with heat pipe is about 47.2 $\pm$0.5°C at 500 W or 11.7 °C reduction of panel's surface temperature..

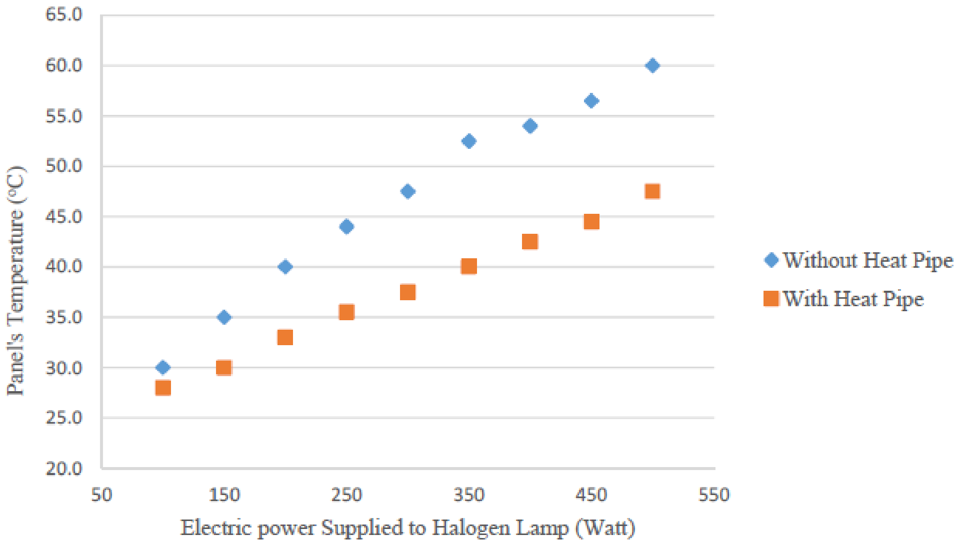

Figure 10 Solar Panel's Surface Temperature .vs. Electric Power Supplied to Halogen Lamp

The temperature different between the evaporator section of heat pipe and the centre section of heat pipe is plotted as shown in Fig.11 for different electric power supply. The different is less than 1°C which indicates that designed heat pipe can maintain saturated condition inside.

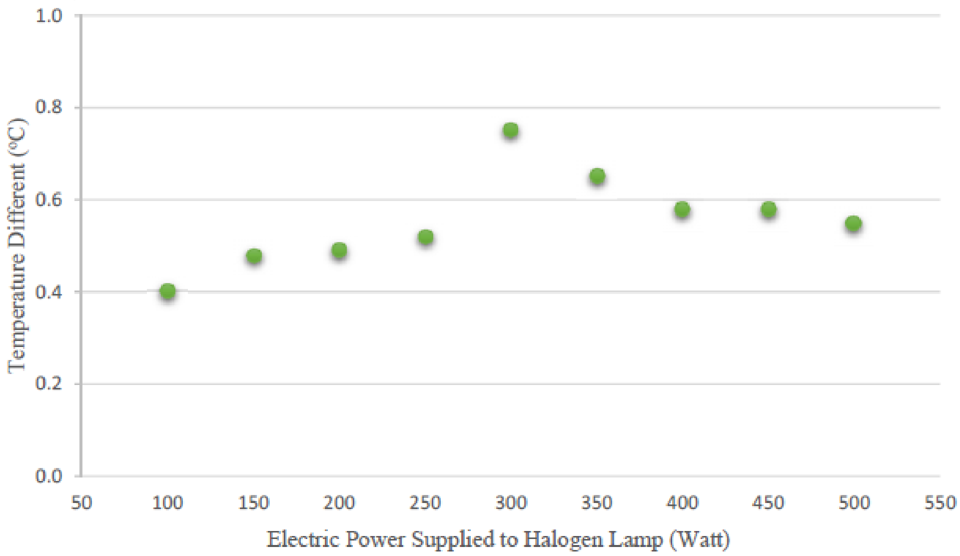

Figure 11 Temperature Different between Evaporator Section and
Centre Section of Heat Pipe .vs. Electric Power Supplied to Halogen Lamp

The percentage increase in electric power produced by solar panel when attached with heat pipe is shown in Fig. 12 along with temperature reduction. The relation between this 2 parameters is found as shown in Eq. 5

$$y_1 = 0.51x_1 + 4.30 \tag{5}$$

where y_1 = Percentage increase in electric power produced, %
x_1 = Solar panel's surface temperature reduction, °C

The equation above states that for every 1°C reduction, the increase in electric power produced by the panel is 0.51% compared with solar panel without heat pipe.

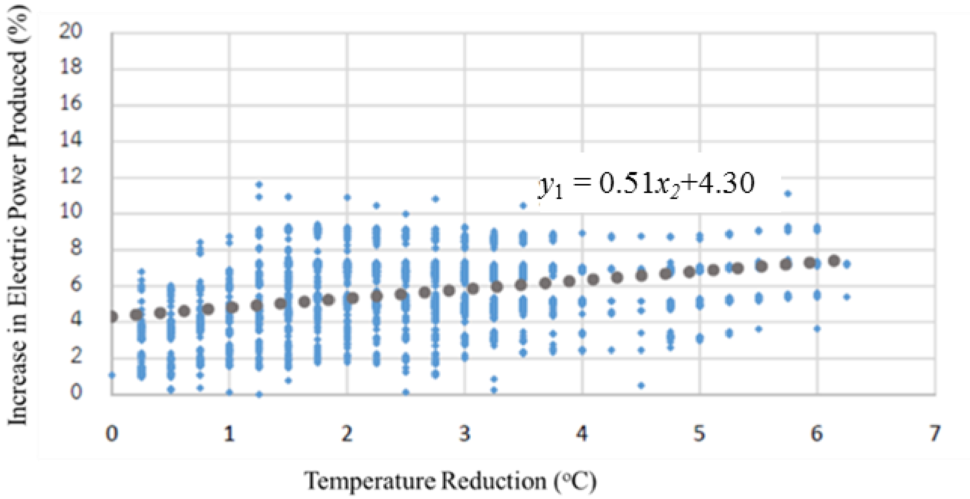

Figure 12 Relation between Temperature Reduction and Increase in Electric Power Produced

The relation between solar panel's surface temperature reduction and solar panel's surface temperature without heat pipe is shown in Fig.13 and equation that relate these 2 parameters is

$$y_2 \;=\; 0.36x_2 - 7.98 \qquad (6)$$

where y_2 = Solar panel's surface temperature reduction due to heat pipe, °C
x_2 = Solar panel's surface temperature without heat pipe, °C

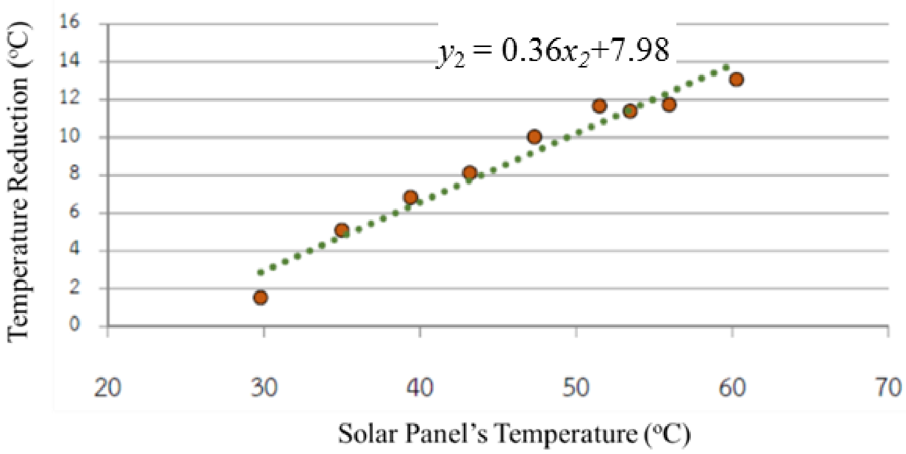

Figure 13 Relation between Temperature Reduction due to Heat Pipe and Solar Panel's Temperature

By taking the average temperature reduction throughout the day, the solar panel with heat pipe can produced electric power at 5.22 % higher than solar panel without heat pipe.
Investigation is done also on simple breakeven point analysis as shown on Table 2. The breakeven point is 4.46 years for solar panel without heat pipe and increase to 6.67 years for solar panel with heat pipe. This represents the feasibility in applying heat pipe to the solar panel since the lifetime of solar panel is 25 years. The different in electrical unit produced is about 0.947 unit per month which is equivalent to 10.15 kg of CO_2 reduction per year as shown in Eq. 7

$$CO_2 \text{ Reduction} = 0.947\ \frac{kWh}{month} \times 12\ \frac{month}{year} \times 0.893\ \frac{kg\mathrm{CO}_2}{kWh} = 10.15\ \text{kg} \tag{7}$$

Table 2 Simple Breakeven Point Analysis

	Solar panel without heat pipe	Solar panel with heat pipe
Electrical power	110 watt	115.74 watt
First cost	3,500 baht	5,500 baht
Operating hours per day	5.5 hrs.	5.5 hrs.
Unit rate	3.5 baht/ kWh	3.5 baht/kWh
Rate of return	21.78 %	16.04 %
Breakeven point	4.46 years	6.67 years

6. Conclusion

The experimental study on the potential of using heat pipe to increase the solar panel's efficiency is done. Heat pipe is designed to look like a sleeping chair shape and is attached to the solar panel. Experiment is conducted under various electric power inputs to halogen lamp in order to simulate the direct sunlight on the solar panel throughout the day. The solar panel's surface temperature reduction is as much as 11.7ºC under 26ºC ambient temperature. The increase in electrical power produced is 5.22 % compare with solar panel without heat pipe. The temperature distribution throughout heat pipe is nearly uniform and hence saturated condition is maintained inside heat pipe. Two equations are setup to find the percentage increase in electrical power produced and solar panel's surface temperature reduction due to heat pipe. The breakeven point is 6.67 years or 2.21 years increase when compared with solar panel without heat pipe. The carbon dioxide reduction is 10.15 kg per year.

References

[1] Supavit V., Chanin S. 2559 *Heat Reduction on Solar Panel Using Aluminium Fin,* Thesis, Department of Environmental Engineering, Chulalongkorn University

[2] A.K. Mozumder, A.F. Akon, M.S.H. Chowdhury and S.C. Banik *Performance of Heat Pipe for Different Working Fluid and Fill Ratios* Department of Mechanical Engineering, Bangladesh University of Engineering & Technology

[3] Patrick J. Brennan and Edward J. Kroliczek 1979 *Heat Pipe Design Handbook* B&K Engineering, Inc.

[4] T.L. Bergman, A.S. Lavine, F.P. Incopera, D.P. Dewitt *Introduction to Heat Transfer*. 6th edition. John Wiley & Sons, Inc. (United States of America)

[5] Green Rhino Energy Ltd. 2016 *Annual Solar Irradiance, Intermittency and Annual Variations* http://www.greenrhinoenergy.com/solar/radiation/empiricalevidence.php

[6] Galen Barbose and Naïm Darghouth 2016 *Tracking the Sun IX.U.S.* (USA)

[7] W.F. Stoecker 1980 *Design of Thermal Systems* 2nd edition McGraw Hill Inc. (United State of America)

[8] R.Manimaran1, K.Palaniradja1, N.Alagumurthi1, K.Velmurugan *An Investigation of Thermal Performance of Heat Pipe Using Di-water* 2012 Science and Technology 2(4) p. 77-80

[9] Madhuri, Ashish Pandey, Anil Kumar, N.P Yadav 2019 *Predicting the Performance of Heat Pipe at Different Inclination Angle* IOP Conf. Series: Materials Science and Engineering 691 012011

TSF0006

The Proper Orthogonal Decomposition and Dynamic Mode Decomposition of Minimal Channel Flow

Worapat Piensuk[1], Peerapong Kumkhuntod[1], Wichayaporn Suthanupaphwuth[1], and Kamthon Septham[1,*]

[1]Department of Mechanical Engineering, Faculty of Engineering, King Mongkut's University of Technology Thonburi, 10140, Thailand

* Corresponding Author: E-mail: kamthon.sep@mail.kmutt.ac.th

Abstract. Wall turbulence is the turbulent flow in a region adjacent to the wall or the surface enclosing the fluid. The study of wall turbulence provides a better understanding of the underlying physics, thus, the improvement of drag reduction strategies. Theoretically solving the Navier-Stokes equations seems to be an ideal approach to extract knowledge of fluid motions. However, wall turbulence cannot be easily described due to the existence of essentially strongly nonlinearity. Therefore, here is where numerical simulation comes into play as it allows us to investigate fluid motions. Direct numerical simulation (DNS) employed in this work is a widely accepted method due to its superior accuracy. One of the most significant features of wall turbulence is the self-sustaining mechanisms, and the minimal flow unit (MFU) is the smallest computational domain capable of capturing this phenomenon. Not only that MFU can dramatically reduce computational costs, but the results from the MFU is also much less complicated than that of the full channel. The numerical data obtained from DNS is then analysed via the proper orthogonal decomposition (POD) and the dynamic mode decomposition (DMD) which allows complex structures of turbulence to be extracted and decomposed into fundamental structures. In this study, the streamwise and spanwise computational domain of the channel was chosen to be $0.6\pi h$ and $0.18\pi h$, respectively, where h is the channel half-height. DNS is performed using Channelflow-1.4.2 which gives the velocity distribution in the domain during the time interval $0 \leq t \leq 400$ at friction Reynolds number of approximately 200. The time duration between two successive timesteps is 0.1. The results from DMD indicate that the most dominant structure likely corresponds to a streak-like structure which is the crucial component of the self-sustaining mechanisms. Other less important structures are responsible for the complexity in the flow. The results from POD can also identify the same dominant structure.

Keywords: Direct numerical simulation, Proper orthogonal decomposition, Dynamic mode decomposition, Wall turbulence, Minimal flow unit

1. Introduction

Fluid dynamics has always been a field of research where the exact explanations to some areas still remain unknowns. There are many engineering-oriented problems which could be improved or solved with better understanding of the underlying flow physics. In the present work, deeper understanding of the underlying structure of wall turbulence is of particular interest due to its application on, for example, drag reduction techniques implemented in various modes of transportation (road, rail, air, water and pipeline). It is certain that the behavior of the fluids can be described by the nonlinear Navier-Stokes equations. It is its nonlinearity sourcing from the existence of the advective term that creates major obstacle to obtain the exact solution.

Direct numerical simulation (DNS) is one of the widely-accepted methods for its superior accuracy as the Navier-Stokes equations are numerically solved. The results using this method also shows well agreement with the experiments [1]. The results from the simulation are pressure and velocity fluctuations at every point in the computational domain at every timestep (discrete time interval).

The minimal flow unit (MFU), firstly introduced by Jimenez and Moin [2] is used as the computational domain since it is the smallest domain where self-sustaining mechanisms can be observed. The near-wall structures mainly contain only one pair of coherent motions (a low-speed streak and a high-speed region) [3] as shown in figure 1. It is suggested that one complete cycle of the periodic behaviour of a single low-speed streak includes growth, instability, bursting, and decay [4] as shown in figure 2.

Proper orthogonal decomposition (POD) introduced by Lumley [5], which merged the independent works of Karhunen [6] and Loéve [7] together, as a method that decomposes complex structures into orthogonal POD modes and each of which with associated energy. The dominance of those modes is ranked based on their contribution to the total energy of the flow, the energy fraction. Webber et al. (1997) [8] applied POD to wall turbulence. It shows that the most dominant modes are streamwise rollers.

Dynamic mode decomposition (DMD) introduced by Schmid [9] is a method assuming that the evolution of the system is linear. This technique decomposes the original flow field into various DMD modes, each one of them is associated with single frequency, and their dominance are determined by their amplitudes. The evolution of wall turbulence during a short-time interval was investigated using DMD [10]. It shows that linear growing modes related to the self-sustaining mechanisms are detected. Furthermore, the application of DMD suggests that the structures of near-wall turbulence are mainly composed of sinuous meandering structures and alternating-sign streamwise structures [11].

In the present work, wall turbulence in the minimal flow unit with the same configuration of that of Jimenez and Moin [2] is analysed using both POD and DMD. The underlying flow physics is explored.

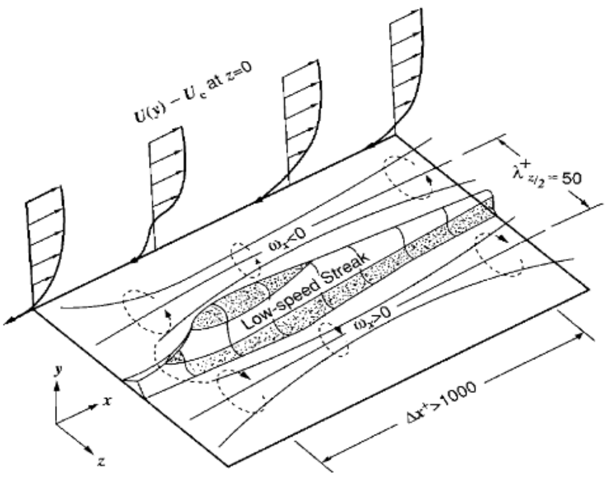

Figure 1. Model of near-wall structures [3].

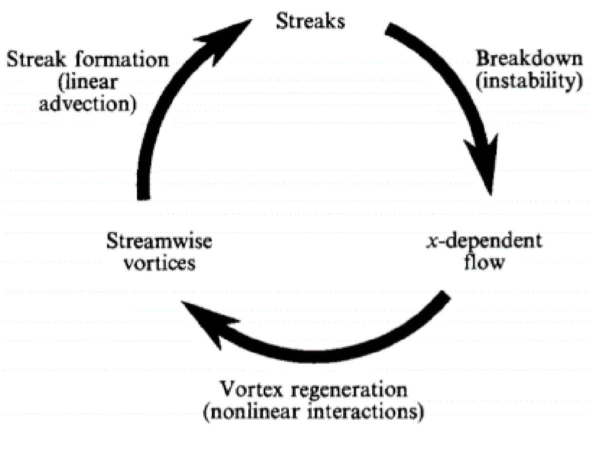

Figure 2. Self-sustaining mechanisms [4].

2. Methodology

2.1 Computational domain

The size of the computational domain as shown in figure 3 is the same as that which had been used by Jimenez and Moin [2].

2.2 Numerical simulation

2.2.1 Direct numerical simulation (DNS)

In this work, Channelflow-1.4.2, which is a DNS algorithm established by Gibson et al. (2008) [12] is employed. The governing equations that are used to generate the numerical data are the incompressible Navier-Stokes equations, where the velocity is written as a sum of two parts: the base part, which is assumed to be the velocity profile of laminar flow, and the fluctuating part. The boundary conditions are presented in figure 3.

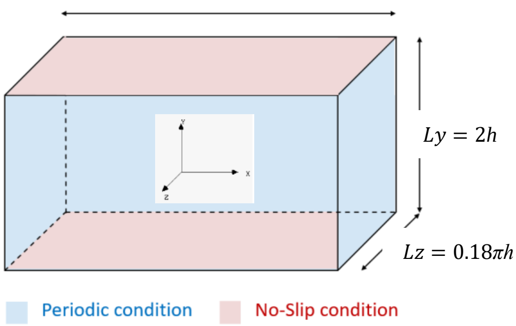

Figure 3. Computational domain.

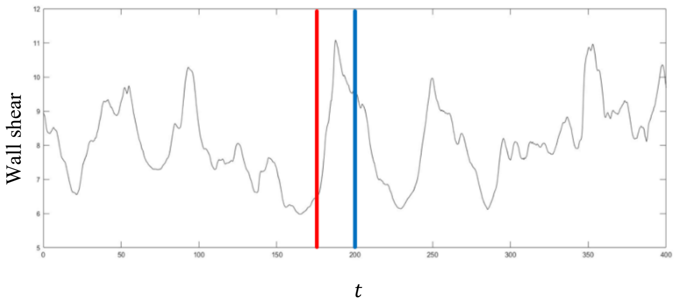

Figure 4. The temporal evolution of wall shear stress.

2.2.2 Proper Orthogonal Decomposition

The domain is imposed with mirror symmetries such that the horizontal plane can be divided into four equal rectangles. Therefore, performing the Fourier transform on the fluctuating velocity field, we get $\boldsymbol{u}(y,n,m)$, where n, $m \geq 0$ are wavenumbers corresponding to variable x and z, respectively. So, the eigenfunctions and eigenvalues are those satisfy

$$\int_{-h}^{h} \mathrm{G_{ij}}(y,y',n,m)\varphi_{\mathrm{j}}(y',n,m)\mathrm{d}y' = \mathrm{g}(n,m)\varphi_{\mathrm{i}}(y), \tag{1}$$

where $\mathrm{G_{ij}}(y,y',n,m) = \langle u_i(y,n,m)\bar{u}_j(y',n,m)\rangle$ is the two-point spatial correlation tensor, and h is the midplane distance measure in wall-normal direction. The eigenfunctions (POD modes) can then be written as

$$\psi^k(x,y,z) = \varphi^k(y,n,m)e^{2\pi nxi/L_x}e^{2\pi mzi/L_z} \tag{2}$$

where $k = (n,m,q)$ denotes unique eigenfunction. Since matrix G is Hermitian, the eigenfunctions are orthonormal allowing us to express the flow field as a linear combination of them with associated coefficients $\mathrm{a}^k(t)$. The energy eigenvalues g can then be obtained from

$$\mathrm{g}^k = \langle\, \mathrm{a}^k(t)\,\overline{\mathrm{a}^k}(t)\rangle \tag{3}$$

Since this formulation is constructed only in a region whose wavenumbers n, m are positive, there are degeneracy of energies when the whole channel is considered. With an effect of degeneracies, a correct energy fraction of each mode can be determined. Practically, only a few of most energetic, high energy fractions, eigenfunctions are needed for the reconstruction of the approximated flow. The work by

Webber et al. (1997) [8] showed that the flow reconstructed from first 100 modes could well approximate that from all 3025 POD modes implying that POD is able to capture the significant feature of the flow using only few modes.

2.2.3 Dynamic Mode Decomposition

It is noted that only the values of velocity are of interest, the script then starts by rearranging these values into a matrix where each column are the data in a single timestep. The streamwise- and spanwise-velocity components (u and w) at a single timestep are rearranged respectively into one column and sorting these columns from the first to the last timesteps results in a sequence of data or a snapshot matrix.

$$\mathbf{D_1^N} = \begin{bmatrix} \mathbf{u_{11}} & \mathbf{u_{12}} & \cdots & \mathbf{u_{1N}} \\ \mathbf{u_{21}} & \mathbf{u_{22}} & \cdots & \mathbf{u_{2N}} \\ \vdots & \vdots & \cdots & \vdots \\ \mathbf{u_{21}} & \mathbf{u_{22}} & \cdots & \mathbf{u_{2N}} \\ \mathbf{w_{11}} & \mathbf{w_{12}} & & \mathbf{w_{1N}} \\ \mathbf{w_{21}} & \mathbf{w_{22}} & \cdots & \mathbf{w_{2N}} \\ \vdots & \vdots & & \vdots \\ \mathbf{w_{M1}} & \mathbf{w_{M2}} & \cdots & \mathbf{w_{MN}} \end{bmatrix}, \tag{4}$$

where the upper and lower indices of matrix **D** denote the first and last timesteps, respectively. The companion matrix can then be determines using the singular value decomposition (SVD) on matrix $\mathbf{D_1^{N-1}}$ such that

$$\mathbf{D_1^{N-1}} = \mathbf{UVW^T}, \tag{5}$$

Where **U** and **W** are unitary matrices and **V** is a diagonal matrix whose elements are eigenvalues (singular values) of $\mathbf{D_1^{N-1}}$. The superscript **T** denotes conjugate transpose. The companion matrix is then

$$\mathbf{\bar{S}} \equiv \mathbf{U^T D^N{}_2\, W V^{-1}} = \mathbf{U^T A U}, \tag{6}$$

where **A** is a linear time-evolution operator such that

$$\mathbf{D_2^N} = \mathbf{A\ D_1^{N-1}} \tag{7}$$

DMD modes and their associated eigenvalues can then be calculated. Consequently, the decay rate and frequency of each DMD mode can then be determined by

$$\sigma_i = \frac{\mathrm{Re}(\lambda_i)}{\Delta t},\ \omega_i = \frac{\mathrm{Im}(\lambda_i)}{\Delta t} \tag{8}$$

However, the level of dominance of modes can only be seen when their amplitudes are found. Here, therefore, Cholesky factorization is used to find the amplitudes, and the selection of modes for reconstruction can now be made appropriately. Figure 4 represents the temporal evolution of wall shear stress. The red and blue lines indicate the starting (t = 175) and ending point (t = 200) of DMD analysis. The time interval between 175 to 200 is selected since the system evolves linearly during the transient growth period, see figure 4, which is in accordance with the assumption on linear evolution of DMD algorithm.

3. Results and Discussion

In the present work, we will be interested in only the velocity distribution (u and w) on a streamwise-spanwise plane at $y^+ \approx 20$ where the production of turbulent kinetic energy is very active.

3.1 Dynamic Mode Decomposition (DMD)

In figure 5, the extracted 1000 eigenvalues at $y^+ \approx 20$ are plotted where real and imaginary parts are x- and y-axes, respectively. Since most of all eigenvalues are on the unit circle, those corresponding modes are then marginally stable. The amplitude is plotted against the frequency in figure 6 illustrating the dominance of all 1000 modes and, thus, it is obvious that the most dominant mode does not oscillate representing a steady-state structure of the flow. Now that with the dominance level of each mode, only the first 25 most dominant modes are properly chosen for the reconstruction. In figure 7, the evolution in time of streamwise velocity fluctuation from DNS and DMD reconstruction are compared showing that DMD can well approximate the behavior of wall turbulence.

Streamwise velocity fluctuation distributions at different timesteps obtained from DNS and DMD reconstruction are compared in figure 8 and the first 6 modes are presented in figure 9.

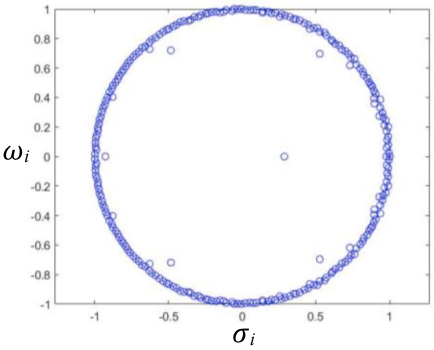

Figure 5. Eigenvalues distribution

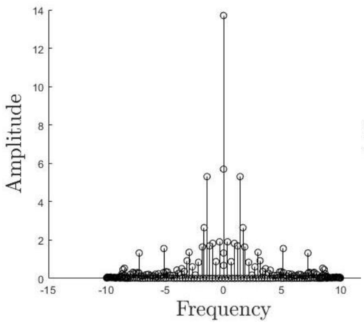

Figure 6. Amplitudes distribution

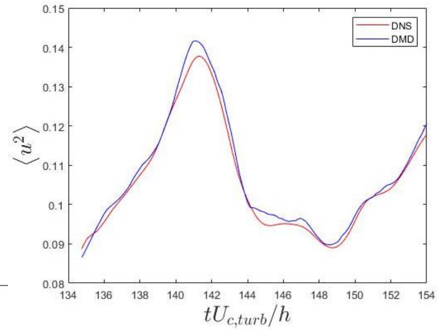

Figure 7. Flow reconstruction

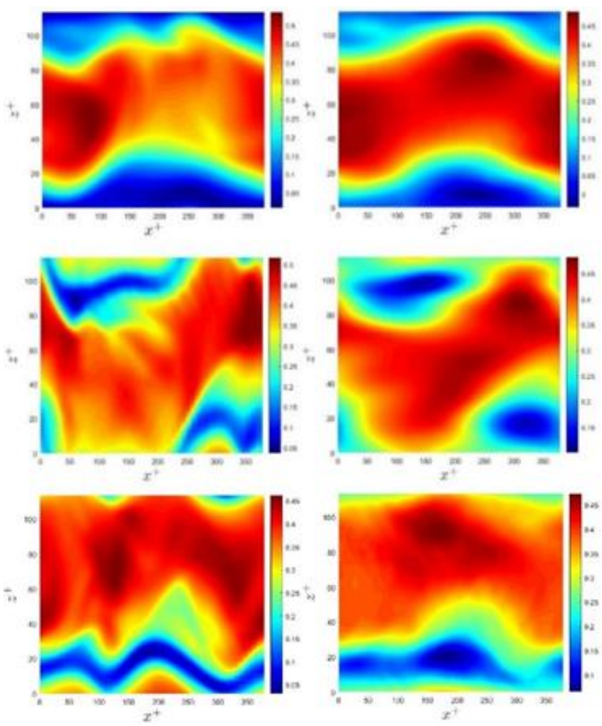

Figure 8. Contours of streamwise velocity fluctuation during self-sustaining mechanism are presented comparing between DNS (left) and DMD reconstruction (right).

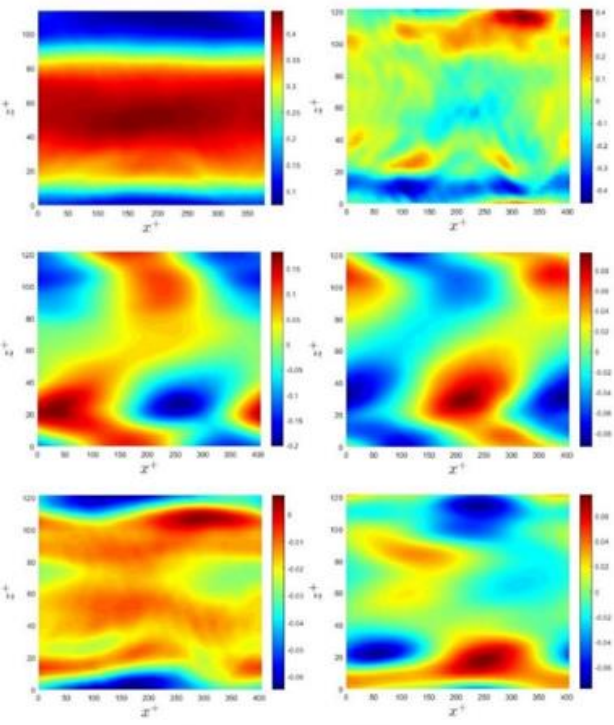

Figure 9. The first 6 most dominant DMD modes are presented. Mode 1 (ω = 0); Mode 2 (ω = 1.416); Mode 3 (ω = 1.663); Mode 4 (ω = 0.345); Mode 5 (ω = 0.922); Mode 6 (ω = 1.202). Mode order: from left to right, top to bottom.

3.2 Proper Orthogonal Decomposition (POD)

The POD analysis is performed at the same plane as in DMD through the same time interval. A total number of 251 POD modes are extracted, and the dominant modes is selected based on their energy fractions. The first 10 modes are shown in figure 10 and, since the fractions of mode 2 to mode 10 are relatively low, another plot of fractions excluding the first mode is presented in figure 11

The velocity distributions during the transient growth are presented in figure 12. The contour plots of the first 6 modes are shown in figure 13. The results from both algorithms show one similarity that they share the same most dominant mode which is a streak-like structure.

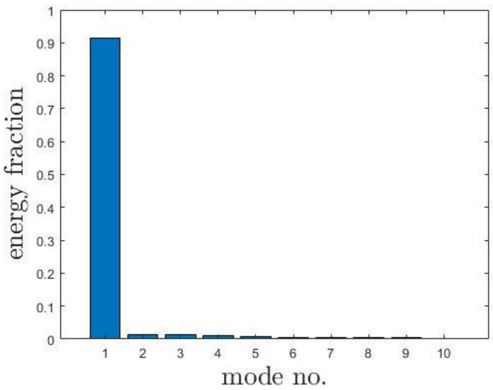

Figure 10. The energy fractions of the first 10 POD modes.

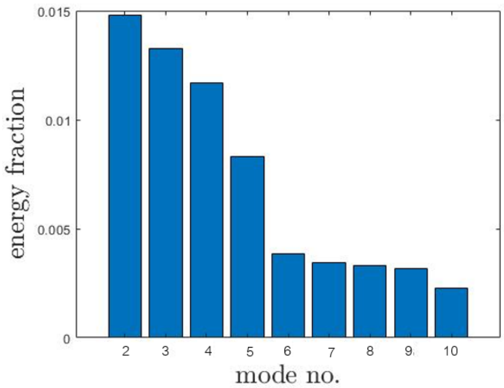

Figure 11. The energy fractions of the POD modes other than the first one.

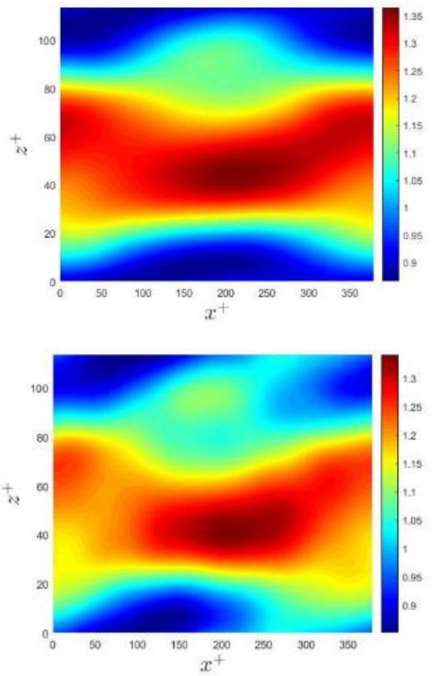

Figure 12. Contours of streamwise velocity fluctuation during self-sustaining mechanism are presented comparing between DNS (top) and POD (bottom).

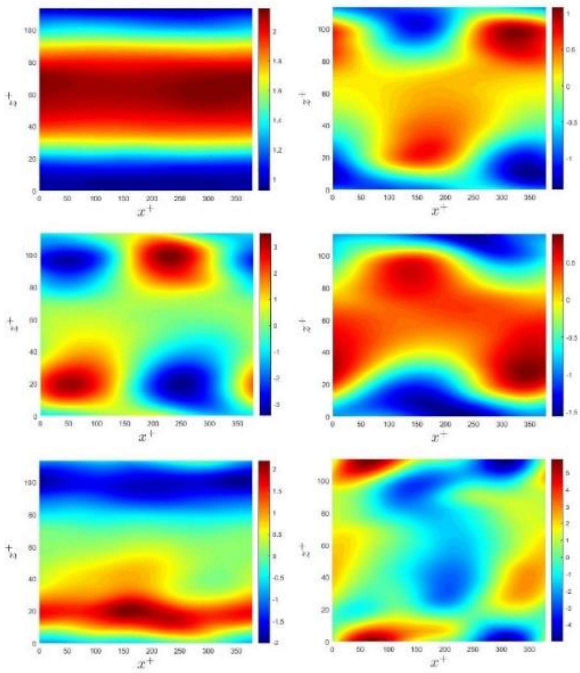

Figure 13. The first 6 most dominant POD modes are presented. Mode order: from left to right, top to bottom.

4. Conclusion

Both dynamic mode decomposition and proper orthogonal decomposition are applied to analyse the underlying structures of wall turbulence in the minimal flow unit. From the results of DMD, we see that only a few most dominant modes are needed to approximate the original flow field from DNS. Moreover, the most dominant DMD mode oscillates with zero frequency. From the results of POD, we find that the most energetic POD mode possesses the same structure, the streak-like structure, as the first mode from DMD analysis and those modes other than the first mode contribute drastically less to the flow. One can see that, since DMD algorithm decomposes the flow into modes with different frequencies, one is then allowed to control the flow more effectively by, for example, exerting the excitation at some specific frequency to achieve the improvement goal. It is likely that both DMD and POD are interesting techniques to extract the underlying physics of wall turbulence.

5. Acknowledgement

We delightfully acknowledge the people who contribute to this work and, also, those who support physically and mentally. We are also in debt the Department of Mechanical Engineering, Faculty of Engineering, King Mongkut’s University of Technology Thonburi for the computing facilities.

6. References

[1] Moin P. and Mahesh K. (1998). Direct Numerical Simulation: A Tool in Turbulence Research. Annual Review of Fluid Mechanics 1998 30:1, 539-578
[2] Jiménez, J. and Moin, P. (1991). The minimal flow unit in near-wall turbulence, Journal of Fluid Mechanics, 225, 213-240.
[3] Blackwelder, R. and Kaplan, R. (1976). On the wall structure of the turbulent boundary layer. Journal of Fluid Mechanics, 76(1), 89-112. doi:10.1017/S002211207600314
[4] Hamilton, J. M., Kim, J. and Waleffe, F. (1995). Regeneration mechanisms of near-wall turbulence structures. Journal of Fluid Mechanics 287, 317-348.
[5] Lumley J. (1970). Stochastic Tools in Turbulence, Academic Press, New York, 1970.
[6] Karhunen K. (1946). Zur Spektraltheorie stochastischer Prozesse, Ann. Acad. Sci. Fennicae, Ser. A 1, 34 (1946).
[7] Loéve M. (1945). Fonctions aleatoires de second ordre, Comptes Rendus De L'Académie des Sciences, vol. 220, 1945.
[8] Webber, G. A., Handler, R. A. and Sirovich, L. (1997). The Karhunen-Loéve decomposition of minimal channel flow, Physics of Fluids, 9, 1054–1066.
[9] Schmid P. (2010). Dynamic mode decomposition of numerical and experimental data, Journal of Fluid Mechanics, Cambridge University Press (CUP), 2010, 656 (August), pp.5-28.
[10] Mizuno, Y., Duke, D., Atkinson, C. and Soria, J. (2011), Investigation of wall-bounded turbulent flow using Dynamic mode decomposition. J. Phys.: Conf. Ser. 318 042040
[11] Cassinelli, A., Giovanetti, M. de, and Hwang, Y. (2017), Streak instability in near-wall turbulence revisited, Journal of Turbulence, 18(5), 443–464.
[12] Gibson, J., Halcrow, J. and Cvitanović, P. (2008). Visualizing the geometry of state space in plane Couette flow, Journal of Fluid Mechanics, 611, 107-130.

TSF0008

Numerical Study on Performance of Crossover Jet Impingement Cooling at Trailing Edge of Gas Turbine Blade with and without Rotation

Napat Kanjeakphong[1], Phongsakorn Thawornsathit[1], Varangrat Juntasaro[2], Pipat Tansakul[3], Panut Bumphenkiattikul[4], Arthit Vongachariya[4] and Ekachai Juntasaro[1*]

[1] Department of Mechanical and Process Engineering, The Sirindhorn International Thai-German Graduate School of Engineering (TGGS), King Mongkut's University of Technology North Bangkok (KMUTNB), 1518 Pracharat 1 Road, Wongsawang, Bangsue, Bangkok, 10800, Thailand
[2] Department of Mechanical Engineering, Faculty of Engineering, Kasetsart University, 50 Ngam Wong Wan Road, Lat Yao, Chatuchack, Bangkok, 10900, Thailand
[3] Electricity Generating Authority of Thailand, 53 Moo 2 Charan Sanitwong Road, Bangkruai, Nonthaburi, 11130, Thailand
[4] SCG Chemicals Co., Ltd., 271 Sukhumvit Rd., Map Ta Phut, Muang Rayong, Thailand, 21150

* Corresponding Author: ekachai.j@tggs.kmutnb.ac.th, +66(0) 89 897 1657

Abstract. For the improvement of gas turbine engines, the performance of gas turbine engines increases when increasing the turbine inlet temperature. At present, the turbine inlet temperature has already been higher than the melting point of the turbine blade material. Therefore, the trailing edge of gas turbine blades requires the effective internal cooling methods because the narrow shape of the trailing-edge region constrains the internal cooling passage. The impingement of a rib-roughened cooling technique is applied to reduce the turbine blade temperature in order to prevent the turbine blade failures. This paper presents the 3D steady numerical study of the flow and the cooling effectiveness indicated by the Nusselt number distribution at the 11 target surfaces based on the Reynolds-Averaged Navier-Stokes (RANS) equations coupled with the energy equation using 5 turbulence models which are Spalart-Allmaras, Wilcox k-ω, SST k-ω, realizable k-ε with enhanced wall treatment and RNG k-ε with enhanced wall treatment. The comparison of the results using 5 turbulence models under the static condition with the experimental data is conducted for the model validation. The Wilcox k-ω turbulence model is qualified and employed for this work. For investigation of the flow and the cooling effectiveness on the rotating turbine blade, only the Wilcox k-ω turbulence model is applied to the same geometry with the rotational velocity of 3000 rpm. The result reveals that the cooling performance of the turbine blade is affected by the centrifugal force, that is, the cooling effectiveness of the rotational case is 22%-59% lower, compared to the static case.

1. Introduction

Thermal efficiency and power output of the gas turbines increase with the increasing turbine rotor inlet temperature. The advanced gas turbines are cooled internally and externally to keep the temperature of turbine blades below its failure temperature. However, this paper focuses on the internal cooling called the impingement cooling which is achieved by passing the high velocity coolant through the nozzles and impinging the coolant jets on the target surfaces that conduct heat from the external surfaces contacting with hot gas. Due to the coolant being the compressor bleed air, the gas turbine cooling system must be designed to minimize the use of the coolant to get the maximum gas turbine performance.

Several previous studies reported about this cooling method. Chupp et al. [1] reported that the averaged Nusselt number at the inner wall of a smooth leading edge of turbine blades increased with increasing Reynolds number. The impingement heat transfer coefficient was measured on a curved surface of the turbine blade leading edge with and without film holes. It was concluded by Metzger and Bunker [2,3] that the Nusselt number increased with approximately 0.6 power of jet Reynolds number. There was the conclusion that there was an optimum nondimensional jet to surface spacing $\frac{z}{d}$ value for the maximum heat transfer coefficient, reported by Chang et al. [4]. Akella and Han [5] reported the study of impingement cooling on the ribbed wall in the rotating two-pass rectangular channels and they concluded that the Nusselt number of the rotating test decreased by 20 percent of the nonrotating test. There were also several leading edge studies with various roughness geometries at the nose inner wall with and without film holes at the leading edge as reported by Taslim [6-11]. The effect of bleed holes on the heat transfer coefficient and the friction factor in the turbine trailing edge cavity with rib roughened surface was also reported by Taslim et al. [12]. Taslim and Nongsaeng [13] and Taslim and Fong [14] studied the heat transfer coefficient affected by the jet impingement at the rib or smooth target surfaces in the trailing edge of turbine blades. Their studies reported that the 5 degree tilted jet produced higher heat transfer coefficients at the target surfaces. Taslim and Xue [15] reported the effect of the rib geometry on the Nusselt number at the target surfaces in the flow passage that was made up of two trapezoidal channels linked to each other by 11 racetrack shaped crossover holes. This study concluded that the 90 degree rib produced the best Nusselt number distribution at the target surfaces.

The objective of this work is to extend the work of Taslim and Xue [15] to investigate the effect of rotation of 3000 rpm on the crossover jet impingement cooling indicated by the Nusselt number at the target surfaces inside the trailing edge of gas turbine blades using the same geometry. The Computational Fluid Dynamics (CFD) simulation is applied to investigate the flow and the heat transfer at the target surfaces.

2. Numerical Method

2.1. Geometry and dimension

The geometry used in the experiment and numerical study of Taslim and Xue [15] is adopted as the fluid domain of the turbine blade cooling channel in this work. The detail of geometry and its dimension are shown in Figure 1. The cooling air flows through the larger trapezoidal channel. Being separated and injected by 11 racetrack shaped nozzles, the cooling air impinges on the heated target surfaces with 90 degree ribs and flows toward the outlet of the smaller trapezoidal channel.

2.2. Mesh generation

The unstructured tetrahedral mesh of 19.5 million cells is generated by the ANSYS Meshing software for numerical calculation in ANSYS FLUENT. To obtain the accurate result of flow and heat transfer, the fine meshes are generated near the wall of the fluid domain using 20 layers of fine prism meshes near the wall with 15% growth rate that covers the boundary layer and are coarser at the core of flow passages with caution of the skewness and orthogonality qualities. Also, y^+ from the wall to the first cell center is about 0.2 over the whole domain.

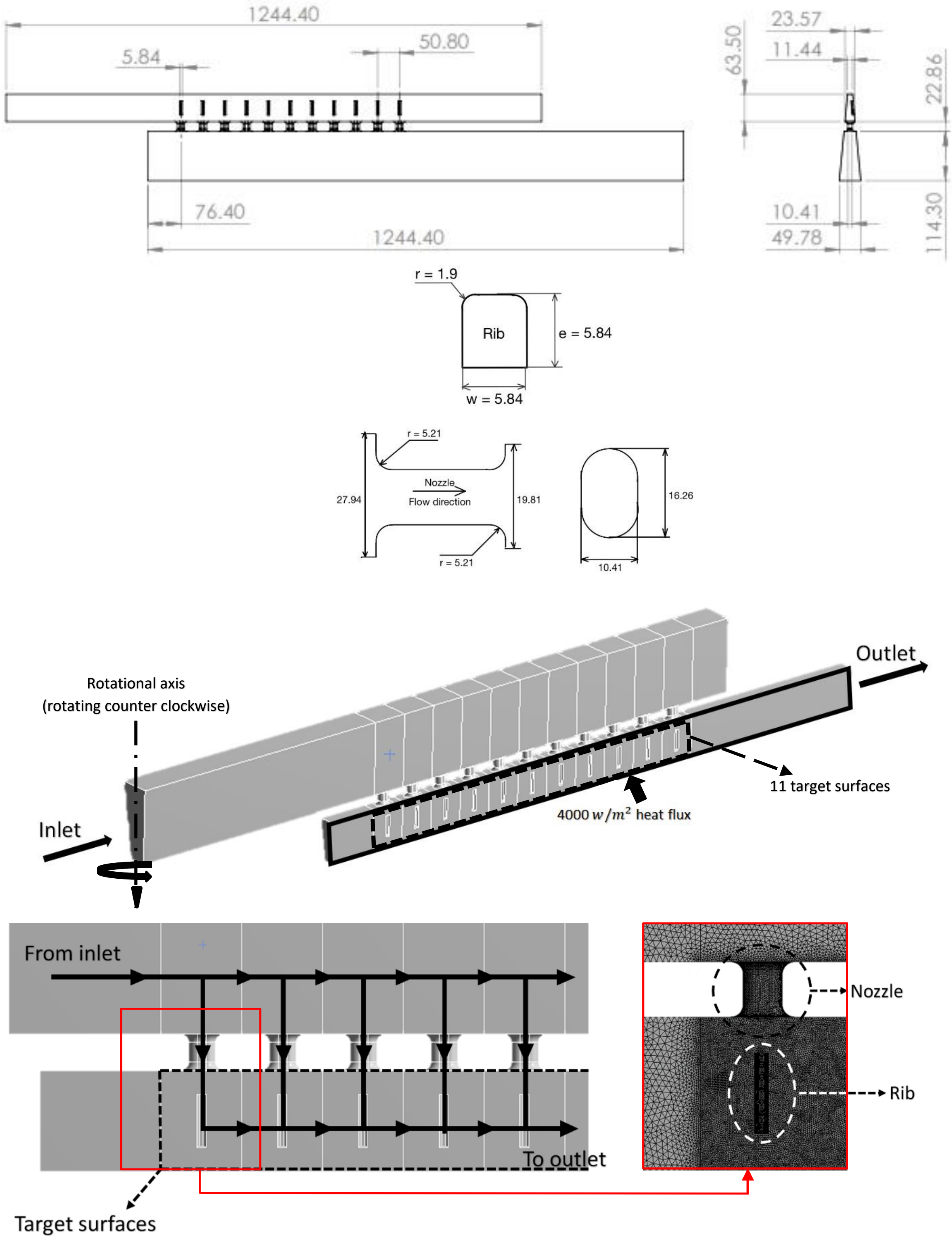

Figure 1. Trailing edge cooling passage geometry.

2.3. Governing equations

The governing equations that are solved by ANSYS FLUENT for the simulation are given as follows:

Continuity Equation:

$$\frac{\partial(\rho\bar{u}_i)}{\partial x_i}=0 \tag{1}$$

Reynolds-Averaged Navier-Stokes Equation:

$$\frac{\partial\left(\rho\bar{u}_j\bar{u}_i\right)}{\partial x_j}=-\frac{\partial\bar{p}}{\partial x_i}+\frac{\partial}{\partial x_j}\left(\mu\frac{\partial\bar{u}_i}{\partial x_j}-\rho\overline{u'_iu'_j}\right) \tag{2}$$

Energy Equation:

$$\frac{\partial}{\partial x_j}\left(\rho c_P\bar{T}\bar{u}_j\right)=\frac{\partial}{\partial x_j}\left(k\frac{\partial\bar{T}}{\partial x_j}-\rho c_P\overline{T'u'_j}\right) \tag{3}$$

Wilcox k-ω Turbulence Model:

$$\frac{\partial\left(\rho u_jk\right)}{\partial x_j}=P_k-\beta^*\rho\omega k+\frac{\partial}{\partial x_j}\left[\left(\mu+\sigma_k\frac{\rho k}{\omega}\right)\frac{\partial k}{\partial x_j}\right] \tag{4}$$

$$\frac{\partial\left(\rho u_j\omega\right)}{\partial x_j}=\frac{\gamma\omega}{k}P_k-\beta\rho\omega^2+\frac{\partial}{\partial x_j}\left[\left(\mu+\sigma_\omega\frac{\rho k}{\omega}\right)\frac{\partial\omega}{\partial x_j}\right]+\frac{\rho\sigma_d}{\omega}\frac{\partial k}{\partial x_j}\frac{\partial\omega}{\partial x_j} \tag{5}$$

2.4. Solution method and boundary conditions

ANSYS FLUENT 2019 R3 is employed to solve 3D viscous steady Reynolds-Averaged Navier-Stokes equations (RANS) coupled with two-equation turbulence model and energy equation. The steady state pressure-based solver is used. Also, the coupled pressure-velocity coupling scheme is utilized with the first-order upwind discretisation method for convection terms in every equation. The calculations were executed on 512 CPU cores CentOS 7.4 Linux cluster by using METIS algorithm for mesh partitioned. For monitoring convergence, the mass and the energy are balanced. The residuals of momentum, energy and turbulence equations are considered to be lower than 1.0e-4 with the mass residual that is approximately decreased below 1.0e-2 and then levels off. The mass flow rate through 11 nozzles, the area-weighted averaged Nusselt number and the static temperature at 11 target surfaces are not changed with the iteration of the simulation. The coolant, 18ºC air, with mass flow rate of 0.028 kg/s, calculated from the jet Reynolds number of 20400, first flows through the inlet of the bigger trapezoidal channel, then is injected by 11 nozzles to impinge on 11 target surfaces and also adjacent surfaces heated uniformly by the heat flux of 4000 W/m^2 and finally flows through the outlet of the smaller trapezoidal channel. For the rotational case, the blade rotates at 3000 rpm around the rotational axis lying on the inlet plane as shown in Figure 1 with the same inlet mass flow rate and heat flux at the target surfaces.

2.5. Turbulence models

In order to verify that the turbulence model used to calculate the rotation case is appropriate for this problem, 5 turbulence models considered (Spalart-Allmaras, Wilcox k-ω (Standard k-ω), SST k- ω, realizable k-ε with enhanced wall treatment and RNG k-ε with enhanced wall treatment) are used to simulate the static case at the jet Reynolds number of 20400 and validate the results with the experimental data of Taslim and Xue [15] in order to select the most accurate turbulence model for this problem and then use it for the rotational case. That turbulence model selected is the Wilcox k-ω.

3. Results and Discussion

3.1. Validation result

The CFD result of the area-weighted averaged Nusselt number at the 11 target surfaces under static condition is compared with the experimental data of Taslim and Xue [15]. The Nusselt number, which is the dimensionless heat transfer coefficient used to evaluate the cooling effectiveness, is defined as

$$Nu = \frac{hD_h}{k} = \frac{q_w D_h}{(T_w - T_{in})k} \tag{6}$$

where q_w is the wall heat flux, T_{in} is the temperature of the fluid at the inlet, T_w is the temperature of the target surface, D_h is the hydraulic diameter and k is the thermal conductivity of fluid. For this problem, the higher Nusselt number means the better cooling effectiveness and hence T_w is decreased while the other physical parameters (q_w, D_h, T_{in} and k) are kept constant in this study.

Figure 2 shows the comparison of the area-weighted averaged Nusselt numbers at target surfaces of the result using the Wilcox k-ω model with the Taslim and Xue [15] experimental data and simulation result of Taslim and Xue [15] with the present CFD result using the Wilcox k-ω model under static condition. It shows the good agreement with the experimental data according to the comparison of the second norms of 5 turbulent models which refer to the experimental data from Taslim and Xue [15] as shown in Table 1. The second norm is defined as

$$Nu_{norm} = \sqrt{\sum_{i=1}^{n} (\Delta Nu_i)^2} \tag{7}$$

where ΔNu_i is the difference between the area-weighted averaged Nusselt numbers at the i^{th} target surface from the CFD results and the experimental data of Nusselt number at the same target surface, while n is the number of target surfaces.

However, the Wilcox k-ω result and the Taslim and Xue [15] simulation result are slightly different because of the difference of mesh. The result shows that the area-weighted averaged Nusselt numbers at target surfaces are quite low at the 1st target surface but increases successively to the target surface. This is related to the result of the mass flow rate of air flowing through the nozzles, i.e. low at nozzle 1, increasing successively to the last nozzle, as shown in Figure 3.

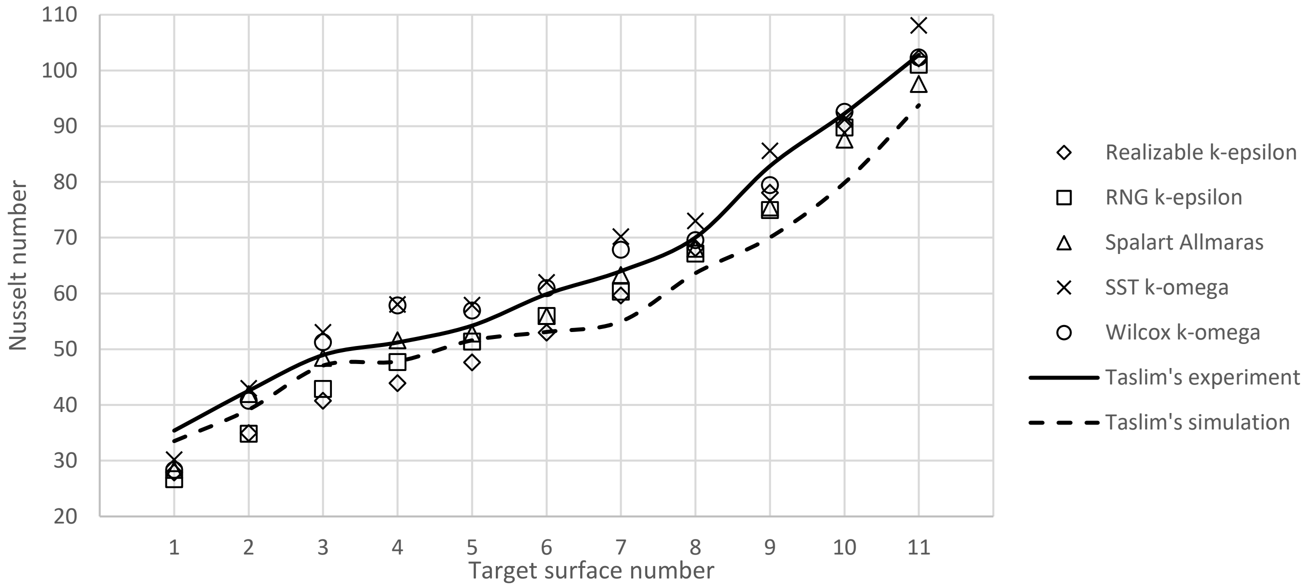

Figure 2. Comparison of the area-weighted averaged Nusselt number at $Re_{jet} = 20400$.

Table 1. The comparison of the second norm of the Nusselt number at the target surfaces of each turbulent model with the Nusselt number at the target surfaces of experiment.

	The comparison of the second norm of the Nusselt number at target surfaces					
	Nusselt number at target surfaces					
Target Surface	**Realizable k-epsilon**	**RNG k-epsilon**	**Spalart Allmaras**	**SST k-omega**	**Wilcox k-omega**	**Taslim's experiment**
1	27.8662261	26.69768682	28.36257555	30.207047	28.34684485	35.39748954
2	34.95315243	34.82662998	41.98331852	42.97306567	40.74800953	42.55230126
3	40.74239089	42.90273703	48.44069164	53.04643029	51.24865532	48.9539749
4	43.9320946	47.68419867	51.58293322	58.02073749	57.87976931	51.21338912
5	47.66125808	51.35301412	52.78648097	57.90667301	56.94125463	54.22594142
6	52.98742303	55.93851094	55.98428106	61.99825894	60.9389762	59.87447699
7	59.63832355	60.32230974	63.30204921	70.22212486	67.82385002	64.0167364
8	68.14934985	67.16599434	68.01935258	72.98459051	69.59087179	70.041841
9	78.05503899	74.96171565	75.45222796	85.57384333	79.43417908	82.84518828
10	90.29469706	89.79852186	87.56535115	91.23672164	92.60774378	92.25941423
11	102.1683736	101.0083451	97.59161696	108.1025845	102.3280897	102.8033473
Second Norm	19.37528814	17.36482698	13.26170842	13.85655614	11.74133727	
Ranking	5	4	2	3	1	

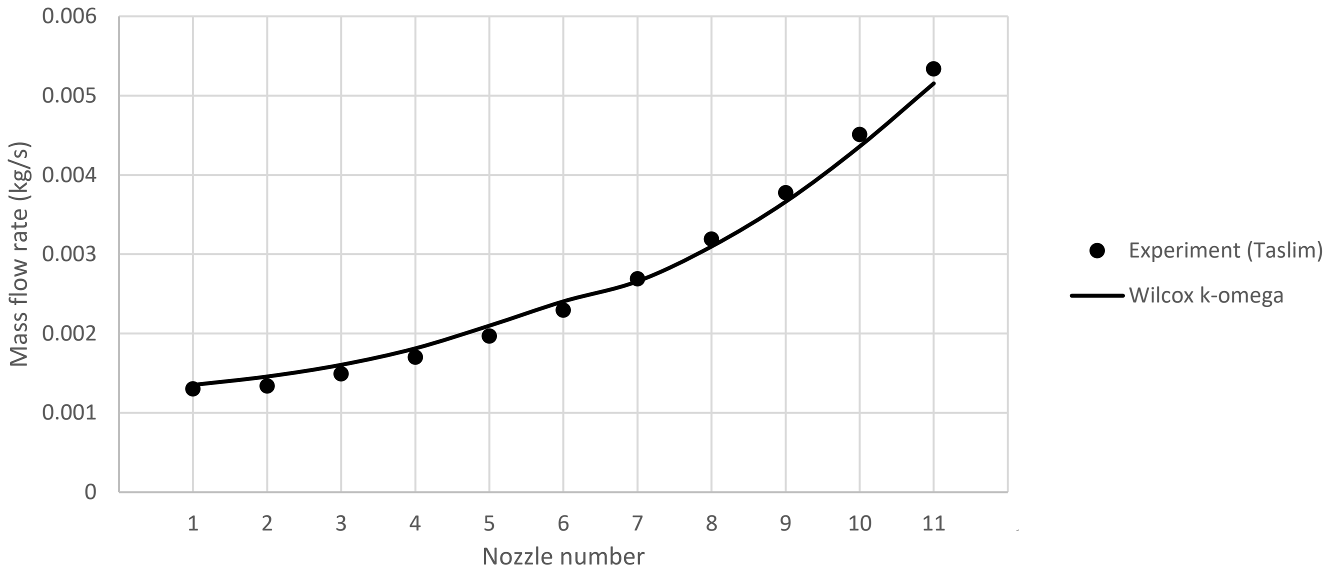

Figure 3. Comparison of the mass flow rate through 11 nozzles at $Re_{jet} = 20400$.

3.2. Effect of rotation on flow and heat transfer phenomena

The Wilcox k-ω turbulence model is applied for the rotational case with 3000 rpm to investigate the effect of the rotation on the cooling effectiveness indicated by the area-weighted averaged Nusselt number distribution at 11 target surfaces as shown in Figure 4. The result shows that the cooling performance of the rotational case is not so effective as the performance of the static case due to the centrifugal force that directs the cooling air toward the end of the inlet chamber. As a result, the cooling air cannot properly enter the early group of nozzles as much as it should have been, and goes out through the outlet, that causes the lack of the cooling effectiveness for the rotational case.

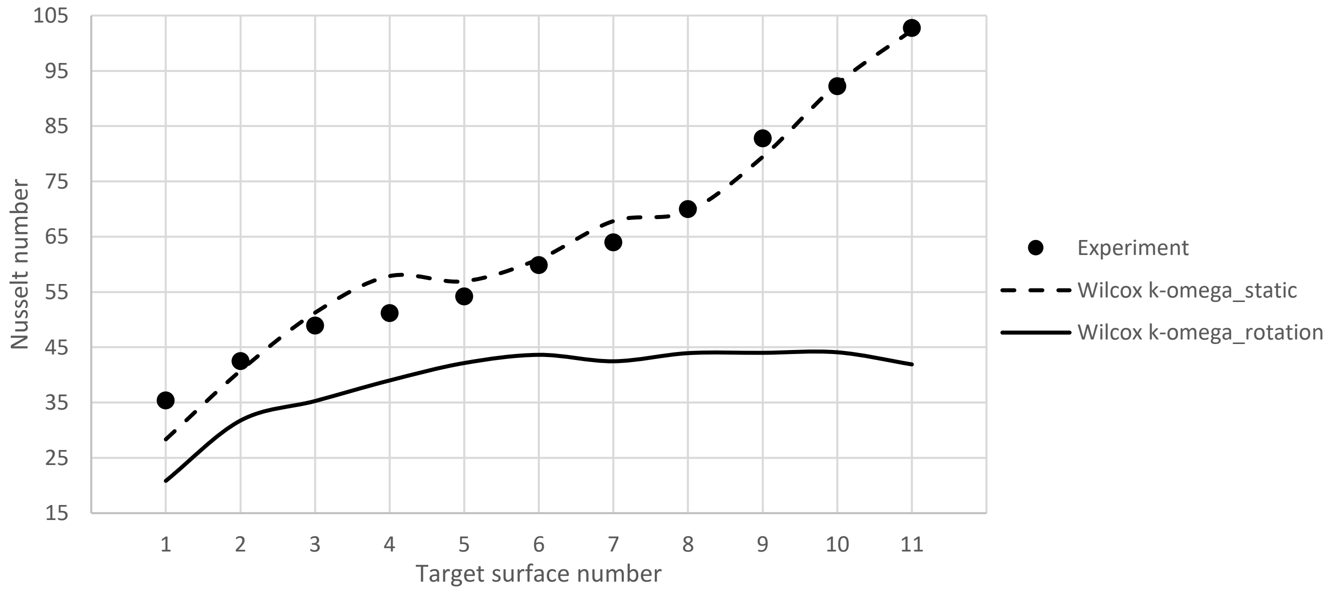

Figure 4. Area-weighted averaged Nusselt number distribution at 11 target surfaces.

4. Conclusion

The cooling effectiveness in the trailing edge of the turbine blade is investigated by the computational fluid dynamics (CFD) with the Wilcox k-ω turbulence model using ANSYS FLUENT. The result shows that the cooling effectiveness, indicated by the area-weighted averaged Nusselt number distribution at the target surfaces, of the rotational case at 3000 rpm is lower than the cooling effectiveness of the static case by 22%-59% due to the centrifugal force affecting the flow of cooling air not to properly enter the early group of nozzles, which is the cause of the lack of cooling effectiveness.

5. Acknowledgement

Napat Kanjeakphong is grateful for the tuition-fee-waiving scholarship from TGGS, KMUTNB, during his Master-Degree study. The support from SCG Chemicals for the high-performance computing power for this work is also appreciated.

References

[1] Chupp, R. E., Helms, H. E. McFadden, P. W., and Brown, T. R., 1969, “Evaluation of Internal Heat transfer Coefficients for Impingement Cooled Turbine Blades,” J. Aircraft, 6(1), pp. 203-208.
[2] Metzger, D. E., and Bunker, R. S., 1990, “Local Heat Transfer in Internally Cooled Turbine Airfoil Leading Edge Regions: Part I—Impingement cooling Without Film Coolant Extraction,” ASME J. Turbomach., 112(3), pp. 451-458.
[3] Bunker, R. S., and Metzger, D. E., 1990 “Local Heat Transfer in Internally Cooled Turbine Airfoil Leading Edge Regions: Part II—Impingement cooling Without Film Coolant Extraction,” ASME J. Turbomach., 112(3), pp. 459-466.
[4] Chang, H., Zhang, D., and Huang, T., 1997, “Impingement Heat Transfer From Rib Roughened Surface Within Arrays of Circular Jet: The Effect of the Relative Position of the Jet Hole to the Ribs,” ASME Paper No. 97-GT-331.
[5] Akella, K. V., and Han, J. C., 1999, “Impingement Cooling in Rotating Two Pass Rectangular Channels With Ribbed Walls,” J. Thermophys. Heat Transfer, 13(3), pp. 364–371.
[6] Taslim, M. E., Setayeshgar, L., and Spring, S. D., 2001, “An Experimental Evaluation of Advanced Leading-Edge Impingement Cooling Concepts,” ASME J. Turbomach., 123(1), pp. 147–153.
[7] Taslim, M. E., Pan, Y., and Spring, S. D., 2001, “An Experimental Study of Impingement on Roughened Airfoil Leading-Edge Walls With Film Holes,” ASME J. Turbomach., 123(4), pp. 766-773.
[8] Taslim, M. E., Bakhtari, K., and Liu, H., 2003, “Experimental and Numerical Investigation of Impingement on a Rib-Roughened Leading-Edge Wall,” ASME J. Turbomach., 125(4), pp. 682–691.
[9] Taslim, M. E., and Khanicheh, A., 2006, “Experimental and Numerical Study of Impingement on an Airfoil Leading-Edge With and Without Showerhead and Gill Film Holes,” ASME J. Turbomach., 128(2), pp. 310–320.
[10] Taslim, M. E., and Bethka, D., 2009, “Experimental and Numerical Impingement Heat Transfer in an Airfoil Leading-Edge Cooling Channel With CrossFlow,” ASME J. Turbomach., 131(1), p. 011021.
[11] Taslim, M. E., and Abdelrassoul, A., 2009, “An Experimental and Numerical Investigation of Impingement Heat Transfer in Airfoils Leading-Edge Cooling Channel,” International Symposium on Heat Transfer in Gas Turbine Systems, Antalya, Turkey, Paper No. JI-41.
[12] Taslim, M. E., Li, T., and Spring, D., 1995, “Experimental Study of the Effects of Bleed Holes on Heat Transfer and Pressure Drop in Trapezoidal Passages With Tapered Turbulators,” ASME J. Turbomach., 117(2), pp. 281–289.
[13] Taslim, M. E., and Nongsaeng, A., 2011, “Experimental and Numerical Crossover Jet Impingement in an Airfoil Trailing-Edge Cooling Channel,” ASME J. Turbomach., 133(3), pp. 1201–1210.
[14] Taslim, M. E., and Fong, M. K. H., 2011, “Experimental and Numerical Crossover Jet Impingement in a Rib-Roughened Airfoil Trailing-Edge Cooling Channel,” ASME J. Turbomach., 135(5), pp. 051014-051014–10.
[15] Taslim, M.E. and Xue, F., 2017, “Crossover Jet Impingement in a Rib-Roughened Trailing-Edge Cooling Channel,” ASME J. Turbomach., 139, p.071007.

TSF0010

Thermal Efficiency Enhancement of High Pressure Gas Stove for Noodle Pot by Using Steel Wire Net Porous Material

P Khantikomol[1,*], M Polsongkram[1] , W Apisitpinyo[1]. and T Poowadin[1]

[1]Renewable Energy Technology Research Laboratory (RTER)
Department of Mechanical Engineering, Rajamangala University of Technology Isan, 744 Suranarai Rd., Muang, Nakhonratchasima, 30000, Thailand

* Corresponding Author: preecha@rmuti.ac.th

Abstract. This research article aims to enhance the thermal efficiency of high pressure cooking gas stove (KB-5) for the noodle pot by stainless steel wire net porous material as cooking stove cover. The stainless steel wire net with pore per inch (PPI) 8, 10 and 12 were examined. Each PPI of porous cover have 3 thickness, which were 10, 20, and 30 mm. Moreover, each cover model have 3 heights, which were 25, 34, and 50 cm. In the experiment, the temperatures at inside and outside the porous cover, at pot bottom, and at the water inside the pot, were measured by the type – K thermocouples. The fuel rate 3.790, 7.584 and 11.370 kW were varied in testing. The results indicated that the stainless steel porous cover with PPI 12, thickness 20 mm, and height 34 mm gave highs thermal efficiency 85.71% at fuel rate 3.790 kW, which was higher than the case without porous cover 35.01%. It was shown that the stainless steel wire net porous material could enhance the thermal efficiency of the cooking stove for the noodle pot due to high heat transfer area and the effect of radiation heat transfer.

1. Introduction

The report on energy statistics of Thailand 2019 by the Energy Policy and Planning Office (EPPO), the Ministry of Energy, Thailand in 2019 [1] indicated the used of LPG gas in the country was about 6.6 million tons. The ratio of LPG use in house hold, industry, petrochemical, vehicle and other were 32.7%, 10.4%, 37.7%, 17.6% and 1.5%, respectively. The tendency of total of energy used in Thailand was increased from the year 2018 about 4.4%. Obviously, the use of LPG in the house hold was quite high leading to do several researches for increasing the thermal efficiency of the gas stove e.g. infrared burner and porous burner. Moreover, the gas stove cover was developed to increase the thermal efficiency of the house hold gas stove e.g. the wind shield gas stove cover developed by the Ministry of Energy [2]. The wind shield gas stove cover (WS cover) was the closed cover that protect the energy loss from the stove to the moving air (wind) by convection. The energy loss, however, also leaves with the exhaust gas and some loss by heat radiation. Later, the gas stove cover was developed using the air preheat concept [3-5] which applied the stainless steel wire net porous material. It was found that the temperature at the bottom of the pot and the surrounding were higher than the case without the porous cover obviously leading to increase the thermal efficiency of the gas stove due to the result of heat radiation and the preheat air. However, those porous cover was a closed system and quite complicate structure, which the structure of the stove was modified.

The survey of noodle shops around Rajamangala University of Technology Isan in Nakhon Ratchasima, Thailand, it was found that LPG energy used for the noodle port was consumed an average of 8 hours per day. The high pressure burner of cooking stove KB-5 was used for these shops to continually heat during the period of opening and closing. There is no materials or equipment that could help protect the heat loss from the gas stove. Therefore, this research article aims to present thermal efficiency enhancement of high pressure gas stove for the noodle pot by using steel wire net porous material. The thermal efficiency enhancement was done by the concept of flow insulation system [6-10] using the porous material as the stove cover. The cases of with and without the cover were compared under the experimental testing according to the DIN EN 203-2 [12] standard.

2. Theory

2.1. The principle of heat recovery

The concept of recovering the enthalpy of exhaust gases from various high-temperature facilities by using the porous materials has been presented by Echigo [1] since the 1982s. The principle of convection-radiation converter by using the porous medium consists of two heat transfer processes namely convection and radiation. The porous medium is capable of converting a part of the enthalpy of the hot gas flowing through it to thermal radiation or vice-versa as shown in figure 1. When the hot gas is flowing through the porous medium, heat is transferred form the gas to the porous medium by convection to decrease the temperature of porous medium. Due to the facts that the porous medium has high surface area to volume ratio and that solids have a higher emissivity than gas, the porous medium would emit thermal radiation into both the upstream and the downstream directions of the flowing gas. However, the main portion of the thermal radiation is directed toward the upstream region. The temperature of the gas was reduced as $\Delta T_f = T_{fu} - T_{fd}$ when flows through the porous media. Where, T_{fu} is the fluid temperature at upstream region and T_{fd} is the fluid temperature at downstream region. It seems that the porous media plays as the insulator of gas flow. Therefore, this porous medium is called the flow insulator.

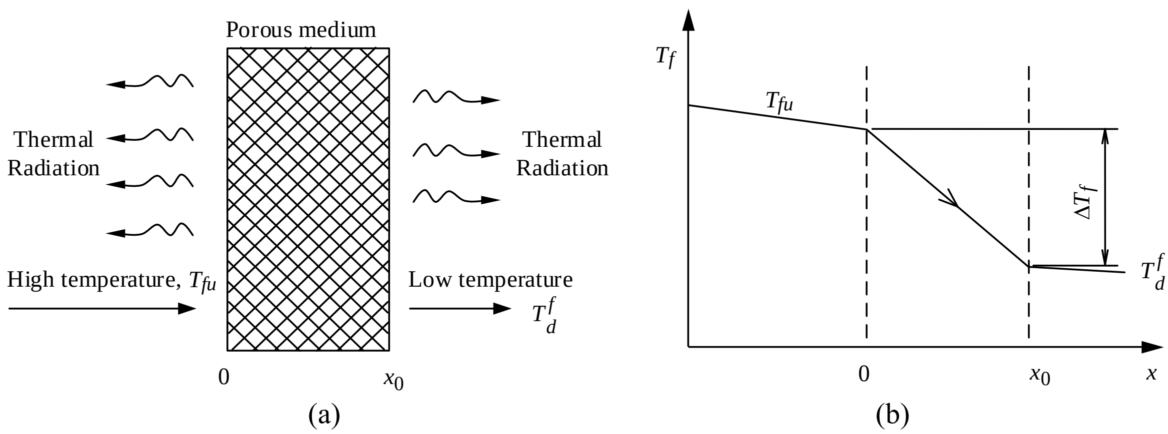

Figure 1 Principle of emitter (a) physical of energy transfer and (b) temperature profile.

Regarding to above definitions, flow insulation system utilizing the stainless steel wire net porous material was applied to construct the stove cover for the noddle port.

2.2. The thermal efficiency

The heat from gas combustion would transfer directly to the bottom of the port as shown in figure 2 by convection of an exhaust gas and the radiation of flame. The amount of energy transfer to the bottom of the port is proportional with the side of the port. However, the energy transfer to the water is the sensible heat of the water. It could calculate using the equation (1).

$$Q = mC(T_2 - T_1) \tag{1}$$

Where, Q is the sensible heat (kW), m is mass of water, C is the specific heat of the water $\left(4.186\times10^{-3}\,\mathrm{MJ/kg\cdot K}\right)$), T_1 and T_2 are the temperature of water at state 1 and 2, respectively.

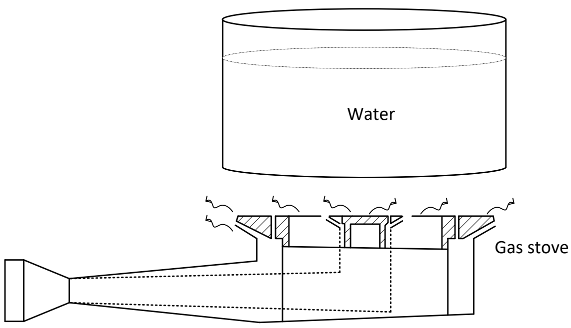

Figure 2. Heat transfer from the stove to the water.

For the thermal efficiency of the gas stove, the boiling test was considered according to the DIN EN 203-2. The experimental apparatus were setup in accordance with the TIS 2312-2549 standard. Before testing, the stove has to warm up with highest combustion rate for 15 minutes, and then turn off. The port with water and thermocouple was installed to the stove. The water was boiled from 30 ^{o}C to 90 ^{o}C. During the boiling test, the amount of gas use was recorded. Then, the thermal efficiency could calculate using equation (2), which is the ratio of sensible heat of the water and the supplied energy.

$$\eta_{th} = \frac{mC\left(363 - T_i\right)}{V\left(LHV\right)t} \times 100\% \tag{2}$$

Where, η_{th} is the thermal efficiency, T_i is the initial temperature of water, V is the volume of supplied gas, LHV is the low heating value of the gas (MJ/Nm^3) at 101.3 kPa, and t is the time of testing.

3. Experimental Setup

Figure 3 shows the experimental apparatus that the schematic diagram of the experimental apparatus according to the DIN EN 203-2 standard for measuring the thermal efficiency (η_{th}) of the cooking gas stove for the noddle port was indicated in figure 3(a). The noodle port having inner diameter 45 cm was examined. The high pressure gas stove KB-5 burner was used for this experiment. The 30 kg water was used for the boiling testing. The thermal efficiency was obtained by the sensible heat, which is the energy to increase the water temperature to 90 ^{o}C comparing to the used LPG. For temperature measurement, several type-K thermocouples were used to measure the temperature at the bottom of the pot and the water in the port. The carbon monoxide (CO) and the nitrogen oxide (NOx) were measured as the same time.

The dimension of stainless steel wire net porous media stove cover was designed as illustrated in figure 3(b). The inner diameter (*d*) and the thickness of the cover were 48.5 cm and 20 mm, respectively. The pore per inch (*PPI*) of the stainless steel wire net porous media were examined as 8, 10, and 12. The height (*h*) of the cover was varied 25, 34, and 50 cm.

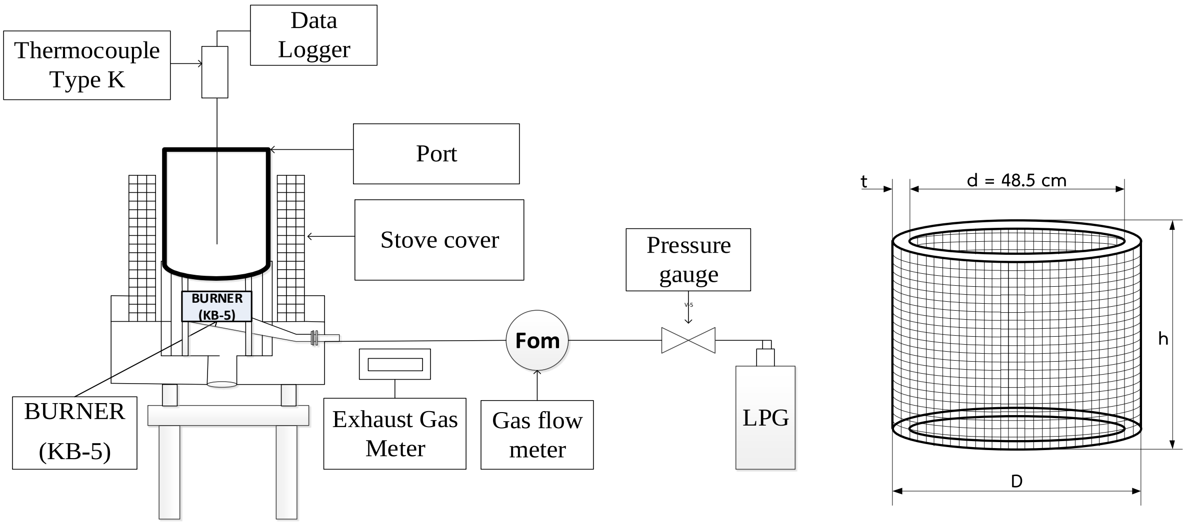

(a) (b)

Figure 3. Experimental apparatus, (a) schematic diagram and (b) porous media stove cover.

4. Results and Discussion

In the present study, the boiling times, the port bottom temperatures, the emission of an exhaust, and the thermal efficiency were considered. The influence of supplying fuel rate, the PPI, and the height of the cover to the consideration results would be investigated. Here, the results have been compared between the case of with and without installing the porous media stove cover.

4.1. Influence of the supplying fuel rate

In this study, the supplying fuel rate were varied 3.790, 7.584, and 11.370 kW, respectively. It was found that the boiling time of the case with the porous media stove cover was short than the case without the cover as shown in figs. 4. While, the pot bottom temperature and thermal efficiency of the case with the porous media stove cover were higher than the case without the cover significantly, as shown in figures 5 and figure 6, respectively

Figure 5 (b) and 6 show the influence of the supplying fuel rate to the pot bottom temperature and the thermal efficiency. The pot bottom temperatures increase with increasing the supplying fuel rate. The thermal efficiency testing according to the DIN EN 203-2 standard increase with increasing the supplying fuel rate corresponding to the pot bottom temperatures and the boiling time. In the case of installing the porous media stove cover, the pot bottom temperature and the thermal efficiency highly increase due to the porous media serves as a converter for the enthalpy of the hot flue gas by radiation and to absorb the heat from the radiation and then transfer back into the pot. This causes to reduce the amount of energy wasted thus leading to increased thermal efficiency.

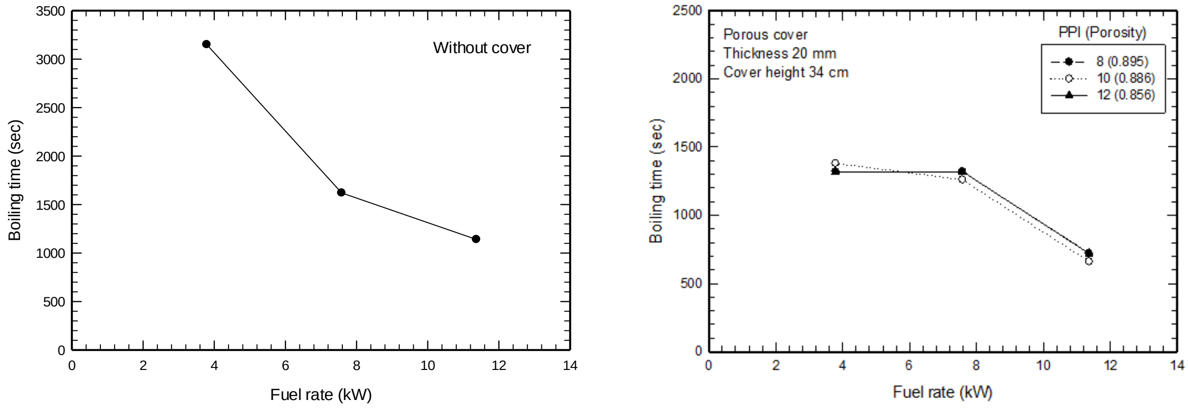

(a) (b)

Figure 4. Influence of the supplying fuel rate to the boiling times, (a) without and (b) with porous media stove cover.

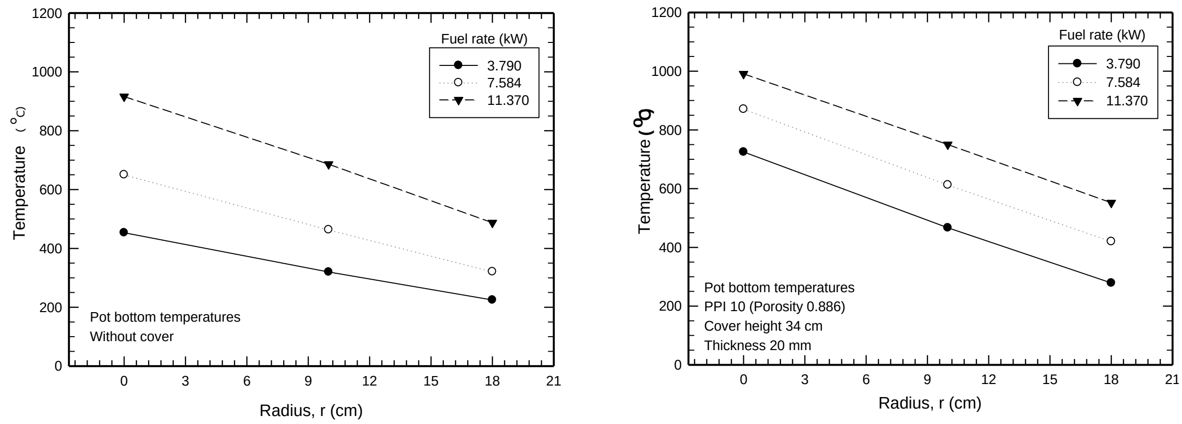

(a) (b)

Figure 5. Influence of the supplying fuel rate to the port bottom temperatures, (a) without and (b) with porous media stove cover.

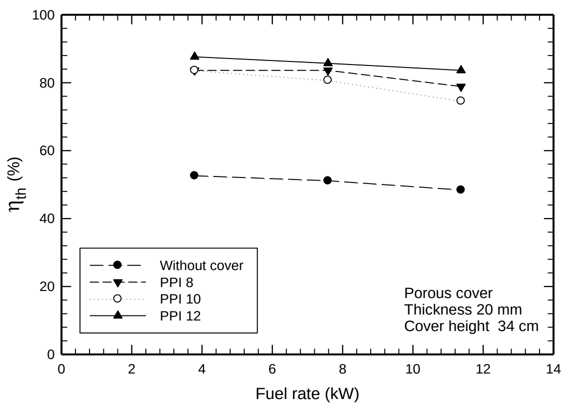

Figure 6. Influence of the supplying fuel rate to the thermal efficiency, comparing between without and with porous media stove cover

4.2. Influence of PPI

In this study, the pore per inch (PPI) of the stainless steel wire net porous material were varied 8, 10, and 12, which have porosity 0.895, 0.886, and 0.856, respectively. The influence of the PPI to the boiling times, the pot bottom temperature and the thermal efficiency were shown in figure 8. The experimental results indicated that the PPI did not strong effect to boiling time, the pot bottom temperature and the thermal efficiency. However, the larger PPI has more heat transfer area thus the porous media stove cover could as the insulator to protect the heat loss from the flue gas. For the emission CO and NOx, it seem that the PPI did not effect to increase or reduce the emission due to the CO and NOx were vary low.

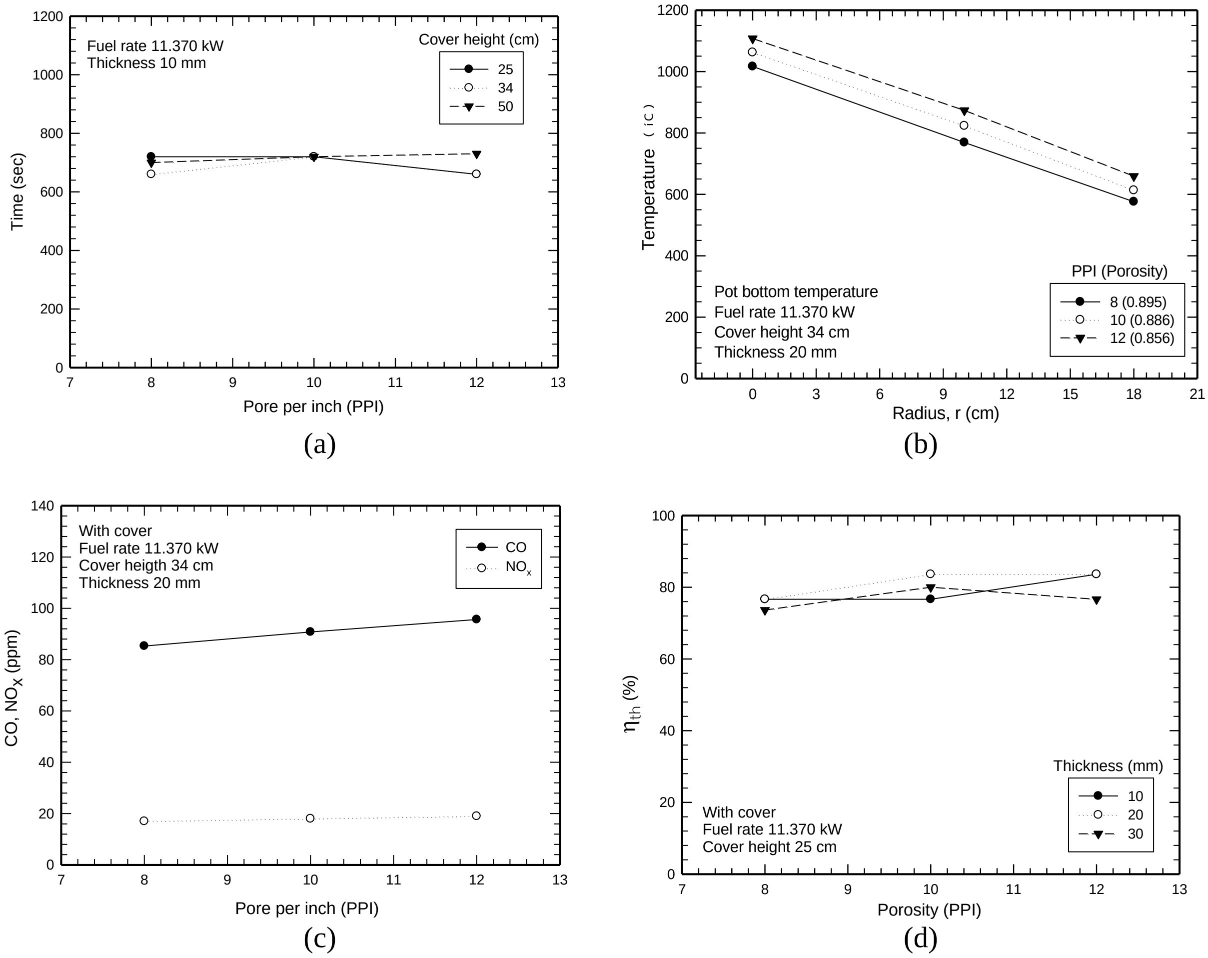

Figure 8. Influence of the PPI to (a) the boiling times, (b) the port bottom temperature, (c) the emission CO and NOx, and (d) the thermal efficiency.

4.3. Influence of the porous media stove cover height

Figure 9 show the influence of the porous media stove cover height to the boiling time, the pot bottom temperature, the emission, and the thermal efficiency. The experimental result illustrated that the porous media stove cover strong effect to these parameters. However, the cover height do not much effect to these parameters. In clearly consideration, pot bottom temperature and the thermal efficiency increase with increasing the cover height.

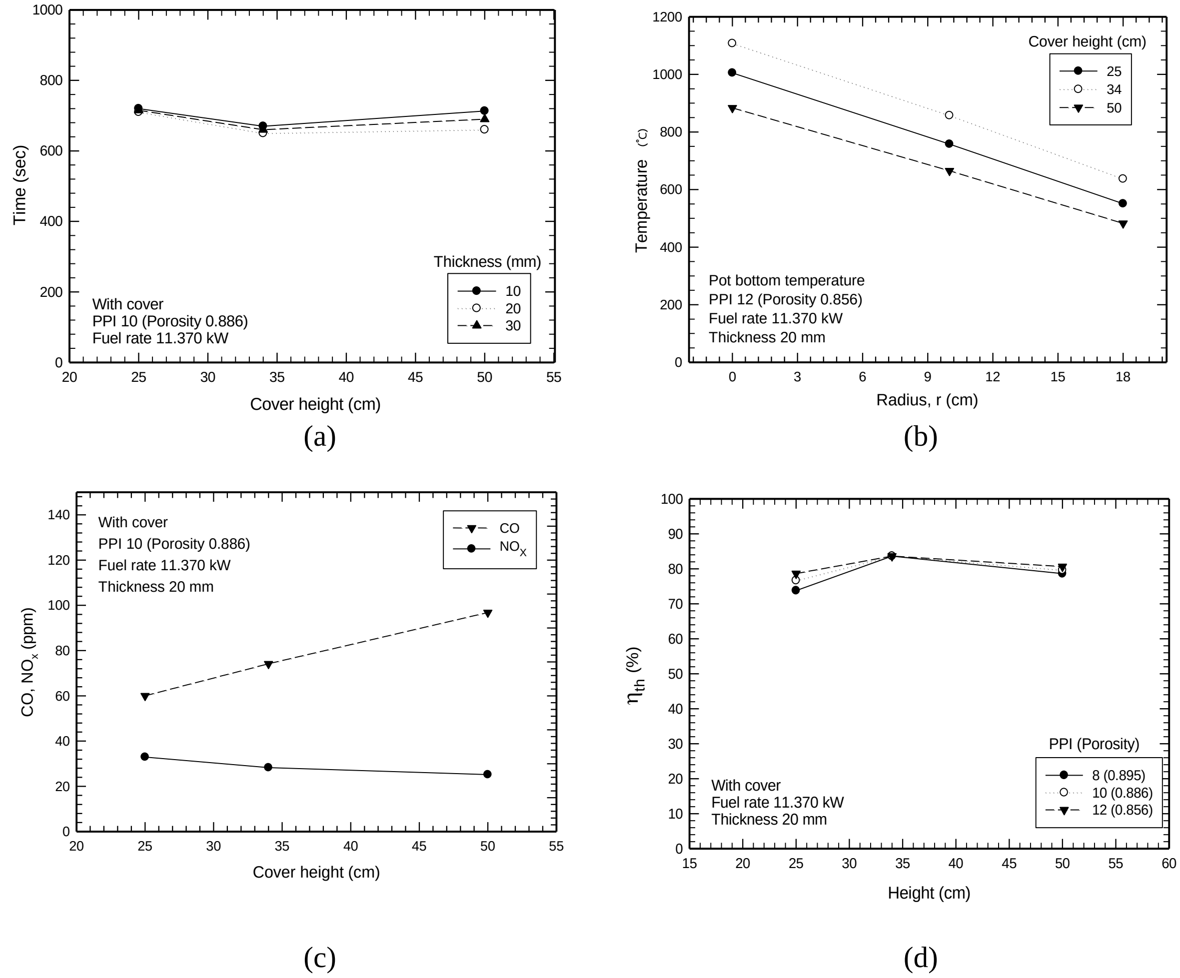

Figure 8. Influence of the porous media stove cover height to (a) the boiling times, (b) the port bottom temperature, (c) the emission CO and NOx, and (d) the thermal efficiency.

Conclusion

The enhancement of thermal efficiency of high pressure cooking gas stove (KB-5) for the noodle pot by using the stainless steel wire net porous material as stove cover. The 45 cm inner diameter of noodle port with containing 30 L water was examined. The boiling test according to the DIN EN 203-2 standard was done comparatively between the case of with and without the stove cover. The experimental results could be concluded as follow.

1) For the boiling times of the water inside the noodle port of the case with the stove cover was shorter than the case without the cover obviously. It was shown that the porous material stove cover highly effect to protect the energy loss and to help the energy transfer to the pot. In consideration of the effect of PPI, cover height and the cover thickness, the boiling time decrease with increasing PPI. The lowest boiling time occurred at 20 mm cover thickness and 34 cm cover height.

2) The temperatures at the port bottom of the case with porous material stove cover was obviously higher than the case without the cover. In the case with the cover, the pot bottom temperature increases with increasing PPI and was highest at 20 mm and 34 cm cover thickness and cover height respectively.

3) The emissions CO and NOx was very low due to the complete combustion of the burner. It could explain that the porous media stove cover was not effected to the emission significantly.

4) Thermal efficiency of the noodle pot gas stove with the porous media cover was higher than the case without the cover significantly. In the case of PPI 12, cover thickness 20 mm, and cover height 3 cm, the thermal efficiency was 87.61% while the thermal efficiency of the case without the cover was 35.01%

References

[1] Energy Policy and Planning Office 2019 Thailand Energy Situation 2019 *Ministry of Energy Thailand*

[2] Department of Alternative Energy Development and Efficiency 2019 Energy situation in 2019 and trends in 2019 *Ministry of Energy Thailand*

[3] Rungsimuntuchat N 2001 *Thesis of Master. Engineering (Mechanical Engineering)* King Mongkut University of Technology Thonburi

[4] Jugjai S and Sanijai S 1996 *International Energy Journal* Vol **18** pp 97-11

[5] Dong L L, Cheung C S and Leung C W 2002 *Int. J. Heat and Mass Transfer* Vol **45** pp 979-992

[6] Echigo R 1982 *Proc.7th Int. Heat Transfer Conf.* Vol **6** p361–366

[7] Wang K Y and Tien C L 1984 *Journal of Heat and Mass Transfer* Vol **106** pp 453-459

[8] Khantikomol P and Kamiuto K 2008 *JSME* , Vol **3** (2) pp319-329

[9] Khantikomol P, Saito S, Kamiuto K and Yokomine T 2010 *International Communications in Heat and Mass Transfer*, Vol.37 (8) pp 1015-1024

[10] Khantikomol P, Saito S and Yokomine T 2010 *J. Energy and Power Engineering*, Vol.**4** (11) pp 21-29

[11] German Standards and Technical Rules 1997 *DIN EN 203-2 : Gas-heated catering Equipment* p 17

TSF0011

A Study of Aerodynamic Performance of an Adaptive Spoiler

C Klinkaesron[1] and K Ruangjirakit[1]

[1] Department of Mechanical Engineering, Faculty of Engineering, King Mongkut's University of Technology Thonburi, 126 Pracha Uthit Rd., Bang Mod, Thung Khru, Bangkok 10140, Thailand.

Corresponding Author: kitchanon.rua@mail.kmutt.ac.th

Abstract. A spoiler is considered as one of many important aerodynamic components of a car used to generate sufficient downforce; hence, improve performance at high speed and during cornering. However, at low speed, less downforce is required in order to achieve faster acceleration. This contrast in downforce requirements leads to a development in adaptive spoiler that is able to be seamlessly morphed at different vehicle speeds, which leads to maximized aerodynamic performance. This research focuses on the study of aerodynamic effects of a 2-D adaptive spoiler to be installed on a passenger sedan car. The vehicle speeds are varied from 30 to 150 km/h and the aerodynamic characteristics of the adaptive spoiler are evaluated using Computational Fluid Dynamics (CFD) analysis in order to propose a suitable shape change and deployment strategy. The preliminary results suggest that the adaptive spoiler can reduce drag while maintaining sufficient downforce; therefore, vehicle stability is increased while fuel consumption is decreased.

1. Introduction

Aerodynamic forces acting on a ground vehicle are important elements that must be carefully analysed in the design process as high drag force will significantly increase the power required to propel the vehicle; hence, the fuel or energy consumption becomes higher, while low downforce will result in poor stability and performance at high speed and during cornering [1]. Therefore, not only aesthetic aspect but also the shape and material of the body shell, and installation of aerodynamic parts, such as front wing and rear spoiler, need to be considered. Extensive research studies [1-2] have been conducted to investigate the aerodynamic effects of different vehicle shapes. In addition, morphing or adaptive structure technology, which can be defined as the structure that its shape can be changed during operation, has been introduced and used with the rear spoiler of high-performance cars. One example of the adaptive spoiler system is Drag Reduction System (DRS) used in Formula one race cars as shown in Figure. 1 [3]. The DRS consists of 2 main parts which are the mainplane that are fixed to the pillar and an adjustable flap that can be closed to generate high downforce and open to reduce the drag during acceleration and overtaking. Apart from Formula one race cars, Porsche also introduced retractable rear spoiler as shown in Figure. 2 [4] by which the spoiler is retracted during low speed drive to reduce the drag induced by the spoiler and is deployed at moderate speed when downforce is required to improve vehicle stability and performance. The examples of moveable spoiler mentioned above rely on mechanical activation which makes the system heavy and complicate. Therefore, the concept of seamless morphing rear spoiler has become attractive as fewer components are required. This was first introduced by Aston Martin as shown in Figure. 3 [5] a concept of adaptive spoiler of Aston Martin AM-RB003 is seamless trailing edge morphing rear spoiler, it can be change trailing edge angle to control aerodynamic characteristic. The concept of seamless morphing rear spoiler has many advantages over the fixed and mechanical adaptive spoiler in terms of drag reduction and improved fuel or energy consumption [6]. In order to obtain the benefit of the positive lift coefficient at zero angle of attack, a cambered airfoil should be used [7]. In addition, to install an actuation mechanism within limited space inside the airfoil section, an airfoil with relatively large maximum thickness is required Therefore, this study aims to investigate the aerodynamic characteristics of a morphing rear spoiler using NACA 4415 airfoil section with 2- and 4-degree trailing edge deflection through Computational Fluid Dynamic (CFD) analysis. The results of this study can be used to identify suitable morphing strategy for the car equipped with the seamless morphing spoiler in order to achieve required downforce and minimize aerodynamic drag at every operational point.

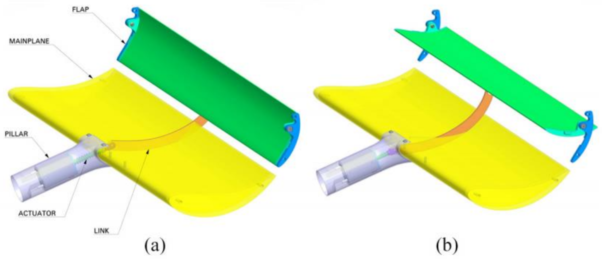

Figure 1. Drag Reduction System in (a) closed configuration and (b) open configuration [3].

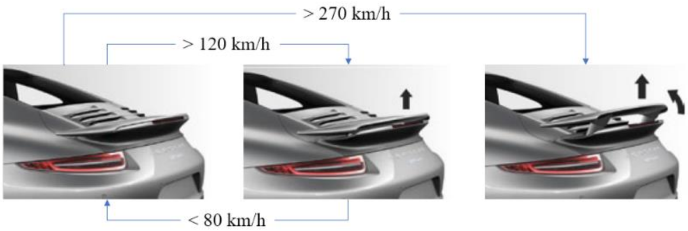

Figure 2. Porsche adaptive spoiler [4].

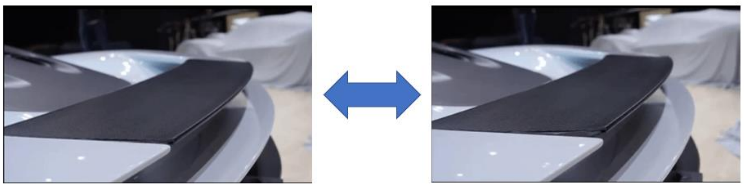

Figure 3. Aston Martin AM-RB003 [5].

2. Computational Fluid Dynamic Modelling

2.1 Morphing Spoiler Model

In this study, NACA 4415 airfoil section with max thickness of 15% at 30.9% chord, max camber of 4% at 40.2% chord as shown in Figure. 4 is used as the based shape of the seamless morphing airfoil. The camber airfoil provides superior aerodynamic benefits than the symmetrical airfoil in terms of lift generated at low angle of attack [7-8].

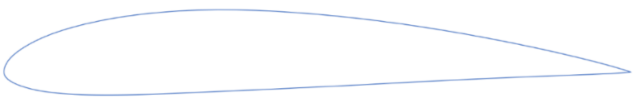

Figure 4. Airfoil NACA4415.

To study the aerodynamic characteristics of the seamless morphing spoiler, the NACA 4415 airfoil is inverted. The trailing edge of the airfoil is deflected upwards by 2- and 4-degree with respect to the pivot point at 30% chord as shown in Figure 5. This morphing concept is based on the adaptive spoiler concept of Aston Martin AM-RB003.

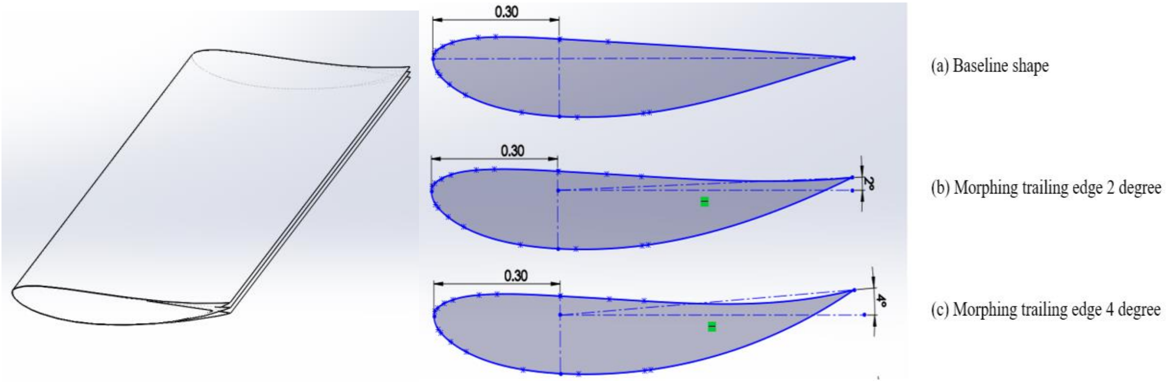

Figure 5. Airfoil NACA4415 (a) baseline shape, (b) morphed trailing edge 2-degree and (c) morphed trailing edge 4-degree.

2.2 Fluid Domain Discretization and Boundary Conditions

In this research, ANSYS Fluent 2020R1 is used as a solver to study the effects morphing spoiler at low vehicle speed (30 km/h) and high vehicle speed (150 km/h). The air with density of 1.225 kg/m3 and viscosity of 1.7894×10-5 kg/m-s, respectively, is used for the fluid domain. Two-dimensional (2-D) domain is discretized using structured mesh as shown in Figure 6. The vertical and horizontal components of freestream velocity are assigned to the top, bottom and semi-circular edges, while the outlet pressure is defined at the right edge. The inverted NACA 4415 airfoil is placed in the fluid domain with no-slip wall conditions. In order to capture viscous effects in the boundary layer close to the airfoil surface, the mesh density is controlled such that very fine elements are assigned near the airfoil surface and coarser away from the airfoil. The angle of attack considered herein ranges between 0 and 16 degrees. The coupled second order upwind scheme is used to solve for momentum and turbulent kinetic energy. Moreover, the RANS k-ω SST turbulent model is selected as it provides accurate prediction over other RANS models and not overly sensitive to inlet boundary conditions [9].

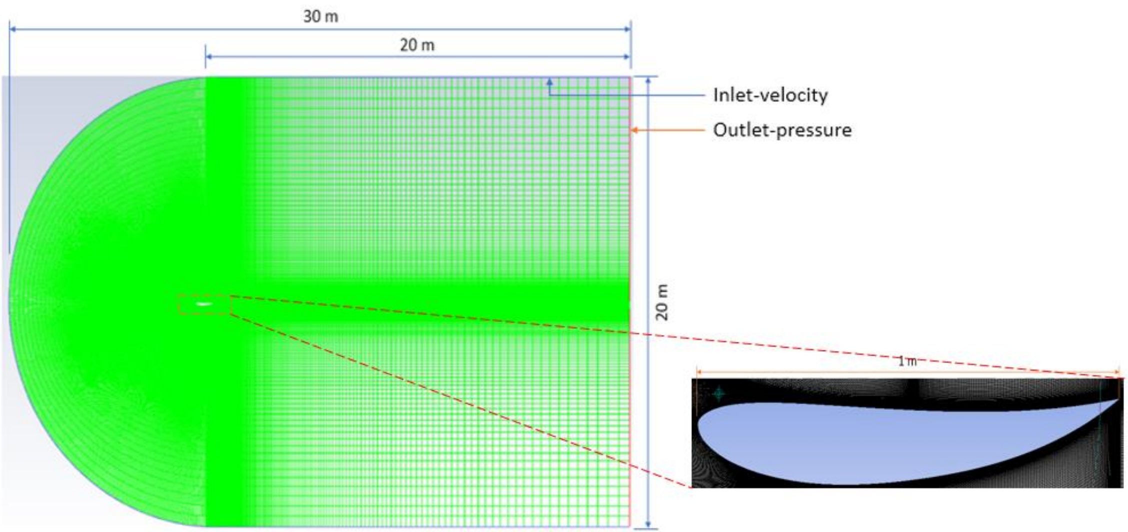

Figure 6. Dimensions and boundary conditions of fluid domain.

3. CFD Model Validation

3.1 Comparison of CFD Model and Experimental Results.

In order to ensure that the CFD settings described in the previous section can be used further to investigate the aerodynamic effects of seamless morphing spoiler, the lift and drag results of NACA 4415 airfoil at Reynolds number of 20,000 obtained from the simulation are compare against the experimental results by Omar Madani Fouatih et al. [10] as shown in Figure 7. The lift results show that the lift coefficients from CFD analysis are slightly lower than the experimental results and drag coefficient from CFD analysis are slightly lower than the experimental results too. Also, the simulation shows that the airfoil stalls at angle of attack of 14 degree while the experimental results suggest the stall angle of 12 degrees. From the comparative study, the results from CFD analysis show similar trend as compared with the experimental results with maximum 18% deviation in lift and 45% deviation in drag coefficients, respectively. with experimental results. Therefore, similar settings as described above can be applied to other morphing configurations.

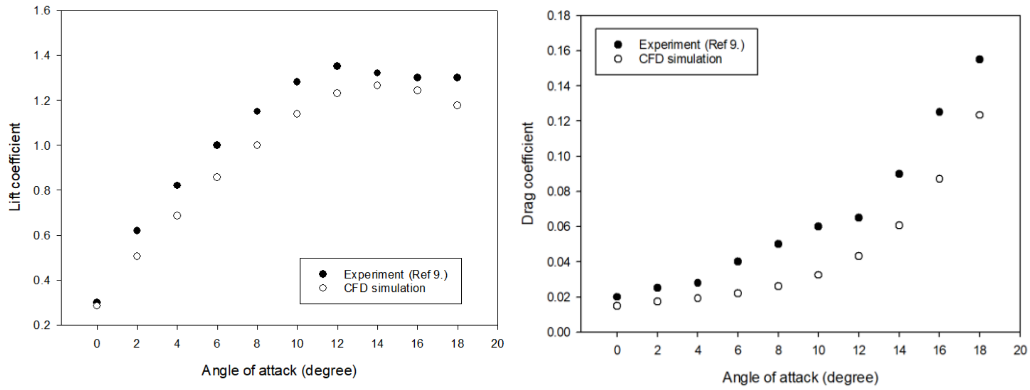

Figure 7. Lift and drag coefficient comparison from NACA4415 CFD simulation and experiment [9].

3.2 Mesh Sensitivity Analysis

In order to balance the computational cost due to increased number of elements and the accuracy of the results, a mesh sensitivity analysis is performed. The lift coefficient of NACA 4415 airfoil at angle of attack of 16 degrees is computed using 5 different mesh sizes: 50,000 80,000 240,000 300,000 and 480,800 elements. The results as shown in Figure 8 suggests that as the number of elements increases from 50,000, the lift coefficient remains relatively unchanged. However, the number of elements of 240,000 is selected in this study to ensure that sufficiently small elements can be allocated near the spoiler surface.

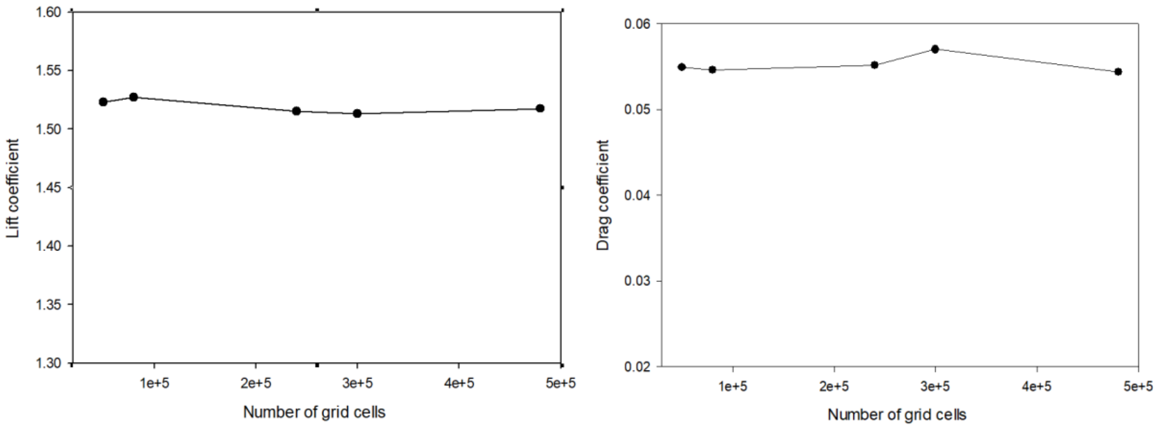

Figure 8. Lift coefficients of NACA 0012 airfoil at 12-degree angle of attack from different mesh sizes.

4. Result and discussion

4.1 Effects of Trailing Edge Morphing Angle

The trailing edge of the NACA 4415 airfoil is deflected by 2 and 4 degrees, respectively. The negative lift (downforce) and drag coefficients are computed at freestream velocity of 30 km/h and 150 km/h. The results as illustrated in Figure 9 show that as the morphing angle increases, more downforce is observed, while more drag is also generated. Similar trend can be seen at the freestream velocity of 150 km/h as at 30 km/h. An increase in downforce when the trailing edge angle is change from 0 to 4 degrees is due to an increase in camber of the airfoil. Lift coefficient is decrease resulting in a larger turbulent zone show in Figure 10. However, the drag is increased because the flow on the lower surface separates from the airfoil skin as shown in Figure 11.

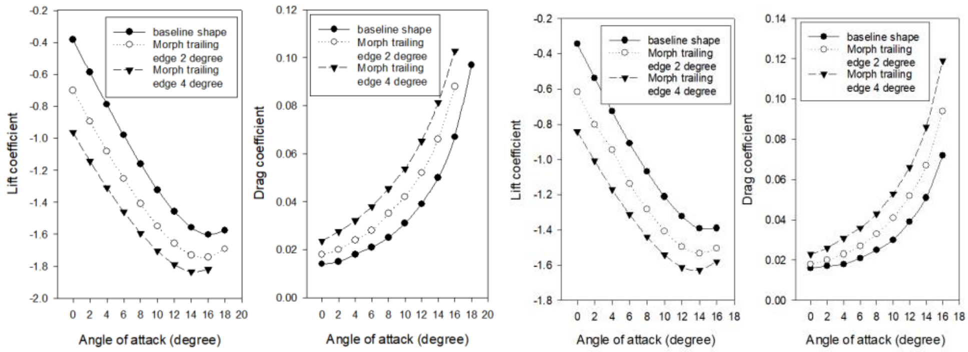

(a) (b)

Figure 9. Lift and drag coefficient comparison of baseline, morph trailing edge 2 and 4 degree (a) 30 km/h, (b) 150 km/h.

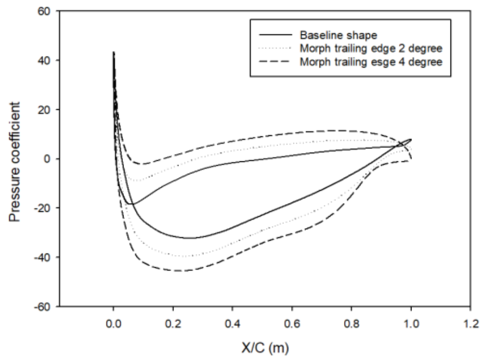

Figure 10. Pressure distribution comparison from speed 30 km/h at angle of attack 0 degree.

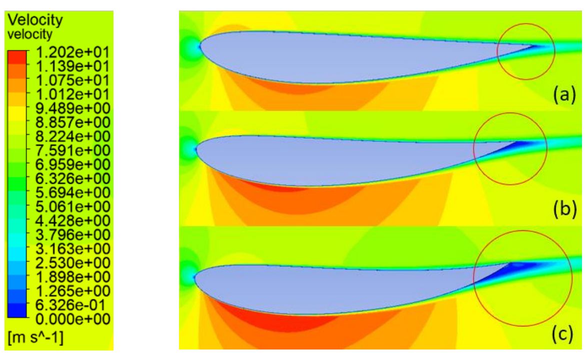

Figure 11. Separate flow on trailing edge (a) baseline shape, (b) morph trailing edge 2 degree (c) morph trailing edge 4 degree.

4.2 Effects of Lift-to-Drag Ratio and Benefits of Morphing Spoiler

The results discussed in Section 4.1 imply that the benefits of maximizing downforce and maintaining relatively low drag can be achieved when the angle of attack of the spoiler is continuously changed with the vehicle speed. However, this approach may not be practical as complicated mechanism is required to change the angle of attack. Therefore, lift-to-drag ratio plots at various angles of attack of 2 freestream velocities are generated as shown in Figure 12. It can be seen that benefits of seamless morphing spoiler are realized when the spoiler's angle of attack is fixed as in the case for current conventional spoiler. To illustrate this, at fixed angle of attack at 2 degrees, the downforce required at low speed may not be as high as in the high-speed regime. Therefore, at low speed drive, the baseline NACA4415 airfoil can be used. However, at high speed drive, the required downforce becomes higher and the trailing edge of the NACA4415 airfoil should be morphed to 2 degrees to generate more downforce.

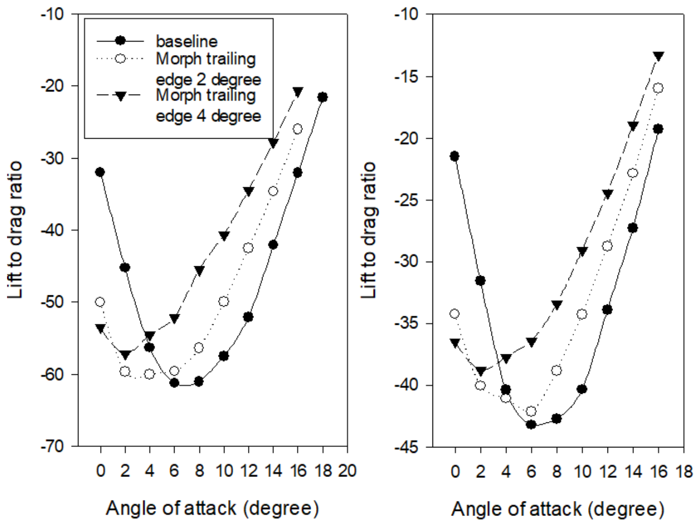

(a) (b)

Figure 12. Lift to drag ratio comparison (a) 30 km/h, (b) 150 km/h.

Finally, the results of lift and drag coefficients of NACA 4415 airfoil at 0-degree angle of attack in freestream velocity of 30 km/h as shown in Figure 13 indicates that as the trailing edge deflects to 2 and 4 degrees, respectively, the lift coefficient increases by 101 and 177 percent. However, the drag coefficient increases only 16.67 and 50 percent, respectively. This clearly shows that the aerodynamic benefits from lift offsets the disadvantage from the drag.

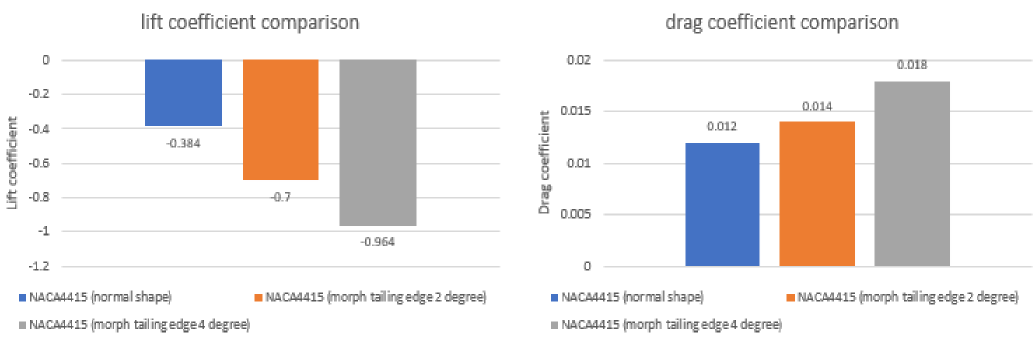

Figure 13. A comparison of lift coefficient decreasing and drag coefficient increasing from speed 30 km/h at angle of attack 0 degree from NACA4415 baseline shape.

5. Conclusion

The main focus of this study is to investigate the aerodynamic benefits of using the seamless morphing spoiler in ground vehicles. The NACA 4415 airfoil is used as a benchmark in this study and its trailing edge is deflected to 2 and 4 degrees, respectively. Computational Fluid Dynamics is performed to obtain the lift and drag results as well as to provide insight information of the flow field. The results suggest that as the trailing edge of the NACA 4415 airfoil is deflected to 2 and 4 degrees, more lift is generated at every angle of attack, while the drag also increases. However, when considering fixed angle of attack as in the case of conventional spoiler, it can be seen that improved aerodynamic performance could be achieved through trailing edge morphing, especially at different vehicle speed. Therefore, seamless morphing spoiler has a potential to be used as a cutting-edge technology of aerodynamic parts for future vehicle.

6. Acknowledgments

This research was supported by King Mongkut’s University of Technology Thonburi (KMUTT). The author would like to acknowledge for personal financial support from Thailand Advance Institute of Science and Technology-Tokyo Institute of Technology (TAIST-Tokyo Tech). The author also appreciates all my advisors from MTEC and KMUTT for their help with the simulation.

7. Reference

[1] Vivek Yakkundi, Shankar Mantha, Vivek Sunnapwar. 2017, “Hatchback versus Sedan – A Review of Drag Issues”, SSRG International Journal of Mechanical Engineering, pp. 5-13.

[2] Zhang, C., Stoll, D., Kuthada, T., & Wiedemann, J. 2019. “Aerodynamic study on the vehicle rear shape parameters with respect to ground simulation”. 2019. Internationales Stuttgarter Symposium, pp. 412–426.

[3] Mauro Dimastrogiovani, Giulio Reina, Andrea Burzoni, 2019, “An improved active drag reduction system for formula race cars”, Prceedings of the Institution of Mechanical Engineering, Part D: Journal of Automobile Engineering, pp. 1-12.

[4] Jochen Mender, Dr. Thomas Wiegand, Michael Pfadenhauer, 2014, Adaptive aerodynamics of the new Porsche 911 Turbi, ATZ Worldwide, 116(2), pp. 42-45.

[5] Mr JWW, (2019, March 5). NEW 'Son Of Valkyrie' Aston Martin AM-RB 003 Hypercar FIRST LOOK [Video], Youtube, https://www.youtube.com/watch?v=WtoRb63zkgg&t=369s

[6] Kota, S., Flick, P., & Collier, F. S, 2016, “Flight Testing of FlexFloilTM Adaptive Compliant Trailing Edge”, 54th AIAA Aerospace Sciences Meeting. 4-8 January 2016, San Diego, California, USA, AIAA 2016. 0036-0049.

[7] NASA, Shape effect on lift [Online], Available: https://www.grc.nasa.gov/WWW/K-12/airplane/shape.html [2020, June 25]

[8] Tuncay Kamas, 2009, “2-D and 3-D assessment of cambered and symmetric airfoils: a cfd study”, M.S. Thesis, Clemson university, South Carolina.

[9] Chapter 6 turbulence modeling [Online], Available: https://www.slideserve.com/thane-beck/chapter-6-turbulence-modeling [2020. June 20]

[10] Omar Madani Fouatih, Marc Medale, Omar Imine and Bachir Imine, 2015, “Design optimization of the aerodamic passive flow control on NACA4415 airfoil using vortex generators”, European journal of mechanics B/Fluids, 56, pp. 82-96.

TSF0013

Flow Visualization and Heat Transfer Characteristics of Refrigerant Gas-liquid Two-phase Flow Passing through Fine Rectangular Grooves in the Evaporation Process

Naoki Maruyama[1,*], Haruki Miyake[2], Kengo Tajima[2] and Masafumi Hirota[1]

[1] Division of Mechanical Engineering, Graduate School of Engineering, Mie University, 1577 Kurimamachiya-cho, Tsu, Mie 514-8507, Japan
[2] Graduate Student, Division of Mechanical Engineering, Graduate School of Engineering, Mie University, 1577 kurimamachiya-cho, Tsu, Mie 514-8507, Japan
*E-mail: maruyama.naoki@mie-u.ac.jp

Abstract: Flow characteristics and heat transfer of refrigerant R134a that pass through the inside of the evaporator were analyzed. In recent practical heat exchangers, the grooves engraved on the heat transfer surface are introduced to increase the heat transfer area. The influence of the cross-sectional shape of fine grooves on the boiling phenomenon of the refrigerant was experimentally examined by flow visualization and heat transfer measurement in this study. The separation of bubbles from the heat transfer surface and the inflow of liquid refrigerant to the fine groove affects heat transfer enhancement. A rectangular concave fine groove path was set on the heat transfer surface in this study. The dimensions of the groove path were set to a groove width of 0.8 mm, a groove depth of 0.4 mm, and a length of 100 mm with reference to apply to an actual evaporator. The heat transfer surface is set with a constant heat flux. In the visualization of the refrigerant two-phase flow, the generation and growth of bubbles were observed by high-speed camera. In addition, the local heat transfer coefficient was simultaneously estimated, and the correlation between the flow transition of refrigerant gas-liquid two-phase flow and the heat transfer enhancement was analyzed.

Keywords: Flow visualization, R134a, Evaporator, Fine groove, Two-phase flow

1. Introduction

As the number of refrigerators and air-conditioners for industrial and private uses increases, it is required to improve the thermal efficiency and reduce the size of refrigerators. Especially, in order to reduce the installation capacity, it is desired to reduce the size of the evaporator which occupies a large volume of the air conditioner indoor unit. Therefore, attention is being paid to heat transfer enhancement of the heat exchanger that is built into the evaporator.

In order to improve the heat transfer coefficient, the heat transfer promotion methods for the refrigerant that passes the fine grooves in the evaporator has been focused. In the practical heat exchanger, the grooves engraved on the heat transfer surface are introduced to increase the heat transfer area. As a result, the total amount of heat transfer increases. Several reviews for two-phase flow and boiling heat transfer in microchannels have been reported[1-3]. It has also been reported that the heat transfer of gas-liquid two-phase flow is closely related to the flow transition of two-phase flow[4-6]. In recent years, the introduction of refrigerants with a low global warming potential has been promoted. The flow boiling heat transfer, pressure drop, and flow pattern in a horizontal fine microchannel has been experimentally investigated for R1234yf[7]. In order to analyze the heat transfer characteristics of the evaporator, it is important to observe the flow condition flowing inside of the microgrooves. In this study, the refrigerant R134a gas-liquid two-phase flow with boiling under constant heat flux is evaluated. The separation of bubbles from the heat transfer surface and the inflow of liquid refrigerant to the fine groove are thought to affect heat transfer enhancement. The bubble behavior at the initial stage of boiling of the refrigerant is analyzed, and the flow mode is evaluated. In addition, the local heat transfer coefficient is estimated at the same time as the flow observation.

The purpose of this study is to analyze and evaluate the influence of the behavior of bubbles and liquid film on the heat transfer coefficient that depends on the shape of the fine grooves. The relationship between the flow characteristics of the refrigerant and the heat transfer characteristics is evaluated, and a cross-sectional shape of a fine groove that contributes to high heat transfer coefficient is proposed.

2. Experimental Apparatus and Procedure

Figure 1 shows the schematic diagram of the experimental apparatus and the details of the test section employed in this experiment. The experimental apparatus consists of four principal equipments to form a refrigerating cycle, that is, a compressor with an inverter control, a condenser, an expansion valve and an evaporator as a flow visualization device. Each piece of equipment in the experimental apparatus is connected by copper tubes that are coated with a heat-insulating material to prevent heat loss to the ambient air. The working fluid in this experiment is refrigerant R134a.

In this system, the flow path is divided into two paths, a test path and a bypath, at the exit of condenser where the refrigerant is kept in liquid phase in order to control the mass flow rate of the test section. In the test path, a cooler and a heater are introduced to control an evaporation temperature and the quality of refrigerant before it flows into the test section. A heater is introduced at the exit of the test section in order to evaporate a refrigerant completely because the refrigerant should be in the gas phase before it flows into the compressor. Typical local bulk temperatures and static pressures are measured by using T-type thermocouples and semiconductor pressure transducers respectively. These are recorded by a multi-channel data logger.

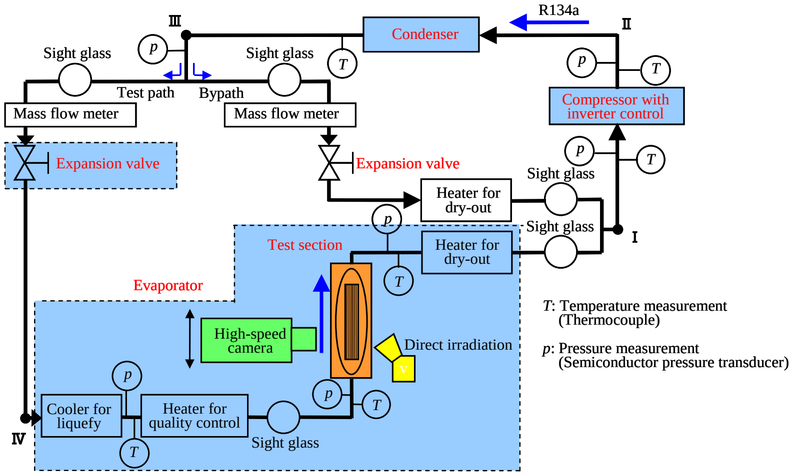

(a) Schematic diagram of experimental apparatus

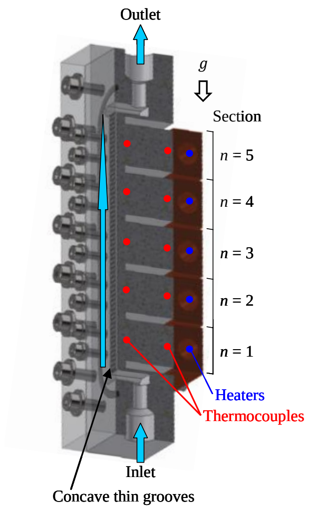

(b) Bird's eye view of test section

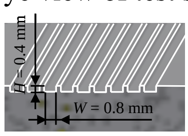

Figure 1 Schematic diagram and test section of experimental apparatus

(c) Concave fine grooves

Figures 1(b) and (c) show the detail of test section, which is installed in the test path. The test section consists of a heat transfer body (aluminum A5052) with flow path grooves, a cover plate (transparent polycarbonate) and cartridge heaters. The body is heated by attaching the copper blocks with the heaters. The dimensions of the rectangular groove are a width of 0.8 mm, a depth of 0.4 mm, and a flow path length of 100 mm in each, as shown in Fig. 2(c). In this study, the flow direction of the refrigerant is set to the vertical upward flow. The phase transition of the refrigerant is observed by a high-speed camera from a direction perpendicular to the heat transfer surface.

3. Experimental Results and Discussion

3.1. Estimation of heat transfer coefficient

The local heat transfer coefficient of the heat transfer surface was calculated using the temperature gradient of the thermocouples installed in the test section. Figure 2 shows a schematic cross-section of the test section. The test section is divided into five sections and the reference temperatures at the center of the each section are measured by ϕ 1.0 sheath-type T-thermocouples. The temperature gradient in each section is estimated by using a pair of reference temperatures. Numbers 1 to 5 were assigned to each section in order toward the exit from inlet.

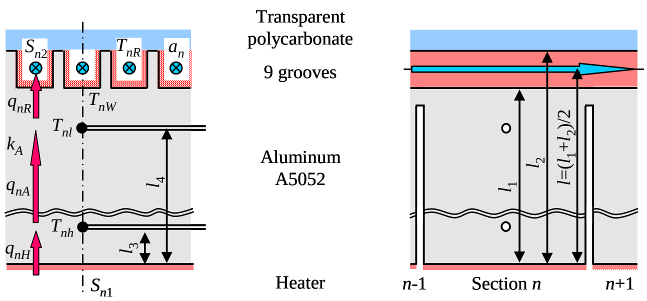

(a) Cross section view (b) Longitudinal cross section

Figure 2 Schematic cross-section of test section

The heat flux q_{nA} estimated from the temperature gradient of the thermocouple in region n was obtained using Fourier's law. And, the heat flux q_{nR} to the refrigerant was obtained by Newton's cooling law. As a result, local heat transfer coefficient a_n in each section n was estimated by Eq. (1).

$$a_n = \frac{k_A S_{n1}\left(T_{nh} - T_{nl}\right)}{S_{n2}\left(l_4 - l_3\right)\left(T_{nW} - T_{nR}\right)} \tag{1}$$

Here the surface temperature T_{nW} of the heat transfer surface is obtained by extrapolation from the temperature gradient between the two points of the thermocouples.

3.2. Experimental condition and results

3.2.1 Flow visualization

An experiment was conducted in a low quality region for the purpose of capturing the phase transition of bubbles in the initial stage of boiling in the fine concave groove. Table 1 shows the experimental conditions.

The amount of heating Q_{total} by the cartridge heater at a constant heat flux from the back of the aluminum body was 30.6 W (30 W class) and 60.3 W (60 W class). The specific enthalpy h_{out} at the outlet of the test section is calculated by Eq. (2) based on the refrigerant physical properties.

$$h_{out} = h_{in} + \sum_{n=1}^{5}\left(\frac{S_{n1} q_{nH}}{m}\right), \qquad \left(\because Q_{total} = \sum_{n=1}^{5}\left(S_{n1} q_{nH}\right)\right) \tag{2}$$

From the above calculation, the superficial velocities of the gas and liquid phases j_{Gout}, j_{Lout} at the exit of the test section can be estimated by Eq. (3), respectively.

$$j_{Gout} = \frac{m x_{out}}{\rho_G A}, \qquad j_{Lout} = \frac{m(1-x_{out})}{\rho_G A} \tag{3}$$

Here, A is the cross-section of the fine grooves, x_{out} is a quality of the outlet, and the density ρ_G and ρ_L for gas and liquid state are calculated using NIST, REFPROP, Ver. 9.1, respectively.

Table 1 Experimental conditions

Test section	Heater input: (Constant heat flux from heater)	Q_{total} [W]	30.6	60.3
	Mass flow rate:	m [g/s]	0.64	0.62
Test section inlet	Pressure:	p_{in} [MPa・abs]	0.41	0.41
	Temperature:	T_{in} [°C]	1.4	1.9
	Quality:	x_{in} [-]	0.0	0.0
	Velocity (Liquid):	u_{in} [m/s]	0.18	0.17
Test section outlet	Pressure:	p_{out} [MPa・abs]	0.40	0.40
	Temperature:	T_{out} [°C]	12.6	13.8
	Quality:	x_{out} [-]	0.34	0.71
	Liquid phase superficial velocity:	j_{Lout} [m/s]	0.14	0.09
	Gas phase superficial velocity:	j_{Gout} [m/s]	2.2	5.0
High-speed camera	Shutter speed:	[sec]	1/20,000	
	Frame rate:	[fps]	16,000	

Figure 3 shows the visualized images and *p-h* diagram when the heating amount was 30.6 W and 60.3 W. Table 2 shows the experimental conditions for the visualized images. In the experiment, the heating condition was set with a constant heat flux from the heaters. The table shows only the conditions for the evaporation process, which is the focus of this study. The table also shows the local heat transfer coefficient estimated by temperature gradient in the heat transfer body.

Figures 3(a-1) and (b-1) show the instant images obtained from the center channel of nine grooves on the heat transfer surface. The channel width is 0.8 mm and the longitudinal evaluation range of flow visualization is 9.0 mm. L_x is the distance from the entrance of the groove.

In the case of Q_{total} = 30.6 W, the bubble generation is observed in the section n = 1. The flow velocity at the center of the flow path is faster than the bubble velocity comes from the side wall of the groove. Therefore, the bubbles grow and flow along the side wall of the groove. As the bubbles grow, they get on the mainstream and become faster. Then the fast-velocity bubbles catch the bubbles flowing in front and merge. The bubbles grow while maintaining a spherical shape due to the surface tension. However, pulsation flow sometimes occurs in the first half of the section n = 1, and a backflow of bubbles is observed. In sections n = 2 to 3, it was observed that the bubbles block the flow path as the bubble diameter increases and the gas plug is formed and grows. After the bubbles contact both sides of the groove, the gas plug expands in volume along the flow direction. Then, the tip of the bubble in the flow direction becomes sharp. The velocity increases and the gas plug becomes elongated as it proceeds downstream. Furthermore, in sections n = 4 to 5, the shape of the gas plug is disturbed and irregular, and the gas-liquid interface changes intricately. It seems that there is a transition from the churn flow to the circular flow.

On the other hand in the case of Q_{total} = 60.3 W, it is observed that more bubbles are generated and they flow faster than that of Q_{total} = 30.6 W. In section n = 1, backflow of bubbles is also observed in the first half of the section even at 60.3 W. It is considered that the pressure in the middle part of the flow path rises locally due to the volume expansion of the slow gas plug. In section n = 2, bubbles are flowing along with the gas plug. No backflow was observed although the flow temporarily stopped due to pulsation. Since the flow velocity of the gas plug in this region is faster than the volume expansion rate of bubble, there is no backflow of bubbles or gas plugs in this section. In sections n = 3 to 5, the quality increased and the droplets or bubbles flow to the center of the groove. The droplets accompany the mainstream since it is faster than the gas plug. In addition, the flow gradually stabilizes from the churn flow to the circular flow. As it gets closer to the outlet of this section, the flow seems to be almost at dry-out condition.

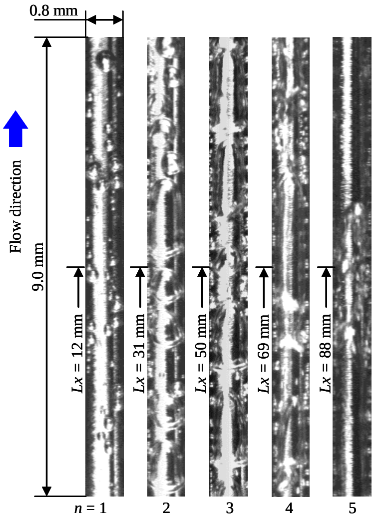

(a-1) Visualized image(30.6W)

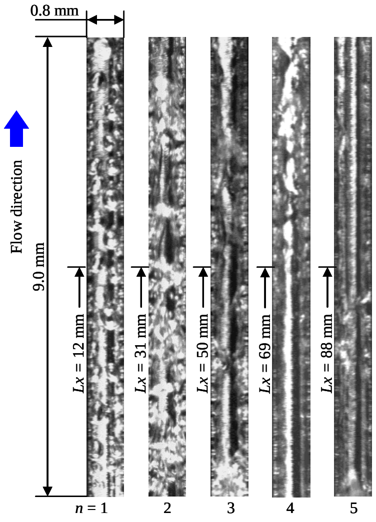

(b-1) Visualized image(60.3W)

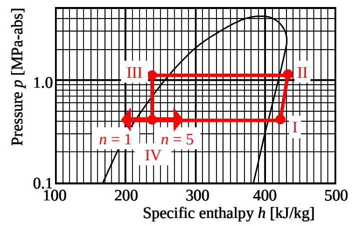

(a-2) p-h diagram(30.6W)

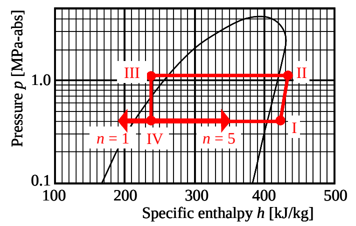

(b-2) p-h diagram(60.3W)

Figure 3 Visualized image and corresponding p-h diagram

Table 2 Experimental results

Q_{total} [W]	Parameter		Section n 1	2	3	4	5
30.6	Heating amount : [W]		6.2	6.1	6.1	6.2	6.0
	Wall temperature: T [°C]	T_{nh}	12.9	14.2	14.3	14.2	13.5
		T_{nl}	11.8	12.3	12.7	12.4	11.8
	Local heat flux estimated from temperature gradient: q_n [kW/m^2]		17.9	24.6	24.1	23.3	22.0
	Local heat transfer coefficient estimated from temperature gradient: a_n [kW/(m^2·K)]		11.4	19.2	13.8	16.8	18.0
60.3	Heating amount : [W]		12.0	12.1	12.0	12.2	12.0
	Wall temperature: T [°C]	T_{nh}	16.3	18.1	18.4	18.0	16.8
		T_{nl}	14.0	15.0	15.3	15.0	13.9
	Local heat flux estimated from temperature gradient: q_n [kW/m^2]		17.9	24.6	24.1	23.3	22.0
	Local heat transfer coefficient estimated from temperature gradient: a_n [kW/(m^2·K)]		11.7	15.2	13.9	14.2	15.0

3.2.2 Gas diameter and velocity

Table 3 shows the size of the bubbles and their velocities obtained from the visualization images. The diameter of the bubble existing in each section was measured from multiple images. Since bubbles are generated in each section, the minimum value of the bubble diameter is 0. The length of the gas plug was measured when it blocks the flow path. If the bubbles were further expanded, the length cannot be measured. For the average value, the bubble diameter was measured when the flow state was visually observed on average. It was quantitatively shown that the bubble diameter increased as it progressed downstream of the flow path. In addition, bubbles block the flow path at a relatively early stage of boiling.

The velocity of the bubbles was determined by taking images at a time interval of 0.02 sec and tracking the same bubble. The velocity of the bubbles tended to increase toward the downstream at any heating rate. In addition, the flow velocity at the center of the cross section of the flow path is high, so that the bubbles are pushed out by the refrigerant at a high flow velocity. The gas phase increases, and the velocity of the gas increases as the heating amount increases. However, the flow velocity is slow at n = 1. A temporary backflow is observed here due to the influence of the pulsate flow. Therefore, some negative values are shown.

It was observed from the image that the velocity of the tip of the gas plug was faster than that of the trailing edge. At the tip of the gas plug, the volume expands downstream to accelerate the mainstream velocity. Then, it merges with the small bubbles in front. On the other hand, the velocity of the small bubbles at the trailing edge of the gas plug was slower than that of the gas plug. Therefore, the small bubbles were united with the subsequent gas plug. In addition, gas plugs and bubbles with a large diameter tended to have unstable shapes and disturbance in velocity. It is considered that the gas coalescence occurs when active, and the gas plug causes pulsation.

From the above discussion, the velocity of the bubble is accelerated by the inertial force from the mainstream velocity. It is important to increase the bubble velocities and gas plugs to promote heat transfer. It is also important to consider not only the bubble diameter but also the growth rate, coalescence frequency and pulsation when evaluating the bubble velocity.

Table 3 Bubble size and gas velocity in the fine groove

Heating amount [W]	Section	Bubble diameter or bubble length [mm]			Gas velocity [m/s]			Note
Q_{total}	n	Min.	Max.	On average	Min.	Max.	On average	
30.6	1	0	0.8	0.4	-0.3	1.1	0.3	Temporarily backflow
	2	0	3.5	1.2	0	0.8	0.5	
	3	0	3.8	1.6	0	1.5	0.8	
	4	0			0	1.7	0.9	
	5	0			0	2.1	1.2	
60.3	1	0	0.8	0.4	-0.5	1.6	0.5	Temporarily backflow
	2	0	3.5	1.0	0	1.9	1.1	
	3	0			0	2.1	1.3	
	4	0			0	2.7	1.4	
	5	0			0	3.5	1.7	
Note		Bubble generation						

3.2.3 Local hear transfer coefficient

Figure 4 shows the local temperature T_n, the heat flux q_{nA} estimated from the temperature gradient, and the local heat transfer coefficient a_n for the heating amounts of 30.6 W and 60.3 W. The temperature shown in Fig. 4 (a) is measured using a temperature-calibrated thermocouple. When the heat input by the heater q_{nH} was set in order to have a constant heat flux, the temperatures at the inlet and outlet sections became low. Along with this, the heat transfer surface temperature T_{nW} also decreased. The temperature difference (T_{nh} - T_{nl}) applied to estimate the heat transfer coefficient is secured at about 2.5 to 4 ºC. The local heat flux on the heat transfer surface calculated from the temperature gradient is shown in Fig. 4 (b). At the inlet n = 1, as shown in Fig. 4 (a), the temperature difference becomes small due to heat dissipation to the inflow area. As a result, the heat flux q_{nA} becomes smaller. Figure 4 (c) shows the local heat transfer coefficient a_n of each section estimated by Eq. (1). When the calculation of heat transfer coefficient, temperature gradient strongly influences on the result. In this study, the thermocouples were calibrated before the experiment. However, the derived a_n include pretty big fluctuation due to the influence of flow instability. Since the experimental conditions of this study are the initial stage of boiling in the low quality region, the heat transfer coefficient increases as it goes on downstream. The flow mode changes from the bubble flow to the slag flow and then churn flow. However, no clear change in heat transfer coefficient is observed due to the constant heat flux condition. It is found that the bubbles maintain a spherical shape from the visualized image. Therefore, it is suggested from both perspective of visualized image and heat transfer coefficient that the liquid refrigerant is supplied to the bottom surface of the flow path by deepening the groove cross section. It is considered that this liquid film flow promotes heat transfer.

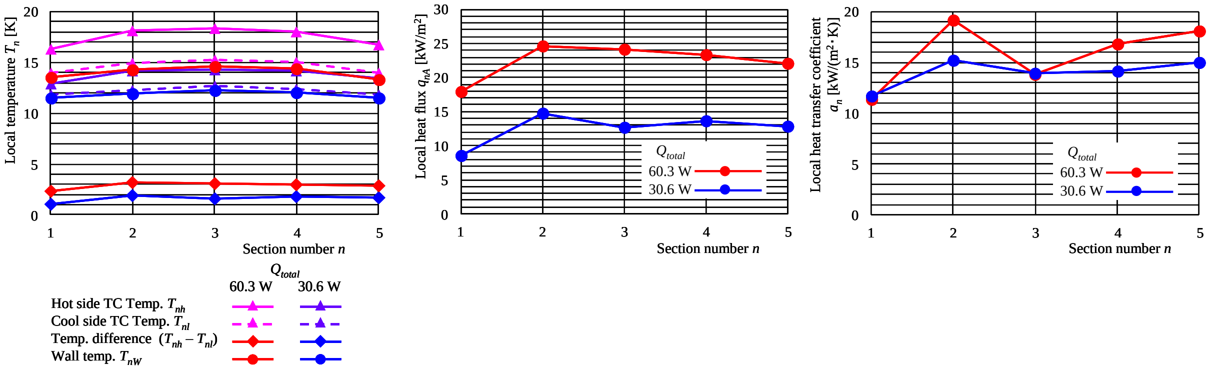

(a) Local temperatures measured by thermocouples (b) Local heat flux (c) Local heat transfer coefficient

Figure 4 Heat transfer coefficient and related parameters

4. Conclusion

The bubble behavior and heat transfer at the initial stage of boiling of the refrigerant R134a that pass through a fine rectangular grooves was evaluated. It was confirmed that the flow mode changed to bubble flow, slag flow, and churn flow. The bubble size and gas flow velocity were quantitatively determined by tracking the behavior of bubbles. The velocity of the bubbles was accelerated by the inertial force received from the mainstream, and the interaction between the bubble diameter and the fine groove size are shown. However, the heat transfer coefficient does not change significantly in this study because of the constant heat flux heating. From the visualized image and the calculated heat transfer coefficient, the bubbles grow while maintaining a spherical shape. Therefore, the liquid refrigerant is supplied to the bottom surface of the flow path by deepening the groove in the case of a rectangular groove flow path, which is expected to enhance heat transfer.

Acknowledgments

This work was supported by JKA-Japan Keirin and Autorace Fundation and its promotion funds from KEIRIN RACE. The test section was processed with the cooperation of the Experiment & Training Factory, Faculty of Engineering, Mie University.

References

[1] Wang, Y., Wang, Z., 2014. An overview of liquid–vapor phase change, flow and heat transfer in mini- and micro-channels. *Int. J. Therm. Sci*. 86, 227–245.

[2] Thome, J.R., 2006. State-of-the-art overview of boiling and two-phase flows in microchannels, Heat *Transf. Eng*. 27, 4–19.

[3] Kim, S.M., Mudawar, I., 2014. Review of databases and predictive methods for heat transfer in condensing and boiling mini/micro-channel flows. *Int. J. Heat Mass Transf.* 77, 627–652.

[4] Jige, D., Sagawa, K., Inoue, N., 2017. Effect of tube diameter on boiling heat transfer and flow characteristic of refrigerant R32 in horizontal small-diameter tubes. *Int. J. Refrig.* 76, 206–218.

[5] Del Col, D., Bortolin, S., Rossetto, L., 2013. Convective boiling inside a single circular microchannel, *Int. J. Heat Mass Transf*. 67, 1231–1245.

[6] Mori, H., 2016. Two-phase flow and boiling flow heat transfer in small-diameter tubes, *Heat Transf. Eng*. 37, 686–695.

[7] Jige, D., Inoue, N., 2019. Boiling heat transfer, pressure drop, and flow pattern in a horizontal square minichannel, *Int. J. of Heat and Fluid Flow*. 78, 108433.

Sponsors and Partners

The 11th TSME
International Conference on Mechanical Engineering
(TSME - ICoME 2020)

Sunee Grand Hotel & Convention Center, Ubon Ratchathani

TSME

ICOME 2020

Challenging Trends in Mechanical Engineering

Department of Mechanical Engineering, Faculty of Engineering, Ubon Ratchathani University

85 Sathonlamark Rd. Warin Chamrap, Ubon Ratchathani 34190, Thailand

Tel: (+66) 4535 3323